HOLOCENE CLIMATE CHANGES IN THE ASIA-PACIFIC REGION

EDITED BY: Liangcheng Tan, Hai Xu and Yehouda Enzel
PUBLISHED IN: Frontiers in Earth Science

frontiers Research Topics

Frontiers eBook Copyright Statement

The copyright in the text of individual articles in this eBook is the property of their respective authors or their respective institutions or funders. The copyright in graphics and images within each article may be subject to copyright of other parties. In both cases this is subject to a license granted to Frontiers.

The compilation of articles constituting this eBook is the property of Frontiers.

Each article within this eBook, and the eBook itself, are published under the most recent version of the Creative Commons CC-BY licence. The version current at the date of publication of this eBook is CC-BY 4.0. If the CC-BY licence is updated, the licence granted by Frontiers is automatically updated to the new version.

When exercising any right under the CC-BY licence, Frontiers must be attributed as the original publisher of the article or eBook, as applicable.

Authors have the responsibility of ensuring that any graphics or other materials which are the property of others may be included in the CC-BY licence, but this should be checked before relying on the CC-BY licence to reproduce those materials. Any copyright notices relating to those materials must be complied with.

Copyright and source acknowledgement notices may not be removed and must be displayed in any copy, derivative work or partial copy which includes the elements in question.

All copyright, and all rights therein, are protected by national and international copyright laws. The above represents a summary only. For further information please read Frontiers' Conditions for Website Use and Copyright Statement, and the applicable CC-BY licence.

ISSN 1664-8714
ISBN 978-2-88966-471-9
DOI 10.3389/978-2-88966-471-9

About Frontiers

Frontiers is more than just an open-access publisher of scholarly articles: it is a pioneering approach to the world of academia, radically improving the way scholarly research is managed. The grand vision of Frontiers is a world where all people have an equal opportunity to seek, share and generate knowledge. Frontiers provides immediate and permanent online open access to all its publications, but this alone is not enough to realize our grand goals.

Frontiers Journal Series

The Frontiers Journal Series is a multi-tier and interdisciplinary set of open-access, online journals, promising a paradigm shift from the current review, selection and dissemination processes in academic publishing. All Frontiers journals are driven by researchers for researchers; therefore, they constitute a service to the scholarly community. At the same time, the Frontiers Journal Series operates on a revolutionary invention, the tiered publishing system, initially addressing specific communities of scholars, and gradually climbing up to broader public understanding, thus serving the interests of the lay society, too.

Dedication to Quality

Each Frontiers article is a landmark of the highest quality, thanks to genuinely collaborative interactions between authors and review editors, who include some of the world's best academicians. Research must be certified by peers before entering a stream of knowledge that may eventually reach the public - and shape society; therefore, Frontiers only applies the most rigorous and unbiased reviews.
Frontiers revolutionizes research publishing by freely delivering the most outstanding research, evaluated with no bias from both the academic and social point of view. By applying the most advanced information technologies, Frontiers is catapulting scholarly publishing into a new generation.

What are Frontiers Research Topics?

Frontiers Research Topics are very popular trademarks of the Frontiers Journals Series: they are collections of at least ten articles, all centered on a particular subject. With their unique mix of varied contributions from Original Research to Review Articles, Frontiers Research Topics unify the most influential researchers, the latest key findings and historical advances in a hot research area! Find out more on how to host your own Frontiers Research Topic or contribute to one as an author by contacting the Frontiers Editorial Office: frontiersin.org/about/contact

HOLOCENE CLIMATE CHANGES IN THE ASIA-PACIFIC REGION

Topic Editors:
Liangcheng Tan, Chinese Academy of Sciences, China
Hai Xu, Tianjin University, China
Yehouda Enzel, Hebrew University of Jerusalem, Israel

Citation: Tan, L., Xu, H., Enzel, Y., eds. (2021). Holocene Climate Changes in the Asia-Pacific Region. Lausanne: Frontiers Media SA. doi: 10.3389/978-2-88966-471-9

Table of Contents

frontiers in Earth Science

EDITORIAL
published: 19 January 2021
doi: 10.3389/feart.2020.622792

Editorial: Holocene Climate Changes in the Asia-Pacific Region

Liangcheng Tan[1,2,3,4]* *and Hai Xu*[5]*

[1]State Key Laboratory of Loess and Quaternary Geology, Institute of Earth Environment, Chinese Academy of Sciences, Xi'an, China, [2]China-Pakistan Joint Research Center on Earth Sciences, CAS-HEC, Islamabad, Pakistan, [3]Center for Excellence in Quaternary Science and Global Change, Chinese Academy of Sciences, Xi'an, China, [4]Institute of Global Environmental Change, Xi'an Jiaotong University, Xi'an, China, [5]Institute of Surface-Earth System Science, Tianjin University, Tianjin, China

Keywords: chronology, lake sediment, peat, delta deposit, marginal sea, monsoon, westerly, climate impact

Editorial on the Research Topic

Holocene Climate Changes in the Asia-Pacific Region

As a fast-growing economic region, more than two-thirds of the global population lives in the Asia-Pacific region. Climate changes in this region not only affect the livelihood and well-being of inhabitants directly, but also influence the world's sustainable development. For example, a recent stalagmite study from southern Thailand suggests extreme wet conditions during the late 14th century. The extreme precipitation caused extensive floods and destruction of the water management systems in Angkor, Cambodia, resulting in the decline of the Khmer Empire (Tan et al., 2019). A 640 year megadrought in central Asia during the mid-Holocene even delayed the opening of the oasis route for trans-Eurasian cultural exchange (Tan et al., 2020a). Despite the recent progress (e.g., Chen et al., 2015; Zhu et al., 2017; Griffiths et al., 2020; Xu et al., 2019; Xu et al., 2020; Tan et al., 2020a; Tan et al., 2020b), both the patterns and the mechanisms of climate change over different sub-regions in the Asia-Pacific during the Holocene, when human civilization developed, are far from well-known. Therefore, reconstructing these changes are essential on the different timescales and shedding light on the driving mechanisms. It will enable a better understanding of the present climatic conditions and their impacts and future trends, especially in the context of continuous global warming (Xu et al., 2019; Tan et al., 2020b). Research Topics of this contribution include improved chronologic methods and new climatic reconstructions and driving forces of climate change on different timescales during the Holocene, covering a broad region from the western Pacific marginal seas to the Asian inland area (**Figure 1**). The environmental and social impacts of climate change during the historical and modern times are also discussed in this research topic. This special issue brings together a collection of papers that bridge vital knowledge gaps in the critical areas human-environment interactions in the Holocene.

IMPROVED CHRONOLOGY

Radiocarbon (^{14}C) dating method was widely applied in various materials of sediments, including plant fossils, bulk organic matter, and carbonates. However, bulk organic matter, and carbonates may be contaminated by the ^{14}C reservoir effect in water bodies. The ^{14}C reservoir effect may be variable through time (An et al., 2012), which brings significant challenges to establish reliable chronologies for lake and delta sediment records. In this collection, Zhou et al. systematically studies the ^{14}C reservoir ages of the sediments from Lake Bosten in Xinjiang, China. They found the ^{14}C reservoir ages during a dry interval (1,800 to 650 BP) was 1,170 years older than those during the wet periods (650–100 BP; 2,200–1,800 BP). This results suggested different ^{14}C exchange rates between the dissolved CO_2 in lake water and corresponding CO_2 in the atmosphere. There is a changing

OPEN ACCESS

Edited and reviewed by:
Steven L. Forman,
Baylor University, United States

***Correspondence:**
Liangcheng Tan
tanlch@ieecas.cn
Hai Xu
xuhai@tju.edu.cn

Specialty section:
This article was submitted to Quaternary Science, Geomorphology and Paleoenvironment, a section of the journal Frontiers in Earth Science

Received: *29 October 2020*
Accepted: *24 November 2020*
Published: *19 January 2021*

Citation:
Tan L and Xu H (2021) Editorial: Holocene Climate Changes in the Asia-Pacific Region. Front. Earth Sci. 8:622792. doi: 10.3389/feart.2020.622792

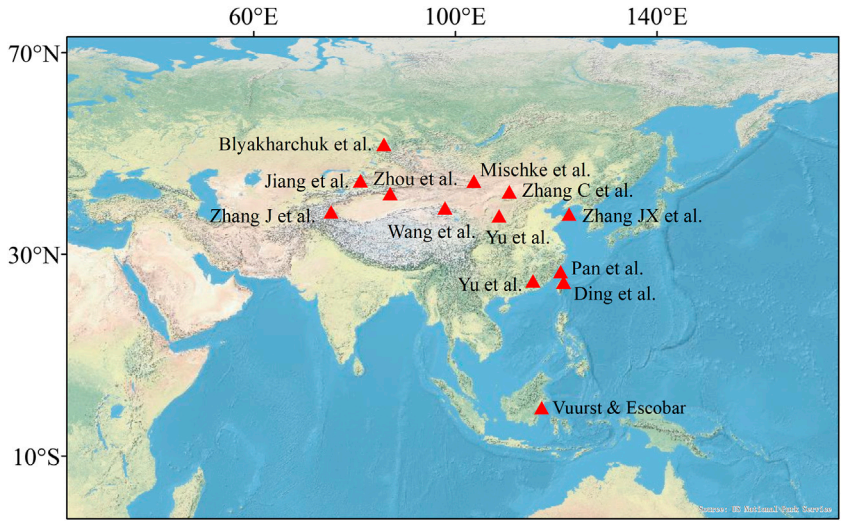

FIGURE 1 | Locations of the study sites included in this volume.

proportion of lake-derived organic matter and detrital organic matter from a catchment during dry and wet conditions, which may affect the resident time for ^{14}C in aquatic environments and can challenge construction of a credible chronology in arid/semiarid regions. Besides, Blyakharchuk et al. identify a possible old CO_2 source from decomposed organic matter from buried, old sediment that may be metabolized by contemporary aquatic algae and submerged plants, may give anomalous old ^{14}C ages. As a result, caution should be exercised on establishing chronologies of sediment cores with just a few ^{14}C dates, even if the ages are in stratigraphic order. A better way is to combine the ^{14}C dating method with ^{210}Pb, ^{137}Cs, OSL, and ^{230}Th dating methods to determine the possible variable ^{14}C reservoir ages, as shown by Blyakharchuk et al. and Xu et al. (2020).

New Insights of Holocene Climate Changes

Since An et al. (2000) proposed the asynchronous Holocene Optimum in the East Asian monsoon region two decades ago, the timing and patterns of the Holocene precipitation changes in Asia are debated widely (e.g. Zhou et al., 2007; Cai et al., 2010; Chen et al., 2019; Tan et al., 2020b; Xu et al., 2020). Ding et al. synthesized the current hydroclimate records from Taiwan, and suggested that the East Asian Summer Monsoon (EASM) rainfall maximum occurred during the early Holocene. They further suggested the EASM rainfall maximum occurred progressively later, from the early Holocene in southern China to the middle Holocene in northern China, contrast to An et al. (2000). The latitudinal shifts of the westerlies and western Pacific Subtropical High caused by interhemispheric or zonal Pacific temperaturt gradients were employed to explain the asynchronous EASM rainfall changes during the Holocene (Xu et al., 2020). Zhang et al. 's multiproxy studies from Tengger Nuur in the Inner Mongolian Plateau, China, support a middle Holocene precipitation maximum in northern China (Chen et al., 2015). However, the ostracod, gastropod, and charophyte records from Lake Ulaan in Mongolia, northwest of Tengger Nuur, indicated the highest inflows and highest productivity in and around the lake, and wettest climate conditions during the early Holocene (Mischke et al.). Cheng et al. also suggested a southward migration of the monsoon fringe during the Holocene, as illustrated in a transient climate-terrestrial ecosystem model simulation. The discrepancies may reflect chronologic uncertainties of the various records, or potentially varying climate sensitivity of the different proxies. Some proxies may reflect annual and seasonal precipitation changes or effective precipitation changes with storm intensity with non-analogous atmospheric circulations. For example, Tan et al. (2020b) suggested that the earlier wetting of the western Chinese Loess Plateau compared to the eastern sector may reflect increased rainfall associated with a stronger Indian summer monsoon during the early Holocene. In contrast, a well-dated record of $\delta^{13}C$ for black carbon from sediment core of Sayram Lake in Xinjiang, China reveals persistently wetter conditions during the Holocene (Jiang et al.), which is consistent with other records from eastern central Asia (Chen et al., 2019; Xu et al., 2019). This increase in effective moisture in eastern central Asia is linked to North Atlantic sea surface temperatures and changes in Westerly circulation. Specifically, the Community Earth System Model simulations show gradually southward and strengthened summer westerly jet over central Asia from the early Holocene to late Holocene (Zhou et al., 2007). In turn, Wang et al. further confirmed the out-of-phase relationship of humidity conditions between westerlies-dominated central Asia and monsoon areas over the past century.

Climatic changes in the western Pacific marginal seas are also studied in this collection. Pan et al. reconstructed the Holocene sea surface temperature (SST) and subsurface water temperature (SWT) of the East China Sea using UK′37 and TEX86, respectively. They found the SWT decreased between 6 and

4 ka with SWT increased in the late Holocene, almost in anti-phase with the SST. These results provide new insight into the interaction mechanism among the winter monsoon, precipitation and the Kuroshio Current.

Environmental and Social Impacts of Climate Change

Li et al. reviewed the global mercury deposition, climate change, and human activities. They found more mercury accumulation during the glacial period and less during the interglacial period. Zhang J. et al. suggested changes in temperature and wind speed may dominate the dust storm's frequency and intensity in northwest China. Global warming may lead to decreased temperature gradients and wind speed. Thus, reducing dust storm frequency and intensity in central Asia in the past century. As a result, less and weaker dust storms are expected under a continuously warming scenario. The social impacts of monsoon precipitation changes are discussed in this collection. Zhang J.X. et al. found close relationships between changes in the Chinese economy and monsoon precipitation for northern China, as reconstructed from northern Yellow Sea sediments. Also, there appears to be an association between the frequency of wars over the past 2000 years and monsoon variability, consistent with Tan et al. (2011) observations. In traditional agriculture societies, low precipitation may lead to crop failure, resulting in famine, which may cause uprisings and ultimately wars (Hus, 1998). Currently, there are many countries in Asia that are and will be impacted by climate change in the 21st century. Case-in-point is the effect of climate change and human overuse of resources upon Jakarta, Indonesia, where the government has recently planned to relocate the capital to the island of Borneo. Vuurst and Escobar discussed the possible adverse effects of the relocation. They called for multidisciplinary research in Borneo to determine its ecosystems' status for a comprehensive assessment, before and after urban expansion to better understand Anthropogenic impacts.

AUTHOR CONTRIBUTIONS

All authors listed have made a substantial, direct, and intellectual contribution to the work and approved it for publication.

FUNDING

LT and HX acknowledge the supports from National Key Research and Development Program of China (2017YFA0603401) and the Strategic Priority Research Program of Chinese Academy of Sciences (XDB40000000).

REFERENCES

An, Z., Colman, S. M., Zhou, W., Li, X., Brown, E. T., Timothy Jull, A. J., et al. (2012). Interplay between the Westerlies and Asian monsoon recorded in Lake Qinghai sediments since 32 ka. *Sci. Rep.* 2, 619. doi:10.1038/srep00619

An, Z., Porter, S. C., Kutzbach, J. E., Wu, X., Wang, S., Liu, X., et al. (2000). Asynchronous Holocene optimum of the East Asian monsoon. *Quat. Sci. Rev.* 19, 743–762. doi:10.1016/S0277-3791(99)00031-1

Cai, Y., Tan, L., Cheng, H., An, Z., Edwards, R. L., Kelly, M. J., et al. (2010). The variation of summer monsoon precipitation in central China since the last deglaciation. *Earth Planet. Sci. Lett.* 291, 21–31. doi:10.1016/j.epsl.2009.12.039

Chen, F., Chen, J., Huang, W., Chen, S., Huang, X., Jin, L., et al. (2019). Westerlies Asia and monsoonal Asia: spatiotemporal differences in climate change and possible mechanisms on decadal to sub-orbital timescales. *Earth Sci. Rev.* 192, 337–354. doi:10.1016/j.earscirev.2019.03.005

Chen, F., Xu, Q., Chen, J., Birks, H. J. B., Liu, J., Zhang, S., et al. (2015). East Asian summer monsoon precipitation variability since the last deglaciation. *Sci. Rep.* 5, 11186. doi:10.1038/srep11186

Griffiths, M. L., Johnson, K. R., Pausata, F. S. R., White, J. C., Henderson, G. M., Wood, C. T., et al. (2020). End of Green Sahara amplified mid- to late Holocene megadroughts in mainland Southeast Asia. *Nat. Commun.* 11, 4204. doi:10.1038/s41467-020-17927-6

Hus, K. J. (1998). Sun, climate, hunger, and mass migration. *Sci. China Earth Sci.* 41, 449–472. doi:10.1007/bf02877737

Tan, L., Cai, Y., An, Z., Edwards, R. L., Cheng, H., Shen, C. C., et al. (2011). Centennial- to decadal-scale monsoon precipitation variability in the semihumid region, northern China during the last 1860 years: records from stalagmites in Huangye Cave. *Holocene* 21, 287–296. doi:10.1177/0959683610378880

Tan, L., Dong, G., An, Z., Edwards, R. L., Li, H., Li, D., et al. (2020a). Megadrought and cultural exchange along the proto-Silk Road. *Sci. Bull.* [Epub ahead of print]. doi:10.1016/j.scib.2020.10.011

Tan, L., Li, Y., Wang, X., Cai, Y., Lin, F., Cheng, H., et al. (2020b). Holocene monsoon change and abrupt events on the western Chinese Loess Plateau as revealed by accurately-dated stalagmites. *Geophys. Res. Lett.* 47 (21), e2020GL090273. doi:10.1029/2020GL090273

Tan, L., Shen, C. C., Löwemark, L., Chawchai, L., Edwards, R. L., Cai, Y., et al. (2019). Rainfall variations in central Indo-Pacific over the past 2700 year. *Proc. Nat. Acad. Sci. U.S.A.* 116 (35), 17201–17206. doi:10.1073/pnas.1903167116

Xu, H., Goldsmith, Y., Lan, J., Tan, L., Wang, X., Zhou, X., et al. (2020). Juxtaposition of western Pacific subtropical high on Asian Summer monsoon shapes subtropical East Asian precipitation. *Geophys. Res. Lett.* 47, 255–258. doi:10.1029/2019GL084705

Xu, H., Zhou, K., Lan, J., Zhang, G., and Zhou, X. (2019). Arid Central Asia saw mid-Holocene drought. *Geology* 47, 255–258. doi:10.1130/G45686.1

Zhou, W., Song, S., Burr, G., Jull, A. J. T., Lu, X., Yu, H., et al. (2007). Is there a time-transgressive Holocene optimum in the East Asian monsoon area? *Radiocarbon* 49 (2), 865–875. doi:10.1017/S0033822200042739

Zhu, Z., Feinberg, J. M., Xie, S., Bourne, M. D., Huang, C., Hu, C., et al. (2017). Holocene ENSO-related cyclic storms recorded by magnetic minerals in speleothems of central China. *Proc. Nat. Acad. Sci. U.S.A.* 114, 852–857. doi:10.1073/pnas.1610930114

Conflict of Interest: The authors declare that the research was conducted in the absence of any commercial or financial relationships that could be construed as a potential conflict of interest.

Copyright © 2021 Tan and Xu. This is an open-access article distributed under the terms of the Creative Commons Attribution License (CC BY). The use, distribution or reproduction in other forums is permitted, provided the original author(s) and the copyright owner(s) are credited and that the original publication in this journal is cited, in accordance with accepted academic practice. No use, distribution or reproduction is permitted which does not comply with these terms.

frontiers in Earth Science

ORIGINAL RESEARCH
published: 22 January 2020
doi: 10.3389/feart.2019.00328

Variable Late Holocene ^{14}C Reservoir Ages in Lake Bosten, Northwestern China

Kang'en Zhou[1,2], Hai Xu[3], Jianghu Lan[1], Dongna Yan[1,2], Enguo Sheng[4], Keke Yu[5], Yunping Song[3], Jin Zhang[3], Pingqing Fu[3] and Sheng Xu[3]*

[1] State Key Laboratory of Loess and Quaternary Geology, Institute of Earth Environment, Chinese Academy of Sciences, Xi'an, China, [2] University of Chinese Academy of Sciences, Beijing, China, [3] Institute of Surface-Earth System Science, Tianjin University, Tianjin, China, [4] College of Resources and Environment, Zunyi Normal University, Zunyi, China, [5] Key Laboratory of Disaster Monitoring and Mechanism Simulating of Shaanxi Province, Baoji University of Arts and Sciences, Baoji, China

Radiocarbon (^{14}C) dating has been widely used in paleoclimate reconstruction. However, the reliability of the ^{14}C age in lake sediments is sensitive to the ^{14}C reservoir effect, especially for a lake in arid regions. In this study, we evaluated the ^{14}C reservoir ages under different hydroclimatic conditions over the past ~2300 years in Lake Bosten, northwestern China, by comparing with different dating results and with multi-proxy indices of a vertical-down sediment core collected in this lake. The ^{14}C reservoir ages during ~1800 to 650 BP (a dry interval) are estimated to be approximately 1170 years older than those during ~650–100 BP and those during 2200–1800 BP (wet intervals). We proposed that variation in ^{14}C exchange rate between the dissolved CO_2 in lake water and CO_2 in the atmosphere, as well as the changing proportion of organic matter in the lake and the catchment, could have contributed to the variable ^{14}C reservoir ages in Lake Bosten. The result of this study suggests that the ^{14}C reservoir effect may be larger in dry periods than in wet periods in the arid/semi-arid area, which should be considered when establishing age models of lake sediment cores from these regions.

Keywords: ^{14}C reservoir age, hydroclimate change, late Holocene, Lake Bosten, arid central Asia

OPEN ACCESS

Edited by:
Michaël Hermoso, Université du Littoral Côte d'Opale, France

Reviewed by:
Philip Alan Meyers, University of Michigan, United States
Li Wu, Anhui Normal University, China

****Correspondence:***
Hai Xu
xuhai@tju.edu.cn

Specialty section:
This article was submitted to Quaternary Science, Geomorphology, and Paleoenvironment, a section of the journal Frontiers in Earth Science

Received: *24 October 2019*
Accepted: *27 November 2019*
Published: *22 January 2020*

Citation:
Zhou K, Xu H, Lan J, Yan D, Sheng E, Yu K, Song Y, Zhang J, Fu P and Xu S (2020) Variable Late Holocene ^{14}C Reservoir Ages in Lake Bosten, Northwestern China. Front. Earth Sci. 7:328. doi: 10.3389/feart.2019.00328

INTRODUCTION

Radiocarbon (^{14}C) dating has been widely used to establish geochronology less than ~50,000 years (Hughen et al., 2004; Reimer et al., 2009), using a variety of dating materials, including fossils of terrestrial and aquatic plants, bulk organic matter, etc. (Snyder et al., 1994; Bennike, 2000). The basis of ^{14}C dating is that the ^{14}C concentration of the living dating material, which exchanges ^{14}C with atmosphere CO_2 directly, is equal to the contemporaneous atmospheric ^{14}C concentration (e.g., Deevey et al., 1954). For example, a terrestrial plant absorbs atmospheric CO_2 during photosynthesis, and its ^{14}C concentration is generally regarded to be identical to the atmospheric ^{14}C concentration. Therefore, land plant debris has been widely used as an ideal ^{14}C dating material in paleolimnology.

However, in many cases, due to the paucity of sufficient terrestrial plant debris in lake sediments, bulk organic matter and aquatic shells are frequently used in radiocarbon dating, and the ^{14}C ages of these materials are generally more or less contaminated by the ^{14}C reservoir effect. This is due to the disequilibrium of ^{14}C concentration between aquatic CO_2 and atmospheric CO_2, and due

to the partial utilization of the dissolved inorganic carbon (DIC) in lake waters to synthesize both organic and inorganic materials. In addition, the input of "old" materials from the catchment to the lake will also lead to "older" ^{14}C ages of bulk organic matter than their real ages.

Previous studies have reported markedly different ^{14}C reservoir ages among different lakes. For example, the ^{14}C reservoir ages in Lake Wulungu (Liu et al., 2008a), Lake Qinghai (Shen et al., 2005), Chaka Salt Lake (Liu et al., 2008b), Lake Zigê Tangco (Herzschuh et al., 2006), Lake Kusai (Liu et al., 2009), and Lake Harnur (Lan et al., 2018) in northwestern China are estimated to be 760, 1073, 1700, 2010, 3400, and 3560 years, respectively, suggesting that the ^{14}C reservoir effects in different lakes can vary from hundreds to thousands of years (**Table 1**). The reservoir ages in the same lake estimated by different studies are also sometimes different. For example, Chen et al. (2006) and Huang et al. (2009) estimated a 1140-year ^{14}C reservoir age in Lake Bosten. Zhang et al. (2004) proposed an old carbon age of 650 years in the same lake, whereas Wünnemann et al. (2006) contended that the reservoir effect in Lake Bosten is minor and neglectable.

Mischke et al. (2013) showed that the ^{14}C reservoir ages change spatially even in different sites of a same lake on the Tibetan Plateau. These spatially variable reservoir ages may be related to different degrees of ^{14}C exchange between atmospheric CO_2 and aquatic CO_2, and may be partly attributed to the different "old" carbon released from erosion of carbon-contained bedrocks. ChongYi et al. (2018) also found that the ^{14}C ages of total organic carbon in surface sediments in Lake Qinghai vary spatially and attributed these ages to different degrees of ^{14}C exchange between aquatic and atmospheric CO_2. Hou et al. (2012) studied the ^{14}C reservoir effect of different lakes in Tibetan Plateau, and they suggested that the ^{14}C reservoir ages are related to geological settings of the catchment, residence time of lake water, peat/wetland development within the lake catchment, etc.

In addition, ^{14}C reservoir ages of different periods in a same lake may be variable as well. For example, Zhou et al. (2014) got different ^{14}C reservoir ages (135, 1143, and 2523 years, respectively) at different depths of a sediment core in Lake Qinghai. The old carbon ages in Lake Xingyun were estimated to vary between 960 and 2200 years over the past 8000 years (Zhou et al., 2015), and these variable old carbon reservoir ages were likely related to the variable input of "old materials" from the catchment under different hydrological conditions. Since changes of ^{14}C reservoir ages in the same lake may largely affect the accuracy of the ^{14}C age model of vertical-down sediment cores, it is necessary to assess the ^{14}C reservoir ages in the same lake in different periods.

Lakes in the arid/semi-arid regions of China, most of which are closed and/or semi-closed lakes, are often high in salinity and alkalinity, and the ^{14}C reservoir ages of these lakes are variable. Lake Bosten is a widely noted site to study paleoclimatic changes, in Xinjiang, northwestern China, arid central Asia (Mischke and Wünnemann, 2006; Wünnemann et al., 2006). However, previous studies have not fully considered the possibly variable ^{14}C reservoir ages, and therefore parts of the previously published age models may need to be improved/corrected. In this study, we assessed the old carbon effects by comparison between the ^{14}C ages of bulk organic matter and the ^{137}Cs and ^{210}Pb ages of sediment in Lake Bosten and by comparison between multi-proxy indices extracted from this lake and those from other works.

BACKGROUND AND METHODS

Lake Bosten is a fault lake located at the southern foot of central Tianshan Mountains (41°56′–42°14′N, 86°40′–87°26′E; modern lake level: 1048 m asl). The catchment area is ∼55,600 km^2, and the modern lake area is ∼1000 km^2, with a maximum water depth of ∼17 m (Xiao et al., 2010). Lake Bosten is supplied by 13 rivers, among which the Kaidu River is the largest one. River water of the Kaidu River mainly comes from alpine glacier and permanent snowmelt water, as well as seasonal snowmelt water and summer precipitation (Wünnemann et al., 2006).

Annual mean temperature around Lake Bosten is ∼8.3°C, and the average temperature in January and July are −9.2°C and 23.6°C, respectively (Huang et al., 2009). Annual precipitation is ∼70 mm, mostly falling in the warm season (**Figure 1**). Annual evaporation is ∼2000 mm (Huang et al., 2009). Precipitation in the lower reaches of the lake basin is relatively high; for example, it reaches ∼400 mm/a in the eastern part of Tianshan Mountain (Hu, 2004). Water vapor in the study area comes from the Atlantic, Mediterranean, and Caspian Sea water supply (Aizen et al., 2006; Chen et al., 2008; Xu et al., 2019b; Yan et al., 2019). Salinity of modern lake water is unevenly distributed, with a spatially increasing trend from west to east (Jiu et al., 1990). The lowest salinity of the lake is in the Kaidu River estuary (0.20–0.28%; Mischke and Wünnemann, 2006), and the maximum value is in the eastern part of the lake (>2.5%; Jiu et al., 1990). The pH value of lake water is 8.3–9.0 (Mischke and Wünnemann, 2006).

A 153-cm-long sediment core (BL13-1-4; 41°59′10.29″N, 87°09′43.70″E; water depth: 12 m) was collected from the central lake (**Figure 1**), in August 2013, using a gravity corer (UWITEC). The uppermost 24 cm is typical gray lacustrine sediment; 25 – 40 cm is gray sandy sediment; 41–137 cm is gray lacustrine sediment; 138–144 cm is sandy gray-white sediment; and 145–153 cm is gray lacustrine sediment. The core was sectioned at every 1-cm interval *in situ* and was stored under low temperature conditions (−20°C) until freeze-dried.

Radioactivities of ^{210}Pb and ^{137}Cs were determined using a gamma detector [Ortec Germanium (HPGe) well detector; GWL-15-250; **Figure 2**]. No macroscopic plant debris for radiocarbon dating was observed in the core, and 12 samples were dated using bulk organic carbon at Institute of Surface-Earth System Science (ISESS), Tianjin University, and Beta Analytic (**Figure 3** and **Table 2**). Sedimentary carbonate contents (carb%) were determined by titration with $HClO_4$ (0.1 mol/L) and NaOH (0.1 mol/L), with uncertainty less than 0.5%. Sedimentary grain size was determined on a Malvern Mastersizer 2000 laser grain-size analyzer, with uncertainty less than 3%. Total organic carbon content (TOC), total nitrogen content (TN), and the organic carbon and nitrogen isotopes were determined (δ^{13}C and

TABLE 1 | Comparison of ^{14}C reservoir ages from different lakes of western China.

Site name	Location	^{14}C reservoir age (years)	References
Lake Wulungu	46.98°N, 87.58°E	760	Liu et al., 2008a
Chaka Salt Lake	36.67°N, 99.10°E	1700	Liu et al., 2008b
Lake Zigê Tangco	32.01°N, 90.91°E	2010	Herzschuh et al., 2006
Lake Kusai	35.67°N, 93.33°E	3400	Liu et al., 2009
Lake Harnur	43.11°N, 83.97°E	3560	Lan et al., 2018
Lake Qinghai	36.87°N,100.17°E	1039	Shen et al., 2005
		658; 737	Henderson et al., 2010
		135; 1143; 2523	Zhou et al., 2014
Lake Bosten	41.99°N, 86.98°E	1140	Chen et al., 2006; Huang et al., 2009
		650	Zhang et al., 2004
		Minor and neglectable	Wünnemann et al., 2006

δ^{15}N) on an elementary analyzer–mass spectrometer (Flash2000-MAT253), with uncertainty less than 0.1% (**Figure 4**).

RESULTS

^{137}Cs and ^{210}Pb Dating

^{137}Cs is an artificial nuclide with a half-life of 30.17 years. After 1945, especially in the 1950s, nuclear tests were widely carried out in the world, which led to the rapid increase of atmospheric ^{137}Cs concentration. A rapid increase in ^{137}Cs activity from natural background (zero) was detected in a large number of undisturbed or weakly disturbed lake sediment cores, and this point was assigned as a time marker of 1952 AD, which is particularly evident in lakes in northwest China (e.g., Yu et al., 2017; Lan et al., 2018; Yan et al., 2019). The atmospheric ^{137}Cs fallout peak in the northern hemisphere occurred at 1963 AD (Robbins and Edgington, 1975), and this peak is widely used as a time marker of 1964 AD in lake sediments. Although the 1986 Chernobyl nuclear leak out may generate a ^{137}Cs peak in lake sediment, this peak can be hardly detected in northwestern China (Xu et al., 2010; Yu et al., 2017; Yan et al., 2019).

The ^{137}Cs curve of the core BL13-1-4 shows no clear peak, suggesting considerable disturbance of the sediments in modern times. Although this disturbance may lead to broadening of the peak, it does not affect the central position of the peak (Xu et al., 2010). The central position of the ^{137}Cs peak of core BL13-1-4 occurred at ∼15 cm, and it can be recognized as the 1964 AD time marker. Sedimentation rate based on this 1964-year time marker is ∼0.29 cm/year. ^{137}Cs activity increases rapidly from zero (the background) at 22 cm, indicating the beginning of atmospheric ^{137}Cs fallout, corresponding to the 1952 AD time marker (Yu et al., 2017; Yan et al., 2019). Sedimentation rate based on this time marker (1952-year) is ∼0.83 cm/year. Such big difference in modern sedimentation rates suggests strong anthropogenic impacts during the recent/modern epoch, such as changes in land use in the catchment and/or roads/factories construction around the lake.

^{210}Pb is a daughter of uranium series, with a half-life of 22.23 years. It has been widely used to determine the age of lake sediments of the past 150 years (e.g., Robbins and Edgington, 1975). The commonly used ^{210}Pb dating methods include constant initial concentration mode (CIC) and constant rate of supply mode (CRS; Robbins and Edgington, 1975). The ^{210}Pb ages of core BL13-1-4 derived from CRS model are similar to the ^{137}Cs ages for the uppermost 10 cm, but deviate more and more as depth increases (**Figure 2**). The ^{210}Pb ages derived from the CIC model are quite different with those derived from CRS model and those derived from the ^{137}Cs time marker (**Figure 2**), and such big differences are most likely due to instable sedimentation rates. Because of such variable sedimentation rates, the ^{210}Pb dating method can hardly generate reliable ages for the upper section of core BL13-1-4. Therefore, we do not use the ^{210}Pb ages, but only use the ^{137}Cs ages to assess the old carbon reservoir effect in this study (see below).

^{14}C Dating

The ^{14}C ages show linear trends in three intervals (20–50 cm, 60–120 cm, 120–153 cm; **Figure 3**). ^{137}Cs age at 20 cm is −8 a BP, while the corresponding ^{14}C age is 1025 a BP. We therefore got an old carbon reservoir age of 1033 years for the upper 20–50 cm. Since the ^{14}C ages of 120–153 cm are linearly correlated to those of 20–50 cm (r^2 = 0.99; **Figure 3**), we assume similar old carbon reservoir ages for both intervals. The ^{14}C ages of 60–120 cm are bigger than those of the upper and lower intervals. After a correction of 2200 years, the corrected ^{14}C ages of 60–120 cm fall on the regression line of ^{14}C ages of the upper and bottom sections (**Figure 3**). The final age model of core BL13-1-4 is a combination of the ^{137}Cs ages of the upper section (0–22 cm) and the corrected ^{14}C ages of the lower section (23–153 cm). We acknowledge that the chronology of core BL13-1-4 may not be accurate enough regarding high-resolution records; however, it does not influence the topic involved in this study (see below).

Proxy Indices and the Climatic Significance

The carbonate content of core BL13-1-4 varies between 31.36% and 54.85%, with an average of 47.61% (**Figure 4**). Autogenic carbonate is generally precipitated faster and more in waters with higher ion concentration, and thus its content in lake sediment can be used to reflect the budget of water input and evaporation of a lake (Chen et al., 2006). In general, lower carb% in lake

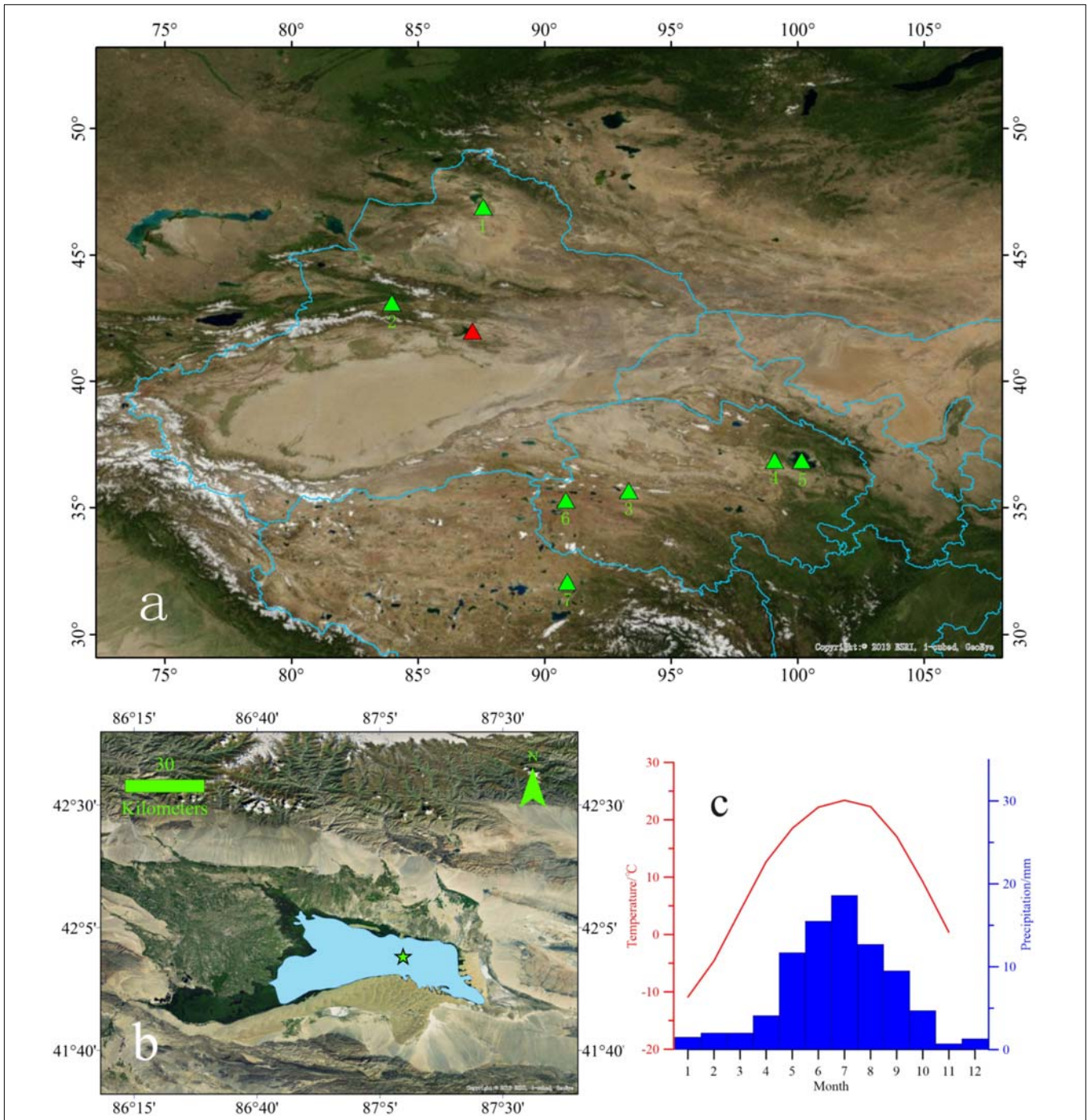

FIGURE 1 | Locations of Lake Bosten (red triangle in panel **a**) and some lakes mentioned in the text (green triangles). 1, Lake Wulungu (Liu et al., 2008a); 2, Lake Harnur (Lan et al., 2018); 3, Lake Kusai (Liu et al., 2009); 4, Lake Chaka (Liu et al., 2008b); 5, Lake Qinghai (Shen et al., 2005); 6, Lake Donggi Cona (Mischke et al., 2013); 7, Lake Zigê Tangco (Herzschuh et al., 2006). **(b)** Shows the modern lake and the sampling site of this study (green star). **(c)** Shows the seasonal temperature and precipitation at Yanqi County (~80 km to Lake Bosten; data from http://data.cma.cn/data/weatherBk.html; 1981–2010).

sediment reflects wetter hydroclimatic condition, while higher carb% reflects dryer condition (Chen et al., 2006).

The grain size of core BL13-1-4 varies between 9.21 and 30.87 μm, with an average of 14.38 μm. Sedimentary grain size has different climatic significance under different conditions and on different time scales. On long-term time scales, the grain size can reflect lake level variations (Liu et al., 2008a), while on short time scales, sediment grain size can record changes in surface runoff intensity, and then changes in precipitation (Xu et al., 2015). As Lake Bosten is an open lake, the decrease in

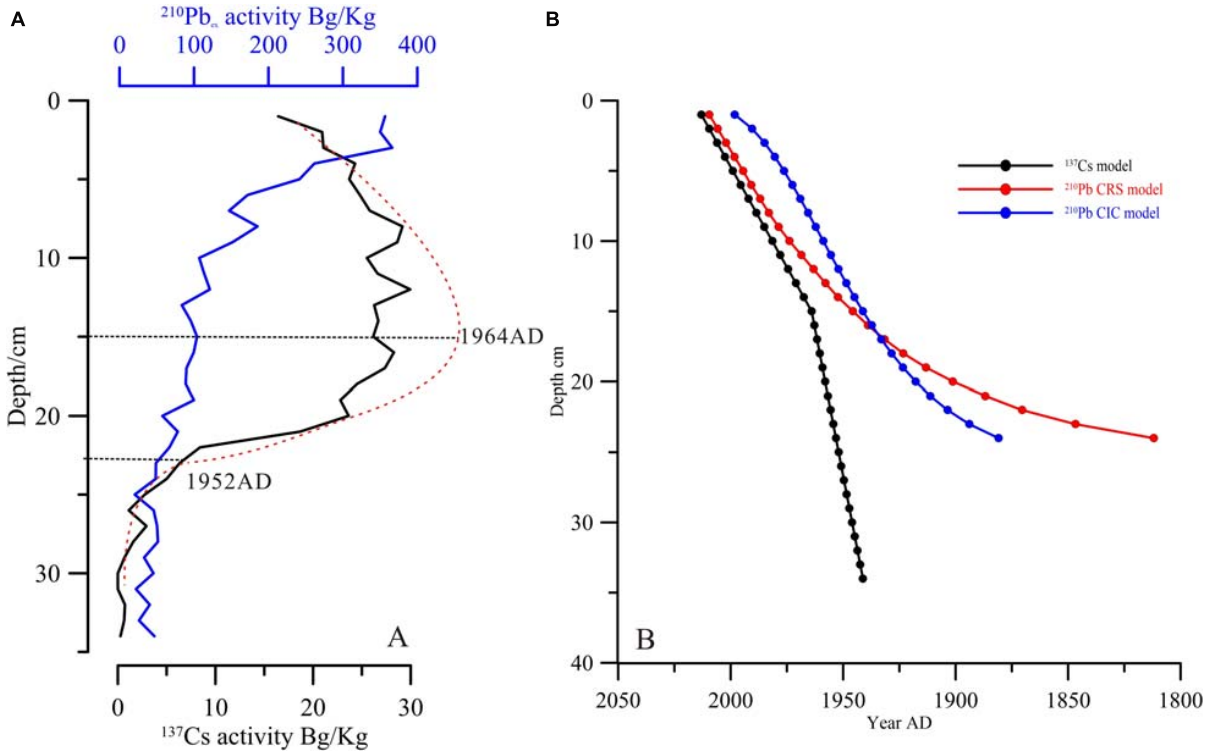

FIGURE 2 | (A) ^{137}Cs and ^{210}Pb activity of the surface sediments in core BL13-1-4. **(B)** ^{137}Cs and ^{210}Pb age models (see text for details).

sedimentary grain size in the late Holocene most likely indicates decrease in surface runoff intensity and precipitation; on the contrary, the increase in grain size indicates increase in regional runoff intensity and precipitation.

The δ^{15}N of core BL13-1-4 ranges from 2.49% to 7.91%, with an average of 5.88%. δ^{15}N of organic matter in lake sediments is closely related to primary productivity in lakes (Talbot and Johannessen, 1992; Xu et al., 2014, 2016b). During photosynthesis, the fractionation of nitrogen isotope is mainly controlled by nitrogen isotope value of dissolved inorganic nitrogen (DIN) in lake water. Phytoplankton in water tends to absorb ^{14}N in photosynthesis, which leads to gradual enrichment of δ^{15}N in lake water DIN pool (Talbot and Johannessen, 1992; Xu et al., 2014, 2016b). Increasing primary productivity in lake would therefore result in higher δ^{15}N values in organic matter, and vice versa.

Total organic carbon content of core BL13-1-4 varies between 1.39 and 7.40%, with an average of 3.46. Sedimentary TOC is a sum of endogenous and exogenous organic carbon, and can reflect the biomass both in lake and in catchment (Meyers, 2003). The primary productivity in the lake is closely related to temperature variations and nutrients supply, while the amount of organic matter transported from the catchment to the lake is also closely related to the biomass and surface runoff intensity in the catchment (Cohen, 2003).

The atomic C/N ratio in core BL13-1-4 varies between 8.36 and 13.47, with an average value of 9.79. Because aquatic phytoplankton and algae contain higher protein content, their C/N ratio is relatively low and generally falls within the range of 4–10. In contrast, terrestrial plants contain more lignin and cellulose, so their C/N values are higher (generally higher than 20). As a result, C/N ratio can reflect the relative contribution of different sources of organic matter in lake sediments; decrease in

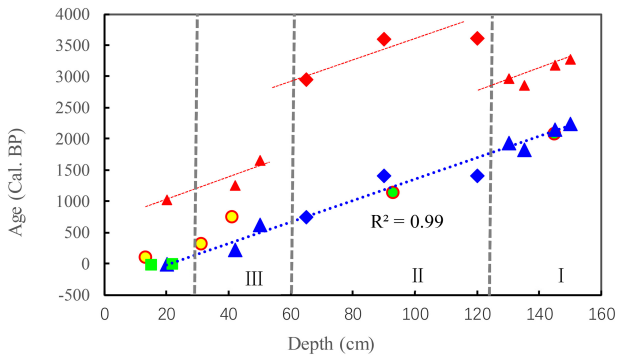

FIGURE 3 | Radiocarbon ages of sediment samples in core BL13-1-4 from Lake Bosten (the red points denote the original ^{14}C ages, blue points denote the ^{14}C ages after old carbon correction). Blue triangles denote ^{14}C ages of wet intervals (interval I and III; see text for details) after a correction of 1033 years. Blue diamonds denote ^{14}C ages of dry interval (interval II) after a correction of 2200 years. The green squares denote the ^{137}Cs time markers (1964-year and 1952-year). Green and yellow filled circles denote ^{14}C ages of plant debris and those of bulk organic matter and humic materials, respectively (data from others' previous work; **Table 3**).

TABLE 2 | ^{14}C ages of sediment samples of core BL13-1-4 in Lake Bosten.

Sample no.	Lab. no.	Depth (cm)	^{137}Cs age	^{14}C age	Cal. ^{14}C age (BP; median prob.)*	Old carbon reservoir	Corrected ages (BP)
BL13-1-4-15	LPR-1402-09	15	1964	/	/	/	−14
BL13-1-4-22	LPR-1402-16	22	1952	/	/	/	−2
BL13-1-4-20	TJU/C97	20	/	1126 ± 30	1025	1033	−8
BL13-1-4-42	TJU/C98	42	/	1320 ± 30	1264	1033	231
BL13-1-4-50	Beta 491266	50	/	1750 ± 30	1658	1033	625
BL13-1-4-65	TJU/C99	65	/	2844 ± 30	2951	2200	751
BL13-1-4-90	TJU/C100	90	/	3363 ± 30	3607	2200	1407
BL13-1-4-120	TJU/C101	120	/	3373 ± 30	3616	2200	1416
BL13-1-4-130	Beta 491269	130	/	2860 ± 30	2976	1033	1943
BL13-1-4-135	Beta 491270	135	/	2770 ± 30	2864	1033	1831
BL13-1-4-145	Beta 491271	145	/	3000 ± 30	3186	1033	2153
BL13-1-4-150	Beta 491272	150	/	3060 ± 30	3278	1033	2245

**Calibrated by CALIB 7.0.2 (Stuiver et al., 1998).*

TABLE 3 | ^{14}C ages of sediments in Lake Bosten from some previous works.

Sample number	Depth (cm)	Dating materials	^{14}C age	Calib. age*	Corrected ages	References
BST04H	31	TOC	1470 ± 40	1358	325**	Huang et al., 2009
XBWu46	13	OM_{mean}	102 ± 24	111	111	Wünnemann et al., 2006
XBWu25	41	OM_{bulk}	840 ± 40	751	751	Wünnemann et al., 2006
XBWu46	93	Plant	1207 ± 23	1129	1129	Wünnemann et al., 2006
BSTC-01	145	Plant	2099 ± 24	2072	2072	Zhang et al., 2004

**Re-calibrated using CALIB 7.0.2. **This age was dated by bulk organic matter and was corrected by 1033 years.*

sedimentary C/N ratio suggests high fraction of organic matter produced in lake, and vice versa (Meyers, 2003).

Late Holocene Climatic Changes at Lake Bosten

The sedimentary proxy indices in core BL13-1-4 in Lake Bosten indicate significant climate change during the late Holocene, and it can be broadly divided into four intervals:

Interval I (126–153 cm), corresponding to 1800–2200 BP: the average sedimentary grain size was relatively big, indicating strong runoff intensities; the carb% was relatively low, both of which suggest higher precipitation during this period. C/N ratio increases, indicating increase in terrestrial organic matter input, which also indicates enhanced runoff transport in the catchment. The coarse sand during 138–144 cm (about 2100–2000 BP) indicates that precipitation may be higher during this period. The sediment δ^{15}N is relatively low, indicating relatively weak lake productivity during this period.

Interval II (60–125 cm), the carb% was at a higher level in the corresponding period of 650–1800 BP, indicating that the lake water salinity was higher and chemical deposition rate was faster, suggesting that the water influx to the lake was less than the evaporation. The average sedimentary grain size decreased obviously compared with that of the previous period, indicating that the runoff intensity was weakened and the surface runoff transport capacity was decreased, suggesting that the precipitation may decrease in that period. The C/N ratio was relatively small, suggesting relatively low contribution of terrestrial organic matter in this period. The high δ^{15}N value in this period indicates that the relative contribution of lake productivity is increasing. All these suggest that the biomass in the catchment was relatively low during this period due to less precipitation.

Interval III (28–59 cm), corresponding to 650–100 BP: the carb% firstly decreased and then increased, and the averaged value was relatively low. Sedimentary grain size shows a first increasing and then slightly decreasing trend, and the averaged grain size of this section was coarser than that of the previous section (60–125 cm; corresponding to 650–1800 BP). A sandy layer (25–40 cm) was found in this section. The TOC, TN, and the C/N ratios are higher, suggesting higher biomass in the catchment and larger contribution of terrestrial organic matter to the bulk sedimentary organic matter. The averaged δ^{15}N is lower, suggesting low primary productivity of the lake. All these suggest that the catchment was wetter in general, but experienced obvious dry and wet transitions during 650–100 BP.

The surface (1–27 cm) sedimentation rates are strongly influenced by human activities, which can be seen from two aspects. (1) From the ^{210}Pb-^{137}Cs chronology of surface sediments, it can be seen that the deposition rate has changed dramatically in the modern times as mentioned above. (2) The correlation between different proxy indices in this interval is weak, implying strong human activities during the modern epoch (strong human activity disturbs the relationship between proxy indices and climatic changes under natural background).

DISCUSSION

Old Carbon Reservoir

The basis of the ^{14}C dating is that the initial ^{14}C concentration of the living sample is equal to the atmospheric ^{14}C concentration of the same period (Deevey et al., 1954). However, factors influencing the old carbon reservoir ages are diverse, including (1) recharge of surface/underground water that contains "old carbon" (Deevey et al., 1954; Hendy and Hall, 2006). When the surface/underground water flows through the limestone area, it erodes the limestone or soils in the catchment, and brings "old carbon" into the lake (Olsson, 2009). (2) The ^{14}C exchange between lake water and atmospheric CO_2. Due to the slow convection rate of some lakes and the lake water stratification, the ^{14}C concentration of lake water is lower than that of atmospheric CO_2 of the same period, and the calculated ^{14}C ages of materials produced in lake are older than the corresponding real ages. For example, some aquatic plants in the lake use CO_2 in atmosphere and DIC in water for photosynthesis, which will result in parts of the "old carbon" used in photosynthesis (Olsson, 2009). (3) the pH value, salinity, and nutrient concentration of lake water may affect the primary productivity of lake, the ^{14}C exchange rate (between aquatic and atmospheric CO_2), and the old carbon reservoir age (Fontes et al., 1996; Shen et al., 2005). (4) The organic matter in lake sediments may be a mixture of terrestrial plants and aquatic plants (phytoplankton/algae), and the relative fraction of these two sources will change with the lake levels and primary productivity over time, which may also affect the age of old carbon reservoir.

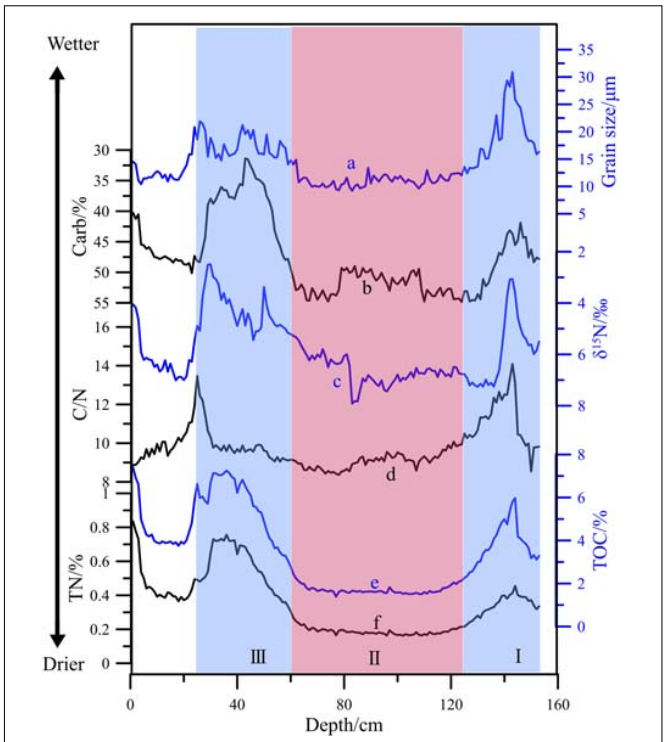

FIGURE 4 | Proxy indices in core BL13-1-4 in Lake Bosten. **(a)** Grain size. **(b)** Carbonate content (Carb%). **(c)** Organic matter δ^{15}N. **(d)** organic matter C/N ratio. **(e,f)** Total organic carbon content and nitrogen content.

Old Carbon Correction

Methods used to correct old carbon reservoir ages generally include three categories: linear regression, stratigraphic correlation, and geochemical modeling.

Linear Regression

Linear regression method has been widely used to estimate the old carbon reservoir age (e.g., Fontes et al., 1996; Sheng et al., 2015; Zhang et al., 2016). Ages of the surface sediments are generally considered to be the time when they were sampled, then the intercept between the linear regression line and age coordinate (at the water-sediment interface) is regarded as the carbon reservoir age. For example, Shen et al. (2005) used linear regression method to estimate the carbon reservoir age in Lake Qinghai, and Fontes et al. (1996) and Hou et al. (2017) used linear regression method to estimate the carbon reservoir ages in Lake Bangongco. By comparing the ^{14}C ages of the bulk organic matter with those of plant residue and inorganic carbonates in sediment core of Lake Zigê Tangco, and by linear regression, Wu et al. (2010) got the carbon reservoir age of 2010 years for this lake. However, the climate, hydrology, and deposition rate should be relatively stable when using linear regression method to evaluate the old carbon effect. If the environment changes largely in different periods, it is better to use piecewise linear regression. For example, by separating linear regression of different layers, Zhou et al. (2014) got old carbon reservoir ages of 135 years, 1143 years, and 2523 years for different sections of a core collected in Lake Qinghai.

Stratigraphic Correlation

Lake sediments of the last hundred years can be determined by ^{210}Pb and ^{137}Cs dating methods; by comparison with the ^{14}C ages of the surface sediment and ^{210}Pb and ^{137}Cs ages of the same depth, the old carbon reservoir ages can be estimated. By comparison between the ^{14}C ages of terrestrial plant residues (no old carbon effect), those of the bulk sedimentary organic matter, aquatic plants, and snail shells in the lake sediments of the same layers, the ^{14}C reservoir effect can also be estimated. The old carbon reservoir ages can also be evaluated by comparing the ^{14}C ages of the same layer with the luminescent ages and varve-counting ages (e.g., Hall and Henderson, 2001; Long et al., 2011). For example, by comparing ^{14}C ages of different samples collected from the same layers in sediment core in Xingyun Lake, Zhou et al. (2015) estimated that the carbon reservoir ages of this lake changed from 1150 to 2200 years in the past 8500 years. By comparing the ^{14}C age of organic matter and inorganic carbonate in the surface layer, and ^{14}C age of dissolved organic matter in lake water in Lake Qinghai, Henderson et al. (2010) got an old carbon reservoir age of 658 years.

Modeling of the Old Carbon Reservoir Age

If different ^{14}C sources of a lake can be identified and quantified, then old carbon reservoir age can be estimated by geochemical

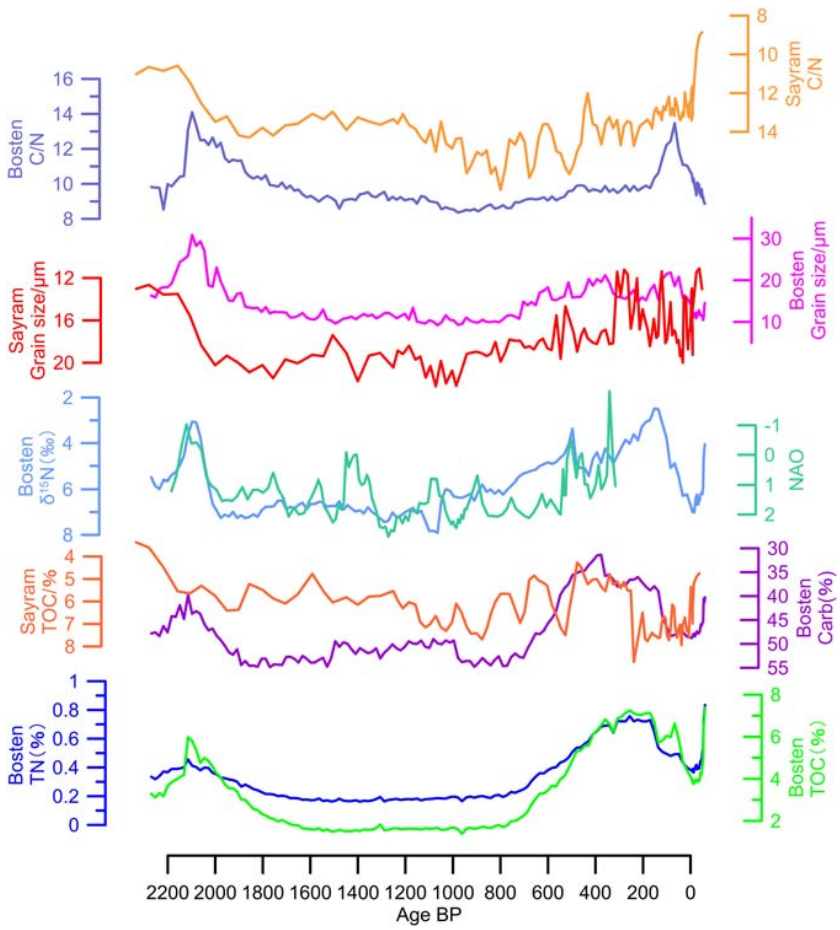

FIGURE 5 | Comparison between proxy indices in core BL13-1-4 in Lake Bosten (this study) and those from some other work. The grain size, C/N, and carbonate content were from Lan et al. (2019) and NAO index is from Olsen et al. (2012).

modeling. For example, Yu et al. (2007) used geochemical modeling to study the old carbon reservoir ages in Lake Qinghai, and they got an old carbon reservoir age of ∼1500 years in this lake. Watanabe et al. (2013) calculated the relative contribution of organic matter produced in lake and those in lakeshore wetland at Lake Pumoyum Co, and estimated the old carbon reservoir age. However, as lakes may have experienced considerable environmental changes in the past, the uncertainty of the parameters limits the application of modeling to evaluate the carbon reservoir ages of the past times. It is therefore generally limited to determine the old carbon effect of modern lakes.

Changing Old Carbon Reservoir Effect in Lake Bosten

The different linear correlations of the ^{14}C ages (as shown in **Figure 3**) and the variation patterns of the proxy indices (**Figure 4**) imply that the carbon reservoir effect of Lake Bosten was relatively smaller in the humid interval I (59–28 cm, 650–100 BP) and interval III (153–126 cm, 2200–1800 BP), but was significantly bigger (about 1170 years) during the dry interval II (125–60 cm, 1800–650 BP). To verify the changing carbon reservoir effect and the reliability of the age model for core BL13-1-4 in Lake Bosten, we compared the age model of this study with those published by some previous work. The results show that parts of previous ^{14}C ages (e.g., Zhang et al., 2004; Wünnemann et al., 2006) have a good correlation with the age model obtained in this study (**Figure 3**). In particular, the ^{14}C ages based on plant residues of some previous work fall on the regression line of this paper, suggesting that our age model (based on separated correction of different old carbon ages in different periods) is rational.

Comparison of Proxy Indices

To further verify the age model in this paper, we compared the proxy indices developed in this study with those of some previous work. As shown in **Figure 5**, the time series of proxy index based on the abovementioned age model in this study show good synchroneity to those of some other previous work. For example, the grain size, δ^{15}N, TOC, and carb% of the core BL13-1-4 show that there is a transition from wet to dry in Lake Bosten area around 2100 BP, while some other records, like the grain size and C/N ratio of Lake Sayram (Lan et al., 2019), North Atlantic NAO

index (Olsen et al., 2012), etc., show similar transitions from wet to dry contemporaneously (**Figure 5**). Another example is that during the period of about 650–500 BP, the grain size, δ^{15}N, TOC, and carb% of Lake Bosten recorded a transition from dry to wet, which is similar to the climatic transitions inferred from grain size and C/N ratio in Lake Sayram (Lan et al., 2019), the NAO index (Olsen et al., 2012), and the Alpine flood records (Wirth et al., 2013). It is interesting to note that such an obvious hydroclimatic transition from dry to wet seems to have an even wider extension, e.g., in the extended Indian summer monsoon areas (Xu et al., 2016a, 2019a). However, the nature of this hydroclimatic transition needs further study and is outside the scope of this work.

However, some differences do exist between the climate changes reconstructed by different studies, and these may be due to (1) certain errors or methodological differences in different chronologies, (2) differences in the resolution of different indicators, and (3) different responses of proxy indices to climate events or atmospheric circulation in different regions. Neglecting these differences, the results of this study are in good agreement with those obtained by previous studies. Therefore, it is rational to evaluate and correct the different old carbon effects in different periods of Lake Bosten.

Possible Causes of the Changing Old Carbon Reservoir Ages in Lake Bosten

The old carbon effect in core BL13-1-4 of Lake Bosten is significantly higher in interval II than those in other intervals, which may be related to the variable proportion of organic matter produced in lake compared to those of the bulk sediment (due to the different climatic conditions). TOC values are relatively low during 1800–650 BP (60–125 cm), suggesting less organic matter transported from the catchment to the lake during this period. The higher lake water salinity would lead to faster chemical deposition rate, and the high sedimentary carb% (as high as 55%) strongly supports the above inference.

The dry hydroclimatic condition during this interval may lead to relatively low lake levels, consistent with the switch from lacustrine sediment to peaty mud during the interval of ∼1000–500 BP in a core collected near the western shoreline in this lake (Mischke and Wünnemann, 2006). The decrease of lake water level and increase of water salinity may have slowed down the ^{14}C exchange between dissolved CO_2 and atmospheric CO_2, resulting in increase of old carbon age of the DIC pool. At the same time, the decrease of lake level during this period favored nutrient transport to the sampling site, resulting in increasing primary productivity surround the sampling site. The higher δ^{15}N values during this period also suggest that the primary productivity around the sampling site was strong. Due to the decrease of organic matter input from the catchment to lake, the relative contribution of organic matter produced in lakes should increase during this period, which can be strongly supported by the significant decreases in sedimentary C/N ratios during this period.

According to the above analysis, the contribution of endogenous organic matter increased during the relatively dry period at Lake Bosten. Due to partial utilization of DIC to synthesize organic matter, and due to the larger reservoir ages in dry period, the bulk organic matter ^{14}C age of lake sediments is older. In contrast, the relative lower contribution of endogenous organic matter in wet periods (100–650 BP and 1800–2200 BP) resulted in a smaller old carbon effect in lake sediment.

CONCLUSION

We focused on influence of different hydroclimatic conditions of the old carbon reservoir effect in Lake Bosten. By comparison between ^{137}Cs/^{210}Pb dating results and radiocarbon ages of the surface sediments and by comparison between multi-proxy indices developed in this study and proxy indices from some previous work, we found that the old carbon effect existed and varied over the past ∼2300 years at Lake Bosten. The old carbon reservoir ages of dry periods are likely to be bigger than those of wet periods. We contend that the changing old carbon reservoir ages could be ascribed to different degrees of ^{14}C exchange between lake water CO_2 and atmospheric CO_2 under different hydroclimatic conditions and to the variable proportion between organic matter produced in the lake and those in the catchment.

As the old carbon effect varies on different temporal and spatial scales for some specific lakes, it would lead to large uncertainty by simply correcting the old carbon effect using one unique old carbon reservoir age. It is necessary to correct parts of the previous ^{14}C ages (especially those over the arid zone) by a proper method. The method of this study, i.e., by comparing the ^{14}C ages with other robust dating results and by comprehensive comparison of multi-proxy indices, may serve as a reference method to get reliable age models in paleolimnology.

DATA AVAILABILITY STATEMENT

All datasets generated for this study are included in the article/supplementary material.

AUTHOR CONTRIBUTIONS

HX designed the research. HX, KZ, JL, DY, ES, KY, JZ, and YS performed the research. KZ, HX, JL, PF, and SX analyzed the data. KZ and HX wrote the manuscript.

FUNDING

This study was supported by the National Natural Science Foundation of China (Nos. 41672169 and 41761144070).

ACKNOWLEDGMENTS

We thank the reviewers for their valuable comments and suggestions.

REFERENCES

Aizen, V. B., Aizen, E. M., Joswiak, D. R., Fujita, K., Takeuchi, N., and Nikitin, S. A. (2006). Climatic and atmospheric circulation pattern variability from ice-core isotope/geochemistry records (Altai, Tien Shan and Tibet). *Ann. Glaciol.* 43, 43–49.

Bennike, O. (2000). Palaeoecological studies of Holocene lake sediments from west Greenland. *Palaeogeogr. Palaeoclimatol. Palaeoecol.* 155, 285–304. doi: 10.1016/s0031-0182(99)00121-2

Chen, F., Huang, X., Zhang, J., Holmes, J. A., and Chen, J. (2006). Humid Little Ice Age in arid central Asia documented by Bosten Lake,Xinjiang,China. *Sci. China Ser. D Earth Sci.* 49, 1280–1290. doi: 10.1007/s11430-006-2027-4

Chen, F. H., Yu, Z. C., Yang, M. L., Ito, E., Wang, S. M., Madsen, D. B., et al. (2008). Holocene moisture evolution in arid central Asia and its out-of-phase relationship with Asian monsoon history. *Quat. Sci. Rev.* 27, 351–364. doi: 10.1016/j.quascirev.2007.10.017

ChongYi, E., Sun, Y. J., Liu, X. J., Hou, G. L., Lv, S. C., Yuan, J., et al. (2018). A comparative study of radiocarbon dating on terrestrial organisms and fish from Qinghai Lake in the northeastern Tibetan Plateau, China. *Holocene* 28, 1712–1719. doi: 10.1177/0959683618788671

Cohen, A. S. (2003). *Paleolimnology: The History and Evolution of Lake Systems*. Oxford: Oxford University Press.

Deevey, E. S., Gross, M. S., Hutchinson, G. E., and Kraybill, H. L. (1954). The Natural C Contents of Materials from Hard-Water Lakes. *Proc. Natl. Acad. Sci. U.S.A.* 40, 285–288. doi: 10.1073/pnas.40.5.285

Fontes, J. C., Gasse, F., and Gibert, E. (1996). Holocene environmental changes in Lake Bangong basin (Western Tibet). Part 1: Chronology and stable isotopes of carbonates of a Holocene lacustrine core. *Palaeogeogr. Palaeoclimatol. Palaeoecol.* 120, 25–47. doi: 10.1016/0031-0182(95)00032-1

Hall, B. L., and Henderson, G. M. (2001). Use of uranium–thorium dating to determine past ^{14}C reservoir effects in lakes: examples from Antarctica. *Earth Planet. Sci. Lett.* 193, 565–577. doi: 10.1016/s0012-821x(01)00524-6

Henderson, A. C. G., Holmes, J. A., and Leng, M. J. (2010). Late Holocene isotope hydrology of Lake Qinghai, NE Tibetan Plateau: effective moisture variability and atmospheric circulation changes. *Quat. Sci. Rev.* 29, 2215–2223. doi: 10.1016/j.quascirev.2010.05.019

Hendy, C. H., and Hall, B. L. (2006). The radiocarbon reservoir effect in proglacial lakes: Examples from Antarctica. *Earth Planet. Sci. Lett.* 241, 413–421. doi: 10.1016/j.epsl.2005.11.045

Herzschuh, U., Winter, K., Wünnemann, B., and Li, S. J. (2006). A general cooling trend on the central Tibetan Plateau throughout the Holocene recorded by the Lake Zigetang pollen spectra. *Quat. Int.* 154, 113–121. doi: 10.1016/j.quaint.2006.02.005

Hou, J., D'andrea, W. J., and Liu, Z. (2012). The influence of ^{14}C reservoir age on interpretation of paleolimnological records from the Tibetan Plateau. *Quat. Sci. Rev.* 48, 67–79. doi: 10.1016/j.quascirev.2012.06.008

Hou, J. Z., D'andrea, W. J., Wang, M. D., He, Y., and Liang, J. (2017). Influence of the Indian monsoon and the subtropical jet on climate change on the Tibetan Plateau since the late Pleistocene. *Quat. Sci. Rev.* 163, 84–94. doi: 10.1016/j.quascirev.2017.03.013

Hu, R. J. (2004). *Physical Geography of the Tianshan Mountains in China*. Beijing: China Environmental Science Press.

Huang, X. Z., Chen, F. H., Fan, Y. X., and Yang, M. L. (2009). Dry late-glacial and early Holocene climate in arid central Asia indicated by lithological and palynological evidence from Bosten Lake. *China. Quat. Int.* 194, 19–27. doi: 10.1016/j.quaint.2007.10.002

Hughen, K., Lehman, S., Southon, J., Overpeck, J., Marchal, O., Herring, C., et al. (2004). ^{14}C activity and global carbon cycle changes over the past 50,000 years. *Science* 303, 202–207. doi: 10.1126/science.1090300

Jiu, X., Liu, H., Tu, Q., Zhang, Z., and Zhu, H. (eds) (1990). "Eutrophication of lakes in China" in *Proceeding of the 4th International Conference on the Conservation and Management of lakes, Hangzhou'90*, Hangzhou.

Lan, J. H., Xu, H., Sheng, E. G., Yu, K. K., Wu, H. X., Zhou, K. G., et al. (2018). Climate changes reconstructed from a glacial lake in High Central Asia over the past two millennia. *Quat. Int.* 487, 43–53. doi: 10.1016/j.quaint.2017.10.035

Lan, J. H., Xu, H., Yu, K. K., Sheng, E. G., Zhou, K. E., Wang, T. L., et al. (2019). Late Holocene hydroclimatic variations and possible forcing mechanisms over the eastern Central Asia. *Sci. China Earth Sci.* 62, 1288–1301. doi: 10.1007/s11430-018-9240-x

Liu, X., Dong, H., Yang, X., Herzschuh, U., Zhang, E., Stuut, J. B. W., et al. (2009). Late Holocene forcing of the Asian winter and summer monsoon as evidenced by proxy records from the northern Qinghai–Tibetan Plateau. *Earth Planet. Sci. Lett.* 280, 276–284. doi: 10.1016/j.epsl.2009.01.041

Liu, X., Herzschuh, U., Shen, J., Jiang, Q. F., and Xiao, X. Y. (2008a). Holocene environmental and climatic changes inferred from Wulungu Lake in northern Xinjiang. China. *Quat. Res.* 70, 412–425. doi: 10.1016/j.yqres.2008.06.005

Liu, X., Dong, H., Rech, J. A., Matsumoto, R., Bo, Y., and Wang, Y. (2008b). Evolution of Chaka Salt Lake in NW China in response to climatic change during the Latest Pleistocene–Holocene. *Quat. Sci. Rev.* 27, 867–879. doi: 10.1016/j.quascirev.2007.12.006

Long, H., Lai, Z. P., Wang, N. A., and Zhang, J. R. (2011). A combined luminescence and radiocarbon dating study of Holocene lacustrine sediments from arid northern China. *Quat. Geochronol.* 6, 1–9. doi: 10.1016/j.quageo.2010.06.001

Meyers, P. A. (2003). Applications of organic geochemistry to paleolimnological reconstructions: a summary of examples from the Laurentian Great Lakes. *Org. Geochem.* 34, 261–289. doi: 10.1016/s0146-6380(02)00168-7

Mischke, S., Weynell, M., Zhang, C., and Wiechert, U. (2013). Spatial variability of ^{14}C reservoir effects in Tibetan Plateau lakes. *Quat. Int.* 31, 147–155. doi: 10.1016/j.quaint.2013.01.030

Mischke, S., and Wünnemann, B. (2006). The Holocene salinity history of Bosten Lake (Xinjiang, China) inferred from ostracod species assemblages and shell chemistry: Possible palaeoclimatic implications. *Quat. Int.* 154, 100–112. doi: 10.1016/j.quaint.2006.02.014

Olsen, J., Anderson, N. J., and Knudsen, M. F. (2012). Variability of the North Atlantic Oscillation over the past 5,200 years. *Nat. Geosci.* 5, 808–812. doi: 10.1038/ngeo1589

Olsson, I. U. (2009). Radiocarbon Dating History: Early Days, Questions, and Problems Met. *Radiocarbon* 51, 1–43. doi: 10.1017/s0033822200033695

Reimer, P. J., Bard, E., Bayliss, A., Beck, J. W., Blackwell, P. G., Ramsey, C. B., et al. (2009). IntCal13 and Marine13 Radiocarbon Age Calibration Curves 0–50,000 Years cal BP. *Radiocarbon* 55, 1869–1887. doi: 10.1016/j.dib.2018.10.040

Robbins, J. A., and Edgington, D. N. (1975). Determination of recent sedimentation rates in Lake Michigan using Pb-210 and Cs-137. *Geochim. Cosmochim. Acta* 39, 285–304. doi: 10.1016/0016-7037(75)90198-2

Shen, J., Liu, X. Q., Wang, S. M., and Matsumoto, R. (2005). Palaeoclimatic changes in the Qinghai Lake area during the last 18,000 years. *Quat. Int.* 136, 131–140. doi: 10.1016/j.quaint.2004.11.014

Sheng, E. G., Yu, K. K., Xu, H., Lan, J. H., Liu, B., and Che, S. (2015). Late Holocene Indian summer monsoon precipitation history at Lake Lugu, northwestern Yunnan Province, southwestern China. *Palaeogeogr. Palaeoclimatol. Palaeoecol.* 438, 24–33. doi: 10.1016/j.palaeo.2015.07.026

Snyder, J. A., Miller, G. H., Werner, A., Jull, A. J. T., and Stafford, T. W. (1994). AMS-radiocarbon dating of organic-poor lake sediment, an example from Linnévatnet, Spitsbergen, Svalbard. *Holocene* 4, 413–421. doi: 10.1177/095968369400400409

Stuiver, M., Reimer, P. J., Bard, E., Beck, J. W., Burr, G. S., Hughen, K. A., et al. (1998). INTCAL98 radiocarbon age calibration, 24,000-0 cal BP. *Radiocarbon* 40, 1041–1083. doi: 10.1017/s0033822200019123

Talbot, M. R., and Johannessen, T. (1992). A high resolution palaeoclimatic record for the last 27,500 years in tropical West Africa from the carbon and nitrogen isotopic composition of lacustrine organic matter. *Earth Planet. Sci. Lett.* 110, 23–37. doi: 10.1016/0012-821x(92)90036-u

Watanabe, T., Nakamura, T., Matsunaka, T., Nara, F. W., Zhu, L., Wang, J., et al. (2013). A chronology of the PY608E–PC sediment core (Lake Pumoyum Co, southern Tibetan Plateau) based on radiocarbon dating of total organic carbon. *Nucl. Instrum. Meth.* 294, 520–523. doi: 10.1016/j.nimb.2012.07.015

Wirth, S. B., Glur, L., Gilli, A., and Anselmetti, F. S. (2013). Holocene flood frequency across the Central Alps - solar forcing and evidence for variations in North Atlantic atmospheric circulation. *Quat. Sci. Rev.* 80, 112–128. doi: 10.1016/j.quascirev.2013.09.002

Wu, Y., Li, S., Lücke, A., Wünnemann, B., Zhou, L., Reimer, P., et al. (2010). Lacustrine radiocarbon reservoir ages in Co Ngoin and Zigê Tangco, central Tibetan Plateau. *Quat. Int.* 212, 21–25. doi: 10.1016/j.quaint.2008.12.009

Wünnemann, B., Mischke, S., and Chen, F. H. (2006). A Holocene sedimentary record from Bosten Lake, China. *Palaeogeogr. Palaeoclimatol. Palaeoecol.* 234, 223–238. doi: 10.1016/j.palaeo.2005.10.016

Xiao, M., Wu, F., Liao, H., Li, W., Lee, X., and Huang, R. (2010). Characteristics and distribution of low molecular weight organic acids in the sediment porewaters in Bosten Lake, China. *J. Environ. Sci.* 22, 328–337. doi: 10.1016/s1001-0742(09)60112-1

Xu, H., Lan, J. H., Sheng, E. G., Liu, B., Yu, K. K., Ye, Y. D., et al. (2016a). Hydroclimatic contrasts over Asian monsoon areas and linkages to tropical Pacific SSTs. *Sci. Rep.* 6:33177. doi: 10.1038/srep33177

Xu, H., Yu, K., Lan, J., Sheng, E., Liu, B., Ye, Y., et al. (2016b). Different responses of sedimentary δ^{15}N to climatic changes and anthropogenic impacts in lakes across the Eastern margin of the Tibetan Plateau. *J. Asian Earth Sci.* 123, 111–118. doi: 10.1016/j.jseaes.2016.03.024

Xu, H., Liu, X. Y., An, Z. S., Hou, Z. H., Dong, J. B., and Liu, B. (2010). Spatial pattern of modern sedimentation rate of Qinghai Lake and a preliminary estimate of the sediment flux. *Chin. Sci. Bull.* 55, 621–627. doi: 10.1007/s11434-009-0580-x

Xu, H., Sheng, E. G., Lan, J. H., Liu, B., Yu, K. K., and Che, S. (2014). Decadal/multi-decadal temperature discrepancies along the eastern margin of the Tibetan Plateau. *Quat. Sci. Rev.* 89, 85–93. doi: 10.1016/j.quascirev.2014.02.011

Xu, H., Song, Y., Goldsmith, Y., and Lang, Y. (2019a). Meridional ITCZ shifts modulate tropical/subtropical Asian monsoon rainfall. *Sci. Bull.* 64, 1737–1739. doi: 10.1016/j.scib.2019.09.025

Xu, H., Zhou, K., Lan, J., Zhou, X., and Zhang, G. (2019b). Arid central Asia saw mid-Holocene drought. *Geology* 47, 255–258. doi: 10.1130/g45686.1

Xu, H., Zhou, X. Y., Lan, J. H., Liu, B., Sheng, E. G., Yu, K. K., et al. (2015). Late Holocene Indian summer monsoon variations recorded at Lake Erhai, Southwestern China. *Quat. Res.* 83, 307–314. doi: 10.1016/j.yqres.2014.12.004

Yan, D. N., Xu, H., Lan, J. H., Zhou, K. G., Ye, Y. D., Zhang, J. X., et al. (2019). Solar activity and the westerlies dominate decadal hydroclimatic changes over arid Central Asia. *Glob. Planet. Change* 173, 53–60. doi: 10.1016/j.gloplacha.2018.12.006

Yu, K. K., Xu, H., Lan, J. H., Sheng, E. G., Liu, B., Wu, H. X., et al. (2017). Climate change and soil erosion in a small alpine lake basin on the Loess Plateau, China. *Earth Surf. Proc. Land.* 42, 1238–1247. doi: 10.1002/esp.4071

Yu, S. Y., Shen, J., and Colman, S. M. (2007). Modeling the radiocarbon reservoir effect in lacustrine systems. *Radiocarbon* 49, 1241–1254. doi: 10.1017/s0033822200043150

Zhang, C., Cao, J., Lei, Y., and Shang, H. (2004). The Chronological Characteristics of Bosten Lake Holocene Sediment Environment in Xinjiang, China. *Acta Sediment. Sin.* 22, 494–499.

Zhang, J. W., Ma, X. Y., Qiang, M. R., Huang, X. Z., Li, S., Guo, X. Y., et al. (2016). Developing inorganic carbon-based radiocarbon chronologies for Holocene lake sediments in arid NW China. *Quat. Sci. Rev.* 144, 66–82. doi: 10.1016/j.quascirev.2016.05.034

Zhou, A., He, Y., Wu, D., Zhang, X., Zhang, C., Liu, Z., et al. (2015). Changes in the radiocarbon reservoir age in Lake Xingyun, Southwestern China during the Holocene. *PLoS One* 10:e0121532. doi: 10.1371/journal.pone.0121532

Zhou, W., Cheng, P., Jull, A. J. T., Lu, X., An, Z., Wang, H., et al. (2014). ^{14}C Chronostratigraphy for Qinghai Lake in China. *Radiocarbon* 56, 143–155. doi: 10.2458/56.16470

Conflict of Interest: The authors declare that the research was conducted in the absence of any commercial or financial relationships that could be construed as a potential conflict of interest.

Copyright © 2020 Zhou, Xu, Lan, Yan, Sheng, Yu, Song, Zhang, Fu and Xu. This is an open-access article distributed under the terms of the Creative Commons Attribution License (CC BY). The use, distribution or reproduction in other forums is permitted, provided the original author(s) and the copyright owner(s) are credited and that the original publication in this journal is cited, in accordance with accepted academic practice. No use, distribution or reproduction is permitted which does not comply with these terms.

frontiers in Earth Science

PERSPECTIVE
published: 30 January 2020
doi: 10.3389/feart.2020.00005

Perspective: Climate Change and the Relocation of Indonesia's Capital to Borneo

*Paige Van de Vuurst and Luis E. Escobar**

Department of Fish and Wildlife Conservation, Virginia Polytechnic Institute and State University, Blacksburg, VA, United States

Indonesia has recently announced the relocation of the country's capital from the island of Java to the island of Borneo. Java's limited sustainability is evident from extreme deforestation, biodiversity loss, intense road traffic, and high pollution. Jakarta, Indonesia's current capital on Java, is both one of the most densely populated cities in the world, and one of the most threatened by climate change. Negative impacts upon Jakarta due to climate change could affect its economy, human health, and biodiversity. These negative factors could be transferred from Jakarta to Borneo, at least partially, during the early stages of moving the capital. Borneo currently houses one of the largest remaining forested areas in Southeast Asia and is considered to be a biodiversity hotspot. However, despite its biological importance, ∼30% of Borneo has been deforested in the last 50 years. Borneo also has high rates of biological endemism, but some of its emblematic endemic species are critically endangered. We argue that Indonesia's announcement to re-locate the capital is one of the first examples of systematic, mass migration expected to occur linked to the climate change crisis. Unless a multidisciplinary and sustainable transition is implemented, the establishment of a new capital in Borneo could be a major biodiversity catastrophe. Research is urgently needed in Borneo to determine the *status quo* of its ecosystems for a large-scale, before-after assessment of the human-footprint to better understand processes in the Anthropocene.

Keywords: Anthropocene, biodiversity, flooding, impacts, Indonesia

OPEN ACCESS

Edited by:
Liangcheng Tan, Institute of Earth Environment (CAS), China

Reviewed by:
Fang Su, Shaanxi University of Science and Technology, China
Agung Wardana, Gadjah Mada University, Indonesia

***Correspondence:**
Luis E. Escobar
escobar1@vt.edu

Specialty section:
This article was submitted to Interdisciplinary Climate Studies, a section of the journal Frontiers in Earth Science

Received: *28 November 2019*
Accepted: *14 January 2020*
Published: *30 January 2020*

Citation:
Van de Vuurst P and Escobar LE (2020) Perspective: Climate Change and the Relocation of Indonesia's Capital to Borneo. Front. Earth Sci. 8:5. doi: 10.3389/feart.2020.00005

Indonesia is a country composed of volcanic islands located off the coast of mainland Southeast Asia (**Figure 1**), resulting in a diverse nation in terms of ethnic groups, culture, and biodiversity (Mavridis, 2015). Indonesia has also been identified as a vulnerable country in the face of climate change, in part due to its geographic location (Measey, 2010). Jakarta, Indonesia's current capital, is both one of the most densely populated cities in the world, and one of the most threatened due to environmental instability (Ward et al., 2013). Jakarta functions as both a political and economic hub for the Southeast Asia region. Nearly two thirds of the Indonesia's Gross Domestic Product is generated within Jakarta, and both the parliament building and presidential palace are located there (Salim and Firman, 2011; The World Bank, 2019). As a result, Jakarta demonstrates a high human density (>4000 people/km^2) (World Population Review, 2019). Recent estimates show that

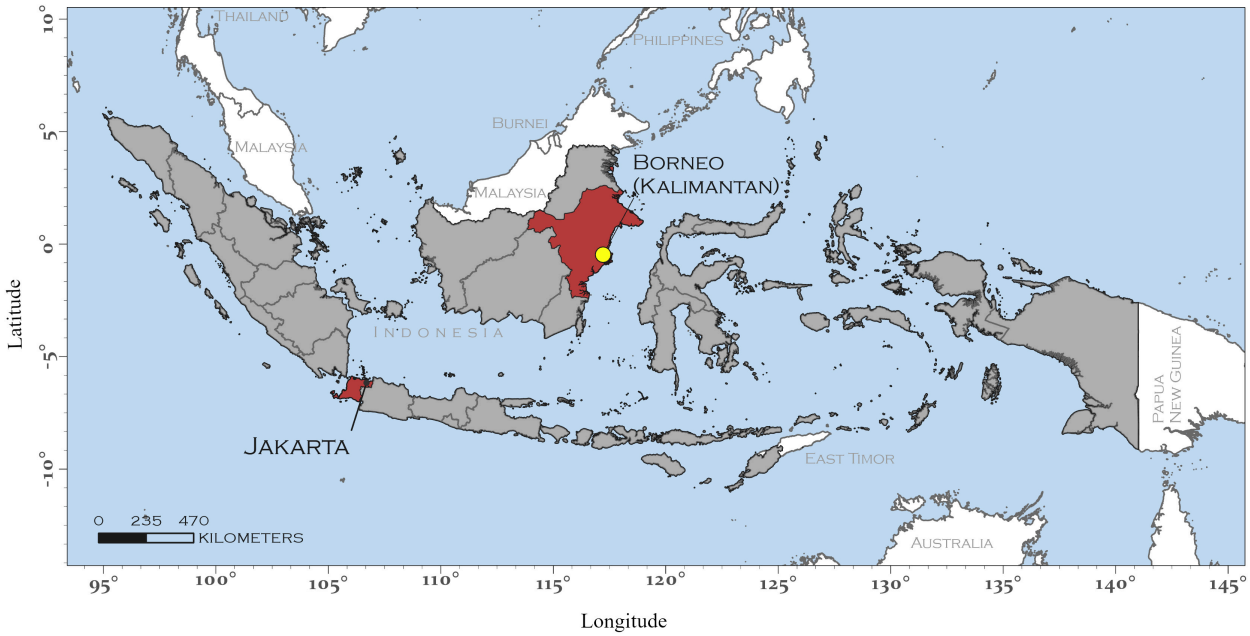

FIGURE 1 | Map of South Asia. Location of Indonesia's current capital, Jakarta, on the Java Island and potential location of the new capital (yellow point) on the island of Borneo. Country borders from Hijmans (2017).

over 10.6 million people live within the city, and that number is only growing (World Population Review, 2019). World Bank estimates that over seven million individuals will have immigrated into the city within the last decade (The World Bank, 2015). This rapid increase of people and other factors, such as poor or unsafe walking paths, have generated overwhelming road traffic (Salim and Firman, 2011). Increased emissions from motor vehicles, numerous nearby coal-fired power plants, frequent and sustained forest fires, and a history of open waste burning have also caused air quality in Jakarta to decline (The World Bank, 2016; Wati and Nasution, 2018; Edwards et al., 2020). Currently, Jakarta's air pollutant particulate concentration is 28.3% above World Health Organization guidelines (45.3 $\mu g/m^3$ annual average of atmospheric particulate matter) (IQAir, 2019). These factors are worsened by the island's susceptibility to recurring inundation due to excessive rain. In fact, in early 2020, over 400,000 residents were displaced and over 60 deaths were attributed to extreme flooding (Berlinger and Yee, 2020; Suhartono and Goldman, 2020).

The potential negative impacts of climate change upon Jakarta have, and could continue to affect its economy, human health, and biodiversity (Measey, 2010). This is worrying notion of concern, particularly for the ∼400,000 impoverished individuals living in Jakarta who are considered to be more vulnerable (Thiede and Gray, 2017). Compounding its exposure to climate change, Jakarta is also one of the fastest sinking cities in the world, with parts of the city having sunk by up to 4 m since leveling surveys began in 1978 (Abidin et al., 2001, 2011). This sinking makes Jakarta vulnerable to flooding, tsunamis, and intense coastal storms expected to increase in frequency in this area due to climate change (Knutson et al., 2012; Siagian et al., 2014; Thiede and Gray, 2017; Watts et al., 2019). Furthermore, Jakarta is located on the island of Java where there is overall limited sustainability. The deforestation rate in Java (3,415 ± 290 km^2 from 1990 to 2015) corresponds to ∼40% of the island's forest (Higginbottom et al., 2019; **Figure 2**). This accelerated deforestation has generated extensive biodiversity loss with projections estimating the extinction of up to 42% of species within the next decades (Sodhi et al., 2004).

In response to the considerable sociological issues, pollution, traffic, climate change risks, and political influences, the government of Indonesia has recently announced plans to relocate the country's political capital to the more sparsely inhabited island of Borneo (**Figure 1**), potentially within the eastern Kalimantan region (Ritter, 2019; Watts, 2019). This move is estimated to cost nearly $33 billion (US), and could signal a new wave of forced relocation or development in tropical areas across the world due to environmental collapse (Thiede and Gray, 2017; Lyons, 2019). This initiative, though made in the good faith of relieving Jakarta of its human burden, could mean that the negative factors driving poor sustainability on Java could be transferred from Jakarta to Borneo, especially during the early stages of moving the capital. We argue that Indonesia's announcement to relocate their political capital is one of the first examples of government sanctioned, systematic, tractable, mass migration expected to occur in the modern Anthropocene.

The island of Borneo has one of the largest remaining forested areas in Southeast Asia and is considered to be a global biodiversity hotspot (Myers et al., 2000). In fact, Borneo has played a key role in the development of the theoretical bases of evolution. For instance, biogeographer Alfred Russel Wallace proposed his first admission of evolution, the Sarawak Law, after

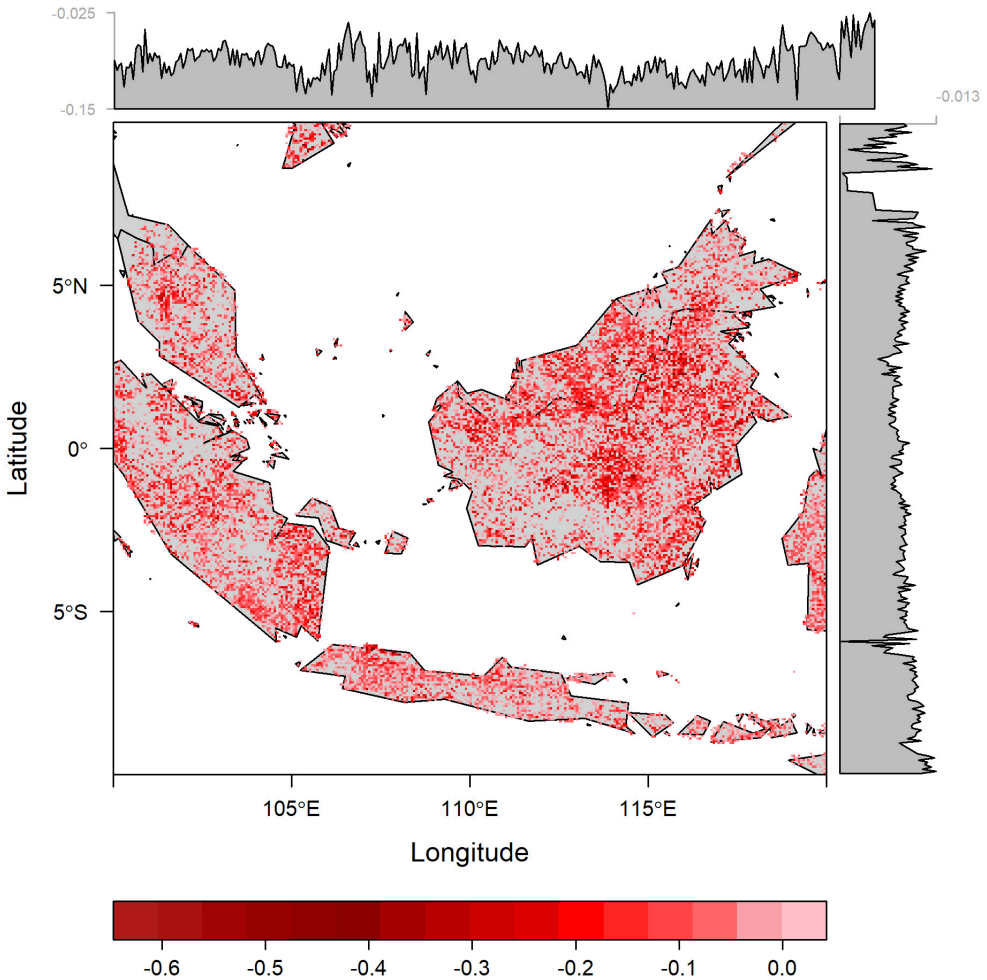

FIGURE 2 | Deforestation across Indonesian islands 2000–2019. Changes in vegetation phenologies as measured by Enhanced Vegetation Index (EVI) values from the Moderate Resolution Imaging Spectroradiometer (MODIS) sensor of the Terra satellite for the month of April in 2000 and 2019 at 16-day temporal resolution and 250 m spatial resolution (LP DAAC, 2019). Vegetation loss: areas from moderated (pink) to severe (dark red) vegetation loss based on EVI values. Note that deforestation is scattered across the Indonesian territory. Areas without vegetation loss detected are shown in gray. Map generated using the maptools package in R (Bivand and Lewin-Koh, 2019; R Core Team, 2019).

his expedition to the Sarawak region in Borneo during the mid 1800s (Wallace, 1855; van Wyhe, 2016). Furthermore, Borneo has high rates of endemism, with over 700 endemic species of vertebrates alone existing on the island (Myers et al., 2000).

Despite its ecological importance, ∼30% of Borneo has been deforested in the last 50 years, with primary forests being the most heavily affected (Margono et al., 2014; Higginbottom et al., 2019). Indeed, Indonesia has struggled to reduce forest degradation in Borneo caused principally by infrastructure expansion, logging, commercial agriculture (e.g., oil palm and wood-pulp), mining, and wildfires associated to recent droughts (Gaveau et al., 2016; Edwards et al., 2020). In 2019 alone Borneo suffered a loss of more than 9,400 km^2 of forests and agricultural land (Suroyo and Diela, 2019). In an economic sense, this corresponds to roughly 0.5% of the country's gross domestic product (Suroyo and Diela, 2019). This loss also comes just 4 years after the extreme fires of 2015 in Indonesia, which burned an area larger than the state of Vermont in the United States, or more than twice the size of London, in the United Kingdom, and Tokyo, in Japan, combined (The World Bank, 2016). The effects of these fires also lead to more than 100,000 premature human deaths (Edwards et al., 2020).

Furthermore, a significant number of Borneo's endemic species of megafauna have been listed as critically endangered (e.g., Bornean Orangutan, *Pogo pygmaeus*) (IUCN, 2019) or have become extinct just recently in all other areas besides Borneo (Sumatran Rhinoceros, *Dicerorhinus sumatrensis*, declared extinct in Malaysia November 24th, 2019) (Bittel, 2019). It has been estimated that, even without the establishment of a new capital in Borneo, even seemingly large populations of Bornean Orangutans will become locally extinct within the next 50 years (Abram et al., 2015). Other threatened or endangered species include the pygmy elephant (*Elephas maximus borneensis*), sunda pangolin (*Manis javanica*), sun bear (*Helarctos malayanus*), and the clouded leopard (*Neofelis diardi*)

(IUCN, 2019). More efforts are necessary to better understand the conservation status of other taxa of potential economic and conservation importance, including arthropods, fish, plants, and fungi.

The Indonesian government's decision to move its capital from Jakarta to Borneo is by no means a new idea. The move has been proposed in the past, and has mostly been attributed to an ongoing effort to centralize the location of governance, or other sociopolitical and economic reasons (Lyons, 2019; Ritter, 2019). The timeline for this endeavor, however, has been accelerated under growing pressures linked to environmental collapse that include flooding and coastal storms in Jakarta (Lyons, 2019; Watts, 2019). The location of the new capital seems to have been specifically selected to minimize the effects of natural disasters as well (Sofyan, 2019; Watts, 2019). For example, East Kalimantan is buffered by the islands of Java to the south and Sulawesi to the east. These geographic features could aid in protecting the city from intense coastal storms in the future. This strategic decision, compounded with the climate change-linked causes for this move in the first place, presents concerning new insights into the current and future effects of the climate crisis.

Considerable uncertainty exists regarding the location, direction, and magnitude of mass human migration due to climate change, as this type of migration is heavily contingent upon the demographics of the affected population (Thiede and Gray, 2017). However, this type of uncertainty could be reduced in this region by analyzing the migration projected to occur in Indonesia, where the government plans to relocate ∼1.5 M federal workers from Jakarta to Borneo by the year 2024 (Lyons, 2019; Watts, 2019). This migration alone could have vast impacts upon Borneo's natural resources, but could also facilitate the study of sustainable development and mass migration linked in part to the negative effects of climate change. Demographic studies on the relocation process could also help to inform policy and decision making during the critical phases of the transition. As environmental extremes continue to occur throughout the Anthropocene these types of global-change driven human migrations may become more common, and understanding the tangled web of sociological, economic, environmental, and societal variables triggering mass migration will become even more crucial (Zalasiewicz et al., 2010; Loon et al., 2016).

Unless a multidisciplinary and sustainable transition is implemented, the establishment of a new capital in Borneo will be a major biodiversity catastrophe in modern time. The expected translocation of the city requires immediate research efforts to document the current biotic and abiotic conditions of the area receiving the new capital, to better understand the effects of anthropogenic perturbation in the biological and physical properties of Borneo. These assessments would require a large-scale, before-after study of the human foot print, which have been conducted retrospectively (Mckinney, 2008; Barlow et al., 2016; Hafsi et al., 2016; Luo et al., 2018; Lu et al., 2019; Marvel et al., 2019) but rarely in near real-time. Defaunation has emerged as a global concern in the Anthropocene, and has been linked to ecosystem imbalances (Pérez-Méndez et al., 2016; Young et al., 2016). This type of biodiversity loss should be mitigated and prevented to retain ecosystem health in Borneo. Some evidence suggests that biodiversity loss could augment the burden of zoonotic diseases, at least at the local level (Rohr et al., 2020). Thus, assessing the levels of biodiversity loss that generate the minimum disease transmission risk (i.e., biodiversity-disease relationship) could help to prevent disease transmission within areas of human-wildlife interface.

Furthermore, more study into the social and economic issues currently effecting Jakarta is needed to prevent these same issues from affecting the new capital. Though environmental issues and climate change could have vast impacts upon this relocation, the original drivers of human migration, such as pollution, inundation due to flooding, and high road traffic must be addressed as well. This will allow for the development of more sustainable cities, and will offer a better understanding of development in resources limited contexts. Sustainable development in the region would also aid in the prevention of many deleterious impacts upon local ecosystem that often come as a consequence of development, urbanization, and population growth (Carley and Christie, 2000). For example, the unsustainable extraction of ground water in Jakarta is linked to the sinking of the city, which makes it prone to flooding (Abidin et al., 2011; Rahman et al., 2018). By developing sustainable management in land use (e.g., agriculture, forestry, water systems, etc.), such over extraction could be prevented, ensuring long-term ecological functions and services (Carley and Christie, 2000). Sustainability has also been called for in this region, both to prevent the over extraction of resources, and to promote equitable dispersal of ownership and power among stakeholders (Kadarusman and Herabadi, 2018; Kurniawan and Managi, 2018).

Studying the relocation of Indonesia's capital to Borneo will provide a unique opportunity to better understand the Anthropocene epoch. This phenomenon is an opportunity to inform mitigation plans regarding ecosystem impacts before they occur. The scientific community should be made aware of this transition, and should direct attention toward documenting and aiding this landmark event in the modern Anthropocene.

DATA AVAILABILITY STATEMENT

The datasets generated for this study are available on request to the corresponding author.

AUTHOR CONTRIBUTIONS

PV and LE wrote the manuscript and conducted the analysis.

ACKNOWLEDGMENTS

The authors thank Steven N. Winter and Mariana Castaneda-Guzman for their assistance in the development of the figures. Fang Su, Agung Wardana, and Juan-Pablo Castaneda provided critical suggestions that improved this manuscript.

REFERENCES

Abidin, H. Z., Andreas, H., Gumilar, I., and Fukuda, Y. (2011). Land subsidence of Jakarta (Indonesia) and its relation with urban development. *Nat. Hazards* 59, 1753–1771. doi: 10.1007/s11069-011-9866-9

Abidin, H. Z., Djaja, R., Darmawan, D., Hadi, S., Akbar, A., Rajiyowiryono, H., et al. (2001). Land subsidence of Jakarta (Indonesia) and its geodetic monitoring system. *Nat. Hazards* 23, 365–387. doi: 10.1023/A:1011144602064

Abram, N. K., Meijaard, E., Wells, J. A., Ancrenaz, M., Pellier, A. S., Runting, R. K., et al. (2015). Mapping perceptions of species' threats and population trends to inform conservation efforts: the Bornean orangutan case study. *Divers. Distrib.* 21, 487–499. doi: 10.1111/ddi.12286

Barlow, J., Lennox, G. D., Ferreira, J., Berenguer, E., Lees, A. C., Nally, R., et al. (2016). Anthropogenic disturbance in tropical forests can double biodiversity loss from deforestation. *Nature* 535, 144–147. doi: 10.1038/nature18326

Berlinger, J., and Yee, I. (2020). *66 People Now Killed by Flooding in Jakarta, and More Rain Appears to be on the Way*. Available at: https://www.cnn.com/2020/01/06/asia/jakarta-floods-intl-hnk/index.html. (accessed January, 2020).

Bittel, J. (2019). *Last Sumatran Rhino in Malaysia Dies*. Available at: https://www.nationalgeographic.com/animals/2019/05/last-sumatran-rhino-malaysia-dies/ (accessed November, 2019).

Bivand, R., and Lewin-Koh, N. (2019). *Maptools: Tools for Handling Spatial Objects*. R package version 0.9.8. Available at: http://maptools.r-forge.r-project.org/ (accessed November, 2019).

Carley, M., and Christie, I. (2000). *Managing Sustainable Development: Second Edition*. New York, NY: Earthscan, 12–177.

Edwards, R. B., Naylor, R. L., Higgins, M. M., and Falcon, W. P. (2020). Causes of Indonesia's forest fires. *World Dev.* 127:104717.

Gaveau, D. L. A., Sheil, D., Salim, M. A., Arjasakusuma, S., Ancrenaz, M., Pacheco, P., et al. (2016). Rapid conversions and avoided deforestation: examining four decades of industrial plantation expansion in Borneo. *Nat. Sci. Rep.* 6, 1–13. doi: 10.1038/srep32017

Hafsi, R., Ouerdachi, L., Kriker, A. E. O., and Boutaghane, H. (2016). Assessment of urbanization/impervious effects on water quality in the urban river Annaba (Eastern Algeria) using physicochemical parameters. *Water Sci. Technol.* 74, 2051–2059. doi: 10.2166/wst.2016.350

Higginbottom, T. P., Collar, N. J., Symeonakis, E., and Marsden, S. J. (2019). Deforestation dynamics in an endemic-rich mountain system: conservation successes and challenges in West Java 1990 – 2015. *Biol. Conserv.* 229, 152–159. doi: 10.1016/j.biocon.2018.11.017

Hijmans, R. J. (2017). *DIVA-GIS (2017) Free Spatial Data by Country*. Available at: http://www.diva-gis.org/gdata (accessed October, 2019).

IQAir (2019). *Jakarta Air Quality Analysis and Statistics. Jakarta*. Available at: https://www.airvisual.com/indonesia/jakarta (accessed September, 2019).

IUCN (2019). *The IUCN Red List of Threatened Species. 2*. Available at: https://www.iucnredlist.org/ (accessed September, 2019).

Kadarusman, Y. B., and Herabadi, A. G. (2018). Improving sustainable development within Indonesian palm oil: the importance of the reward system. *Sustain. Dev.* 26, 422–434. doi: 10.1002/sd.1715

Knutson, T. R., McBride, J. L., Chan, J., Emanuel, K., Holland, G., Landsea, C., et al. (2012). Tropical cyclones and climate change. *Nat. Geosci.* 3, 157–163. doi: 10.1002/wcc.371

Kurniawan, R., and Managi, S. (2018). Economic growth and sustainable development in Indonesia: an assessment. *Bull. Indones Econ. Stud.* 54, 339–361. doi: 10.1080/00074918.2018.1450962

Loon, A. F., Van, Gleeson, T., Clark, J., Dijk, A. I. J. M., Van, et al. (2016). Drought in the Anthropocene. *Nat. Geosci.* 9, 89–91. doi: 10.1038/ngeo2646

LP DAAC (2019). *MOD13Q1 MODIS/Terra Vegetation Indices 16-Day L3 Global 250m SIN Grid V006 [Data set]. NASA EOSDIS Land Processes DAAC*. Available at: https://lpdaac.usgs.gov/products/mod13q1v006/ (accessed September, 2019).

Lu, X., Lin, C., Li, W., Chen, Y., Huang, Y., Fung, J. C. H., et al. (2019). Analysis of the adverse health effects of PM2.5 from 2001 to 2017 in China and the role of urbanization in aggravating the health burden. *Sci. Total Environ.* 652, 683–695. doi: 10.1016/j.scitotenv.2018.10.140

Luo, K., Hu, X., He, Q., Wu, Z., Cheng, H., Hu, Z., et al. (2018). Impacts of rapid urbanization on the water quality and macroinvertebrate communities of streams: a case study in Liangjiang New Area. *China Sci. Total Environ.* 621, 1601–1614. doi: 10.1016/j.scitotenv.2017.10.068

Lyons, K. (2019). *Why is Indonesia Moving its Capital City? Everything you Need to Know*. Available at: https://www.theguardian.com/world/2019/aug/27/why-is-indonesia-moving-its-capital-city-everything-you-need-to-know (accessed November, 2019).

Margono, B. A., Potapov, P. V., Turubanova, S., Stolle, F., and Hansen, M. C. (2014). Primary forest cover loss in Indonesia over 2000–2012. *Nat. Clim. Chang.* 4, 730–735. doi: 10.1038/nclimate2277

Marvel, K., Cook, B. I., Bonfils, C. J. W., Durach, P. J., Smerdon, J. E., and Williams, A. P. (2019). Twentieth-century hydroclimate changes consistent with human influence. *Nature* 569, 59–65. doi: 10.1038/s41586-019-1149-8

Mavridis, D. (2015). Ethnic diversity and social capital in Indonesia. *World Dev.* 67, 376–395. doi: 10.1016/j.worlddev.2014.10.028

Mckinney, M. L. (2008). Effects of urbanization on species richness: a review of plants and animals. *Urban Ecosyst.* 11, 161–176. doi: 10.1007/s11252-007-0045-4

Measey, M. (2010). Indonesia: a vulnerable country in the face of climate change. *Glob. Major E-J.* 1, 31–45.

Myers, N., Mittermeier, R. A., Mittermeier, C. G., Fonseca, G. A. B., and Kent, J. (2000). Biodiversity hotspots for conservation priorities. *Nature* 403, 853–882. doi: 10.1038/35002501

Pérez-Méndez, N., Jordano, P., García, C., and Valido, A. (2016). The signatures of Anthropocene defaunation: cascading effects of the seed dispersal collapse. *Sci. Rep.* 6:24820. doi: 10.1038/srep24820

R Core Team (2019). *R: A Language and Environment for Statistical Computing*. Vienna, Austria: R Foundation for Statistical Computing. Available at: http://www.R-project.org/ (accessed September, 2019).

Rahman, S., Sumotarto, U., and Pramudito, H. (2018). Influence the condition land subsidence and groundwater impact of Jakarta coastal area. *IOP Conf. Ser. Earth Environ. Sci.* 106:012006. doi: 10.1088/1755-1315/106/1/012006

Ritter, M. (2019). "President Joko Widodo: new captial city will be on Borneo," in *Proceedings of the Palace Press Conference Aug. 26, 2019*, (Jakarta).

Rohr, J. R., Civitello, D. J., Halliday, F. W., Hudson, P. J., Lafferty, K. D., Wood, C. L., et al. (2020). Towards common ground in the biodiversity– disease debate. *Nat. Ecol. Evol.* 4, 24–33. doi: 10.1038/s41559-019-1060-6

Salim, W., and Firman, T. (2011). "Governing the Jakarta city-region: history, challenges, risks and strategies," in *Planning Asian Cities: Risks and Resilience*, eds S. Hamnett, and D. Forbes, (London: Routledge), 240–263.

Siagian, T., Tinggi, S., Statistik, I., Purhadi, P., and Suhartono, S. (2014). Social vulnerability to natural hazards in Indonesia: driving factors and policy implications. *Nat. Hazards* 70, 1603–1617. doi: 10.1007/s11069-013-0888-3

Sodhi, N. S., Koh, L. P., Brook, B. W., and Ng, P. K. L. (2004). Southeast Asian biodiversity: an impending disaster. *Trends Ecol. Evol.* 19, 654–660. doi: 10.1016/j.tree.2004.09.006

Sofyan, L. (2019). *Indonesia to Move Capital to Borneo. Digital Media Nusantara. ASEAN Post* 2019:2–5. Available at: https://theaseanpost.com/article/indonesia-move-capital-borneo (accessed September, 2019).

Suhartono, M., and Goldman, R. (2020). *Flash Floods in Indonesia Leave Hundreds of Thousands Homeless*. Available at: https://www.nytimes.com/2020/01/02/world/asia/indonesia-jakarta-rain-floods.html?auth=link-dismiss-google1tap (accessed January, 2020).

Suroyo, G., and Diela, T. (2019). *World Bank Says Indonesia Forest Fires Cost $5.2 Billion in Economic Losses*. Available at: https://www.reuters.com/article/us-indonesia-environment/world-bank-says-indonesia-forest-fires-cost-5-2-billion-in-economic-losses-idUSKBN1YF0FJ (accessed January, 2020).

The World Bank (2015). *Urban Expansion in East Asia – Indonesia. Jakarta*. Available at: https://www.worldbank.org/en/news/feature/2015/01/26/urban-expansion-in-east-asia-indonesia (accessed January, 2020).

The World Bank (2016). *The Cost of Fire: An Econimic Analysis of Indonesia's 2015 Fire Crisis. In: Indonesia Sustainable Landscapes Knowledge Note:1*. Washington DC: The World Bank Group, 7–12.

The World Bank (2019). *East Asia and Pacific Economic Update October 2019: Weathering Growing Risks*. Washington DC: World Bank Group, 17–180.

Thiede, B. C., and Gray, C. L. (2017). Heterogeneous climate effects on human migration in Indonesia. *Popul. Environ.* 39, 173–195. doi: 10.1007/s11111-017-0282-2

van Wyhe, J. (2016). The impact of A. R. Wallace ' s Sarawak Law paper reassessed. *Stud. Hist. Philos. Biol. Biomed. Sci.* 60, 56–66. doi: 10.1016/j.shpsc.2016.09.004

Wallace, A. R. (1855). On the law which has regulated the introduction of new species. *Ann. Mag. Nat. Hist.* 2, 184–196. doi: 10.1080/03745480949 5509

Ward, P. J., Pauw, W. P., Buuren, M. W., Van, and Marfai, M. A. (2013). Governance of flood risk management in a time of climate change: the cases of Jakarta and Rotterdam. *Env. Polit.* 22, 518–536. doi: 10.1080/09644016.2012. 683155

Wati, T., and Nasution, R. (2018). Evaluation of urban pollution and bio-climate using total suspended particles and discomfort index in Jakarta City. *IOP Conf. Ser. Earth Envrion. Sci.* 203:012003. doi: 10.1088/1755-1315/203/1/ 012003

Watts, J. (2019). *Indonesia Announces Site of Capital City to Replace Sinking Jakarta*. Available at: https://www.theguardian.com/world/2019/aug/26/ indonesia-new-capital-city-borneo-forests-jakarta (accessed September, 2019).

Watts, N., Amann, M., Arnell, N., Ayeb-karlsson, S., Belesova, K., Boykoff, M., et al. (2019). The 2019 report of The Lancet Countdown on health and climate change: ensuring that the health of a child born today is not defined by a changing climate. *Lancet* 6736, 1–43. doi: 10.1016/S0140-6736(19)32596-6

World Population Review (2019). *Jakarta Population 2019. Walnut*. Available at: http://worldpopulationreview.com/world-cities/jakarta-population/ (accessed September, 2019).

Young, H. S., Mccauley, D. J., Galetti, M., and Dirzo, R. (2016). Patterns, causes, and consequences of Anthropocene defaunation. *Annu. Rev. Ecol. Evol. Syst.* 47, 333–358. doi: 10.1146/annurev-ecolsys-112414-054142

Zalasiewicz, J., Williams, M., Steffen, W., and Crutzen, P. (2010). The new world of the Anthropocene. *Environ. Sci. Technol.* 44, 2228–2231. doi: 10.1021/ es903118j

Conflict of Interest: The authors declare that the research was conducted in the absence of any commercial or financial relationships that could be construed as a potential conflict of interest.

Copyright © 2020 Van de Vuurst and Escobar. This is an open-access article distributed under the terms of the Creative Commons Attribution License (CC BY). The use, distribution or reproduction in other forums is permitted, provided the original author(s) and the copyright owner(s) are credited and that the original publication in this journal is cited, in accordance with accepted academic practice. No use, distribution or reproduction is permitted which does not comply with these terms.

frontiers in Earth Science

CORRECTION
published: 12 March 2020
doi: 10.3389/feart.2020.00071

Corrigendum: Perspective: Climate Change and the Relocation of Indonesia's Capital to Borneo

*Paige Van de Vuurst and Luis E. Escobar**

Department of Fish and Wildlife Conservation, Virginia Polytechnic Institute and State University, Blacksburg, VA, United States

Keywords: Anthropocene, biodiversity, flooding, impacts, Indonesia

A Corrigendum on

Perspective: Climate Change and the Relocation of Indonesia's Capital to Borneo
by Van de Vuurst, P., and Escobar, L. E. (2020). Front. Earth Sci. 8:5. doi: 10.3389/feart.2020.00005

In the original article, there was an error. Page two, paragraph three stated that the estimated cost of moving the political capital from Java to Borneo was 3.3 billion United States dollars, the correct number is 33 billion. A correction has been made to the 4th paragraph

"In response to the considerable sociological issues, pollution, traffic, climate change risks, and political influences, the government of Indonesia has recently announced plans to relocate the country's political capital to the more sparsely inhabited island of Borneo (**Figure 1**), potentially within the eastern Kalimantan region (Ritter, 2019; Watts, 2019). This move is estimated to cost nearly $33 billion (US), and could signal a new wave of forced relocation or development in tropical areas across the world due to environmental collapse (Thiede and Gray, 2017; Lyons, 2019). This initiative, though made in the good faith of relieving Jakarta of its human burden, could mean that the negative factors driving poor sustainability on Java could be transferred from Jakarta to Borneo, especially during the early stages of moving the capital."

The authors apologize for this error and state that this does not change the scientific conclusions of the article in any way. The original article has been updated.

OPEN ACCESS

Edited and reviewed by:
Liangcheng Tan, Institute of Earth Environment (CAS), China

***Correspondence:**
Luis E. Escobar
escobar1@vt.edu

Specialty section:
This article was submitted to Interdisciplinary Climate Studies, a section of the journal Frontiers in Earth Science

Received: *12 February 2020*
Accepted: *26 February 2020*
Published: *12 March 2020*

Citation:
Van de Vuurst P and Escobar LE (2020) Corrigendum: Perspective: Climate Change and the Relocation of Indonesia's Capital to Borneo. Front. Earth Sci. 8:71. doi: 10.3389/feart.2020.00071

ACKNOWLEDGMENTS

The authors thank Tiffany M. Tran for informing them of this error.

REFERENCES

Lyons, K. (2019). *Why is Indonesia Moving its Capital City? Everything you Need to Know*. Available at: https://www.theguardian.com/world/2019/aug/27/why-is-indonesia-moving-its-capital-city-everything-you-need-to-know (accessed November, 2019).

Ritter, M. (2019). "President Joko Widodo: new captial city will be on Borneo," in *Proceedings of the Palace Press Conference Aug. 26, 2019*, (Jakarta).

Thiede, B. C., and Gray, C. L. (2017). Heterogeneous climate effects on human migration in Indonesia. *Popul. Environ.* 39, 173–195. doi: 10.1007/s11111-017-0282-2

Watts, J. (2019). *Indonesia Announces Site of Capital City to Replace Sinking Jakarta*. Available at: https://www.theguardian.com/world/2019/aug/26/indonesia-new-capital-city-borneo-forests-jakarta (accessed September, 2019).

Copyright © 2020 Van de Vuurst and Escobar. This is an open-access article distributed under the terms of the Creative Commons Attribution License (CC BY). The use, distribution or reproduction in other forums is permitted, provided the original author(s) and the copyright owner(s) are credited and that the original publication in this journal is cited, in accordance with accepted academic practice. No use, distribution or reproduction is permitted which does not comply with these terms.

frontiers in Earth Science

ORIGINAL RESEARCH
published: 05 June 2020
doi: 10.3389/feart.2020.00192

Anti-phase Variation of Hydrology and In-Phase Carbon Accumulations in Two Wetlands in Southern and Northern China Since the Last Deglaciation

Xuefeng Yu[1,2], Jiquan Chen[3], Yanhong Zheng[4], Wei Zhong[5], Zutao Ouyang[6] and Weijian Zhou[1,2]*

[1] State Key Laboratory of Loess and Quaternary Geology, Institute of Earth Environment, Chinese Academy of Sciences, Xi'an, China, [2] Shaanxi Key Laboratory of Accelerator Mass Spectrometry (AMS) Technology and Application, Xi'an AMS Center, Xi'an, China, [3] Department of Geography, Michigan State University, East Lansing, MI, United States, [4] State Key Laboratory of Continental Dynamics, Department of Geology, Northwest University, Xi'an, China, [5] School of Geography Science, South China Normal University, Guangzhou, China, [6] Department of Earth System Science, Stanford University, Stanford, CA, United States

OPEN ACCESS

Edited by:
Hai Xu,
Tianjin University, China

Reviewed by:
Li Wu,
Anhui Normal University, China
Yan Zhang,
Fujian Normal University, China

***Correspondence:**
Xuefeng Yu
xfyu@loess.llqg.ac.cn

Specialty section:
This article was submitted to Quaternary Science, Geomorphology and Paleoenvironment, a section of the journal Frontiers in Earth Science

Received: *11 March 2020*
Accepted: *14 May 2020*
Published: *05 June 2020*

Citation:
Yu X, Chen J, Zheng Y, Zhong W, Ouyang Z and Zhou W (2020) Anti-phase Variation of Hydrology and In-Phase Carbon Accumulations in Two Wetlands in Southern and Northern China Since the Last Deglaciation. Front. Earth Sci. 8:192. doi: 10.3389/feart.2020.00192

To examine the spatial patterns of hydrological variations in the southern and northern East Asia Monsoonal (EAM) region on millennial time scales, as well as to investigate the relationship between hydrological changes and carbon accumulation in these regions with contrasting environmental backgrounds, we performed facies-based hydrological reconstructions in two wetlands, Midiwan wetland (37°39′N, 108°37′E) and Dahu wetland (24°45′N, 115°2′E), located in a semi-arid loess-desert transitional zone and humid southern China, respectively. Our reconstructions revealed an anti-phase pattern of the precipitation in these two wetlands on a millennial time scale. However, with the different responses to the contrasting hydrological conditions, the carbon accumulations at these two sites showed an in-phase patterns on a millennial time scale. Our results imply that the carbon accumulations at these two sites are mainly controlled by local hydrologic conditions. The wetlands in both southern and northern China were found to be expanding during the interval from 6 to 4 cal. ka BP (ka = kilo annum), as inferred by a higher total organic carbon (TOC) content. For the Mystery Interval (MI, from 17.5 to 14.5 cal. ka BP), however, both hydrological conditions and carbon accumulations at these two sites showed an in-phase pattern.

Keywords: hydrological reconstruction, carbon accumulation, wetland, spatial pattern, monsoon precipitation

INTRODUCTION

Wetland represents one of the most important terrestrial ecosystems with its natural accumulation of organic matter closely related to hydrological processes (Billett et al., 2004; Holden, 2005). Although it only accounts for 3% of the global terrestrial land area, wetlants are regarded as one of the most important carbon reservoirs due to its high carbon density (Frolking and Crill, 1994; Blodau, 2002; Strack et al., 2006; Limpens et al., 2008; Yu et al., 2010; Leifeld et al., 2019). It is both

a natural and an anthropogenic source of greenhouse gases (e.g., CH_4) emission to the atmosphere because of its significant changes in decomposition processes under different climates, harvests, and disturbances such as fires (Zoltai et al., 1998; Page et al., 2002; Olson et al., 2013; Chimner et al., 2017; Rigney et al., 2018).

Carbon accumulation in a wetland is determined by the balance of the photosynthetic uptake and decomposition loss mainly controlled by regional climatic conditions, especially the hydrological process (Frolking et al., 2010; Rennermalm et al., 2010). Generally, carbon accumulation increases with an increase in soil moisture that is influenced by groundwater level or precipitation (Nijp et al., 2019; Lazcano et al., 2020). However, at some waterlogged sites, carbon accumulation decreases with the increase in soil water because of the inhibition of a seeper to the growth of plants (**Figure 1**). Here, we put forward a conceptual framework by hypothesizing that there will be two cases for the relationship between total organic carbon (TOC) accumulation and soil moisture conditions in wetlands with typical hydrological conditions of A and B types (**Figure 1**): (1) the variations in TOC at two wetlands would be anti-phased if the variations in precipitation at the two sites are in-phase, or (2) the variations in TOC would be in-phased if precipitation at the two sites is anti-phase. For the latter case, there may exist several periods during which the proportions of both wetlands increase. Therefore, the total carbon accumulation is ultimately determined by the spatial pattern of hydrology.

From a global perspective, there are spatial differences in precipitation as well as in trends in different regions (Wang et al., 2012). Numerical modeling studies revealed that the variation in summer precipitation in northern and southern East Asia exhibits an anti-phase pattern on the orbital time scale due to the ENSO-like response to orbital forcing (Shi et al., 2012). Stable carbon isotope records of peat sequences from the eastern Tibetan Plateau and northeastern China also show an anti-phase pattern of monsoon precipitation on the millennial-centennial time scale (Hong et al., 2005, 2010, 2014). A recent reconstruction of lake levels at Lake Chenghai in southwest China also showed an out-phase variation of precipitation on orbital time scale in southwest China with boreal summer insolation that was regarded as the driver of Asian summer monsoon precipitation (Xu et al., 2020). For northern and southern East Asia, however, it is unclear whether the anti-phased spatial pattern of monsoonal precipitation exists on the millennial time scale. More importantly, the relationship between carbon accumulation and regional hydrological conditions in southern and northern East Asia remains unknown. More studies on archives containing information about hydrological processes and carbon cycling are needed for understanding the history, variability, and dynamics of environmental change in these two regions.

Here, we chose two well-dated peat sequences that represent contrasting hydrological and temperature regimes to test our hypotheses. The objectives of this study were: (1) to examine the spatial variation of changes in precipitation (i.e., hydrological cycle) in southern and northern East Asia on a millennial time scale and (2) to investigate the relationship between hydrological changes and carbon accumulation in wetlands located in a semi-arid loess-desert transitional zone and in humid southern China.

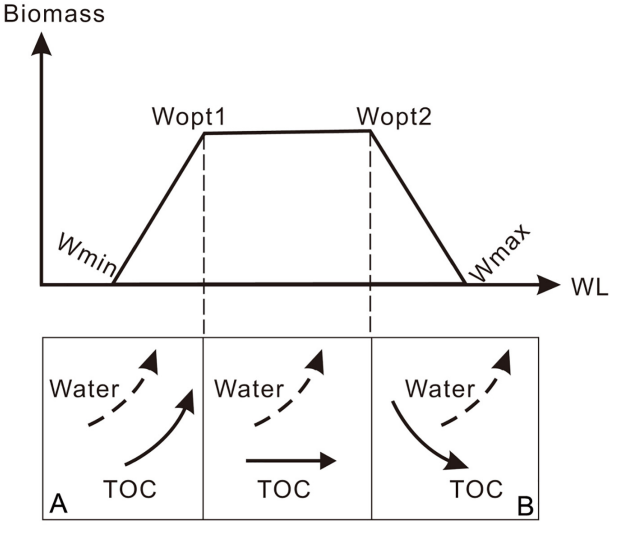

FIGURE 1 | Conceptual model showing the relationship between the water content of soil (WL) and soil carbon accumulation (CA). The upper plot is for the WL (horizontal axis) and plant production (ordinates) and the lower for the WL and carbon accumulation. A and B show the typical relationship between the WL and CA in two contrasting hydrological conditions.

STUDY SITES

The two wetlands used in this study are Midiwan (MDW, 37°39′N, 108°37′E) located in the loess-desert transitional zone in northern China and Dahu (DH, 24°45′N, 115°2′E) located in the Nanling Mountain area in southern China (**Figure 2**). These wetlands are located in a semi-arid area and humid area, respectively, where the contrasting changes in precipitation yield different hydrological conditions and, consequently, determine the TOC accumulation. Like scenario A in **Figure 1**, in the semi-arid region (i.e., MDW), the higher soil moisture would favor the growth of plants and carbon accumulation, whereas in the humid region (i.e., DH), like scenario B in **Figure 1**, more water would hinder the growth of plants and carbon accumulation when the water content of soil (WL) exceeds the optimum values (**Figure 1**).

Midiwan (MDW) Wetland

The MDW wetland, with an altitude of 1400 m a.s.l., is located in southwest of Yulin City in northern Shaanxi Province, in the southern margin of the Mu Us Desert region. As showed in **Table 1**, a quadrat survey of Lake Hongjiannao near the MDW site shows that the modern plants in this site are mainly grasses from 9 families. The climate is characterized by semi-arid continental monsoon activity with an annual precipitation of 395 mm and annual mean temperature of 7.8°C (**Figures 3A,B**).

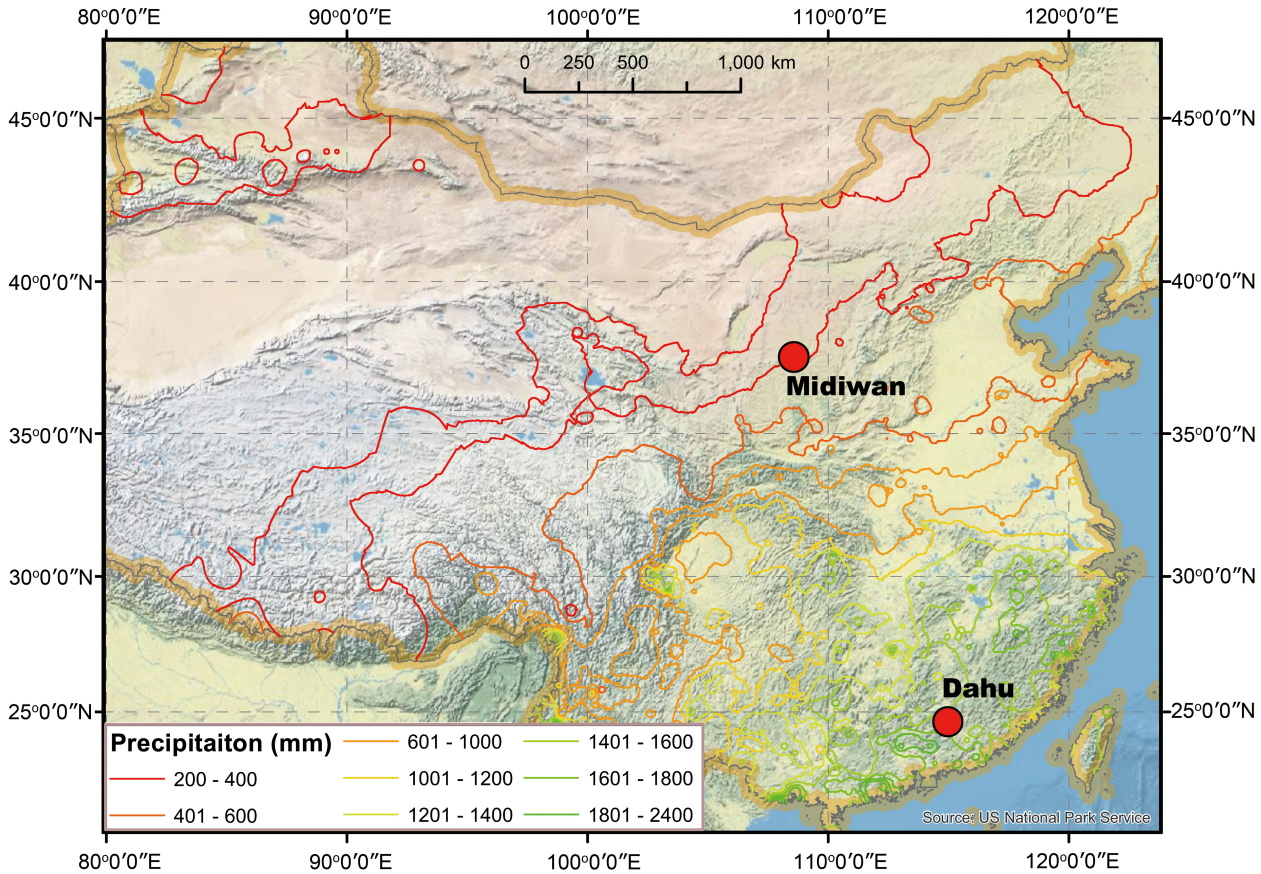

FIGURE 2 | Locations of the two peatlands used in this study. Lines in different colors show the isolines of annual precipitations.

Water is the most important limiting factor for the growth of plants at this site; the amount and timing of precipitation are critical. During the humid periods, with the retreat of the desert, the palaeosol or peat was deposited. During the drier periods, with the advance of the desert, loess or eolian dust was deposited on the land surface (Porter and Zhou, 2006). Therefore, regarding the depositional sequences in this loess-desert transitional zone, the alternative deposition of wetland and wind-blown dust reflects the history and variability of summer monsoon activities (Porter and Zhou, 2006). Specifically, wetland deposits reflect the stronger monsoon activity that brings more precipitation to this region, while eolian dust deposits reflect the retreat of the monsoon front, which causes drier conditions and desertification in this region. Following the stratigraphic description of Zhou et al. (1996), the MDW peat sequence with a length of 13.8 m was divided into 13 depositional units (**Table 2**), reflecting millennial-scale changes in hydrological conditions in northern China.

Dahu (DH) Wetland

The DH swamp, covering an area of 0.8 km^2 and located at about 260 m a.s.l., has developed in a small, closed intermontane basin in the eastern Nanling Mountain region in southern China (Zhou et al., 2004; Zhong et al., 2010, 2011). The hydrological conditions of the swamp depend largely on precipitation because there is no river discharging into the swamp (Xue et al., 2009). In this area, the present-day annual average temperature is 17.8°C and the annual precipitation is ∼1600 mm, mainly occurring from March to September (**Figure 3C**). The modern vegetation around this site is the shrubbery with ferns and grasses (**Table 3**) (Zhong et al., 2010). Ferns and grasses are the main plants in the peat accumulations. Zheng et al. (2008) conducted systematic drilling along a track line from the northeast to the southwest. The cross section along the drilling sites was reconstructed based on stratigraphic correlation (**Figure 4**). In the region, where the WL is usually higher than W_{opt2}, an increase in WL would inhibit plant growth and carbon accumulation. During humid times, lacustrine mud or sand deposits on the surface because the valley is covered with water. It is only during relatively drier periods, accompanied by the shrinking of the lake, that plants that contribute to the peat accumulations flourish. The stratigraphical sequence at this site is composed of peat interbedded with lacustrine sediments (Zhou et al., 2004; Zheng et al., 2008; Xue et al., 2009). The lacustrine sand represents a waterlogged condition caused by excessive precipitation, while the peat layer represents a relatively drier environment caused by moderate precipitation. The thickest deposits occurred at the center of the swamp, covering a time back to 42 cal. ka BP (Zheng

TABLE 1 | Modern plant species around Lake Hongjiannao.

Poaceae
Achnatherum extremiorientale (Hara) Keng
Agropyron cristatum
Eragrostis pilosa
Imperata cylindrica (Linn.) Beauv
Pennisetum alopecuroides (L.) Spreng
Phragmites australis (Cav.) Trin. ex Steud
Calamagrostis epigejos (L.) Roth
Setaira viridis (L.) Beauv
Allium tenuissimum L.
Allium bidentatum Fisch. ex Prokh. & Ikonn.- Gal.
Setaria glauca
Liliaceae
Allium tenuissimum L.
Allium bidentatum Fisch. ex Prokh. & Ikonn. - Gal.
Boraginaceae
Cynoglossum fu Crcatum Wall
Chenopodiaceae
Chenopodium glaucum Linn
Salsola collina Pall
Herba Suaedae Glaucae Suaeda glauca Bge
Agriophyllum squarrosum (L.) Moq
Zygophyllaceae
Peganum multisectum (Maxim.) Bobr
Convolvulaceae
Cuscuta chinensis Lam
Bignoniaceae
Incarvillea sinensis
Asteraceae
Artemisia anethifolia Weber
Artemisia verlotorum Lamotte
Aster ageratoides
Cirsium setosum
Heteropappus altaicus (Willd) Novopokr
Ixeridium sonchifolium (Maxium).shih
Leontopodium alpinum
Taraxacum mongolicum
Sonchus oleraceus Linn.
Artemisia frigida Willd. Sp. Pl.
Saussurea japonica
Artemisia desterorum Spreng
Leguminosae
Thermopsis lanceolata
Medicago sativa L.
Melilotus alba

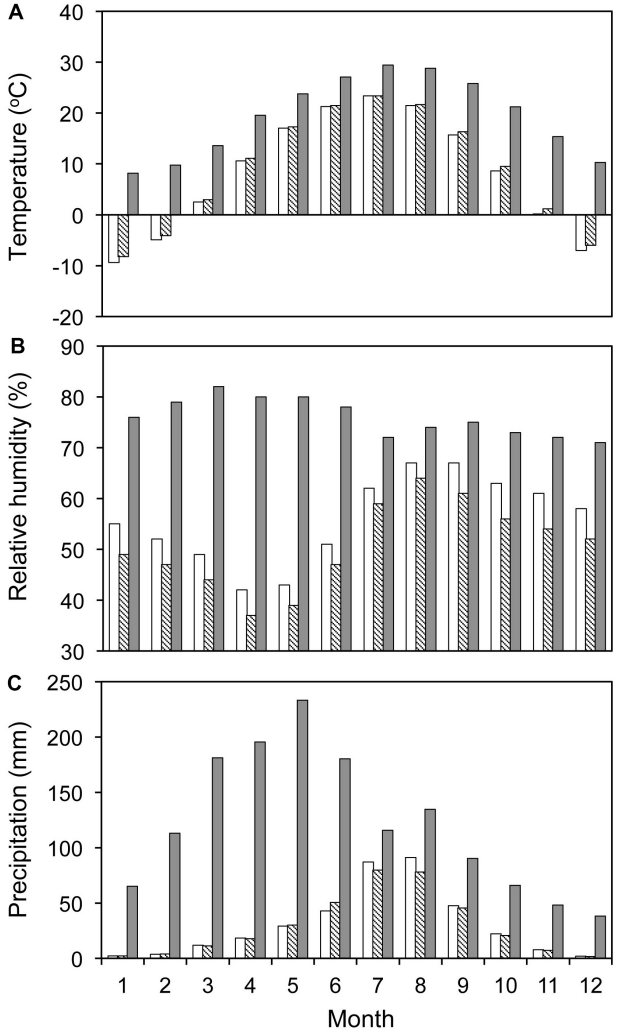

FIGURE 3 | Meteorological data near the study sites. **(A)** Temperature (°C), **(B)** relative humidity (%), and **(C)** annual precipitation (mm). Gray-filled bars show the data from the Ganzhou Meteorological Observatory near the DH site, white-filled bars and black diagonal-filled bars show the data from the Meteorological Observatories of Yulin and Hengshan near the MDW site, respectively.

et al., 2008). In this study, a 3.5 m long core was taken at the center of the swamp and divided into 10 depositional units (**Table 2**; Zhou et al., 2004).

MATERIALS AND METHODS

Hydrologic Grades of Different Facies

Based on our conceptual model, the production of plants that affects the accumulation of organic carbon in the soil is controlled by the WL. As shown in **Figure 1**, when the WL is lower than the minimum value (W_{min}), plants cannot survive; accordingly, there will be no organic carbon deposits in the stratigraphic section. When the WL increases from W_{min} to W_{opt1} (the lower optimum threshold WL for plant growth), plant production increases. For a WL between W_{opt1} and W_{opt2} (the highest optimum threshold WL for plant growth), the production will be consistent. With a WL > W_{opt2}, the production will decrease due to the inhibition of the waterlogged condition to the growth of plants.

For the MDW site, we assigned the value of 0 to peat layers to represent the hydrologic grade, 2 to lacustrine deposits, and -1 to -3 to eolian deposits to mark the dry conditions (**Figure 5**). Based on the description of the MDW profile (Zhou et al., 1996), by using the aforementioned protocol and also consulting the results of pollen analyses and stable carbon isotope measurements, the hydrological condition of the MDW area since 16 cal. ka BP was reconstructed (**Table 2**).

Similarly, for the DH site, we assigned the value of 0 to peat layers and 1–3 to lacustrine deposits (**Figure 5**). Based on

TABLE 2 | Stratigraphic description and hydrologic reconstruction at the Midiwan site (MDW) (see Zhou et al., 1996 for more details) and the Dahu site (DH) (see Zhou et al., 2004 for more details).

Site	Depth (cm)	Stratigraphic unit	Hydrologic grade
MDW	0–80	Grayish-brown to grayish-green silty paleosol	−1
	80–310	Grayish-yellow to grayish-green silt with mud bands	−2
	310–550	Grayish-black to black silty peat	0
	550–650	Grayish-black to grayish-yellow silt	−2
	650–710	Black silty peat	0
	710–740	Grayish-black and grayish-green silt	−2
	740–835	Black silty peat	0
	835–900	Light yellow eolian sand	−2
	900–970	Grayish-black silty peat	0
	970–1090	Heiheze silt	−2
	1090–1140	Grayish-black silty peat	0
	1140–1240	Pale-yellow to light grayish-green silts	2
	1240–1380	Grayish-yellow eolian sand; average grain size 70 mm	−2
DH	0–40	Brownish-yellow soil cultivated for rice	1
	40–118	Brown herb rich peat	0
	118–141	Grayish-green organic mud	1
	141–161	Black sandy mud	2
	161–180	Grayish-green organic mud	1
	180–210	Black sandy mud	2
	210–228	Brown herb rich peat	0
	228–254	Grayish-green sandy mud	2
	254–280	Brown herb rich peat	0
	280–300	Sandy mud	2

TABLE 3 | Modern plant species around Dahu swamp (Zhong et al., 2010).

Taxodiaceae
Cunninghamia lanceolata (Lamb.) Hook.
Caprifoliaceae
Viburnum fordiae Hance
Pinaceae
Pinus massoniana L.
Meliaceae
Cedrela toona Roxb.
Fagaceae
Castanopsis fissa (Champ. ex Benth.) Rehd. et Wits
Lauraceae
Litsea cubeba (Lour.) Pers.
Myrtaceae
Syzygium championii (Benth.) Merr. et Perry
Theaceae
Camellia oleifera Abel
Moraceae
Ficus pumila L.
Ficus hirta Vahl
Myrsinaceae
Maesa perlarius (Lour.) Merr.
Rosaceae
Rhaphiolepis indica (L.) Lindl.
Rubus reflexus Ker.
Rubus pirifolius Sm.
Ericaceae
Rhododendron simsii Planch
Blechnaceae
Blechnum orientale L.
Cyperaceae
Gahnia tristis Nees
Gleicheniaceae
Dicranopteris dichotoma (Thunb.) Bernh.
Labiatae
Callicarpa rubella Lindl.

the description of each stratigraphic unit (Zhou et al., 2004), the hydrological grade in the DH core since 18 cal. ka BP was reconstructed (**Table 2**).

Chronological Framework

The chronological frameworks for these two peat sites were established by radiocarbon dating (Zhou et al., 1996, 2004). A total of 23 and 17 samples from the MDW and DH profiles, respectively, including fossil wood, charcoal, and peat, were collected for dating. Radiocarbon dating results were calibrated using the CALIB software (Stuiver et al., 1998) to obtain calendar ages. The chronological framework for each profile was established by the linear regression between the calibrated age and depths. The details of the dating materials, methods, and chronological framework can be found in Zhou et al. (1996) for the MDW site and in Zhou et al. (2004) for the DH site.

Total Organic Carbon (TOC)

The TOC was determined for the two studied sections (Zhou et al., 1996, 2004). At both the MDW and DH sites, the stratigraphic sequence is composed of inter-bedded peat and sand layers, indicating a great difference in carbon accumulation at different times. Organic carbon was only deposited during the periods when peat layers were formed. For those sites with drastic facies changes, carbon accumulations are mainly determined by the organic carbon input into the layers. Compared to organic carbon input, other factors, such as microbial activities and depositional factors, are negligible. Therefore, combining the reconstructed hydrological conditions, we used the TOC data to explore the relationships between hydrology and carbon accumulation at these two sites with contrasting climate condition.

RESULTS

Hydrological Variations in MDW and DH

There were five periods with wetter conditions and six periods with drier conditions at MDW since the last 16 cal. ka BP (**Figure 6A**). The highest WL at this site was found from 14.5 to 13.5 cal. ka BP, as indicated by the layer of light grayish-green lacustrine silt and silty peat. During the Younger Dryas event, the deposition at the MDW site varied from silt to silty peat, then to eolian sand (1090–815 cm), indicating an unstable, variable hydrological condition between dry and humid (Zhou et al., 1996). The hydrological condition at the MDW site was generally humid during the early Holocene (11.5–8.5 cal. ka BP), except for an aberrant dry event occurring at ∼10 cal. ka BP.

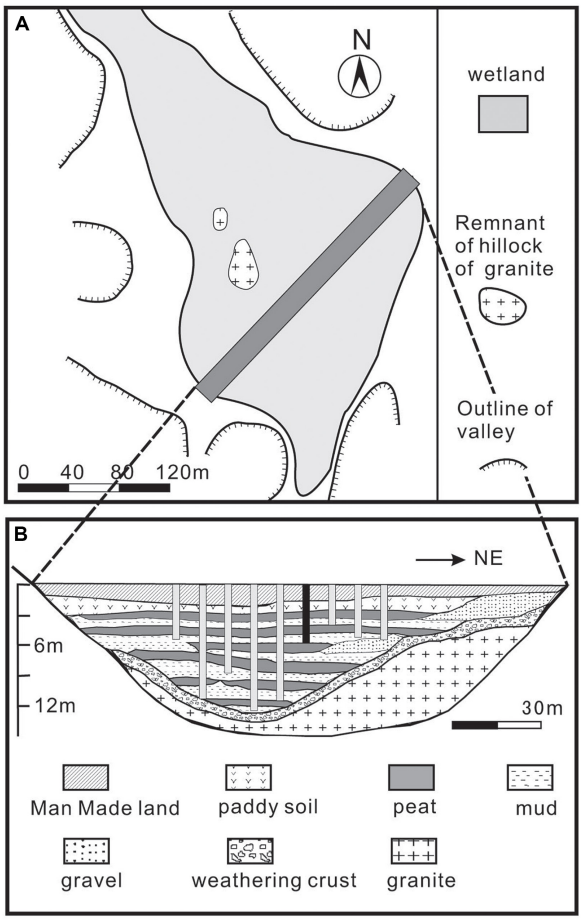

FIGURE 4 | Distribution **(A)** and cross section **(B)** of Dahu swamp (redrawn after Zhou et al., 2004; Zheng et al., 2008).

A prolonged dry period occurred from 8.5 to 6.5 cal. ka BP, as indicated by a set of grayish-yellow eolian deposits. The WL resumed to high level in the period from 6.5 to 3.5 cal. ka BP, as indicated by a set of silty peat deposits (550–310 cm). We note that the deposits during this humid period contained more minerals than those in the early Holocene, suggesting that this humid period occurred along with a drying trend. A set of silt-with-mud bands developed, and this is mantled by a modern active dune on the top, suggesting a strengthened drying trend after 3.5 cal. ka BP.

The general trend of the hydrological variation in the DH area since 18 cal. ka BP represents a cyclic pattern: the WL decreasing in the period from 18 to 15 cal. ka BP, increasing from 15 to 11 cal. ka BP, and then decreasing from 11 to 3.5 cal. ka BP (**Figure 6B**). The WL changed from a peak at 18 cal. ka BP to a low at ∼15 cal. ka BP. There was a dry period from 15.5 to 14.5 cal. ka BP, as inferred by a brown herbaceous-rich peat layer from 280 to 254 cm in the section. This dry period was followed by a humid period from 14.5 cal. ka BP to the beginning of the Holocene, with a hiatus corresponding to the Younger Dryas event. The hydrological condition in this area during the early Holocene was relatively high. A dry event occurred at ∼9 cal. ka BP and lasted for ∼1000 years (9.5–8.5 cal. ka BP). The WL began to decrease after 7 cal. ka BP and reached its lowest level again in the period from 6 to 3.5 cal. ka BP. The WL showed a slight increase after 3.5 cal. ka BP.

Hydrology and Carbon Accumulation

The variations in carbon accumulation, indicated by TOC proxy and hydrological conditions in the MDW area during the last 16 cal. ka BP, are generally synchronous (**Figure 6A**): a higher WL was accompanied by a higher carbon accumulation, except during a wetter period with lower carbon accumulation from 14.5 to 14 cal. ka BP, as recorded by a layer of lacustrine silt. The hydrology and carbon accumulation in the DH area during the last 18 cal. ka BP, in contrast, represents an asynchronous pattern (**Figure 6B**): a higher WL was concurrent with a lower carbon accumulation.

The carbon accumulations at these two wetlands on the millennial time scale show a general in-phase relationship (**Figure 6**). For example, during 10–8 cal. ka BP and 6–4 cal. ka BP, there were high carbon accumulations at both sites. However, during 8–6 cal. ka BP, both sites had low carbon accumulation. The highest rate of carbon accumulation at these two sites occurred at different times, although their trends on the millennial time scale are generally synchronous. The highest rate occurred during the early Holocene in northern China, but during the middle Holocene in southern China.

DISCUSSION

Comparison of Hydrological Reconstruction With Other Proxies

To validate our conceptual model, we compared the facies-based reconstruction of the hydrological condition with other proxy-based reconstructions. The results show that our reconstructions of hydrology at these two peatlands through facies analysis are comparable with other proxy-based reconstructions, implying that the facies analysis is a sound approach for hydrological reconstruction for these sections with drastic facies variation. Our result at the MDW site is generally consistent with the results of pollen and stable carbon isotope analyses performed in the same section (Zhou et al., 1996). The dry episodes are usually correlated to those with low levels of pollen concentrations and the positive bias of stable carbon isotope. The proxy-based reconstruction of lake level from Lake Daihai (Sun et al., 2009) northeast of the MDW site also showed a similar trend in hydrological fluctuation to that in the MDW area. The rhythm from the dry (9–7 cal. ka BP) to the humid period (7–3.5 cal. ka BP) in the MDW area can be correlated to the lake-level change in Lake Daihai, implying that the MDW site might have the potential to record hydrology at a regional scale. The archaeo-biological evidence showed that rice agriculture in northwest China first emerged > 5000 years ago and lasted for > 1000 years (Li et al., 2007). This evidence, showing a relatively humid period from 5 to 4 cal. ka BP in northern China, further

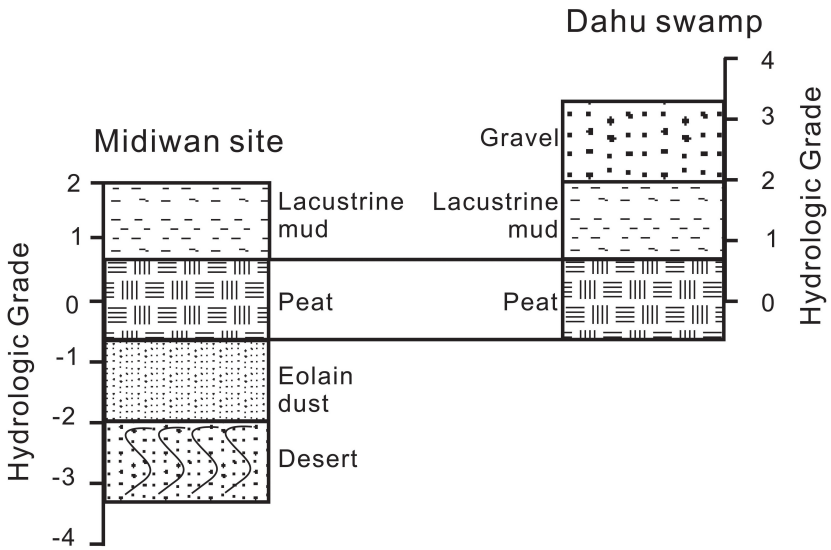

FIGURE 5 | Relationship between the hydrologic grade and the depositional facies in Midiwan and Dahu. Axes beside the facies show the hydrologic grades of the corresponding facies. The order of each facies in this map does not represent the sequences in these sections.

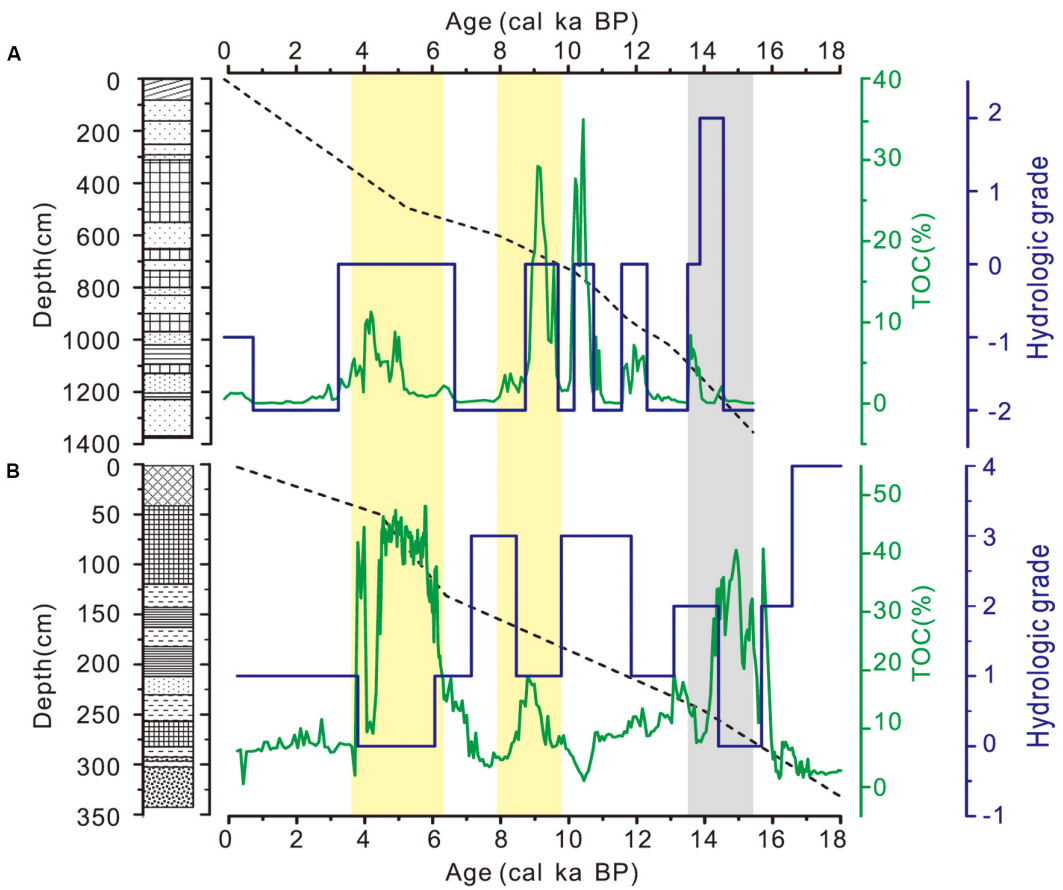

FIGURE 6 | Variations in hydrological conditions and carbon accumulation in two peatlands since the Last Deglaciation (**A** for MDW and **B** for DH). Blue lines are the reconstructed hydrological conditions of two sites, green lines are for the carbon accumulation, dashed lines are for the depth-age relationships of two sections, light yellow bars are the in-phase pattern for carbon accumulation and the anti-phase pattern for hydrology in the two sites, and the light gray bar indicates the in-phase pattern for hydrology in the two sites in the interval from 15 to 13.5 cal. ka BP.

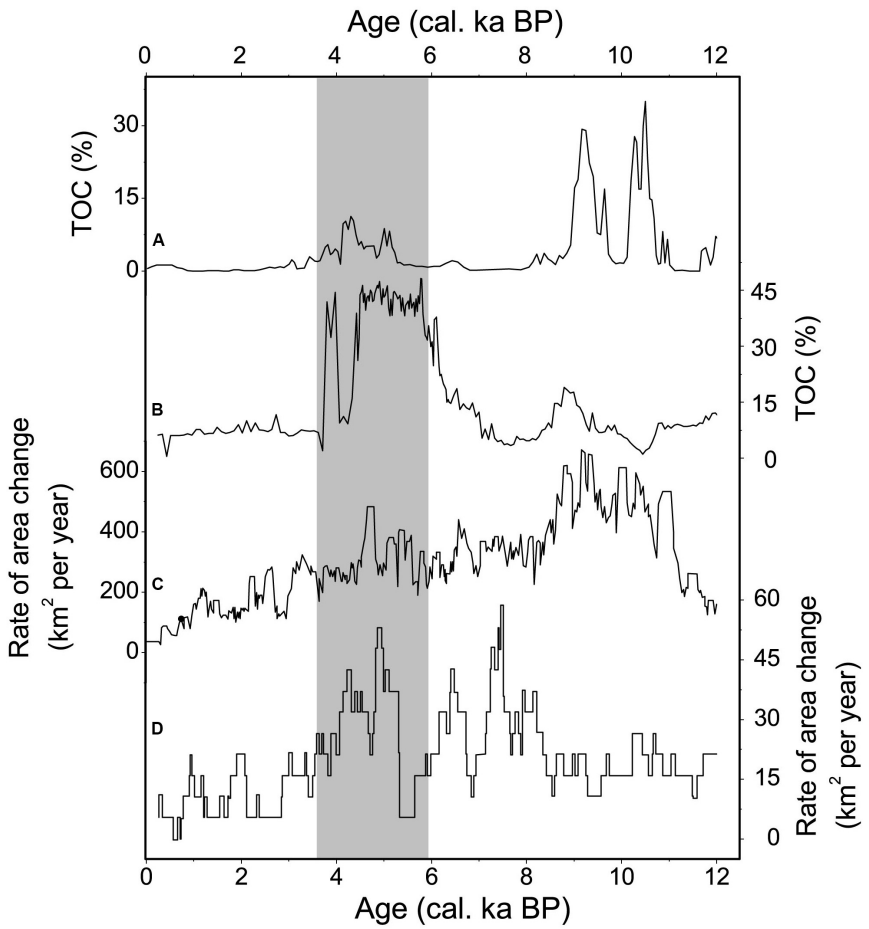

FIGURE 7 | Carbon accumulations in MDW and DH with the area of change in global peatlands during the Holocene. Panel **(A,B)** are the carbon accumulations in MDW and DH, respectively. Panel **(C,D)** are the rates of area change, respectively, for the northern peatlands and the tropical peatlands (Yu et al., 2010).

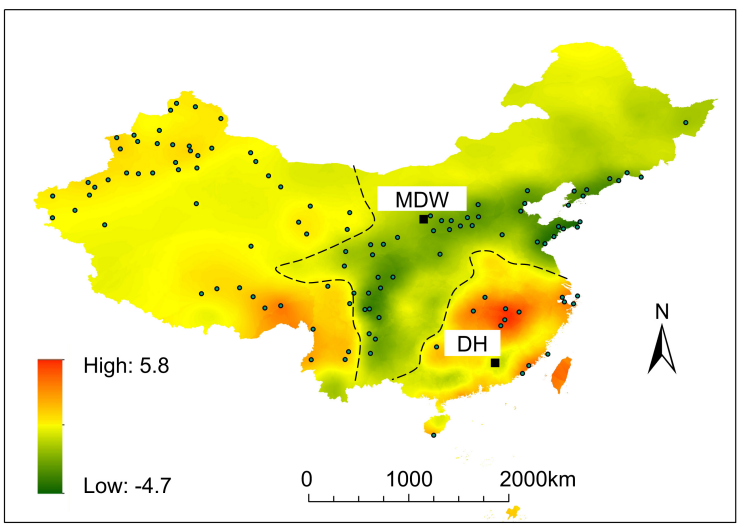

FIGURE 8 | Gridded trends of annual precipitation in China. Annual precipitation data of 591 meteorological observatories from 1960 to 2005 were obtained from the China Meteorological Data Service Center (CMDC). A linear trend of precipitation was calculated at each site, and only the 110 sites with a significant level of $p < 0.05$ were reserved. The Kriging interpolation method was applied to obtain the gridded precipitation trends.

explains the expansion of wetlands in the mid-Holocene. For the DH site, other proxies such as pollen concentration (Zhou et al., 2004), humification (Zhong et al., 2011), and biomarker records (Zhou et al., 2005; Zheng et al., 2009) agreed well with our findings.

Hydrology and Carbon Accumulation During the Holocene

The reconstructed hydrological conditions with carbon accumulation at these two sites show that carbon accumulations are generally controlled by regional hydrological conditions. The result rejects the first case in the aforementioned hypothesis, that carbon accumulation is anti-phased. However, it supports the second case in our hypothesis. We noticed that, in several periods, such as 9.5–8.5 cal. ka BP and 6–4 cal. ka BP, the carbon accumulation increased in both northern and southern East Asia (**Figure 7**), which matches well with the change of global peatlands coverage (Yu et al., 2010).

The period from 6 to 4 cal. ka BP was a unique period, during which precipitation in northern and southern East Asia showed an anti-phased spatial pattern. The environment in northern East Asia in this period was relatively humid, as indicated by our results in MDW and the proxy-based reconstruction from Lake Daihai (Sun et al., 2009), while in southern East Asia, the environment during the same period was relatively dry, as indicated by the hydrological reconstruction and other reports (Zhou et al., 2004, 2005; Xiao et al., 2007; Zheng et al., 2009; Zhong et al., 2010, 2011). This type of spatial pattern in precipitation in East Asia favored the development of wetlands during the mid-Holocene. The total area of global peatlands expanded in this period (Yu et al., 2010), which matches well with the peatland expansion in both the MDW and DH areas (**Figure 7**).

The results from this study filled a major knowledge gap regarding the seesaw pattern of hydrological changes in the northern and southern East Asia monsoonal (EAM) regions on the millennial time scale. As showed in **Figure 8**, the gridded linear trends in precipitation in China can be divided into three regions. The MDW and DH sites are located in regions with contrasting trends of precipitation. Intergrading the seesaw pattern of the East Asia monsoon on an orbital timescale (Shi et al., 2012), millennial time scale, and inter-decadal scale, we propose that the monsoon dynamics on different timescales might be similar. Thus, modern instrumental records can provide an analog for understanding the environmental processes in the past.

Spatial Pattern of Hydrology and Carbon Accumulation During the Mystery Interval (MI)

It is worthwhile to note that the variations in precipitation in northern and southern East Asia are synchronous during 16–14 cal. ka BP (**Figure 6**), which is different from the anti-phase pattern during the Holocene. This episode is known as the Mystery Interval (MI), a period with a series of enigmatic climate features from 17.5 to 14.5 cal. ka BP: temperatures in Greenland were lower than that during the Last Glacial Maximum as inferred by low $\delta^{18}O$ values, but the mountain glaciers in eastern Greenland, northern Europe, and North America retreated during this period (Williams et al., 2012; Zhang et al., 2014). Our results in the DH area show that the hydrological conditions during the MI varied from a high during 18 cal. ka BP to a low in 15 cal. ka BP, then returned to a higher level in 14 cal. ka BP, which is consistent with the two-phase pattern of northern hemisphere records (Broecker and Putnam, 2012). For the MDW site, the WL reached its peak at 14.5 cal. ka BP. The spatial pattern of hydrology, as inferred from these two sites during the MI, is itself a mystery. It shows an in-phase pattern, while during the Holocene there experienced an anti-phase pattern. The cause of this variation in spatial pattern during the MI remains unclear.

DATA AVAILABILITY STATEMENT

The raw data supporting the conclusions of this article will be made available by the authors, without undue reservation, to any qualified researcher.

AUTHOR CONTRIBUTIONS

XY conceived this study and performed the hydrological reconstruction. WJZ provided radiocarbon dating and TOC data. ZO calculated the modern precipitation trend. XY and JC prepared the manuscript. All authors participated in the discussion and edited the manuscript.

FUNDING

This work was supported by the National Key Research and Development Program of China (2016YFA0601902) and the MOST special fund for SKLLQG (LQ0703).

REFERENCES

Billett, M. F., Palmer, S. M., Hope, D., Deacon, C., Storeton-West, R., Hargreaves, K. J., et al. (2004). Linking land-atmosphere-stream carbon fluxes in a lowland peatland system. *Glob. Biogeochem. Cycles* 18:GB1024. doi: 10.1029/2003gb002058

Blodau, C. (2002). Carbon cycling in peatlands: a review of processes and controls. *Environ. Rev.* 10, 111–134. doi: 10.1139/a02-004

Broecker, W., and Putnam, A. E. (2012). How did the hydrologic cycle respond to the two-phase mystery interval? *Q. Sci. Rev.* 57, 17–25. doi: 10.1016/j.quascirev.2012.09.024

Chimner, R. A., Pypker, T. G., Hribljan, J. A., Moore, P. A., and Waddington, J. M. (2017). Multi-decadal changes in water table levels alter peatland carbon cycling. *Ecosystems* 20, 1042–1057. doi: 10.1007/s10021-016-0092-x

Frolking, S., and Crill, P. (1994). Climate controls on temporal variability of methane flux from a poor fen in southeastern New-Hampshire - measurement and modeling. *Glob. Biogeochem. Cycles* 8, 385–397. doi: 10.1029/94gb01839

Frolking, S., Roulet, N. T., Tuittila, E., Bubier, J. L., Quillet, A., Talbot, J., et al. (2010). A new model of Holocene peatland net primary production, decomposition, water balance, and peat accumulation. *Earth Syst. Dyn.* 1, 1–21. doi: 10.1111/gcb.12672

Holden, J. (2005). Peatland hydrology and carbon release: why small-scale process matters. *Philos. Trans. R. Soc. a Math. Phys. Eng. Sci.* 363, 2891–2913. doi: 10.1098/rsta.2005.1671

Hong, B., Hong, Y., Uchida, M., Shibata, Y., Cai, C., Peng, H., et al. (2014). Abrupt variations of Indian and East Asian summer monsoons during the last deglacial stadial and interstadial. *Q. Sci. Rev.* 97, 58–70. doi: 10.1016/j.quascirev.2014.05.006

Hong, B., Hong, Y. T., Lin, Q. H., Shibata, Y., Uchida, M., Zhu, Y. X., et al. (2010). Anti-phase oscillation of Asian monsoons during the Younger Dryas period: evidence from peat cellulose delta C-13 of Hani. Northeast China. *Palaeogeogr. Palaeoclimatol. Palaeoecol.* 297, 214–222. doi: 10.1016/j.palaeo.2010.08.004

Hong, Y. T., Hong, B., Lin, Q. H., Shibata, Y., Hirota, M., Zhu, Y. X., et al. (2005). Inverse phase oscillations between the East Asian and Indian Ocean summer monsoons during the last 12 000 years and paleo-El Nino. *Earth Planet. Sci. Lett.* 231, 337–346. doi: 10.1016/j.epsl.2004.12.025

Lazcano, C., Deol, A. S., Brummell, M. E., and Strack, M. (2020). Interactive effects of vegetation and water table depth on belowground C and N mobilization and greenhouse gas emissions in a restored peatland. *Plant Soil* 448, 299–313. doi: 10.1007/s11104-020-04434-4432

Leifeld, J., Wust-Galley, C., and Page, S. (2019). Intact and managed peatland soils as a source and sink of GHGs from 1850 to 2100. *Nat. Clim. Change* 9, 945–947. doi: 10.1038/s41558-019-0615-615

Li, X., Zhou, X., Zhang, H., Zhou, J., Shang, X., and Dodson, J. (2007). The record of cultivated rice from archaeobiotogical evidence in northwestern China 5000 years ago. *Chin. Sci. Bull.* 52, 1372–1378. doi: 10.1007/s11434-007-0186-180

Limpens, J., Berendse, F., Blodau, C., Canadell, J. G., Freeman, C., Holden, J., et al. (2008). Peatlands and the carbon cycle: from local processes to global implications - a synthesis. *Biogeosciences* 5, 1475–1491. doi: 10.5194/bg-5-1475-2008

Nijp, J. J., Metselaar, K., Limpens, J., Bartholomeus, H. M., Nilsson, M. B., Berendse, F., et al. (2019). High-resolution peat volume change in a northern peatland: spatial variability, main drivers, and impact on ecohydrology. *Ecohydrology* 12:e2114. doi: 10.1002/eco.2114

Olson, D. M., Griffis, T. J., Noormets, A., Kolka, R., and Chen, J. (2013). Interannual, seasonal, and retrospective analysis of the methane and carbon dioxide budgets of a temperate peatland. *J. Geophys. Res. Biogeosci.* 118, 226–238. doi: 10.1002/jgrg.20031

Page, S. E., Siegert, F., Rieley, J. O., Boehm, H. D. V., Jaya, A., and Limin, S. (2002). The amount of carbon released from peat and forest fires in Indonesia during 1997. *Nature* 420, 61–65. doi: 10.1038/nature01131

Porter, S. C., and Zhou, W. (2006). Synchronism of Holocene East Asian monsoon variations and North Atlantic drift-ice tracers. *Quternary Res.* 65, 443–449. doi: 10.1016/j.yqres.2006.01.007

Rennermalm, A. K., Nordbotten, J. M., and Wood, E. F. (2010). Hydrologic variability and its influence on long-term peat dynamics. *Water Resour. Res.* 46:W12546.

Rigney, C., Wilson, D., Renou-Wilson, F., Mueller, C., Moser, G., and Byrne, K. A. (2018). Greenhouse gas emissions from two rewetted peatlands previously managed for forestry. *Mires Peat* 21, 1–23. doi: 10.19189/MaP.2017.OMB.314

Shi, Z., Liu, X., and Cheng, X. (2012). Anti-phased response of northern and southern East Asian summer precipitation to ENSO modulation of orbital forcing. *Q. Sci. Rev.* 40, 30–38. doi: 10.1016/j.quascirev.2012.02.019

Strack, M., Waddington, J. M., Rochefort, L., and Tuittila, E. S. (2006). Response of vegetation and net ecosystem carbon dioxide exchange at different peatland microforms following water table drawdown. *J. Geophys. Res. Biogeosci.* 111:G02006. doi: 10.1029/2005jg000145

Stuiver, M., Reimer, P. J., and Braziunas, T. F. (1998). High-precision radiocarbon age calibration for terrestrial and marine samples. *Radiocarbon* 40, 1127–1151. doi: 10.1017/s0033822200019172

Sun, Q., Wang, S., Zhou, J., Shen, J., Cheng, P., Xie, X., et al. (2009). Lake surface fluctuations since the late glaciation at Lake Daihai, North central China: a direct indicator of hydrological process response to East Asian monsoon climate. *Q. Int.* 194, 45–54. doi: 10.1016/j.quaint.2008.01.006

Wang, B., Liu, J., Kim, H.-J., Webster, P. J., and Yim, S.-Y. (2012). Recent change of the global monsoon precipitation (1979-2008). *Clim. Dyn.* 39, 1123–1135. doi: 10.1007/s00382-011-1266-z

Williams, C., Flower, B. P., and Hastings, D. W. (2012). Seasonal Laurentide Ice Sheet melting during the "Mystery Interval" (17.5-14.5 ka). *Geology* 40, 955–958. doi: 10.1130/g33279.1

Xiao, J., Lue, H., Zhou, W., Zhao, Z., and Hao, R. (2007). Evolution of vegetation and climate since the last glacial maximum recorded at Dahu peat site, South China. *Sci. China Ser. D Earth Sci.* 50, 1209–1217. doi: 10.1007/s11430-007-0068-y

Xu, H., Goldsmith, Y., Lan, J., Tan, L., Wang, X., Zhou, X., et al. (2020). Juxtaposition of western Pacific subtropical high on Asian Summer Monsoon shapes subtropical East Asian precipitation. *Geophys. Res. Lett.* 47:e2019GL084705. doi: 10.1029/2019GL084705

Xue, J., Zhong, W., Zheng, Y., Ma, Q., Cai, Y., and Ouyang, J. (2009). A new high-resolution Late Glacial-Holocene climatic record from eastern Nanling Mountains in South China. *Chin. Geograph. Sci.* 19, 274–282. doi: 10.1007/s11769-009-0274-y

Yu, Z., Loisel, J., Brosseau, D. P., Beilman, D. W., and Hunt, S. J. (2010). Global peatland dynamics since the Last Glacial Maximum. *Geophys. Res. Lett.* 37:L13402. doi: 10.1029/2010gl043584

Zhang, W., Wu, J., Wang, Y., Wang, Y., Cheng, H., Kong, X., et al. (2014). A detailed East Asian monsoon history surrounding the 'Mystery Interval' derived from three Chinese speleothem records. *Q. Res.* 82, 154–163. doi: 10.1016/j.yqres.2014.01.010

Zheng, Y., Zhong, W., Xue, J., Fan, X., Zhen, Z., Liu, W., et al. (2008). Sedimentary characteristics of Dahu lacustrine swamp at Dingnan, Jiangxi Province, eastern Nanling Mountains. *J. South China Normal Univ.* 2008, 129–135.

Zheng, Y., Zhou, W., Xie, S., and Yu, X. (2009). A comparative study of n-alkane biomarker and pollen records: an example from southern China. *Chin. Sci. Bull.* 54, 1065–1072. doi: 10.1007/s11434-008-0563-3

Zhong, W., Ma, Q., Xue, J., Zheng, Y., Cai, Y., Ouyang, Y., et al. (2011). Humification degree as a proxy climatic record since the last deglaciation derived from a limnological sequence in South China. *Geochem. Int.* 49, 407–414. doi: 10.1134/s0016702911040094

Zhong, W., Xue, J., Zheng, Y., Ouyang, J., Ma, Q., Cai, Y., et al. (2010). Climatic changes since the last deglaciation inferred from a lacustrine sedimentary sequence in the eastern Nanling Mountains, south China. *J. Q. Sci.* 25, 975–984. doi: 10.1002/jqs.1384

Zhou, W. J., Donahue, D. J., Porter, S. C., Jull, T. A., Li, X. Q., Stuiver, M., et al. (1996). Variability of monsoon climate in East Asia at the end of the last glaciation. *Q. Res.* 46, 219–229. doi: 10.1006/qres.1996.0062

Zhou, W. J., Xie, S. C., Meyers, P. A., and Zheng, Y. H. (2005). Reconstruction of late glacial and Holocene climate evolution in southern China from geolipids and pollen in the Dingnan peat sequence. *Organ. Geochem.* 36, 1272–1284. doi: 10.1016/j.orggeochem.2005.04.005

Zhou, W. J., Yu, X. F., Jull, A. J. T., Burr, G., Xiao, J. Y., Lu, X. F., et al. (2004). High-resolution evidence from southern China of an early Holocene optimum and a mid-Holocene dry event during the past 18,000 years. *Q. Res.* 62, 39–48. doi: 10.1016/j.yqres.2004.05.004

Zoltai, S. C., Morrissey, L. A., Livingston, G. P., and De Groot, W. J. (1998). Effects of fires on carbon cycling in North American boreal peatlands. *Environ. Rev.* 6, 13–24. doi: 10.1139/a98-002

Conflict of Interest: The authors declare that the research was conducted in the absence of any commercial or financial relationships that could be construed as a potential conflict of interest.

Copyright © 2020 Yu, Chen, Zheng, Zhong, Ouyang and Zhou. This is an open-access article distributed under the terms of the Creative Commons Attribution License (CC BY). The use, distribution or reproduction in other forums is permitted, provided the original author(s) and the copyright owner(s) are credited and that the original publication in this journal is cited, in accordance with accepted academic practice. No use, distribution or reproduction is permitted which does not comply with these terms.

frontiers in Earth Science

ORIGINAL RESEARCH
published: 17 June 2020
doi: 10.3389/feart.2020.00221

Climate History of Southern Mongolia Since 17 ka: The Ostracod, Gastropod and Charophyte Record From Lake Ulaan

Steffen Mischke[1], Min Kyung Lee[2] and Yong Il Lee[3]*

[1] Institute of Earth Sciences, University of Iceland, Reykjavík, Iceland, [2] Korea Polar Research Institute, Incheon, South Korea, [3] School of Earth and Environmental Sciences, Seoul National University, Seoul, South Korea

Late glacial and Holocene environmental and climate change in the Gobi Desert is poorly understood due to the lack of appropriate geological archives and commonly faced difficulties in establishing reliable chronologies. Here, the relatively well-dated sediment record from the terminal Lake Ulaan (Ulaan Nuur) is used to reconstruct the lake history and climate in the region. Most abundant calcareous fossils in the lake sediments are ostracod (micro-crustacean) valves. The ostracod assemblage is dominated by *Limnocythere inopinata*, and generally very shallow conditions and sodium-dominated waters are inferred for Lake Ulaan. A single period of significantly increased silt accumulation in the late glacial was recorded at ca. 16 ka, probably as a result of melting glaciers in the uppermost reaches of the lake's main tributary, the Ongin River, and the influx of glacially ground, fine materials. Lake Ulaan had a higher salinity afterward during the Greenland Interstadial 1, and dry climate prevailed in the region. The lake level started to rise and the salinity decreased since ca. 12.3 ka, leading to the establishment of freshwater conditions in the early Holocene. Highest inflows and highest productivity in and around the lake, and wettest climate conditions in the region were recorded in the early Holocene. Lake conditions, most favorable for the aquatic fauna, culminated ca. 10 ka. Afterward, Lake Ulaan experienced a step-wise lake-level decline and salinity increase at ca. 9.4 and 6.8 ka. The further shrinkage of the lake and the approaching Ongin River mouth near the central part of the basin is recorded since ca. 3.2 ka.

Keywords: Central Asia, Gobi Desert, late glacial, Holocene, palaeoenvironment, micropalaeontology

OPEN ACCESS

Edited by:
Hai Xu,
Tianjin University, China

Reviewed by:
Liping Zhu,
Chinese Academy of Sciences, China
Hao Long,
Chinese Academy of Sciences, China

****Correspondence:***
Steffen Mischke
smi@hi.is

Specialty section:
This article was submitted to Quaternary Science, Geomorphology and Paleoenvironment, a section of the journal Frontiers in Earth Science

Received: *11 April 2020*
Accepted: *26 May 2020*
Published: *17 June 2020*

Citation:
Mischke S, Lee MK and Lee YI (2020) Climate History of Southern Mongolia Since 17 ka: The Ostracod, Gastropod and Charophyte Record From Lake Ulaan. Front. Earth Sci. 8:221. doi: 10.3389/feart.2020.00221

INTRODUCTION

The late glacial and Holocene climate conditions in Central Asia are intensively debated due to the aridity in most parts of the region and the resulting vulnerability of local ecosystems (Chen et al., 2008; Wang et al., 2010). Precipitation arrives in Central Asia with the landward-penetrating East Asian and Indian summer monsoons (EASM and ISM, respectively), and the westerlies. High pressure and dry air predominates over the cooling continental land mass in winter. Future climate change and rapidly increasing population in parts of Central Asia require a good understanding of the potential extent and rapidity or lag times of especially hydrological changes; and periods of rapid warming in the late glacial and Holocene may serve as analogs of future climate change. The

current understanding of the Holocene climate history in Central Asia is not sufficient, although 101 Holocene climate records were recently analyzed from arid Central Asia (ACA, here defined as Mongolia and Central Asia west of the 110th degree of longitude and north of the Tibetan Plateau and its foreland), from the Tibetan Plateau and from East Asia by Herzschuh et al. (2019). Deficiencies mostly result from the uneven spatial distribution of the available climate records, uncertainties of the established chronologies, and the partly poor sample resolution of records in general or at least for specific periods of the Holocene. The largest gap where climate records were not available in the study by Herzschuh et al. (2019) or those of earlier assessments by Chen et al. (2008) and Wang et al. (2010) remains in the central, southern and eastern parts of Mongolia, covering a distance of ca. 1500 km from west to east and of ca. 700 km from north to south. Holocene sediments from the lakes Ulaan, Bayan Tohomin Nuur (BTN), Tatsain Tsagaan Nuur (also written Taatsiin Tsagaan Nuur or Taatsïn Tsagaan Nuur; TTN), Orog Nuur (ON) and Uigi Nuur within this region were investigated in studies by Lee et al. (2011, 2013), Wang et al. (2011), Felauer et al. (2012) and Yu et al. (2017, 2019), but chronologies of these lake records are partly very poorly constrained (BTN and ON), or analyses remained cursory so far (TTN), did not include the early Holocene (Uigi Nuur) or focussed on the assessment of different dating techniques and the provenance of accumulated deposits and weathering conditions rather than the climate history (Lake Ulaan; **Figure 1**). To improve this situation, we investigated the calcareous fossils and additional proxies from the relatively well-dated ULB core from Lake Ulaan in southern Mongolia studied by Lee et al. (2011, 2013). Our aim is the reconstruction of climate conditions in the catchment of the lake in the late glacial and Holocene. In addition, we aim to reconstruct the lake ecosystem with a focus on its palaeo-salinity, and to compare the results to the remote-sensing-based inference of a large freshwater lake with a surface area of up to 19,000 km^2 and an estimated volume of 3150 km^3 that possibly existed in the basin in the past and that led to the assumption of a large freshwater aquifer in the region (Sternberg and Paillou, 2015). Sternberg and Paillou (2015, p. 26) concluded "Thus a fossil groundwater resource of unknown quality may still be present in the Ulaan Nuur depression and accessible using current drilling techniques."

Climate in the region of Lake Ulaan is arid with 127 mm mean annual precipitation (observation period 1982–2012) at the station Dalanzadgad 120 km to the southeast (Climate-Data.org; **Figure 1**). More than half of the precipitation falls during the summer months from June to August. However, precipitation is significantly higher in the upper catchment of the Khangai Mountains with ca. 300–400 mm per year, also mostly falling during summer. Mean January, July and annual temperatures in Dalanzadgad are −14.4, 21.2, and 4.6°C (Climate-Data.org).

Lake Ulaan is the easternmost of the Valley of the Gobi Lakes. It has a relatively large catchment area with the 435-km long Ongin River (also Ongi, Ongiin) as its main tributary (Suzuki, 2013; **Figure 1**). The upper catchment includes the southeastern ranges of the Khangai Mountains as the main source of generated runoff. Exposed bedrock in the southeastern Khangai Mountains mostly represents intensively deformed Devonian sedimentary rocks intruded by late Palaeozoic granitoids (Ganbat and Demberel, 2010). The region around Lake Ulaan is covered by Quaternary unconsolidated alluvial and aeolian sediments.

The lake was a relatively large, endorheic, permanent and generally shallow water body. The surface area of the lake was 65 km^2 in the 1960s or 175 km^2 after occasional heavy rains (Tserensodnom, 2000; Lee et al., 2011). Mean and maximum water depths were 0.9 and 1.6 m, respectively, after strong rains (Tserensodnom, 2000). Lake Ulaan was almost completely dry in 1952–1953 (Tserensodnom, 1971). It was a saline lake similar to most of the better known large lakes of the Gobi Valley (Dulma, 1979; Shvartsev et al., 2014; Lehmkuhl et al., 2018).

The lake shrank in the early 1990s when the main inflow of the lake dried as a result of intensely increased placer-gold mining in the middle reaches of Ongin River (Suzuki, 2013). The permanent lake is replaced by a playa since 1995 which is occasionally partly flooded after heavy rains (Beck et al., 2007; Holguín and Sternberg, 2018). Springs are located at the southern margin of the playa and marshy areas support the growth of reed and sedges (Holguín and Sternberg, 2018). Active and partially vegetated dunes are mostly located in the northwest and north of the playa (Lehmkuhl et al., 2018). Their alignment indicates prevailing winds from the northwest. Local vegetation is sparse and dominated by low shrubs and herbaceous plants (*Haloxylon, Kalidium, Salsola, Artemisia, Calligonum, Nitraria, Ephedra*; Murad, 2011).

MATERIALS AND METHODS

Summary of Previous Analyses

The 588-cm long core ULB was obtained from the southern part of Lake Ulaan (44.5139°N, 103.6544°E) in 2007. The core chronology was established based on optically stimulated luminescence (OSL; 12 samples) and radiocarbon dating (17 samples) by Lee et al. (2011). According to their work, the sediment core represents the lake history of the last 17 ka (Lee et al., 2013). The relatively high mean standard deviation of the twelve OSL-dating ages of 1 ka requires that inferred periods in the discussion below are viewed with caution. However, age data are discussed here with the same precision as was used by Lee et al. (2011, 2013) to ensure consistency and to allow useful comparisons. In addition to radiocarbon and OSL age data, grain-size data were presented by Lee et al. (2011). Major element, total organic carbon (TOC), and carbonate concentrations, and C/N ratios of sediments of the same core were investigated by Lee et al. (2013).

Measurements of Magnetic Susceptibility

For measurements of the magnetic susceptibility (MS), sediment cubes of 1 cm^3 volume were collected at 1-cm resolution (584 samples) from the core continuously without gaps, and measured using a Bartington MS2 system at the Korea Polar Research Institute.

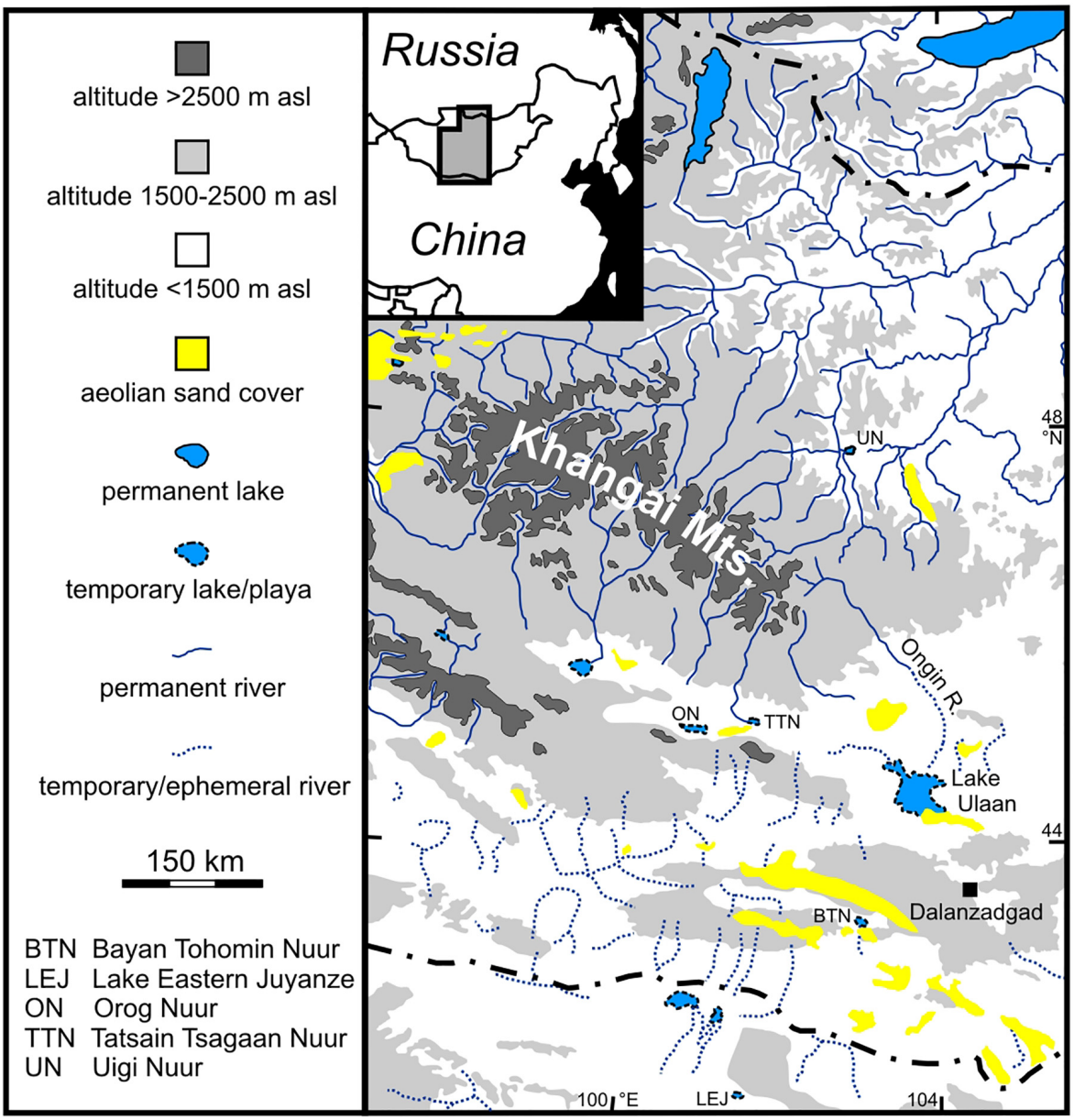

FIGURE 1 | Location of Lake Ulaan and its main tributary, the Ongin River, in Mongolia. Based on Lehmkuhl et al. (2018), modified.

Assessment of Aeolian Sand Contribution

A rough assessment of the potential contribution of aeolian sand to the sand fraction of the ULB core was conducted by the separation of the 180–250 μm fraction through wet sieving of ten selected samples with known high sand contents based on the initial grain-size analysis of Lee et al. (2011). The 180–250 μm fraction was selected as proxy for the aeolian sand contribution because mean grain sizes of aeolian sands of a dune field near ON (Nugin Els dune field) and in the Badain Jaran Desert in the southeast of Lake Eastern Juyanze (LEJ) are ca. 200 μm (Hempelmann, 2011; Dong et al., 2013). In addition, the aeolian end member of lake-surface sediments of five lakes in the southeastern part of the Badain Jaran Desert has grain-size frequency distribution curves with modes at a grain size of ca. 200 μm (Li et al., 2018).

Analyses of Fossils and Inference of Specific Conductivity

In total, 48 samples from core ULB were used for palaeontological analysis. On average, 15 g (8–32 g) of dry sediment was treated with a 3% solution of H_2O_2 for 48 hours. Afterward, sediment was washed through a set of sieves with 90, 250, and 1000 μm pore sizes, respectively.

Ostracod valves were picked from the sieve residues under an Olympus SZ 60 low-power binocular microscope. All valves were picked. Adult and juvenile valves were distinguished separately and identified according to Meisch (2000) and Fuhrmann (2012). A few well-preserved, left valves of adult *Ilyocypris* specimens were examined with a Zeiss Supra 40 VP Scanning Electron Microscope (SEM) at Freie Universität Berlin and identified as valves of *Ilyocypris* cf. *inermis* Kaufmann, 1900 and *Ilyocypris* cf. *bradyi* Sars, 1890 based on the marginal ripplets on the inner lamella (van Harten, 1979; Janz, 1994). Valves of *Ilyocypris* examined under the Olympus SZ 60 microscope were pooled in *I*. gr. *inermis*, probably representing the two identified taxa *I*. cf. *inermis* and *I*. cf. *bradyi*.

Shells of two gastropod taxa were recorded in the sediments of the core ULB. Shells of *Gyraulus*, probably belonging to *Gyraulus chinensis* (Dunker, 1848) or *Gyraulus terekholicus* (Prozorova et Starobogatov, 1997), were pooled in the group *G.* gr. *chinensis.* Shells of *Radix* are partly damaged, and exclusively represent juvenile specimens. Thus, they were assigned as *Radix* sp. In addition to ostracod valves and gastropod shells, charophyte remains were recorded.

Major changes in the distribution and abundance of fossils of the Ulaan-Nuur record were used to define six different zones of the core. Other proxies were considered in addition at zone boundaries with low temporal resolution of samples analyzed for fossils.

Past levels of specific conductivity (SC) were estimated as the mutual SC tolerance range for all taxa recorded in a specific sample. Published SC tolerance ranges of the ostracod taxa recorded at Lake Ulaan are based on calibration data sets of transfer functions of Van der Meeren et al. (2012) and Mischke et al. (2007, 2014; **Table 1**). *Gyraulus* and *Radix* are both regarded as freshwater gastropods. *G. chinensis* is the commonest species in Mongolia and it was recorded in Lake Airag which has a SC of 5.3 mS cm^{-1} regarded as upper SC tolerance limit here (Van der Meeren et al., 2012; Vinarski et al., 2017; **Table 1**). Members of the genus *Radix* such as *R. balthica* with wide distribution in Mongolia, can tolerate relatively brackish conditions with a maximum salinity of 14‰ (Jaeckel, 1962). The charophyte *Chara vulgaris* L. occurs in lakes and rivers in Mongolia, and cultivation experiments suggest an upper salinity limit of ca. 10‰ (Winter and Kirst, 1990; Romanov et al., 2014; **Table 1**). Reported salinity values were converted to SC using the conversion factor of 1.5 recommended by Hem (1982).

Assessment of Holocene Moisture Availability at Other, Previously Studied Locations

Available moisture during the Holocene was assessed for 89 pollen records from Central and East Asia based on quantitative precipitation reconstructions of Herzschuh et al. (2019). Reconstructed precipitation for the early, middle and late Holocene of each studied location was assigned to three categories: (1) dry, (2) moderate, and (3) wet. In addition to these 89 records, twelve relevant Holocene lake-sediment and speleothem records from northwestern China and Mongolia not included in the study of Herzschuh et al. (2019) were assessed using the same three categories.

RESULTS

The recorded MS values in the core ULB range from 4.8–36.1 $\times 10^{-5}$ SI with an average of 15.6 $\times 10^{-5}$ SI (**Figure 2**). The MS increases from the base to ca. 411 cm core depth (ca. 11.7 ka), decreases from 411 to ca. 355 cm (11.7–10.1 ka), remains close or slightly beneath average between 355 and 114 cm (10.1–3.2 ka) and is higher than average above 114 cm (<3.2 ka; **Figure 2**).

In total, 1559 ostracod valves were recorded in 40 samples from the core ULB (**Figure 3**). Eight samples did not contain ostracod valves. Most valves (1425) represent the species *Limnocythere inopinata* (Baird, 1843; **Figures 3**, **4**). *I.* gr. *inermis* was recorded with 97 valves, *Cypridopsis vidua* (Müller, 1776) with 22 valves, *Heterocypris salina* with nine valves and both, *Pseudocandona* sp. and *Sarscypridopsis aculeata* (Costa, 1847) with three valves, respectively. The majority of valves (ca. 85%) are those of juvenile specimens.

Gastropod shells of two different taxa were recovered from the sixth part of the samples: 42 shells of *G.* gr. *chinensis* were recorded in a total of seven samples, and twelve shells of *Radix* sp. were found in four samples.

In addition, 65 gyrogonites and four oospores of the charophyte *C. vulgaris* were recorded in a total of 19 sediment samples (**Figures 3**, **4**).

DISCUSSION

The MS Data and Their Relation to Grain Size and Other Proxies

The MS of lacustrine sediments is a proxy for the concentration of ferromagnetic iron oxides such as (titano)magnetite and maghemite and potentially for iron sulfides such as greigite (Hatfield et al., 2020). The MS data of the ULB core show relatively systematic trends within four core sections which are separated by rapid changes at 11.7 ka (411 cm), 10.1 ka (355 cm), and 3.2 ka (114 cm; **Figure 2**). The rapid changes and trends such as the continuous decrease from high values at 11.7 ka to the minimum at 10.1 ka are apparently not controlled by grain-size variations in the sediment core which change most rapidly at 15.2 ka (534 cm) and 11.1 ka (390 cm). In contrast, MS variations are apparently at least partly controlled by concentrations of $CaCO_3$ and TOC. The continuous MS decrease between 11.7 and 10.1 ka is accompanied by the strongest increase of the $CaCO_3$ and TOC concentrations showing that dilution effects due to the contribution of carbonate and organic matter (OM) are significant. Pearson correlation coefficients for MS and $CaCO_3$ or MS and TOC in this section of the core are −0.9 and −0.8, respectively. However, there is no correlation between these parameters or MS and mean grain size if the complete data set is considered (Pearson's *r* is 0.1, 0.3, and −0.3, respectively). Lee et al. (2013) demonstrated in their study of the provenance of the detrital sediments of the ULB core that their origin changed over

TABLE 1 | Published specific conductivity (SC) tolerance ranges (minima and maxima) for taxa recorded in the sediments of Lake Ulaan.

Taxon	SC min.	SC max.	*n*	References
Limnocythere inopinata	1.1	6.6	46	Van der Meeren et al., 2012
Ilyocypris cf. *bradyi**	0.4	0.9	13	Van der Meeren et al., 2012
Ilyocypris cf. *inermis*#	0.7	3.0	11	Van der Meeren et al., 2012
Heterocypris salina	0.7	6.3	85	Mischke et al., 2014
Pseudocandona	0.3	1.3	11	Van der Meeren et al., 2012
Sarscypridopsis aculeata	2.6	17.0	8	Mischke et al., 2007
Cypridopsis vidua	0.3	0.8	9	Van der Meeren et al., 2012
Gyraulus chinensis	0.0	5.3		Van der Meeren et al., 2012; Vinarski et al., 2017
Radix balthica	0.0	21.5		Jaeckel, 1962
Chara vulgaris	0.0	16.0		Winter and Kirst, 1990

*n is number of water bodies where remains of a specific taxon were recorded in surface-sediment sample calibration-data sets; max. SC for C. vulgaris was calculated from salinity value using a conversion factor of 1.5 (Hem, 1982); *I. cf. bradyi was pooled together with I. cf. mongolica; #I. cf. inermis was pooled together with I. cf. decipiens.*

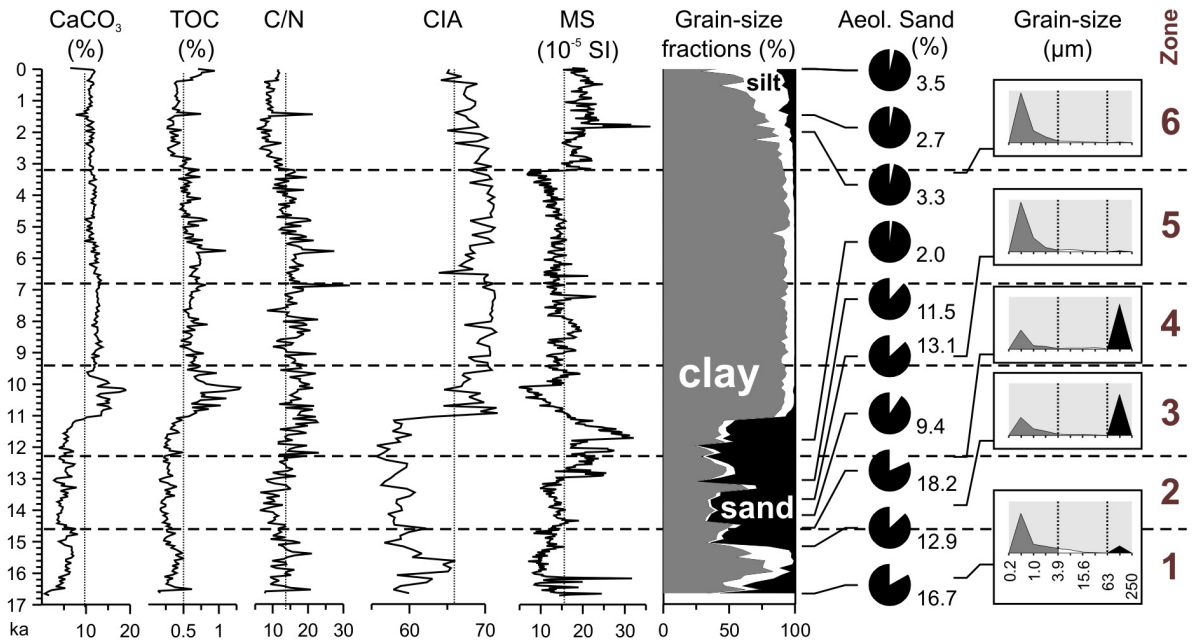

FIGURE 2 | Magnetic susceptibility (MS) of the ULB core in comparison to carbonate content, TOC concentration, C/N ratio, the CIA and grain-size data (Lee et al., 2011, 2013). Differences in the contribution of aeolian sand to the sand fraction of ten selected samples are estimated semi-quantitatively assuming that the grain-size fraction 180–250 μm mostly represents air-borne particles. Typical dune sand in the region has a mode at ca. 200 μm. The height of the gray boxes of the grain-size distributions at the right represents 70%. Zonation based on the fossil record (**Figure 3**).

time. Thus, the MS data are not easily interpreted as a proxy of a single controlling factor.

In comparison to other late glacial and Holocene lake sediments from the Valley of the Gobi Lakes or further south, the sediments from Lake Ulaan have significantly higher clay (73% on average for the entire core) and lower silt (11%) contents (**Figure 2**). For example, sediments from BTN ca. 110 km to the south-southwest, TTN ca. 190 km to the west-northwest, or ON ca. 240 km to the west-northwest, have significantly higher silt contents of ca. 65, 85, or 60%, respectively (Felauer et al., 2012; Yu et al., 2017; Lehmkuhl et al., 2018; **Figure 1**). However, the silty lake deposits from BTN have the main grain size mode at ca. 5 μm (i.e., very fine silt), close to the grain-size classification boundary between silt and clay at 3.9 μm (Felauer et al., 2012). Grain-size analysis was conducted at Lake Ulaan by wet sieving of the fraction coarser than 63 μm and using a Micromeritics Sedigraph 5100 device for the finer fraction. In contrast, a laser diffraction particle size analyzer was used for analyses of sediments from ON and BTN (Felauer et al., 2012; Yu et al., 2017). Wet sieving of the fraction >63 μm and the pipette method for the finer fraction were applied to sediments from TTN (Lehmkuhl et al., 2018). Comparative analyses of sediments for the application of the Sedigraph and the laser diffraction particle size analyzer revealed typically a ca. 20% higher clay content of sediments analyzed

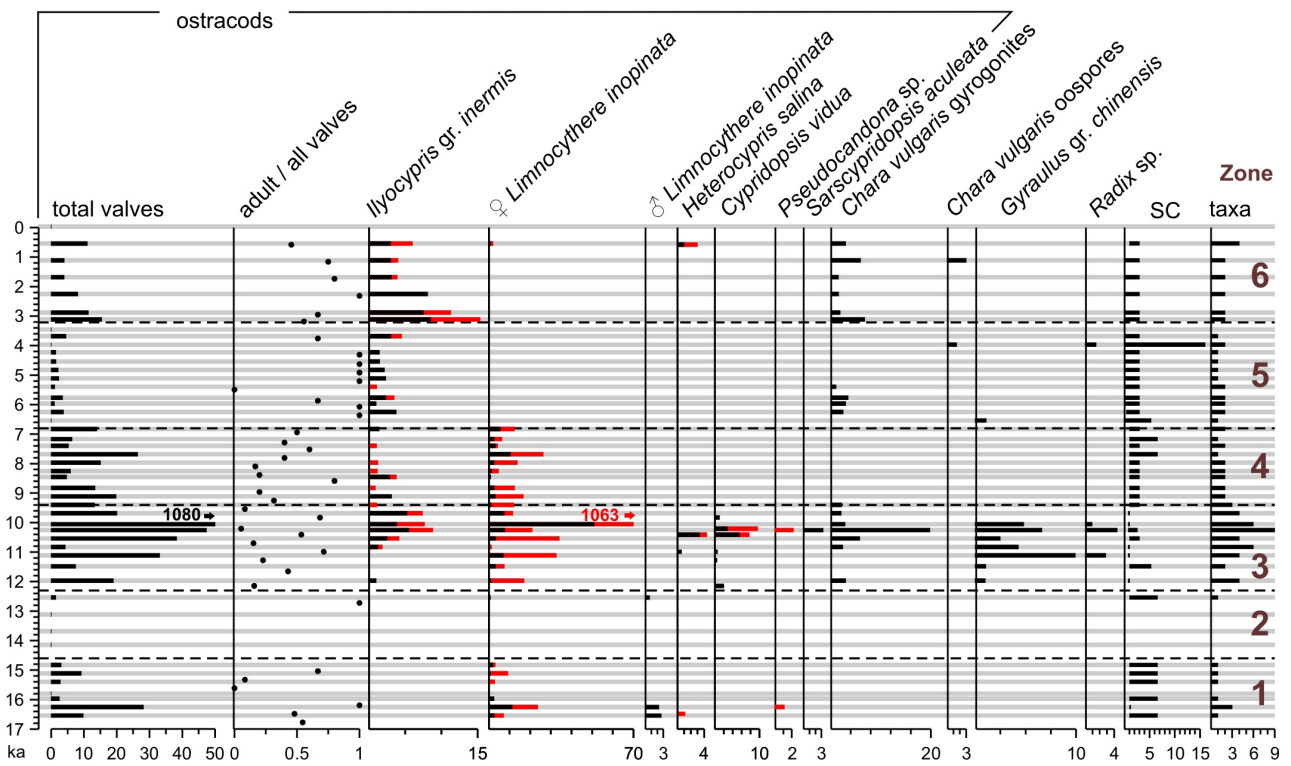

FIGURE 3 | The fossil record from Lake Ulaan. Absolute count data given for 15 g dry sediment material per sample. Black bars indicate adult ostracod valves and red bars show juvenile valves. Underlying gray bars mark positions of samples. Specific conductivity (SC) is estimated based on mutual ranges of known SC tolerance ranges of taxa recorded from individual samples (**Table 1**).

using a Sedigraph device at the expense of the silt fraction (Magno et al., 2017). Also the Sedigraph approach typically resulted in higher contents of fine materials in comparison to the pipette approach (Buchan et al., 1993; Müller et al., 2009). However, it remains unclear whether the high clay and low silt contents in the sediments of the ULB core in comparison to nearby Gobi-Desert lakes reflect methodological differences in grain-size analysis of generally very clay or very fine-silt-rich sediments, or possibly different particle-transport controls and different depositional settings.

The Ostracod Assemblage and Other Fossils From Lake Ulaan

Observed changes in the abundance of fossil remains in the ULB core were used to differentiate six distinct periods in the history of Lake Ulaan since 17 ka (**Figure 3**). The ostracod assemblage from Lake Ulaan is largely dominated by the species *L. inopinata*. The species was recorded as the most widely distributed ostracod taxon in modern lakes in western and central Mongolia where it was present in 46 of the investigated 56 lakes (Van der Meeren et al., 2012). A similar dominance of the species in late glacial and Holocene sediments was also observed at other Gobi-Desert lakes such as ON and Eastern Juyanze (ca. 330 km in the south-southwest; Mischke et al., 2002; Yu et al., 2019; **Figure 1**). In contrast, and unexpected considering its wide distribution and wide ecological tolerances, the species is completely absent from the fragmentary late glacial and Holocene ostracod record of BTN (Meisch, 2000; Felauer et al., 2012).

Valves of *I.* cf. *inermis* and *I.* cf. *bradyi* were recorded in the sediments of Lake Ulaan and also in the late Pleistocene deposits of ON (Yu et al., 2019). In addition, those of the probably more freshwater-restricted *I.* cf. *bradyi* were also found in the Holocene deposits of ON, of BTN and of LEJ (Mischke et al., 2002; Felauer et al., 2012). The species *C. vidua* and *H. salina* were both recorded in Lake Ulaan, the BTN and in LEJ. Valves of *Pseudocandona* sp. were recovered (partly as *P.* cf. *compressa* or *P. compressa*) from all four lakes including also ON. A few valves of *S. aculeata* were not only recorded in the sediments from Lake Ulaan but also in those of ON and LEJ.

In addition to ostracods, the gastropods *G.* gr. *chinensis* and *Radix* sp., and charophyte oospores and gyrogonites were recorded in Lake Ulaan. Shells of *Gyraulus* and *Radix*, and charophyte oospores were also reported from LEJ whilst similar remains were not recorded in the sediments of ON. A few gastropod shells and shell fragments were separated from the sediments of BTN but were not identified (unpublished data *S. Mischke*).

In contrast to the ostracod records from the other three Gobi-Desert lakes, valves of *Candona*, *Neglecandona*, and *Fabaeformiscandona*, and of the species *Darwinula stevensoni*

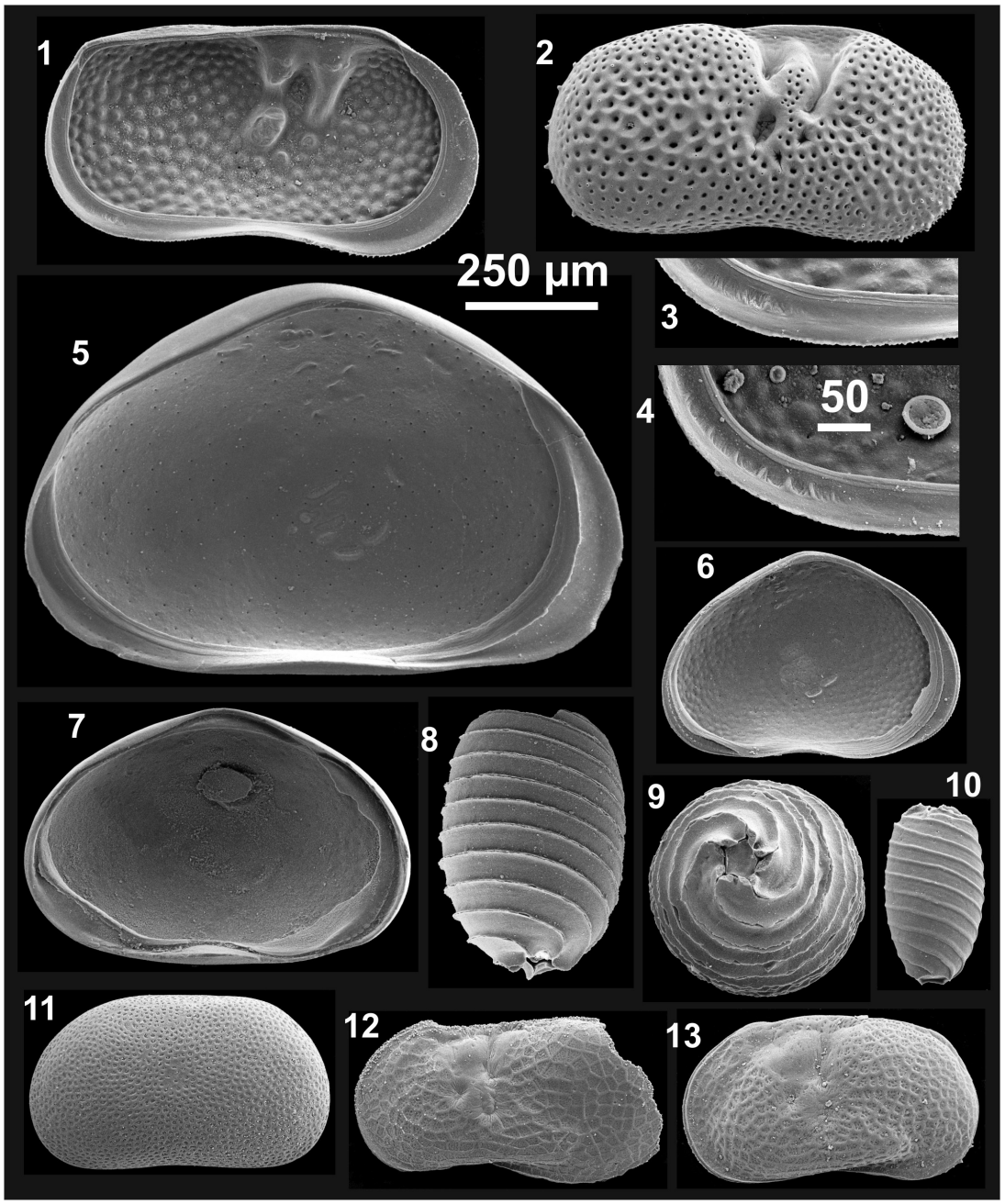

FIGURE 4 | Recorded fossils from Lake Ulaan. 1 *Ilyocypris* cf. *inermis* left valve (LV) internal view (iv); 2 *I.* gr. *inermis* right valve (RV) external view (ev); 3 *I.* cf. *inermis*, marginal ripplets on posteroventral part of inner lamella; 4 *Ilyocypris* cf. *bradyi*, marginal ripplets on posteroventral part of inner lamella; 5 *Heterocypris salina* LV iv; 6 *Sarscypridopsis aculeata* LV iv; 7 *Cypridopsis vidua* LV iv; 8–10 *Chara vulgaris*, 8 gyrogonite lateral view, 9 gyrogonite basal view, 10 oospore lateral view; 11 *Pseudocandona* sp. (juvenile) LV ev; 12, 13 *Limnocythere inopinata*, 12 ♂ LV ev, 13 ♀ LV ev. Scale bar is 250 µm apart for 3 and 4. Specimens housed at Institute of Geological Sciences of the Free University of Berlin (Germany).

were not recovered from the ULB core, possibly suggesting that Lake Ulaan was a permanent and relatively brackish lake which was not supporting taxa with freshwater to slightly brackish-water preferences. Among these taxa, only *D. stevensoni* reached high abundances in the Holocene sediments of one of the other three records – that from Eastern Juyanze. Van der Meeren et al. (2012) reported a maximum SC tolerance of ca. 0.6 mS cm^{-1} for *D. stevensoni* in Mongolia based on six water bodies where the species was recorded. Thus, the absence of valves of *D. stevensoni* from the sediments of the Lake-Ulaan record possibly implies that the water was never as fresh as 0.6 mS cm^{-1} during the late glacial and Holocene. However, the

species was observed to tolerate significantly higher salinities in other regions (Meisch, 2000).

The predominance of valves of *L. inopinata* (91% of all valves) in sediments of Lake Ulaan is comparable to almost monospecific assemblages of 16 lakes among 440 investigated modern lakes of the Tibetan Plateau and in Xinjiang, Inner Mongolia, Heilongjiang (all China) and Mongolia where the relative abundance of the species' valves in surface-sediment samples was exceeding 90% (Mischke et al., 2007; and additional unpublished data *S. Mischke*). Altitude, SC, concentration of dissolved oxygen and other key parameters of these 16 lakes cover large gradients whilst all 16 lakes have shallow water depths ranging from 0.08–2.10 m and high sodium-ion and low calcium-ion concentrations (42–99% and 0–27% of the cations, respectively) in common (unpublished data *S. Mischke*). Thus, the ostracod assemblage from Lake Ulaan implies that the lake was probably mostly shallow and waters were likely dominated by sodium due to evaporative concentration and removal of calcium by carbonate precipitation in a terminal lake. The inference of Holocene lake levels 44, 124, and 259 m above the present dry basin surface based on remote-sensing data of structures interpreted as palaeo-shorelines is not supported by the ostracod record from Lake Ulaan (Sternberg and Paillou, 2015). In contrast, lake levels of 2–3 m above the dry basin floor described by Lehmkuhl et al. (2018) for the most recent highstand until the 1960s are consistent with the predominance of *L. inopinata* and the mono-specific or almost mono-specific occurrence of the species' in very shallow modern lakes in Central Asia.

Late Glacial and Holocene History of Lake Ulaan

Zone 1: 17–14.6 ka (588–512 cm)

Apart from one sample, sediments of Zone 1 contain only ostracod valves of *L. inopinata*. Valves represent both juvenile and adult specimens, indicating that they probably not experienced post-mortem transport and re-deposition (**Figure 3**). Valves of *H. salina* and *Pseudocandona* sp. were recorded in one sample, with the former suggesting shallow, fluctuating, possibly temporary and slightly brackish conditions (Meisch, 2000). The low species diversity and dominance of *L. inopinata* suggests that Lake Ulaan was a very shallow lake with sodium-dominated water. Low TOC concentrations and C/N ratios of ca. 13 in Zone 1 indicate that bioproductivity in the lake was low and that OM mostly derived from lake productivity and not from terrestrial vegetation. The detrital sediment fraction shows a bimodal grain-size frequency distribution with similarly large clay and sand fractions near the base and top of Zone 1 (Lee et al., 2013; **Figure 2**). The clay fraction increases in the middle of the zone similar to the silt fraction, and both decrease in the upper part at the expense of the sand fraction. Ca. 17% of the sand fraction of a sample from the lower part of the zone is in the size range from 180 to 250 μm which encompasses the particle-size distribution mode of typical dune sand in the region, suggesting that a significant fraction of the sand was not transported to Lake Ulaan by the Ongin River but by wind (Hempelmann, 2011; Dong et al., 2013; Li et al., 2018). Lee et al. (2011) already argued that the accumulation of detrital sediments in Lake Ulaan was dominated by aeolian processes with the fine fraction representing locally derived dust and the coarse fraction representing aeolian sands. The fine fraction of Zone 1 was geochemically traced to originate from the Gobi Altai terrane by Lee et al. (2013). The increase of the clay but also of the silt fraction in the middle of the zone requires a different explanation. The parallel increase of clay and silt contents at ca. 16 ka can be possibly explained by two different processes: (1) the decrease of storm frequencies and wind strength, leading to a lower influx of aeolian sand in Lake Ulaan, or (2) a higher contribution of suspended sediments of runoff entering Lake Ulaan. The latter could have resulted from increased runoff in general, or from a higher suspension load of the Ongin River, possibly caused by a higher meltwater contribution to the drainage of the catchment. The last major late glacial glacier advances in the Khangai Mountains were dated to ca. 18–17 or 17–16 ka, and melting of glaciers and the release of glacially ground materials (i.e., rock flour, glacial milk) and subsequent transport and deposition in Lake Ulaan possibly caused the increase of the clay and silt fraction ca. 16 ka (Rother et al., 2014; Pötsch et al., 2015). Alternatively, fluvial sediment accumulation and lake-level changes or re-locations of the Ongin River delta in Lake Ulaan cannot explain the detrital sediment-accumulation change from the base to the middle of Zone 1, because an increasing lake level (or larger distance to the delta and shores) would result in a decreased accumulation of fluvial grains in comparison to air-borne particles at the core site. In contrast, a falling lake level (or closer delta position or distance to the shores) should lead to a decrease of the clay fraction and increase of fluvially transported silt and sand grains, accompanied by a higher influx of aeolian sands. Thus, accumulation of aeolian sand during storms, clay-sized dust particles following stormy days and during windy days, and suspended particles from the Ongin River better explains the observed grain-size pattern in the middle of Zone 1.

The weathering proxy CIA increases in the middle of Zone 1, obviously mirroring the significant grain-size changes and not necessarily tracing changes in weathering or climate conditions (**Figure 2**).

Zone 2: 14.6–12.3 ka (512–430 cm)

Ostracod valves are almost completely absent in Zone 2 (**Figure 3**). One sample from Zone 2 contains a few adult valves of *L. inopinata* which are not accompanied by juvenile valves, and it is not possible to rule out that these valves were not reworked from older deposits or transported by currents from other locations in the lake. The almost complete lack of organism remains could have resulted from (1) the desiccation of Lake Ulaan, (2) the establishment of hypoxic conditions, or (3) the increase of the salinity above the tolerance maxima of the lake dwellers. The relatively high clay content and low C/N ratios in Zone 2 show that Lake Ulaan was not dry and that fine-grained dust particles were trapped on the lake surface. The sand fraction is ca. 55% in the zone, and the fraction within the 180–250 μm range is relatively high, suggesting that the influx of aeolian sand was significant. The inference of hypoxic conditions and related enhanced OM preservation is not supported by the low

TOC concentrations in Zone 2. Thus, conditions were apparently too brackish to support a thriving ostracod population in Lake Ulaan. Based on upper tolerance boundaries of *L. inopinata*, *H. Salina*, and *Pseudocandona* sp., conductivities exceeded probably 7 mS cm^{-1} (equivalent to a salinity of 4.5‰; Hem, 1982; **Table 1**). Low $CaCO_3$ and TOC concentrations support the inference of more brackish conditions: relatively low inflows resulted in insignificant precipitation of authigenic carbonate from the water column, and relatively high salinity suppressed bioproductivity of the lake. Relatively brackish conditions of the lake may have resulted from arid climate conditions and low inflows and high evaporation due to the first significant late-glacial warming because sediments of Zone 2 accumulated more or less during the period of the Greenland Interstadial 1 (GI-1; 14.7–12.9 ka; Lowe et al., 2008). The lower and upper boundaries of Zone 2 are only poorly constrained due to a poor sample resolution for analysis of fossils and the relatively low sediment-accumulation rate with the two neighboring samples representing ages of 14.8 and 14.1 ka at the lower boundary or ages of 12.5 and 12.0 ka at the upper one, respectively. Low C/N ratios indicate that terrestrial vegetation around the lake was sparse, supporting the inference of arid climate conditions. C/N ratios slightly increase from the middle of Zone 2 toward the top. However, increasingly wetter climate toward to the zone's top is not indicated by the generally low CIA. MS values, increasing toward the zone's top, possibly also suggest sparse-vegetation cover and increasing soil erosion. The slight C/N ratio increase in the upper half of Zone 2 results probably from the establishment of a reed belt along the lake shore or enlargement of the reed belt rather than increasing density of terrestrial vegetation in the region. Reed was widely distributed in the marshy areas of the lake basin in 2015, and it is the taxon *Phragmites australis* which is widely distributed in the marshy areas of the Valley of the Gobi Lakes (Gunin et al., 1999; Orkhonselenge et al., 2018). Modern *P. australis* in northeastern China has a mean C/N ratio of 18, similar to C/N ratios near the top of Zone2, and typically higher values in southern China (Liu et al., 2015; Jia et al., 2018).

Zone 3: 12.3–9.4 ka (430–331 cm)

Ostracod valves reach relatively high numbers in Zone 3, and valves include both juvenile and adult specimens and are dominated by the former, suggesting that they represent autochthonous death assemblages which were not affected by post-mortem transport (**Figure 3**). The assemblage has a relatively high diversity with up to six species recorded from a single sample. The assemblage is dominated by *L. inopinata* with relative abundances of 75% on average. Valves of *I.* gr. *inermis* occur in all samples from the upper half of the zone. Shells of *G.* gr. *chinensis* and gyrogonites of *C. vulgaris* are relatively abundant too. *G. chinensis* is widely distributed in Mongolia today and common in a wide range of habitats including large mountain lakes, rivers, ponds, and pools (Glöer et al., 2014; Vinarski et al., 2017). It was recorded in fresh to slightly brackish waters in Mongolia (Van der Meeren et al., 2012; **Table 1**). However, SC estimates based on the mutual tolerance ranges of the taxa recorded in the sediments of Zone 3 suggest that Lake Ulaan was probably mostly a freshwater lake during the formation of Zone 3. The abundant charophyte remains indicate that the lake was relatively shallow and that the delta of the Ongin River was probably relatively distant to the core position, causing sufficient light penetration to the lake floor. According to the OSL-dating based age-depth relationship of Lee et al. (2011), sediment formation during Zone 3 is equivalent to the time of the second half of the Greenland Stadial 1 [GS-1 (Younger Dryas); 12.9–11.7 ka] and most of the early Holocene.

$CaCO_3$ and TOC concentrations remained relatively constant and low during the initial period of Zone 3 (i.e., the second half of GS-1), suggesting that inflows to the lake and productivity in its waters remained low. The CIA increased slightly during this period, starting at lowest values for the entire record. MS values fluctuated and reached a maximum near the end of the GS-1, probably resulting from further enhanced soil erosion. The inference of low inflows to Lake Ulaan and low productivity in the lake, and a decreasing salinity is consistent with colder temperatures and lower evaporation effects as would be expected for the time of the GS-1. The 180–250 μm fraction of sand in a sample from the top of the GS-1 is significantly smaller than the values determined for earlier periods showing that the influx of aeolian sand to Lake Ulaan was significantly reduced.

$CaCO_3$ and TOC concentrations show a slight increase in the initial period of the early Holocene before they increase more significantly and reach maximum values ca. 10 ka (**Figure 2**). Increasing runoff entering the lake and higher bioproductivity, probably as a result of warmer temperatures, are inferred. The MS values decrease constantly from the beginning of the Holocene to 10.1 ka probably as a result of decreasing soil erosion. C/N ratios of 18 on average, similar to the average ratios for *P. australis* in northeastern China today, suggest that a dense reed belt surrounded Lake Ulaan (Liu et al., 2015). Shells of *Radix* sp. first occurred during the early Holocene. The $CaCO_3$ and TOC maxima, the corresponding MS minimum and the highest diversity of fossil remains at ca. 10 ka probably represent the wettest and warmest conditions in the early Holocene in southern Mongolia. The TOC and $CaCO_3$ concentrations, the C/N ratios and ostracod valve abundances decrease abruptly after 10 ka, suggesting a return to less favorable conditions. Lee et al. (2011) explained the lowest difference between radiocarbon- and regressed OSL-dating results at 350 cm (ca. 10 ka) in the ULB core as result of the lowest influence of old reworked carbon and based their inference of most humid conditions on this observation. Thus, different lines of evidence (the fossil assemblage, the $CaCO_3$ and TOC maxima, the age difference between radiocarbon- and OSL-age data) suggest that wettest conditions occurred at Lake Ulaan ca. 10 ka.

The abrupt sedimentary change from bimodal clay- and sand-rich sediments to clayey sediments at ca. 11 ka is accompanied by a similarly abrupt change of the CIA, apparently reflecting grain-size changes rather than rapidly changing weathering conditions. In addition, it is accompanied by the occurrence of high numbers of *G.* gr. *chinensis* shells and the first occurrence of *Radix*

sp. in the record, but not by rapid changes of other proxies. Thus, a threshold mechanism apparently decreased the influx of sand-sized particles in Lake Ulaan, possibly related to habitat conditions for the gastropod fauna. We may speculate that the increasing lake size, possibly in conjunction with the enlargement of the reed belt upwind of the core location and in the delta region, largely reduced the accumulation of fluvial and aeolian sand at ca. 11 ka. Reed provides an important micro-habitat for gastropods, and the maximum in *G.* gr. *chinensis* shells at ca. 11 ka possibly reflects a significant increase in the spatial distribution and density of emergent vegetation in Lake Ulaan (Glöer and Pešić, 2007).

Zone 4: 9.4–6.8 ka (331–238 cm)

The lower number of ostracod valves and the reduced species diversity of only two taxa suggest that habitat conditions became less favorable during the formation of sediments of Zone 4. Charophyte remains are almost absent and gastropod shells were not recorded (**Figure 3**). Lower $CaCO_3$ and TOC concentrations point to reduced inflows and lower bioproductivity, and increased salinities in Lake Ulaan in the last third of the early and first half of the middle Holocene (**Figure 2**). Larger fluctuations of C/N ratios and generally higher MS values probably suggest sporadic influxes of terrestrial OM and increased soil erosion. The detrital particles remain dominated by the clay fraction. The CIA is high apart from three short-lived minima at ca. 9.2, 8.7, and 8.1 ka, indicating efficient weathering conditions. However, generally drier climate conditions and an increased salinity of Lake Ulaan in comparison to conditions during the previous zone are inferred for the period of Zone 4 based on the other proxies.

Zone 5: 6.8–3.2 ka (238–114 cm)

Very low ostracod-valve numbers and the predominance of valves of adult *Ilyocypris* specimens suggest that the ostracod assemblage of Zone 5 mostly or exclusively represents allochthonous specimens (**Figure 3**). *I. bradyi* commonly inhabits slowly flowing waters, and it is likely the case that the recorded valves of Zone 5 were transported to the core site by wave-driven currents (Meisch, 2000). The inferred absence of autochthonous ostracod valves in Zone 5 probably results from relatively brackish conditions in the lake with a salinity that exceeded the upper tolerance limits of commonly recorded taxa. The slightly decreasing C/N ratios probably suggest that OM from *Phragmites* or terrestrial vegetation contributed less to the OM accumulation at the core location. The CIA and MS values are more or less comparable to those of the previous zone (**Figure 2**).

Lehmkuhl et al. (2018) described a "smoothened beach ridge" at the position of their investigated UN1 section ca. 10 km northeast of the core location and ca. 13 m above the dry lake floor. They reported two middle Holocene radiocarbon and OSL ages for a humic silt and fine sand layer at 100 cm depth (4.4 ka) and fluvial sand at 160 cm (7.8 ka), respectively. They used the 1040-m altitude contour to estimate a middle Holocene lake extent of ca. 500 km^2 due to "missing well expressed shore lines" (Lehmkuhl et al., 2018). However, it is questionable that the beach-bar remnants were formed contemporaneously with the humic layer regarded as lacustrine sediment due to the layer's position 100 cm beneath the shoreline deposits. Instead, the 4.4-ka age of the humic layer represents the time when aquatic conditions, lacustrine or possibly spatially more restricted wetland conditions, existed at their section location. The 4.4-ka age should be further regarded as maximum age for the formation of the shoreline deposit on the surface of the UN1 section. However, the ULB-core record does not provide supporting evidence for a 13-m high lake level and generally wet conditions at 4.4 ka or afterward (see below).

Zone 6: 3.2 ka to Present (114–0 cm)

Ostracod-valve numbers are higher in Zone 6 again, and they represent both juvenile and adult valves (**Figure 3**). However, they almost exclusively originate from *I.* gr. *inermis* including valves of *I.* cf. *bradyi* which is regarded as a river- and stream-dwelling species. Apart from one sample including a few valves of *H. salina*, valves of other ostracod species were not recorded in Zone 6. Gastropod shells are also lacking, pointing to a relatively high salinity of Lake Ulaan. Gyrogonites of *C. vulgaris* were consistently recorded in the sediments of Zone 6, indicating that Lake Ulaan was relatively shallow and that the transparency of water was sufficient for macro-algae growth. *C. vulgaris* has an upper SC tolerance of 16 mS cm^{-1} (salinity of ca. 10.4‰; Hem, 1982; **Table 1**). The salinity of Lake Ulaan was probably close to the upper tolerance limit of *C. vulgaris* and we assume that the *I.* cf. *inermis* valves originate from the approaching Ongin River mouth. This scenario is supported by sedimentological evidence. The silt and sand fractions increase continuously at the expense of clay-sized particles from the lower zone boundary at 3.2 ka toward the top (**Figure 2**). The 180–250 μm fraction of the sand is constantly low, suggesting that the influx of aeolian sand was insignificant. Thus, the continuously increasing silt and sand proportions indicate a gradual decrease of the lake level, and the Ongin River mouth approaching the core position. The CIA decreases in Zone 6, probably reflecting the gradual grain-size increase rather than changing weathering conditions.

The initial decrease of the C/N ratios at the base of Zone 6 and mostly low ratios afterward suggest that OM production resulted mostly from phytoplankton growth. In contrast, *Phragmites* or terrestrial catchment vegetation did not contribute significantly to the OM accumulation in Lake Ulaan in the late Holocene. The MS values show an abrupt rise at 3.2 ka and increase slightly afterward, probably as a result of lower $CaCO_3$ and TOC concentrations at the zone base and increased soil erosion in the catchment of the lake. The inferred lake-level decrease since 3.2 and related lowering of the base level probably resulted in down-cutting of tributaries and soil erosion in the vicinity of Lake Ulaan.

The TOC concentrations are mostly low in the late Holocene due to low productivity in relatively saline lake waters and the poor preservation of OM in a shallow lake. The TOC concentrations increase significantly near the core top, starting ca. 350 years ago. The strong TOC concentration increase possibly reflects the onset of significant human impact due to

increasing livestock numbers in the lake's catchment and the related higher influx of nutrients in the lake. Human impacts on environments in Mongolia beyond the most recent decades were rarely addressed so far but charcoal records from western Mongolia were assessed and used to relate declining charcoal concentrations in lake sediments to increasing livestock numbers following the establishment of the Manchu rule in the late seventeenth century (Umbanhowar et al., 2009). Miehe et al. (2007) interpreted pollen data from the southern Gobi Altai (ca. 50 km southwest of Dalanzadgad; **Figure 1**) as proxy of drier climate conditions since ca. 1600 CE but they also speculated that the observed increase of *Artemisia*, *Potentilla*-type and Brassicaceae pollen resulted from increased animal husbandry.

Comparison With Regional Climate Records

Significantly less brackish conditions in Lake Ulaan, causing more or less freshwater conditions in the early Holocene, were first established at ca. 12.3 ka in the middle of GS-1. Wetter conditions during the GS-1 are typically not inferred from other climate records from Central Asia due to the assumption of generally cold and dry conditions in the region (Li et al., 2011; Goldsmith et al., 2017; Yu et al., 2019). Considering the assumed constant sediment accumulation rate (SAR) for the ULB core which is implied by the simple linear regression of the OSL age data used for the establishment of the age-depth relationship by Lee et al. (2011), the timing of the initiation of less brackish conditions in Lake Ulaan is possibly not well constrained. Assuming that the SAR changed over time and using linear interpolation between the two OSL ages below and above the boundary between Zones 2 and 3 results in a slightly earlier inferred establishment of less brackish conditions in Lake Ulaan at ca. 12.7 ka, almost contemporaneous with the beginning of the GS-1. Thus, different ways of age-data assessments support the inference that wetter conditions were established in Lake Ulaan's catchment sometime during the GS-1. This unexpected inference is supported by the reconstructed spread of steppe vegetation and onset of loess formation in the Qilian Mountains between 13 and 11 ka, and the reconstruction of increasing runoff and the initial establishment of the terminal Zhuyeze Lake at the southern margin of the Gobi Desert during GS-1 (Küster et al., 2006; Mischke et al., 2016). The lower temperatures and reduced evaporation during GS-1 may have caused a more positive water balance of some of the desert lakes in the Gobi region already before the onset of the Holocene given that the inferred less brackish conditions did not result from local hydrological peculiarities in the catchment areas. However, detailed studies of the local late glacial conditions and the transition to the Holocene are required to assess the climatic significance of the GS-1 in Central Asia.

Lowest salinities in Lake Ulaan in the early Holocene and inferred wettest conditions were also reconstructed for the majority of climate records in ACA (**Figure 5**). Contrary inferences such as one based on dating of aeolian deposits in the Tian Shan Mountains by Long et al. (2017) exist and testify that available moisture may have varied significantly on a local scale, that the presence and accumulation of aeolian sands could have resulted from the higher activity of fluvial systems during wetter periods as suggested by Nottebaum et al. (2015), and/or that our understanding of geological processes in response to past climate change is at least partly far from sufficient. However, wettest conditions in the early Holocene in ACA derived from most available pollen-based records correspond also to wettest conditions inferred from the northeastern part of the Tibetan Plateau whilst only few similar inferences originate from more central or southern positions (**Figure 5**). In addition, wettest conditions in the early Holocene were suggested only for few records from East Asia. Thus, an assumed more northern penetration of the EASM and ISM during the early Holocene alone cannot fully explain the observed pattern. Instead, a more northern position of the westerlies jet earlier in the year and/or a less zonal and rather SW-NE alignment of the jet over Central Asia possibly existed in the early Holocene due to stronger summer insolation as proposed by Herzschuh et al. (2019). As a result, the prolongation of the monsoonal period possibly caused the higher moisture availability in the northeastern part of the Tibetan Plateau. Whether the EASM penetrated to central Mongolia or even farther to the west cannot be assessed based on the available data. Mostly dry or moderately wet conditions reconstructed for East Asian locations in the early Holocene probably resulted from the EASM which traversed the region relatively rapidly (Kong et al., 2017; Herzschuh et al., 2019). Decreasing moisture availability was recorded at Lake Ulaan soon after 10 ka. A dry and cool climate event was recorded in coastal East Asia and the western tropical Pacific at 9.8 ka which possibly contributed to the climate deterioration in the catchment of Lake Ulaan after 10 ka (Stott et al., 2004; Park et al., 2019).

The transition from wetter conditions during Zone 3 to drier conditions of Zone 4 at 9.4 ka more or less coincides with the 9.2 ka event widely recorded in the Mediterranean region and the Middle East (Magny et al., 2013; Dean et al., 2015; Flohr et al., 2016). Thus, the termination of the wettest and warmest Holocene conditions in central and southern Mongolia was possibly triggered by colder conditions and less incoming moisture delivered by the westerlies. However, the most significant reduction in the EASM and an abrupt sea surface temperature decrease in the western tropical Pacific was also recorded at 9.2 ka, and we cannot rule out that monsoonal precipitation had reached the catchment of Lake Ulaan during the wettest conditions in the early Holocene but not afterward anymore (Stott et al., 2004; Zhang et al., 2018).

Moderately wet conditions in the middle Holocene were inferred from the record of Lake Ulaan and were also reconstructed for the majority (80%) of the records from ACA. Wettest conditions during the middle Holocene were proposed for about a third of the records from the Tibetan Plateau and half of the records from East Asia (**Figure 5**). The resulting moisture distribution pattern in the middle Holocene is consistent with a proposed southward-shifted, almost zonal alignment of the westerlies-jet-stream axis (Herzschuh et al., 2019). High monsoonal precipitation was apparently mostly confined to East Asia during the middle Holocene.

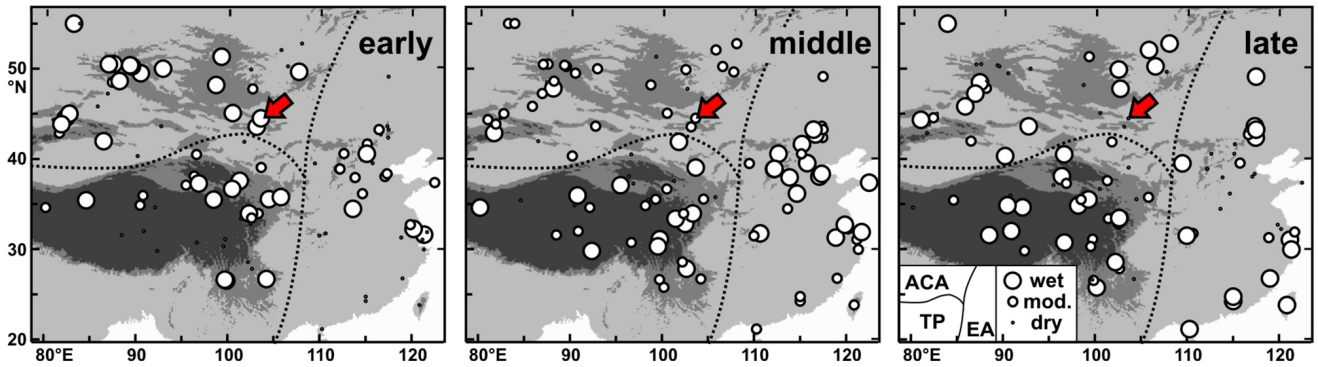

FIGURE 5 | Comparison of early, middle, and late Holocene moisture inferences (dry, moderate, or wet) for 101 records from arid Central Asia (ACA), the Tibetan Plateau (TP) and East Asia (EA). The majority (89) are pollen records examined by Herzschuh et al. (2019). In addition, 12 records from Bayan Tohomin Nuur (Felauer et al., 2012), Orog Nuur (Yu et al., 2019), Uigi Nuur (Wang et al., 2011), Hoton Nur (Rudaya and Li, 2013), the Nur *Sphagnum* Bog (Fukumoto et al., 2012), Wulungu Lake (Liu et al., 2008), the Yili Section (Li et al., 2011), the peat record BBP-13 (Xu et al., 2019), Kesang Cave (Cai et al., 2017), Zhuyeze Lake (Mischke et al., 2016), Lake Dali (Goldsmith et al., 2017), and this study (red arrow) are included.

The decline of Lake Ulaan's level and inferred dry climate conditions in its catchment in the late Holocene are supported by similar inferences from the nearby BTN and ON, and records from western Mongolia (Felauer et al., 2012; Yu et al., 2019; **Figure 5**). A series of closely spaced cold-dry events at 5.3, 4.7, 4.2, 3.7, 3.2, 2.8, and 2.4 ka was recorded in South Korea and the western tropical Pacific (Stott et al., 2004; Park et al., 2019). TOC concentrations and C/N ratios of the Lake-Ulaan record show coinciding decreases at 5.3, 4.7, 3.2, and especially 2.8 ka, and possibly suggest that cold-dry spells in the late part of the middle and first third of the late Holocene in East Asia contributed to the observed lake-level lowering and drier conditions in Lake Ulaan's catchment in the late Holocene. More precise age data are clearly required to discuss the occurrence of such short-lived climate events in more detail. However, significant aridification was also observed in the eastern Mediterranean ca. 3.5–2.8 ka which was possibly conveyed to Central and East Asia by the westerlies jet (Schilman et al., 2001; Kaniewski et al., 2008; Magny et al., 2013; Kagan et al., 2015). In contrast to the inference of dry conditions at Lake Ulaan in the late Holocene, wettest climate conditions were reconstructed at about a third of the locations investigated in ACA (**Figure 5**). In addition, wettest climate conditions in the late Holocene were also inferred from a third of the records from the Tibetan Plateau and slightly more than a third (38%) of the records in East Asia. The reconstructed moisture-distribution pattern in the late Holocene shows that locations where wettest Holocene conditions were reconstructed are more or less evenly spread over ACA, the Tibetan Plateau and East Asia. On a local scale, climate records where wettest and dry conditions were reconstructed occur more often next to each other in comparison to the early or middle Holocene. It could be argued that the insolation-driven later onset and shorter duration of the monsoon season and cooler conditions in the late Holocene caused not only less precipitation at higher latitudes but also reduced evaporation. Thus, the decrease of both precipitation and evaporation may have resulted in reduced effective moisture at one location if the former dominated or in higher effective moisture if the latter governed local conditions. Specific catchment conditions such as exposure of slopes, alignment of mountain ranges in relation to main wind directions, relative size of the upper reaches of a catchment, rock, soil, and vegetation types and related infiltration characteristics, extend of wetlands upstream or at the margins of a lake, etc., probably resulted in significant differences in effective moisture in neighboring regions. However, reconstructions based on proxy data and their assessment in comparison to results of atmospheric general circulation models are required to shed more light on the spatial distribution of effective moisture in the late Holocene in ACA, the Tibetan Plateau and East Asia.

CONCLUSION

Lee et al. (2011, 2013) had already suggested that the sediments of the ULB core mostly represent aeolian deposits. The re-assessment of the available grain-size data and additional examination of the 180–250 μm fraction showed that river-derived materials were accumulated predominantly during two different periods in Lake Ulaan. Silt-rich sediments which were accumulated ca. 16 ka in the lake likely derived from high meltwater discharge to the lake, generated from melting glaciers in the uppermost reaches of the Ongin River in the southeastern Khangai Mountains. A second major pulse of fluvial sediments is recorded near the top of the core where increasing silt and sand fractions at the expense of clay-sized particles point to the approaching Ongin River mouth as a result of the shrinkage of Lake Ulaan in the late Holocene.

Our study shows that the lake waters were apparently too brackish for a flourishing ostracod population during GI-1 and that the salinity decreased in the GS-1. This result is surprising, given that cold and dry conditions are typically inferred for the period of GS-1 in Central Asia (Wang et al., 2010). Future studies will show whether the inferred rising lake levels during GS-1 mostly resulted from reduced evaporation and increasing

moisture availability in the catchment or whether catchment-specific peculiarities independent of regional climate conditions affected the lake. However, our study shows also that wettest conditions were established soon afterward in the catchment of Lake Ulaan, leading to more or less freshwater conditions in the lake in the early Holocene.

The fossil assemblage from Lake Ulaan suggests optimal, freshest conditions in the lake at ca. 10 ka and a stepwise decline of the lake level starting soon afterward at 9.4 ka, and later in the middle and late Holocene at 6.8 and 3.2 ka. At least the former and latter lake-level drops where apparently triggered by global or at least regional aridification events.

Current occasional flooding of the modern playa probably contributes to freshwater discharge of the surficial local aquifer. However, the fossil record from the ULB core indicates that Lake Ulaan was mostly a brackish-water lake during the late glacial and Holocene, and that abundant freshwater resources beneath the ground cannot be expected in the region which was covered by the lake since ca. at least 17 ka.

Our study of the ULB core sediments cannot provide robust evidence for the assessment of proposed shorelines high above the current, dry lake floor (Sternberg and Paillou, 2015). Detailed, field-based mapping campaigns including the dating of shoreline features are required in addition to remote-sensing analysis to assess the extent and timing of Pleistocene or possibly even Holocene mega-lakes in this part of the Gobi Desert.

DATA AVAILABILITY STATEMENT

The raw data supporting the conclusions of this article will be made available by the authors, without undue reservation, to any qualified researcher.

AUTHOR CONTRIBUTIONS

YL designed the study. ML performed magnetic susceptibility measurements, treated sediment sub-samples for palaeontological analysis, and provided resulting sieve residues to SM who did the palaeontological analysis. SM wrote the original manuscript draft. All authors contributed to the revision of the text.

FUNDING

This work was partially supported by the Korea Polar Research Institute (Project PE20180).

ACKNOWLEDGMENTS

We thank LZ and HL who provided very constructive suggestions for the improvement of the original manuscript.

REFERENCES

Beck, L., Mendel, T., and Thindwa, J. (2007). *The Enabling Environment for Social Accountability in Mongolia*. Washington, DC: World Bank.

Buchan, G. D., Grewal, K. S., Claydon, J. J., and McPherson, R. J. (1993). A comparison of Sedigraph and Pipette methods for soil particle-size analysis. *Aust. J. Soil Res.* 31, 407–417.

Cai, Y., Chiang, J. C. H., Breitenbach, S. F. M., Tan, L., Cheng, H., Edwards, R. L., et al. (2017). Holocene moisture changes in western China, Central Asia, inferred from stalagmites. *Quat. Sci. Rev.* 158, 15–28. doi: 10.1016/j.quascirev.2016.12.014

Chen, F., Yu, Z., Yang, M., Ito, E., Wang, S., Madsen, D. B., et al. (2008). Holocene moisture evolution in arid central Asia and its out-of-phase relationship with Asian monsoon history. *Quat. Sci. Rev.* 27, 351–364. doi: 10.1016/j.quascirev.2007.10.017

Dean, J. R., Jones, M. D., Leng, M. J., Noble, S. R., Metcalfe, S. E., Sloane, H. J., et al. (2015). Eastern Mediterranean hydroclimate over the late glacial and Holocene, reconstructed from the sediments of Nar lake, central Turkey, using stable isotopes and carbonate mineralogy. *Quat. Sci. Rev.* 124, 162–174. doi: 10.1016/j.quascirev.2015.07.023

Dong, Z., Qian, G., Lv, P., and Hu, G. (2013). Investigation of the sand sea with the tallest dunes on Earth: China's Badain Jaran Sand Sea. *Earth Sci. Rev.* 120, 20–39. doi: 10.1016/j.earscirev.2013.02.003

Dulma, A. (1979). Hydrobiological outline of the Mongolian lakes. *Int. Rev. Gesamten Hydrobiol.* 64, 709–736. doi: 10.1002/iroh.19790640602

Felauer, T., Schlütz, F., Murad, W., Mischke, S., and Lehmkuhl, F. (2012). Late Quaternary climate and landscape evolution in arid Central Asia: a multiproxy study of lake archive Bayan Tohomin Nuur, Gobi desert, southern Mongolia. *J. Asian Earth Sci.* 48, 125–135. doi: 10.1016/j.jseaes.2011.12.002

Flohr, P., Fleitmann, D., Matthews, R., Matthews, W., and Black, S. (2016). Evidence of resilience to past climate change in Southwest Asia: early farming communities and the 9.2 and 8.2 ka events. *Quat. Sci. Rev.* 136, 23–39. doi: 10.1016/j.quascirev.2015.06.022

Fuhrmann, R. (2012). Atlas quartärer und rezenter Ostrakoden Mitteldeutschlands. *Altenburger Naturwissenschaftliche Forschungen* 15, 1–320.

Fukumoto, Y., Kashima, K., Orkhonselenge, A., and Ganzorig, U. (2012). Holocene environmental changes in northern Mongolia inferred from diatom and pollen records of peat sediment. *Quat. Int.* 254, 83–91. doi: 10.1016/j.quaint.2011.10.014

Ganbat, E., and Demberel, O. (2010). "Geologic background of the Hangay geothermal system, west-central Mongolia," in *Proceedings of the World Geothermal Congress*, Bali, 1–6.

Glöer, P., Boeters, H. D., and Pešić, V. (2014). Freshwater molluscs of Kyrgyzstan with description of one new genus and species (Mollusca: Gastropoda). *Folia Malacol.* 22, 73–81. doi: 10.12657/folmal.022.009

Glöer, P., and Pešić, V. (2007). *Gyraulus meierbrooki*, *G. ioanis*, and *G. shasi* – three new *Gyraulus* spp. from the Skadar Lake Basin, Montenegro (Gastropoda: Planorbidae). *Mollusca* 25, 131–137.

Goldsmith, Y., Broecker, W. S., Xu, H., Polissar, P. J., de Menocal, P. B., Porat, N., et al. (2017). Northward extent of East Asian monsoon covaries with intensity on orbital and millennial timescales. *Proc. Nat. Acad. Sci. U.S.A.* 114, 1817–1821. doi: 10.1073/pnas.1616708114

Gunin, P. D., Vostokova, E. A., Dorofeyuk, N. I., Tarasov, P. E., and Black, C. C. (1999). *Vegetation Dynamics of Mongolia*. Dordrecht: Springer.

Hatfield, R. G., Woods, A., Lehmann, S. B., Weidhaas, N., Chen, C. Y., Kück, J., et al. (2020). Stratigraphic correlation and splice generation for sediments recovered from a large-lake drilling project: an example from Lake Junín. *Peru. J. Paleolimnol.* 63, 83–100. doi: 10.1007/s10933-019-00098-w

Hem, J. D. (1982). "Conductance: a collective measure of dissolved ions," in *Water Analysis, Inorganic Species*, Vol. 1, Part 1, eds R. A. Minear and L. H. Keith (Cambridge, MA: Academic Press), 137–161. doi: 10.1016/b978-0-12-498301-4.50009-8

Hempelmann, N. (2011). *Aeolian Geomorphodynamics in Endorheic Basins of the Mongolian Gobi Desert*. Ph.D. thesis, University Mainz, Mainz.

Herzschuh, U., Cao, X., Laepple, T., Dallmeyer, A., Telford, R. J., Ni, J., et al. (2019). Position and orientation of the westerly jet determined Holocene rainfall patterns in China. *Nat. Commun.* 10:2376.

Holguín, L. R., and Sternberg, T. (2018). A GIS based approach to Holocene hydrology and social connectivity in the Gobi Desert. Mongolia. *Archaeol. Res. Asia* 15, 137–145. doi: 10.1016/j.ara.2016.12.001

Jaeckel, S. G. A. (1962). "Ergänzungen und Berichtigungen zum rezenten und quartären Vorkommen der mitteleuropäischen Mollusken," in *Die Tierwelt Mitteleuropas, 2: Weichtiere – Mollusca*, eds P. Brohmer, P. Ehrmann, and P. Ulmer (Leipzig: Quelle & Meyer), 225–294.

Janz, H. (1994). Zur Bedeutung des Schalenmerkmals, Marginalrippen' der Gattung *Ilyocypris* (Ostracoda, Crustacea). *Stuttgarter Beiträge zur Naturkunde Ser. B* 206, 1–19.

Jia, J., Bai, J., Wang, W., Zhang, G., Wang, X., Zhao, Q., et al. (2018). Changes of biogenic elements in *Phragmites australis* and *Suaeda salsa* from salt marshes in Yellow River Delta, China. *Chin. Geogr. Sci.* 28, 411–419. doi: 10.1007/s11769-018-0959-1

Kagan, E. J., Langgut, D., Boaretto, E., Neumann, F. H., and Stein, M. (2015). Dead Sea levels during the Bronze and Iron ages. *Radiocarbon* 57, 237–252. doi: 10.2458/azu_rc.57.18560

Kaniewski, D., Paulissen, E., van Campo, E., Al-Maqdissi, M., Bretschneider, J., and Van Lerberghe, K. (2008). Middle East coastal ecosystem response to middle-to-Late-Holocene abrupt climate changes. *Proc. Natl. Acad. Sci. U.S.A.* 105, 13941–13946. doi: 10.1073/pnas.0803533105

Kong, W., Swenson, L. M., and Chiang, J. C. H. (2017). Seasonal transitions and the westerly jet in the Holocene East Asian summer monsoon. *J. Clim.* 30, 3343–3365. doi: 10.1175/jcli-d-16-0087.1

Küster, Y., Hetzel, R., Krbetschek, M., and Tao, M. (2006). Holocene loess sedimentation along the Qilian Shan (China): Significance for understanding the processes and timing of loess deposition. *Quat. Sci. Rev.* 25, 114–125. doi: 10.1016/j.quascirev.2005.03.003

Lee, M. K., Lee, Y. I., Lim, H. S., Lee, J. I., Choi, J. H., and Yoon, H. I. (2011). Comparison of radiocarbon and OSL dating methods for a Late Quaternary sediment core from Lake Ulaan, Mongolia. *J. Paleolimnol.* 45, 127–135. doi: 10.1007/s10933-010-9484-7

Lee, M. K., Lee, Y. I., Lim, H. S., Lee, J. I., and Yoon, H. I. (2013). Late Pleistocene-Holocene records from Lake Ulaan, Southern Mongolia: implications for east Asian palaeomonsoonal climate changes. *J. Quat. Sci.* 28, 370–378. doi: 10.1002/jqs.2626

Lehmkuhl, F., Grunert, J., Hülle, D., Batkhishig, O., and Stauch, G. (2018). Paleolakes in the Gobi region of southern Mongolia. *Quat. Sci. Rev.* 179, 1–23. doi: 10.1016/j.quascirev.2017.10.035

Li, X., Zhao, K., Dodson, J., and Zhou, X. (2011). Moisture dynamics in central Asia for the last 15 kyr: new evidence from Yili Valley, Xinjiang, NW China. *Quat. Sci. Rev.* 30, 3457–3466. doi: 10.1016/j.quascirev.2011.09.010

Li, Z., Wei, Z., Dong, S., and Chen, Q. (2018). The paleoenvironmental significance of spatial distributions of grain size in groundwater-recharged lakes: a case study in the hinterland of the Badain Jaran Desert, northwest China. *Earth Surf. Process. Landforms* 43, 363–372. doi: 10.1002/esp.4248

Liu, X., Herzschuh, U., Shen, J., Jiang, Q., and Xiao, X. (2008). Holocene environmental and climatic changes inferred from Wulungu Lake in northern Xinjiang, China. *Quat. Res.* 70, 412–425. doi: 10.1016/j.yqres.2008.06.005

Liu, Y., Jiang, M., Lu, X., Zhang, Z., and Lou, Y. (2015). Leaf carbon, nitrogen and phosphorus stoichiometry of *Phragmites australis* in northeastern China. *Fresenius Env. Bull.* 24, 4711–4719.

Long, H., Shen, J., Chen, J., Tsukamoto, S., Yang, L., Cheng, H., et al. (2017). Holocene moisture variations over the semiarid-arid central Asia revealed by a comprehensive sand-dune record from the central Tian Shan, NW China. *Quat. Sci. Rev.* 174, 13–32. doi: 10.1016/j.quascirev.2017.08.024

Lowe, J. J., Rasmussen, S. O., Björck, S., Hoek, W. Z., Steffensen, J. P., Walker, M. J. C., et al. (2008). Synchronisation of palaeoenvironmental events in the North Atlantic region during the Last Termination: a revised protocol recommended by the INTIMATE group. *Quat. Sci. Rev.* 27, 6–17. doi: 10.1016/j.quascirev.2007.09.016

Magno, M. C., Venti, F., Gaglianone, G., Pierfranceschi, G., and Romano, E. (2017). "Grain size analysis: a comparison between laser granulometer and sedigraph," in *Proceedings of the IMEKO Int. Conf. Metrology for the Sea*, Naples, 210–214.

Magny, M., Combourieu Nebout, N., De Beaulieu, J. L., Bout-Roumazeilles, V., Colombaroli, D., Desprat, S., et al. (2013). North–south palaeohydrological contrasts in the central Mediterranean during the Holocene: tentative synthesis and working hypotheses. *Clim. Past.* 9, 2043–2071. doi: 10.5194/cp-9-2043-2013

Meisch, C. (2000). *Freshwater Ostracoda of Western and Central Europe*. Heidelberg: Spektrum.

Miehe, G., Schlütz, F., Miehe, S., Opgenoorth, L., Cermak, J., Samiya, R., et al. (2007). Mountain forest islands and Holocene environmental changes in Central Asia: a case study from the southern Gobi Altay, Mongolia. *Palaeogeogr. Palaeoclimatol. Palaeoecol.* 250, 150–166. doi: 10.1016/j.palaeo.2007.03.022

Mischke, S., Almogi-Labin, A., Al-Saqarat, B., Rosenfeld, A., Elyashiv, H., Boomer, I., et al. (2014). An expanded ostracod-based conductivity transfer function for climate reconstruction in the Levant. *Quat. Sci. Rev.* 93, 91–105. doi: 10.1016/j.quascirev.2014.04.004

Mischke, S., Fuchs, D., Riedel, F., and Schudack, M. E. (2002). Mid to Late Holocene palaeoenvironment of Lake Eastern Juyanze (north-western China) based on ostracods and stable isotopes. *Geobios* 35, 99–110. doi: 10.1016/s0016-6995(02)00013-x

Mischke, S., Herzschuh, U., Massmann, G., and Zhang, C. (2007). An ostracod-conductivity transfer-function for Tibetan lakes. *J. Paleolimnol.* 38, 509–524. doi: 10.1007/s10933-006-9087-5

Mischke, S., Lai, Z., Long, H., and Tian, F. (2016). Holocene climate and landscape change in the northeastern Tibetan Plateau foreland inferred from the Zhuyeze Lake record. *Holocene* 26, 643–654. doi: 10.1177/0959683615612570

Müller, H.-W., Dohrmann, R., Klosa, D., Rehder, S., and Eckelmann, W. (2009). Comparison of two procedures for particle-size analysis: köhn pipette and X-ray granulometry. *J. Plant Nutr. Soi Sci.* 172, 172–179. doi: 10.1002/jpln.200800065

Murad, W. (2011). *Late Quaternary Vegetation History and Climate Change in the Gobi Desert, South Mongolia*. Ph.D. thesis, Georg-August-Universität Göttingen, Göttingen.

Nottebaum, V., Lehmkuhl, F., Stauch, G., Lu, H., and Yi, S. (2015). Late Quaternary aeolian sand deposition sustained by fluvial reworking and sediment supply in the Hexi Corridor - An example from northern Chinese drylands. *Geomorphology* 250, 113–127. doi: 10.1016/j.geomorph.2015.08.014

Orkhonselenge, A., Komatsu, G., and Uuganzaya, M. (2018). Middle to late Holocene sedimentation dynamics and paleoclimate conditions in the Lake Ulaan basin, southern Mongolia. *Géomorphologie* 24, 351–363. doi: 10.4000/geomorphologie.12219

Park, J., Park, J., Yi, S., Cheul Kim, J., Lee, E., and Choi, J. (2019). Abrupt Holocene climate shifts in coastal East Asia, including the 8.2 ka, 4.2 ka, and 2.8 ka BP events, and societal responses on the Korean peninsula. *Sci. Rep.* 9:10806.

Pötsch, S., Rother, H., Lorenz, S., Walther, M., and Lehmkuhl, F. (2015). Timing of late Pleistocene glaciation in Mongolia: surface exposure dating reveals a differentiated pattern of glacial forcing. *Geophys. Res. Abstr.* 17:EGU2015-4815.

Romanov, R. E., Zhakova, L. V., Bazarova, B. B., and Kipriyanova, L. M. (2014). The charophytes (Charales, Charophyceae) of Mongolia: a checklist and synopsis of localities, including new records. *Nova Hedwigia* 98, 127–150. doi: 10.1127/0029-5035/2013/0134

Rother, H., Lehmkuhl, F., Fink, D., and Nottebaum, V. (2014). Surface exposure dating reveals MIS-3 glacial maximum in the Khangai Mountains of Mongolia. *Quat. Res.* 82, 297–308. doi: 10.1016/j.yqres.2014.04.006

Rudaya, N., and Li, H.-C. (2013). A new approach for reconstruction of the Holocene climate in the Mongolian Altai: the high-resolution $\delta^{13}C$ records of TOC and pollen complexes in Hoton-Nur Lake sediments. *J. Asian Earth Sci.* 69, 185–195. doi: 10.1016/j.jseaes.2012.12.002

Schilman, B., Bar-Matthews, M., Almogi-Labin, A., and Luz, B. (2001). Global climate instability reflected by eastern Mediterranean marine records during the late Holocene. *Palaeogeogr. Palaeoclimatol. Palaeoecol.* 176, 157–176. doi: 10.1016/s0031-0182(01)00336-4

Shvartsev, S., Kolpakova, M. N., Isupov, V. P., Vladimirov, A. G., and Ariunbileg, S. (2014). Geochemistry and chemical evolution of saline lakes of Western Mongolia. *Geochem. Int.* 52, 388–403. doi: 10.1134/s0016702914030070

Sternberg, T., and Paillou, P. (2015). Mapping potential shallow groundwater in the Gobi Desert using remote sensing: Lake Ulaan Nuur. *J. Arid Env.* 118, 21–27. doi: 10.1016/j.jaridenv.2015.02.020

Stott, L., Cannariato, K., Thunell, R., Haug, G. H., Koutavas, A., and Lund, S. (2004). Decline of surface temperature and salinity in the western tropical

Pacific Ocean in the Holocene epoch. *Nature* 431, 56–59. doi: 10.1038/nature02903

Suzuki, Y. (2013). "Conflict between mining development and nomadism in Mongolia," in *The Mongolian Ecosystem Network*, eds N. Yamamura, N. Fujita, and A. Maekawa (Cham: Springer), 269–294. doi: 10.1007/978-4-431-54052-6_20

Tserensodnom, J. (1971). *Lakes of Mongolia*. Ulaanbaatar: State Publishing.

Tserensodnom, J. (2000). *A Catalog of Lakes in Mongolia*. Ulaanbaatar: Shuvuum Saaral Publishing.

Umbanhowar, C. E., Shinneman, A. L. C., Tserenkhand, G., Hammon, E. R., Lor, P., and Nail, K. (2009). Regional fire history based on charcoal analysis of sediments from nine lakes in western Mongolia. *Holocene* 19, 611–624. doi: 10.1177/0959683609104039

Van der Meeren, T., Mischke, S., Sunjidmaa, N., Herzschuh, U., Ito, E., Martens, K., et al. (2012). Subfossil ostracode assemblages from Mongolia – Quantifying response for paleolimnological applications. *Ecol. Indic.* 14, 138–151. doi: 10.1016/j.ecolind.2011.07.004

van Harten, D. (1979). "Some new shell characters to diagnose the species of the *Ilyocypris gibba - biplicata - bradyi* group and their ecological significance," in *Taxonomy, Biostratigraphy and Distribution of Ostracodes, Proceedings of the 7th International Symposium on Ostracodes*, (Belgrade: Serbian Geological Society), 71–76.

Vinarski, M. V., Palatov, D. M., and Marinskiy, V. V. (2017). Checklist of the freshwater snails (Mollusca: Gastropoda) of Mongolia. *Zootaxa* 4317, 45–78.

Wang, W., Ma, Y., Feng, Z., Narantsetseg, T., Liu, K.-B., and Zhai, X. (2011). A prolonged dry mid-Holocene climate revealed by pollen and diatom records from Lake Ugii Nuur in central Mongolia. *Quat. Int.* 229, 74–83. doi: 10.1016/j.quaint.2010.06.005

Wang, Y., Liu, X., and Herzschuh, U. (2010). Asynchronous evolution of the Indian and East Asian Summer Monsoon indicated by Holocene moisture patterns in monsoonal central Asia. *Earth Sci. Rev.* 103, 135–153. doi: 10.1016/j.earscirev.2010.09.004

Winter, U., and Kirst, G. O. (1990). Salinity response of a freshwater charophyte, *Chara vulgaris*. *Plant Cell Env.* 13, 123–134. doi: 10.1111/j.1365-3040.1990.tb01284.x

Xu, H., Zhou, K., Lan, J., Zhang, G., and Zhou, X. (2019). Arid Central Asia saw mid-Holocene drought. *Geology* 47, 255–258. doi: 10.1130/g45686.1

Yu, K., Lehmkuhl, F., Diekmann, B., Zeeden, C., Nottebaum, V., and Stauch, G. (2017). Geochemical imprints of coupled paleoenvironmental and provenance change in the lacustrine sequence of Orog Nuur, Gobi Desert of Mongolia. *J. Paleolimnol.* 58, 511–532. doi: 10.1007/s10933-017-0007-7

Yu, K., Lehmkuhl, F., Schlütz, F., Diekmann, B., Mischke, S., Grunert, J., et al. (2019). Late Quaternary environments in the Gobi Desert of Mongolia: vegetation, hydrological, and palaeoclimate evolution. *Palaeogeogr. Palaeoclimatol. Palaeoecol.* 514, 77–91. doi: 10.1016/j.palaeo.2018.10.004

Zhang, W., Yan, H., Dodson, J., Cheng, P., Liu, C., Li, J., et al. (2018). The 9.2 ka event in Asian summer monsoon area: the strongest millennial scale collapse of the monsoon during the Holocene. *Clim. Dyn.* 50, 2767–2782. doi: 10.1007/s00382-017-3770-2

Conflict of Interest: The authors declare that the research was conducted in the absence of any commercial or financial relationships that could be construed as a potential conflict of interest.

Copyright © 2020 Mischke, Lee and Lee. This is an open-access article distributed under the terms of the Creative Commons Attribution License (CC BY). The use, distribution or reproduction in other forums is permitted, provided the original author(s) and the copyright owner(s) are credited and that the original publication in this journal is cited, in accordance with accepted academic practice. No use, distribution or reproduction is permitted which does not comply with these terms.

frontiers in Earth Science

ORIGINAL RESEARCH
published: 19 June 2020
doi: 10.3389/feart.2020.00200

Surface Ocean Hydrographic Changes in the Western Pacific Marginal Seas Since the Early Holocene

Hui-Juan Pan[1], Min-Te Chen[1,2,3]*, Deming Kong[4], Xiaopei Lin[5], Kuo-Tsan Wong[6], Hung-Ling Tsai[1], Shengfa Liu[7,8], Xuefa Shi[7,8] and Yosuke Yokoyama[9]*

[1] Institute of Earth Sciences, College of Ocean Science and Resource, National Taiwan Ocean University, Keelung, Taiwan, [2] Center of Excellence for Ocean Engineering, College of Engineering, National Taiwan Ocean University, Keelung, Taiwan, [3] Center of Excellence for Oceans, National Taiwan Ocean University, Keelung, Taiwan, [4] Laboratory for Coastal Ocean Variation and Disaster Prediction, College of Ocean and Meteorology, Guangdong Ocean University, Zhanjiang, China, [5] Key Laboratory of Physical Oceanography, College of Ocean and Atmospheric Science, Ocean University of China, Qingdao, China, [6] Central Geological Survey, Ministry of Economic Affairs, New Taipei City, Taiwan, [7] Key Laboratory of Marine Sedimentology and Environmental Geology, First Institute of Oceanography, State Oceanic Administration, Qingdao, China, [8] Laboratory for Marine Geology, Qingdao National Laboratory for Marine Science and Technology, Qingdao, China, [9] Atmosphere and Ocean Research Institute, The University of Tokyo, Kashiwa, Japan

OPEN ACCESS

Edited by:
Hai Xu,
Tianjin University, China

Reviewed by:
Xin Zhou,
University of Science and Technology of China, China
Xianyu Huang,
China University of Geosciences Wuhan, China

***Correspondence:**
Hui-Juan Pan
hjpan76@gmail.com
Min-Te Chen
mtchen@mail.ntou.edu.tw

Specialty section:
This article was submitted to Quaternary Science, Geomorphology and Paleoenvironment, a section of the journal Frontiers in Earth Science

Received: *03 March 2020*
Accepted: *18 May 2020*
Published: *19 June 2020*

Citation:
Pan H-J, Chen M-T, Kong D, Lin X, Wong K-T, Tsai H-L, Liu S, Shi X and Yokoyama Y (2020) Surface Ocean Hydrographic Changes in the Western Pacific Marginal Seas Since the Early Holocene. Front. Earth Sci. 8:200. doi: 10.3389/feart.2020.00200

Climatic changes in the western Pacific marginal seas are influenced by global forcing and regional processes, including monsoons, and ocean circulation. To better understand the process of hydrographic and temperature changes, we applied the $U^{K'}_{37}$ as our index of Sea Surface Temperature (SST) and TEX_{86} as the index of Subsurface Water Temperature (SWT) for the last 8400 years using the sediment core MZ01 from the continental shelf of the East China Sea (ECS). To focus on centennial and millennial variabilities, the original SST and SWT are filtered with the Ensemble Empirical Mode Decomposition (EEMD) of the Hilbert-Huang Transform (HHT), with the confidence defined by a new method, the Continuity Superposition Error Calculation Method (CSECM). The SST and SWT both have a quasi-period of 1000–2000 years, exhibiting some teleconnection with the north Atlantic climatic changes. The SWT decreased during approximately 6–4 ka and then increased by ∼4°C to the late Holocene, almost anti-phase with the SST. The stronger Asian winter monsoon and China Coastal Current (CCC), are very likely responsible for the decreased SST in the late Holocene. In contrast, the increased SWT may imply that the stronger CCC has brought more Changjiang Diluted Water (CDW) southward and formed a thicker barrier layer in the ECS, which dampened bottom water heat loss that was transported from the Taiwan Warm Current (TWC), and Western Kuroshio Branch Current (WKBC). This process is tested by the hosing experiment that supports stronger stratification when the north Atlantic cooled. The combined results by $U^{K'}_{37}$ and TEX_{86} provide a new insight into the interaction mechanism among the winter monsoon, precipitation and the Kuroshio Current, and also raises caution to take more regional factors into account in the application of TEX_{86}.

Keywords: East China Sea, $U^{K'}_{37}$, TEX_{86}, Sea Surface Temperature, East Asia Monsoon, Kuroshio, Hilbert Huang Transform, Ensemble Empirical Mode Decomposition

INTRODUCTION

In past decades, sea surface temperature (SST) reconstructions have depicted quite a consistent portrait of Holocene climatic changes over the open oceans (Leduc et al., 2010; PAGES Ocean 2k Working Group, 2012). In contrast, climatic records from marginal seas always show high complexity and discordance among different regions. This is partly due to the complex effect of terrestrial process, regional currents, and tidal and depositional processes on the marginal seas. In other words, the paleoceanographic records in marginal seas usually contain more climatic information than the open oceans. It is sometimes important to decipher the complex interaction between different forcing, particularly land-ocean interaction. In addition, marginal sea sediments usually provide a higher depositional rate and temporal resolution, which is crucial to reconstruct and understand high resolution climatic changes on centennial to millennial scales.

Previous reconstructions in the western Pacific marginal seas, including the East China Sea (ESC), South China Sea (SCS), and Yellow Sea, show significant influence from the continental climatic system, such as the winter monsoon. Initial comparison between the Holocene SST trend from marginal sea (Kong et al., 2014) and the North Atlantic (Sachs, 2007; Rodrigues et al., 2009) exhibit good agreement in the cooling trend during the mid-late Holocene. This implies possible teleconnection between high latitudes of the North Atlantic Ocean and Pacific marginal seas. The Holocene climate in the North Atlantic has been found to have ∼1500 years quasi-periodic cycles (Bond et al., 1997; Bond et al., 2001). However, little is known about these quasi-periodic cycles in the western Pacific marginal seas (Jian et al., 2000; Kubota et al., 2010; Yi et al., 2015), partly due to the lack of studies and an effective method to extract periodic signals from complicated reconstructions.

Here we report paired temperature reconstruction based on long-chain alkenones and Glycerol Dialkyl Glycerol Tetraethers (GDGTs) over the last 8400 years, and introduce a Continuity Superposition Error Calculation Method (CSECM) to assess the errors in both ages and proxies. We focus on the general trend of surface and subsurface temperature at millennial scales, and attempt to investigate the hydrographic changes in the Western Pacific marginal seas since the early Holocene.

MATERIALS AND METHODS

Sediment Core

The study is based on the continental shelf mud area of the ECS. A sediment core MZ01 (120°50.94′E, 26°32.82′N) was collected from the ECS inner shelf (Liu et al., 2010). The core site is about 65 m in depth and 90 km from the mouth of the Min River, which has a catchment area of approximately 6×10^4 km^2. About 500 km to the north of the core site is the mouth of China's largest river, the Yangtze River (Changjiang; **Figure 1**). The climate system and the hydrological regime prevailing in the study area are demonstrated in the **Supplementary Material**.

The core MZ01 was 2.96 m in total, and it was subsampled at 2 cm intervals and analyzed for grain size, major elements, and clay minerals with five old age dating (Liu et al., 2010). In this study we presented a new age model of core MZ01 that was based on new 12 AMS ^{14}C ages using strictly-selected, mixtures of benthic foraminifers (mainly epifauna; **Supplementary Table S1**). All the calibration and establishment of age are discussed in the **Supplementary Material**.

Analysis of Alkenones and GDGTs

The analyses for long-chain alkenones and GDGTs were performed at the National Taiwan Ocean University using the procedures described by Hung (2013), Tsai (2013), and Lin et al. (2014). The SST was calculated using the empirical equation established by Conte et al. (2006):

$$\mathrm{SST} = -0.957 + 54.293\left(\mathrm{U}^{\mathrm{K}'}_{37}\right) - 52.894\left(\mathrm{U}^{\mathrm{K}'}_{37}\right)^2 + 28.321\left(\mathrm{U}^{\mathrm{K}'}_{37}\right)^3$$

The TEX_{86} was calculated to temperature in the BAYSPAR (BAYesian SPAtially-varying Regression) system[1] (Tierney and Tingley, 2014, 2015), which allows us to predict the temperature empirically derived from regional environmental and biological factors. The uncertainties originating from the BAYSPAR calibration is about ±2.5°C. The BIT (Branched and Isoprenoid Tetraether) index that reflects the terrestrial contribution were established by Hung (2013) and shown in **Supplementary Figure S3**.

Data Processing

Uncertainties in the age controls (X) and proxy data (Y) are always inevitable in paleoclimatic reconstructions. The commonly used methods to assess the uncertainties of a paleoclimatic record include plotting error bars on the X or Y axis, or just describing them in words. However, these methods usually fail to take into account the interrelationship between the errors in X and Y. In an effort to overcome such problems, we introduce the method named CSECM that combines the errors in both X and Y. The CSECM method generally includes four steps, which are elaborated in the **Supplementary Material**.

The Hosing Experiment

To test the impact of global climatic forcing such as the change of AMOC (Atlantic Meridional Ocean Circulation; van Oldenborgh et al., 2009; Svendsen et al., 2014) to the surface hydrographies in the western Pacific marginal seas, we used data from the run the National Center for Atmospheric Research (NCAR) Community Climate System Model version 3 (CCSM3). The CCSM3 is a fully coupled model, comprised of the Parallel Ocean Program (POP), the Community Atmosphere Model (CAM), the Community Sea Ice Model (CSIM), and the Community Land Model (CLM). The resolution configuration of the model is referred to as T42 × 1. CAM uses spectral dynamics at T42 resolution (grid spacing of approximately 2.8° in latitude and longitude with 26 vertical

[1]https://github.com/jesstierney/BAYSPAR

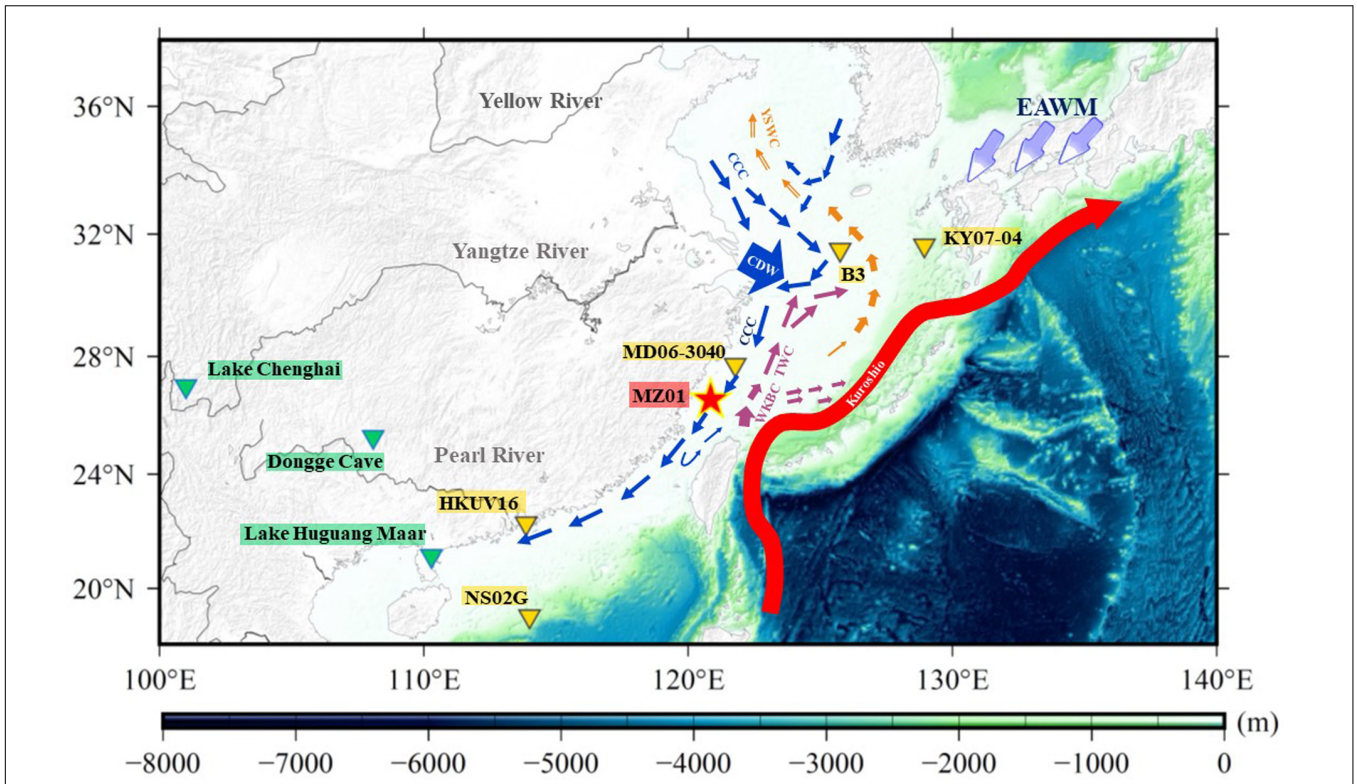

FIGURE 1 | Topography of the study area close to site MZ01 (red star) and the fluvial systems on surrounding continents. Also shown are locations of oceanic archive KY07-04 (Nakanishi et al., 2012), B3 (Zhao et al., 2014), MD063040 (Wang et al., 2014), HKUV16 (Kong et al., 2014), NS02G (Kong et al., 2014) labeled with yellow triangles; and terrestrial archives Dongge Cave (Dykoski et al., 2005), Lake Huguang Maar (Yancheva et al., 2007), and Lake Chenghai (Xu et al., 2020) labeled with green triangles. The arrows show monsoon winds and current systems: Kuroshio Current, Western Kuroshio Branch Current (WKBC), Taiwan Warm Current (TWC), and Changjiang Diluted Water (CDW) after Lie and Cho (2016); Chinese Coastal Current (CCC) after Lee and Chao (2003); and Yellow Sea Warm Current (YSWC) after Bian et al. (2013).

hybrid levels). The ocean grid has 320 × 384 horizontal points, with enhanced meridional resolution near the equator and high-latitude North Atlantic, and 40 levels in the vertical z-coordinate. The ice model shares the same horizontal resolution with the ocean model. The North Pole is set in Greenland to avoid singularity problems.

The control setting is Holocene climatological means, which is represented using the mean condition of the last 30 years. The experimental setting is the shut-down status of AMOC caused by 1 Sv (Sverdrup) fresh water impulses during the Bond or Heinrich-type cold events (Stouffer et al., 2006). The fresh water hosing lasts for 100-years, which is sufficient to shut down the AMOC, and the experiments are termed hosing experiments. Based on the hosing experiment results, parameter differences between experimental and control settings were plotted, respectively, for winter and summer (**Figure 2**).

RESULTS

According to the age model, the core MZ01 extends back to 8400 years BP, with an average sedimentation rate ∼33.6 cm/kyr. The sedimentation rate was much higher during the period 8.5–7.5, 6–5, and 1–0 ka (**Supplementary Figure S2**). As a result, the resolution of the reconstructed record varied greatly at different stages, possibly due to dynamic sedimentation processes in the shelves of the ECS (Yang et al., 2016; Liu et al., 2018).

The $U^{K'}_{37}$-SST of MZ01 ranges within 23.2–26.8°C and can be roughly divided into 3 stages: fast fluctuation from 8.4 to 6 ka, warming from ∼6 to 3 ka, and mild cooling since 3 ka (**Figure 3**). The record is imbedded with several fast cooling events at ∼7.6, ∼6.1, ∼5.5, and ∼1.0 ka. In the past 1 ky, relatively warmer and cooler periods could be identified, within the ranges of age and proxy uncertainties, at approximately 0.8–0.4 and 0.4–0.1 ky BP. Despite the age uncertainties and small temperature differences between these two periods, they might be hydrographic fingerprints from the widely found "Medieval Warm Period" and "Little Ice Age."

The TEX_{86}-derived temperature calculated by the BAYSPAR system range from 14.5–24.7°C (**Figure 3**), about 2°C lower than the result obtained from calibration by Kim et al. (2010). The core top TEX_{86}-Subsurface Water Temperature (SWT) is about 17.4°C, lower than the observed subsurface seawater temperature (21°C) near the core site. Generally, the TEX_{86}-derived temperature shows quite different changes from the $U^{K'}_{37}$-SST. It fluctuated greatly and decreased from 8.4 ka to

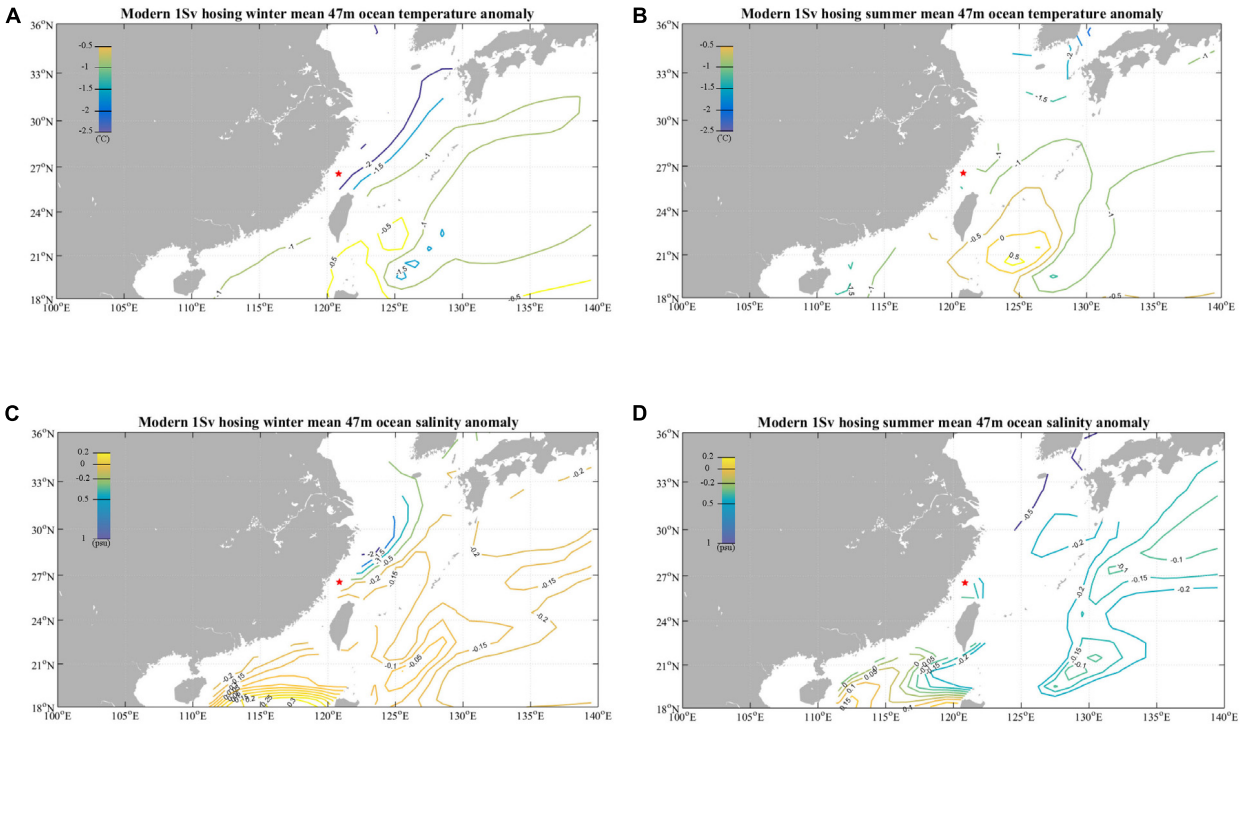

FIGURE 2 | Spatial distribution of temperature **(A,B)** and salinity **(C,D)** in winter **(A,C)** and summer **(B,D)**. Contours reveal the status at a depth of 47 m during AMOC shut-down according to the hosting experiments.

~6.6 ka. After a cold period between 7–6 ka, the temperature rapidly increased to the episodic maximum at 6 ka, and decreased to ~4 ka. It then exhibits an apparently increasing trend with two coolings at 2.4 ka and 1.0ka.

As the original $U^{K'}_{37}$-SST and TEX_{86}-SWT contain some noise signal and errors in both age and proxy data, we prefer to discuss the trend of these two proxies. The trend of $U^{K'}_{37}$-SST and TEX_{86}-SWT were named the $U^{K'}_{37}$-SST-trend2 ($=\sum_{i=2}^{n} IMFi + R$), and TEX_{86}-SWT-trend2 ($=\sum_{i=2}^{n} IMFi + R$). The trend lines were plotted with the error range provided by the CSECM (**Figure 3**).

The TEX_{86}-SWT of MZ01 shows several warming-cooling cycles, with episodic peaks at 7.1, 6.0, 2.8, 1.7, and 0.4 ka. The Hilbert-Huang Transform (HHT) spectrum exhibits cyclicity of approximately 1000–2000 years over the last 8000 years (**Figure 4**).

DISCUSSION

Interpretation of the $U^{K'}_{37}$ and TEX_{86} Proxies

The proxy $U^{K'}_{37}$ has been widely accepted as a good indicator for SST. In this study, the estimated SST from core top (2-points average) $U^{K'}_{37}$ of MZ01 is 26°C, ~4.4°C higher than the observed annual mean SST (21.6°C). The offset between this estimated $U^{K'}_{37}$-SST and the observed SST was also reported in the Pearl River Estuary (Kong et al., 2014). This systematic offset might relate to the different species fraction of coccolithphores (Kang et al., 2016), as well as the different seasonality of alkenone production in various environmental settings (Popp et al., 2006). However, we prefer to consider that the offset between the estimated $U^{K'}_{37}$-SST and "actual" SST had not changed much as long as the environment was relatively stable during the investigated period. In addition, we focus on the general trend rather than details. Thus, the $U^{K'}_{37}$ is expected to be able to reflect the general SST changes in the study area.

The TEX_{86} derived temperature of core top (2-points average) is 21°C, quite close to the annual mean temperature of the whole water column. Analysis of GDGTs in suspended particulate matter suggest that TEX_{86} correlates well with annual mean temperature when the water depth exceeds 70 m in the ECS (Zhang et al., 2017). While sediment TEX_{86} usually shows a much lower estimated value than the observed temperature in the inner shelf (Wei et al., 2011; Zhang et al., 2013). The TEX_{86} was proposed to reflect SWT (Huguet et al., 2006; Jia et al., 2012) and has been adopted by many studies (Li et al., 2013). With the best interpretation on the TEX_{86} proxy,

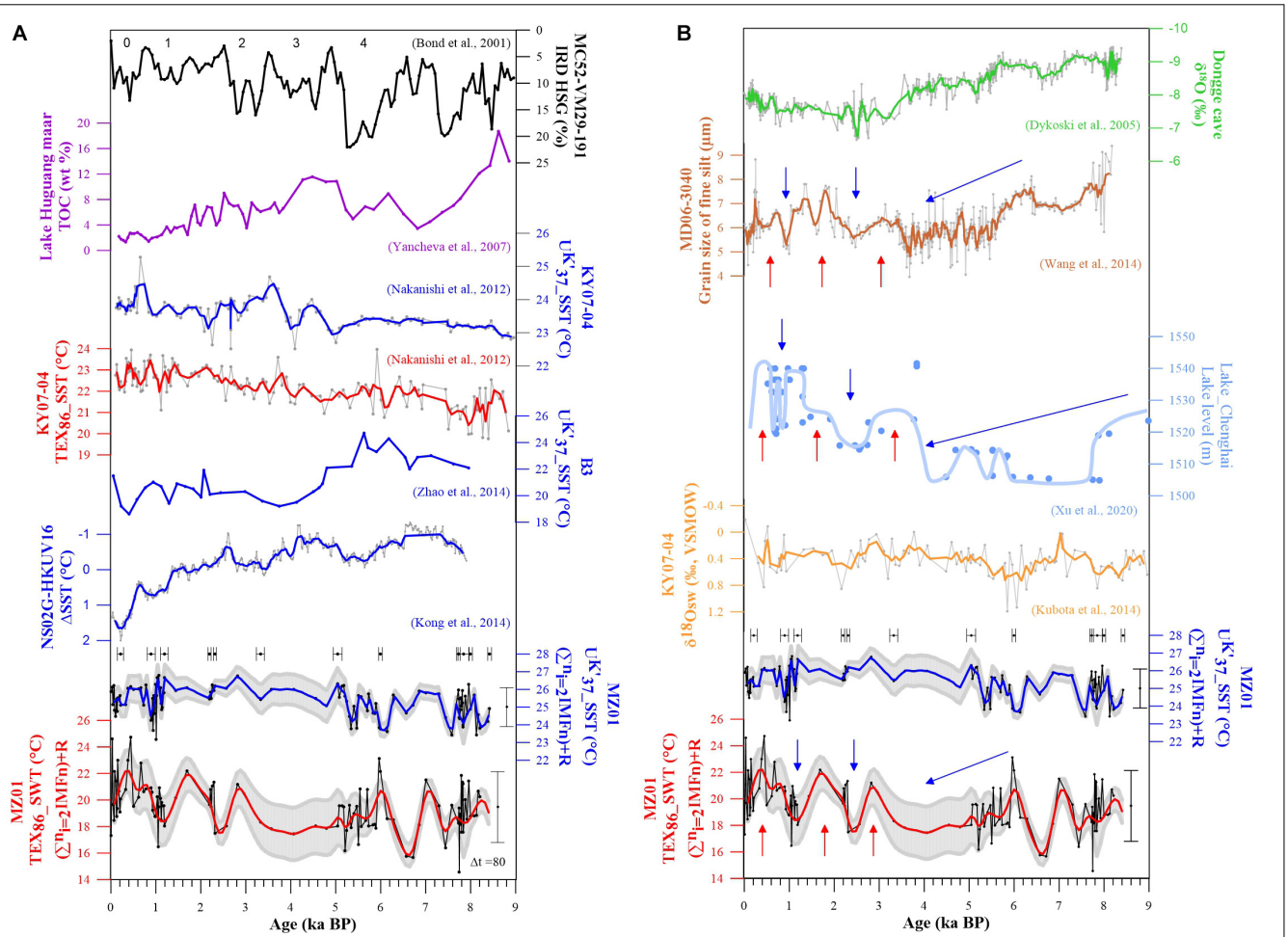

FIGURE 3 | (A) from top to bottom: the variations of hematite-stained grains derived from ice-rafted debris in the North Atlantic (Bond et al., 2001), total organic carbon content in Lake Huguang Maar (Yancheva et al., 2007), $U^{K'}_{37}$-SST and TEX_{86} -derived temperature of core KY07-04 in East China Sea (ECS; Nakanishi et al., 2012), $U^{K'}_{37}$-SST of core B3 in the continental shelf of the ECS (Zhao et al., 2014), and the temperature difference between sites HKUV16 and NS02G neighboring Pearl River estuary (Kong et al., 2014). **(B)** from top to bottom: the fluctuations of $\delta^{18}O$ in Dongge Cave (Dykoski et al., 2005), fine silt grain size of core MD06-3040 from mud belt off the Zhejiang-Fujian coast on the inner shelf of ECS (Wang et al., 2014), lake level variation of Chenghai (Xu et al., 2020), and $\delta^{18}O$ of core KY07-04 (Kubota et al., 2015). The gray curves represent the original data before 3-points smoothing. The last two curves in both **(A)** and **(B)** display the $U^{K'}_{37}$ and TEX_{86} -derived temperature of core MZ01. The gray strip region indicates the temperature range generated from CSECM conversion (**Supplementary Material Part 3**).

it was assumed to record changes in the SWT during our investigational period.

Regional SST and SWT in the ECS Since the Early Holocene

Regional circulations have a strong influence on the temperature and salinity distribution in the ECS. It has been suggested that the modern circulation pattern had not been established until approximately 7–6 ka when the sea level rose to almost modern height (Li et al., 2009; Yuan et al., 2018). The $U^{K'}_{37}$-SST and TEX_{86}-SWT of MZ01 both experienced a cooling between 7–6 ka, implying an impact of the circulation changes on these two proxies. However, it might not be so convincing to give too much weight to the interpretation of temperature changes before 6 ka based on the knowledge of modern circulation.

The $U^{K'}_{37}$-SST of MZ01 increased by ∼2°C from approximately 6 to 3 ka; this seems to coincide with the warming in $U^{K'}_{37}$-SST of the northeastern ECS (site KY07-04) from 6 to 3.5 ka (Nakanishi et al., 2012). Both circumstances may arise from the weakened EAWM that not only caused the warming at site KY0704 but also diminished the cold freshwater supply from China Coastal Current (CCC) to the MZ01. Nevertheless, another $U^{K'}_{37}$-SST (core B3) in the northern ECS shows extraordinary cooling by ∼4°C during this period (Zhao et al., 2014). It was proposed that such cooling anomaly likely relates to the southward migration of the Intertropical Convergence Zone (ITCZ), Western Pacific Subtropical High moving north-westward and strengthening of the Yellow Sea Coastal Current inducing the cold eddy formation (Zhao et al., 2014; Yuan et al., 2018; Xu et al., 2020).

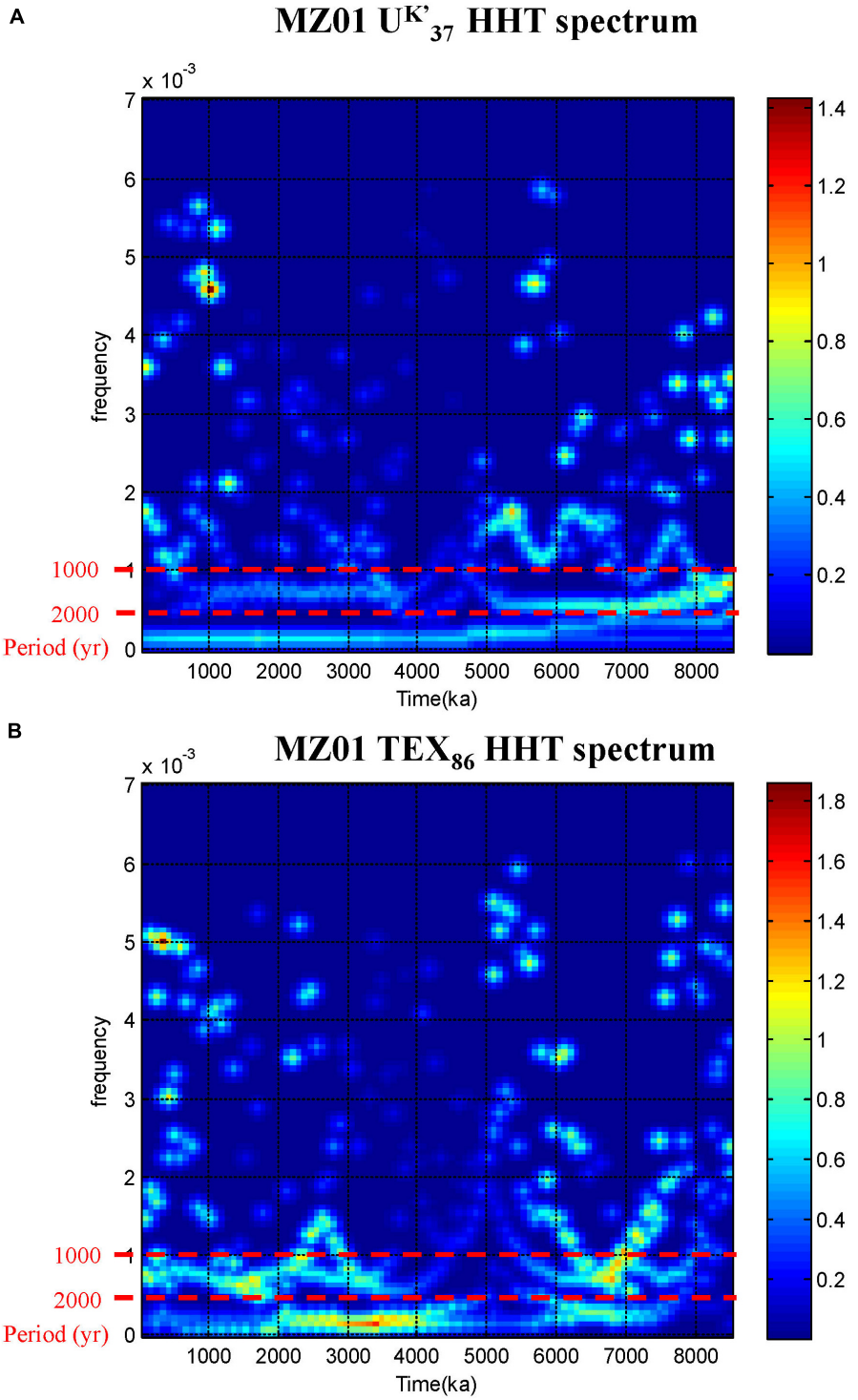

FIGURE 4 | HHT spectrum of MZ01 $U^{K'}_{37}$ SST **(A)** and TEX_{86} -derived temperature **(B)**. The colors between the periodicities of 1000 to 2000 year shown by dash lines indicate the spectral power. We note that the interpretation on spectral power of <1000–2000 year between ~5–2.5 ka is uncertain due to very low sedimentation rate of core MZ01.

On the other hand, the TEX_{86} -derived temperature of core KY07-04 show an overall warming through the Holocene (Nakanishi et al., 2012), which was ascribed to the strengthening of EAWM (**Figure 3**). However, the TEX_{86}-SWT of MZ01 recorded several warming and cooling fluctuations since 6 ka. It represents that the TEX_{86}-SWT of MZ01 is a sensitive

index which not only reflecting the EAWM but also the other impacts such as the Taiwan Warm Current (TWC) and West Kuroshio Branch Current (WKBC) in ECS (see discussion in the next two sections).

Impact of the EAWM and WKBC

Changes in the EAWM over the Holocene have been controversial. The magnetic susceptibility and total organic carbon (TOC) of the Lake Huguang Maar have been used as the indicator of EAWM in the tropics (Yancheva et al., 2007). They show an overall strengthening of EAWM over the Holocene, with episodic weakening during approximately 7–4 ka (Yancheva et al., 2007; **Figure 3A**). Stronger EAWM in the late Holocene has also been supported by marine records in the northern SCS. The vertical and east-west gradient of reconstructed temperatures in the SCS also show that the EAWM became stronger since ∼4 ka (Huang et al., 2011; Steinke et al., 2011). The significant decrease of $U^{K'}_{37}$-SST in coastal areas and the increased gradient between the open sea of the northern SCS have also been proposed to be caused by stronger EAWM in the late Holocene (Kong et al., 2014).

The $U^{K'}_{37}$-SST-trend of MZ01 shows an increase during approximately 7–3 ka and a decrease during 3–0 ka, in good agreement with changes of EAWM in these two periods. It suggests that the long term variability of $U^{K'}_{37}$-SST was controlled by the EAWM in the inner shelf of ECS, comparable to the SCS (Kong et al., 2014, 2017). Though the $U^{K'}_{37}$ is considered a proxy of annual mean SST, some modern investigations suggest the alkenone-producing coccolithophores are more abundant in colder seasons in tropical and sub-tropical seas (Chen et al., 2007). Even if we ignore the seasonality of alkenone production, the larger variability of winter SST would contribute more to the long-term variability of sediment $U^{K'}_{37}$ and thus reflect colder season temperature changes.

The TEX_{86}-SWT-trend of MZ01 exhibits an overall decrease from approximately 6 ka to 4 ka and an increase since ∼4 ka (**Figure 3**). This is in opposite to the trend in the $U^{K'}_{37}$-SST. The discrepancy may lie in the different temperatures that TEX_{86} and $U^{K'}_{37}$ recorded. It has been proposed that the TEX_{86} reflects the bottom water temperature in the ECS (Xing et al., 2015; Yuan et al., 2018), while the $U^{K'}_{37}$ is widely accepted as a SST indicator (Nakanishi et al., 2012; Yuan et al., 2018). Therefore, the opposite changes in these two proxies suggest different controlling mechanisms for temperature change at the surface and bottom of the sea.

To understand this mechanism, it is of prime importance to investigate the modern hydrographic conditions. Modern observed temperature (1955–2012, WOA2013) shows very distinctive seasonal distributions in our studied area (Locarnini et al., 2013; Zweng et al., 2013). The surface temperature is ∼2°C higher than the subsurface (55 m) temperature during summer. It's easy to understand this, as strong stratification dampens the heat convection to deeper waters. In contrast, the subsurface temperature is ∼1°C higher than the surface during fall and winter. And according to the WOA2013 observation data, the mean annual temperature difference between the sea surface and bottom water at MZ01 is around 3–5°C. This phenomenon is quite extraordinary as it's usually thought that the EAWM induced strong mixing that would make the upper layer of the ocean almost homogenous. Nevertheless, the mixing might be weakened by the stratification in the ECS shelf even during cold seasons (Wu, 2015; Xuan et al., 2017). Though the Changjiang River fluxes in winter and fall are not as large as in summer, the plume is driven southwardly by the EAWM and forms a diluted water layer in the ECS. In addition, the TWC and WKBC carry high temperature and salinity water to the ECS shelf and encounter the diluted water (Kako et al., 2016; Wang et al., 2017). The diluted water confronts the warmer and saltier Kuroshio water, dampening the vertical mixing, and heat exchange. As a result, the subsurface water remains warmer when the EAWM causes strong cooling in the diluted surface (Wang and Oey, 2016).

In short, the fluctuations of SST and SWT at MZ01 site are closely associated with the intensity of EAWM and its induced WKBC intrusion. The opposite trends of SST and SWT from approximately 6 ka to 4 ka observed in this study supports this mechanism. The $U^{K'}_{37}$-SST has been increased by weakened EAWM, which may block the intrusions of TWC and WKBC that would decreased the TEX_{86}-SWT. Similarly, stronger EAWM prevailed since 4 ka has promoted the SST decreased and reinforced the TWC and WKBC intrusions, resulting in the TEX_{86}-SWT in the ECS from 4 ka.

Holocene Hydrographic Changes in the ECS

The TEX_{86}-SWT of MZ01 shows several warming-cooling cycles, with episodic peaks at approximately 7.1, 6.0, 2.8, 1.7, and 0.4 ka (**Figure 3**). The HHT spectrum exhibits cyclicity of about 1000–2000 years over the last 8000 years (**Figure 4**). This cyclicity was comparable to the 1500-year quasi-periodicity of the drift-ice record from the north Atlantic (Bond et al., 1997; Bond et al., 2001). Despite some minor mismatch in the ages, the major warmings in the TEX_{86}-SWT show patterns similar to the increase of drift-ice, which were reflected by the hematite-stained grains (HSG) changes in the sediment (**Figure 3A**). The drift-ice indicated large amount of fresh water into the North Atlantic, causing shut down of the AMOC and cold events in the North Atlantic. This process possibly amplified the signal of solar signals and transmitted them globally (Bond et al., 2001). To test the impact of this process in the ECS, we run the hosing experiment as described in the method section. The results show the surface salinity and temperature in the ECS shelf would significantly decrease during Bond's cold events. In contrast, the subsurface (47 m) exhibits much less freshening, particularly in boreal winter (**Figure 2**). This is likely due to the strengthening of the winter monsoon and the fact that the more diluted water of Changjiang River was driven southward. Consequently, the surface salinity dropped greatly in the studied area. While the subsurface water in the ECS shelf was affected by the intrusion of TWC and WKBC, it thus experienced less

freshening. This process would intensify stratification and may have led to the subsurface warming in contrast to the apparent surface cooling.

The sediment grain size of core MD06-3040, which is about 200 km north to the MZ01 on the inner shelf of ECS, was used to study the Changjiang River drainage (Wang et al., 2014; Wang et al., 2020). It was found that the discharge of the Changjiang River has decreased from approximately 6 to 4 ka, then increased by ∼3 ka. The discharge has dropped again by 2.5 ka, with subsequently increased to 1.8 ka, and decreased to 1 ka (**Figure 3B**). The overall pattern of the Changjiang River discharge since 6 ka was in-phase with our TEX_{86}-derived temperature of MZ01. The grain size shows good agreement with the East Asian summer monsoon (EASM) derived from the Dongge Cave stalagmite $\delta^{18}O$ from 6 to 2 ka (Dykoski et al., 2005; **Figure 3B**). After 2 ka, the $\delta^{18}O$ derived EASM intensified, while the grain size indicates the Changjiang discharge decreased (Zhao et al., 2013). This might relate to the asynchronous performance of EASM at different latitudes (An et al., 2000), the location of Western subtropical high (Xu et al., 2019), or the southward migration of ITCZ since 2 ka (Haug et al., 2001).

Further, the variation pattern of the TEX86-derived temperature of MZ01 not only coincides with that of Changjiang River discharge but also shares a similar pattern with the lake level of Chenghai which affected by the summer monsoon precipitation in subtropical East Asia (Xu et al., 2020; **Figure 3B**). The TEX_{86}-SWT of MZ01 and Changjiang River discharge are both characterized by a decreasing trend since 6 ka to a minimum at 4 ka. It implies the EASM has become weak and/or the ITCZ has moved southward during the interval. With the evidence indicated here we argue that the precipitation in the northern region (at the latitude of Chenghai Lake and Changjiang River drainage) has been reduced but might maintained in the south (Dykoski et al., 2005). Reduced precipitation would make the flux of Changjiang Diluted Water (CDW) decreased, that in turn, would make fresh water barrier layer near the coast of the ECS thin, heat convection from the subsurface water increased and thus the TEX_{86}-SWT decreased at site MZ01. The similar migration of ITCZ and weakened EASM with cooling TEX86-derived SWT of MZ01 have happened persistently at ∼2.5 ka, and ∼1 ka (**Figure 3B**).

In contrast, the rising levels of Lake Chenghai between 4–3, 2.5–1.8, and 1–0.4 ka coincide with the increases of Changjiang River discharge and MZ01 TEX_{86}-SWT, suggesting stronger EASM and/or a northern migration of ITCZ (**Figure 3B**). Stronger EASM would lead to more CDW flowing into the ECS and a thicker fresh water barrier layer. In winter, such a thicker barrier layer could dampen heat release of the subsurface water and thus lead to temperature increase. This could be observed from the vertical temperature profile in winter. Surface water has lower salinity and temperature than subsurface shoreward (**Supplementary Figure S1**). But salinity becomes homogenous and surface temperature is higher than subsurface off shore. This feature could be explained by the intrusion of TWC and WKBC on shoreward (Lie and Cho, 2016). Though there is no observational evidence that the TWC and WKBC could reach as shallow as the core MZ01 site, they are speculated here to exert some influence on regional hydrological conditions at millennial scales.

CONCLUSION

The proxies $U^{K'}_{37}$ and TEX_{86} from sediment core MZ01 in the ECS are used to indicate SST and SWT changes over the last 8400-years. After being filtered with the Ensemble Empirical Mode Decomposition (EEMD) of HHT, the fluctuating SST and SWT both have a quasi-periodicity of approximately 1000–2000 years, in accordance with the north Atlantic drift ice activities. This suggests the impact of high latitude forcings on the ECS climate changes. The variability of SST and SWT at centennial and millennial scales reveals some anti-phase since 6 ka. Decrease of SST since approximately 3 ka suggests a cooling effect from intensified Asian winter monsoons and the CCC. This process could also lead to a thicker fresh water barrier layer on the surface, which could apparently dampen heat loss from the bottom water that is evidenced by modern observations. Therefore, the increase of SWT since approximately 4 ka, likely indicates regional hydrographic changes that relate to stronger winter and summer monsoons, as well as possibly stronger WKBC and TWC. The hosing experiment is also lends support to more obvious stratification during the cold period in north Atlantic high latitudes. Finally, our results revealed a close relationship between paleo-temperatures and hydrographic conditions, particularly in the western Pacific marginal seas, and provided a new approach to assess the interaction between regional hydrographic conditions and global climate forcing.

DATA AVAILABILITY STATEMENT

All datasets generated for this study are included in the article/**Supplementary Material**.

AUTHOR CONTRIBUTIONS

M-TC designed the research. H-JP and DK composed the main text and **Supplementary Material**. XL ran the hosting experiment. K-TW was responsible for the CSECM calculation. H-LT, SL, XS, and YY conducted the data analysis.

FUNDING

This study was supported by the research projects MOST 108-2116-M-019-004 and MOST 108-2116-M-019-008-MY2 from the Ministry of Science and Technology, Taiwan.

SUPPLEMENTARY MATERIAL

The Supplementary Material for this article can be found online at: https://www.frontiersin.org/articles/10.3389/feart.2020.00200/full#supplementary-material

REFERENCES

An, Z., Porter, S. C., Kutzbach, J. E., Xihao, W., Suming, W., Xiaodong, L., et al. (2000). Asynchronous Holocene optimum of the East Asian monsoon. *Quatern. Sci. Rev.* 19, 743–762. doi: 10.1016/S0277-3791(99)00031-31

Bian, C., Jiang, W., and Greatbatch, R. J. (2013). An exploratory model study of sediment transport sources and deposits in the Bohai Sea, Yellow Sea, and East China Sea. *J. Geophys. Res. Oceans* 118, 5908–5923. doi: 10.1002/2013JC009116

Bond, G., Kromer, B., Beer, J., Muscheler, R., Evans, M. N., Showers, W., et al. (2001). Persistent solar influence on North Atlantic climate during the holocene. *Science* 294, 2130–2136. doi: 10.1126/science.1065680

Bond, G., Showers, W., Cheseby, M., Lotti, R., Almasi, P., deMenocal, P., et al. (1997). A pervasive millennial-scale cycle in North Atlantic holocene and glacial Climates. *Science* 278, 1257–1266. doi: 10.1126/science.278.5341.1257

Chen, Y.-L. L., Chen, H.-Y., and Chung, C.-W. (2007). Seasonal variability of coccolithophore abundance and assemblage in the northern South China Sea. *Deep Sea Res. II Top. Stud. Oceanogr.* 54, 1617–1633. doi: 10.1016/j.dsr2.2007.05.005

Conte, M. H., Sicre, M.-A., Rühlemann, C., Weber, J. C., Schulte, S., Schulz-Bull, D., et al. (2006). Global temperature calibration of the alkenone unsaturation index (UK′37) in surface waters and comparison with surface sediments. *Geochem. Geophys. Geosyst.* 7:GC001054. doi: 10.1029/2005GC001054

Dykoski, C. A., Edwards, R. L., Cheng, H., Yuan, D., Cai, Y., Zhang, M., et al. (2005). A high-resolution, absolute-dated Holocene and deglacial Asian monsoon record from Dongge Cave, China. *Earth Planet. Sci. Lett.* 233, 71–86. doi: 10.1016/j.epsl.2005.01.036

Haug, G. H., Hughen, K. A., Sigman, D. M., Peterson, L. C., and Röhl, U. (2001). Southward migration of the intertropical convergence zone through the holocene. *Science* 293:1304. doi: 10.1126/science.1059725

Huang, E., Tian, J., and Steinke, S. (2011). Millennial-scale dynamics of the winter cold tongue in the southern South China Sea over the past 26 ka and the East Asian winter monsoon. *Quatern. Res.* 75, 196–204. doi: 10.1016/j.yqres.2010.08.014

Huguet, C., Kim, J.-H., Sinninghe Damsté, J. S., and Schouten, S. (2006). Reconstruction of sea surface temperature variations in the Arabian Sea over the last 23 kyr using organic proxies (TEX86 and $U^{K'}_{37}$). *Paleoceanography* 21:PA3003. doi: 10.1029/2005PA001215

Hung, T.-Y. (2013). *The Application of TEX86 and BIT organic biomarkers to reconstruct climate chagnes in the East China Sea over the past 8000 years*. Keelung: National Taiwan Ocean University.

Jia, G., Zhang, J., Chen, J., Peng, P. A., and Zhang, C. L. (2012). Archaeal tetraether lipids record subsurface water temperature in the South China Sea. *Organ. Geochem.* 50, 68–77. doi: 10.1016/j.orggeochem.2012.07.002

Jian, Z., Wang, P., Saito, Y., Wang, J., Pflaumann, U., Oba, T., et al. (2000). Holocene variability of the Kuroshio Current in the Okinawa Trough, northwestern Pacific Ocean. *Earth Planet. Sci. Lett.* 184, 305–319. doi: 10.1016/S0012-821X(00)00321-326

Kako, S. I, Nakagawa, T., Takayama, K., Hirose, N., and Isobe, A. (2016). Impact of changjiang river discharge on sea surface temperature in the East China Sea. *J. Phys. Oceanogr.* 46, 1735–1750. doi: 10.1175/JPO-D-15-0167.1

Kang, L. K., Lu, H. M., Sung, P. T., Chan, Y. F., Lin, Y. C., Gong, G. C., et al. (2016). The summer distribution of coccolithophores and its relationship to water masses in the East China Sea. *J. Oceanogr.* 72, 883–893. doi: 10.1007/s10872-016-0385-x

Kim, J.-H., van der Meer, J., Schouten, S., Helmke, P., Willmott, V., Sangiorgi, F., et al. (2010). New indices and calibrations derived from the distribution of crenarchaeal isoprenoid tetraether lipids: implications for past sea surface temperature reconstructions. *Geochim. Cosmochim. Acta* 74, 4639–4654. doi: 10.1016/j.gca.2010.05.027

Kong, D., Wei, G., Chen, M.-T., Peng, S., and Liu, Z. (2017). Northern South China Sea SST changes over the last two millennia and possible linkage with solar irradiance. *Quatern. Int.* 459, 29–34. doi: 10.1016/j.quaint.2017.10.001

Kong, D., Zong, Y., Jia, G., Wei, G., Chen, M. T., and Liu, Z. (2014). The development of late Holocene coastal cooling in the northern South China Sea. *Quatern. Int.* 349, 300–307. doi: 10.1016/j.quaint.2013.08.055

Kubota, Y., Kimoto, K., Tada, R., Oda, H., Yokoyama, Y., and Matsuzaki, H. (2010). Variations of East Asian summer monsoon since the last deglaciation based on Mg/Ca and oxygen isotope of planktic foraminifera in the northern East China Sea. *Paleoceanography* 25:PA4205. doi: 10.1029/2009PA001891

Kubota, Y., Tada, R., and Kimoto, K. (2015). Changes in East Asian summer monsoon precipitation during the Holocene deduced from a freshwater flux reconstruction of the Changjiang (Yangtze River) based on the oxygen isotope mass balance in the northern East China Sea. *Clim. Past* 11:265. doi: 10.5194/cp-11-265-2015

Leduc, G., Schneider, R., Kim, J. H., and Lohmann, G. (2010). Holocene and Eemian sea surface temperature trends as revealed by alkenone and Mg/Ca paleothermometry. *Quatern. Sci. Rev.* 29, 989–1004. doi: 10.1016/j.quascirev.2010.01.004

Lee, H.-J., and Chao, S.-Y. (2003). A climatological description of circulation in and around the East China Sea. *Deep Sea Res. II Top. Stud. Oceanogr.* 50, 1065–1084. doi: 10.1016/S0967-0645(03)00010-19

Li, D., Zhao, M., Tian, J., and Li, L. (2013). Comparison and implication of TEX86 and $U^{K'}_{37}$ temperature records over the last 356kyr of ODP Site 1147 from the northern South China Sea. *Palaeogeogr. Palaeoclimatol. Palaeoecol.* 376, 213–223. doi: 10.1016/j.palaeo.2013.02.031

Li, T., Nan, Q., Jiang, B., Sun, R., Zhang, D., and Li, Q. (2009). Formation and evolution of the modern warm current system in the East China Sea and the Yellow Sea since the last deglaciation. *Chinese J. Oceanol. Limnol.* 27, 237–249. doi: 10.1007/s00343-009-9149-9144

Lie, H.-J., and Cho, C.-H. (2016). Seasonal circulation patterns of the Yellow and East China Seas derived from satellite-tracked drifter trajectories and hydrographic observations. *Prog. Oceanogr.* 146, 121–141. doi: 10.1016/j.pocean.2016.06.004

Lin, D.-C., Chen, M.-T., Yamamoto, M., and Yokoyama, Y. (2014). Millennial-scale alkenone sea surface temperature changes in the northern South China Sea during the past 45,000 years (MD972146). *Quatern. Int.* 333, 207–215. doi: 10.1016/j.quaint.2014.03.062

Liu, J. T., Hsu, R. T., Yang, R. J., Wang, Y. P., Wu, H., Du, X., et al. (2018). A comprehensive sediment dynamics study of a major mud belt system on the inner shelf along an energetic coast. *Sci. Rep.* 8:4229. doi: 10.1038/s41598-018-22696-w

Liu, S., Shi, X., Liu, Y., Qiao, S., Yang, G., Fang, X., et al. (2010). Records of the East Asian winter monsoon from the mud area on the inner shelf of the East China Sea since the mid-Holocene. *Chinese Sci. Bull.* 55, 2306–2314. doi: 10.1007/s11434-010-3215-3213

Locarnini, R. A., Mishonov, A. V., Antonov, J. I., Boyer, T. P., Garcia, H. E., Baranova, O. K., et al. (2013). *World ocean atlas 2013 Temperature*. Silver Spring, MA: NOAA.

Nakanishi, T., Yamamoto, M., Tada, R., and Oda, H. (2012). Centennial-scale winter monsoon variability in the northern East China Sea during the Holocene. *J. Quatern. Sci.* 27, 956–963. doi: 10.1002/jqs.2589

PAGES Ocean 2k Working Group (2012). "Synthesis of marine sediment-derived SST records for the past 2 millennia: first-order results from the PAGES/Ocean2k project," in *Proceedings of the AGU Fall Meeting, PP11F-07* (Washington, DC: American Geophysical Union).

Popp, B. N., Prahl, F. G., Wallsgrove, R. J., and Tanimoto, J. (2006). Seasonal patterns of alkenone production in the subtropical oligotrophic North Pacific. *Paleoceanography* 21, 1–15. doi: 10.1029/2005PA001165

Rodrigues, T., Grimalt, J. O., Abrantes, F. G., Flores, J. A., and Lebreiro, S. M. (2009). Holocene interdependences of changes in sea surface temperature, productivity, and fluvial inputs in the Iberian continental shelf (Tagus mud patch). *Geochem. Geophys. Geosyst.* 10:Q07U06. doi: 10.1029/2008GC002367

Sachs, J. P. (2007). Cooling of Northwest Atlantic slope waters during the Holocene. *Geophys. Res. Lett.* 34:L03609. doi: 10.1029/2006GL028495

Steinke, S., Glatz, C., Mohtadi, M., Groeneveld, J., Li, Q., and Jian, Z. (2011). Past dynamics of the East Asian monsoon: no inverse behaviour between the summer and winter monsoon during the Holocene. *Glob. Planet. Change* 78, 170–177. doi: 10.1016/j.gloplacha.2011.06.006

Stouffer, R. J., Yin, J., Gregory, J. M., Dixon, K. W., Spelman, M. J., Hurlin, W., et al. (2006). Investigating the causes of the response of the thermohaline circulation to past and future climate changes. *J. Clim.* 19, 1365–1387. doi: 10.1175/JCLI3689.1

Svendsen, L., Kvamstø, N. G., and Keenlyside, N. (2014). Weakening AMOC connects Equatorial Atlantic and Pacific interannual variability. *Clim. Dyn.* 43, 2931–2941. doi: 10.1007/s00382-013-1904-1908

Tierney, J. E., and Tingley, M. P. (2014). A Bayesian, spatially-varying calibration model for the TEX86 proxy. *Geochim. Cosmochim. Acta* 127, 83–106. doi: 10.1016/j.gca.2013.11.026

Tierney, J. E., and Tingley, M. P. (2015). A TEX86 surface sediment database and extended Bayesian calibration. *Sci. Data* 2, 1–10. doi: 10.1038/sdata.2015.29

Tsai, H. L. (2013). *The Application of Alkenone Unsaturation Organic Biomarkers to Reconstruct Sea Surface Temperature and Climate Changes in the East China Sea over the Past 8000 years*. Keelung: National Taiwan Ocean University.

van Oldenborgh, G. J., te Raa, L. A., Dijkstra, H. A., and Philip, S. Y. (2009). Frequency- or amplitude-dependent effects of the Atlantic meridional overturning on the tropical Pacific Ocean. *Ocean Sci.* 5, 293–301. doi: 10.5194/os-5-293-2009

Wang, B., Hirose, N., Yuan, D., Moon, J.-H., and Pan, X. (2017). Effects of tides on the cross-isobath movement of the low-salinity plume in the western Yellow and East China Seas in winter. *Continent. Shelf Res.* 143, 228–239. doi: 10.1016/j.csr.2016.06.011

Wang, J., and Oey, L. Y. (2016). Seasonal exchanges of the kuroshio and shelf waters and their impacts on the shelf currents of the East China Sea. *J. Phys. Oceanogr.* 46, 1615–1632. doi: 10.1175/JPO-D-15-0183.1

Wang, K., Tada, R., Zheng, H., Irino, T., Zhou, B., and Saito, K. (2020). Provenance changes in fine detrital quartz in the inner shelf sediments of the East China Sea associated with shifts in the East Asian summer monsoon front during the last 6 kyrs. *Prog. Earth Planet. Sci.* 7:5. doi: 10.1186/s40645-019-0319-315

Wang, K., Zheng, H., Tada, R., Irino, T., Zheng, Y., Saito, K., et al. (2014). Millennial-scale East Asian Summer Monsoon variability recorded in grain size and provenance of mud belt sediments on the inner shelf of the East China Sea during mid-to late Holocene. *Quatern. Int.* 349, 79–89. doi: 10.1016/j.quaint.2014.09.014

Wei, Y., Wang, J., Liu, J., Dong, L., Li, L., Wang, H., et al. (2011). Spatial variations in archaeal lipids of surface water and core-top sediments in the South China Sea and their implications for paleoclimate studies. *Appl. Environ. Microbiol.* 77:7479. doi: 10.1128/AEM.00580-511

Wu, H. (2015). Cross-shelf penetrating fronts: a response of buoyant coastal water to ambient pycnocline undulation. *J. Geophys. Res. Oceans* 120, 5101–5119. doi: 10.1002/2014JC010686

Xing, L., Sachs, J. P., Gao, W., Tao, S., Zhao, X., Li, L., et al. (2015). TEX86 paleothermometer as an indication of bottom water temperature in the Yellow Sea. *Organ. Geochem.* 86, 19–31. doi: 10.1016/j.orggeochem.2015.05.007

Xu, H., Goldsmith, Y., Lan, J., Tan, L., Wang, X., Zhou, X., et al. (2020). Juxtaposition of western pacific subtropical high on asian summer monsoon shapes subtropical east asian precipitation. *Geophys. Res. Lett.* 47:e2019GL084705. doi: 10.1029/2019GL084705

Xu, H., Song, Y., Goldsmith, Y., and Lang, Y. (2019). Meridional ITCZ shifts modulate tropical/subtropical Asian monsoon rainfall. *Sci. Bull.* 64, 1737–1739. doi: 10.1016/j.scib.2019.09.025

Xuan, J., Huang, D., Pohlmann, T., Su, J., Mayer, B., Ding, R., et al. (2017). Synoptic fluctuation of the Taiwan Warm Current in winter on the East China Sea shelf. *Ocean Sci.* 13:55332710.

Yancheva, G., Nowaczyk, N. R., Mingram, J., Dulski, P., Schettler, G., Negendank, J. F. W., et al. (2007). Influence of the intertropical convergence zone on the East Asian monsoon. *Nature* 445, 74–77. doi: 10.1038/nature05431

Yang, S., Bi, L., Li, C., Wang, Z., and Dou, Y. (2016). Major sinks of the Changjiang (Yangtze River)-derived sediments in the East China Sea during the late Quaternary. *Geol. Soc.* 429, 137–152. doi: 10.1144/sp429.6

Yi, L., Chen, S., Ortiz, J. D., Chen, G., Peng, J., Liu, F., et al. (2015). 1500-year cycle dominated Holocene dynamics of the Yellow River delta. China. *Holocene* 26, 222–234. doi: 10.1177/0959683615596834

Yuan, Z., Xiao, X., Wang, F., Xing, L., Wang, Z., Zhang, H., et al. (2018). Spatiotemporal temperature variations in the East China Sea shelf during the Holocene in response to surface circulation evolution. *Quatern. Int.* 482, 46–55. doi: 10.1016/j.quaint.2018.04.025

Zhang, J., Bai, Y., Xu, S., Lei, F., and Jia, G. (2013). Alkenone and tetraether lipids reflect different seasonal seawater temperatures in the coastal northern South China Sea. *Organ. Geochem.* 58, 115–120. doi: 10.1016/j.orggeochem.2013.02.012

Zhang, J., Jia, G., Guo, W., Wang, X., and Lei, F. (2017). Isoprenoid tetraether lipids in suspended particulate matter from the East China Sea and implication for sedimentary records. *Organ. Geochem.* 114, 81–90. doi: 10.1016/j.orggeochem.2017.09.006

Zhao, C., Chang, Y.-P., Chen, M.-T., and Liu, Z. (2013). Possible reverse trend in Asian summer monsoon strength during the late Holocene. *J. Asian Earth Sci.* 69, 102–112. doi: 10.1016/j.jseaes.2012.09.028

Zhao, M., Ding, L., Xing, L., Qiao, S., and Yang, Z. (2014). Major mid-late Holocene cooling in the East China Sea revealed by an alkenone sea surface temperature record. *J. Ocean Univ. China* 13, 935–940. doi: 10.1007/s11802-014-2641-2642

Zweng, M. M., Reagan, J. R., Antonov, J. I., Locarnini, R. A., Mishonov, A. V., Boyer, T. P., et al. (2013). *World Ocean Atlas 2013 Salinity*. Silver Spring, MA: NOAA.

Conflict of Interest: The authors declare that the research was conducted in the absence of any commercial or financial relationships that could be construed as a potential conflict of interest.

Copyright © 2020 Pan, Chen, Kong, Lin, Wong, Tsai, Liu, Shi and Yokoyama. This is an open-access article distributed under the terms of the Creative Commons Attribution License (CC BY). The use, distribution or reproduction in other forums is permitted, provided the original author(s) and the copyright owner(s) are credited and that the original publication in this journal is cited, in accordance with accepted academic practice. No use, distribution or reproduction is permitted which does not comply with these terms.

frontiers in Earth Science

ORIGINAL RESEARCH
published: 03 July 2020
doi: 10.3389/feart.2020.00262

Chronology of a Holocene Core From the Pearl River Delta in Southern China

XiaoLin Xu[1†], HongWei Li[2†], LinJie Tang[1], ZhongPing Lai[1], GuanJun Xu[2], XianHe Zhang[2] and YiXuan Wang[3]*

[1] Institute of Marine Sciences, Guangdong Provincial Key Laboratory of Marine Biotechnology, Shantou University, Shantou, China, [2] Guangdong Geological Survey Institute, Guangzhou, China, [3] Salt Lake Chemistry Analysis and Test Center, Qinghai Institute of Salt Lakes, Chinese Academy of Sciences, Xining, China

Establishing a reliable chronological framework for sediments is crucial to the reconstruction of evolution process of estuarine delta, and the study of regional paleoenvironmental history, e.g., sea level fluctuations due to global climatic changes. High resolution chronology is still very limited for Holocene sediments in the Pearl River delta (PRD) in southern China. This study tries to construct a detailed chronology for core DA of 37.7 m in depth by using luminescence (seven samples) and radiocarbon (fourteen samples) dating techniques. Our results indicate that both luminescence and radiocarbon dating methods are suitable for the Holocene sediments in the PRD and that sediments of core DA were deposited during 7.3–0.18 ka. The ^{14}C age is generally older than the OSL age for the sediment at the similar depths, and the age difference increased from 0.45 ka at the depth of 21 m to 0.98 ka at the depth of 35 m. The reason that ^{14}C ages are relatively older might be caused by the carbon-reservoir effect which requires further study. The sedimentation rate increased from 3.74 m/ka during 7.3–2 ka to 7.92 m/ka in the last 2 ka. The appearances of rusty stains in upper unit of the core revealed that the water level was gradually falling. After the formation of underwater sand body at about 2 ka, the sediment was subject to continuous shifting between submergence and exposure.

Keywords: optically stimulated luminescence dating, radiocarbon dating, drilling core, Holocene environment, the Pearl River delta in southern China

OPEN ACCESS

Edited by:
Hai Xu,
Tianjin University, China

Reviewed by:
Junyi Ge,
Institute of Vertebrate Paleontology and Paleoanthropology (CAS), China
Anchuan Fan,
University of Science and Technology of China, China

****Correspondence:***
ZhongPing Lai
zhongping.lai@yahoo.com;
zhongping_lai@stu.edu.cn

[†] These authors have contributed equally to this work

Specialty section:
This article was submitted to Quaternary Science, Geomorphology and Paleoenvironment, a section of the journal Frontiers in Earth Science

Received: *11 March 2020*
Accepted: *11 June 2020*
Published: *03 July 2020*

Citation:
Xu X, Li H, Tang L, Lai Z, Xu G, Zhang X and Wang Y (2020) Chronology of a Holocene Core From the Pearl River Delta in Southern China. Front. Earth Sci. 8:262. doi: 10.3389/feart.2020.00262

INTRODUCTION

As the product of complex dynamic actions in littoral zones, estuarine delta is a key area in studying the regional paleoenvironmental history, and provides an important window to understand the coupling interplay among eustasy, climate, and tectonics on the deltaic evolution (e.g., Hori et al., 2001; Saito et al., 2001; Sarkar et al., 2009; Tang et al., 2010; He et al., 2017; Pennington et al., 2017; Li et al., 2018; Bomer et al., 2019; Pleuger et al., 2019; Xu et al., 2019). To obtain such information, accurate and reliable chronology is of crucial importance. Radiocarbon dating (e.g., Hori et al., 2001; Nageswara Rao et al., 2012; Xu et al., 2019) and luminescence dating (e.g., Shen and Mauz, 2012; Sugisaki et al., 2015; Nian et al., 2018;

Wang F. et al., 2018; Wang Z. H. et al., 2018; Wang et al., 2019) have been widely used for dating the Holocene deltaic sediments.

The Pearl River delta (PRD) is one of the biggest estuarine deltas in China. Based on seismic reflection profiles and borehole data, studies on the Quaternary deposits showed that the PRD has experienced a major transgressive-regressive cycle during the Holocene, and formed a corresponding terrestrial unit and a marine unit (Fyfe et al., 1997; Owen et al., 1998; Zong et al., 2009b; Yu, 2017). Zong et al. (2009a) proposed an evolution model of PRD for the time interval of the last 9 cal ka BP, based on lithological characteristics, microfossil assemblages and 34 new or published radiocarbon dates of 35 cores drilled from north to the south of PRD, together with the archaeological and historical documents. They showed that three driving factors, including sea level changes, monsoon-drive discharge and human activities, played important roles in different stages of delta formation, respectively. Ten ^{14}C ages of core PRD11 in the central PRD showed that the regional Holocene stratum was formed during 8.6 to 0.4 cal ka BP, and that the sedimentation rate decreased from 1.74 m/ka (8.6 to 4.7 cal ka BP) to 0.72 m/ka (4.7–0.4 cal ka BP) (Liu et al., 2016). Hu et al. (2013) obtained ten AMS ^{14}C ages, ranging from 8.0 to 1.2 cal ka BP, on mollusk fossils for a 6 m-thick mud layer with occasional shell-rich intervals from core B2/1, which was located in the mouth of the Pearl River Bay. They also reported an event of enhanced sediment weathering intensity during the last 2.5 cal ka BP. Again by radiocarbon dating on core HKUV11 from a near-shore location of the northern South China Sea, seven marine shell ages revealed that the stratum above the hard and mottled sandy-clayey silt was formed during 9.2–1.6 cal ka BP, with a stable sedimentation rate of 1.8 m/ka (Wu et al., 2017).

From the above mentioned studies, it seems that an ideal chronological framework can be obtained in most radiocarbon studies. However, problems also exist in these previous studies. The age data density of some sediment cores is relatively low. For instance, core PK16 (20 m long) in Zong et al. (2009a) had only three ages. Core B2/1 (10 m long) had the best dating density with only ten ^{14}C ages (Hu et al., 2013). In a few studies, the radiocarbon ages from the top part of the cores were relatively older than expected (e.g., Hu et al., 2013; Wu et al., 2017). Some other studies reported that the ^{14}C dates from the surface samples were abnormally old by up to 2 ka, and that these dating samples might be the allochthonous materials transported by flow and tides (Yim et al., 2006; Kong et al., 2014). Study on the natural Δ^{14}C data of river water from carbonate-rich PRD revealed that PRD could release negative particulate organic carbon (POC) that represented old carbon from deeper sediments and sedimentary rocks, which had significant effect on the organic carbon ages (Liu et al., 2017). For instance, the Δ^{14}C-POC value obtained from the Xijiang River in the dry season corresponds to a radiocarbon age of 2820 a BP (Liu et al., 2017).

Compared with the numerous ^{14}C dating ages reported, there are only a few case studies using optical stimulated luminescence (OSL) technique in the PRD. In order to determine the position of ancient coastal lines, Peng et al. (2014) recognized that the marine muddy-silt outcrop, deposited on a wave-cut platform in the central PRD, was formed at 5.5–5.0 ka, based on three samples by fine-grained quartz OSL dating. Using seven cores from Dongjiang River sub-delta, Guo et al. (2013) built a relatively rough chronological framework of late Quaternary sediments based on 13 fine-grained quartz OSL ages and 13 radiocarbon ages, and pointed out that most of the OSL ages are consistent with ^{14}C ages in Holocene stratum. But this claim was based on only a pair of OSL and ^{14}C ages from similar depths. They also concluded that the marine transgression inundated almost the whole Dongjiang River sub-delta during the Holocene transgression event (ages $<$ 8 ka).

Although there are many stratigraphic studies and radiocarbon dating data of the Holocene sediments in the PRD, the application of OSL dating and the comparative analysis of OSL and ^{14}C techniques is still limited. This study attempts to build a high resolution chronological framework for a 37.7-m-long core drilled from southern PRD using both OSL (seven samples) and radiocarbon dating (fourteen samples).

THE STUDIED AREA AND SAMPLING

The Studied Area

The Pearl River delta is located in the central of Guangdong province, southeast coast of China, covering an area of 8601 km^2. It is composed of deltas of Dongjiang River, Xijiang-Beijiang River and Tanjiang River (Huang et al., 1982). The neotectonic movement in the PRD is mainly characterized by faulting and differential uplift of fault blocks (Huang et al., 1982; Yao et al., 2008). The main fault zones have been active during the Quaternary (Liu, 1994). To some extent, the faults controlled the topography of the basement and river direction of the delta (Yu et al., 2016). Since the Holocene, the fault activity in the PRD became weaker, and the river system basically inherited the pattern before the last marine transgression (Yao et al., 2008). In geomorphic features, the north, east, west sides of delta are surrounded by mountains and hills, and the south is facing the South China Sea (**Figure 1**). The delta plain is also dotted with hilly platforms, while the delta front has low hills. The basement is characterized by gentle undulation, two parallel ridges and valleys and checkerboard pattern (Huang et al., 1982). The average sedimentary thickness of Quaternary strata was only about 25.1 m, with the Xijiang River and Beijiang River deltas relatively thicker (25.6 m on average; Huang et al., 1982).

Core DA and Sampling

Core DA was drilled from a sand bar, located in the Xijiang River estuary of western PRD (**Figure 1**), and had a length of 37.7 m. The core was drilled by direct mud rotary with $>$90% recovery rate. The sediments are mainly composed of clay and silt, mixed with thin layers or lens of fine sand with horizontal beddings (**Figure 2**), and can be divided into three units. From bottom to top: Unit 1 (37.7–22.52 m) shows light gray silt with a small amount of clay; Unit 2 (22.52–18.0 m) is a dark gray silt mixed with thin layers of clay, and with thicker sandy layers occurring at the depths of 20.00–19.70 and 19.00–18.10 m; and Unit 3 (18.0–5.0 m) is brown clay mixed with silt. The upper five meters are reworked materials by human re-filling.

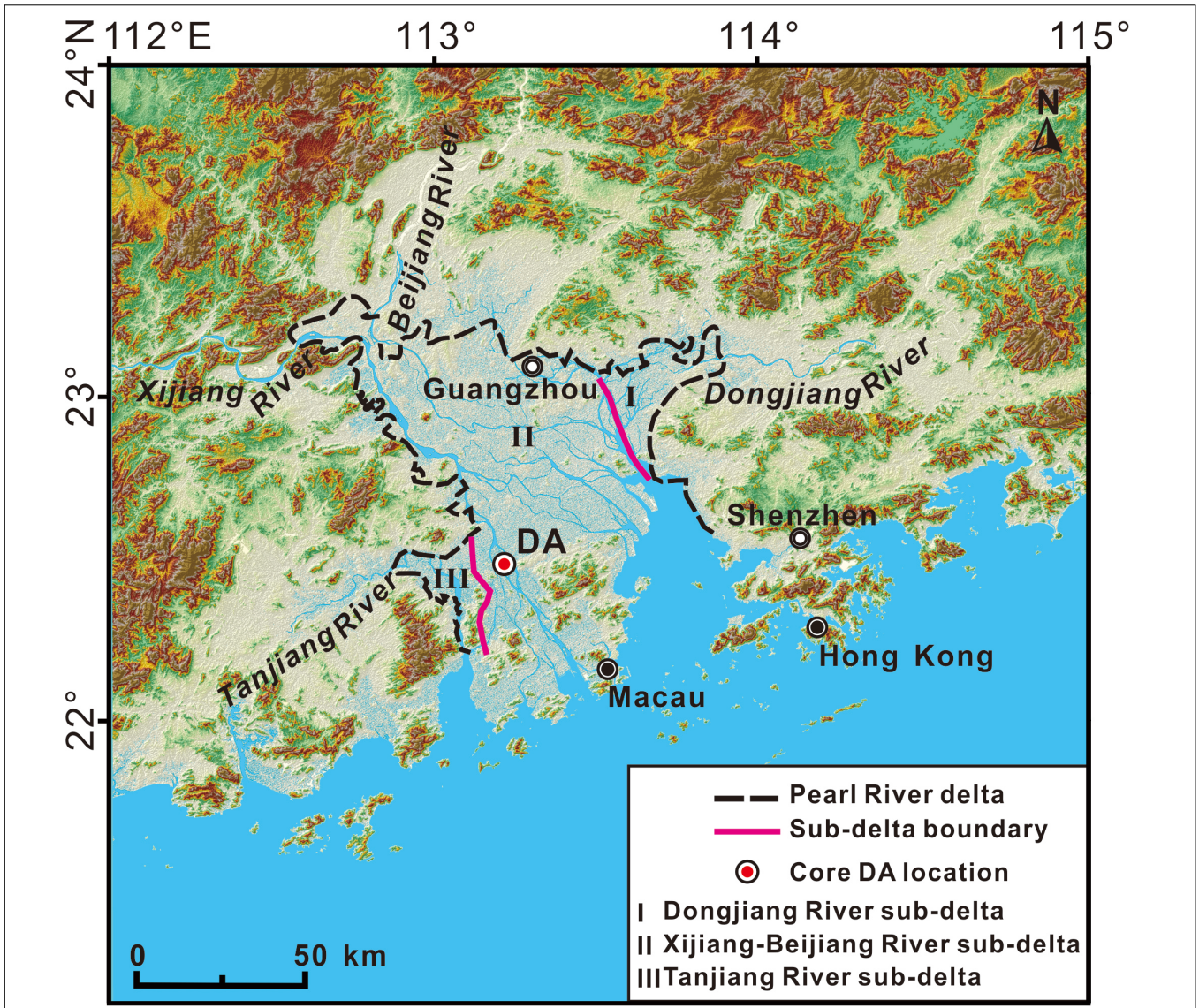

FIGURE 1 | Topographic characteristics of the Pearl River delta (PRD) and location of core DA. The PRD can be divided into Dongjiang River sub-delta (zone I), Xijiang-Beijiang River sub-delta (zone II) and Tanjiang River sub-delta (zone III). Core DA is located in the south of zone II.

The core contains many rust stains (**Figure 2**). The mild rust stain first occurred at the depth of 25.55 m and the moderate rust stain first occurred at 24.40 m. The moderate rust stain was found at 16.85 m with a thickness of about 3 cm. The frequency of upward rust stains increased after the occurrence of thin layer sand with severe rust stains at 13.80 m.

MATERIALS AND METHODS

OSL Dating

Sample Preparation

Seven samples were dated. All operations followed the routines of luminescence dating procedures (Lai, 2010), and were carried out under subdued red light in the laboratory. The out layer of the sample that might have been light-exposed was removed, and the remaining samples were successively treated to remove carbonate and organic matter with 10% HCl and 30% H_2O_2. The samples were then wet sieved to obtain 38–63 or 90–125 μm grain size particles, depending on availability. Samples with a grain size of 90–125 μm were then etched with 40% HF for ~60 min to remove feldspar minerals, while samples of 38–63 μm were treated with 35% H_2SiF_6 for about 2–3 weeks, and both were then washed with 10% HCl for about 30 min to remove the chloride precipitation generated during the reaction. To ensure the quartz purity, infrared stimulated luminescence (IRSL) measurement was conducted. Finally, the quartz sample was uniformly coated as a mono-layer on the central part (~0.7 cm diameter) of stainless-steel discs (~0.97 cm diameter) by silicone oil.

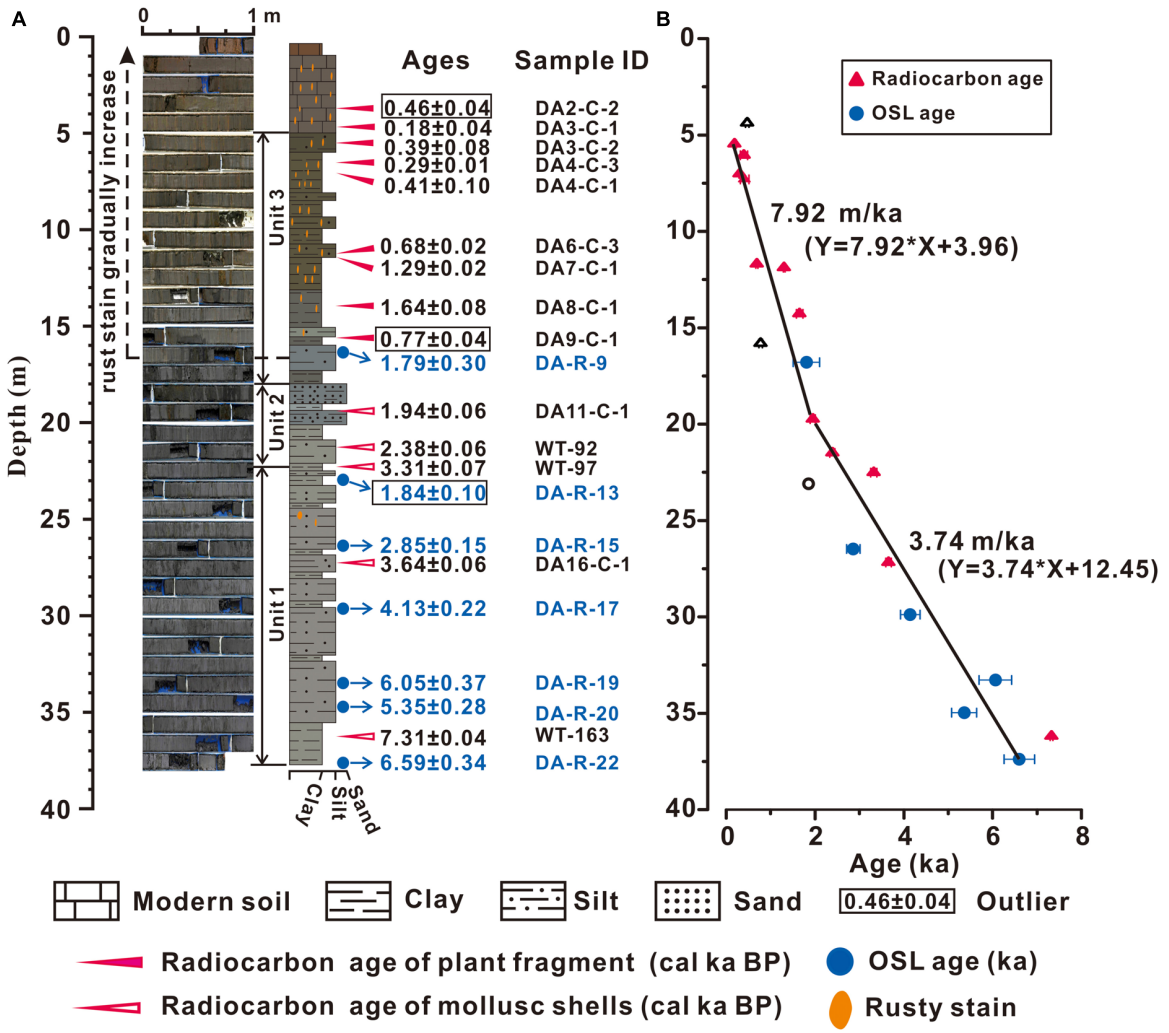

FIGURE 2 | Profile of core DA showing **(A)** the lithology, OSL and radiocarbon ages; **(B)** the age-depth model. The color of core profile represents the color observed from field. The hollow triangle and circle in **(B)** represent the outlier age of ^{14}C and OSL, respectively.

Equivalent Dose (D_e) Determination

OSL measurements were performed on a Risø TL/OSL-DA-20 reader equipped with a $^{90}Sr/^{90}Y$ beta source. Quartz signals were stimulated by a blue light (λ = 470 ± 20 nm) for 40 s at 130°C. The signal was recorded by 9235QA photomultiplier through a 7.5 mm Hoya U-340 filter. The equivalent dose (D_e) was determined by a combination of single aliquot regenerative-dose (SAR) protocol (Murray and Wintle, 2000) and standard growth curve (SGC) protocol (Roberts and Duller, 2004; Lai, 2006). The experiment results of preheat plateau test and dose recovery test from Yu (2017) showed that it is feasible to choose the preheat temperature of 260°C with duration of 10 s during the SAR and SGC protocol for dating deltaic samples from PRD. Therefore, the preheat temperature for regeneration doses is chosen to be of 260°C for 10 s, and the preheating temperature for test doses 220°C for 10 s. Four to six aliquots of each sample were measured by using SAR protocol and an SGC curve was established for each sample. To determinate the natural signal (L_N) and the test dose signal (T_N), another six to twelve aliquots under the same measurement parameters were measured. Each value of L_N/T_N was projected into the SGC curve to obtain a D_e value. The final D_e value is the average of all D_e values measured by both SAR and SGC protocols.

Dose Rate Determination

Neutron activation analysis (NAA) was used to obtaining U, Th, and K. The cosmic ray dose was calculated based on the altitude, geographical location and depth of the samples (Prescott and Hutton, 1994). The contribution of alpha particles was also taken into account in the quartz grains of 38–63 μm with a coefficient of 0.035 ± 0.003 (Lai et al., 2008). The measured moisture content was used, with an uncertainty of ± 8% in the age calculation by considering seasonal variation of precipitation in the studied area. The dose rates and final ages were calculated on the website program of DARC (Durcan et al., 2015).

Radiocarbon Dating

A total of 14 radiocarbon samples were collected from core DA. Eight plant fragment samples collected at depths of 4.43, 5.51, 6.09, 7.06, 11.72, 11.91, 14.30, and 15.84 m were sent to Peking University. One plant fragment collected at the depth of 7.34 m and five mollusk shells at depths of 19.76, 21.51, 22.52, 27.18, and 36.18 m were sent to the Beta Analytic Radiocarbon Dating Laboratory. Based on the difference of sample properties, the IntCal04 (Reimer et al., 2004) and the Marine13 (Reimer et al., 2013) calibration curves were chosen for the calibration of plant fragment samples and mollusk shells samples, respectively. Calibrated ages were obtained by using the procedure OxCal v3.10 (2).

RESULTS

Luminescence Characteristics and OSL Ages

Most samples showed good luminescence behavior. OSL growth curves and decay curves of represented aliquot for samples DA-R-09 (90–125 μm) and DA-R-20 (38–63 μm) are shown in **Figure 3**. As can be seen from the decay curves, the OSL signal rapidly decreases to the background value within 1 s, indicating that quartzes are mainly composed of fast components. The recycle ratio of sample DA-R-09 (1.00–1.05) and DA-R-20 (0.98–1.07) indicate that the correction of test dose for sensitivity changes is ideal. The ratio of zero dose to natural dose $[(L_0/T_0)/(L_N/T_N)]$, sample DA-R-09 at 0.07–1.4%, and DA-R-20 at 0.5–0.9% are all lower than the threshold of 5%, indicating that the recuperation is negligible. Laboratory known-dose can also be recovered with 10% error.

The OSL dating results are listed in **Table 1**. OSL ages range from 6.59 ± 0.34 ka to 1.79 ± 0.30 ka. Overall, the OSL ages increase with depth and conform to the general stratum sequences.

Radiocarbon Ages

The radiocarbon dating results are listed in **Table 2** and **Figure 2**. The AMS ^{14}C ages range from 7,306 ± 36 cal a BP to 180 ± 37 cal a BP. Among them, Sample DA2-C-2 (462 ± 40 cal a BP) from the top might be re-deposited material. And Sample DA9-C-1 (766 ± 38 cal a BP) at a depth of 15.84 m shows an abnormally young age, which may be due to the introduction

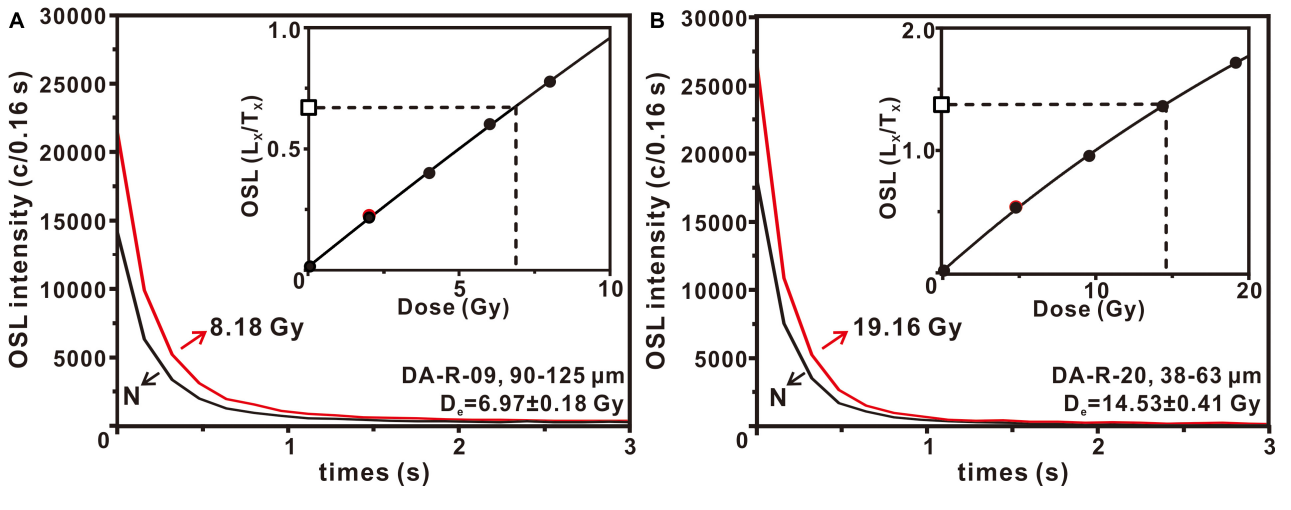

FIGURE 3 | Luminescence properties of sample DA-R-09 **(A)** and DA-R-20 **(B)**. The black lines and red lines represent OSL decay curves of the natural signal and regeneration signal, respectively. The growth curves are shown in the set charts. Black cycles, regenerative doses; Red cycles, recycled doses; hollow square, natural doses.

TABLE 1 | OSL dating results from core DA.

Sample ID	Depth (m)	Grain size (μm)	Aliquot number	K (%)	Th (ppm)	U (ppm)	Moisture (%)	Dose rate (Gy/ka)	D_e (Gy)	OSL age (ka)
DA-R-9	16.8	90–125	$6^a + 12^b$	1.4 ± 0.1	11.8 ± 0.3	2.2 ± 0.1	28.8 ± 8	2.09 ± 0.11	3.7 ± 0.6	1.79 ± 0.30
DA-R-13	23.09	38–63	$4^a + 6^b$	1.3 ± 0.1	15.9 ± 0.4	3.4 ± 0.1	27.4 ± 8	2.63 ± 0.14	4.8 ± 0.1	1.84 ± 0.10
DA-R-15	26.49	38–63	$4^a + 6^b$	1.5 ± 0.1	14.1 ± 0.4	2.6 ± 0.1	33.1 ± 8	2.42 ± 0.12	6.9 ± 0.1	2.85 ± 0.15
DA-R-17	29.89	38–63	$4^a + 6^b$	1.6 ± 0.1	14.5 ± 0.4	2.8 ± 0.1	31.6 ± 8	2.57 ± 0.13	10.6 ± 0.1	4.13 ± 0.22
DA-R-19	33.28	38–63	$4^a + 6^b$	1.4 ± 0.1	12.1 ± 0.3	2.7 ± 0.1	28.6 ± 8	2.32 ± 0.12	14.0 ± 0.4	6.05 ± 0.37
DA-R-20	34.98	38–63	$4^a + 12^b$	1.6 ± 0.1	15.9 ± 0.4	2.7 ± 0.1	30.4 ± 8	2.62 ± 0.14	14.0 ± 0.2	5.35 ± 0.28
DA-R-22	37.39	38–63	$4^a + 12^b$	1.8 ± 0.1	17.6 ± 0.5	3.1 ± 0.1	30.9 ± 8	2.92 ± 0.15	19.2 ± 0.2	6.59 ± 0.34

The superscript "a" means aliquot numbers for SAR protocol and superscript "b" means aliquot numbers for SGC protocol.

TABLE 2 | Radiocarbon dates from core DA.

Sample ID	Depth (m)	Dating material	^{14}C age (a BP)	Calibrated age (2σ; cal a BP)
DA2-C-2	4.43	Plant fragment	365 ± 30	462 ± 40
DA3-C-1	5.51	Plant fragment	330 ± 30	180 ± 37
DA3-C-2	6.09	Plant fragment	185 ± 20	390 ± 82
DA4-C-3	7.06	Plant fragment	235 ± 20	294 ± 13
DA4-C-1	7.34	Plant fragment	350 ± 30	405 ± 95
DA6-C-3	11.72	Plant fragment	730 ± 25	678 ± 23
DA7-C-1	11.91	Plant fragment	1370 ± 20	1293 ± 18
DA8-C-1	14.3	Plant fragment	1745 ± 30	1642 ± 76
DA9-C-1	15.84	Plant fragment	875 ± 25	766 ± 38
DA11-C-1	19.76	Gastropod shell	1990 ± 30	1938 ± 58
WT-92	21.51	Clam shell fragment	2340 ± 30	2377 ± 62
WT-97	22.52	Oyster shell fragment	3100 ± 30	3307 ± 74
DA16-C-1	27.18	Gastropod shell	3400 ± 30	3638 ± 62
WT-163	36.18	Oyster shell fragment	6400 ± 30	7306 ± 36

of "new" carbon during burial or sample treatment. Samples DA2-C-2 and DA9-C-1 are treated as outliers, and will not be considered in the sedimentation rate discussion. Apart from these two samples, ^{14}C ages increase with depth and conform to the general stratum sequences.

DISCUSSION

Assessment of the Radiocarbon and OSL Ages

Previous studies compared ages by both radiocarbon and OSL dating methods on delta deposits. In studies of transgression events during the last glacial-interglacial period in coastal areas of eastern China, most ^{14}C dating ages fell into MIS 3 (e.g., Huang et al., 1982; Lin et al., 1989; Yim et al., 1990; Liu et al., 2009; Yin et al., 2016; Ye et al., 2017). These dating results could be problematic due to the limits of ^{14}C dating (Yim et al., 1990; Yi et al., 2013; Lai et al., 2014; Song et al., 2015; Yu et al., 2019), including the "reservoir effects" in coastal deposits (Stanley and Chen, 2000; Alves et al., 2015), the "new" carbon introduction during exposure (Yim et al., 1990), and the restricted theoretic upper limit to 50 ka (Reimer et al., 2013) or pracitcal upper limit to only 25–30 ka (Lai et al., 2014; Song et al., 2015; Yu et al., 2019). The dating results of similar transgression deposits by other dating methods are mostly concentrated in MIS 5, such as OSL (e.g., Owen et al., 1998; Yi et al., 2013; Yu et al., 2017), or uranium-series dating (Yim et al., 1990).

For Holocene samples, most of the radiocarbon ages agree well with the OSL ages along the south Bohai Sea (Yi et al., 2013). In eastern PRD, Guo et al. (2013) found out that most of the Holocene ^{14}C ages were consistent with the OSL ages, but a few ^{14}C results were obviously younger. The radiocarbon results from incised valley of the Yangtze River delta are mostly not in stratigraphic order due to contamination by old carbon material, while the OSL ages shows better results (Nian et al., 2018).

In this study, OSL and ^{14}C ages are in general consistent with the stratigraphic order. The cross validation between OSL and ^{14}C ages only appeared below the depth of 16.8 m. Therefore, we chose results that below 16.8 m in depth for detailed comparison. The linear curve fittings of both the calculated ^{14}C ages and OSL ages within the depths of 16.8 to 37.4 m show that the fitting results are satisfactory, with R square of 0.96 for ^{14}C ages, and 0.89 for OSL ages, respectively (**Figure 4**). According to the fittings, the ^{14}C ages are in general older than OSL ages, and the difference between these two dating results become larger with the increase of depth. The discrepancy can be directly reflected by taking the depth data into these two fitting equations for calculation. For instance, at the depth of 21 m, the fitted OSL age is 1.81 ± 0.14 ka while the fitted ^{14}C age is 2.26 cal ka BP, with a difference of 0.45 ka. At the depth of 35 m, the fitted OSL age is 5.87 ± 0.46 ka while the fitted ^{14}C age is 6.85 cal ka BP, with a difference of 0.98 ka. The error of OSL age is taken from the average error of all the measured OSL ages.

Accurate radiocarbon dating of shells requires evaluation of local marine reservoir effect. In the study of marine reservoir correction for Southeast Asia, Southon et al. (2002) suggested that source waters entering the South China Sea were quite equilibrated with the atmospheric ^{14}C, which gave low regional corrections (mean ΔR values = −25 ± 20 years) for the southern and central part of South China Sea, and that a probably ΔR values lies between −25 ± 20 years and −149 ± 7 years for the South China coast. Compared with marine samples, mollusks from estuarine environment might have higher reservoir correction due to the additional carbonates input from bedrock and soil (Reimer, 2014). River water from carbonate-rich PRD can carry old carbon from deeper sediments and sedimentary rocks, and this hard water effect will cause abnormally higher ^{14}C ages (Liu et al., 2017). The fact that the ^{14}C ages are older than OSL ages in this study may be due to this carbon-reservoir effect. Meanwhile, carbon-reservoir effect in Holocene marine samples in the southwestern Pacific may have large ΔR values variation (maximum difference for about 410 years) during 8–5.4 ka, while the ΔR values are close to modern values after 5.4 ka (Hua et al., 2015). ^{14}C reservoir effect in Lake Bosten, northwestern China, trended to be greater in dry periods than in wet periods (Zhou et al., 2020). And this change might be related to the variable proportion of organic matter, which due to the different hydroclimatic conditions (Zhou et al., 2020). The reason for temporal difference in the ^{14}C reservoir effect in the PRD, as we found in core DA, requires further study.

Chronology of Core DA and the Paleoenvironmental Implications for the Pearl River Delta

As shown in **Figure 2**, the sediment of core DA was deposited during 7.3–0.18 ka. Unit 1 (37.73–22.52 m) was deposited since 7.3–3.3 ka. This unit is composed of light gray silt, with rich broken bivalve shells and assemblages dominated by marine and estuary species. The rusty stain first appeared in this unit at depths 25.55–24.40 m with an age of about 3.0 ka. The appearance of rusty stain indicates that there might be a sea level dropping

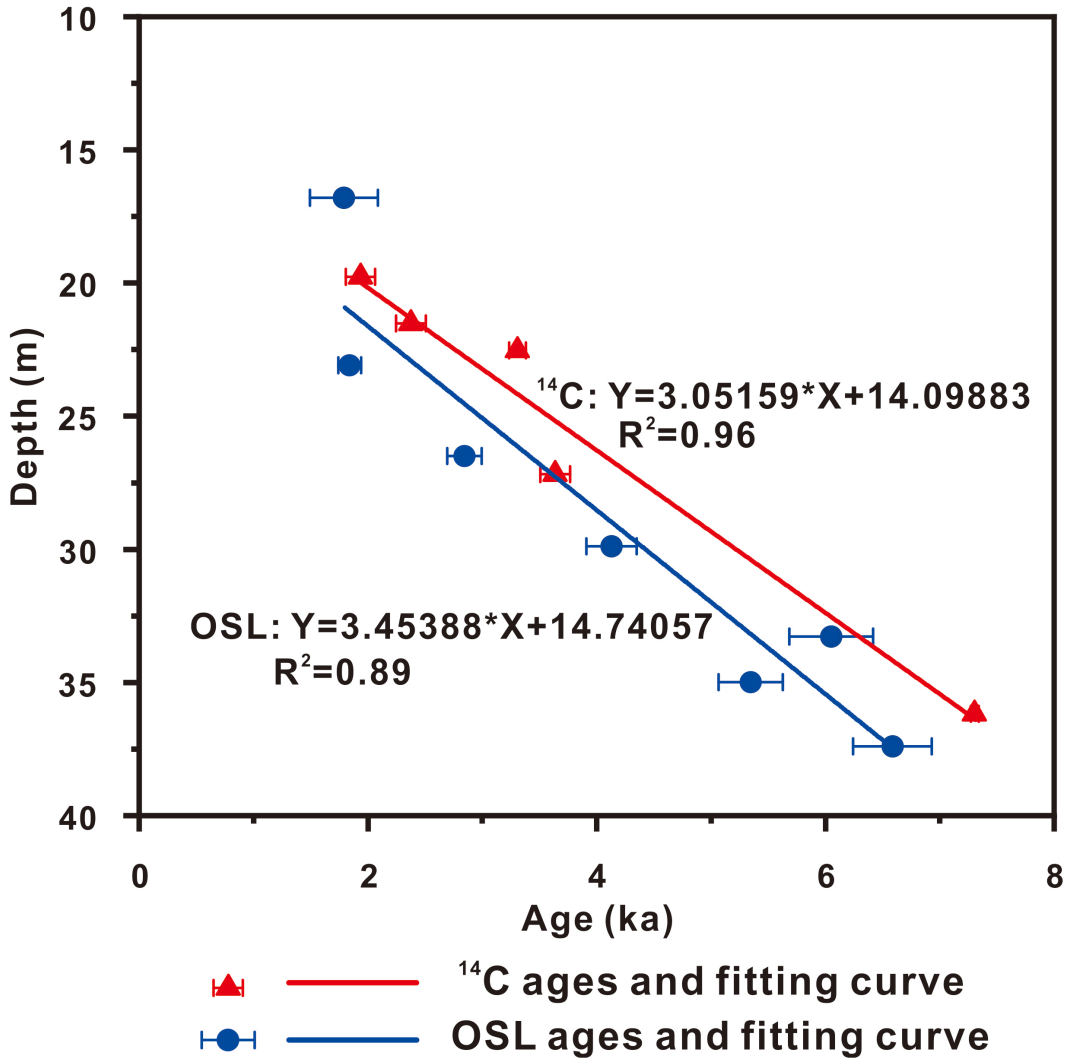

FIGURE 4 | Linear fitting curves for ^{14}C ages and OSL ages of core DA that obtained from depth 16.8 to 37.4 m.

event. Study in the PRD have shown that the iron nodules appeared in marine deposits that formed in mid-Holocene, and it might due to the laterization process during later exposure (Huang et al., 1982). Others suggested that sea level was relatively high or stable during that time (Fang et al., 1991; Zong, 2004; Xiong et al., 2018).

Unit 2 (22.52–18.0 m) consists of dark gray silt with thin layers of clay, and two thick sandy layers appears at depths 20.00–18.10 m. This unit represents two sets of underwater sand body and the formation age is about 3.3–2.0 ka. Unit 3 (18.0–5.0 m) was deposited since about 2.0 ka. From 16.85 m upwards, the number of horizontal thin layer with rusty stain and iron nodules gradually increase and become common in sediments. The accumulation of Fe^{3+} indicates frequent fluctuation of water level. A study on cores from southern PRD also found out that after 2.5 ka the weathering intensity sharply increased till the present day (Hu et al., 2013). Huang et al. (2018) presented similar results for samples from northern South China Sea, showing that intense chemical weathering in the northern shelf after 2 cal ka BP.

The sediment accumulation rate shows two-phase changes (**Figure 2**). During 7.3–2 ka (37.73–19.76 m), the rate is around 3.74 m/ka. It increases to around 7.92 m/ka during the last 2 ka (19.76–5.51 m). The PRD is a composite delta formed by several rivers in a semi-closed bay, which may result in different rates in different locations (Fu et al., 2020). A study on the sedimentary rates in different locations of PRD revealed that the deltaic shoreline advanced and the sedimentation rate in the north and south wings of the central basin increased after about 4 ka (Fu et al., 2020). Meanwhile, core PRD11, which was drilled from the central PRD, showed that the sedimentation rate decreased from 1.74 m/ka (8.6–4.7 cal ka BP) to 0.72 m/ka (4.7–0.4 cal ka BP), due to the regional sedimentary environment changed into a alluvial plain setting in the later period (Liu et al., 2016). However, the statistical results of 92 cores in PRD revealed that the deposition center had shifted to the estuary area since 2.5

ka, and the sedimentary rate is 5.33 m/ka, compared to 2.15 m/ka during 5.0–2.5 ka (Wei et al., 2011).

The extremely high accumulation rate since 2 ka was also observed in the Yangtze River delta. For instance, core SD recorded an accumulation rate of 48 m/ka in the last 2 ka (Nian et al., 2018). The sediment trapping rate has increased from 99–113 Mt/a during 6–2 cal ka BP to 162 Mt/a in the last 2 ka at the Yangtze River mouth (Wang Z. H. et al., 2018). Most studies linked this increase to the influence of intensified human activities, such as extensive influx of migrants and the expansion of agricultural land (Hori et al., 2001; Xu et al., 2012; Wang Z. H. et al., 2018). Other researches rather linked it to the paleo-coastline change and the shift of deposition center (Feng et al., 2016; Nian et al., 2018). In the PRD, the sea level already reached the modern position and stayed stable during the last 2 ka (Xiong et al., 2018). Zong et al. (2009a) and Huang et al. (2018) mentioned that after the sea level reached the present stable level, the whole delta was dominated by fluvial force, and the increased fluxes of river deposit was mainly contributed by the enhanced human activities. Core DA is located at the head area of the Xijiang River estuary. The acceleration of accumulation rate occurs after the formation of underwater sand body at 2 ka. According to the characters of lithologic and assemblages of microfossils revealed by core DA (data unpublished), the regional environment changed from relatively open estuary bay to relatively closed one at 2 ka, which caused the reduction in outward sediment flux and trapping of a large amount of sediment. In this case, the high sedimentation rate since 2 ka recorded by core DA could be interpreted as reflecting the enhanced fluvial force and the increased deposition flux, rather than the increased human activities.

CONCLUSION

Our results indicate that both luminescence and radiocarbon methods are applicable for dating the Holocene sediments in the PRD. However, ^{14}C age is generally older than the OSL age for samples from similar depths. The age difference increased from 0.45 ka (OSL age is 1.81 $\pm$ 0.14 ka while ^{14}C age is 2.26 cal ka BP) at the depth of 21 m to 0.98 ka (OSL age is 5.87 $\pm$ 0.46 ka while ^{14}C age is 6.85 cal ka BP) at the depth of 35 m. The reason for this discrepancy might be due to the carbon-reservoir effect. This requires further study.

The core DA was deposited during 7.3–0.18 ka. The first appearance of rust stains at about 3.0 ka (depths 25.55–24.40 m) may be caused by marine regression. Two sets of underwater sand bodies were formed during about 3.3–2.0 ka. And after that time, rust stains in horizontal thin layers gradually increased and become common, which indicate frequent fluctuation of water level. A significant increase in sedimentation rate was observed, from 3.74 m/ka before 2 ka to 7.92 m/ka since 2 ka.

DATA AVAILABILITY STATEMENT

The datasets generated for this study are available on request to the corresponding author.

AUTHOR CONTRIBUTIONS

ZL was in over-all charge. XX and HL contributed to the analysis and writing work equally. LT, GX, and XZ finished the drilling and sampling work. YW was responsible to the OSL dating. All authors contributed to the article and approved the submitted version.

FUNDING

This research was supported by the special funds for Geological Survey Projects of the China Geological Survey Bureau (Grant No. 12120113066000), Special Project of Geological Hazard Control, Guangdong Province, China (Grant No. 2017201), and NSFC (Grant No. 41877438).

ACKNOWLEDGMENTS

We thank Prof. XiaoQiang Yang for help in dating work.

REFERENCES

Alves, E., Macario, K., Souza, R., Pimenta, A., Douka, K., Oliveira, F., et al. (2015). Radiocarbon reservoir corrections on the Brazilian coast from prebomb marine shells. *Q. Geochronol.* 29, 30–35.

Bomer, E. J., Bentley, S. J., Hughes, J. E. T., Wilson, C. A., Crawford, F., and Xu, K. (2019). Deltaic morphodynamics and stratigraphic evolution of middle Barataria bay and middle Breton sound regions, Louisiana, USA: implications for river-sediment diversions. *Estuar. Coast. Shelf Sci.* 224, 20–33. doi: 10.1016/j.ecss.2019.03.017

Durcan, J. A., King, G. E., and Duller, G. A. T. (2015). DRAC: dose rate and age calculator for trapped charge dating. *Q. Geochronol.* 28, 54–61. doi: 10.1016/j.quageo.2015.03.012

Fang, G. X., Li, P. R., and Huang, G. Q. (1991). Sea level changes in Zhujiang delta during the past 8000 years. *Georaph. Res.* 10, 1–11.

Feng, Z. B., Liu, B. H., Zhao, Y. X., Li, X. S., Jiang, L., and Si, S. K. (2016). Spatial and temporal variations and controlling factors of sediment accumulation in the Yangtze River estuary and its adjacent sea area in the Holocene, especially in the Early Holocene. *Continent. Shelf Res.* 125, 1–17. doi: 10.1016/j.csr.2016.06.007

Fu, S. Q., Xiong, H. X., Zong, Y. Q., and Huang, G. Q. (2020). Reasons for the low sedimentation and slow progradation in the Pearl River delta, southern China, during the middle Holocene. *Mar. Geol.* 423, 106–133.

Fyfe, J. A., Selby, I. C., Shaw, R., James, J. W. C., and Evans, C. D. R. (1997). Quaternary sea-level change on the continental shelf of Hong Kong. *J. Geol. Soc.* 154, 1031–1038. doi: 10.1144/gsjgs.154.6.1031

Guo, L. T., Wang, P., Zhang, K., Sheng, Q., Zhao, H., and Wang, C. M. (2013). OSL and 14C ages of the Late Quaternary sediments in the east Pearl River Delta. *Geol. China* 40, 1842–1849.

He, M., Zhuo, H. T., Chen, W. T., Wang, Y. M., Du, J. Y., Liu, L. H., et al. (2017). Sequence stratigraphy and depositional architecture of the Pearl River Delta system, northern South China Sea: an interactive response to sea level, tectonics and paleoceanography. *Mar. Petrol. Geol.* 84, 76–101. doi: 10.1016/j.marpetgeo.2017.03.022

Hori, K., Saito, Y., Zhao, Q. H., Cheng, X. R., Wang, P. X., Sato, Y., et al. (2001). Sedimentary facies and holocene progradation rates of the changjiang (Yangtze) delta, China. *Geomorphology* 41, 233–248. doi: 10.1016/s0169-555x(01)00119-2

Hu, D. K., Clift, P., Böning, P., Hannigan, R., Hillier, S., Blusztajn, J., et al. (2013). Holocene evolution in weathering and erosion patterns in the Pearl River delta: weathering in holocene Southern China. *Geochem. Geophys. Geosyst.* 14, 2349–2368. doi: 10.1002/ggge.20166

Hua, Q., Webb, G. E., Zhao, J. X., Nothdurft, L. D., Lybolt, M., Price, G. J., et al. (2015). Large variations in the Holocene marine radiocarbon reservoir effect reflect ocean circulation and climatic changes. *Earth Planet. Sci. Lett.* 422, 33–44. doi: 10.1016/j.epsl.2015.03.049

Huang, C., Zeng, T., Ye, F., Xie, L. H., Wang, Z. B., Wei, G. J., et al. (2018). Natural and anthropogenic impacts on environmental changes over the past 7500 years based on the multi-proxy study of shelf sediments in the northern South China Sea. *Q. Sci. Rev.* 197, 35–48. doi: 10.1016/j.quascirev.2018.08.005

Huang, Z. G., Li, P. R., Zhang, Z. Y., Li, K. H., and Qiao, P. N. (1982). *The Formation and Evolution of Pearl River Delta*. Guangzhou: Science Popularizaiton Press.

Kong, D. M., Zong, Y. Q., Jia, G. D., Wei, G. J., Chen, M. T., and Liu, Z. H. (2014). The development of late holocene coastal cooling in the northern South China Sea. *Q. Intern.* 349, 300–307. doi: 10.1016/j.quaint.2013.08.055

Lai, Z. P. (2006). Testing the use of an OSL standardised growth curve (SGC) for De determination on quartz from the Chinese Loess Plateau. *Rad. Measur.* 41, 9–16. doi: 10.1016/j.radmeas.2005.06.031

Lai, Z. P. (2010). Chronology and the upper dating limit for loesssamples from Luochuan section in the Chinese Loess Plateau using quartz OSL SAR protocol. *J. Asian Earth Sci.* 37, 176–185. doi: 10.1016/j.jseaes.2009.08.003

Lai, Z. P., Mischke, S., and Madsen, D. (2014). Paleoenvironmental implications of new OSL dates on the formation of the "Shell Bar" in the Qaidam Basin, northeastern Qinghai-Tibetan Plateau. *J. Paleolimnol.* 51, 197–210. doi: 10.1007/s10933-013-9710-1

Lai, Z. P., Zöller, L., Fuchs, M., and Brückner, H. (2008). Alpha efficiency determination for OSL of quartz extracted from Chinese loess. *Rad. Measur.* 43, 767–770. doi: 10.1016/j.radmeas.2008.01.022

Li, Y., Shang, Z. W., Tsukamoto, S., Tamura, T., Yi, L., Wang, H., et al. (2018). Quartz and K-feldspar luminescence dating of sedimentation in the North Bohai coastal area (NE China) since the late pleistocene. *J. Asian Earth Sci.* 152, 103–115. doi: 10.1016/j.jseaes.2017.10.036

Lin, J. X., Zhang, S. L., Qiu, J. B., Wu, B. Y., Huang, H. Z., Huang, H. Z., et al. (1989). Quaternary marine transgressions and paleoclimate in the Yangtze River delta region. *Q. Res.* 32, 296–306. doi: 10.1016/0033-5894(89)90096-3

Liu, C. Y., Yin, J., Lian, L. C., Huang, Y., and Wu, Y. Q. (2016). Holocene mollusc records and palaeoenvironmental changes in the Pearl River delta. *Trop. Geogr.* 36, 355–363.

Liu, J., Yoshiki, S., Hong, W., Liang, Y. Z., and Zi, G. Y. (2009). Stratigraphic development during the Late Pleistocene and Holocene offshore of the Yellow River delta, Bohai Sea. *J. Asian Earth Sci.* 36, 318–331. doi: 10.1016/j.jseaes.2009.06.007

Liu, Z. H. (1994). Neorectonics at the Pearl river mouth basin in South China Sea. *Geol. Res. South China Sea* 6, 30–50.

Liu, Z. H., Zhao, M., Sun, H. L., Yang, R., Chen, B., Yang, M. X., et al. (2017). "Old" carbon entering the South China Sea from the carbonate-rich Pearl River Basin: coupled action of carbonate weathering and aquatic photosynthesis. *Appl. Geochem.* 78, 96–104. doi: 10.1016/j.apgeochem.2016.12.014

Murray, A. S., and Wintle, A. G. (2000). Luminescence dating of quartz using an improved single-aliquot regenerative-dose protocol. *Rad. Measur.* 32, 57–73. doi: 10.1016/s1350-4487(99)00253-x

Nageswara Rao, K., Saito, Y., Nagakumar, K. C. V., Demudu, G., Basavaiah, N., Rajawat, A. S., et al. (2012). Holocene environmental changes of the Godavari Delta, east coast of India, inferred from sediment core analyses and AMS14C dating. *Geomorphology* 175-176, 163–175. doi: 10.1016/j.geomorph.2012.07.007

Nian, X. M., Zhang, W. G., Wang, Z. H., Sun, Q. L., and Hutchinson, S. M. (2018). The chronology of a sediment core from incised valley of the Yangtze River delta: comparative OSL and AMS14C dating. *Mar. Geol.* 395, 320–330. doi: 10.1016/j.margeo.2017.11.008

Owen, R. B., Neller, R. J., Shaw, R., and Cheung, P. C. T. (1998). Late Quaternary environmental changes in Hong Kong. *Palaeogeogr. Palaeoclimatol. Palaeoecol.* 138, 151–173. doi: 10.1016/s0031-0182(97)00129-6

Peng, Z. L., Chen, G. N., Grapes, P., Qiu, Y., Zhang, K., and Wang, J. (2014). Optically Stimulated Luminescence dating of sediments from the Pearl River delta, Southeast China. *J. Earth Sci. Eng.* 4, 378–384.

Pennington, B. T., Sturt, F., Wilson, P., Rowland, J., and Brown, A. G. (2017). The fluvial evolution of the holocene Nile Delta. *Q. Sci. Rev.* 170, 212–231. doi: 10.1016/j.quascirev.2017.06.017

Pleuger, E., Goiran, J. P., Mazzini, I., Delile, H., Abichou, A., Gadhoum, A., et al. (2019). Palaeogeographical and palaeoenvironmental reconstruction of the Medjerda delta (Tunisia) during the Holocene. *Q. Sci. Rev.* 220, 263–278. doi: 10.1016/j.quascirev.2019.07.017

Prescott, J. R., and Hutton, J. T. (1994). Cosmic ray contributions to dose rates for luminescence and ESR dating: large depths and long-term time variations. *Rad. Measur.* 23, 497–500. doi: 10.1016/1350-4487(94)90086-8

Reimer, P. J. (2014). Marine or estuarine radiocarbon reservoir corrections for mollusks? A case study from a medieval site in the south of England. *J. Archaeol. Sci.* 49, 142–146. doi: 10.1016/j.jas.2014.05.002

Reimer, P. J., Baillie, M. G. L., Bard, E., Bayliss, A., Beck, J., Bertrand, C. H., et al. (2004). IntCal04 Terrestrial radiocarbon age calibration, 0–26 cal kyr BP. *Radiocarbon* 46, 1029–1058. doi: 10.1017/s0033822200032999

Reimer, P. J., Bard, E., Bayliss, A., Beck, J. W., Blackwell, P. G., Ramsey, C. B., et al. (2013). IntCal13 and Marine13 radiocarbon age calibration curves 0–50,000 years cal BP. *Radiocarbon* 55, 1869–1887. doi: 10.2458/azu_js_rc.55.16947

Roberts, H. M., and Duller, G. A. T. (2004). Standardised growth curves for optical dating of sediment using multiple-grain aliquots. *Rad. Measur.* 38, 241–252. doi: 10.1016/j.radmeas.2003.10.001

Saito, Y., Yang, Z. S., and Hori, K. (2001). The Huanghe (Yellow River) and Changjiang (Yangtze River) deltas: a review on their characteristics, evolution and sediment discharge during the Holocene. *Geomorphology* 41, 219–231. doi: 10.1016/s0169-555x(01)00118-0

Sarkar, A., Sengupta, S., Mcarthur, J. M., Ravenscroft, P., Bera, M. K., Bhushan, R., et al. (2009). Evolution of ganges–brahmaputra western delta plain: clues from sedimentology and carbon isotopes. *Q. Sci. Rev.* 28, 2564–2581. doi: 10.1016/j.quascirev.2009.05.016

Shen, Z. X., and Mauz, B. (2012). Optical dating of young deltaic deposits on a decadal time scale. *Q. Geochronol.* 10, 110–116. doi: 10.1016/j.quageo.2012.01.014

Song, Y., Lai, Z., Li, Y., Chen, T., and Wang, Y. (2015). Comparison between luminescence and radiocarbon dating of late quaternary loess from the Ili Basin in Central Asia. *Q. Geochronol.* 30, 405–410. doi: 10.1016/j.quageo.2015.01.012

Southon, J., Kashgarian, M., Fontugne, M., Metivier, B., and Yim, W.-S. W. (2002). Marine reservoir corrections for the Indian Ocean and Southeast Asia. *Radiocarbon* 44, 167–180. doi: 10.1017/s0033822200064778

Stanley, D. J., and Chen, Z. Y. (2000). Radiocarbon dates in China's Holocene Yangtze delta: record of sediment storage and reworking, not timing of deposition. *J. Coast. Res.* 16, 1126–1132.

Sugisaki, S., Buylaert, J. P., Murray, A., Tada, R., Zheng, H., Bo Ke, W., et al. (2015). OSL dating of fine-grained quartz from Holocene Yangtze delta sediments. *Q. Geochronol.* 30, 226–232. doi: 10.1016/j.quageo.2015.02.021

Tang, C., Zhou, D., Endler, R., Lin, J. Q., and Harff, J. (2010). Sedimentary development of the Pearl River Estuary based on seismic stratigraphy. *J. Mar. Syst.* 82, S3–S16.

Wang, F., Nian, X. M., Wang, J. L., Zhang, W. G., Peng, G. Y., Ge, C., et al. (2018). Multiple dating approaches applied to the recent sediments in the Yangtze River (Changjiang) subaqueous delta. *Holocene* 28, 858–866. doi: 10.1177/0959683617752847

Wang, Z. H., Saito, Y., Zhan, Q., Nian, X. M., Pan, D. D., Wang, L., et al. (2018). Three-dimensional evolution of the Yangtze River mouth, China during the holocene: impacts of sea level, climate and human activity. *Earth Sci. Rev.* 185, 938–955. doi: 10.1016/j.earscirev.2018.08.012

Wang, F., Zhang, W. G., Nian, X. M., Ge, C., Zhao, X. Q., Cheng, Q. Z., et al. (2019). Refining the late-Holocene coastline and delta development of the northern Yangtze River delta: combining historical archives and OSL dating. *Holocene* 29, 1439–1449. doi: 10.1177/0959683619854522

Wei, X., Mo, W. J., and Wu, C. Y. (2011). Analysis on the sedimentation rates and depositional environment of the Pearl River delta Area since Holocene. *Acta Sedimentol. Sin.* 29, 329–335.

Wu, M. S., Zong, Y. Q., Mok, K. M., Cheung, K. M., Xiong, H. X., and Huang, G. Q. (2017). Holocene hydrological and sea surface temperature changes in the northern coast of the South China Sea. *J. Asian Earth Sci.* 135, 268–280. doi: 10.1016/j.jseaes.2017.01.004

Xiong, H. X., Zong, Y. Q., Qian, P., Huang, G. Q., and Fu, S. (2018). Holocene sea-level history of the northern coast of South China Sea. *Q. Sci. Rev.* 194, 12–26. doi: 10.1016/j.quascirev.2018.06.022

Xu, K. H., Li, A. C., Liu, J. P., Milliman, J. D., Yang, Z. S., Liu, C.-S., et al. (2012). Provenance, structure, and formation of the mud wedge along inner continental shelf of the East China Sea: a synthesis of the Yangtze dispersal system. *Mar. Geol.* 291-294, 176–191. doi: 10.1016/j.margeo.2011.06.003

Xu, Y. T., Lai, Z. P., and Li, C. A. (2019). Sea-level change as the driver for lake formation in the Yangtze plain – a review. *Glob. Planet. Chang.* 181:102980. doi: 10.1016/j.gloplacha.2019.102980

Yao, Y. T., Zhan, W. H., Liu, Z. F., Zhang, Z. Q., and Zhan, M. Z. (2008). Neotectonics of the Pear River delta and its relationship with the deltaic evolution. *South China J. Selsmol.* 28, 29–40.

Ye, L. T., Yu, G., Liao, M. N., Hu, S. Y., Wang, L. S., and Gao, L. (2017). Terrestrial-marine sedimentary cycles in the South Yellow Sea, China: implications for paleoenvironmental reconstruction since MIS 5. *Turk. J. Earth Sci.* 26, 170–188. doi: 10.3906/yer-1608-18

Yi, L., Lai, Z. P., Yu, H. J., Xu, X. Y., Su, Q., Yao, J., et al. (2013). Chronologies of sedimentary changes in the south Bohai Sea, China: constraints from luminescence and radiocarbon dating. *Boreas* 42, 267–284. doi: 10.1111/j.1502-3885.2012.00271.x

Yim, W. W. S., Huang, G., Fontugne, M. R., Hale, R. E., Paterne, M., Pirazzoli, P. A., et al. (2006). Postglacial sea-level changes in the northern South China Sea continental shelf: evidence for a post-8200 calendar yr BP meltwater pulse. *Q. Intern.* 145-146, 55–67. doi: 10.1016/j.quaint.2005.07.005

Yim, W. W. S., Ivanovich, M., and Yu, K. F. (1990). Young age bias of radiocarbon dates in pre-holocene marine deposits of Hong Kong and implications for pleistocene stratigraphy. *Geo Mar. Lett.* 10, 165–172. doi: 10.1007/bf02085932

Yin, J., Liu, C. L., Wu, J., Huang, Y., and Wu, Y. Q. (2016). Foraminiferal records and palaeoenvironmental changes since the late pleistocene in central Pearl River Delta. *J. Palaeogeogr.* 18, 677–690.

Yu, S. Y., Colman, S. M., and Lai, Z. P. (2019). Late-Quaternary history of 'great lakes' on the Tibetan Plateau and palaeoclimatic implications – A review. *Boreas* 48, 1–19. doi: 10.1111/bor.12349

Yu, Z. X. (2017). *The Age of the Lower Transgression Cycle in the Pearl River Delta and Its Implication of Sea-Level Changes and Neotectonic Movements*. Ph. D. thesis, Sun Yat-sen University, Guangzhou.

Yu, Z. X., Zhang, K., Li, X. Y., Liang, H., and Li, Z. Y. (2017). The age of the old transgression sequence in the Pearl River delta, China. *Acta Geol. Sin.* 91, 1515–1516. doi: 10.1111/1755-6724.13388

Yu, Z. X., Zhang, K., Liang, H., and Li, Z. Y. (2016). Late quaternary tectonic movements in the Pearl River delta, china, revealed from stratigraphic profiles. *Trop. Geogr.* 36, 334–342.

Zhou, K. E., Xu, H., Lan, J. H., Yan, D. N., Sheng, E. G., Yu, K. K., et al. (2020). Variable late Holocene 14C reservoir ages in Lake Bosten, Northwestern China. *Front. Earth Sci.* 7:328. doi: 10.3389/feart.2019.00328

Zong, Y. Q. (2004). Mid-Holocene sea-level highstand along the Southeast Coast of China. *Q. Intern.* 117, 55–67. doi: 10.1016/s1040-6182(03)00116-2

Zong, Y. Q., Huang, G. X., Switzer, A. D., Yu, F. L., and Yim, W. W. S. (2009a). An evolutionary model for the holocene formation of the Pearl River delta, China. *Holocene* 19, 129–142. doi: 10.1177/0959683608098957

Zong, Y. Q., Yim, W. W. S., Yu, F. L., and Huang, G. Q. (2009b). Late Quaternary environmental changes in the Pearl River mouth region, China. *Q. Intern.* 206, 35–45. doi: 10.1016/j.quaint.2008.10.012

Conflict of Interest: The authors declare that the research was conducted in the absence of any commercial or financial relationships that could be construed as a potential conflict of interest.

Copyright © 2020 Xu, Li, Tang, Lai, Xu, Zhang and Wang. This is an open-access article distributed under the terms of the Creative Commons Attribution License (CC BY). The use, distribution or reproduction in other forums is permitted, provided the original author(s) and the copyright owner(s) are credited and that the original publication in this journal is cited, in accordance with accepted academic practice. No use, distribution or reproduction is permitted which does not comply with these terms.

frontiers in Earth Science

ORIGINAL RESEARCH
published: 03 July 2020
doi: 10.3389/feart.2020.00206

AMS ^{14}C Dating Problem and High-Resolution Geochemical Record in Manzherok Lake Sediment Core From Siberia: Climatic and Environmental Reconstruction for Northwest Altai Over the Past 1,500 Years

Tatiana Blyakharchuk[1], Valerii Udachin[2], Hong-Chun Li[3,4] and Su-Chen Kang[3]*

[1] Institute of Monitoring of Climatic and Ecological Systems, Siberian Branch of Russian Academy of Sciences (IMCES SB RAS), Tomsk, Russia, [2] Institute of Mineralogy, Ural Branch of Russian Academy of Sciences (IM UrB RAS), Tomsk, Russia, [3] Department of Geosciences, National Taiwan University, Taipei, Taiwan, [4] Frontiers Science Center for Deep Ocean Multispheres and Earth System and Key Laboratory of Marine Chemistry Theory and Technology, Ministry of Education, Ocean University of China, Qingdao, China

OPEN ACCESS

Edited by:
Liangcheng Tan,
Chinese Academy of Sciences, China

Reviewed by:
Cheng Peng,
Institute of Earth Environment (CAS), China
Jiawu Zhang,
Lanzhou University, China

***Correspondence:**
Hong-Chun Li
hcli1960@ntu.edu.tw

Specialty section:
This article was submitted to Quaternary Science, Geomorphology and Paleoenvironment, a section of the journal Frontiers in Earth Science

Received: *19 March 2020*
Accepted: *18 May 2020*
Published: *03 July 2020*

Citation:
Blyakharchuk T, Udachin V, Li H-C and Kang S-C (2020) AMS ^{14}C Dating Problem and High-Resolution Geochemical Record in Manzherok Lake Sediment Core From Siberia: Climatic and Environmental Reconstruction for Northwest Altai Over the Past 1,500 Years. Front. Earth Sci. 8:206. doi: 10.3389/feart.2020.00206

This study presents high-resolution multi-proxy biological and geochemical records in an 82-cm sediment core from Manzherok Lake located in a forest–steppe zone on the western piedmonts of Altai Mountain, Russia. Based on ^{210}Pb dating and 48 accelerator mass spectrometry ^{14}C dates as well as pollen data and geochemical proxies, detailed lake history and local climatic changes over 1,500 years are obtained. Prior to the Medieval Warm Period (MWP), the lake had high productivity under stable moderately wet and warm conditions. During 1,150–1,070 year BP, strong surface runoff led to a high detritus input and an increasing lake level, reflecting the onset of MWP. The lake was deep and fresh under the warm and wet conditions of MWP (1,070–850 year BP). In this interval, more aquatic algae and submerged plants on the lake bottom were generated, which would use dissolved CO_2 partially decomposed from organic matters in the deeper sediment layers. Consequently, many acid–base–acid-treated samples contain old carbon influence on their ^{14}C dates. This calls for attention on the chronological construction of lake sediments. During 850–700 year BP, the lake level started to drop with reduced sediment load under cooling and drying conditions. Low sedimentation and lake productivity occurred due to cold and dry climates during 700–500 years BP. Very low sedimentation and hiatus were attributed to ice cover and weak water input between 500 and 50 years BP, corresponding to cold and dry Little Ice Age. Manzherok Lake has recovered productivity and deposition during the current warming century. Change in the total solar irradiance (TSI) is an important factor to influence the climate in the Altai Mountains. With decreased TSI, the Siberian High became strong, which led to the Westerly and the polar front being pushed away from this region, resulting in arid climates. The situation was reversed *vice versa*.

Keywords: radiocarbon dating, pollen, geochemical proxy, lake sediment, Russian altai

INTRODUCTION

A small endorheic or closed lake often leads to a high assimilation potential of living matters, which allows the lake to produce high organogenic masses and to form sapropel-type sediments (Korde, 1960; Popolzin, 1967; Lopatko, 1978). The source materials of sapropel formations in a lake normally include the remains of aquatic organisms such as plankton (phytoplankton and zooplankton), algae, macrophytes, and organic matters as well as mineral substances coming from the catchment area. As organic (humus) substances and inorganic mineral impurities (clay and sand) are introduced into the autochthonous organic matter (formed in the lake) under the influence of biochemical, microbiological, and mechanical processes, sapropel of allochthon origin is formed (Korde, 1960; Vine and Tourtelot, 1970; Lopatko, 1978; Poplavko et al., 1978; Gurari and Gavshin, 1981; Neruchev, 1982; Kuzin, 2007). When interpreting geochemical proxies in lake sediments, it is necessary to identify the source and the migration of those elements and isotopes. For instance, Leonova and Bobrov (2012) studied plankton development in reservoirs of the Siberian region. They revealed that, in small lakes, the organic matter of plankton detritus did not significantly change its micronutrient composition while sinking down to the lake bottom. They quantitatively calculated the supply of chemical elements directly through the "plankton channel" into the lake sediments. Vetrov and Kuznetsova (1997) and Granina (2008) studied the geochemistry of diatom pelagic silts and the microelement composition of plankton in Baikal Lake.

In recent years, interesting work has begun to be devoted to the study of the climatic indicator role of chemical elements in sediments (Syso and Yu, 2007; Kalugin et al., 2014; Darin et al., 2014). Syso and Yu (2007) proposed several geochemical indicators for determining the soil properties. It is believed that the enrichment of lake sapropel by mineral components reflects the enhancement of the surface flow of water (Kalugin et al., 2014). Indicators of this phenomena are considered to be "cluster" elements to which Si, Al, Ti, Fe, Mg, Ca, and K belong. The organic fraction of the sediment is more closely related to the increase of temperature at which the bio-productivity of the catchment basin and the water body increases. Some geochemical indices can be directly used for the paleo-reconstruction of the environment. For example, elements with variable valence can be specific indicators of external conditions (Kalugin et al., 2014). Fe is strictly connected with sulfur in sulfate under anoxic conditions. Additionally, Fe forms siderite in carbonate, whereas Mn-enriched layers mark long-term pauses of sedimentation in oxide systems. The Mo/Mn ratio is correlated well with the anoxic environment. According to Kalugin et al. (2014), the Sr/Rb ratio reflects a portion of clay fraction in annually laminated lake deposits of Shira Lake, which marks a stable sedimentation period in winter time. They divided the elements of the bottom sediments of Lake Shira into three clusters: carbonate (Sr, Sc, and Ca), clastic (Zn, Mo, As, Cu, Ni, U, Nb, Ba, Zr, Ga, Mn, Y, Co, Fe, Ti, Rb, and K), and organic pore water (Br, Cl, and S).

The trace metal elements (TME), heavy metal elements (HME), and rare earth elements (REE) in lake sediments are also used for environmental studies. Li (1991) and Leonova et al. (2010) investigated a number of elements that enrich the upper layers of modern lake deposits relatively to clay shale, including their sources and ways to migration in lake sediments. The groups of elements enriching the upper horizons of lake sapropel with respect to clayey shales are singled out as "highly sapropelophilic" elements (the ash concentration coefficients of which KK = 28–15)—P, Br, Mn, As, and Hg; "sapropelophilic" elements (KK = 7–8)—Fe, Mo, Zn, Cd, Cu, Pb, Ag, and Sb; "weakly sapropelophilic" elements (KK = 2–1)—Se and U; and "non-sapropelophilic" elements (KK <1)—alkaline, alkaline earth elements, and rare earth elements (Leonova et al., 2010). In general, it was found that, in small lakes, the plankton contribution significantly exceeds the supply of the microelements from the plant (macrophytic) source, with the exception of Mn. The share of Mn supply through vegetable detritus is about 15 vs. 1% through the plankton supply channel. Plankton is found as a biogeochemical barrier between the atmosphere and the water surface boundary, which intensively retards the chalcophile elements (Cd, As, Sb, Zn, Pb, Hg, Se, *etc.*) emanating from atmospheric precipitation (Leonova and Bobrov, 2012). Low-biophilic elements of Al, Ti, and Zr are used to characterize the role of clastic and clay material in suspended matter and precipitation (Perelman, 1979).

According to previous studies (Boyarkina et al., 1993; Kutsenogiy and Kutsenogiy, 2000; Raputa et al., 2000; Smolyakov, 2000; Moiseenko et al., 2006), an important additional source of micronutrient supply in small closed lakes is atmospheric mineral matter, and the role of the plankton biofilter is very strongly manifested in such environments (Leonova and Bobrov, 2012). Phyto- and zooplankton are mainly the first substance (biofilter) which involves chemical elements in the biological cycle at the atmosphere–water interface. On this barrier, phyto- and zooplankton get enriched by chalcophile elements which enter the water surface of lakes mainly as part of atmospheric precipitation. These elements are separated into a group of so-called "volatile" elements (Malakhov and Makhonko, 1990; Shotyk et al., 1996; Gavshin et al., 2004; Bobrov, 2007; Dauvalter et al., 2008; Bobrov et al., 2011). While precipitating on the earth's surface as part of atmospheric aerosols, chalcophile "volatile" elements get actively induced in the processes of biodifferentiation by living matter as well as by plankton in small lakes (Leonova et al., 2006; Bobrov et al., 2007). The further fate of these elements is determined by the hydrochemical characteristics of the lake water. Moreover, these elements enter the bottom sediments of the plankton detrital composition if the hydrocarbonate class of water shows a pH range of 7–8 (Leonova et al., 2008, 2011; Leonova and Bobrov, 2012). In lakes with sulfate class of water with low pH ranging 5–6, these elements would be leached out from plankton detritus into an aqueous solution and get re-introduced into trophic chains. As, Se, Cd, Hg, and Pb are toxic elements with extremely low background concentrations in water. However, they are characterized by high accumulation coefficients in living organisms (Leonova and Bychinsky, 1998; Leonova, 2004; Leonova et al., 2007). Sc, Zr, Nb, Hf, and Th are included in the group of terrigenous elements. Sc is characterized by low solubility, and it has been suggested

to use, for standardization, the basic elements to evaluate the accumulation of elements in various water bodies using the "enrichment factor" (Shotyk et al., 1996).

In Blyakharchuk et al. (2017), detailed palaeopollen and diatom data and brief elemental data with 21 accelerator mass spectrometry (AMS) ^{14}C dates in an 82-cm sediment core from Manzherok Lake located in a forest–steppe zone on the western piedmonts of Altai Mountain were used for climate and environmental reconstruction over the last 1,400 years. Among the 21 ^{14}C dates, nine non-acid–base–acid (ABA)-treated samples are older than their ABA-treated pairs, even though the ABA-treated samples show a rather scattered chronological stratigraphy (Blyakharchuk et al., 2017). Thus, we have dated more layers with ABA treatment. In this study, a total of 48 AMS ^{14}C dates plus ^{210}Pb dating results from the 82-cm core yield better chronology. The present study reveals detailed TME, HME, and REE contents in the core. Together with physical, biological, and geochemical data sets, a detailed history of the lake and the environmental conditions under climate influence over the past 1,500 years has been discussed. In addition, archeological activity and human impact in the study area will be addressed.

AREA OF STUDY

Manzherok Lake [51.822° N, 85.811° E, 373 m above sea level (a.s.l.)] is a small, freshwater lake located in the western periphery of the Altai Mountains of Southern Siberia on a terrace of the right-hand bend of the Katun' River, 18 km southwest of Gorno-Altaisk City (51°49′15.5" N, 85°48′35.7" E, 423 m a.s.l.) (**Figure 1**). The lake has an elevation of 373 m, which is much higher than that of Katun' River (297 m a.s.l.). Therefore, although the lake is about 2 km away from the river, there is no evidence that the river has invaded the lake over the late Holocene. Geologically, Manzherok Lake lies within the tectonic unit of Bijsk-Katun' anticlinorium—exhibiting more ancient geological structures of the Altai Early Caledonian fold system. Consequently, in the area of Manzherok Lake, a positive element of relief is presented by ancient carbonate rocks of the Baratalsk series (R3-V), formed in the Proterozoik marine environment (Geology of the USSA, 1997). The low mountains around the lake are covered by forest–steppe vegetation with *Betula pendula* (BP) and *Pinus sylvestris*, with patches of *Pinus sibirica*. The climate is moist with a relatively mild temperature even though it is classified as of the West Siberian continental type (Ogureeva, 1980). A more detailed regional setting with detailed pollen and diatom data of Manzherok Lake is presented in an earlier publication (Blyakharchuk et al., 2017).

Although the origin and the history of Manzherok is still under study, Rusanov and Vazhov (2017) provided the most comprehensive summary of the Manzherok Lake studies. The origin of Lake Manzherok was probably caused by a catastrophic breakthrough of the large glacial-dammed lakes of Altai at the

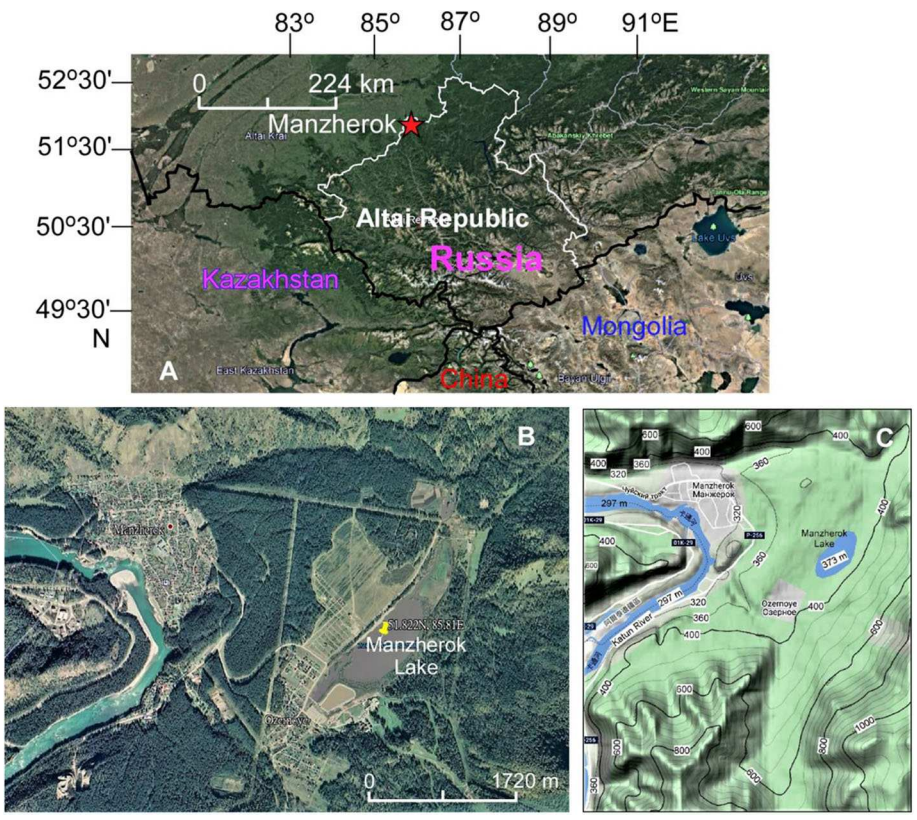

FIGURE 1 | Location of the study area. **(A)** Map of Altai and the surrounding areas. **(B)** Satellite map of the Manzherok area. **(C)** Topographic map with contour lines of the Manzherok area. The figures are modified from maps that have been downloaded from Google Map.

end of the Ice Age. Fed by streams flowing from the surrounding slopes, precipitation, and groundwater, the lake is elliptical in shape and elongated from southwest to northeast. Manzherok Lake is a freshwater open lake, with an outlet at the southwest end through a swampy runoff hollow. The lake water has low pH of 6.2–7.2 and contains low ionic concentrations. The salinity and the alkalinity of the lake are quite low, e.g., CO_3^{2-} and HCO_3^- measurements in the lake in 1972 were 0.0 (non-detectable) and 0.28 mg/100 g water, respectively (Ilyin, 1982). The modern Manzherok Lake is a popular recreation area. Human activities around the lake, such as fishing, farming, and grazing, may have impact on the sedimentary processes to the lake.

METHODS

Elemental Geochemical Analyses of Lake Sediment Samples

About 0.05 g of dry powder lake sediment from every 1-cm horizon of the upper 31-cm section and every 2-cm interval of the 32–82-cm section of the core was precisely weighted and then digested with a mixed acid solution ($HF + HNO_3 + HCl$) in a polytetrafluoroethylene beaker using a microwave system (SpeedWave 3, Berghof, Germany). The microwave program ran for 15 min at about 145°C, for 20 min at 200°C, and a holding time of 15 min, followed by a cool-down procedure of 10 min. After the residue was completely diluted, the evaporate was dissolved repeatedly with concentrated HCl to convert the solution in chloride medium. Then, the solution was diluted to 100 ml volume with 0.5 N HCl. The acid solution was filtered through an acetate filter membrane with 0.45-μm pore size to remove any undissolved particles. The filtered solution was analyzed for 45 elements using inductively coupled plasma-mass spectrometry (Agilent Technologies 7700×, Japan).

Multi-element standards (Agilent) were routinely analyzed as quality control. The analytical performance was assessed through related materials including lake Baikal sediment reference material BIL-1 (Russia) and LKSD-1 (Canada), which all have certified or recommended values. The relative standard deviation was <8%. The recovery of the reference materials ranges 91–112%. A total of 54 samples have been analyzed for TME, HME, and REE.

^{210}Pb Dating and Sedimentation Models

Lead-210 measurement can be achieved by either directly using low-background gamma spectrometry or measuring its decay product (^{210}Po) via alpha spectrometry. Despite being proven efficient for low-density samples (e.g., peat, lake sediment), gamma spectrometry is limited in small samples (e.g., Ebaid and Khater, 2006), while the measurement of low-energy ^{210}Pb gamma photons ($E_{210Pb} = 46.5$ keV) is virtually impossible. The ^{210}Pb dating of the Manzherok Lake core was determined by the ^{210}Po method (Pawlyta et al., 2004; Cooke et al., 2007; Baskaran et al., 2014).

Dry sediment samples of 1.0 g for the top core section and 2.0 g for the bottom position with a known amount of ^{209}Po spike solution were placed into Teflon vessels and digested at a temperature of 120°C using concentrated $HNO_3 + HClO_4 +$ HF. After 12 h of digestion, the solution was centrifuged. The supernatant was transferred into a Teflon beaker and evaporated with 6 M HCl until dryness. The evaporate in the Teflon beaker was dissolved in 10 ml 0.5 N HCl and transferred into a 50-ml centrifuge tube. Ascorbic acid powder was added into the solution to form Fe complex ions in order to prevent the Fe ions to be co-precipitated with Po ions. A silver disk, 8 mm in diameter, was placed in the solution of the centrifuge tube. Then, the centrifuge tube was placed in a water bath at 60°C. Polonium isotopes were spontaneously deposited within 4 h on the Ag disk. The activities of ^{209}Po and ^{210}Po were measured by an alpha spectrometer. Two blank samples were analyzed with each sample batch to verify the quality of the chemical extraction. The procedure of acid extraction and deposition of polonium was outlined in Suriyanarayanan et al. (2008) and Ugur et al. (2003). The total ^{210}Pb activity reached a relatively constant below 13 cm in depth (**Figure 2**). We use the average ^{210}Pb activity below the 13-cm depth as the supported ^{210}Pb activity. The excessive ^{210}Pb ($^{210}Pb_{ex}$) in each sample was obtained by the measured total activity of ^{210}Pb subtracted by the supported ^{210}Pb activity (**Figure 2**). The Constant Rate of Supply model (Appleby, 2001) was applied to the ^{210}Pb inventories calculated from the $^{210}Pb_{ex}$ data to generate ages.

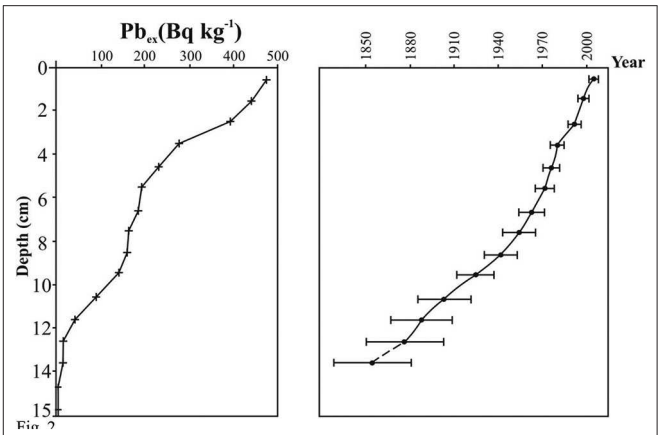

FIGURE 2 | Vertical profiles of ^{210}Pbex of Manzherok Lake sediment core and ^{210}Pb chronologies. The dashed line indicates an interpolation result of age (see text for interpretation).

AMS Radiocarbon Dating

In Blyakharchuk et al. (2017), we reported 21 AMS ^{14}C dates from the core. In that study, we have found that the lake sediments need ABA treatment (Brock et al., 2010). Otherwise, the ^{14}C dates became older than their true ages. Therefore, in the present study, about 0.1 g of bulk gyttja sample from different depths of the core was treated with 0.5 N HCl, 0.5 M NaOH, and 0.5 N HCl sequentially. The dry-treated sample was then placed into a 9-mm quartz tube with pre-combusted CuO powder and a piece of silver and then placed on a vacuum line. The quartz tube was sealed under vacuum of 1e-5 mbar and then combusted for 6 h at 850°C in a muffle furnace. The CO_2 produced by oxidation was transferred and purified cryogenically on the vacuum line

and sealed into combination tubes, which included a 9-mm glass tube with Zn and TiH_2 powders and an inner 6-mm center tube containing Fe powder (Xu et al., 2007). Graphitization of the CO_2 in the tube took place in the muffle furnace at 550°C for 6 h.

Sample graphite was pressed into a target holder and measured for its $^{14}C/^{12}C$ and $^{13}C/^{12}C$ ratios with a 1.0 MV Tandetron Model 4110 BO-Accelerator Mass Spectrometer in the NTUAMS Lab. Every sample batch contains at least three international standards (OXII, 4,900 C), three backgrounds (BKG), and two inter-comparison samples (IRIs). The measurement mode was $^{14}C^{3+}$ to avoid $2Li^{+}$ interference with $^{14}C^{2+}$. Using the $^{14}C/^{12}C$ and the $^{13}C/^{12}C$ ratios of OXII, BKG, and the samples, the percentages of modern carbon (pMC), $D^{14}C$ (= pMC/100–1) × 1,000, and ^{14}C conventional age were calculated with the Libby half-life of 5,568 years (Stuiver and Polach, 1977). $\delta(^{13}C)$ is calculated from the $^{13}C/^{12}C$ ratios of OXII ($\delta^{13}C = -18‰$) and sample, which is used for the correction of carbon isotopic fractionation (against −25‰) during natural and AMS dating laboratory processes. Hence, the $\delta(^{13}C)$ value is not only determined by the carbon isotopic composition of the sample but also strongly influenced by the ABA treatment and the AMS measurement. Measured by AMS, the $\delta(^{13}C)$ is different from $\delta^{13}C$ (measured by isotope-ratio mass spectrometry) and cannot be used for stable isotope interpretation. The conventional age is transferred into calibrated ^{14}C ages with 1σ error using the calibration curve IntCal13 (Stuiver and Reimer, 1993; Niu et al., 2013; Reimer et al., 2013). The ^{14}C ages expressed in this paper are calibrated ^{14}C ages in years BP (0 year BP = 1,950 CE). A total of 48 AMS ^{14}C dates from the core are listed in **Table 1**.

RESULTS AND DISCUSSIONS

Problems of ^{14}C Dates and New Chronology

Table 1 and **Figure 3** show all the ^{14}C dates. First of all, the core contains very high organic content (>20 wt.%) (**Figure 3B**). The core materials have black color with swamp odor, which look totally different from the river sediments and the surrounding debris. The latter ones contain much lower organic matter. The materials in the core are very suitable for ^{14}C dating, especially the lower part which contains organic matter like peat as high as 35 wt.%. However, these organic matters are well-decomposed and difficult to be isolated from the bulk sediments. In the earlier publication (Blyakharchuk et al., 2017), several plant remain samples were AMS ^{14}C dated, even though those plant remains still show old carbon influence on the non-ABA treated ^{14}C dates (**Table 1**). In fact, all non-ABA-treated samples have older ages than those of ABA-treated samples from the same bulk sample pairs. Since the remaining core materials could not pick up more plant remains, in this study we have dated bulk gyttja (sapropel) samples from multiple horizons above 35 cm in depth, with ABA pre-treatment. As the lake sediments were deposited stratigraphically, their ages should become older from top to bottom. In **Table 1**, the first criterion for selecting the corrected dates is to remove all the non-ABA treated samples. The second criterion is to remove an older date (ABA-treated) in the upper layer as the younger dates contain least old carbon influence. If an age in the upper layer is slightly older that in the level below but is within uncertainties, we will keep it.

Although the lake has low pH (6.2–7.2), the carbonate content in the bulk sample still has about 2–5% (**Figure 3**). Those carbonates contain normally old carbon from detritus carried by surface runoff. With ABA treatment, those carbonates can be removed. Another older carbon source comes from organic carbon such as humic acids and/or CO_2 decomposed from deeper sediments. The humic acids decomposed from older organic matter in the deeper sediments may migrate upward and enter the bulk gyttja. The function of base treatment in the ABA procedure is to remove such mobile humic acids. Thus, the ABA-treated samples should be able to eliminate the influence of carbonate and mobile humic acid. However, there are many newly measured ABA-treated samples showing reversed ^{14}C ages (**Table 1** and **Figure 3**). Our hypothesis of this old carbon influence is that dissolved CO_2 in the lake water contained CO_2 decomposed from organic matters in the deeper sediments that was uptaken by submerged plants and aquatic algae to form organic compounds which could not be removed by ABA treatment.

Since the CO_2 decomposed from organic matters in the deeper sediments is a function of lake chemistry such as redox condition, water temperature, pH, and bacterial activity, *etc*., the later ones are affected by water depth and climatic condition. Thus, this old carbon influence is different from "hard water effect" or "reservoir effect." "Hard water effect" is caused by high concentrations of HCO_3^- and CO_3^{2-} in lake water, which commonly exist in closed alkaline lakes. Manzherok Lake does not belong to such a lake. "Reservoir effect" including hard water effect sometimes can be caused by organic carbon input from inflow sediments, for example, Teletskoye Lake in Altai has reservoir age in the ^{14}C ages of bulk organic carbon in the sediments (Rudaya et al., 2016). This lake is also a freshwater lake, but its sediments contain a low percentage of total organic carbon. A total of 16 AMS ^{14}C dates (from two labs) on the TOC of bulk sediments from the lake core show about 2,400–3,000 years of "reservoir age" throughout the sediment core. This is not the case for Manzherok Lake core. In the Manzherok Lake core, there are several ^{14}C dates from plant remains. Even on the bulk gyttja samples from the upper 5-cm part, four ABA-treated samples contain nuclear bomb ^{14}C signal, indicating no reservoir effect (**Table 1**). Thus, the old carbon influence on the ^{14}C age of the Manzherok Lake sediments is not considered as "hard water effect" or "reservoir effect." This influence varies with lake condition with time. **Figure 3A** shows that the old carbon influence was negligible above 19 cm in depth and was relatively weak below 46 cm in depth.

In general, deeper water (higher lake level) is in favor of the anoxic condition in the bottom of the lake. Warmer lake water provides a stronger bacterial activity. The reduced environment would generate CH_4, which would be oxidized into CO_2 during degassing in the lake bottom. In **Figure 3**, most ABA-treated samples with rejected ^{14}C ages are in 40–20-cm depths. This interval belongs to the Medieval Warm Period (MWP). In later

TABLE 1 | Accelerator mass spectrometry ^{14}C dates of the samples from Manzherok Lake core.

Lab code	Sample ID	Depth (cm)	Pretreatment	pMC (%)	^{14}C age (year BP)	Calibrated ^{14}C age (year BP)	$\delta(^{13}C)$ ‰	Type
NTUAMS-3319	MZh 1-2 Pb	1.5	ABA	100.09 ± 1.15	−8 ± 92	Modern	−19.88	Bulk gyttja
NTUAMS-3320	MZh 2-3	2.5	ABA	101.88 ± 0.79	−150 ± 62	Modern	−18.24	Bulk gyttja
NTUAMS-3321	MZh 3-4	3.5	ABA	100.48 ± 0.79	−38 ± 63	Modern	−21.51	Bulk gyttja
NTUAMS-2876	MZh 4-5	4.5	No ABA	98.17 ± 0.72	149 ± 58	145 ± 60*	−25.39	Peat
NTUAMS-2876c	MZh 4-5	4.5	ABA	101.73 ± 0.81	−138 ± 64	Modern	−24.06	Peat
NTUAMS-3322	MZh 5-6	5.5	ABA	94.92 ± 0.75	419 ± 63	505 ± 60	−15.41	Bulk gyttja
NTUAMS-3323	MZh 6-7	6.5	ABA	95.90 ± 0.81	337 ± 68	390 ± 115	−34.75	Bulk gyttja
NTUAMS-3324	MZh 8-9 Pb	8.5	ABA	93.39 ± 1.15	550 ± 99	580 ± 130	−18.59	Bulk gyttja
NTUAMS-3325	MZh 9-10	9.5	ABA	90.43 ± 0.76	808 ± 67	720 ± 30	−31.19	Bulk gyttja
NTUAMS-3326	MZh 11-12	11.5	ABA	90.78 ± 0.72	777 ± 64	710 ± 80	−24.60	Bulk gyttja
NTUAMS-3327	MZh 12-13	12.5	ABA	91.72 ± 0.73	694 ± 64	670 ± 90	−17.95	Bulk gyttja
NTUAMS-3328	MZh 13-14	13.5	ABA	90.28 ± 0.74	821 ± 65	730 ± 30	−36.07	Bulk gyttja
NTUAMS-3329	MZh 14-15	14.5	ABA	91.82 ± 0.73	686 ± 63	670 ± 85	−29.53	Bulk gyttja
NTUAMS-3330	MZh 16-17 Pb	16.5	ABA	88.84 ± 0.77	950 ± 69	875 ± 125	−43.56	Bulk gyttja
NTUAMS-3331	MZh 17-18	17.5	ABA	89.06 ± 0.71	931 ± 64	860 ± 115	−25.09	Bulk gyttja
NTUAMS-3332	MZh 18-19	18.5	ABA	89.02 ± 0.75	935 ± 65	860 ± 115	−34.75	Bulk gyttja
NTUAMS-3333	MZh 19-20	19.5	ABA	85.79 ± 0.66	1,231 ± 61	1,175 ± 120#	−14.62	Bulk gyttja
NTUAMS-3335	MZh 21-22	21.5	ABA	85.81 ± 0.71	1,229 ± 66	1,175 ± 120#	−35.51	Bulk gyttja
NTUAMS-3336	MZh 22-23	22.5	ABA	86.71 ± 0.67	1,146 ± 62	1,040 ± 125#	−24.81	Bulk gyttja
NTUAMS-3337	MZh 23-24	23.5	ABA	85.93 ± 0.68	1,218 ± 64	1,140 ± 120#	−32.04	Bulk gyttja
NTUAMS-2877	MZh 25-26,	25.5	Partial ABA	84.81 ± 0.66	1,323 ± 63	1,280 ± 85*	−37.75	Bulk gyttja
NTUAMS-2877b	MZh 25-26	25.5	ABA	89.09 ± 0.72	928 ± 65	855 ± 115	−19.41	Bulk gyttja
NTUAMS-3248	MZh 26-27	26.5	ABA	86.74 ± 0.70	1,142 ± 65	1,040 ± 130#	−33.74	Bulk gyttja
NTUAMS-3249	MZh 27-28	27.5	ABA	85.44 ± 0.77	1,264 ± 73	1,225 ± 130#	−35.34	Bulk gyttja
NTUAMS-2920	MZh 28-29,	28.5	No ABA	84.70 ± 0.54	1,334 ± 51	1,290 ± 85*	−25.30	Bulk gyttja
NTUAMS-2920b	MZh 28-29	28.5	ABA	87.73 ± 0.70	1,051 ± 64	980 ± 145	−15.67	Bulk gyttja
NTUAMS-3250	MZh 28-29	28.5	ABA	89.02 ± 0.70	934 ± 63	860 ± 115	−36.75	Bulk gyttja
NTUAMS-3251	MZh 29-30	29.5	ABA	85.85 ± 0.67	1,226 ± 63	1,165 ± 130	−28.52	Bulk gyttja
NTUAMS-3253	MZh 30-31	30.5	ABA	83.14 ± 0.92	1,483 ± 88	1,370 ± 150#	−12.37	Bulk gyttja
NTUAMS-3254	MZh 31-32	31.5	ABA	85.19 ± 0.93	1,288 ± 88	1,235 ± 150#	−15.54	Bulk gyttja
NTUAMS-3255	MZh 32-33	32.5	ABA	85.28 ± 0.92	1,280 ± 87	1,230 ± 145#	−17.04	Bulk gyttja
NTUAMS-3255	MZh 33-34	33.5	ABA	85.59 ± 0.92	1,250 ± 86	1,215 ± 130#	−14.97	Bulk gyttja
NTUAMS-3256	MZh 34-35	34.5	ABA	83.41 ± 0.91	1,457 ± 88	1,350 ± 145#	−18.32	Bulk gyttja
NTUAMS-2878	MZh 39-40	39.5	ABA	96.12 ± 0.61	318 ± 51	380 ± 95*	−25.71	Plant remain
IAAA-150551		40.5	No ABA		1,550 ± 20	1,460 ± 35*	−27.94	Bulk gyttja
NTUAMS-2917	MZh Sc 46-47	46.5	No ABA	84.63 ± 0.59	1,341 ± 56	1,290 ± 90*	−16.72	Macrofossils
NTUAMS-2917b	MZh 46-47	46.5	ABA	86.74 ± 0.74	1,143 ± 68	1,065 ± 130	−32.68	Macrofossils
NTUAMS-2879	MZh Sc-53-54	53.5	ABA	83.67 ± 0.57	1,432 ± 55	1,330 ± 35#	−39.42	Macrofossils
NTUAMS-2880	MZh 60-61	60.5	ABA	85.27 ± 0.55	1,280 ± 52	1,230 ± 70	−33.10	Plant remain
NTUAMS-2918	MZh Sc-63-64,	63.5	No ABA	80.53 ± 0.57	1,740 ± 57	1,660 ± 105*	−24.44	Macrofossils
NTUAMS-2918b	MZh Sc 63-64	63.5	ABA	82.23 ± 0.66	1,572 ± 64	1,470 ± 120#	−17.51	Macrofossils
NTUAMS-2921	MZh 70-71	70.5	No ABA	80.88 ± 0.51	1,705 ± 50	1,605 ± 105*	−21.25	Bulk gyttja
NTUAMS-2921b	MZh 70-71	70.5	ABA	85.29 ± 0.84	1,278 ± 80	1,215 ± 140	−37.39	Bulk gyttja
NSK_UGAMS-21783		70.5	No ABA		1,742 ± 22	1,660 ± 55*	−32.10	Bulk gyttja
NTUAMS-2881	MZh 71-72	71.5	ABA	84.44 ± 0.64	1,358 ± 61	1,295 ± 90	−45.75	Plant remain
NTUAMS-2919	MZh Sc-72-73	72.5	No ABA	79.80 ± 0.51	1,813 ± 51	1,765 ± 100*	−37.06	Bulk gyttja
NTUAMS-2919b	MZh Sc 72-73	72.5	ABA	82.54 ± 0.66	1,541 ± 64	1,445 ± 120	−20.44	Bulk gyttja
IAAA-150552		81.5		83.38 ± 1.14	1,460 ± 20	1,350 ± 35	−17.51	Plant remain

*The symbols * and # mean that the dates are rejected in the chronological construction due to possible multiple carbon sources.*
The errors for percent of modern carbon (pMC) and measured ^{14}C age are 2σ error. The calibrated ^{14}C ages with 1σ error are used in the IntCal13 curve. ABA stands for acid–base–acid treatment.

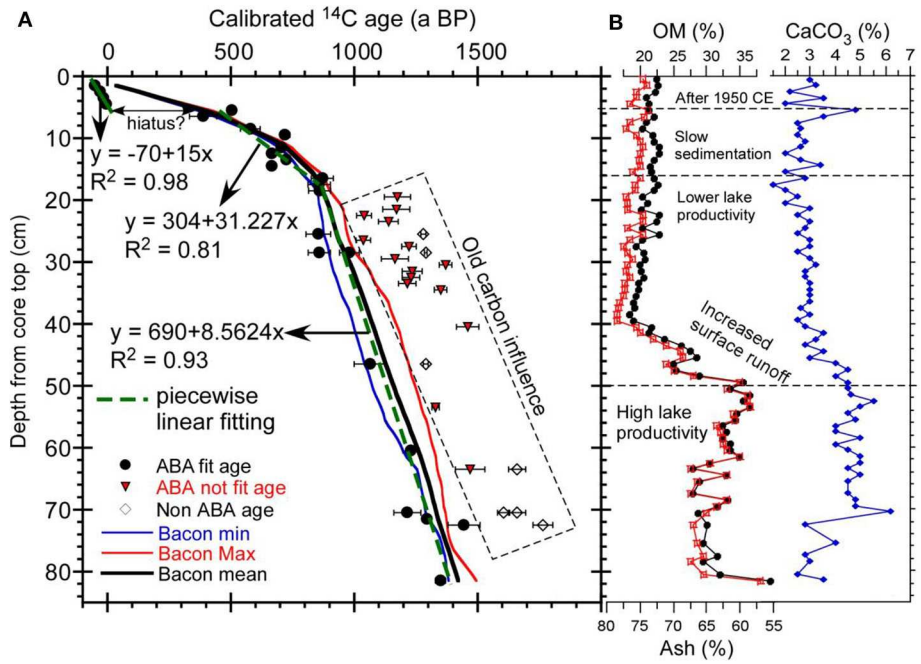

FIGURE 3 | (A) Accelerator mass spectrometry ^{14}C dating and chronology of the core. The three linear equations are used in available ^{14}C ages in three segments: 0–5, 6–20, and 20–82 cm. **(B)** Organic matter (OM, black), ash (red), and $CaCO_3$ contents of the core. Note that the scale axis of OM and ash are opposite so that one can see the lake sediments that contain mainly OM and detritus, which are linearly negatively correlated ($R^2 = 0.99$).

sections, we will interpret that this interval had a higher lake level under warm and wet climatic conditions. Since the lake sediments should be deposited in age sequence, those reversed ages could not be used for chronology construction. Based on the criteria described above, we remain as many reasonable ^{14}C dates as possible for the Bacon age model (Blaauw and Christen, 2011). **Figure 4** exhibits the Bacon age model of the Manzherok Lake core, which shows the core to contain deposition from 1,440 years BP to the present.

Our findings about the problems of ^{14}C dating on the Manzherok Lake sediments call for attention about chronological construction: (1) it is necessary to perform ABA treatment for lake sediments and (2) ABA treatment cannot remove old carbon influence if uptake is older dissolved CO_2 (non-equilibrium with the atmospheric CO_2) by organisms in the lake. In freshwater lakes, terrestrial plant remains in lake cores are often difficult to be obtained for dating. Old carbon influence and age reversion are common, e.g., in Rudaya et al. (2016). Sometimes, with a few ^{14}C dates, the chronology may be not good even if the dates are in a stratigraphic order.

Although the new Bacon age model provides a better chronology than that in Blyakharchuk et al. (2017), it has a problem in the upper 5-cm part. The Bacon age model results yielded ages in the upper 5-cm part of 0–305 years BP. However, four ^{14}C dates in the upper 5 cm show nuclear bomb ^{14}C, reflecting that the lake sediments in this interval must be deposited after 1,950 CE. The ^{14}C ages from 5- to 9-cm depths quickly jumped to 390–580 years BP, indicating that the lake deposition between 5- and 7-cm depths could have hiatus. Because the Bacon age model does not allow sedimentary hiatus, the modeled result forces the ages in the upper 5 cm to become older. Besides that, the ^{210}Pb dating result also indicates that the upper 10-cm part has an apparent $^{210}Pb_{ex}$ decay trend, reflecting modern deposition (**Figure 2**). Therefore, the results of the Bacon age model for the upper 5-cm part were not used. We instead use a linear sedimentation rate given by the ^{210}Pb dating for the upper 5-cm part. The reason that we do not use the ^{210}Pb ages shown in **Figure 2** is that ^{210}Pb in the surface sediments of a freshwater lake can diffuse downward (Benoit and Hemond, 1991), whereas the majority of the organic carbon (plant remains) in the lake sediments are not mobile. Hence, we use the age–depth relationship of the Bacon age model below the 5-cm depth. In the new chronology, there is only one data point (1-cm layer) between 0 year BP (4.5-cm depth) and 465 years BP (6.5-cm depth). This interval represents the depositional period of the Little Ice Age. Nevertheless, the new chronology is significantly improved by more ^{14}C dates and ^{210}Pb. We shall re-interpret the Manzherok Lake record based on the new chronology.

Spore–Pollen Data for Manzherok Lake

A detailed spore–pollen diagram, with descriptions of the pollen zones and the phases of vegetation development in the study area obtained from the Lake Manzherok core, was published earlier (Blyakharchuk et al., 2017). According to the new chronology, the time boundaries of the phases in vegetation development reconstructed based on the pollen zones have changed slightly (**Figure 5**), which can be summarized as follows:

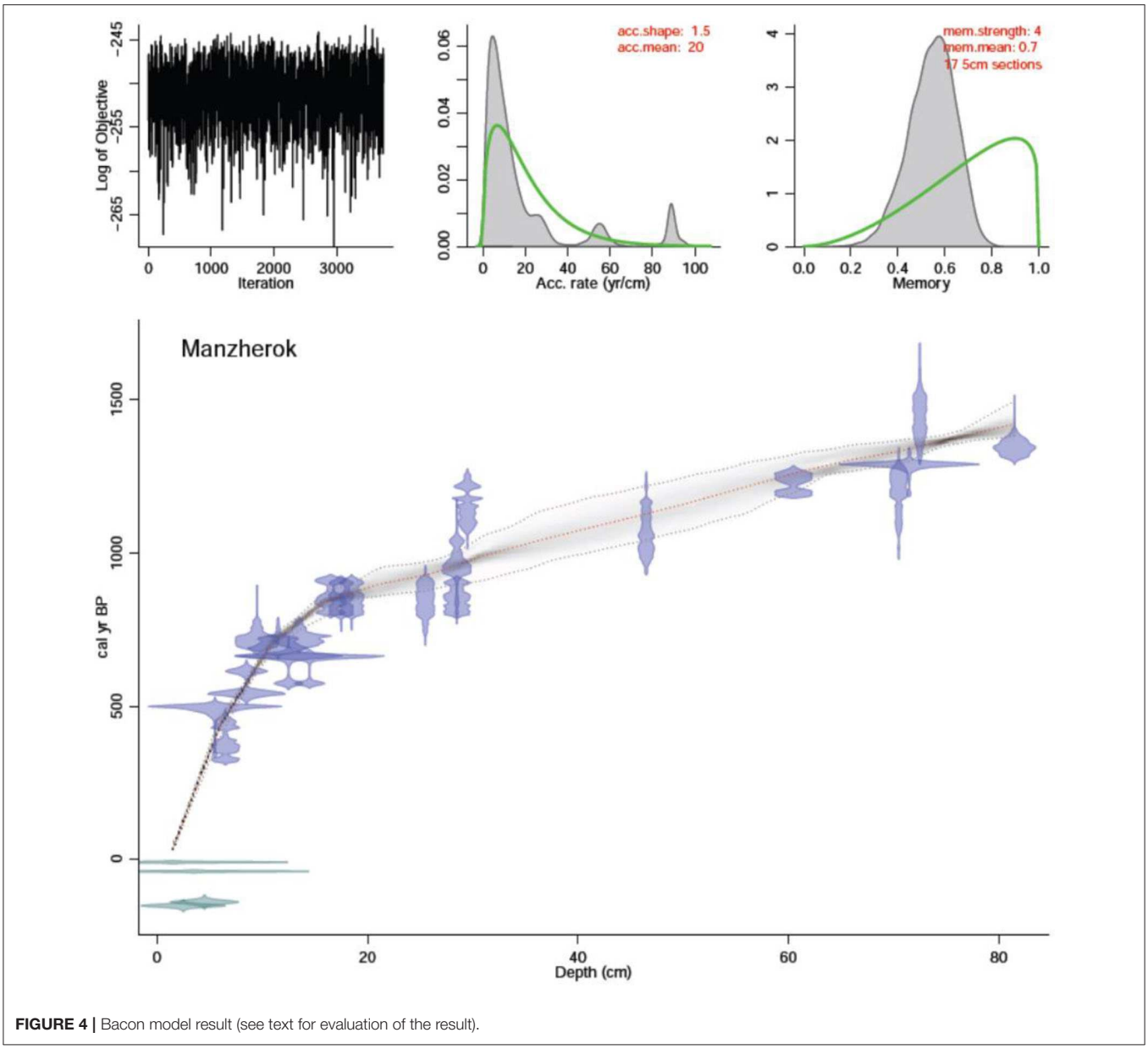

FIGURE 4 | Bacon model result (see text for evaluation of the result).

1. The phase of the birch forest–steppe (pollen zone 1 at 82–50 cm) now is dated 1,440–1,150 years BP or VI–IX centuries AD. (In old chronology, it was 1,350–1,200 years BP).
2. The transitional phase from the birch forest–steppe to birch and pine forests (pollen zone 2 at 50–40 cm) took place at 1,150–1,070 years BP or IX–X centuries AD. (In old chronology, it was 12,00–1,150 years BP).
3. The phase of the birch and pine forests (pollen zone 3 at 40–20 cm) now is dated 1,070–850 years BP or X–XII centuries AD. (In old chronology, it was 1,100–700 years BP).
4. The phase of the pine–birch forest–steppe (pollen zone 4 at 20-cm depth to the surface) now is 850 a BP—contemporary. (In old chronology, it was 700 a BP—contemporary).

Based on the Manzherok pollen data, we reconstruct climate changes in terms of humidity and compare with neighboring palaeoecological data of Teletskoye Lake record (Rudaya et al., 2016) (**Figure 6**). Although the new chronology practically has no significant influence on the interpretations which were made in Blyakharchuk et al. (2017), some differences are addressed below:

1. According to the modified chronology, the period of humid climates during medieval episode became shorter than that in the previous chronology (200 years compared with 400 years). Consequently, it can be concluded that the climate of the medieval climatic anomaly in the western foothills of the Altai was not uniform in terms of the degree of wetness. The early Middle Ages (1,050–900 years BP) was wet, which is marked by the spread of dark coniferous

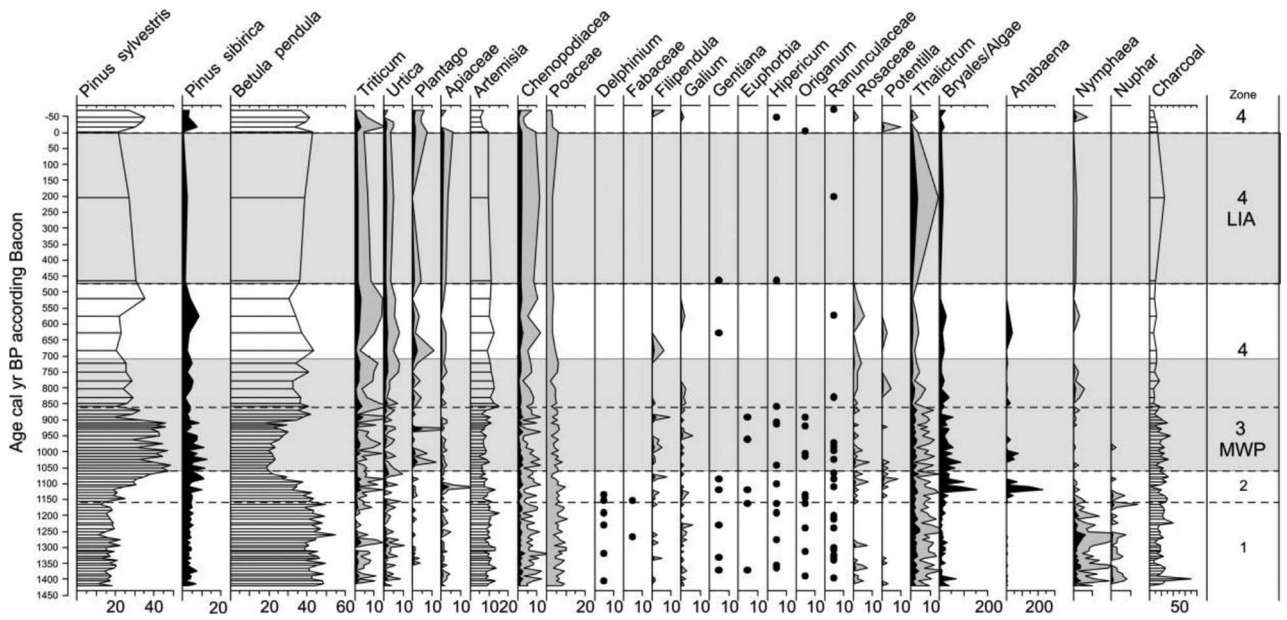

FIGURE 5 | Pollen diagram of Manzherok Lake on even time scale. The pollen types are presented in % from the pollen of terrestrial plants.

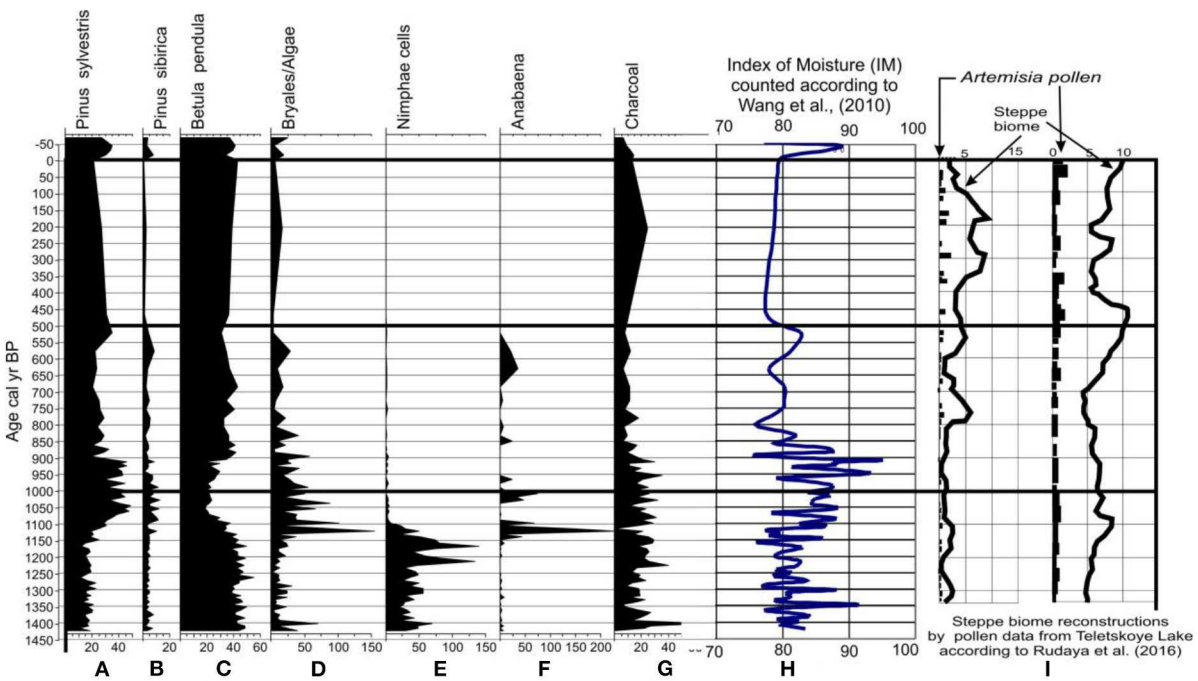

FIGURE 6 | Diagnostic palynomophs of Manzherok Lake and the pollen-based index of humidity of the climate from this study compared with the content of diagnostic *Artemisia* pollen and steppe biome reconstructions in the neighboring Teletskoye Lake (Rudaya et al., 2016). (**A-I**) indicator pollen types and indices based on pollen.

and pine forests in the vicinity of the Manzherok Lake. The late Middle Ages (900–700 years BP) was characterized by relatively dry climate and domination of the birch forest–steppe.

2. The Mongolian invasion (1,236–1,242 years CE) in the territory of Altai to the new chronology is synchronous with the layer of lake sediment at the depth of 11–13 cm or ∼710 years BP (25–30 cm in the old version). During this period,

the climate became less arid than before, and the area occupied by wormwood steppes in the foothills of the Altai decreased. Below this layer of sediment (850–750 years BP), a new series of geochemical data shows two high maxima of Zn and an increase of Cu and Fe content. In the pollen spectrum of this layer, the abundance of pollen of anthropogenic indicators and charcoal was slightly decreased. These indicators confirm our earlier interpretation of the influence of Mongolian invasion on the Altai region (Blyakharchuk et al., 2017).

3. During the cold Little Ice Age (LIA), according to the modified chronology, the rate of sediment accumulation in Manzherok Lake was very low or even absent. The cold and dry climates during LIA could lead to a longer period of frozen lake surface and very low biological productivity in the lake. Low surface runoff under the dry climates reduced the sediment input into the lake. Unfortunately, based on the new chronology, there is only a 2-cm layer falling into LIA. Thus, it is not possible to trace the detailed effect of LIA climates on the lake deposition by biological and geochemical proxies. Besides the very low sedimentation which indicates cold/dry climatic condition, our interpretation on the biological and geochemical results of the 5–7-cm sediment sample deposited during the LIA should be with caution.

Results of High-Resolution Geochemical Analysis

In this study, a new and detailed series of geochemical data (**Table 2**) was obtained for samples of the same core for which spore–pollen, diatom, and preliminary geochemical analyses were made earlier (Blyakharchuk et al., 2017). A total of 54 samples (every 1 cm in the upper 31-cm part and every 2 cm below the 31-cm depth) were used for high-resolution geochemical analysis. A total of 46 elements, including TME, HME, and REE, were analyzed for every sample. It is important to point out that these elements are from the bulk sediment samples which were completely dissolved in HF + HNO_3 + HCl acids by microwave digestion. Therefore, the majority of the elements should come from detritus, mainly from exogenous origins. Their variations probably are mainly due to input change instead of lake chemistry, except for some elements such as alkaline and alkaline earth elements.

Figure 7 plots the variations of selected elements in the core. Among the measured elements, Al, Fe, and Ti are the dominant elements and have high concentrations in the order of mg/g, whereas the other elements are on the orders of mg/kg. Al, Fe, and Ti mainly come from detritus and have a strong positive correlation ($R^2 > 0.9$) with the ash content of the sediment which was determined by loss of ignition at 550°C (Blyakharchuk et al., 2017). Some trace metal and heavy metal elements such as Li, Rb, Th, Nb, Zr, Cr, V, Hf, Sc, and Y have similar patterns as those of Al, Fe, and Ti, indicating that they have the same origins. Together Al, Fe, Ti, Li, Rb, Th, Nb, Zr, Cr, V, Hf, Sc, and Y are considered as lithophilic elements, and their variations are chiefly controlled by detrital input. Furthermore, the REE contents are also strongly correlated with the ash content ($R^2 = 0.88$) (**Figure 8**). Thus, the detrital content of the sediments is the main dominant factor to control the variations of the above-mentioned elements (Dobrovolsky, 1999). Hence, we can classify the geochemical variation of the core as follows:

Zone I: 1,440–1,150 years BP (82–50 cm): high organic (OM) and $CaCO_3$ contents, low ash content, and low TME, HME, and REE contents.

Zone II: 1,150–1,070 years BP (50–40 cm): strongly increased ash content but decreased OM and $CaCO_3$ contents and strongly increased TME, HME, and REE contents.

Zone III: 1,070–850 years BP (40–17 cm): maximum values of ash, lithophilic element, and REE contents, but low OM and $CaCO_3$ contents in the beginning. Then, the lithophilic element and the REE contents gradually decreased.

Zone IV: 850–500 years BP (17–7 cm): the lithophilic element and the REE contents were stable at moderate levels. The sedimentation rate had a significant decrease.

Zone V: 500–50 years BP (7–5 cm): very low sedimentation rate; $CaCO_3$ content increased. Except As and Pb, most elemental concentrations were relatively low.

Zone VI: The last century (5–0 cm): OM and $CaCO_3$ contents increase. Most elemental concentrations are reduced to low values.

The geochemical records shown in **Figures 7**, **8** provide us the lake history under climate influence. During zone I, the lake had relatively high biological productivity as reflected by high OM and $CaCO_3$. The lake was a freshwater lake with a moderate lake level because the organic matter was generally high (28–35%) and the $CaCO_3$ content was only 2–5% in the bulk sediments. With relatively low detritus content, the lake sediments contained low TME, HME, and REE. During zone II, as the surface runoff sharply increased, the OM and the $CaCO_3$ contents rapidly decreased and the ash contents strongly increased, which resulted in strong increases of TME, HME, and REE. During zone III, the surface runoff could be still high. However, as the lake became deeper and larger, sediment loading in the coring site became finer and detritus/OM ratio gradually decreased. The lake level was still high in the beginning of zone IV. Then, as the climate became cooling and drying, the lake input decreased, resulting to lowering of the sedimentation rate during zone IV. The lake had very low sedimentation during zone V due to cold and dry climatic conditions. Until about 100 years ago, the lake started to recover its biological productivity and water input.

Rare earth elements include La, Ce, Pr, Nd, Sm, Eu, Gd, Tb, Dy, Ho, Er, Tm, Tu, Yb, and Lu. Light REEs involve La to Gd, and heavy REEs contain Tb to Lu. Many previous studies have used REE patterns to trace the depositional processes and identify the sediment provenances since they behave conservatively during sediment formation (Prajith et al., 2015; Xu et al., 2017). However, most REE studies of sediment provenances are used in marine environments. For the Manzherok Lake core, the sediment source is relatively simple and the depositional time is relatively short. Therefore, we only use the REE pattern to discuss the sediment feature throughout the core.

Figure 9 shows the REE normalized to North American Shale Composite (NASC) and **Figure 10** reveals the REE normalized to chondrite in different sediment layers. We averaged the patterns

TABLE 2 | Rare earth elements of the Manzherok Lake core samples.

Depth (cm)	Age (a BP)	La	Ce	Pr	Nd	Sm	Eu	Gd	Tb	Dy	Ho	Er	Tm	Yb	Lu	ΣLREE	ΣHREE	ΣLREE/ ΣHREE	ΣREE	δEn	δCe
0–1	−63	20.2	48.5	5.51	21.8	4.60	1.14	4.95	0.72	4.29	0.80	2.28	0.31	2.19	0.30	106.8	10.9	9.8	117.7	1.06	1.07
1–2	−48	20.3	49.5	5.69	22.6	4.84	1.18	5.12	0.74	4.44	0.83	2.36	0.32	2.31	0.32	109.2	11.3	9.7	120.6	1.05	1.07
2–3	−33	20.6	50.2	5.81	23.0	4.86	1.18	5.17	0.75	4.60	0.85	2.39	0.33	2.31	0.33	110.9	11.6	9.6	122.4	1.05	1.06
3–4	−18	21.8	52.8	5.96	23.7	5.05	1.22	5.37	0.78	4.71	0.88	2.53	0.34	2.39	0.34	115.9	12.0	9.7	127.8	1.04	1.08
4–5	−3	27.0	60.5	6.07	24.1	5.16	1.29	5.33	0.75	4.67	0.85	2.55	0.34	2.55	0.33	129.5	12.0	10.8	141.5	1.09	1.10
5–6	203	24.9	55.1	5.57	22.2	4.87	1.13	5.06	0.72	4.14	0.81	2.27	0.31	2.16	0.30	118.9	10.7	11.1	129.6	1.01	1.09
6–7	465	24.7	58.4	5.84	22.6	4.99	1.20	5.24	0.73	4.49	0.85	2.38	0.35	2.40	0.30	123.0	11.5	10.7	134.5	1.04	1.13
7–8	520	24.9	59.4	5.82	22.9	4.98	1.23	5.28	0.74	4.54	0.85	2.41	0.34	2.37	0.35	124.5	11.6	10.7	136.1	1.06	1.15
8–9	574	24.9	60.1	5.90	23.4	4.87	1.24	5.30	0.79	4.61	0.84	2.51	0.33	2.52	0.35	125.8	11.9	10.5	137.7	1.08	1.15
9–10	629	23.9	58.3	5.62	22.2	4.86	1.13	5.16	0.72	4.53	0.83	2.34	0.33	2.46	0.34	121.1	11.6	10.5	132.7	1.00	1.17
10–11	683	23.4	56.9	5.54	22.3	4.74	1.11	5.07	0.69	4.30	0.80	2.33	0.33	2.34	0.33	119.1	11.1	10.7	130.2	1.01	1.16
11–12	724	24.4	58.9	5.81	23.4	4.75	1.18	5.12	0.74	4.42	0.85	2.36	0.35	2.50	0.35	123.6	11.6	10.7	135.1	1.06	1.15
12–13	750	24.5	60.4	5.91	23.0	4.86	1.23	5.29	0.75	4.54	0.84	2.52	0.32	2.64	0.32	125.2	11.9	10.5	137.1	1.08	1.16
13–14	777	23.4	58.2	5.70	21.9	4.82	1.15	5.03	0.73	4.42	0.84	2.39	0.32	2.33	0.31	120.2	11.3	10.6	131.6	1.03	1.17
14–15	803	23.7	58.4	5.62	22.5	4.91	1.19	5.11	0.74	4.37	0.83	2.52	0.34	2.39	0.34	121.4	11.5	10.5	133.0	1.05	1.17
15–16	830	24.6	59.4	5.92	23.0	4.93	1.22	5.07	0.77	4.42	0.84	2.47	0.35	2.32	0.34	124.2	11.5	10.8	135.7	1.08	1.14
16–17	848	23.7	57.1	5.50	22.0	4.92	1.09	5.00	0.73	4.25	0.81	2.36	0.32	2.39	0.35	119.3	11.2	10.6	130.5	0.98	1.16
17–18	859	24.0	59.6	5.76	23.2	5.08	1.18	5.27	0.74	4.56	0.85	2.46	0.33	2.41	0.34	124.2	11.7	10.6	135.8	1.01	1.18
18–19	871	25.7	62.6	6.16	24.6	5.27	1.28	5.50	0.81	4.82	0.90	2.67	0.36	2.39	0.35	131.0	12.3	10.6	143.3	1.06	1.15
19–20	882	26.5	63.7	6.40	25.1	5.78	1.35	5.68	0.80	4.91	0.93	2.75	0.38	2.62	0.36	134.5	12.7	10.5	147.2	1.05	1.13
20–21	893	25.1	60.7	5.92	23.6	4.86	1.20	5.35	0.76	4.57	0.85	2.46	0.35	2.46	0.33	126.7	11.8	10.8	138.5	1.05	1.16
21–22	902	24.7	60.9	5.97	23.9	5.05	1.28	5.28	0.75	4.80	0.87	2.61	0.36	2.57	0.36	127.0	12.3	10.3	139.3	1.10	1.16
22–23	909	25.1	61.2	6.08	24.0	5.18	1.25	5.45	0.78	4.69	0.87	2.59	0.36	2.54	0.37	128.3	12.2	10.5	140.5	1.04	1.15
23–24	915	28.1	60.4	5.98	23.2	4.96	1.24	5.43	0.76	4.81	0.87	2.60	0.36	2.51	0.35	129.3	12.3	10.5	141.5	1.06	1.08
24–25	922	25.4	60.4	5.94	23.5	5.15	1.19	5.19	0.76	4.55	0.84	2.55	0.37	2.42	0.35	126.8	11.8	10.7	138.6	1.02	1.14
25–26	929	24.8	59.1	5.83	23.0	4.98	1.24	5.20	0.75	4.57	0.88	2.58	0.37	2.44	0.35	124.1	11.9	10.4	136.1	1.08	1.14
26–27	938	24.8	59.2	5.75	23.2	5.02	1.23	5.28	0.76	4.66	0.83	2.52	0.37	2.49	0.35	124.4	12.0	10.4	136.4	1.06	1.15
27–28	950	26.6	61.8	6.02	24.0	5.05	1.25	5.29	0.77	4.53	0.88	2.65	0.36	2.58	0.35	129.9	12.1	10.7	142.0	1.07	1.13
28–29	962	28.2	61.1	5.99	23.3	4.92	1.17	5.26	0.77	4.75	0.88	2.52	0.35	2.69	0.37	130.0	12.3	10.5	142.3	1.02	1.09
29–30	974	24.0	61.1	5.92	23.8	5.26	1.31	5.24	0.82	4.79	0.89	2.66	0.38	2.67	0.39	126.7	12.6	10.1	139.3	1.11	1.19
30–31	986	24.9	63.2	6.16	24.7	5.16	1.29	5.43	0.78	4.97	0.93	2.75	0.38	2.52	0.36	130.8	12.7	10.3	143.5	1.09	1.18
32–33	1006	25.7	63.8	6.34	25.2	5.43	1.33	5.33	0.83	4.88	0.93	2.81	0.38	2.74	0.39	133.1	13.0	10.3	146.1	1.10	1.16
34–35	1025	26.9	65.0	6.60	26.2	5.54	1.37	5.76	0.89	5.21	0.99	2.79	0.40	2.80	0.38	137.4	13.5	10.2	150.8	1.08	1.13
36–37	1043	27.8	66.6	7.08	27.3	5.98	1.41	6.23	0.90	5.32	1.00	2.99	0.43	2.97	0.41	142.3	14.0	10.1	156.4	1.03	1.10
38–39	1060	29.1	68.7	7.27	28.2	6.12	1.38	6.23	0.93	5.39	1.02	3.24	0.41	2.94	0.41	147.0	14.4	10.2	161.4	0.99	1.10
41–42	1086	23.9	57.1	5.77	23.3	5.04	1.28	5.34	0.74	4.77	0.89	2.67	0.34	2.59	0.36	121.7	12.4	9.8	134.0	1.09	1.13
43–44	1103	20.5	53.9	5.35	21.5	4.64	1.09	4.67	0.70	4.40	0.79	2.38	0.33	2.36	0.32	111.7	11.3	9.9	123.0	1.04	1.20
45–46	1120	17.9	48.4	4.68	18.9	4.02	1.00	4.35	0.62	3.75	0.70	2.05	0.28	1.95	0.27	99.3	9.6	10.3	108.9	1.06	1.23
47–48	1137	15.9	43.3	4.15	16.5	3.66	0.88	3.84	0.57	3.24	0.61	1.86	0.24	1.79	0.22	88.2	8.5	10.3	96.8	1.04	1.24
49–50	1155	14.9	40.9	3.87	15.2	3.25	0.80	3.45	0.52	3.14	0.56	1.68	0.23	1.58	0.22	82.3	7.9	10.4	90.3	1.06	1.25
51–52	1173	13.7	37.8	3.48	13.7	3.04	0.74	3.30	0.46	2.69	0.54	1.47	0.22	1.47	0.20	75.8	7.1	10.8	82.9	1.04	1.27
53–54	1193	13.6	38.0	3.44	14.1	3.13	0.73	3.09	0.44	2.76	0.50	1.48	0.21	1.41	0.21	76.1	7.0	10.8	83.1	1.03	1.28
55–56	1212	13.7	37.0	3.46	13.8	2.91	0.76	3.20	0.46	2.83	0.52	1.51	0.21	1.44	0.19	74.9	7.2	10.4	82.0	1.11	1.25
57–58	1231	13.9	37.7	3.55	14.4	3.01	0.78	3.34	0.46	2.80	0.54	1.52	0.22	1.52	0.20	76.6	7.2	10.6	83.8	1.09	1.25
59–60	1251	13.4	37.1	3.52	13.7	2.97	0.72	3.14	0.44	2.76	0.50	1.49	0.21	1.36	0.22	74.5	7.0	10.7	81.5	1.04	1.25
61–62	1269	13.4	37.2	3.50	14.0	2.99	0.76	3.40	0.45	2.76	0.55	1.57	0.21	1.50	0.20	75.3	7.3	10.4	82.6	1.06	1.26
63–64	1285	14.3	38.9	3.71	14.7	3.16	0.77	3.30	0.48	2.95	0.56	1.50	0.22	1.54	0.21	78.8	7.5	10.6	86.3	1.05	1.24
65–66	1301	15.4	40.9	3.88	15.3	3.32	0.84	3.48	0.51	3.06	0.57	1.63	0.23	1.64	0.23	83.1	7.9	10.6	91.0	1.09	1.23
68–69	1320	14.7	39.6	3.75	15.4	3.19	0.79	3.15	0.49	3.01	0.53	1.58	0.24	1.49	0.21	80.5	7.5	10.7	88.0	1.10	1.24
70–71	1333	19.0	40.1	4.03	16.0	3.40	0.85	3.56	0.51	3.12	0.59	1.67	0.22	1.62	0.22	87.0	8.0	10.9	94.9	1.08	1.06

(Continued)

TABLE 2 | Continued

Depth (cm)	Age (a BP)	La	Ce	Pr	Nd	Sm	Eu	Gd	Tb	Dy	Ho	Er	Tm	Yb	Lu	SLREE	SHREE	SLREE/ SHREE	SREE	dEn	dCe
72–73	1348	13.8	38.3	3.61	14.9	3.06	0.74	3.25	0.47	2.95	0.57	1.57	0.21	1.48	0.22	77.8	7.5	10.4	85.2	1.05	1.26
73–74	1357	13.8	38.3	3.49	14.2	3.10	0.76	3.28	0.49	2.83	0.53	1.46	0.21	1.50	0.20	76.9	7.2	10.7	84.1	1.06	1.28
75–76	1373	14.8	39.2	3.82	15.3	3.33	0.77	3.34	0.47	2.98	0.55	1.56	0.22	1.55	0.23	80.5	7.6	10.7	88.0	1.02	1.21
77–78	1390	14.0	37.5	3.62	14.3	3.31	0.79	3.32	0.48	2.98	0.53	1.58	0.22	1.53	0.20	76.8	7.5	10.2	84.4	1.06	1.22
79–80	1406	14.1	38.5	3.74	14.7	3.27	0.78	3.39	0.49	3.15	0.56	1.61	0.21	1.60	0.21	78.4	7.8	10.0	86.2	1.04	1.23
81–82	1421	14.3	38.0	3.61	14.8	3.22	0.79	3.53	0.50	2.93	0.53	1.56	0.20	1.47	0.23	78.2	7.4	10.5	85.6	1.03	1.23
Average		21.3	52.5	5.20	20.6	4.44	1.08	4.66	0.67	4.08	0.76	2.22	0.31	2.17	0.30	109.8	10.5	10.4	120.3	1.05	1.17
St. Deviation	5.2	10.3	1.12	4.3	0.93	0.22	0.95	0.14	0.83	0.16	0.49	0.07	0.48	0.07	22.8	2.2	0.3	25.0	0.03	0.06	

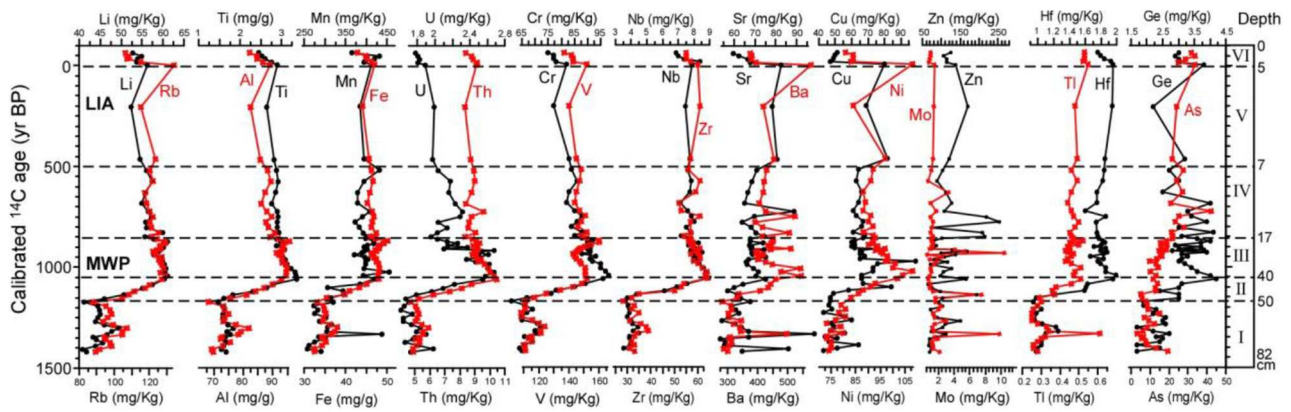

FIGURE 7 | Selected elemental concentrations in the lake sediments throughout the Manzherok Lake sediment core. Note that the units for Al, Ti, and Fe are in mg/g, whereas the rest of the elements are in mg/kg.

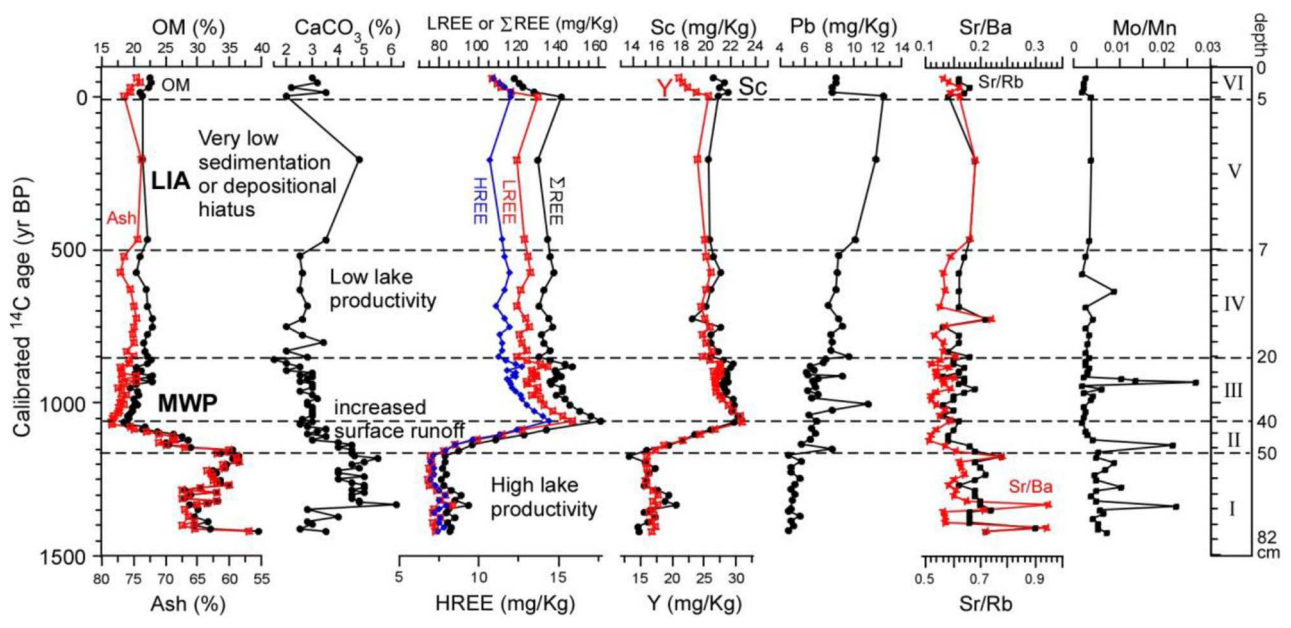

FIGURE 8 | Classification of the geochemical zones in the Manzherok Lake sediment core.

of 51–82 cm as their ratios in the different layers of this zone are quite similar. In the two figures, although the patterns are all similar, the values of the normalized ratios can be grouped into three categories: (1) 51–82 cm, (2) above 29–33-cm layer, and (3) between 34–35-cm layer and 49–50-cm layer. In the first category which is corresponding to zone I, both NASC and chondrite normalized ratios are the lowest, and the ratios of Ho, Er, Tm, Yb, and Lu to NASC are the same (**Figure 9**). The feature of the first category can be considered as the organic-rich sediments with a relatively constant input, which can be regarded as an end-member of the mixed lake sediments with another end-member from the surface runoff. In the second category, the values of both NASC and chondrite normalized patterns increased from the 49–50-cm layer to the 38–39-cm layer and then slightly decreased to the 34–35-cm layer (**Figures 9, 10**). In principle, the REEs in the lake sediments are mainly from detrital input carried by surface runoff. When the detrital input increases with the surface runoff under wet climates, the REE contents should increase. The patterns at different layers are basically the same, indicating that the detrital source, which is from the surrounding area of the lake, remains relatively constant. The variations in the NASC and chondrite normalized ratios shown in **Figures 9, 10** depend on the percentage of the input detritus in the lake sediments. The higher ratios reflect a higher percentage of the input detritus, which is confirmed by the increasing ash content from the 49–50-cm layer to 38–39-cm layer. Therefore, the changes in the geochemical proxies during the depositional period of 50–40 cm in the lake core (zone II, 1,150–1,070 years BP) reflected strongly the increased detrital input due to the enhanced surface runoff under wet climates. The third category shows that the patterns and the ratios are similar, especially for the chondrite normalized ratios (**Figure 10**). This means that the amount of detrital input to the lake sediments at the coring site from the surface runoff reduced after deposition at 33-cm depth (1,005 years BP). Such a situation could be caused by both increased lake level, so that it was difficult for the sediments from the surface runoff to reach the depo-center where the core was retrieved, and reduced surface runoff.

The variation trends of As, Cd (not shown), and Pb are different from those of lithophilic elements (**Figures 7, 8**). Except

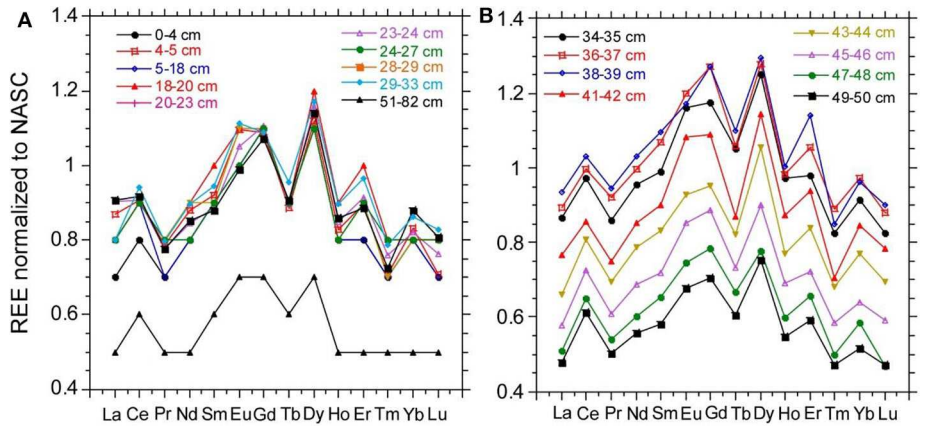

FIGURE 9 | (A,B) Rare earth element patterns normalized to chondrite at different depths in the Manzherok Lake sediment core.

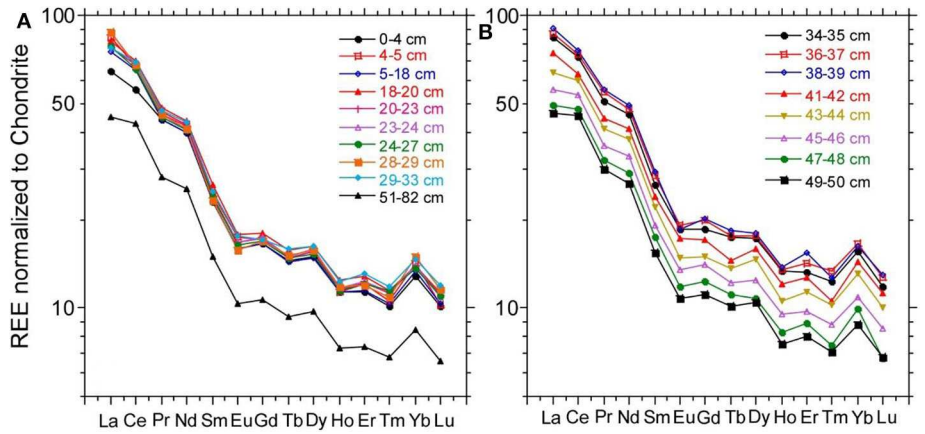

FIGURE 10 | (A,B) Rare earth element patterns normalized to North American shale composition at different depths in the Manzherok Lake sediment core.

at the surface 5 cm, these elements have a general increasing trend from the bottom to the upper section. **Figure 11** exhibits that those toxic elements have some positive correlations (R^2 = 0.39 for Pb vs. Cd and R^2 = 0.46 for Pb vs. As). Normally, these elements have low concentration in the natural background so that their origins should not come from detrital materials. The accumulation of these elements in the lake sediments may be related to the metabolic processes of living organisms and anthropogenic activities.

Sr, Ba, and Rb are IIA elements in the periodic table and have similar chemical characteristics. However, Sr is more influenced by lake water chemistry, whereas Ba and Rb are mainly from detritus. **Figure 11** shows the significant correlation ($R^2 = 0.735$) between Rb and Ba, but weak or no correlation (R^2 = 0.15) between Rb and Sr. Using the Sr/Ba and the Sr/Rb ratios, one may eliminate detrital influence so that the effect of lake chemistry can be seen. Sr prefers to co-precipitate with carbonate and favors high alkalinity and lake productivity. The variations of Sr/Ba and Sr/Rb in the core show peaks at 1,410, 1,335, 1,175, and 725 year BP, which also correspond to peaks in $CaCO_3$ (**Figure 8**). During those periods, the lake had relatively high productivity and alkalinity. A slight increase in Sr/Ba, Sr/Rb, and $CaCO_3$ during LIA might not reflect an increase in lake productivity. Under dry climatic condition during LIA, the lake level or volume decreased so that the concentrations of Ca^{2+} and CO_3^{2-} in the lake might be enhanced to raise alkalinity and pH, resulting in carbonate precipitation.

The Mo/Mn ratio is correlated well with the anoxic environment (Kalugin et al., 2014), whereas the Mn-enriched layer marks a long-term pause of sedimentation in the oxidized systems. In **Figure 8**, the Mo/Mn peaks appeared at 1,335, 1,270, 1,140, 930, and 630 years BP, indicating the anoxic conditions in the lake, which reflected high lake productivity under relatively warm and moist conditions on decadal time scales in the study area.

High Sr/Ba, Sr/Rb, Mo/Mn, and $CaCO_3$ appeared at around 1,335, 1,140, and 930 years BP, reflecting high lake productivity. These periods also coincide with the mass bloom of algae and cyanobacteria *Anabaena*. Thus, the geochemical proxies and the biological proxies agree with each other, confirming the observations.

BIOLOGICAL AND GEOCHEMICAL PROXIES IN THE MANZHEROK LAKE CORE AS INDICATORS OF CLIMATIC AND ENVIRONMENTAL CHANGE OVER THE PAST 1,500 YEARS

The biological and the geochemical records of the Manzherok Lake core with the new chronology provide us with details on lake history and vegetation change under climate regimes and human impacts since 1,440 years BP. In **Figure 12**, we summarize the major geochemical proxies in the core and compare them with the total solar irradiance (Bard et al., 2000; Steinhilber et al., 2009). The OM, ash, and $CaCO_3$ contents reflect the sediment feature which briefly dominate the lake geochemical and productivity signals. The concentrations of total REE, Al, and Ti represent detrital inputs. Sr/Ba and Sr/Rb can be considered as indicators of lake alkalinity and productivity. Mo/Mn may illustrate anoxic conditions. The shortage of this record is that the sedimentation rate was too low during the Little Ice Age so that the interpretation for this period is brief. In the following, we shall describe the record for each lake and climate stages one by one:

1,440–1,150 years BP (zone I for geochemical proxies and zone 1 for pollen records): This period is prior to the Medieval Warm Period. During this period, the lake had a moderately high level, with relatively high productivity and alkalinity under a frequently anoxic condition, which was shown by high organic matter and carbonate contents, peaks of Sr/Ba, Sr/Rb, and Mo/Mn, and mass bloom of algae and cyanobacteria *Anabaena*. Vegetation in the area was a phase of birch forest–steppe with a high abundance

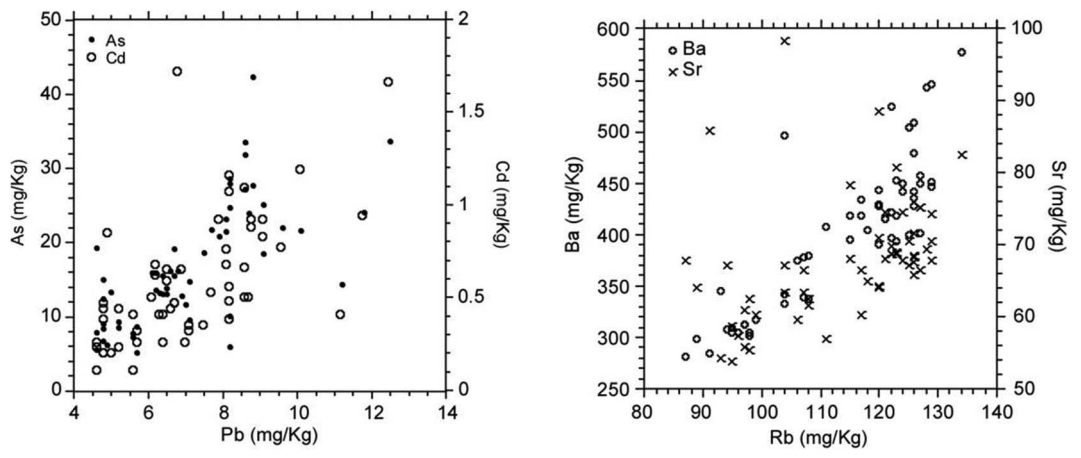

FIGURE 11 | Left: correlations among toxic elements of Pb, Cd, and As. **Right**: relationships among Sr, Ba, and Rb.

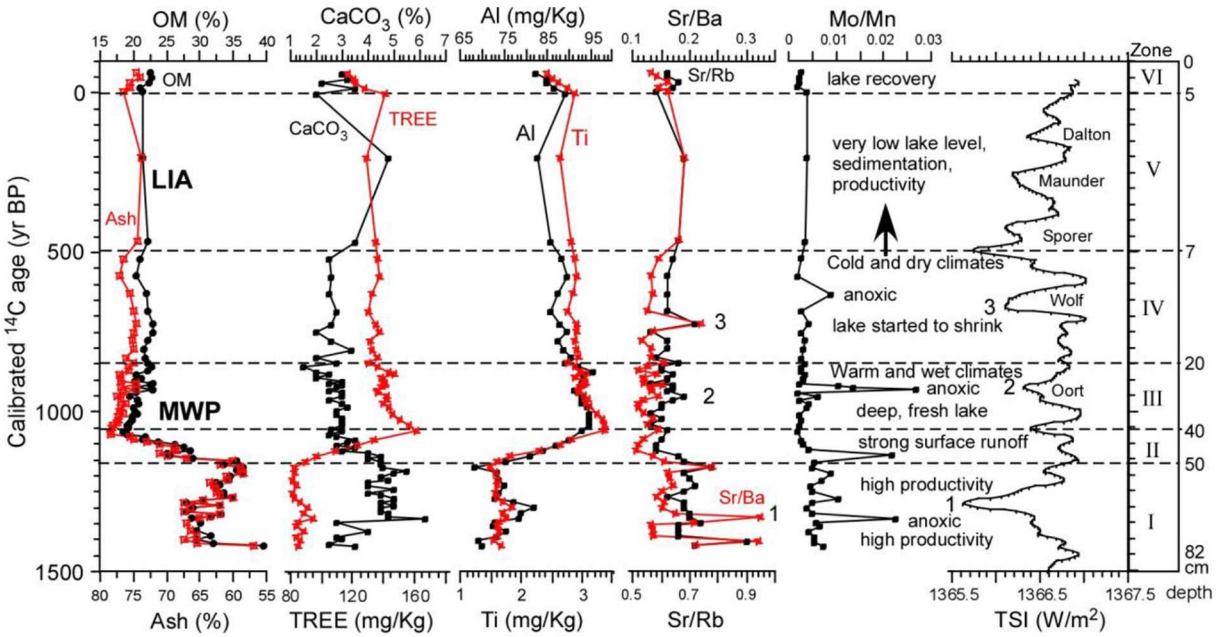

FIGURE 12 | Comparison of important geochemical indices in the Manzherok Lake core with the total solar irradiance (TSI). The TSI curve is a five-point running average of the 5-years resolution TSI data from Steinhilber et al. (2009). Numerical numbers 1, 2, and 3 for the Sr/Ba and the TSI plots denote their correlations.

of *Nymphaea* and *B. pendula* and relatively low *P. sylvestris*. The climatic conditions were moderately warm and wet. Surface runoff to the lake was not strong so that detrital input from the surrounding lake was low. Decadal scales of warm but dry episodes appeared at 1,335, 1,270, and 1,140 years BP.

1,150–1,070 years BP (zone II for geochemical proxies and zone 2 for pollen records): Manzherok Lake had a sudden change due to wet climates. The surface runoff strongly increased and brought high sediment input to the lake, shown by strongly decreased OM and $CaCO_3$ and strongly increased ash content, lithophilic elements, and REE. The lake level increased so that lake productivity and alkalinity decreased (Sr/Ba and Sr/Rb strongly dropped) and the anoxic condition (Mo/Mn peak) was further enhanced. The REE concentrations continuously increased and reached a maximum at 1,070 years BP. The vegetation in the area became transitional phase from birch forest–steppe to birch and pine forests. The abundance of *B. pendula* sharply decreased and *Nymphaea* disappeared, while *P. sylvestris* increased. In the lake, algae and *Anabaena* were abundant, reflecting that the lake was still productive. The wet and warm climates marked the onset of MWP.

Anthropogenic influence on the landscape began. Approximately from 1,130 years BP or slightly earlier, one can see permanent findings of the pollen of cultivated plant *Triticum* supplemented by the pollen of field weeds. Simultaneously, we count abundant microcharcoal in pollen slides. It is evidence of spreading of fire-cutting agriculture on the western piedmonts of the Altai Mountains. According to these evidences, fire-cutting agriculture began to spread here a few centuries before the Russian colonization. It is worth to mention that human activity could cause the loosening of the earth surface, which might introduce more sediment input to the lake.

1,070–850 years BP (zone III for geochemical proxies and zone 3 for pollen records): This interval had warm and wet climates corresponding to MWP. Manzherok Lake was the largest and deepest during this period over the past 1,500 years. Due to the deepening of the lake throughout high and frequent surface runoffs in the previous stage, the sediments at the depo-center, where the core was retrieved, contained less detritus as shown by reduced contents of ash, REE, and lithophilic elements. In the early half of this period, the lake was very fresh and had low productivity (very low Sr/Ba and Sr/Rb). However, during the late half of the period, the lake productivity and the alkalinity (increased Sr/Ba, Sr/Rb, and OM content) increased, and the anoxic condition (highest Mo/Mn peak) at the bottom of the lake became very strong. The vegetation in the area was a phase of birch and pine forests during this period, reflecting warm and moist conditions. The abundance of *P. sylvestris* reached its maximum (ca. 40%), *B. pendula* dropped to its minimum (∼20%), and *Nymphaea* disappeared, showing the dynamic change of the local vegetation. The enhanced *Bryales*/algae and *anabaena* abundances and the REE and lithophilic elements before the end of this stage indicate that the lake started to drop its level (**Figure 8**). The humidity index, as reconstructed by the pollen data using the equation of Wang et al. (2010), provided a semi-quantitative moisture change (Blyakharchuk et al., 2017), showing the highest humidity at around 950–900 years BP (**Figure 6**). After 900 years BP, the climate became dry.

Owing to the deep and anoxic conditions of Manzherok Lake during MWP, the submerged plants and algae would uptake dissolved CO_2 which could not fully exchange with the atmospheric CO_2. Because the dissolved CO_2 contained partial CO_2 which was decomposed from old organic matter in the deeper sediments, its ^{14}C had an initial age. Therefore, even though many samples from this interval were gone through ABA treatment, their ages are still older than their true ages because the ABA treatment could not remove the old carbon influence caused by the uptake of dissolved CO_2.

The anthropogenic influence during this period became more significant as shown by the accumulation of toxic elements including Pb, As, and Cd. Metal elements such as Ni, Cu, and Zn commonly exit in the copper ore. The joint finding of Zn and Cu in the bones of people was considered as an indicator of their involvement in the metallurgical process (Aleksandrovskaya and Aleksandrovsky, 2007). The same authors pointed out that during the smelting of copper from copper and polymetallic ores and even during the remelting of copper objects, Zn could evaporate together with metallurgical gases. When the metallurgical gases contacted with cold air, Zn could condense and fall on the ground. The maximum Cu concentration appeared at 980 years BP, probably reflected as ancient smelting in the local area.

850–500 years BP (zone IV for geochemical proxies and lower zone 4 for pollen records): The vegetation after 850 years BP was determined as a phase of pine–birch forest–steppe. The lake sedimentation rate began to drop rapidly due to drying and cooling climatic conditions. The humidity index based on the pollen data dropped significantly and was kept at a low level (**Figure 6**). The concentrations of REEs and lithophilic elements in this interval was kept relatively constant at lower values than those in zone III, indicating a lower detrital input corresponding to reduced sedimentation rate under a dry climate. The lake level declined gradually so that carbonate precipitation slightly increased at 800 years BP (**Figure 12**). A slight increase in REE and lithophilic elements at 750 years BP probably indicated that the lake reached a low steady level with moderate productivity. The lake enhanced its alkalinity at 725 years BP as reflected by the peaks of Sr/Ba and Sr/Rb due to the further shrinking of the lake volume. As the lake volume shrank, its nutrient concentration increased so that the lake productivity also slightly increased, as shown by the enhanced abundance of algae and *Anabaena* between 700 and 600 years BP (**Figure 6**). A weak but apparent anoxic condition of the lake occurred at around 630 years BP. After 600 years BP, the climatic condition in the study area entered into cold LIA.

According to history record, the first Mongolian invasion to Siberia was 1,207 CE (743 years BP). The time period that Mongolia conquered the Altai region was 1,236–1,242 years CE (714–708 years BP). Thus, the two Zn peaks, together with a slight increase in the Cu and the Ba contents at 850–830 and 770–750 years BP, in our record might reflect the metallurgical practice of local human tribes who lived on the western piedmonts of the Altai Mountains in XII century CE. The humidity index based on the pollen record and the geochemical proxies of the Manzherok core illustrate that the climate was moist during the beginning of the Mongolian invasion, although the climate during this period was not as wet as that during MWP. The Mongol Empire can be divided in two parts: 1,206 CE (744 years BP) to 1,270 CE (680 years BP) before the Yuan Dynasty and 1,271 CE (679 years BP) to 1,368 CE (582 years BP) of the Yuan Dynasty. The first part, especially during the Chenghis Khan reign, was mainly active in the north regions including Altai, Siberia, whereas the second part was mainly active in Mongolia and northern China. According to the Manzherok Lake record, the climate in the study area began cooling and drying at around 750 years BP and became much worse after 600 years BP. The climatic conditions certainly affected human activity in the study area.

500–50 years BP (zone V for geochemical proxies and middle zone 4 for pollen records): The lake depositional record in this interval corresponds to LIA. The sedimentation rate was very low and often had depositional hiatuses due to cold and dry conditions during this period. For only the 2-cm sediments in this interval, the pollen and geochemical data were not good enough to interpret the detailed lake history. Nevertheless, the extreme sedimentation was attributed not only to low surface runoff under dry climates but also to longer frozen time under cold conditions.

After 1,950 CE (zone VI for geochemical proxies and upper zone 4 for pollen records): The top 5-cm sediments containing nuclear bomb ^{14}C indicate that they were deposited after 1,950 CE. In the 5-cm layer, one can still see clear trends of increasing OM, decreasing ash content, and declining concentrations of REE and lithophilic elements. These trends reflect the recovery of lake productivity and deposition in the current warming centenary.

The above description of Manzherok Lake history and the local climatic conditions over the past 1,500 years refine our findings in Blyakharchuk et al. (2017). The detailed pollen data and the geochemical proxies consistently illustrate the climate changes well. We have compared this record with the pollen and geochemical records from Teletskoye Lake which is 100 km east during the past 1,000 years (Andreev et al., 2007; Kalugin et al., 2007). The climate reconstruction-based pollen record (**Figure 6**) in Teletskoye Lake during the last 1,000 years (Andreev et al., 2007) are summarized as follows: (1) humid climate of late MWP 1,000–880 years BP and dry climate 880–750 years BP, (2) humid climate 750–550 years BP, and (3) dry climate of LIA 520–110 years BP. Our Manzherok Lake record agrees well with the above-mentioned climate reconstructions. We have also found a good correlation of Sr/Rb index between the Manzherok Lake record and the Teletskoye Lake record (Kalugin et al., 2007). However, we should mention that Manzherok Lake is much smaller and shallower than Teletskoye Lake so that the sedimentations in the two lakes are different. In the Teletskoye Lake sediments, annual laminations can be found, whereas the Manzherok Lake sediments do not show laminations; they instead contain much more plant remains (OM > 20%). In addition, because Manzherok Lake is small and shallow, it has a longer frozen time than Teletskoye Lake. Hence, the sedimentary hiatus during LIA did not occur in Teletskoye Lake. Under such circumstances, Manzherok Lake is more

sensitive to climate change than Teletskoye Lake in terms of geochemical proxies.

In **Figure 12**, a comparison of the Manzherok Lake record to the TSI record shows good correlations not only on the long-term major changes of the lake but also on decadal events corresponding to the climate changes. In general, a large, deep, and fresh lake with high sedimentation exists under warm and wet climates such as MWP. A small and shallow lake stage with low sedimentation appears under cold and dry climates such as LIA. During a long relatively warm and wet period, a TSI minimum resulting in a dry episode would lead to lake shrinkage that will cause a rise in lake alkalinity and productivity so that increased Sr/Ba and Sr/Rb could result. In **Figure 12**, numbers 1, 2, and 3 denote the correlations between Sr/Ba (and Sr/Rb) and TSI minimum within age uncertainties. Thus, we conclude that the climate of the study area is strongly influenced by total solar irradiance, with higher TSI resulting in warmer and wetter conditions. Since the westerly and the polar easterly are the two major moisture jet streams to the area, when lower TSI causes a stronger Siberian High, the latter probably pushes both the westerly and the polar front away from the study area, resulting in arid climates. The situation is reversed *vice versa*.

CONCLUSIONS

The high-resolution multiproxy analyses including pollen, diatom, contents of total organic carbon, carbonate and ash, concentrations of trace metal elements, heavy metal elements, and rare earth elements in an 82-cm sediment core from Manzherok Lake reveal detailed changes in vegetation and climate in the western foothills of the Altai Mountains over the past 1,500 years. A total of 48 AMS ^{14}C dates combined with ^{210}Pb dating indicate that the lake had very low sedimentation (only ∼2 cm) during LIA due to cold and dry climates. There are many ABA-treated samples that show old carbon influence on their ^{14}C ages because ABA treatment cannot remove organic compounds which used old dissolved CO_2 in the lake at high and anoxic stages. High-resolution ^{14}C dating on such lake cores should apply for solving such a problem.

Vegetation development in this region can be classified as (1) phase of birch forest–steppe during 1,440–1,150 years BP, (2) transitional phase from birch forest–steppe to birch and pine forests dated 1,150–1,070 years BP, (3) phase of birch and pine forests during 1,070–850 years BP, and (4) phase of pine–birch forest–steppe after 850 years BP. Aquatic pollen species such as algae, *Nimphae* cell, and cianobacterium *Anabaena* provide details on the changes in the lake ecosystem.

Changes in the contents of organic matter, ash, and $CaCO_3$ (dominant sediment feature), concentrations of lithophilic and REE elements (detrital inputs), Sr/Ba and Sr/Rb (indicators of lake alkalinity and productivity), and Mo/Mn (anoxic conditions) identify six stages in the lake history corresponding to the climate changes: (1) 1,440–1,150 years BP. The lake was moderately deep with high productivity under relatively warm and wet climates: (2) 1,150–1,070 years BP. Strong surface runoff into the lake resulting from wet climates marked the onset of MWP: (3) 1,070–850 years BP. Large, deep, and fresh lake exited due to warm and wet climates during MWP. Decomposed old organic matter in the anoxic bottom caused old carbon influence on the ^{14}C ages: (4) 850–500 years BP. In the early stage, the lake dropped its level slowly until about 700 years BP. Then, the lake shrank its size quickly corresponding to the cooling and drying climates: (5) 500–50 years BP. Small and shallow lake with very low sediment deposition corresponded to cold and dry LIA. (6) The lake has been recovered during the current warming century.

The Manzherok record compares well with the total solar irradiance record, indicating that changes in TSI is an important factor to influence climate in the Altai Mountains. The Siberian High became strong during the TSI minima. Consequently, the westerly and the polar front would be pushed away from this region, resulting in arid climates.

The pollen and charcoal records and the metal elemental concentrations indicate that fire-cutting agriculture began to spread in the Altai Mountains several centuries before the Russian colonization, and the metallurgical practice of local human tribes who lived on the western piedmonts of the Altai Mountains took place in XII century AD before the Mongolian invasion.

DATA AVAILABILITY STATEMENT

The raw data supporting the conclusions of this article will be made available by the authors, without undue reservation, to any qualified researcher.

AUTHOR CONTRIBUTIONS

TB and H-CL designed Research Topic and wrote the manuscript. H-CL and S-CK performed ^{14}C dating. TB and VU conducted pollen and geochemical analyses. All authors contributed to the article and approved the submitted version.

FUNDING

This study was carried out in the framework of the state budget theme of IMCES SB RAS No. AAAAA-A16-116041356666-6 and with the support of the RFBR grants 13-04-00984a, 14-04-10054/k, 52020/MHT_a, and 20-55-53015/20. Funding support to H-CL in Taiwan include MOST 106-2923-M-002—002 -MY3, MOST 106-2116-M-002-012, and MOST 107-2116-M-002-005.

ACKNOWLEDGMENTS

We are thankful to T. S. Papina and P. A. Blyakharchuk for assistance in the field drilling of the Manzherok Lake sediments.

REFERENCES

Aleksandrovskaya, E. I., and Aleksandrovsky, A. L. (2007). *Anthropochemistry. Tutorial*. Moscow: "Class-Mb" Press.

Andreev, A. A., Pierau, R., Kalugin, I. A., Daryin, A. V., Smolyaninova, L. G., and Diekmann, B. (2007). Environmental changes in the northern Altai during the last millennium documented in Lake Teletskoye pollen record. *Quat. Res.* 67, 394–399. doi: 10.1016/j.yqres.2006.11.004

Appleby, P. G. (2001). "Chronostratigraphic techniques in recent sediments," in *Tracking Environmental Change Using Lake Sediments 1,* eds W. M. Last and J. P. Smol (Nedherlands: Springer E-Publishing Inc.), 171–203. doi: 10.1007/0-306-47669-X_9

Bard, E., Raisbeck, G., Yiou, F., and Jouzel, J. (2000). Solar irradiance during the last 1200 years based on cosmogenic nuclides. *TELLUS B* 52, 985–992. doi: 10.3402/tellusb.v52i3.17080

Baskaran, M., Nix, J., Kuyper, C., and Karunakara, N. (2014). Problems with the dating of sediment core using excess 210Pb in a freshwater system impacted by large scale watershed changes. *J. Environ. Radioact.* 138, 355–363. doi: 10.1016/j.jenvrad.2014.07.006

Benoit, G., and Hemond, H. F. (1991). Evidence for diffusive redistribution of ^{210}Pb in lake sediments. *Geochim. Cosmochim. Acta* 55, 1963–1975. doi: 10.1016/0016-7037(91)90036-5

Blaauw, M., and Christen, J. A. (2011). Flexible paleoclimate age-depth models using an autoregressive gamma process. *Bayesian Anal.* 6, 457–474. doi: 10.1214/ba/1339616472

Blyakharchuk, T. A., Eirikh, A., Mitrofanova, E., Li, H. -C., and Su-Chen Kang, S. -C. (2017). High resolution palaeoecological records for climatic and environmental changes during last 1500 years from Manzherok Lake, western foothills of the Altai Mountains, Russia. *Quat. Int.* 447, 59–74. doi: 10.1016/j.quaint.2017.06.014

Bobrov, V. A. (2007). "Estimation of the flows of mineral matter from the atmosphere in the late Holocene. Problems of geochemistry of endogenous processes in the environment: materials of all russian scientific," in *Conf. Publishing house of the Institute of Geography SB RAS*, Irkutsk, v.1, 128–132. (In Russian).

Bobrov, V. A., Bogush, A. A., and Leonova, P. F. (2011). Abnormal manifestations of zinc and copper concentrations in the peat bog of the upper marsh of the southern urals. *Rep. Rus. Acad. Sci.* 439, 784–788. (In Russian). doi: 10.1134/S1028334X11080228

Bobrov, V. A., Leonova, G. A., Strakhovenko, V. D., and Krasnobaev, V. A. (2007). Geochemical role of living matter (plankton, macrophytes) in the formation of organogenic deposits of some lakes in siberia. ecology of biosystems: problems of study, indication and forecasting: *Proceedings of the Intern. Scientific. -Pract. Conf.*, 20-25 Aug. (2007). Publishing house of ASU, Astrakhan, v. 1., 17-24. (In Russian).

Boyarkina, A. P., Baikovsky, V. V., and Vasiliev, N. V. (1993). *Aerosols in Natural Plates in Siberia*. TSU Press, Tomsk. (In Russian).

Brock, F., Higham, T., Ditchfield, P., and Ramsey, C. B. (2010). Current pretreatment methods for AMS radiocarbon dating at the Oxford radiocarbon accelerator unit (ORAU). *Radiocarbon* 52, 103–112. doi: 10.1017/S0033822200045069

Cooke, C. A., Abbott, M. B., Wolfe, A. P., John, L., and Kittleson, J. L. (2007). A millennium of metallurgy recorded by lake sediments from morococha, peruvian andes. *Environ. Sci. Technol.* 41, 3469–3474. doi: 10.1021/es062930+

Darin, A., Kalugin, I., Tretiakov, G., Maksimov, M., Rogozin, D., Zykov, V., (2014). "Reconstruction of the lake Dhira level diring the last 1500 years according to microstratigraphic studies bottom sediments," in *Paleolimnology of Northern Eurasia. Proceedings of the International Conference*, eds D. Subetto, T. Regerand, A. Sidorova (Petrozavodsk: Karelian Reserch Centre Press), 30–32 (In Russian).

Dauvalter, V. A., Dauvalter, M. V., Saltan, N. V., and Semenov, E. N. (2008). Chemical composition of atmospheric precipitates within the influence zone of the severonikel smelter. *Geochemistry* 10, 1131–1136. doi: 10.1134/S0016702908100108

Dobrovolsky, V. V. (1999). Fine particles of soils as a factor of mass transfer of heavy minerals in the biosphere. *Soil Sci.* 11, 1309–1317. (In Russian).

Ebaid, Y. Y., and Khater, A. M. (2006). Determination of ^{210}Pb in environmental samples. *J. Radioanal. Nuclear Chem.* 270, 609–619. doi: 10.1007/s10967-006-0470-5

Gavshin, V. M., Bobrov, V. A., and Sukhorukov, F. V. (2004). Evidence of the fractionation of chemical elements in the atmosphere of western siberia according to the research of the upper peat bog. *Doklady Russiiskoi Academii Nayk* 396, 804-807. (In Russian).

Geology of the USSA (1997). *Western Siberia. Part I. Geological Description*. Vol. XIV. Nedra, Moscow. (in Russian).

Granina, L. Z. (2008). *Early Diagenesis of Bottom Sediments of Lake Baikal*. Academ. Publishing house "Geo", Novosibirsk (In Russian).

Gurari, F. G., and Gavshin, V. M. (1981). *Planktonic deposits of the Phanerozoic as an indicator of the stability of the content in sea water of rare and radioactive elements. Evolution of the sedimentary process on continents and oceans*. IGiG SBO AN SSSR Press, Novosibirsk, 207–208.

Ilyin, V. V. (1982). Flora and vegetation of manzherok lake (Altai). *Bot J*, 67, 210–220.

Kalugin, I., Darin, A., and Rogosin, D. (2014). "Geochemical signals of paleoclimate recorded in the varved clastic and carbonate lake sediments," in *Paleolimnology of northern Eurasia. Proceedings of the International Conference,* eds D. Subetto, T. Regerand, and A. Sidorova (Petrozavodsk: Karelian Research Centre Press). 47–49. (In Russian). doi: 10.5593/SGEM2013/BD4/S19.018

Kalugin, I., Daryin, A., Smolyaninova, L., Andreev, A., Diekmann, B., and Khlystov, O. (2007). 800-yr-long records of annual air temperature and precipitation over southern Siberia inferred from Teletskoye Lake sediments. *Quat. Res.* 67, 400–410. doi: 10.1016/j.yqres.2007.01.007

Korde, N. V. (1960). *Biostratigraphy and Typology of Russian Sapropels*. Moscow: Publishing House of the USSR Academy of Sciences, 219. (In Russian).

Kutsenogiy, K. P., and Kutsenogiy, P. K. (2000). Aerosols of Siberia. The results of seven years of research. Siberian Ecol. J. VII, 11–20. (In Russian).

Kuzin, I. L. (2007). On the geological role of blue-green algae and the natural conditions of the Precambrian. *News RGO* 139, 48–64. (In Russian).

Leonova, G. A. (2004). Biogeochemical indications of pollution of aquatic ecosystems by heavy metals. *Water Resour.* 31, 215–222. (In Russian). doi: 10.1023/B:WARE.0000021580.73140.51

Leonova, G. A., and Bobrov, V. A. (2012). *Geochemical Role of the Plankton of the Continental Reservoirs of Siberia in the Concentration and Biosedimentation of Microelements*. Academic Publishing House "Hero", Novosibirsk, 308. (In Russian).

Leonova, G. A., Bobrov, V. A., Bogush, A. A., Bychinsky, V. A., and Anoshin, G. N. (2007). Geochemical characteristics of the current state of salt lakes in the altai territory. *Geochemistry* 10, 1114–1128. (In Russian). doi: 10.1134/S0016702907100060

Leonova, G. A., Bobrov, V. A., and Krivonogov, S. K. (2010). "*Biogeochemical Characteristics of Varieties of Lake Sapropels of the Siberian Region. Mineralogy and Geochemistry of Landscapes of Mining Territories*," Modern mineral formation: *Proceedings of the III All-Russian Symposium*. Readings of the memory of Academician A.E. Fersman, November 29 - December 2, 2010. Chita Russia. Publishing house of the Institute of Natural Resources, Ecology and Cryology SB RAS, Chita, 74-78. (In Russian).

Leonova, G. A., Bobrov, V. A., Lazareva, E. V., Bogush, A. A., and Krivonogov, S. K. (2011). Biogenic contribution of microelements to the organic matter of modern lake sapropels (on the example of Lake Kirek). *Lithol. Minerals* 2, 115–131. (In Russian). doi: 10.1134/S0024490211010044

Leonova, G. A., Bobrov, V. A., Lazareva, E. V., and Krivonogov, S. K. (2008). Evaluation of biogenic supply of microelements of lake sapropels (plankton and macrophyte "channels"). Mineralogy and geochemistry of landscapes of mining territories: *Proceedings of the II All-Russian Symposium with International Participation November 10-13, 2008.* Publishing House of the Institute of Natural Resources and Cryology SB RAS, Chita, 70-74. (In Russian).

Leonova, G. A., Bobrov, V. A., and Palesskiy, S. V. (2006). "Use of the elemental composition of plankton and sapropels to estimate the fluxes of matter from the atmosphere (on the example of Lake Kirek, Tomsk Region)," in *Control and rehabilitation of the environment*. eds M. V. Kabanov and A. A. Tikhomirov (Tomsk: Materials of the symposium), 98-100. (In Russian).

Leonova, G. A., and Bychinsky, V. A. (1998). Hydrobionts of the Bratsk water reservoir as objects for monitoring heavy metals. *Water Resour.* 25, 603–610. (In Russian).

Li, Y. -H. (1991). Distribution pattern of the elements in the ocean. *A synthesis. Geochim. Cosmochim. Acta*, 55, 3223–3240. doi: 10.1016/0016-7037(91)90485-N

Lopatko, M. Z. (1978). *The Lake and Sapropel*. Minsk: Science and technology Press.

Malakhov, S. G., and Makhonko, E. P. (1990). Emission of toxic metals and their accumulation in the surface layer of the Earth. *Adv. Chem.* 59, 1777–1798. doi: 10.1070/RC1990v059n11ABEH003575

Moiseenko, T. I., Gashkina, N. A., and Kudryavtseva, L. P. (2006). Zonal features of formation of the chemical composition of the waters of small lakes in the territory of the European part of Russia. *Water Resour.* 33, 163–180. doi: 10.1134/S0097807806020047

Neruchev, S. G. (1982). *Uranium and life in the history of the Earth*. Leningrad: Nedra Press Leningrad branch.

Niu, M., Heaton, T. J., Blackwell, P. G., and Buck, C. E. (2013). The bayesian approach to radiocarbon calibration curve estimation: the IntCal13, Marine13, and SHCal13 methodologies. *Radiocarbon* 55, 1905–1922. doi: 10.2458/azu_js_rc.55.17222

Ogureeva, G. N. (1980). *Botanical Geography of Altai*. Moscow: Nauka Press. (In Russian).

Pawlyta, J., Pazur, A., Piotrowska, N., Poreba, G., Sikorski, J., Szczepanek, M., et al. (2004). Isotopic investigations of uppermost sediments from lake Wigry (NE Poland) and its environment. *Geochronometria*. 23, 71–78.

Perelman, A. I. (1979). *Geochemistry*. Moscow: High school Press (In Russian).

Poplavko, E. M., Ivanov, V. V., Orekhov, V. S., and Tarkhov, Y.A. (1978). Peculiarities of metallicity of combustible shales and some assumptions about their genesis. *Geochemistry* 9, 1411–1418.

Popolzin, A. G. (1967). *Lakes of the South of the Ob-Irtysh Basin (Zonal Complex Characteristic)*. Novosibirsk: West Siberian book publishing house.

Prajith, A., Rao, V. P., and Kessarkar, P. M. (2015). Controls on the distribution and fractionation of yttrium and rare earth elements in core sediments from the Mandovi estuary, western India. *Cont. Shelf Res*. 92, 59–71. doi: 10.1016/j.csr.2014.11.003

Raputa, V. F., Smolyakov, B. S., and Kutsenogiy, K. P. (2000). Analysis of the temporal dynamics of changes in the composition of atmospheric aerosol in the north of Western Siberia. *Siberian Ecol. J.* 1, 97–101.

Reimer, P. J., Bard, E., Bayliss, A., Beck, J. W., Blackwell, P. G., Bronk, R. C., et al. (2013). IntCal13 and Marine13 radiocarbon age calibration curves 0–50,000 years cal BP. *Radiocarbon* 55, 1869–1887. doi: 10.2458/azu_js_rc.55.16947

Rudaya, N., Nazarova, L., Novenko, E., Andreev, A., Kalugin, I., Daryim, A., et al. (2016). Quantitative reconstructions of mid- to late Holocene climate and vegetation in the north-eastern Altai mountains recorded in lake teletskoye. *Glob. Planet. Change* 141, 12–24. doi: 10.1016/j.gloplacha.2016.04.002

Rusanov, G. G., and Vazhov, S. V. (2017). *Unsolved Problems of Lakes Manzherok and Aya*. Biysk, FGBOU VO "AGGGU named after V.V. Shukshina," 168. (in Russian)

Shotyk, W., Cheburkin, A. K., Appleby, P. G., Fankhauser, A., and Kraumers, Y. D. (1996). Two thousand years of atmospheric arsenic, antimony and lead deposition in an ombrotrophic bog profile, Jura Mountains Switzerland. Earth and Planet. *Sci. Lett*. 145, 1–7. doi: 10.1016/S0012-821X(96)00197-5

Smolyakov, B. S. (2000). Problems of acid deposition in the north of Western Siberia. *Siberian Ecol. J. VII* (1), 21–30. doi: 10.1016/S0021-8502(99)80311-5

Steinhilber, F., Beer, J., and Fröhlich, C. (2009). Total solar irradiance during the holocene. *Geophys. Res. Lett*. 36:L19704. doi: 10.1029/2009GL040142

Stuiver, M., and Polach, H. A. (1977). Discussion: reporting of ^{14}C data. *Radiocarbon* 19, 355–363. doi: 10.1017/S0033822200003672

Stuiver, M., and Reimer, P. J. (1993). Extended ^{14}C data base and revised CALIB 3.0 ^{14}C age calibration program. *Radiocarbon* 35, 215–230. doi: 10.1017/S0033822200013904

Suriyanarayanan, S., Brahmanandhan, G. M., Malathi, J., Kumar, S. R., Masilamani, V., Hameed, P. S., et al. (2008). Studies on the distribution of ^{210}Po and ^{210}Pb in the ecosystem of point Calimere coast (Palk Strait), India. *J. Environ. Radioact.* 99, 766–771. doi: 10.1016/j.jenvrad.2007.10.003

Syso, A., and Yu. (2007). *Regularities in the distribution of chemical elements in soil-forming rocks and soils in Western Siberia*. Novosibirsk: SB RAS Press.

Ugur, A., Miquel, J. C., Fowler, S. W., and Appleby, P. (2003). Radiometric dating of sediment cores from a hydrothermal vent zone off Milos Island in the Aegean Sea. *Sci. Total Environ.* 307, 203–214. doi: 10.1016/S0048-9697(02)00542-9

Vetrov, V. A., and Kuznetsova, A. I. (1997). *Microelements in the Natural Environment of Lake Baikal*. Novosibirsk: SB RAS Press, 234.

Vine, J. D., and Tourtelot, E. B. (1970). Geochemistry of black shale deposits. *Econ. Geol*. 65, 253–272. doi: 10.2113/gsecongeo.65.3.253

Wang, W., Ma, Y., Feng, Z., Narantsetseg, T., Liu, K.-B., and Zhai, X. (2010). A prolonged dry mid-Holocene climate revealed by pollen and diatom records from lake ugii nuur in central Mongolia. *Quat. Int*. 229, 74–83. doi: 10.1016/j.quaint.2010.06.005

Xu, F. J., Hu, B. Q., Dou, Y. G., Liu, X. T., Wan, S. M., Xu, Z. K., et al. (2017). Sediment provenance and paleoenvironmental changes in the northwestern shelf mud area of the South China Sea since the mid-Holocene. *Contin. Shelf Res.* 144, 21–30. doi: 10.1016/j.csr.2017.06.013

Xu, X., Trumbore, S. E., Zheng, S., Southon, J. R., McDuffee, K. E., Luttgen, M., et al. (2007). Modifying a sealed tube zinc reduction method for preparation of AMS graphite targets: reducing background and attaining high precision. *Nucl. Instrum. Methods Phys. Res. B* 259, 320–329. doi: 10.1016/j.nimb.2007.01.175

Conflict of Interest: The authors declare that the research was conducted in the absence of any commercial or financial relationships that could be construed as a potential conflict of interest.

Copyright © 2020 Blyakharchuk, Udachin, Li and Kang. This is an open-access article distributed under the terms of the Creative Commons Attribution License (CC BY). The use, distribution or reproduction in other forums is permitted, provided the original author(s) and the copyright owner(s) are credited and that the original publication in this journal is cited, in accordance with accepted academic practice. No use, distribution or reproduction is permitted which does not comply with these terms.

frontiers in Earth Science

ORIGINAL RESEARCH
published: 17 July 2020
doi: 10.3389/feart.2020.00228

A Persistently Increasing Precipitation Trend Through the Holocene in Northwest China Recorded by Black Carbon $\delta^{13}C$ From Sayram Lake

Qingfeng Jiang[1], Jianan Zheng[1], Yufeng Yang[1], Wenwei Zhao[1] and Dongliang Ning[1,2]*

[1] School of Geography Sciences, Nantong University, Nantong, China, [2] State Key Laboratory of Lake Science and Environment, Nanjing Institute of Geography and Limnology, Chinese Academy of Sciences, Nanjing, China

Precipitation is an important requirement for the stable and sustainable development of ecosystems and communities in arid areas, which are vulnerable to the influences of climate change. The changes in precipitation throughout the Holocene, as well as its long-term characteristics in arid northwest China, are not well understood, and records to reconstruct the precipitation trends are needed. Therefore, this study established a well-dated black carbon (BC) stable isotope-inferred ($\delta^{13}C$) precipitation record based on a sediment core from Sayram Lake, Tianshan Mountains (Xinjiang province, northwest China). The record spans the last 12880 cal. yr BP. Variations in BC $\delta^{13}C$ showed that between ∼12280 and 9260 cal. yr BP, regional precipitation gradually decreased, but then increased continually until the present, with millennial to centennial scale fluctuations. During the Holocene, a distinct period of low precipitation was observed between 9800 and 8800 cal. yr BP, and two episodes of high precipitation were observed between 8000 and 7600, and 5800 and 2500 cal. yr BP. The maximum precipitation occurred at ∼3800 cal. yr BP. Generally, the persistently increasing precipitation trend is consistent with other records from arid northwest China and adjacent areas. The trend was possibly controlled by Northern Hemisphere solar insolation and associated substantial ice sheet remnants, due to the influence of the North Atlantic Ocean sea surface temperatures and intensities of the Westerlies, which regulate the transport of water vapor to Xinjiang. The results provide a better understanding of the mechanisms driving the evolution of precipitation through the Holocene.

Keywords: black carbon isotope, northwest China, precipitation, Holocene, Sayram Lake

OPEN ACCESS

Edited by:
Liangcheng Tan,
Chinese Academy of Sciences, China

Reviewed by:
Jianghu Lan,
Chinese Academy of Sciences, China
Yu Li,
Lanzhou University, China

****Correspondence:***
Qingfeng Jiang
qfjiangz@163.com;
qfjiangz@ntu.edu.cn

Specialty section:
This article was submitted to Quaternary Science, Geomorphology and Paleoenvironment, a section of the journal Frontiers in Earth Science

Received: *29 February 2020*
Accepted: *27 May 2020*
Published: *17 July 2020*

Citation:
Jiang Q, Zheng J, Yang Y, Zhao W and Ning D (2020) A Persistently Increasing Precipitation Trend Through the Holocene in Northwest China Recorded by Black Carbon $\delta^{13}C$ From Sayram Lake. Front. Earth Sci. 8:228. doi: 10.3389/feart.2020.00228

INTRODUCTION

Northwest China is a vast territory characterized by an arid climate and fragile ecosystem (Chen et al., 2008). To maintain such a fragile regional ecosystem and ensure the sustainable development of human communities in these areas, water is a crucial factor. Precipitation, which has significantly affected the evolution of human civilizations, is one of the most important sources

of water in northwest China (Zhao et al., 1995). Considering the impact of potential changes to water availability on ecosystems and societies, it is important to assess their vulnerability to predicted warming of the climate. For such an assessment, understanding the evolution of regional precipitation over a historical period is necessary (Swann et al., 2018). Meteorological observations from northwest China, however, have been recorded over a duration that is too short to evaluate the evolution of precipitation over different timescales, or to predict future changes. Therefore, to provide a scientific basis for understanding regional water availability in response to future climate warming, over the past two decades, geological archives have been used to reconstruct the long-term evolution of precipitation/moisture in the region. Examples of such geological archives include: cave stalagmites (Cheng et al., 2012, 2016; Cai et al., 2017), desert sand dunes (Ran and Feng, 2014; Long et al., 2017), loess deposits (Chen et al., 2016; Xie et al., 2018), tree rings (Gou et al., 2015; Deng et al., 2016, 2017; Yang et al., 2019), lake sediments (Jiang et al., 2007, 2013; Liu et al., 2008; An et al., 2011; Li et al., 2011; Wang W. et al., 2013; Huang et al., 2015, 2018; Zhao et al., 2015, 2018), ice cores (Thompson et al., 1997, 2018), and peat deposits (Zhang and Feng, 2018; Xu et al., 2019). However, the results of these studies are contradictory with regard to the evolution of precipitation/moisture (Chen et al., 2008; Long et al., 2017). For example, arboreal pollen abundances from Bosten Lake, which are indicative of the moisture level in the lake catchment area, indicated that the Holocene climate was the wettest during 8–6 ka (Tarasov et al., 2019), whereas abundances of *Ephedra* from the same area and same elevation range suggested that the climate was relatively dry throughout the Holocene (Huang et al., 2009). As another example, a profile of the Big Black Peatland in the Southern Altay Mountains showed the middle Holocene to be dry, while a profile of the Kelashizi Peat, only 140 km away, showed a wet middle Holocene (Wang and Zhang, 2019; Xu et al., 2019). The reasons for these different understandings and interpretations of the same climate proxy are unclear. Similarly, the proposed mechanisms, as well as the sensitivity of indexes, that reflect responses to precipitation are inconsistent. Thus, more records on precipitation variation are needed to deepen our understanding of regional Holocene moisture changes, as well as the associated mechanisms.

Black carbon (BC) is a product of the incomplete combustion and pyrolysis of biomass and fossil fuels. It includes a series of carbonaceous materials with different degrees of carbonization, such as charcoal, carbon chips, graphite carbon, and soot (Masiello, 2004; Bird and Ascough, 2012). Owing to its chemical stability, including a strong resistance to oxidation and decomposition, it can remain unchanged in soil, and in ocean, lake, and other sediments for a long time. Recently, the stable isotope, $\delta^{13}C_{BC}$, which is present in the BC in lake sediments, has been extensively used in the reconstruction of paleofires, paleovegetations, paleoclimates, and paleoenvironments. This is because it can trace and provide information on the features of burned plants and their surrounding climatic and environmental conditions (Bird and Gröcke, 1997; Wang X. et al., 2013; Sun et al., 2015, 2017; Zhang et al., 2015; Zhang E. et al., 2018).

To enable the reconstruction of the evolution of regional precipitation, this study will generate a well-dated BC stable isotope-inferred precipitation record using Holocene sediments from Sayram Lake in arid northwest China. The record will be compared with published Holocene precipitation data from the study area as well as from adjacent areas, to identify potential correlations and understand possible driving mechanisms for climate change on millennial to centennial scales.

STUDY SITE

Sayram Lake (44°30′–44°42′ N, 81°05′–81°15′ E, 2071.9 m a.s.l.) is located on the western side of the Tianshan Mountains in Xinjiang province, northwest China. It is a vast closed alpine lake (**Figure 1a**) that is approximately elliptical (30 km long from east to west, and 27 km wide from north to south) (**Figure 1b**). It covers a total area of 453.0 km^2 and its catchment has a total area of 1408 km^2 (Wang and Dou, 1998). The lake has a storage capacity of 261×10^8 m^3 and in 2012 its maximum and average water depths were 99 and 56 m, respectively (Wu et al., 2012).

The Sayram Lake area, climate within the Eurasian continental temperate zone, is characterized by a continental semi-arid. It freezes in late October, and remains frozen (ice thickness: 0.7–1.1 m) for ∼150 days (i.e., from October to early May) (Wang and Dou, 1998). According to observational data collected during 1958–2018 from the nearest Wenquan County meteorological station (∼30 km away, and 1354.6 m a.s.l.), the annual average temperature and precipitation were ∼3.9°C and ∼236 mm, respectively. About 80% of precipitation (primarily derived from water vapor carried by westerly circulation) occurs between May and September (Zhang and Deng, 1987; Aizen et al., 2001). Between October and April, precipitation primarily results from the Siberian anticyclone, which accounts for <20% of the mean annual precipitation (Zhang and Deng, 1987; Aizen et al., 2001).

Water supply into Sayram Lake primarily results from precipitation, groundwater flow, and melted ice and snow. Thirty-two rivers (predominantly distributed along the western- and northwestern lake margins) drain into the lake (Hu, 2004). Among the rivers, seven are perennial and the others are seasonal. Sagakele River is the largest river (18.0 km long) and the only river that flows directly into the lake. Its average annual runoff is $\sim 0.24 \times 10^8$ m^3, which mainly results from precipitation. The other rivers recharge the lake via surface runoff or groundwater flow, with an inflow of $\sim 0.68 \times 10^8$ m^3. Surface precipitation into the lake is $\sim 1.6 \times 10^8$ m^3, and accounts for 63% of the total lake water recharge. Water loss from the lake is primarily due to evaporation on the lake surface, with an average annual evaporation of 550.0 mm (Wang and Dou, 1998) and total annual evaporation of 2.49×10^8 m^3. Presently, annual inflow is $\sim 2.52 \times 10^8$ m^3, and there is an approximate balance between inflow and outflow (Wang and Dou, 1998). Additionally, the glacier area in the Sayram Lake basin is small, i.e., ∼ 4.28 km^2 (Hu, 2004). It only accounts for ∼0.3% of the total basin area. Thus, the impact of glacial melt water on surface runoff and lake water level/area may be negligible (Lan et al., 2019).

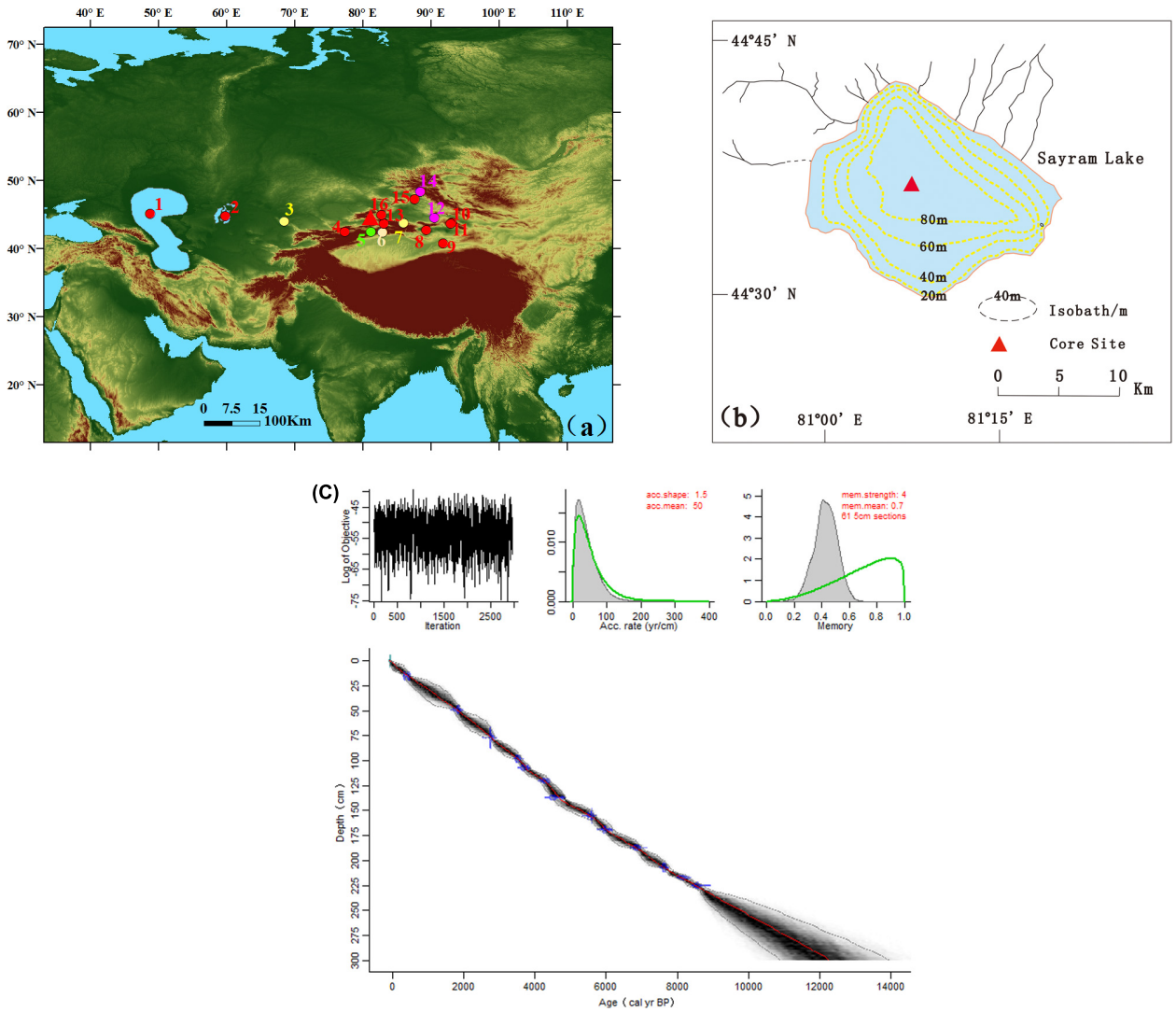

FIGURE 1 | (a) Location map of Sayram Lake (red triangle) and other mentioned and discussed research sites (colored circles with numbers). 1, Caspian Sea (Leroy et al., 2014); 2, Aral Sea (Cretaux et al., 2013); 3, VA loess section in central Kazakhstan (Ran and Feng, 2014); 4, Issyk-Kul in north-western Tianshan Mountains, Kyrgyzstan (Ricketts et al., 2001); 5, Kesang cave stalagmites (Cheng et al., 2012, 2016; Cai et al., 2017); 6, Sand dune in the central TianShan Mountains (Long et al., 2017); 7, LJW loess-paleosol section in the Tianshan Mountains (Chen et al., 2016; Xie et al., 2018); 8, Bosten Lake (Huang et al., 2009); 9, Lop Nur (Liu et al., 2016; Jia et al., 2017); 10, Balikun Lake (An et al., 2011; Zhao et al., 2015); 11, Tuolekule Lake (An et al., 2011); 12, Chaiwopu peat (Hong et al., 2014); 13, Lake sediments profile in Yili Valley (Li et al., 2011; Zhao et al., 2013); 14, Narenxia and Tielisha peat in Altai Mountains (Zhang et al., 2016, Zhang D. et al., 2018); 15, Wulungu Lake (Jiang et al., 2007; Liu et al., 2008); 16, Aibi Lake (Wang W. et al., 2013). **(b)** The SLM2009 core site (red triangle) and the isobathymetric map of Sayram Lake. **(c)** Bayesian model age-depth curve.

MATERIALS AND METHODS

In July 2009, a 300-cm long sedimentary core was extracted from the center of Sayram Lake (**Figure 1b**, SLMH2009, 44°34′59.0″ N, 81°09′12.3″ E) at a depth of 86.0 m using a piston corer attached to a UWITEC drilling platform. After extraction, the sediment core was transported to the laboratory, where it was cut longitudinally, and sampled at 1-cm intervals. The samples were then stored in a refrigerator at 4°C until analysis.

To establish the sedimentary chronology, the accelerator mass spectrometry (AMS) ^{14}C dating method was used. Without any suitable terrestrial plant residues, only bulk organic matter in the lake sediments was used for dating. Fourteen samples from different depths along the core were dated. The dating analyses were performed by the AMS Laboratory of Tokyo University (Japan) and by the Beta Analytic Radiocarbon Dating Laboratory in Miami (United States). All AMS ^{14}C dates, of which twelve had been previously reported by Jiang et al. (2013), were calibrated to calendar years using the Calib 7.1 program under the IntCal13 model (Reimer et al., 2013). Additionally, an age-depth curve was derived using the Bayesian model in the

Bacon 2.2 program in R v3.4.4 (Blaauw and Christen, 2011; R Development Core Team, 2013).

For $\delta^{13}C_{BC}$ analyses, 150 samples of bulk sediment were collected at 2-cm intervals. To extract and isolate BC from the lake sediments, the chemical oxidation method developed by Lim and Cachier (1996) was used. About 1.0 g of the dry powder bulk sediment was weighed. Carbonates and some of the silicates were removed via treatment with HCl (3 mol/L), HF (10 mol/L), HCl (1 mol/L), and HCl (3 mol/L) in sequence. To completely remove kerogen and soluble organic matter, $K_2Cr_2O_7$ (0.2 mol/L) and H_2SO_4 (2 mol/L) were added to oxidize the acid-treated samples (60 h, 55°C). After treatment, refractory carbon in the sediment was considered to be BC, which represents charcoal and soot resulting from regional fires and other earlier sources (Lim and Cachier, 1996). Determination of $\delta^{13}C_{BC}$ was performed by the State Key Laboratory of Lake Science and Environment, Nanjing Institute of Geography and Limnology, Chinese Academy of Sciences using a Thermo Delta V Advantage isotope mass spectrometer coupled with a Flash EA 1112 element analyzer. The $\delta^{13}C_{BC}$ values obtained were expressed using the delta per mil (δ, %) notation relative to Vienna Pee Dee Belemnite (V-PDB) as a standard. The accuracy of isotopic analyses was calibrated and evaluated based on replicate measurements using standard laboratory materials, and an accuracy of greater than $\pm$0.2% was obtained.

RESULTS

Table 1 shows the dating results of the 14 sediment samples. One sample, Slm1-245, diverged from the age-depth line that fits the other dates and has been excluded from the chronology of Sayram Lake. Lakes with carbonates in their basin can be affected by the "reservoir" effect, which is caused by the mixing of "old carbon" from the bedrock. There is usually uncertainty in age-depth models established using radiocarbon dates of bulk organic matter samples from such lakes (Hou et al., 2012). Generally, the "reservoir" effect is considered as the difference between zero and the age at the sediment-water interface obtained via linear extrapolation of the age-depth curve. The carbon reservoir age of the Sayram Lake was inferred to be 778a (**Figure 1c** and **Table 1**). This is approximately equal to the difference (~800a) between AMS^{14}C and ^{137}Cs dating results at a core depth of 15 cm (**Supplementary Figures 1–3**). Even though this estimation for the late Holocene radiocarbon reservoir effect is slightly smaller than that proposed by Lan et al. (2019) (1073a), which could be attributed to the estimations being made at different times, it is still close to the reservoir effect estimated for other lakes in Xinjiang province, including Wulungu Lake (760a, Liu et al., 2008), Balikun Lake (790a, An et al., 2011), and Bosten Lake (200–1140a, Huang, 2006). Therefore, the reservoir-corrected estimation of 778a was considered reliable. After subtracting 778a from the final age-depth model presented in **Figure 1c**, the 13 reliable dating results were converted to calendar years. The mean weighted age at the base of the SLMH2009 core was found to be ~12280 cal. yr BP, and the sedimentation rate through the core was between 0.17–0.34 cm/yr. With an average sedimentation rate of 0.26 cm/yr, the average resolution of the $\delta^{13}C_{BC}$ record from Sayram Lake was ~50 yr.

The $\delta^{13}C_{BC}$ values ranged from −30.9 to −22.1%, with a mean of −27.4% (**Figure 2a**). The general variation in $\delta^{13}C_{BC}$ could be roughly divided into three stages: Stage 1, 12280–9260 cal. yr BP, during which $\delta^{13}C_{BC}$ increased from −26.9 to −22.1%, with a mean of −25.0%; Stage 2, 9260–8000 cal. yr BP, during which $\delta^{13}C_{BC}$ decreased abruptly from −22.1 to −30.4%; and Stage 3, 8000 cal. yr BP to present, during which $\delta^{13}C_{BC}$ increased from −30.9 to −26.8%, with a mean of −28.1%. These overall $\delta^{13}C_{BC}$ trends were punctuated by several millennial-scale excursions, which included $\delta^{13}C_{BC}$ enrichments centered at 9200 and 7400 cal. yr BP, and depletions at ~8000–7600 and 5800–2500 cal. yr BP.

DISCUSSION

Interpretation of the $\delta^{13}C_{BC}$ in Sayram Lake

Studies have demonstrated that $\delta^{13}C_{BC}$ can be influenced by several factors (Bird and Ascough, 2012), including the stable carbon isotope compositions of the burned precursors (e.g., Street-Perrott et al., 1997; Huang et al., 2001; Zhang et al., 2003), relative abundances of different burned plant species (e.g., Wang X. et al., 2013; Sun et al., 2015, 2017; Zhang et al., 2015), isotope fractionation during pyrolysis, and modification that occurs during diagenesis (e.g., Bird and Ascough, 2012; Sun et al., 2015, 2017).

During photosynthesis, the $\delta^{13}C$ values of terrestrial plants can be modified via carbon isotope fractionation, and plants can be classified into three types depending on their carbon-fixation pathways: C_3, C_4, and CAM plants (O'Leary, 1981, 1988). The C_3 plants, which include trees, most shrubs and grasses, and sedges, are characterized by the C_3 carbon-fixation pathway under cold climatic conditions, and their $\delta^{13}C$ values range from −34 to −20%, with a mean of −27% (Bird et al., 1996). The C_4 plants, which include most grasses and sedges, are characterized by the C_4 carbon-fixation pathway under warm climatic conditions, and their $\delta^{13}C$ values are relatively higher, and range between approximately −16 to −10%, with a mean of −13% (Smith and Epstein, 1971; O'Leary, 1981; Farquhar et al., 1989). The CAM plants, which include most succulents, and can survive in extremely dry environments, are characterized by both the C_3 and C_4 carbon-fixation pathways, and they have a large range of $\delta^{13}C$ values, from −28% to −11% (O'Leary, 1988; Lüttge, 2004).

Carbon isotope fractionation of plants during pyrolysis to BC varies with pyrolysis temperature and the amount of oxygen available. It also varies with the proportion of carbon components as well as the isotopic composition of different plant tissues (Sun et al., 2017). Most pyrolysis experiments have confirmed that the variation of plant carbon-isotope fractionation during pyrolysis is in the range of 1–2%, with an average carbon-isotope depletion of 0.3 and 1.7% for C_3 and C_4 plants, respectively (Bird and Gröcke, 1997; Bird and Ascough, 2012; Wang X. et al., 2013).

TABLE 1 | AMS ^{14}C dating results.

Sample number	Laboratory I.D.	Depth/cm	Dating material	^{14}C age/aBP	$\delta^{13}C$/‰	C/N	Reservoir-corrected ^{14}C age by 778a	Calendar age/cal. yr BP(2σ)
Slm1-15	Tka-15142	14–15	TOC	1150 ± 25	−25.7	13.4	372	426–501 (464)
Slm1-49	Tka-15163	48–49	TOC	2670 ± 35	−26.3	14.9	1892	1727–1899 (1813)
Slm1-77	Tka-15143	76–77	TOC	3425 ± 30	−27.6	14.0	2647	2739–2796 (2768)
Slm1-98	Beta469443	97–98	TOC	4080 ± 30	−27.1	15.4	3302	3454–359 (3524)
Slm1-107	Tka-15144	106–107	TOC	4215 ± 35	−29.6	18.1	3437	3608–3780 (3694)
Slm1-120	Beta469444	119–120	TOC	4640 ± 30	−26.5	13.7	3862	4225–4411 (4318)
Slm1-137	Tka-15164	136–137	TOC	4815 ± 45	−28.9	12.9	4037	4416–4629 (4523)
Slm1-155	Tka-15145	154–155	TOC	5625 ± 35	−28.7	15.4	4847	5578–5651 (5615)
Slm1-169	Tka-15165	168–169	TOC	5980 ± 45	−25.4	17.2	5202	5893–6029 (5961)
Slm1-187	Tka-15146	186–187	TOC	6795 ± 35	−26.8	12.0	6017	6776–6949 (6863)
Slm1-207	Tka-15147	206–207	TOC	7555 ± 40	−28.0	10.5	6777	7577–7677 (7627)
Slm1-217	Tka-15166	216–217	TOC	8120 ± 50	−25.2	14.6	7342	8021–8220 (8121)
Slm1-225	Tka-15148	224–225	TOC	8560 ± 45	−26.7	10.3	7782	8455–8639 (8542)
Slm1-245	Tka-15149	244–245	TOC	14550 ± 60	−18.2	4.2	/	/

Black carbon is usually considered stable, and remains unchanged after deposition (Bird and Ascough, 2012), especially if buried in low-temperature and non-oxidizing environments. Due to the relatively high altitude, relatively deep, low temperature, and anoxic bottom of Sayram Lake, post-depositional modification of the isotopes in BC was considered negligible. Thus, the $\delta^{13}C_{BC}$ values of the lake sediment samples were primarily determined by the variation in C_3 and C_4 terrestrial plants inhabiting the area, as well as the variation of their proportions during combustion. This means that $\delta^{13}C_{BC}$ values are generally indicative of the regional paleovegetation in a given area (Bird and Gröcke, 1997; Bird and Cali, 1998; Clark et al., 2001; Jia et al., 2003; Sun et al., 2015; Zhang et al., 2015). The $\delta^{13}C_{BC}$ values for Sayram Lake were less than −27‰, suggesting that over the past ∼12280 yr, the lake basin and surrounding region were predominantly inhabited by C_3 plants. This is consistent with the findings from loess areas of Xinjiang, which also suggested that arid northwest China was mainly inhabited by C_3 plants throughout the Holocene (Xie et al., 2018).

During photosynthesis in C_3 plants, climatic factors including temperature, precipitation, and atmospheric CO_2 concentration, as well as vital effects, directly affect the fractionation of carbon isotopes (Sage et al., 1999; Kohn, 2010). Globally, there is a significant negative correlation between $\delta^{13}C$ and mean annual precipitation. Furthermore, for C_3 plants, the correlation between $\delta^{13}C$ and mean annual precipitation is much more significant than that between $\delta^{13}C$ and mean annual temperature (Rao et al., 2017). This has been confirmed by studies on the Loess Plateau in China, which showed that the $\delta^{13}C$ of C_3 plants generally increased with decreasing precipitation (Wang et al., 2008, 2018). The atmospheric CO_2 concentration was generally stable during the Holocene (Monnin et al., 2004), and its effects on carbon-isotope fractionation in C_3 plants were considered negligible (Schubert and Jahren, 2012). Even though these factors are uncertain for the Sayram Lake area, the $\delta^{13}C_{BC}$ values of the Sayram Lake sediment samples can be used as a paleo-precipitation proxy, with more positive $\delta^{13}C_{BC}$ values indicating lower precipitation, and vice versa.

The relationship between BC isotope composition and climate factors, such as precipitation and temperature in the study area, had not been investigated. However, studies on the correlation between climate factors and the carbon isotopes in modern plants, as well as topsoil organic matter in the Tianshan Mountains (**Supplementary Figures 4–9**), have shown that the organic carbon isotope composition of modern plants and topsoil organic matter are strongly negatively correlated with precipitation, and weakly positively correlated with temperature. These relationships were stronger when only the isotope compositions of samples from the northern slope of the Tianshan Mountains, where Sayram Lake is located, were considered. These findings establish precipitation as a key factor that controls the organic carbon isotope composition in modern plants and topsoil organic matter. Most importantly, BC isotopes can be used as an alternative indicator of precipitation and its evolution in an area.

Variations of Holocene Precipitation in Northwest China

The variation of $\delta^{13}C_{BC}$ from ∼12280 to 9260 cal. yr BP revealed a gradual decrease in precipitation in the study area. Thereafter, it increased persistently through the Holocene with millennial- to centennial-scale fluctuations superimposed (**Figure 2a**). A distinct low-precipitation episode appeared between 9800 and 8800 cal. yr BP, with the lowest precipitation at 9260 cal. yr BP. Two high precipitation episodes were also observed between 8000 and 7600, and 5800 and 2500 cal. yr BP, and the highest precipitation was observed at ∼3800 cal. yr BP.

The gradually decreasing and increasing precipitation trends before and after 9260 cal. yr BP, respectively, based on the $\delta^{13}C_{BC}$ data from Sayram Lake, were found to be consistent with the moisture changes reconstructed using *Artemisia* and Chenopodiaceae pollen percentage ratios (i.e., A/C, **Figure 2b**) from the same sediment core (Jiang et al., 2013). However,

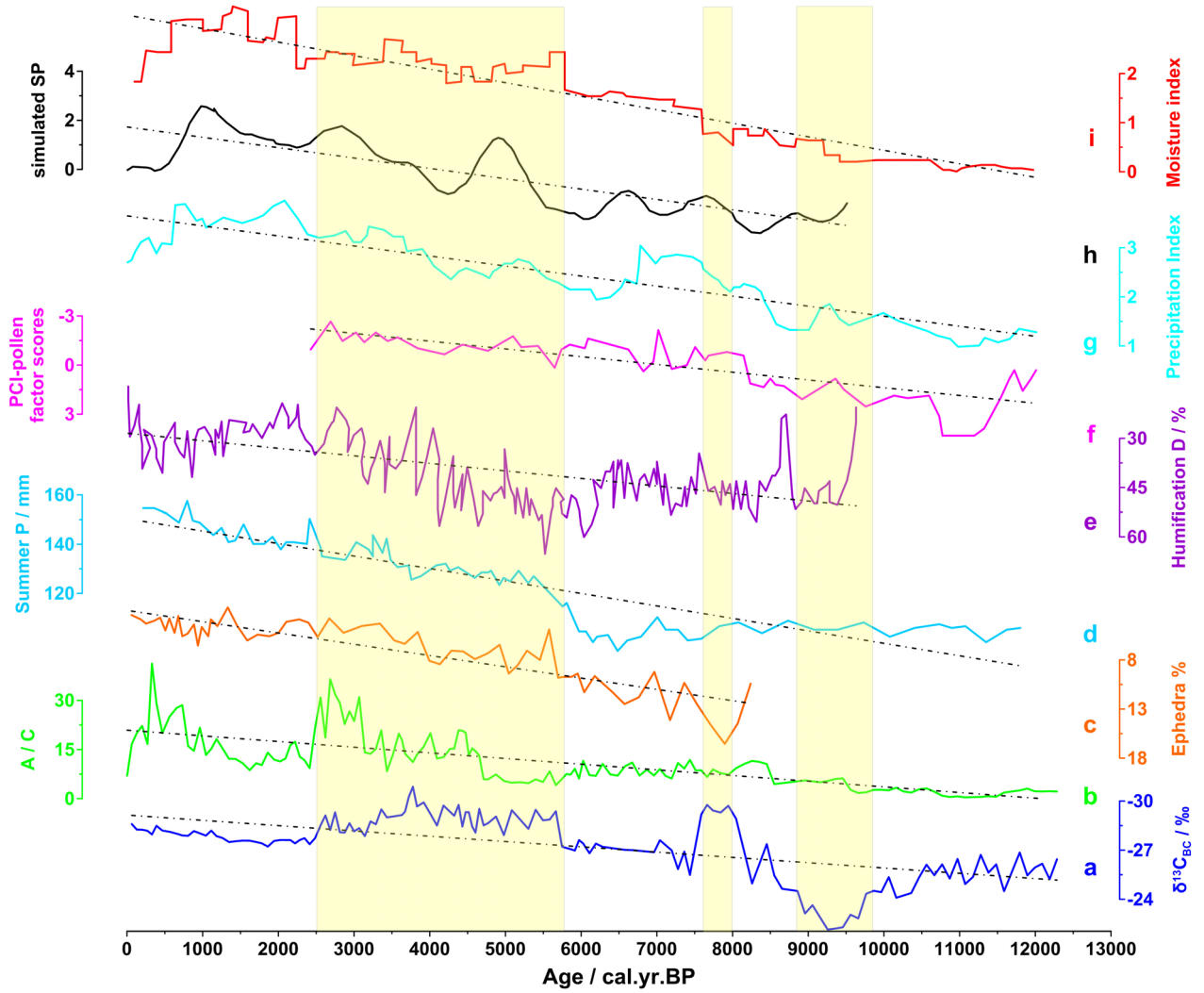

FIGURE 2 | Comparisons between a BC carbon isotope record of Sayram Lake **(a)** and other records from arid northwest China and the adjacent regions. **(b)** A/C Ratio of Sayram Lake (Jiang et al., 2013). **(c)** Ephedra% of Bosten Lake (Huang et al., 2009). **(d)** Summer precipitation reconstruction from Tianshan Mountains Loess (Xie et al., 2018). **(e)** Humification degree in Tielisha Peat (Zhang et al., 2016). **(f)** PC1-pollen factor scores of the Caspian Sea (Leroy et al., 2014). **(g)** Synthesized pollen-based Holocene precipitation-index from Altai Mountains and its adjacent areas (Zhang D. et al., 2018). **(h)** Simulated summer precipitation in arid central Asia (Zhang et al., 2017). **(i)** Synthesis moisture index from the Mongolian Plateau and its adjacent areas (Wang and Feng, 2013); Black dotted dash line represents proxies' variation trend.

there were also some differences between the precipitation and moisture levels recorded in this study and those reported in previous studies. Jiang et al. (2013) reported that precipitation increased sharply during the early Holocene, while moisture levels increased at a relatively slower pace. This difference could be attributed to the higher evaporation rate caused by higher temperature instability during this period.

Variations in $\delta^{13}C_{BC}$-inferred Holocene precipitation observed in this study generally resemble those observed in other lake sediment records from adjacent regions in northwest China. Even though characterized by significant fluctuations, similar moisture evolution trends have been observed in Bosten, Wulungur, and Swan Lake based on *Ephedra* abundance, A/C ratios, and Cyperaceae/Poaceae ratios, respectively, as shown in **Figure 2c** (Jiang et al., 2007; Liu et al., 2008; Huang et al., 2009, 2015). The principle component 1 values of pollen abundance and carbonate content in sediments from Balikun Lake showed a moisture threshold at ~8000 cal. yr BP, which increased rapidly for a short while, and thereafter decreased slowly, accompanied by significant fluctuations. The studies on Balikun Lake showed a very wet late Holocene period (An et al., 2011; Zhao et al., 2015). Based on A/C ratios, moisture records from Aibi Lake sediments also showed a mildly dry early Holocene, a progressively wet middle Holocene, and a very wet late Holocene after 2000 cal. yr BP (Wang W. et al., 2013). The annual precipitation record from Kanas Lake reconstructed using a palynological transfer function also showed a continuously increasing Holocene wetness trend (Huang et al., 2018).

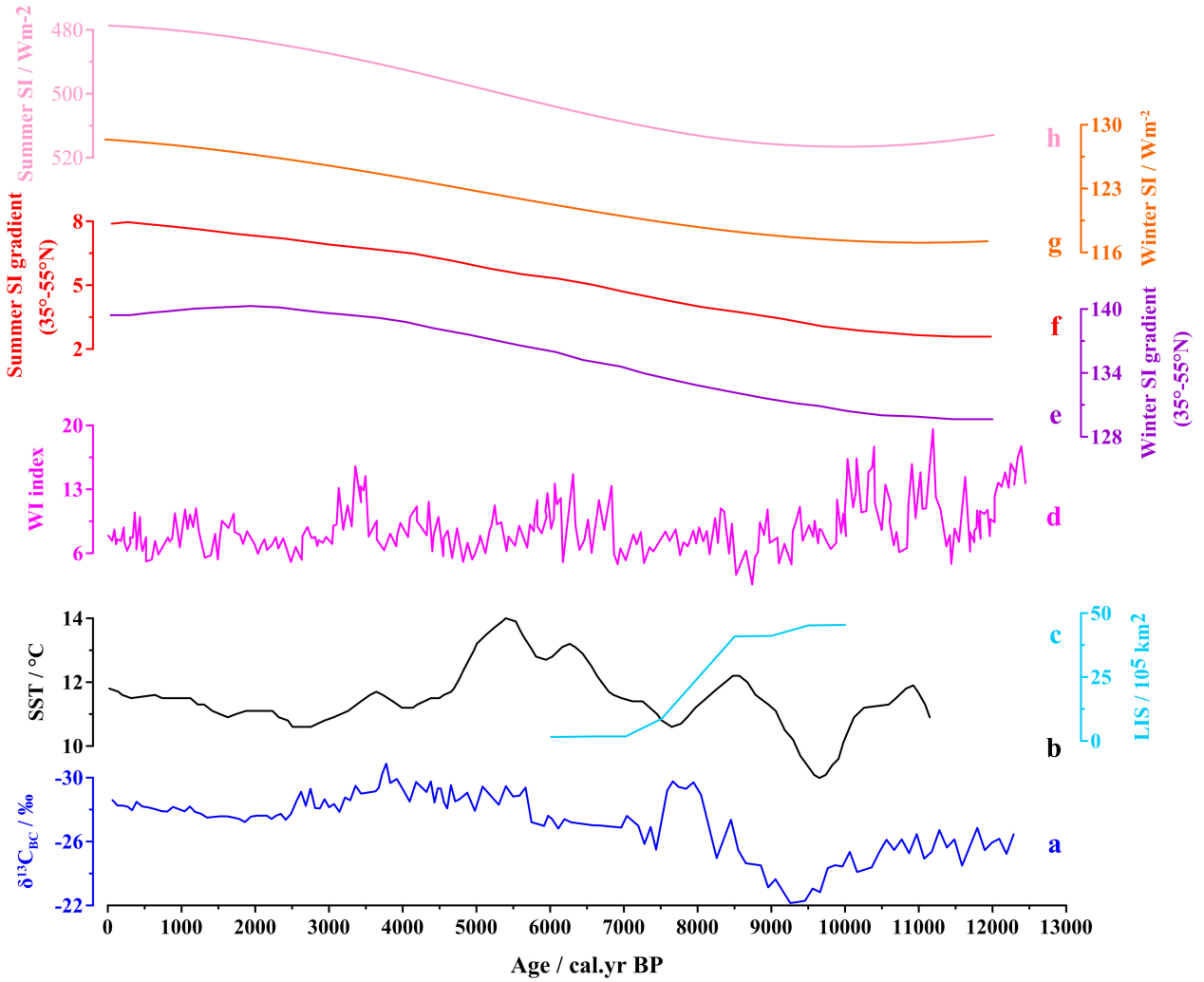

FIGURE 3 | Possible forcing for Holocene precipitation changes in northwest China. **(a)** Black carbon isotope record from Sayram Lake (This study). **(b)** Holocene sea surface temperature (SST) of North Atlantic (Berner et al., 2008). **(c)** Substantial remnants of ice sheets in the Northern Hemisphere (Carlson et al., 2008). **(d)** Reconstruction of sunspot number in the past 11400 yr (Solanki et al., 2004). **(e,f)** Summer and winter solar insolation on 45°N (Berger and Loutre, 1991). **(g,h)** Summer and winter insolation gradient between middle and high latitudes (Routson et al., 2019).

Moreover, other sedimentary records within arid northwest China also support the generally increasing precipitation pattern recorded in Sayram Lake. Holocene moisture variation based on magnetic parameters χ_{ARM}/SIRM from a loess-paleosol section in the Tianshan Mountains showed a continuously increasing humidity trend, with the wettest period during the late Holocene (Chen et al., 2016). An organic carbon isotope-based summer precipitation reconstruction from the same loess-paleosol profile also indicated an increasing precipitation trend throughout the Holocene (**Figure 2d**; Xie et al., 2018). Additionally, AP/NAP pollen ratios from Narenxia Peat (Altay Mountains), humification degree data from Tielisha Peat (Altay Mountains), and $\delta^{13}C$ value of α-cellulose from Chaiwopu Peat (eastern Tianshan Mountains) also showed gradually increasing Holocene moisture trends with large fluctuations (**Figure 2e**; Hong et al., 2014; Zhang et al., 2016; Feng et al., 2017).

Records from studies outside the northwest China region also confirm a persistently increasing precipitation trend in arid areas during the Holocene. Organic carbon $\delta^{13}C$ from the VA loess section in Kazakhstan showed that the moisture level fluctuated along a constant line between early to mid-Holocene, and then increased during the last ca. 5000 yr (Ran and Feng, 2014). The principle component 1 scores based on pollen measurements from the Caspian Sea indicated that moisture levels increased consistently from 12440 to 2430 cal. yr BP (**Figure 2f**; Leroy et al., 2014). In addition to the pollen data, dinocyst assemblages from the Caspian Sea clearly revealed a 6000-yr long highstand sea level between 10550 and 4110 cal. yr BP, implying a higher precipitation/moisture level (Leroy et al., 2014).

The synthesized pollen-based Holocene precipitation-index for the lowland Altay Mountains and adjacent areas (**Figure 2g**; Zhang D. et al., 2018), the simulated summer precipitation

variations in arid central Asia (**Figure 2h**; Zhang et al., 2017), and the synthesized moisture index from the Mongolian Plateau and adjacent areas (**Figure 2i**; Wang and Feng, 2013) also indicated an increasing precipitation trend throughout the Holocene, even though since 1000 cal. yr BPit has been declining.

Notably, all the above-mentioned precipitation and moisture level records showed different precipitation rate and range changes. However, the general trend is for gradually decreasing precipitation during the early Holocene, followed by a persistent increase in precipitation until the present. The tread is clear even though the proxy records are possibly affected by age uncertainties, regional climate differences, and the impacts of a variety of climate factors (Liu et al., 2006; Rao et al., 2019).

Possible Forcing for Holocene Precipitation Changes in Northwest China

Modern observations and paleoclimate simulations have confirmed that water vapor originating from the North Atlantic Ocean, and the Mediterranean, Black, and Caspian Seas, and transported by Westerlies, represents the dominant moisture source that supplies precipitation to arid northwest China (Zhang and Deng, 1987; Aizen et al., 1997, 2001; Jin et al., 2012; Wang B.L. et al., 2013; Zhao et al., 2013; Huang et al., 2017; Xu et al., 2019). Therefore, sea surface temperatures (SST) of the North Atlantic Ocean and the intensity of the Westerlies are probably the primary factors that directly influence rainfall patterns in the study area. This inference is supported by the nearly synchronous Holocene evolution of the precipitation changes recorded in Sayram Lake and changes in the intensity of the Westerlies recorded in the Tianshan Mountains (Jia et al., 2018), Qinghai Lake (An et al., 2012), and SST data from the North Atlantic Ocean (Berner et al., 2008).

Previous studies have shown that solar insolation in the Northern Hemisphere is the main factor that controls the intensity of Westerlies (Jin et al., 2012). The winter and summer insolations at mid-latitudes increase and decrease, respectively, faster than that at high latitudes; the insolation gradient between the middle and high latitudes has increased gradually from the early Holocene period onward (**Figure 3**; Jin et al., 2012; Routson et al., 2019). This increased insolation gradient possibly results in more intense Westerlies (Routson et al., 2019), which could have potentially transported more moisture from the North Atlantic Ocean to northwestern China, bringing about the increase in precipitation during the Holocene.

Additionally, both Northern Hemisphere solar insolation and the substantial ice sheet remnants, including the Laurentide and Fennoscandian ice sheets (Peltier and Fairbanks, 2006; Carlson et al., 2008), can significantly influence SSTs of the North Atlantic Ocean (Chen et al., 2016; He et al., 2017). Increasing winter insolation during the Holocene could have possibly warmed the sea surface, thereby enhancing evaporation over the North Atlantic Ocean (Chen et al., 2016). Thus, both the strengthened Westerly wind and the increased evaporation could have increased the moisture supply to northwestern China, leading to a wetter winter climate through the Holocene (Chen et al., 2016). The corresponding decreasing summer insolation possibly resulted in the decreasing summer precipitation in northwestern China. However, a higher summer temperature during the early Holocene would have increased the melting of ice sheets, resulting in their expansion over the North Atlantic Ocean (**Figure 3**). This probably slowed down the Atlantic Meridional overturning circulation and reduced thermal transport from the equator to the middle and high latitudes, resulting in decreases in SSTs (McManus et al., 2004). As the Northern Hemisphere ice sheets gradually diminished, SST increased; coupled with more intense Westerlies, much more vapor was transported to northwest China, resulting in a persistently wet summer climate. Furthermore, a higher summer temperature resulting from higher summer insolation during the early Holocene could have caused northward displacement of the subtropical high, which inhibits precipitation development in northwest China (Chen et al., 2016). As summer temperatures decreased from the middle to late Holocene, the subtropical high could have migrated southward, leading to higher precipitation in this area. The enhanced precipitation in both summer and winter probably resulted in the increasing precipitation trend observed in the Sayram Lake area.

It is suggested that the persistently increasing precipitation trend observed in northwest China during the Holocene resulted from changes in Northern Hemisphere solar insolation and the substantial ice sheet remnants due to the influence of North Atlantic Ocean SSTs and increased intensity of the Westerlies.

CONCLUSION

In this study, to illustrate Holocene precipitation variation in arid northwest China, a BC isotope-inferred precipitation record of an alpine lake in the Tianshan Mountains in Xinjiang was presented. The chronology of the studied lake sediment core, which had a mean basal age of ∼12280 years, was established using 13 AMS ^{14}C dates. The $\delta^{13}C_{BC}$ record showed that precipitation decreased between ∼12280 and 9260 cal. yr BP, and then increased during the mid- to late Holocene. The reliability of the $\delta^{13}C_{BC}$ record, particularly the persistently increasing precipitation trend throughout the Holocene, was further supported by published precipitation and moisture records from northwest China and surrounding regions. It was inferred that the evolution of precipitation in arid northwest China throughout the Holocene was linked to Northern Hemisphere solar insolation and the substantial ice sheet remnants due to the influence of North Atlantic Ocean SSTs and the intensity of the Westerlies. Considering the importance of understanding the Holocene evolution of regional precipitation, as well as its driving mechanisms in arid areas, more reliable Holocene precipitation reconstructions are needed for further study.

DATA AVAILABILITY STATEMENT

The datasets generated for this study are available on request to the corresponding author.

AUTHOR CONTRIBUTIONS

QJ designed the research. QJ, JZ, YY, WZ, and DN performed the research. QJ, JZ, and YY analyzed the data. QJ, WZ, and DN wrote the manuscript. All authors contributed to the article and approved the submitted version.

FUNDING

This study was supported by the National Natural Science Foundation of China (Grant Nos. 41672349 and 40802084).

ACKNOWLEDGMENTS

We thank the reviewers for their very valuable comments and suggestions. We also thank Dr. Chao Zhenhua and Dr. Zhou Tong from the School of Geography Sciences, Nantong University, for their assistance during field measurements.

SUPPLEMENTARY MATERIAL

The Supplementary Material for this article can be found online at: https://www.frontiersin.org/articles/10.3389/feart.2020.00228/full#supplementary-material

REFERENCES

Aizen, E. M., Aizen, V. B., Melack, J. M., Nakamura, T., and Ohta, T. (2001). Precipitation and atmospheric circulation patterns at mid-latitudes of Asia. *Int. J. Climatol.* 21, 535–556. doi: 10.1002/joc.626

Aizen, V. B., Aizen, E. M., Melack, J. M., and Dozier, J. (1997). Climatic and hydrologic changes in the Tien shan, Central Asia. *J. Climate* 10, 1393–1404. doi: 10.1175/1520-0442(1997)010<1393:cahcit>2.0.co;2

An, C. B., Zhao, J. J., Tao, S. C., Lv, Y. B., Dong, W. M., Li, H., et al. (2011). Dust variation recorded by lacustrine sediments from arid Central Asia since similar to 15 cal ka BP and its implication for atmospheric circulation. *Quat. Res.* 75, 566–573. doi: 10.1016/j.yqres.2010.12.015

An, Z., Colman, S. M., Zhou, W., Li, X., Brown, E. T., Jull, A. J., et al. (2012). Interplay between the Westerlies and Asian monsoon recorded in Lake Qinghai sediments since 32 ka. *Sci. Rep.* 2:619. doi: 10.1038/srep00619

Berger, A., and Loutre, M. F. (1991). Insolation values for the climate of the last 10 million years. *Quat. Sci. Rev.* 10, 297–317. doi: 10.1016/0277-3791(91)90033-q

Berner, K. S., Koc, N., Divine, D., Godtliebsen, F., and Moros, M. (2008). A decadal-scale Holocene sea surface temperature record from the subpolar North Atlantic constructed using diatoms and statistics and its relation to other climate parameters. *Paleoceanography* 23, 2211–2215. doi: 10.1029/2006pa001339

Bird, M. I., and Ascough, P. L. (2012). Isotopes in pyrogenic carbon: a review. *Org. Geochem.* 42, 1529–1539. doi: 10.1016/j.orggeochem.2010.09.005

Bird, M. I., and Cali, J. A. (1998). A million-year record of fire in sub-Saharan Africa. *Nature* 394, 767–769. doi: 10.1038/29507

Bird, M. I., Chivas, A. R., and Head, J. (1996). A latitudinal gradient in carbon turnover times in forest soils. *Nature* 381, 143–146. doi: 10.1038/381143a0

Bird, M. I., and Gröcke, D. R. (1997). Determination of the abundance and carbon isotope composition of elemental carbon in sediments. *Geochim. Cosmochim. Acta* 61, 3413–3423. doi: 10.1016/s0016-7037(97)00157-9

Blaauw, M., and Christen, J. A. (2011). Flexible paleoclimate age-depth models using an autoregressive gamma process. *Bayesian Anal.* 6, 457–474. doi: 10.1214/11-ba618

Cai, Y. J., Chiang, J. C. H., Breitenbach, S. F. M., Tan, L. C., Cheng, H., Edwards, R. L., et al. (2017). Holocene moisture changes in western China, Central Asia, inferred from stalagmites. *Quat. Sci. Rev.* 158, 15–28. doi: 10.1016/j.quascirev.2016.12.014

Carlson, A. E., Legrande, A. N., Oppo, D. W., Came, R. E., Schmidt, G. A., Anslow, F. S., et al. (2008). Rapid early Holocene deglaciation of the Laurentide ice sheet. *Nat. Geosci.* 1, 620–624. doi: 10.1038/ngeo285

Chen, F. H., Jia, J., Chen, J. H., Li, G. Q., Zhang, X. J., Xie, H. C., et al. (2016). A persistent Holocene wetting trend in arid central Asia, with wettest conditions in the late Holocene, revealed by multi-proxy analyses of loess-paleosol sequences in Xinjiang, China. *Quat. Sci. Rev.* 146, 134–146. doi: 10.1016/j.quascirev.2016.06.002

Chen, F. H., Yu, Z. C., Yang, M. L., Ito, E., Wang, S. M., Madsen, D. B., et al. (2008). Holocene moisture evolution in arid central Asia and its out-of-phase relationship with Asian monsoon history. *Quat. Sci. Rev.* 27, 351–364. doi: 10.1016/j.quascirev.2007.10.017

Cheng, H., Spotl, C., Breitenbach, S. F., Sinha, A., Wassenburg, J. A., Jochum, K. P., et al. (2016). Climate variations of Central Asia on orbital to millennial timescales. *Sci. Rep.* 5:36975. doi: 10.1038/srep36975

Cheng, H., Zhang, P. Z., Spotl, C., Edwards, R. L., Cai, Y. J., Zhang, D. Z., et al. (2012). The climatic cyclicity in semiarid-arid central Asia over the past 500,000 years. *Geophys. Res. Lett.* 39:L01705. doi: 10.1029/2011gl050202

Clark, J. S., Grimm, E. C., Lynch, J., and Mueller, P. G. (2001). Effects of Holocene climate change on the C 4 grassland/woodland boundary in the Northern Plains, USA. *Ecology* 82, 620–636. doi: 10.2307/2680184

Cretaux, J. F., Letolle, R., and Berge-Nguyen, M. (2013). History of Aral Sea level variability and current scientific debates. *Glob. Planet Change* 110, 99–113. doi: 10.1016/j.gloplacha.2013.05.006

Deng, Y., Gou, X., Gao, L., Yang, M., and Zhang, F. (2016). Spatiotemporal drought variability of the eastern Tibetan Plateau during the last millennium. *Clim. Dynam.* 49, 2077–2091. doi: 10.1007/s00382-016-3433-8

Deng, Y., Gou, X. H., Gao, L. L., Yang, M. X., and Zhang, F. (2017). Tree-ring recorded moisture variations over the past millennium in the Hexi Corridor, northwest China. *Environ. Earth Sci.* 76:272. doi: 10.1007/s12665-017-6581-1

Farquhar, G., Ehleringer, J. R., and Hubick, K. T. (1989). Carbon isotope discrimination and photosynthesis. *Annu. Rev. Plant Phys.* 40, 503–537.

Feng, Z., Sun, A., Abdusalih, N., Ran, M., Kurban, A., Lan, B., et al. (2017). Vegetation changes and associated climatic changes in the southern Altai Mountains within China during the Holocene. *Holocene* 27, 683–693. doi: 10.1177/0959683616670469

Gou, X., Deng, Y., Gao, L., Chen, F., Cook, E., Yang, M., et al. (2015). Millennium tree-ring reconstruction of drought variability in the eastern Qilian Mountains, northwest China. *Clim. Dynam.* 45, 1761–1770. doi: 10.1007/s00382-014-2431-y

He, S., Gao, Y., Li, F., Wang, H., and He, Y. (2017). Impact of Arctic Oscillation on the East Asian climate: a review. *Earth Sci. Rev.* 164, 48–62. doi: 10.1016/j.earscirev.2016.10.014

Hong, B., Gasse, F., Uchida, M., Hong, Y., Leng, X., Shibata, Y., et al. (2014). Increasing summer rainfall in arid eastern-Central Asia over the past 8500 years. *Sci. Rep.* 4:5279. doi: 10.1038/srep05279

Hou, J., D'andrea, W. J., and Liu, Z. (2012). The influence of 14C reservoir age on interpretation of paleolimnological records from the Tibetan Plateau. *Quat. Sci. Rev.* 48, 67–79. doi: 10.1016/j.quascirev.2012.06.008

Hu, R. J. (2004). *Physical Geography of the Tianshan Mountaions in China*. Beijing: China Environmental Science Press, 278–284.

Huang, W., Chang, S. Q., Xie, C. L., and Zhang, Z. P. (2017). Moisture sources of extreme summer precipitation events in North Xinjiang and their relationship with atmospheric circulation. *Adv. Clim. Change Res.* 8, 12–17. doi: 10.1016/j.accre.2017.02.001

Huang, X., Peng, W., Rudaya, N., Grimm, E. C., Chen, X., Cao, X., et al. (2018). Holocene vegetation and climate dynamics in the altai mountains and surrounding areas. *Geophys. Res. Lett.* 45, 6628–6636. doi: 10.1029/2018gl078028

Huang X. Z. (2006). *Holocene Climate Variability of Arid Central Asia Documented by Bosten Lake, Xinjiang, China*. Ph.D. thesis, Lanzhou Uinversity, Lanzhou, 71–80.

Huang, X. Z., Chen, C. Z., Jia, W. N., An, C. B., Zhou, A. F., Zhang, J. W., et al. (2015). Vegetation and climate history reconstructed from an alpine lake in central Tienshan Mountains since 8.5 ka BP. *Palaeogeogr. Palaeoclimatol. Palaeoecol.* 432, 36–48. doi: 10.1016/j.palaeo.2015.04.027

Huang, X. Z., Chen, F. H., Fan, Y. X., and Yang, M. L. (2009). Dry late-glacial and early Holocene climate in arid central Asia indicated by lithological and palynological evidence from Bosten Lake, China. *Quat. Int.* 194, 19–27. doi: 10.1016/j.quaint.2007.10.002

Huang, Y., Street-Perrott, F. A., Metcalfe, S. E., Brenner, M., Moreland, M., and Freeman, K. H. (2001). Climate change as the dominant control on glacial-interglacial variations in C3 and C4 plant abundance. *Science* 293, 1647–1651. doi: 10.1126/science.1060143

Jia, G. D., Peng, P. A., Zhao, Q. H., and Jian, Z. M. (2003). Changes in terrestrial ecosystem since 30 Ma in East Asia: stable isotope evidence from black carbon in the South China Sea. *Geology* 31, 1093–1096.

Jia, H. J., Wang, J. Z., Qin, X. G., and Yi, S. (2017). Palynological implications for Late Glacial to middle Holocene vegetation and environmental history of the Lop Nur Xinjiang Uygur autonomous region, northwestern China. *Quat. Int.* 436, 162–169. doi: 10.1016/j.quaint.2016.11.024

Jia, J., Liu, H., Gao, F. Y., and Xia, D. S. (2018). Variations in the westerlies in Central Asia since 16 ka recorded by a loess section from the Tien Shan Mountains. *Palaeogeogr. Palaeoclimatol. Palaeoecol.* 504, 156–161. doi: 10.1016/j.palaeo.2018.05.021

Jiang, Q. F., Ji, J. F., Shen, J., Matsumoto, R., Tong, G. B., Qian, P., et al. (2013). Holocene vegetational and climatic variation in westerly-dominated areas of Central Asia inferred from the Sayram Lake in northern Xinjiang, China. *Sci. China Earth Sci.* 56, 339–353. doi: 10.1007/s11430-012-4550-9

Jiang, Q. F., Shen, J., Liu, X. Q., Zhang, E. L., and Xiao, X. Y. (2007). A high-resolution climatic change since Holocene inferred from multi-proxy of lake sediment in westerly area of China. *Chin. Sci. Bull.* 52, 1970–1979. doi: 10.1007/S11434-007-0245-6

Jin, L., Chen, F., Morrill, C., Otto-Bliesner, B. L., and Rosenbloom, N. (2012). Causes of early Holocene desertification in arid central Asia. *Clim. Dynam.* 38, 1577–1591. doi: 10.1007/s00382-011-1086-1

Kohn, M. J. (2010). Carbon isotope compositions of terrestrial C3 plants as indicators of (paleo)ecology and (paleo)climate. *Proc. Natl. Acad. Sci. U.S.A.* 107, 19691–19695. doi: 10.1073/pnas.1004933107

Lan, J., Xu, H., Yu, K., Sheng, E., Zhou, K., Wang, T., et al. (2019). Late Holocene hydroclimatic variations and possible forcing mechanisms over the eastern Central Asia. *Sci. China Earth Sci.* 62, 1288–1301. doi: 10.1007/s11430-018-9240-x

Leroy, S. A. G., Lopez-Merino, L., Tudryn, A., Chalie, F., and Gasse, F. (2014). Late Pleistocene and Holocene palaeoenvironments in and around the middle Caspian basin as reconstructed from a deep-sea core. *Quat. Sci. Rev.* 101, 91–110. doi: 10.1016/j.quascirev.2014.07.011

Li, X. Q., Zhao, K. L., Dodson, J., and Zhou, X. Y. (2011). Moisture dynamics in central Asia for the last 15 kyr: new evidence from Yili Valley, Xinjiang, NW China. *Quat. Sci. Rev.* 30, 3457–3466. doi: 10.1016/j.quascirev.2011.09.010

Lim, B., and Cachier, H. (1996). Determination of black carbon by chemical oxidation and thermal treatment in recent marine and lake sediments and Cretaceous-Tertiary clays. *Chem. Geol.* 131, 143–154. doi: 10.1016/0009-2541(96)00031-9

Liu, C. L., Zhang, J. F., Jiao, P. C., and Mischke, S. (2016). The Holocene history of Lop Nur and its palaeoclimate implications. *Quat. Sci. Rev.* 148, 163–175. doi: 10.1016/j.quascirev.2016.07.016

Liu, X. Q., Herzschuh, U., Shen, J., Jiang, Q. F., and Xiao, X. Y. (2008). Holocene environmental and climatic changes inferred from Wulungu Lake in northern Xinjiang. *China Quat. Res.* 70, 412–425. doi: 10.1016/j.yqres.2008.06.005

Liu, Z., Henderson, A. C. G., and Huang, Y. (2006). Alkenone-based reconstruction of late-Holocene surface temperature and salinity changes in Lake Qinghai, China. *Geophys. Res. Lett.* 33:L09707. doi: 10.1029/2006gl026151

Long, H., Shen, J., Chen, J. H., Tsukamoto, S., Yang, L. H., Cheng, H. Y., et al. (2017). Holocene moisture variations over the arid central Asia revealed by a comprehensive sand-dune record from the central Tian Shan, NW China. *Quat. Sci. Rev.* 174, 13–32. doi: 10.1016/j.quascirev.2017.08.024

Lüttge, U. (2004). Ecophysiology of crassulacean acid metabolism (CAM). *Ann. Bot.* 93, 629–652. doi: 10.1093/aob/mch087

Masiello, C. A. (2004). New directions in black carbon organic geochemistry. *Mar. Chem.* 92, 201–213. doi: 10.1016/j.marchem.2004.06.043

McManus, J. F., Francois, R., Gherardi, J.-M., Keigwin, L. D., and Brown-Leger, S. (2004). Collapse and rapid resumption of Atlantic meridional circulation linked to deglacial climate changes. *Nature* 428, 834–837. doi: 10.1038/nature02494

Monnin, E., Steig, E. J., Siegenthaler, U., Kawamura, K., Schwander, J., Stauffer, B., et al. (2004). Evidence for substantial accumulation rate variability in Antarctica during the Holocene, through synchronization of CO_2 in the Taylor Dome, Dome C and DML ice cores. *Earth Planet Sci. Lett.* 224, 45–54. doi: 10.1016/j.epsl.2004.05.007

O'Leary, M. H. (1981). Carbon isotope fractionation in plants. *Phytochemistry* 20, 553–567. doi: 10.1016/0031-9422(81)85134-5

O'Leary, M. H. (1988). Carbon isotopes in photosynthesis. *Bioscience* 38, 328–336. doi: 10.2307/1310735

Peltier, W. R., and Fairbanks, R. G. (2006). Global glacial ice volume and Last Glacial maximum duration from an extended Barbados sea level record. *Quat. Sci. Rev.* 25, 3322–3337. doi: 10.1016/j.quascirev.2006.04.010

R Development Core Team (2013). *R: A Language and Environment for Statistical Computing*. Vienna: R Foundation for Statistical Computing.

Ran, M., and Feng, Z. (2014). Variation in carbon isotopic composition over the past ca. 46,000yr in the loess–paleosol sequence in central Kazakhstan and paleoclimatic significance. *Org. Geochem.* 73, 47–55. doi: 10.1016/j.orggeochem.2014.05.006

Rao, Z., Wu, D., Shi, F., Guo, H., Cao, J., and Chen, F. (2019). Reconciling the 'westerlies' and 'monsoon' models: a new hypothesis for the Holocene moisture evolution of the Xinjiang region, NW China. *Earth Sci. Rev.* 191, 263–272. doi: 10.1016/j.earscirev.2019.03.002

Rao, Z. G., Guo, W. K., Cao, J. T., Shi, F. X., Jiang, H., and Li, C. Z. (2017). Relationship between the stable carbon isotopic composition of modern plants and surface soils and climate: a global review. *Earth Sci. Rev.* 165, 110–119. doi: 10.1016/j.earscirev.2016.12.007

Reimer, P. J., Bard, E., Bayliss, A., Beck, J. W., Blackwell, P. G., Ramsey, C. B., et al. (2013). IntCal13 and Marine13 radiocarbon age calibration curves 0–50,000 Years cal BP. *Radiocarbon* 55, 1869–1887. doi: 10.2458/azu_js_rc.55.16947

Ricketts, R. D., Johnson, T. C., Brown, E. T., Rasmussen, K. A., and Romanovsky, V. V. (2001). The Holocene paleolimnology of Lake Issyk-Kul, Kyrgyzstan: trace element and stable isotope composition of ostracodes. *Palaeogeogr. Palaeoclimatol. Palaeoecol.* 176, 207–227. doi: 10.1016/s0031-0182(01)00339-x

Routson, C. C., McKay, N. P., Kaufman, D. S., Erb, M. P., Goosse, H., Shuman, B. N., et al. (2019). Mid-latitude net precipitation decreased with Arctic warming during the Holocene. *Nature* 568, 83–89. doi: 10.1038/s41586-019-1060-3

Sage, R. F., Wedin, D. A., and Li, M. (1999). "The biogeography of C4 photosynthesis: patterns and controlling factors," in *C4 Plant Biology*, eds R. F. Sage and R. K. Monson (San Diego, CA: Academic Press), 313–373. doi: 10.1016/b978-012614440-6/50011-2

Schubert, B. A., and Jahren, A. H. (2012). The effect of atmospheric CO2 concentration on carbon isotope fractionation in C3 land plants. *Geochim. Cosmochim. Acta* 96, 29–43. doi: 10.1016/j.gca.2012.08.003

Smith, B. N., and Epstein, S. (1971). Two categories of 13c/12c ratios for higher plants. *Plant Physiol.* 47, 380–384. doi: 10.1104/pp.47.3.380

Solanki, S. K., Usoskin, I. G., Kromer, B., Schussler, M., and Beer, J. (2004). Unusual activity of the sun during recent decades compared to the previous 11,000 years. *Nature* 431, 1084–1087. doi: 10.1038/nature02995

Street-Perrott, F. A., Huang, Y., Perrott, R. A., Eglinton, G., Barker, P., Khelifa, L. B., et al. (1997). Impact of lower atmospheric carbon dioxide on tropical mountain ecosystems. *Science* 278, 1422–1426. doi: 10.1126/science.278.5342.1422

Sun, W. W., Zhang, E. L., Jones, R. T., Liu, E. F., and Shen, J. (2015). Asian summer monsoon variability during the late glacial and Holocene inferred from the stable carbon isotope record of black carbon in the sediments of Muge Co, southeastern Tibetan Plateau, China. *Holocene* 25, 1857–1868. doi: 10.1177/0959683615605743

Sun, W. W., Zhang, E. L., Liu, E. F., Ji, M., Chen, R., Zhao, C., et al. (2017). Oscillations in the Indian summer monsoon during the Holocene inferred from a stable isotope record from pyrogenic carbon from Lake Chenghai, southwest China. *J. Asian Earth Sci.* 134, 29–36. doi: 10.1016/j.jseaes.2016.11.002

Swann, G. E. A., Mackay, A. W., Vologina, E., Jones, M. D., Panizzo, V. N., Leng, M. J., et al. (2018). Lake Baikal isotope records of Holocene Central

Asian precipitation. *Quat. Sci. Rev.* 189, 210–222. doi: 10.1016/j.quascirev.2018.04.013

Tarasov, P. E., Demske, D., Leipe, C., Long, T. W., Muller, S., Hoelzmann, P., et al. (2019). An 8500-year palynological record of vegetation, climate change and human activity in the Bosten Lake region of Northwest China. *Palaeogeogr. Palaeoclimatol. Palaeoecol.* 516, 166–178. doi: 10.1016/j.palaeo.2018.11.038

Thompson, L. G., Yao, T. D., Davis, M. E., Henderson, E., Mosley-Thompson, E., Lin, P. M., et al. (1997). Tropical climate instability: the last glacial cycle from a qinghai-tibetan ice core. *Science* 276, 1821–1825. doi: 10.1126/science.276.5320.1821

Thompson, L. G., Yao, T. D., Davis, M. E., Mosley-Thompson, E., Wu, G. J., Porter, S. E., et al. (2018). Ice core records of climate variability on the Third Pole with emphasis on the Guliya ice cap, western Kunlun Mountains. *Quat. Sci. Rev.* 188, 1–14. doi: 10.1016/j.quascirev.2018.03.003

Wang, B. L., Zhang, M. J., Wei, J. L., Wang, S. J., Li, S. S., Ma, Q., et al. (2013). Changes in extreme events of temperature and precipitation over Xinjiang, northwest China, during 1960-2009. *Quat. Int.* 298, 141–151. doi: 10.1016/j.quaint.2012.09.010

Wang, G., Feng, X., Han, J., Zhou, L., Tan, W., and Su, F. (2008). Paleovegetation reconstruction using δ13C of Soil Organic Matter. *Biogeosciences* 5, 1325–1337. doi: 10.5194/bg-5-1325-2008

Wang, S. M., and Dou, H. S. (1998). *China Lake Records*. Beijing: Science Press, 348–349.

Wang, W., and Feng, Z. (2013). Holocene moisture evolution across the Mongolian Plateau and its surrounding areas: a synthesis of climatic records. *Earth Sci. Rev.* 122, 38–57. doi: 10.1016/j.earscirev.2013.03.005

Wang, W., Feng, Z. D., Ran, M., and Zhang, C. J. (2013). Holocene climate and vegetation changes inferred from pollen records of Lake Aibi, northern Xinjiang, China: a potential contribution to understanding of Holocene climate pattern in East-central Asia. *Quat. Int.* 311, 54–62. doi: 10.1016/j.quaint.2013.07.034

Wang, W., and Zhang, D. (2019). Holocene vegetation evolution and climatic dynamics inferred from an ombrotrophic peat sequence in the southern Altai Mountains within China. *Glob. Planet Change* 179, 10–22. doi: 10.1016/j.gloplacha.2019.05.003

Wang, X., Cui, L. L., Xiao, J. L., and Ding, Z. L. (2013). Stable carbon isotope of black carbon in lake sediments as an indicator of terrestrial environmental changes: an evaluation on paleorecord from Daihai Lake, Inner Mongolia, China. *Chem. Geol.* 347, 123–134. doi: 10.1016/j.chemgeo.2013.03.009

Wang, X., Cui, L. L., Yang, S. L., Zhai, J. X., and Ding, Z. L. (2018). Stable carbon isotope records of black carbon on Chinese Loess Plateau since last glacial maximum: an evaluation on their usefulness for paleorainfall and paleovegetation reconstruction. *Palaeogeogr. Palaeoclimatol., Palaeoecol.* 509, 98–104. doi: 10.1016/j.palaeo.2017.08.008

Wu, J. L., Zeng, H. A., Ma, L., and Bai, R. D. (2012). Recent changes of selected lake water resources in arid Xinjiang, northwest China. *Quat. Sci.* 32, 142–150.

Xie, H. C., Zhang, H. W., Ma, J. Y., Li, G. Q., Wang, Q., Rao, Z. G., et al. (2018). Trend of increasing Holocene summer precipitation in arid central Asia: evidence from an organic carbon isotopic record from the LJW10 loess section in Xinjiang, NW China. *Palaeogeogr. Palaeoclimatol. Palaeoecol.* 509, 24–32. doi: 10.1016/j.palaeo.2018.04.006

Xu, H., Zhou, K. E., Lan, J. H., Zhang, G. L., and Zhou, X. Y. (2019). Arid Central Asia saw mid-Holocene drought. *Geology* 47, 255–258. doi: 10.1130/G45686.1

Yang, B., Wang, J. L., and Liu, J. J. (2019). A 1556 year-long early summer moisture reconstruction for the Hexi Corridor, Northwestern China. *Sci. China Earth Sci.* 62, 953–963. doi: 10.1007/s11430-018-9327-1

Zhang, D., Feng, Z., Yang, Y., Lan, B., Ran, M., and Mu, G. (2018). Peat δ13Ccelluose-recorded wetting trend during the past 8000 years in the southern Altai Mountains, northern Xinjiang, NW China. *J. Asian Earth Sci.* 156, 174–179. doi: 10.1016/j.jseaes.2018.01.029

Zhang, D. L., and Feng, Z. D. (2018). Holocene climate variations in the Altai Mountains and the surrounding areas: a synthesis of pollen records. *Earth Sci. Rev.* 185, 847–869. doi: 10.1016/j.earscirev.2018.08.007

Zhang, E., Sun, W., Chang, J., Ning, D., and Shulmeister, J. (2018). Variations of the Indian summer monsoon over the last 30 000 years inferred from a pyrogenic carbon record from south-west China. *J. Quat. Sci.* 33, 131–138. doi: 10.1002/jqs.3008

Zhang, E., Sun, W., Zhao, C., Wang, Y., Xue, B., and Shen, J. (2015). Linkages between climate, fire and vegetation in southwest China during the last 18.5ka based on a sedimentary record of black carbon and its isotopic composition. *Palaeogeogr. Palaeoclimatol. Palaeoecol.* 435, 86–94. doi: 10.1016/j.palaeo.2015.06.004

Zhang, J. B., and Deng, Z. F. (1987). *Precipitations in Xinjiang*. Beijing: China Meteorological Press, 1–70.

Zhang, X. J., Jin, L. Y., Chen, J., Chen, F. H., Park, W., Schneider, B., et al. (2017). Detecting the relationship between moisture changes in arid central Asia and East Asia during the Holocene by model-proxy comparison. *Quat. Sci. Rev.* 176, 36–50. doi: 10.1016/j.quascirev.2017.09.012

Zhang, Y., Meyers, P. A., Liu, X. T., Wang, G. P., Ma, X. H., Li, X. Y., et al. (2016). Holocene climate changes in the central Asia mountain region inferred from a peat sequence from the Altai Mountains, Xinjiang, northwestern China. *Quat. Sci. Rev.* 152, 19–30. doi: 10.1016/j.quascirev.2016.09.016

Zhang, Z., Zhao, M., Lu, H., and Faiia, A. M. (2003). Lower temperature as the main cause of C4 plant declines during the glacial periods on the Chinese Loess Plateau. *Earth Planet Sci. Lett.* 214, 467–481. doi: 10.1016/s0012-821x(03)00387-x

Zhao, J., Chen, Y. W., Han, Y. F., Li, Z., Liu, Y. Z., and Li, W. (1995). *Physical Geography of China*, 3rd Edn. Beijing: Higher Education Press.

Zhao, J. J., Thomas, E. K., Yao, Y., Dearaujo, J., and Huang, Y. S. (2018). Major increase in winter and spring precipitation during the Little Ice Age in the westerly dominated northern Qinghai-Tibetan Plateau. *Quat. Sci. Rev.* 199, 30–40. doi: 10.1016/j.quascirev.2018.09.022

Zhao, Y., Wang, M., Huang, A., Li, H., Huo, W., and Yang, Q. (2013). Relationships between the West Asian subtropical westerly jet and summer precipitation in northern Xinjiang. *Theor. Appl. Climatol.* 116, 403–411. doi: 10.1007/s00704-013-0948-3

Zhao, Y. T., An, C. B., Mao, L. M., Zhao, J. J., Tang, L. Y., Zhou, A. F., et al. (2015). Vegetation and climate history in arid western China during MIS2: new insights from pollen and grain-size data of the Balikun Lake, eastern Tien Shan. *Quat. Sci. Rev.* 126, 112–125. doi: 10.1016/j.quascirev.2015.08.027

Conflict of Interest: The authors declare that the research was conducted in the absence of any commercial or financial relationships that could be construed as a potential conflict of interest.

Copyright © 2020 Jiang, Zheng, Yang, Zhao and Ning. This is an open-access article distributed under the terms of the Creative Commons Attribution License (CC BY). The use, distribution or reproduction in other forums is permitted, provided the original author(s) and the copyright owner(s) are credited and that the original publication in this journal is cited, in accordance with accepted academic practice. No use, distribution or reproduction is permitted which does not comply with these terms.

frontiers in Earth Science

ORIGINAL RESEARCH
published: 21 July 2020
doi: 10.3389/feart.2020.00284

Weakening Dust Storm Intensity in Arid Central Asia Due to Global Warming Over the Past 160 Years

Jin Zhang[1], Hai Xu[1], Jianghu Lan[2], Li Ai[2], Enguo Sheng[2], Dongna Yan[2], Kang'en Zhou[2], Keke Yu[2], Yunping Song[1], Shuang Zhang[1] and Adi Torfstein[3]*

[1] Institute of Surface-Earth System Science, Tianjin University, Tianjin, China, [2] State Key Laboratory of Loess and Quaternary Geology, Institute of Earth Environment, Chinese Academy of Sciences, Xi'an, China, [3] Institute of Earth Sciences, The Hebrew University of Jerusalem, Jerusalem, Israel

Dust storms occur frequently in arid central Asia (ACA) and greatly influence the regional ecology/environment, human health, and security, as well as the global climate. To date, neither the patterns nor the underlying mechanisms of dust storms in ACA are fully understood, partly due to the lack of long-term historical records. Here, we reconstruct a dust storm history of the past ~160 years in northwest China, based on high-resolution sedimentary proxies retrieved from Lake Karakul (located in the core zone of ACA). We find that changes in the sedimentary coarse fraction (grain size > 64 μm) in Lake Karakul are correlated with both historical and modern observed dust storms. The reconstructed dust storm intensity shows a decreasing trend since AD 1850s, with three high occurrence intervals at AD 1870s–1910s, AD 1930s–1940s, and AD 1960s–1980s. We contend that changes in temperature and wind speed could have dominated the frequency and intensity of dust storms in northwest China during the record periods: temperature controls the wind speed and then the dust storm frequency/intensity; lower temperature corresponding to higher wind speed, and higher dust storm frequency/intensity, and vice versa. The observed anthropogenic global warming could have led to a decrease in atmospheric temperature gradients and decline in wind speed and then decreasing dust storm frequency/intensity. Providing this stands, less and weaker dust storms are expected under a continuously anthropogenic warming scenario.

Keywords: dust storm, global warming, arid central Asia, Lake Karakul, grain size

OPEN ACCESS

Edited by:
Gary E. Stinchcomb, Murray State University, United States

Reviewed by:
Fahu Chen, Institute of Tibetan Plateau Research (CAS), China
Zongli Wang, Lanzhou University, China

****Correspondence:***
Hai Xu
xuhai@tju.edu.cn

Specialty section:
This article was submitted to Quaternary Science, Geomorphology and Paleoenvironment, a section of the journal Frontiers in Earth Science

Received: *27 April 2020*
Accepted: *18 June 2020*
Published: *21 July 2020*

Citation:
Zhang J, Xu H, Lan J, Ai L, Sheng E, Yan D, Zhou K, Yu K, Song Y, Zhang S and Torfstein A (2020) Weakening Dust Storm Intensity in Arid Central Asia Due to Global Warming Over the Past 160 Years. Front. Earth Sci. 8:284. doi: 10.3389/feart.2020.00284

KEY POINTS

- A 160-year dust storm history over arid central Asia was reconstructed based on high-resolution (0.8-year per sample) sedimentary records.
- Both the dust storm frequency and intensity are attenuated against the recent global warming.
- Temperature-sensitive wind speed is the controlling factor of arid central Asia dust storms.

INTRODUCTION

The dust storms over arid central Asia (ACA), including their frequency/intensity, sources, and transport paths, are widely concerned in studies on global dust and climate changes. Dust emitted from ACA accounts for ∼25% of total global dust emissions, which may exert significant influences on global climate and hydrological and biogeochemical cycles (Jickells et al., 2005; Uno et al., 2009; Booth et al., 2012), by altering the Earth's solar radiation budget (Booth et al., 2012), and oceanic primary productivity through iron fertilization (Jickells et al., 2005), etc. However, to date, the patterns and the underlying mechanisms of dust storms over ACA are not fully understood. Viewpoints are divergent with regards to the relationship between the dust storms (frequency, intensity, etc.) and climate factors (e.g., precipitation, temperature, and wind speed). For example, several studies contend that changes in dust storm frequency/intensity over central Asia could possibly be attributed to precipitation (Liu et al., 2004; Wang, 2005; Tenzin et al., 2016), whereas other studies, based on modeling, lake sediment, and ice core records, suggest that the dust storm activity could be largely influenced by temperature (Wang et al., 2006; Liu et al., 2014b; Grigholm et al., 2015; Zhou et al., 2019). The role of temperature is also under debate. A large number of researchers contend that dust storms frequently occur in cold conditions (Wang et al., 2006; Chen et al., 2013; Wu et al., 2013; Zhou et al., 2019), whereas some others, like Liu et al. (2014b), argued that the increased temperatures may also lead to intensified dust activity. Therefore, it is necessary to develop more solid long-term high-resolution records to understand how dust storms respond to climate changes over ACA.

Lake sediments in arid/semiarid areas are one of the most important archives to record the dust storm history (Wang et al., 2009; Huang et al., 2011; Chen et al., 2013, 2020; Qiang et al., 2014). Wang et al. (2009) reconstructed a past 4,000-year dust storm history in northern Tibetan Plateau, based on the coarse fraction (>64 μm) retrieved from Lake Kusai. Huang et al. (2011) recovered a 2,000-year history of wind intensity/dust storm in western central Asia, using both the grain-size fraction ratio (6–32/2–6 μm) and Ti contents from Aral Sea sediments. Here, we reconstruct a ∼160-year history of dust storm frequency/intensity at Lake Karakul, ACA, based on a high-resolution (∼0.8-year per sample) sedimentary grain size sequence, with an attempt to explore the possible driving mechanisms of dust storms over ACA.

BACKGROUND AND METHOD

Lake Karakul (38°25′50″–38°27′34″N; 75°02′16″–75°04′10″E; 3,650 m asl; **Figures 1a,b**) is a semiclosed alpine moraine lake located in the Pamir Plateau, surrounded by the Karakum and Kyzylkum deserts in the west, the Taklimakan desert in the east, and the Thar desert in the south (**Figure 1a**). The lake currently has a surface area of ∼10 km^2, with a maximum depth of 20 m (Yan et al., 2019). According to meteorological records from Tashkurghan station (**Figure 1a**; ∼75 km southwards to Lake Karakul; altitude, 3,090 m; 1957–2015 AD), annual temperature around the study area ranges between 2.15 and 5.25°C, with an average of 3.61°C; annual precipitation varies between 20.1 and 141.8 mm, with a mean of 74.9 mm, and 65% of the rainfall occurs from May to September (Yan et al., 2019). Annual evaporation around the study area is over 1,500 mm (Yan et al., 2019), much higher than annual precipitation. The seasonal distribution of temperature indicates that the ice cover in Lake Karakul should be melted before April (**Supplementary Figure S1**). Lake water is mainly fed by snowmelt from Muztagh Glacier in the southeast (Liu et al., 2014a). Lake Karakul watershed has sparse vegetation, and 90% of the land in the catchment is desert (Adilijiang et al., 2016; **Figure 1b**). Modern observations show that the high average wind speed, strong winds (≥10 m/s), and dust storm events mainly occur during spring (**Figure 1c** and **Supplementary Figure S2**).

In August 2013, a 1.11-m surface sediment core (KLKL 13-2) was retrieved from the deepest part of Lake Karakul, using a 60-mm UWITEC gravity corer (100% sediment recovery; N 38.4428°, E 75.06104°; and water depth, ∼19.5 m; **Figure 1b**). The core was subsampled *in situ* at 0.5-cm intervals, and an accurate age model was established by ^{210}Pb–^{137}Cs dating method (Yan et al., 2019). Considering the great and variable old carbon effects that widely existed in lake sediments in northwest China (Zhou et al., 2020), we did not use the ^{14}C ages to augment our age model (Yan et al., 2019). The average sedimentation rate is ∼0.7 cm/year, and such a high sedimentation rate enables a potential reconstruction of a high-resolution dust storm history. The sedimentary grain size and total organic carbon content (TOC) of this core were previously determined (Yan et al., 2019). The fine fraction (<10 μm) of the last 60 years has been used to support the viewpoint that temperature variations dominated by changes in solar activity could have influenced the local glacier sizes and hydroclimatic conditions (Yan et al., 2019). In this study, we use the coarse fraction (>64 μm) to trace the dust storms and discuss the potential dust source and forcing mechanisms. The observed dust storm days, temperature, and wind speed data of surrounding stations are obtained from the Chinese Meteorological Administration.

RESULTS

Grain Size Fractions Analysis

As shown in **Figure 2A**, the grain-size frequency distributions of core KLKL13-2 at different depths were characterized by trimodal, including three obvious peaks approximately at 0.8, 8, and 500 μm. Overall, the sedimentary particles of core KLKL13-2 are mainly composed of three apparent grain-size fractions, namely, clay fraction (<4 μm), silt fraction (4–64 μm), and sand fraction (>64 μm), and the variations of these three fractions versus depth are shown in **Figure 2B**. Thereinto, the silt (4–64 μm), and clay (<4 μm) are the major fractions, accounting for 63.5% (ranging from 51.6 to 85.5%),

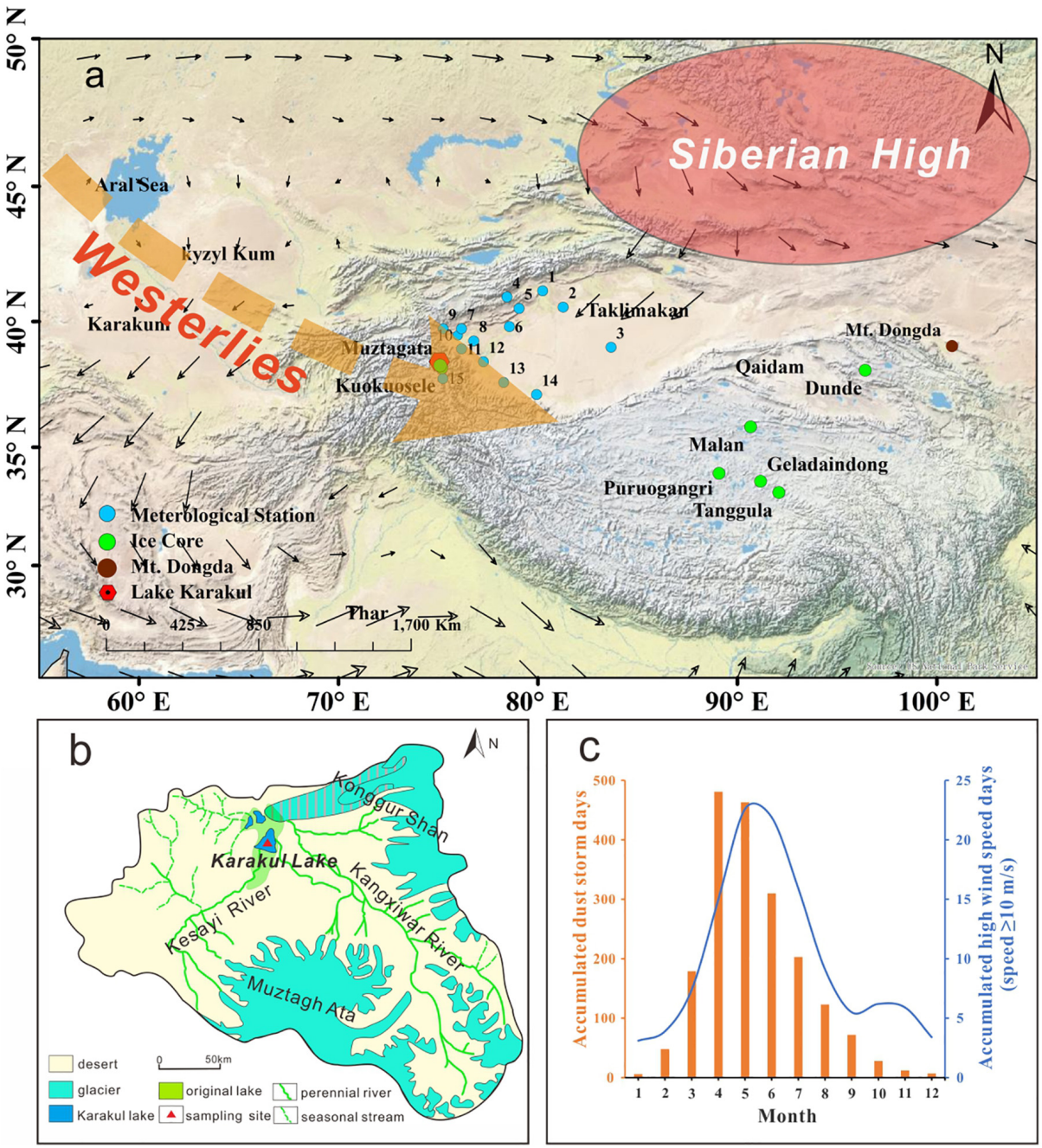

FIGURE 1 | Panel **(a)** Overview map showing the location of Lake Karakul (red hexagon) and ice core sites (green circles) and tree ring site (purple circle) mentioned in the text. Site numbers in panel a denote meteorological stations (blue circles; **Supplementary Table S1**). Arrows show wind field of April-June [850 hPa; 1979–2008 NCEP (National Centers for Environmental Prediction) reanalysis data]. Panel **(b)** shows the Lake Karakul catchment (redrawn from Yan et al., 2019), and the sampling site (red triangle). Panel **(c)** shows seasonal distribution of dust storm and high wind speed days (speed ≥ 10 m/s) in the central and western Tarim Basin. The dust storm days in panel **(c)** are the accumulated monthly dust storm days of 9 stations during 1960–2005 AD (**Supplementary Table S1**); and the accumulated high wind speed days are the monthly high wind speed days of 5 stations during 1981–2010 AD (**Supplementary Table S1**).

and 33.5% (ranging from 14.5 to 48.1%) on average, respectively (**Figure 2B**). The proportion of sand fraction (>64 μm) is relatively low, only contributing 3% on average (varying from 0 to 14.8%; **Figure 2B**). The sand fraction shows three obvious high stages, namely, AD 1870s–1910s, AD 1930s–1940s, and AD 1960s–1980s. Among those high stages, AD 1870s–1900s is the most striking one, during which the >64 μm fraction increased dramatically from approximately 0 up to 14%, indicating that a large number of coarse particles were reloaded into the lake at that time.

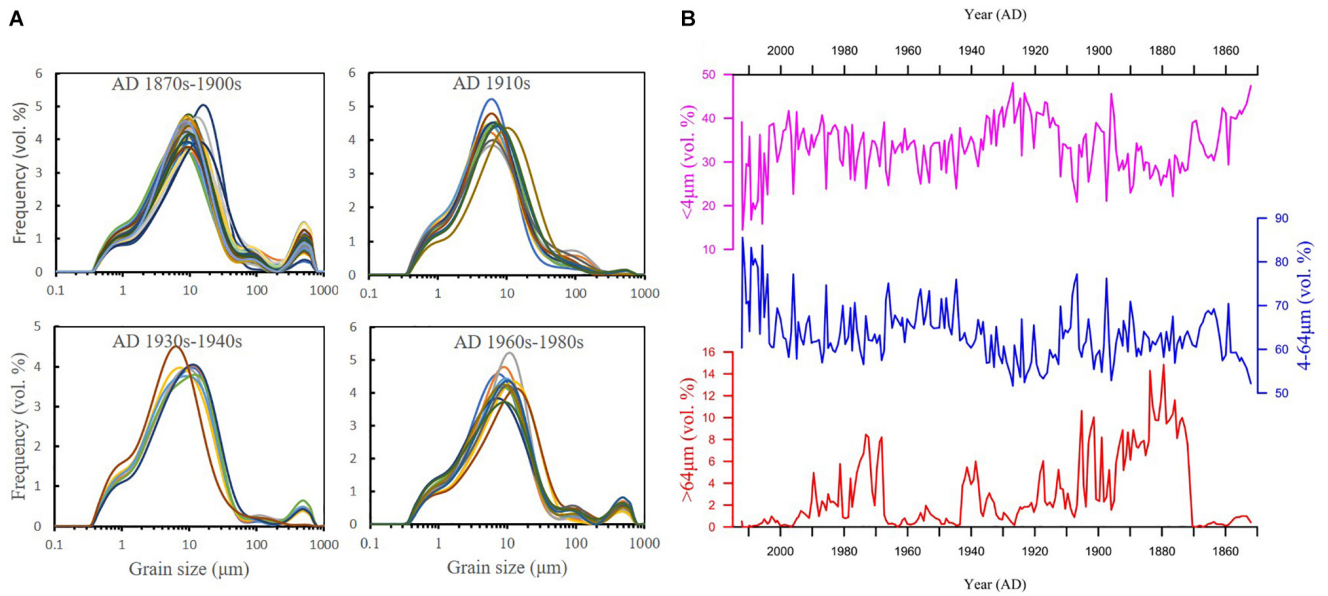

FIGURE 2 | (A) Grain-size frequency distribution patterns of sediments of core KLKL13-2 during the intervals of AD 1870s–1900s, AD1910s, AD 1930s–1940s, and AD 1960s–1980s (the relevant dust storm events are shown in **Figure 4**); **(B)** Proportions of three major fractions: clay (<4 μm, pink), silt (4–64 μm, blue), sand (>64 μm, red) fraction in core KLKL13-2.

Proxy for Dust Storm and Comparison With Metrological Records

The grain-size trimodal distribution patterns in core KLKL13-2 reflect that the particles were transported by different processes. Around the lake, there is no evident surface runoff except the glacier-fed streams; coarse particles can hardly be brought to the central deepest basin except through the air. The contribution of ice-trapped sand particles as suggested by Chen et al. (2013, 2020) cannot be excluded, but it could be insignificant because dust particles deposited on ice surface can hardly be accumulated and kept for a long time; they tend to be quickly moved away by winds. Recent studies suggest that the dust particles with diameters >75 μm could be transported by a long distance (even > 1,000 km; Maring et al., 2003; van der Does et al., 2018). Meteorological observations confirm that the sand fraction accounts for more than 60% of deposits during dust storms, with a modal grain size mainly distributed between 100 and 300 μm (Qiang et al., 2010). We examined the components of >64 and 64–300 μm in lake sediment of Lake Karakul and found that they are similar in trends (**Supplementary Figure S3**), suggesting that the >300 μm component could also share similar behavior with the 64–300 μm component in this case study. Previous studies also interpret such sand-sized particles as products of episodic suspension dust from adjacent sources during strong dust outbreaks (Chen et al., 2013; Qiang et al., 2014; Han et al., 2019) and frequently use the variations of the coarse components to trace dust storm history. The observed dust storm events of seven stations in the western Tarim Basin do not synchronize very well with one another during 1960–2005 AD (see **Supplementary Figure S4**), which possibly suggests that the dust storm occurrences are somewhat regional on short-term scales, like seasonal to annual scales. However, almost all the stations show a decreasing long-term trend in dust storm occurrences, suggesting that although the dust storm events are rather regional, the long-term trends are similar for adjacent sites. As shown in **Figure 3**, the sedimentary proportion of sand fraction (>64 μm) in core KLKL13-2 exhibits a similarly decreasing trend with the observed dust storm days in northwest China over the past 45 years (Zhou et al., 2006; Li et al., 2008), suggesting that the sand fraction (>64 μm) in core KLKL13-2 can be used as an indicator of dust storm activity.

Reconstruction of Dust Storm History in Arid Central Asia

The dust storm frequency/intensity changes inferred from the sedimentary sand fraction at Lake Karakul show an obvious decreasing trend over the past 160 years, characterized by three obvious strengthened periods, namely, AD 1870s–1910s, AD 1930s–1940s, and AD 1960s–1980s (**Figure 4i**). These high dust storm intervals are broadly correlated with those captured in ice cores in ACA, such as Kuokuosele in the Pamirs (**Figure 4b**; Tenzin et al., 2016), and Geladaindong (**Figure 4c**; Grigholm et al., 2015), Tanggula (**Figure 4d**; Wu et al., 2013), and Malan (**Figure 4f**; Wang, 2005) in the Tibetan Plateau.

The Little Ice Age (LIA) cold climate and the twentieth century warming are global phenomena, and lines of evidence indicate that the LIA approximately ended at the beginning of the twentieth century around the study area (Yan et al., 2019). The proportion of sand fraction (>64 μm) was distinctively higher

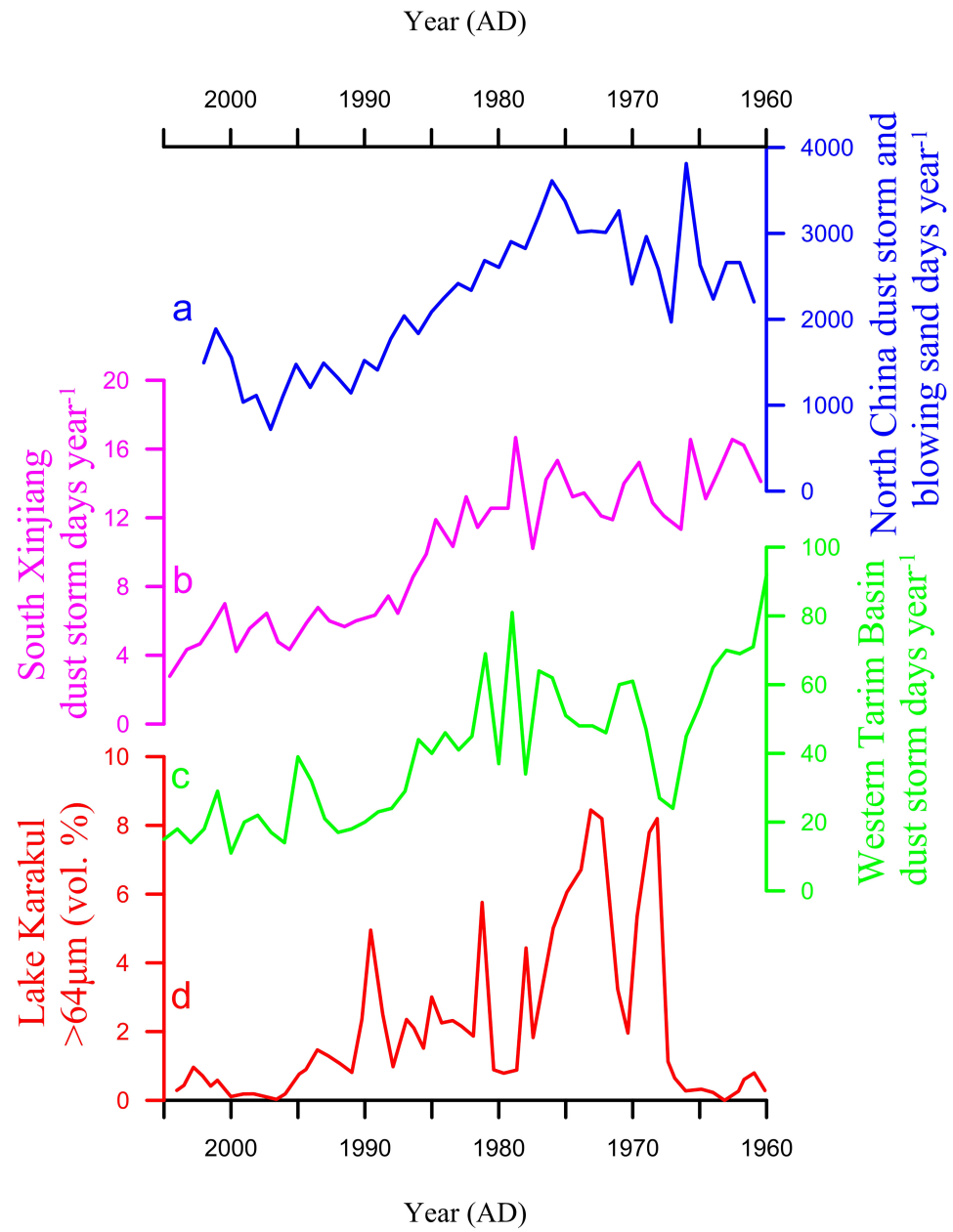

FIGURE 3 | Comparison of the volume percentage of the >64 μm fraction in Lake Karakul sediments (curve d, red, and this study) with observed dust storm days in arid northwest China (curve a–c). Curve a (blue) accumulated dust storm and blowing sand days at 175 stations in north China from 1962 to 2002 AD (Zhou et al., 2006). Curve b (pink) averaged dust storm days of 38 stations in south Xinjiang from 1961 to 2005 AD (Li et al., 2008). Curve c (green) dust storm days at 7 stations in western Tarim Basin from 1960 to 2005 AD (the dust storm time series of each station are provided in **Supplementary Figure S4**).

before AD 1910s, suggesting high dust storm frequency/intensity at the end of the LIA, which is also recorded by the Chinese historical literatures (Zhang, 1984; **Figure 4a**), and by the dirty ratio in the Kuokuosele ice core (Tenzin et al., 2016; **Figure 4b**), while the relative higher sand fraction during AD 1930s–1940s is documented by the variations in Ca concentrations of the Geladaindong ice core (Grigholm et al., 2015; **Figure 4c**), by the mean diameter of dust in the Tanggula ice core (Wu et al., 2013; **Figure 4d**), and by the observed dust event records in Korea (Chun et al., 2008; **Figure 4e**). Dust records from the Malan ice core (**Figure 4f**) also show that dust events in northern China frequently occurred during the period 1930–1940 AD (Wang et al., 2007). The proportion of sand fraction (>64 μm) shows an obviously decreasing trend over the past 50 years, suggesting generally low dust storm activity. The grain size-inferred dust storms from AD 1960s to AD 1980s broadly coincided with the observed windstorm disasters around the study area during 1960–1990 AD (He et al., 2004; see stars in **Figure 4h**).

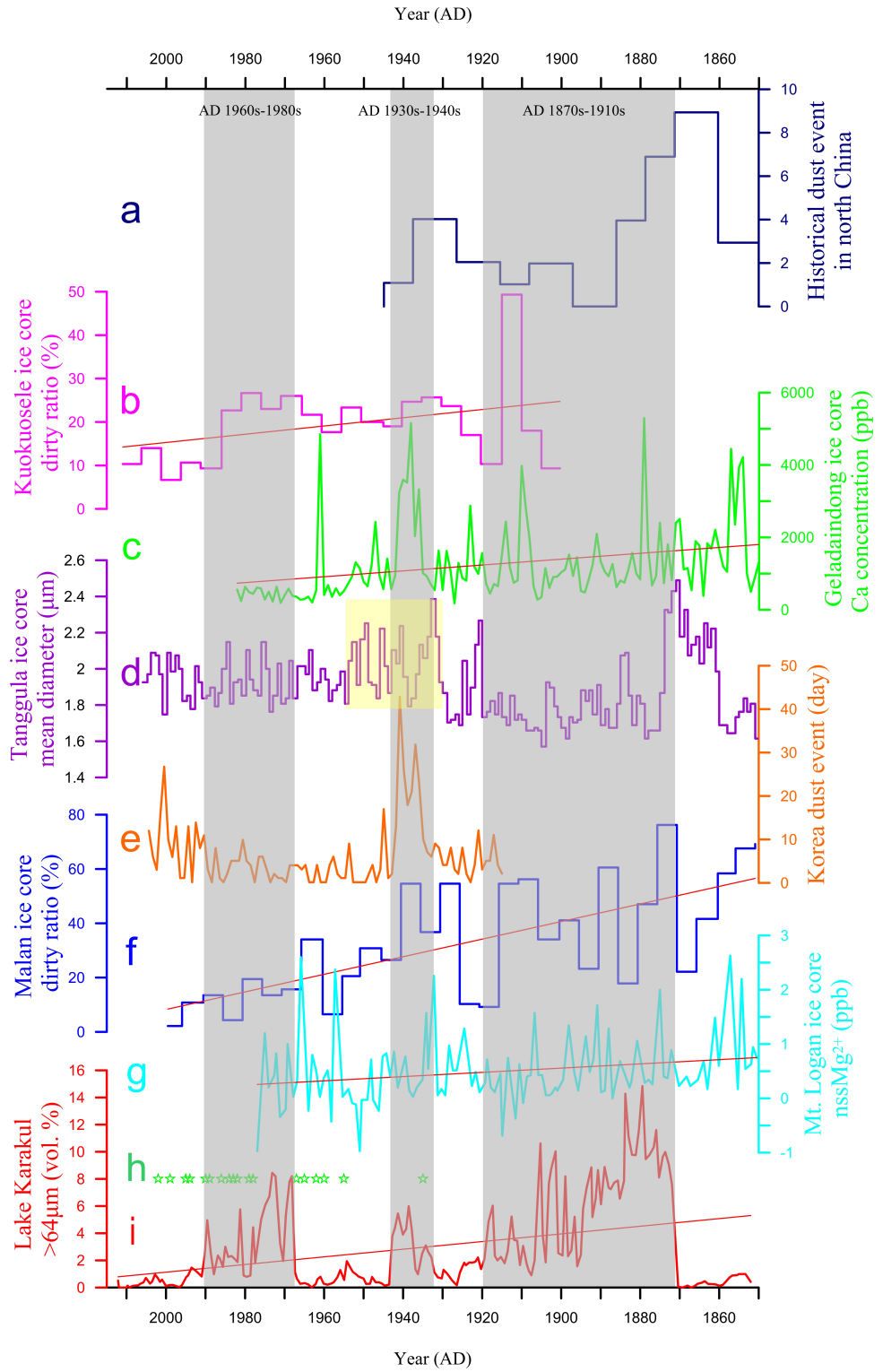

FIGURE 4 | Comparison between dust storm history at Lake Karakul (curve i; inferred from the >64 μm sedimentary gain-size fraction; this study), historical dust events frequency records in northern China (curve a; Zhang, 1984), dirty ratio in the Kuokuosele ice core (curve b; Tenzin et al., 2016), Ca concentrations in the Geladaindong ice core (curve c; Grigholm et al., 2015), mean diameter of dust in the Tanggula ice core (curve d; Wu et al., 2013), historical dust events in Korea (curve e; Chun et al., 2008), dirty ratio in the Malan ice core (curve f; Wang et al., 2007), nssMg^{2+} from ice core in Mt. Logan, Canada (curve g; Kang et al., 2003), and historical dust event records around Lake Karakul (curve h; He et al., 2004). Red thin lines in plots b, c, f, g, and i show the linear trends; the vertical gray shaded bars indicate high frequent/intensive dust storm stages; the pale-yellow rectangle in curve d shows the AD 1930s–1950s dustiness period recorded in Tanggula ice core.

DISCUSSION

Correlation of Dust Storm Activity With Climate Factors

Climate elements (e.g., precipitation, wind speed, and temperature) are important factors influencing the dust storm occurrence or frequency/intensity (Qian et al., 2002; Gao et al., 2003; Kurosaki and Mikami, 2003; Zhang et al., 2017). However, which climate element dominates remains controversial. In fact, most dust sources in northwest China are located in superarid regions, where annual evaporation is significantly higher than annual precipitation. Although several studies have shown that precipitation may impact dust storm activity by changing soil moisture and vegetation coverage (Gao et al., 2003; Liu et al., 2004; Tenzin et al., 2016), whether the increase in precipitation can significantly improve the surface moisture contents in arid zone is still uncertain (Zhou et al., 2019) because the increases in evaporation could be larger than those in precipitation. The sedimentary TOC content in Lake Karakul has been documented to be well correlated with precipitation (Yan et al., 2019); higher TOC content generally corresponding to increased precipitation, and vice versa (**Figures 5f,g**). The comparison between the sand fraction and TOC content in Lake Karakul shows a loose connection (**Figures 5g,h**), implying a weak linkage between the dust storm frequency/intensity and precipitation in this area. According to Adilijiang et al. (2016), the proportion of vegetation coverage in Lake Karakul area had a limited increase, growing from 3.61% in 1990 AD to 3.79% in 2010 AD. Therefore, the increase in precipitation can hardly obviously change the surface conditions (e.g., soil moisture and vegetation coverage) in the dust source areas, at least in the Lake Karakul area. Consequently, contrasting to the previous studies, we infer that precipitation may not be the primary controlling factor of dust storm outbreaks in the study area.

Wind speed is also suggested to have a positive correlation with dust storm frequency/intensity across northern China (Kurosaki and Mikami, 2003; Liu et al., 2004; Zhou et al., 2006; Chen et al., 2013; Grigholm et al., 2015). According to the meteorological observations around Lake Karakul, the dust storms most frequently occurred during spring (from March to June; **Figure 1c**), coinciding with those along the path of Northern Hemisphere dust transport, such as north China (Wang et al., 2005), Korea (Kurosaki and Mikami, 2003), Japan (Kurosaki and Mikami, 2003), north America (Hahnenberger and Nicoll, 2012), and Greenland (Bory et al., 2003). The temporal consistency among dust storms may be related to wind speed at a global scale (Mahowald et al., 2007). Whereas, the wind speed threshold value of dust storm outbreaks is closely related to the land surface conditions, including the vegetation coverage and soil moisture (Yang et al., 2017). Considering the sparse vegetation cover around Lake Karakul, the wind speed of 10 m/s was used as a threshold value of dust storm outbreaks in this study. As mentioned in *Background and Method*, the seasonal distribution of the observed dust storms and strong winds ($\geq$10 m/s) are similar with the maximal peak in spring over the past decades (**Figure 1c**). Furthermore, the sand fraction (>64 μm) in Lake Karakul correlated well with the average annual wind speed in the west of Tarim Basin (**Figures 5a,h**; r = 0.46), supporting again that the wind speed could significantly influence the dust storm frequency/intensity, which has been further substantiated in studies in Xinjiang and the Tibetan Plateau (Li et al., 2008; Grigholm et al., 2015).

Temperature is an important controlling factor for wind speed and then for the dust storm activity (Wang et al., 2006; Grigholm et al., 2015; Han et al., 2019). Based on the oxygen isotope and grain size records retrieved from the Tanggula ice core in Tibetan Plateau, Wu et al. (2013) pointed out that dust storms frequently occurred in cold conditions. A recent study by Han et al. (2019) also suggested that the decreasing temperature could have led to the outbreak of dust storms in the Tarim Basin. Dust storm activities revealed by the grain size of the sediments of Lake Karakul show a negative correlation to the total solar irradiance (Coddington et al., 2016; **Figure 5e**), to temperatures in northwest China reconstructed by tree-ring width (Liu et al., 2016; **Figure 5d**), and to temperatures inferred from $\delta^{18}O$ in the Guliya ice core (Yao et al., 2006; **Figure 5c**), suggesting that the decreasing trend of dust storm activity in northwest China might be attributed to the rising temperature. According to meteorological data, the average annual wind speed in the west of Tarim Basin is negatively correlated with temperature over the past 50 years (1960–2012 AD; r = -0.324; **Figures 5a,b**). The decreased temperature could greatly promote the surface pressure gradient, hence increase the wind speed, and eventually leading to the outbreak of dust storms, as supported by the meteorological data in north China and dust records in Tarim Basin and Tibetan Plateau (Zhou et al., 2006; Grigholm et al., 2015; Han et al., 2019). To summarize, a lower temperature corresponds to higher wind speed and higher dust storm frequency/intensity over the study area, and vice versa.

Possible Dust Sources

The sources of dust over ACA are complex. Recent researches generally argued that the sand fraction (>64 μm) mainly derived from local sources with relatively limited transport distance (Chen et al., 2013; Qiang et al., 2014; Han et al., 2019). Based on the geographical and geological setting of Lake Karakul, the sand-sized particles may primarily originate from the surrounding high-altitude mountains via glacial grinding, frost, and salt weathering. These mountain processes can produce abundant detritus sediments (Sun, 2002); once formed, the coarse sediments were deflated by strong winds and transported to the lake. Consequently, the local moraine may be a primary source of the sedimentary coarse particles. However, besides partly contributed from proximal areas, the sedimentary fine fraction could have distant source regions. According to back trajectory analysis, the major air mass trajectories at Lake Karakul come from the west (Yan et al., 2019), suggesting that the deserts in ACA areas such as Karakum and Kyzylkum could be the potential dust sources. On the other hand, dust storm events in northwest China occur frequently in the south Xinjiang (Tarim) region (Wang et al., 2005), and dust clouds produced from the dust events in Taklimakan desert can be lifted up to the Tibetan Plateau (Uno et al., 2009). From the dust transport routes proposed by Sun et al. (2001), an eastward branch of

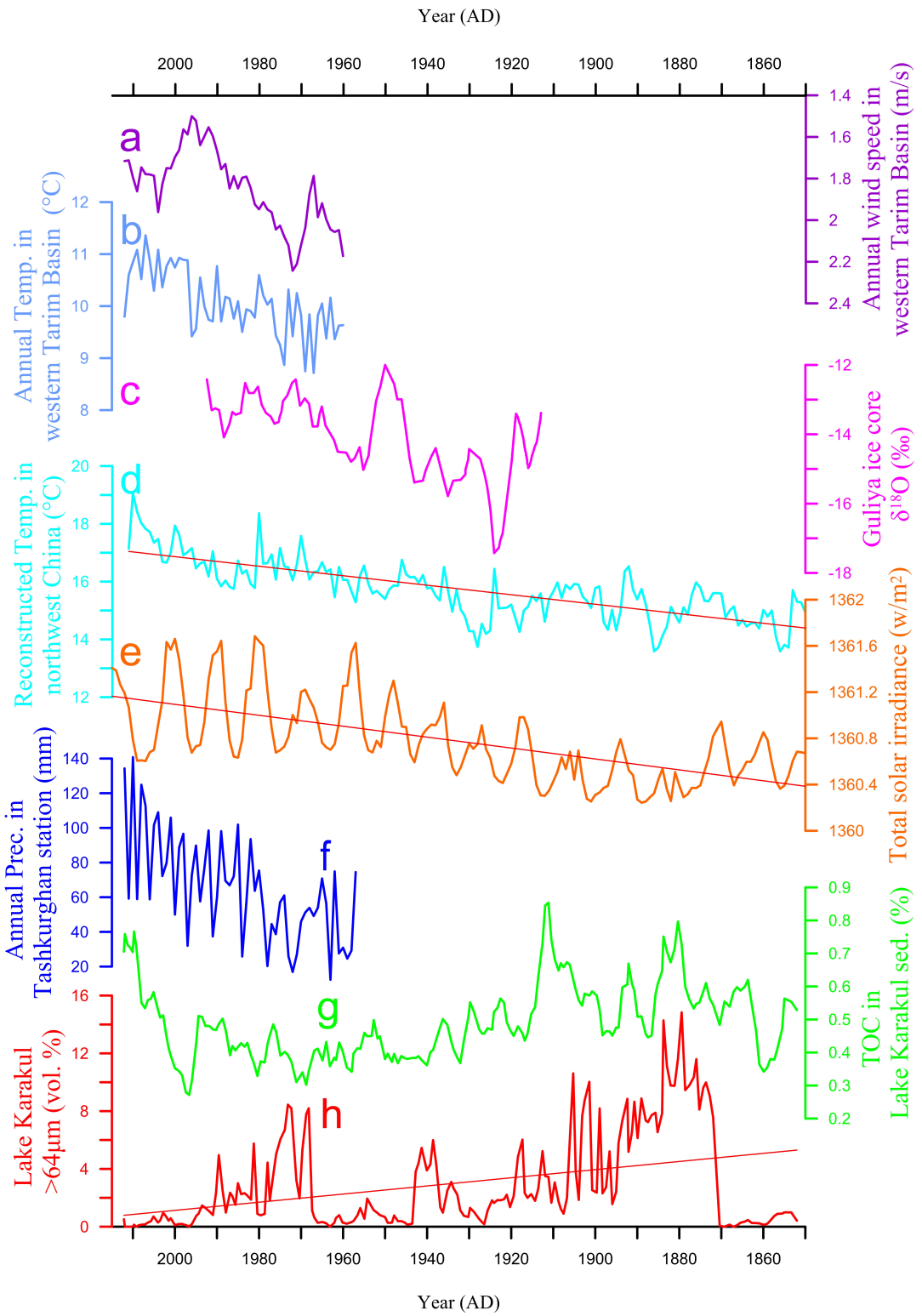

FIGURE 5 | Comparison between the dust storm records at Lake Karakul (curve h; this study), annual mean wind speed (curve a; note it is inversely plotted), and temperature (curve b) recorded by 11 stations in the western Tarim Basin (**Supplementary Table S1** and **Figure 1a**), $\delta^{18}O$ in Guliya ice core (curve c; Yao et al., 2006), the reconstructed temperature in northwest China by tree-ring width (curve d; Liu et al., 2016), total solar irradiance (curve e; Coddington et al., 2016), annual precipitation recorded at Tashkurghan station (curve f), and sedimentary TOC in Lake Karakul sediments (curve g; Yan et al., 2019). Red thin lines in plots d, e, and h show the linear trends.

the cold air mass might contribute dust particles from the Tarim Basin (Taklimakan desert) to Lake Karakul. Based on the Sr–Nd isotopic compositions of insoluble particles, Xu et al. (2012) also suggested that the Taklimakan desert may be a potential dust source for the Muztagata glacier area. Tenzin et al. (2016) presented a significant positive correlation between the Kuokuosele ice core dirty ratio and the observed dust storms over ACA as well as those over northern Tibetan Plateau, suggesting both sources could have contributed dust to the ice core. Lake Karakul, the Muztagata glacier, and the Kuokuosele glacier are all located in the eastern Pamirs, sharing a similar atmospheric circulation background and therefore could have similar dust sources. To summarize, the fine dust particles in Lake Karakul area likely originate from both the deserts over ACA areas to its west, such as the Karakum, Kyzylkum, and the Taklimakan desert to its east.

Possible Forcing for Dust Storm Frequency/Intensity Changes

Some studies proposed that the Siberian High could play an important role in dominating the dust storm occurrence at ACA (Sun et al., 2001; Chen et al., 2013; Zhou et al., 2019). For example, Chen et al. (2013) suggested that occurrence of dust storms in northwest China is largely related to the strengthening of Siberian High. However, some others contend that the dust storm activity could be possibly correlated to the changes in the westerly jet stream (Wang, 2005; Zhong and Li, 2005; Han et al., 2019), i.e., strengthened westerlies during colder climatic conditions could increase surface wind speed by facilitating downward transfer of high-level momentum to near earth surface, and hence intensified dust storm activities (Han et al., 2019), vice versa. Recent studies show that wind speed is reduced gradually with the decrease in temperature gradient caused by recent warming in northwest China (Wang, 2005; Grigholm et al., 2015; Zhang et al., 2017), which may lead to reduced dust outbreaks. For instance, some studies have ascribed the declined dust storm activity on the Tibetan Plateau over the past 200 years (Wang, 2005) and that in north China over the past 50 years (Zhu et al., 2008) to the weakening in wind speed.

The arid southwestern United States is also identified as a dust source for the Atlantic coast and Greenland (Donarummo et al., 2003; Park et al., 2007). The dust fall events in North America also showed a decreasing trend for the past 150 years, as inferred from the dust records from an ice core in Yukon Territory of Canada (Kang et al., 2003; **Figure 4g**). We propose that the similarly decreasing dust storm trends between Lake Karakul area, ACA areas, and north America possibly suggest similar changes in northern hemisphere westerly jet stream.

As temperature gradients may influence the location of the westerly jet stream and hydroclimatic conditions across the westerly route (Xu et al., 2019), they may also potentially influence the location and occurrence of dust storms. Therefore, factors that modulate regional or global temperature gradients are also expected to influence global dust storm occurrence. One hot issue is that whether the recent decreasing dust storm frequency is related to the greenhouse-gas-triggered global warming. Numerical simulations suggest that, in contrast to the natural solar forced warming, the greenhouse-gas-triggered warming may lead to a decrease in zonal sea surface temperature gradient and a noticeable increase in atmospheric static stability (Vecchi et al., 2006; Liu et al., 2013), which is therefore potentially conducive to decreasing wind speed and dust storm frequency/intensity. Therefore, providing the anthropogenic global warming continues, the dust storm frequency/intensity over ACA is expected to remain low or further decrease.

CONCLUSION

We reconstructed an approximately 160-year long dust storm history using high-resolution sedimentary sand fraction (>64 μm) retrieved from a core in Lake Karakul, ACA, and examined the relationship between dust storms, climate factors, and general atmospheric circulations. Our results show that the sand fraction (>64 μm) in lake sediments significantly decreased over the past 160 years, suggesting an obvious decrease in dust storm frequency/intensity during the recent/modern epoch. The dust storm frequency/intensity generally became high during the cold conditions (AD 1870s–1910s), and remained relatively low in the current warm period. The decrease in dust storm frequency/intensity was tentatively attributed to the rising temperature and decreasing wind speed. We contend that the dust storm activity may remain low or further decrease over the ACA area in the context of continued global warming.

DATA AVAILABILITY STATEMENT

The raw data supporting the conclusions of this article will be made available by the authors, without undue reservation.

AUTHOR CONTRIBUTIONS

HX designed the research. JZ and HX wrote the manuscript. JZ, HX, JL, ES, DY, KZ, KY, YS, and SZ performed the research. JZ, HX, and JL analyzed the data. LA and AT collaborated with the corresponding author in the development of the manuscript. All authors read and approved the final manuscript.

FUNDING

This work is funded by the program (No. 41672169) and by the joint NSFC-ISF research program (NSFC grant no. 41761144070 and ISF grant no. 2487/17) supported by the National Natural Science Foundation of China.

SUPPLEMENTARY MATERIAL

The Supplementary Material for this article can be found online at: https://www.frontiersin.org/articles/10.3389/feart.2020.00284/full#supplementary-material

REFERENCES

Adilijiang, K., Chu, X. Z., and Yusupujiang, A. (2016). Dynamic change of landscape spatial pattern in karakul lake region in Xinjiang. *Chin. Agric. Sci. Bull.* 32, 78–84.

Booth, B. B., Dunstone, N. J., Halloran, P. R., Andrews, T., and Bellouin, N. (2012). Aerosols implicated as a prime driver of twentieth-century North Atlantic climate variability. *Nature* 484, 228–232. doi: 10.1038/nature10946

Bory, A. J. M., Biscaye, P. E., and Grousset, F. E. (2003). Two distinct seasonal Asian source regions for mineral dust deposited in Greenland (NorthGRIP). *Geophys. Res. Lett.* 30:L016446. doi: 10.1029/2002gl016446

Chen, F. H., Chen, S. Q., Zhang, X., Chen, J. H., Wang, X., Gowan, E. J., et al. (2020). Asian dust-storm activity dominated by Chinese dynasty changes since 2000 BP. *Nat. Commun.* 11:992. doi: 10.1038/s41467-020-14765-4

Chen, F. H., Qiang, M. R., Zhou, A. F., Xiao, S., Chen, J. H., and Sun, D. H. (2013). A 2000-year dust storm record from Lake Sugan in the dust source area of arid China. *J. Geophys. Res. Atmos.* 118, 2149–2160. doi: 10.1002/jgrd.50140

Chun, Y., Cho, H., Chung, H., and Lee, M. (2008). Historical records of Asian dust events (Hwangsa) in Korea. *Bull. Amer. Meteorol. Soc.* 89, 823–828. doi: 10.1175/2008BAMS2159.1

Coddington, O., Lean, J. L., Pilewskie, P., Snow, M., and Lindholm, D. (2016). A solar irradiance climate data record. *Bull. Amer. Meteorol. Soc.* 97, 1265–1282. doi: 10.1175/bams-d-14-00265.1

Donarummo, J., Ram, M., and Stoermer, E. F. (2003). Possible deposit of soil dust from the 1930's U.S. dust bowl identified in Greenland ice. *Geophys. Res. Lett.* 30:L016641. doi: 10.1029/2002gl016641

Gao, T., Su, L. J., Ma, Q. X., Li, H. Y., Li, X. C., and Yu, X. (2003). Climatic analyses on increasing dust storm frequency in the springs of 2000 and 2001 in inner Mongolia. *Int. J. Climatol.* 23, 1743–1755. doi: 10.1002/joc.970

Grigholm, B., Mayewski, P. A., Kang, S., Zhang, Y., Morgenstern, U., Schwikowski, M., et al. (2015). Twentieth century dust lows and the weakening of the westerly winds over the Tibetan Plateau. *Geophys. Res. Lett.* 42, 2434–2441. doi: 10.1002/2015gl063217

Hahnenberger, M., and Nicoll, K. (2012). Meteorological characteristics of dust storm events in the eastern Great Basin of Utah, U.S.A. *Atmos. Environ.* 60, 601–612. doi: 10.1016/j.atmosenv.2012.06.029

Han, W. X., Lü, S., Appel, E., Berger, A., Madsen, D., Vandenberghe, J., et al. (2019). Dust storm outbreak in central Asia After ˜3.5 *kyr BP*. *Geophys. Res. Lett.* 46, 7624–7633. doi: 10.1029/2018gl081795

He, J. H., Cheng, H. X., Liu, Y. J., and Chang, A. (2004). *Kizilsu Kirghiz Autonomous Prefecture*. Urumqi: Xinjiang People's Publishing House.

Huang, X. T., Oberhänsli, H., von Suchodoletz, H., and Sorrel, P. (2011). Dust deposition in the Aral Sea: implications for changes in atmospheric circulation in central Asia during the past 2000 years. *Quat. Sci. Rev.* 30, 3661–3674. doi: 10.1016/j.quascirev.2011.09.011

Jickells, T. D., An, Z. S., Andersen, K. K., Baker, A. R., Bergametti, G., Brooks, N., et al. (2005). Global iron connections between desert dust, ocean biogeochemistry, and climate. *Science* 308, 67–71. doi: 10.1126/science.1105959

Kang, S. C., Mayewski, P. A., Yan, Y. P., Qin, D. H., Yao, T. D., and Ren, J. W. (2003). Dust records from three ice cores: relationships to spring atmospheric circulation over the Northern Hemisphere. *Atmos. Environ.* 37, 4823–4835. doi: 10.1016/j.atmosenv.2003.08.010

Kurosaki, Y., and Mikami, M. (2003). Recent frequent dust events and their relation to surface wind in East Asia. *Geophys. Res. Lett.* 30:1736. doi: 10.1029/2003gl017261

Li, H. J., Li, J., and He, Q. (2008). Study on sandstorm trend and abrupt change in Xinjiang. *J. Desert. Res.* 28, 915–919.

Liu, J., Wang, B., Cane, M. A., Yim, S. Y., and Lee, J. Y. (2013). Divergent global precipitation changes induced by natural versus anthropogenic forcing. *Nature* 493, 656–659. doi: 10.1038/nature11784

Liu, X. D., Yin, Z. Y., Zhang, X. Y., and Yang, X. C. (2004). Analyses of the spring dust storm frequency of northern China in relation to antecedent and concurrent wind, precipitation, vegetation, and soil moisture conditions. *J. Geophys. Res. Atmos.* 109:D16210. doi: 10.1029/2004jd004615

Liu, X. Q., Herzschuh, U., Wang, Y. B., Kuhn, G., and Yu, Z. T. (2014a). Glacier fluctuations of Muztagh Ata and temperature changes during the late holocene in westernmost Tibetan Plateau, based on glaciolacustrine sediment records. *Geophys. Res. Lett.* 41, 6265–6273. doi: 10.1002/2014gl060444

Liu, X. Q., Yu, Z. T., Dong, H. L., and Chen, H. F. (2014b). A less or more dusty future in the Northern Qinghai-Tibetan plateau? *Sci. Rep.* 4:6672. doi: 10.1038/srep06672

Liu, Y., Sun, C. F., Li, Q., and Cai, Q. F. (2016). A Picea crassifolia tree-ring width-based temperature reconstruction for the Mt. Dongda Region, Northwest China, and its relationship to large-scale climate forcing. *PLoS One* 11:e0160963. doi: 10.1371/journal.pone.0160963

Mahowald, N. M., Ballantine, J. A., Feddema, J., and Ramankutty, N. (2007). Global trends in visibility: implications for dust sources. *Atmos. Chem. Phys.* 7, 3309–3339. doi: 10.5194/acp-7-3309-2007

Maring, H., Savoie, D. L., Izaguirre, M. A., and Custals, L. (2003). Mineral dust aerosol size distribution change during atmospheric transport. *J. Geophys. Res. Atmos.* 108:8592. doi: 10.1029/2002jd002536

Park, S. H., Gong, S. L., Zhao, T. L., Vet, R. J., Bouchet, V. S., Gong, W., et al. (2007). Simulation of entrainment and transport of dust particles within North America in April 2001 ("Red Dust Episode"). *J. Geophys. Res. Atmos.* 112:8443. doi: 10.1029/2007jd008443

Qian, W. H., Quan, L. S., and Shi, S. Y. (2002). Variations of the dust storm in China and its climatic control. *J. Clim.* 15, 1216–1229. doi: 10.1175/1520-0442(2002)015<1216:votdsi>2.0.co;2

Qiang, M., Lang, L., and Wang, Z. (2010). Do fine-grained components of loess indicate westerlies: insights from observations of dust storm deposits at Lenghu (Qaidam Basin. China). *J. Arid. Environ.* 74, 1232–1239. doi: 10.1016/j.jaridenv.2010.06.002

Qiang, M. R., Liu, Y. Y., Jin, Y. X., Song, L., Huang, X. T., and Chen, F. H. (2014). Holocene record of eolian activity from Genggahai Lake, northeastern Qinghai-Tibetan Plateau, China. *Geophys. Res. Lett.* 41, 589–595. doi: 10.1002/2013gl058806

Sun, J. M. (2002). Provenance of loess material and formation of loess deposits on the Chinese Loess Plateau. *Earth Planet. Sci. Lett.* 203, 845–859. doi: 10.1016/S0012-821X(02)00921-4

Sun, J. M., Zhang, M. Y., and Liu, T. S. (2001). Spatial and temporal characteristics of dust storms in China and its surrounding regions, 1960-1999: relations to source area and climate. *J. Geophys. Res. Atmos.* 106, 10325–10333. doi: 10.1029/2000jd900665

Tenzin, D., Yao, T. D., Yao, P., Deji, L., Xu, B. Q., Zhao, H. B., et al. (2016). Variation of atmospheric dust over the past 100 years recorded by visible dusty layers of the Kuokuosele ice core, western Tibetan Plateau. *Chin. Sci. Bull.* 61, 1695–1705. doi: 10.1360/n972015-01309

Uno, I., Eguchi, K., Yumimoto, K., Takemura, T., Shimizu, A., Uematsu, M., et al. (2009). Asian dust transported one full circuit around the globe. *Nat. Geosci.* 2, 557–560. doi: 10.1038/ngeo583

van der Does, M., Knippertz, P., Zschenderlein, P., Harrison, R. G., and Stuut, J. B. W. (2018). The mysterious long-range transport of giant mineral dust particles. *Sci. Adv.* 4:eaau2768. doi: 10.1126/sciadv.aau2768

Vecchi, G. A., Soden, B. J., Wittenberg, A. T., Held, I. M., Leetmaa, A., and Harrison, M. J. (2006). Weakening of tropical Pacific atmospheric circulation due to anthropogenic forcing. *Nature* 441, 73–76. doi: 10.1038/nature04744

Wang, N. L. (2005). Decrease trend of dust event frequency over the past 200 years recorded in the Malan ice core from the northern Tibetan Plateau. *Chin. Sci. Bull.* 50, 2866–2871. doi: 10.1360/982005-237

Wang, N. L., Yao, T. D., Pu, J. C., Zhang, Y. L., and Sun, W. Z. (2006). Climatic and environmental changes over the last millennium recorded in the Malan ice core from the northern Tibetan Plateau. *Sci. Chin. Ser. D Earth Sci.* 49, 1079–1089. doi: 10.1007/s11430-006-1079-9

Wang, N. L., Yao, T. D., Yang, X. D., Shen, J., and Wang, Y. (2007). Variations in dust event frequency over the past century reflected by ice-core and lacustrine records in north China. *Sci. Chin. Ser. D Earth Sci.* 50, 736–744. doi: 10.1007/s11430-007-0037-5

Wang, S. G., Wang, J. Y., Zhou, Z. J., and Shang, K. Z. (2005). Regional characteristics of three kinds of dust storm events in China. *Atmos. Environ.* 39, 509–520. doi: 10.1016/j.atmosenv.2004.09.033

Wang, Y. B., Liu, X. Q., Zhang, E. L., Yang, X. D., and Yao, B. (2009). Dust-storm events in Kekexili Area, Northern Tibetan Plateau during the past 4000 years:

evidence from grain-size analysis of lacustrine sediments in Kusai Lake. *Acta Sedimentol. Sin.* 27:691.

Wu, G. J., Zhang, C. L., Xu, B. Q., Mao, R., Joswiak, D., Wang, N. L., et al. (2013). Atmospheric dust from a shallow ice core from Tanggula: implications for drought in the central Tibetan Plateau over the past 155 years. *Quat. Sci. Rev.* 59, 57–66. doi: 10.1016/j.quascirev.2012.10.003

Xu, H., Zhou, K. E., Lan, J. H., Zhang, G. L., and Zhou, X. Y. (2019). Arid central Asia saw mid-Holocene drought. *Geology* 47, 255–258. doi: 10.1130/g45686.1

Xu, J. Z., Yu, G. M., Kang, S. C., Hou, S. G., Zhang, Q. G., Ren, J. W., et al. (2012). Sr-Nd isotope evidence for modern aeolian dust sources in mountain glaciers of western China. *J. Glaciol.* 58, 859–865. doi: 10.3189/2012JoG12J006

Yan, D. N., Xu, H., Lan, J. H., Zhou, K. E., Ye, Y. D., Zhang, J. X., et al. (2019). Solar activity and the westerlies dominate decadal hydroclimatic changes over arid Central Asia. *Glob. Planet. Chang.* 173, 53–60. doi: 10.1016/j.gloplacha.2018.12.006

Yang, X. H., He, Q., Matimin, A., Yang, F., Huo, W., Liu, X. C., et al. (2017). Threshold velocity for saltation activity in the Taklimakan desert. *Pure Appl. Geophys.* 174, 4459–4470. doi: 10.1007/s00024-017-1644-5

Yao, T. D., Guo, X. J., Thompson, L., Duan, K. Q., Wang, N. L., Pu, J. C., et al. (2006). δ18O record and temperature change over the past 100 years in ice cores on the Tibetan Plateau. *Sci. Chin. Ser. D Earth Sci.* 49, 1–9. doi: 10.1007/s11430-004-5096-2

Zhang, D. E. (1984). Synoptic-climatic studies of dust fall in China since historic times. *Sci. Chin. Ser. B Chem.* 27, 825–836. doi: 10.1360/yb1984-27-8-825

Zhang, W. B., Hou, S. G., Liu, Y. P., Wu, S. Y., An, W. L., Pang, H. X., et al. (2017). A high-resolution atmospheric dust record for 1810-2004 AD derived from an ice core in eastern Tien Shan, central Asia. *J. Geophys. Res. Atmos.* 122, 7505–7518. doi: 10.1002/2017JD026699

Zhong, H. L., and Li, D. L. (2005). Relationship between sand dust storm in northern China in April and westerly circulation. *Plate. Meteor.* 24, 104–111. doi: 10.3321/j.issn:1000-0534.2005.01.016

Zhou, G. P., Huang, X. Z., Wang, Z. L., Zhang, J., and Xie, H. C. (2019). Eolian activity history reconstructed by bosten lake grain size data over the Past ˜2000 years. *J. Desert. Res.* 39, 86–95.

Zhou, K. E., Xu, H., Lan, J. H., Yan, D. N., Sheng, E. G., Yu, K. K., et al. (2020). Variable late holocene 14C reservoir ages in lake Bosten, Northwestern China. *Front. Earth Sci.* 7:328. doi: 10.3389/feart.2019.00328

Zhou, Z. J., Zhang, G. C., Ai, W. X., Zhang, H. Z., and Niu, R. Y. (2006). Time series of spring dust emission and its correlative climatic factors in northern China. *J. Desert. Res.* 26, 935–941. doi: 10.3321/j.issn:1000-694X.2006.06.013

Zhu, C. W., Wang, B., and Qian, W. H. (2008). Why do dust storms decrease in northern China concurrently with the recent global warming?. *Geophys. Res. Lett.* 35:L18702. doi: 10.1029/2008gl034886

Conflict of Interest: The authors declare that the research was conducted in the absence of any commercial or financial relationships that could be construed as a potential conflict of interest.

Copyright © 2020 Zhang, Xu, Lan, Ai, Sheng, Yan, Zhou, Yu, Song, Zhang and Torfstein. This is an open-access article distributed under the terms of the Creative Commons Attribution License (CC BY). The use, distribution or reproduction in other forums is permitted, provided the original author(s) and the copyright owner(s) are credited and that the original publication in this journal is cited, in accordance with accepted academic practice. No use, distribution or reproduction is permitted which does not comply with these terms.

frontiers in Earth Science

ORIGINAL RESEARCH
published: 23 July 2020
doi: 10.3389/feart.2020.00282

Response of Westerly Jet Over the Northern Hemisphere to Astronomical Insolation During the Holocene

Peng Zhou[1,2], Zhengguo Shi[2,3,4], Xinzhou Li[2,5] and Weijian Zhou[2]*

[1] Interdisciplinary Research Center of Earth Science Frontier, Beijing Normal University, Beijing, China, [2] State Key Laboratory of Loess and Quaternary Geology, Institute of Earth Environment, Chinese Academy of Sciences, Xi'an, China, [3] Center for Excellence in Quaternary Science and Global Change, Chinese Academy of Sciences, Xi'an, China, [4] Institute of Global Environmental Change, School of Human Settlements and Civil Engineering, Xi'an Jiaotong University, Xi'an, China, [5] Center for Excellence in Tibetan Plateau Earth Sciences, Chinese Academy of Sciences, Beijing, China

The westerly jet (WJ) in the upper troposphere, an important atmospheric circulation system, is critical for influencing global climate by changes of its north–south migration and intensity. However, its variations during the Holocene across the Eurasian and North America are not well evaluated, which restricts our understanding of climate change in those regions. Using general circulation model experiments, here we simulate the variations of WJ over the past 10 ka to show its intensity and position of WJ responding to astronomical insolation. Our results suggest that the summer WJ gradually migrates southward and strengthens over the Central Asia (CA), Japan, and North America from the early Holocene (EH) to late Holocene (LH); meanwhile, the positions of the winter WJ barely move and its intensity slightly change. These seasonally asymmetric changes can be attributed to the temperature structure, in which the surface latent and sensible heat flux both contribute.

Keywords: westerly jet, insolation, Holocene, Asia, climate model

OPEN ACCESS

Edited by:
Hai Xu,
Tianjin University, China

Reviewed by:
Li Wu,
Anhui Normal University, China
Jun Cheng,
Nanjing University of Information Science and Technology, China

***Correspondence:**
Zhengguo Shi
shizg@ieecas.cn

Specialty section:
This article was submitted to Quaternary Science, Geomorphology and Paleoenvironment, a section of the journal Frontiers in Earth Science

Received: *10 April 2020*
Accepted: *18 June 2020*
Published: *23 July 2020*

Citation:
Zhou P, Shi Z, Li X and Zhou W (2020) Response of Westerly Jet Over the Northern Hemisphere to Astronomical Insolation During the Holocene. Front. Earth Sci. 8:282. doi: 10.3389/feart.2020.00282

INTRODUCTION

The westerly jet (WJ), located in the upper troposphere, is the strong and narrow westerly wind belt with horizontal and vertical wind shears over the Northern Hemisphere (NH) throughout whole year. It is an important planetary-scale atmospheric circulation system affecting weather and climate anomalies; especially, its variations in the intensity and position play a vital role in affecting precipitation patterns in the middle and low latitudes (Yang et al., 2002; Schiemann et al., 2009; Zhao et al., 2014). Given the significance of WJ for global and regional climate, its variations have been widely investigated in recent years (Liang and Wang, 1998; Sung et al., 2006; Sampe and Xie, 2010; Huang et al., 2013, 2015; Wei et al., 2017).

Taken into consideration of the topographical complexity, such as the uneven of land and sea distribution and the topography of the Tibetan Plateau, the WJ has unique structural and seasonal characteristics in Asia (Kuang and Zhang, 2005; Shi et al., 2015). In view of the blocking effect of the Tibet Plateau, the south branch of the WJ is located at the south side of the Tibet Plateau in spring and winter with gradually northward migration in May; whereas it rapidly jumps to north site of Tibetan Plateau in June with continually northward migration in July away from the Tibetan

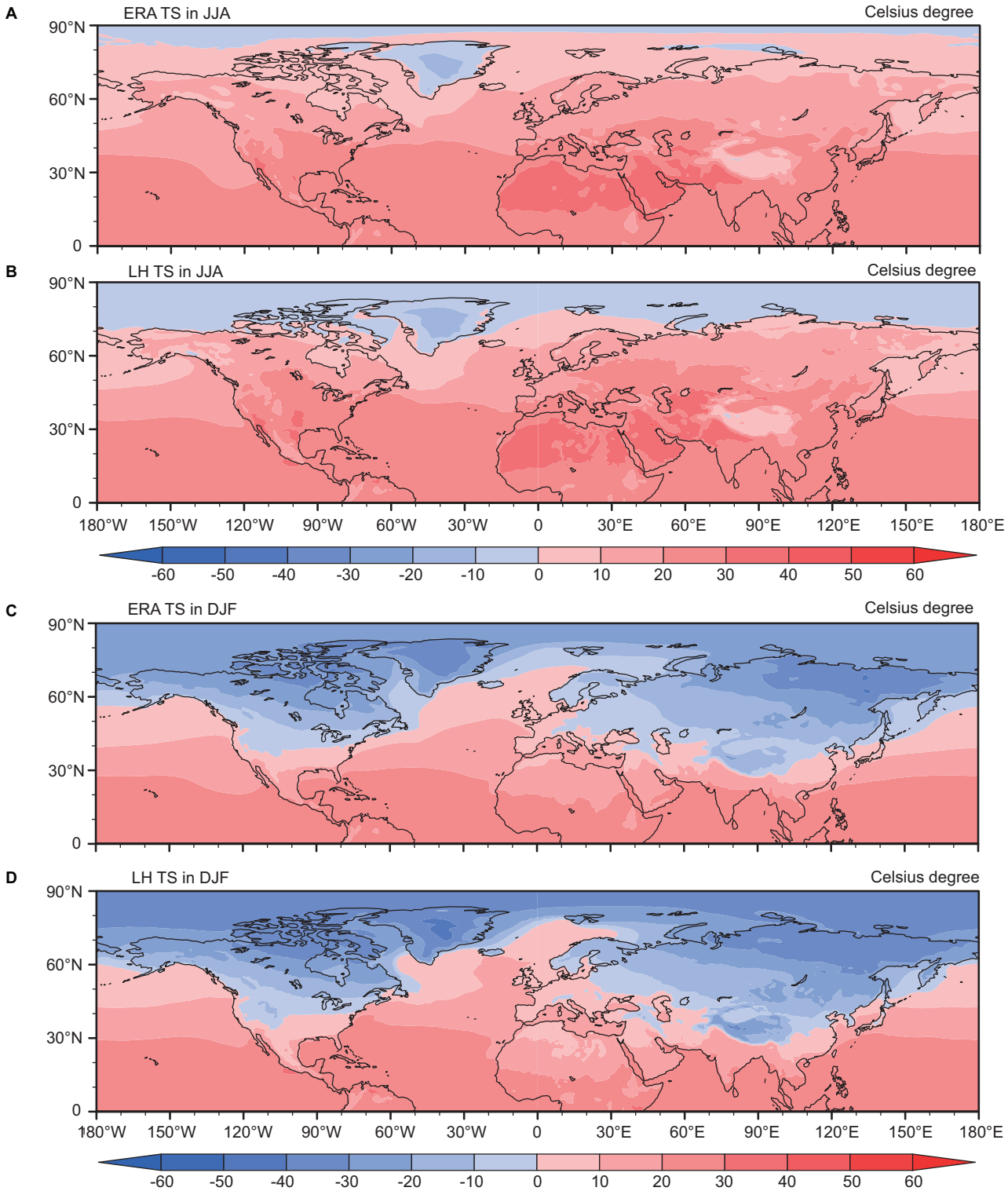

FIGURE 1 | Northern Hemisphere surface temperature (°C). The ERA-Interim reanalysis data for 1979–2014 **(A,C)**, and the simulated results averaged for 1-0 ka BP **(B,D)**.

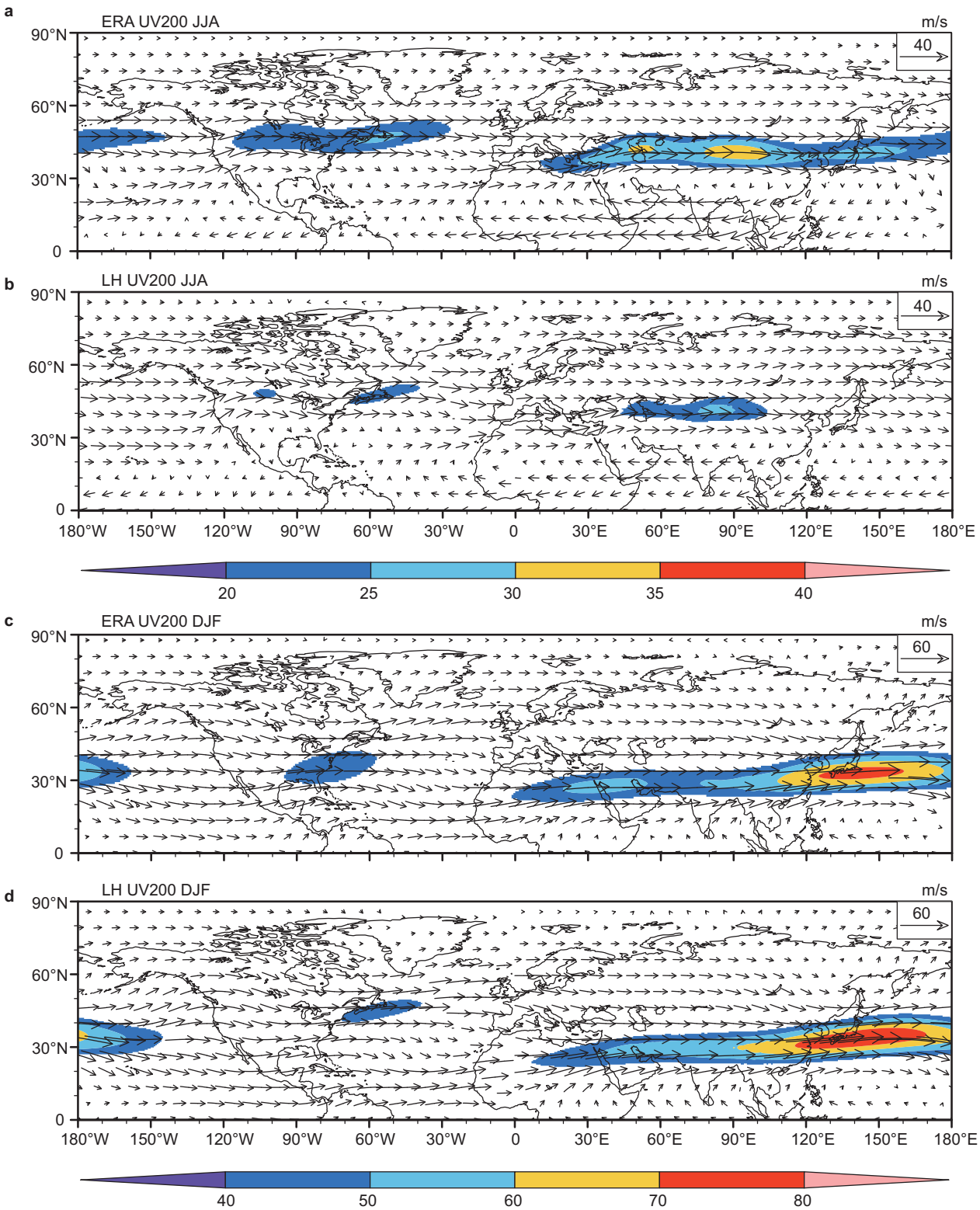

FIGURE 2 | The 200 hPa wind fields (m/s) in boreal summer and winter for the ERA-Interim reanalysis data for 1979–2014 in **(a,c)** and simulated results averaged for 1-0 ka BP **(b,d)**. Vectors are the 200 hPa horizontal winds (m/s) and the shading represents the jets with wind speeds more than 20 m/s in summer and 40 m/s in winter, respectively.

Plateau (Lin and Lu, 2008). Due to intensification of the westerlies across the Tibetan Plateau, a pronounced enhancement of the East Asian rain band during the pre-Meiyu stage is proposed (Chiang et al., 2019).

Based on the synchronically occurrence time of modern westerly circulation and East Asian summer monsoon (EASM) precipitation, the synergistic changes of WJ and EASM during the Holocene have been widely investigated (Nagashima et al., 2007, 2011, 2013; Zhang et al., 2018; Herzschuh et al., 2019). By analysis of geochemical data of marginal sediments in Japan sea, Nagashima et al. (2007) proposed that, on the orbital timescale, the southward migration of WJ is accompanied by the intensified winter monsoon and southeastward migration of summer monsoon when the summer solar insolation decreased in NH. From 101 fossil pollen records, Herzschuh et al. (2019) proposed that the WJ-stream axis shifted gradually southward during the Holocene, which significantly influences the position of EASM rainband.

In addition to paleoclimate proxies, climate simulations have been employed to study the Holocene westerlies and monsoon changes, which are closely associated with the precipitation or moisture over Central and East Asia (Jin et al., 2012; Shi et al., 2012; Li et al., 2013; Chiang et al., 2015; Shi, 2016; Zhang et al., 2016, 2017; Kong et al., 2017). Nevertheless, there are apparently significant differences of westerly winds during the Holocene. For example, a strengthening trend of westerly during the Holocene in NW China has been suggested by the coupled climate models (Jiang et al., 2007; Jin et al., 2012; Zhang et al., 2016, 2017); meanwhile, the transient simulation, forced by Earth's orbital parameters, draw an opposite relationship between the westerly and precipitation during the Holocene (Li et al., 2013).

Although the geological archives and modeling simulations gave useful information, the basic mechanisms for WJ during Holocene are still unclear and controversial. Thus, a better understanding of the temporal and spatial variation of the WJ and its forcing mechanisms is important for validating the regional-scale moisture conditions, which are paramount in assessing future climate change impacts. In this study, based on the Community Earth System Model (CESM) with a relatively high horizontal resolution, we explore the seasonal characteristics of WJ in the NH, especially the Asia, during the Holocene responding to astronomical insolation.

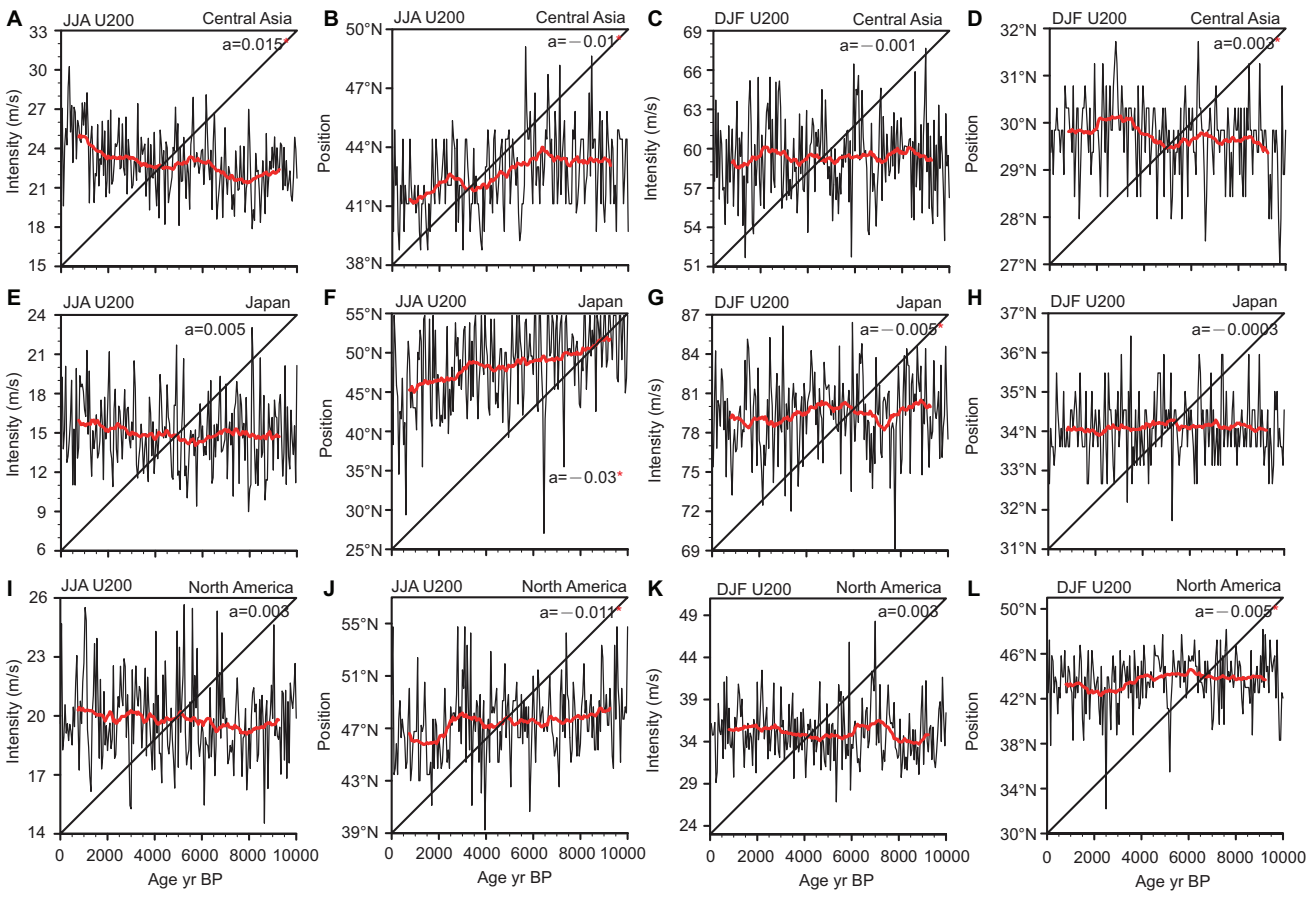

FIGURE 3 | Simulated changes in the intensity and position of WJ during the Holocene over Central Asia **(a–d)**, Japan **(e–h)**, and North America **(i–l)**. The red line represents a 31-simulation-year moving average. The red pentagram indicates that slope is significant at the 99% significance level.

NUMERICAL MODEL AND TRANSIENT EXPERIMENTS

The CESM, released by National Center for Atmospheric Research (NCAR), was conducted in this study. The CESM is a fully coupled model of the earth system, mainly including atmosphere, ocean, ice, river, and carbon cycle (Kay et al., 2015). It is a flexible and extensible tool for studying global change and can be applied to explore the relationship of subsystems in the earth system at multiple time and spatial scale, providing up-to-date simulations of the earth's past, present, and future. To save calculation resources, the atmospheric module CAM5 is coupled with a slab ocean, in which only the feedback of sea surface temperature is included. The horizontal resolution of the atmospheric module is chosen to be 0.47° × 0.63° in latitude and longitude, so that it provides a relatively high resolution to better capture regional features.

We conducted an accelerated transient experiment covering the past 10 ka by orbit acceleration technology (Li et al., 2013). In the simulation, only the changes in orbital parameters are included to purely examine the effect of astronomical insolation on the westerlies. Setting the orbital parameters to 10 ka BP, the model is integrated for 50 years as a spin up time. After that, the orbital parameters are prescribed to the values of every 50-year intervals at the end of each model year. Hence, a total of 200 model years are calculated for the whole of 10 ka by accelerating the variations in the orbital cycles with a factor of 50.

In addition, a more modern reanalysis product, the European Centre for Medium-Range Weather Forecasts (ECMWF)-Interim reanalysis (ERA-Interim) dataset from 1979 to 2014 is used for comparison with the simulated results. The horizontal resolution of the ERA data is 0.75° × 0.75°. In the analysis, the climate state in boreal summer refers to the average of June, July, and August (JJA), and the winter refers to the average of December, January, and February (DJF).

RESULTS

Model Validation

To verify the reliability on the spatiotemporal changes of WJ, the model results are compared with the observed meteorological data (**Figures 1**, **2**). **Figure 1** shows the winter and summer mean surface temperature in NH from the ERA data and the averaged data for 1-0 ka BP in our experiments. The model slightly underestimates the summer surface temperature over the high latitudes and overestimate over the North America and Eurasia (**Figures 1A,B**). Similarly, the simulated mean surface temperature in winter is also slightly lower than that of the ERA data over the high latitudes (**Figures 1C,D**). Considered that the simulated temperature is averaged for the

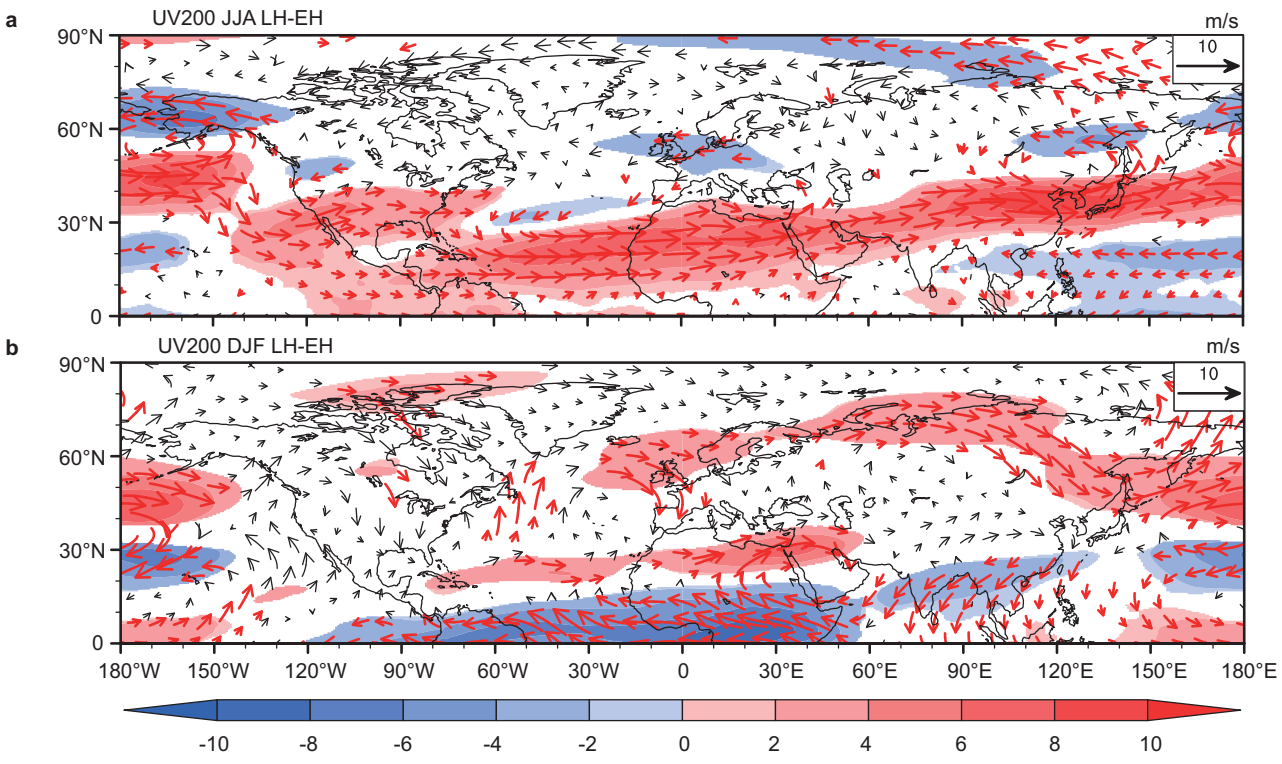

FIGURE 4 | The differences in 200 hPa wind field (m/s) between late Holocene and early Holocene in summer **(a)** and winter **(b)**. Red vectors indicate that the differences are significant at the 95% confidence level and the shading represents the differences in 200 hPa westerly winds are significant.

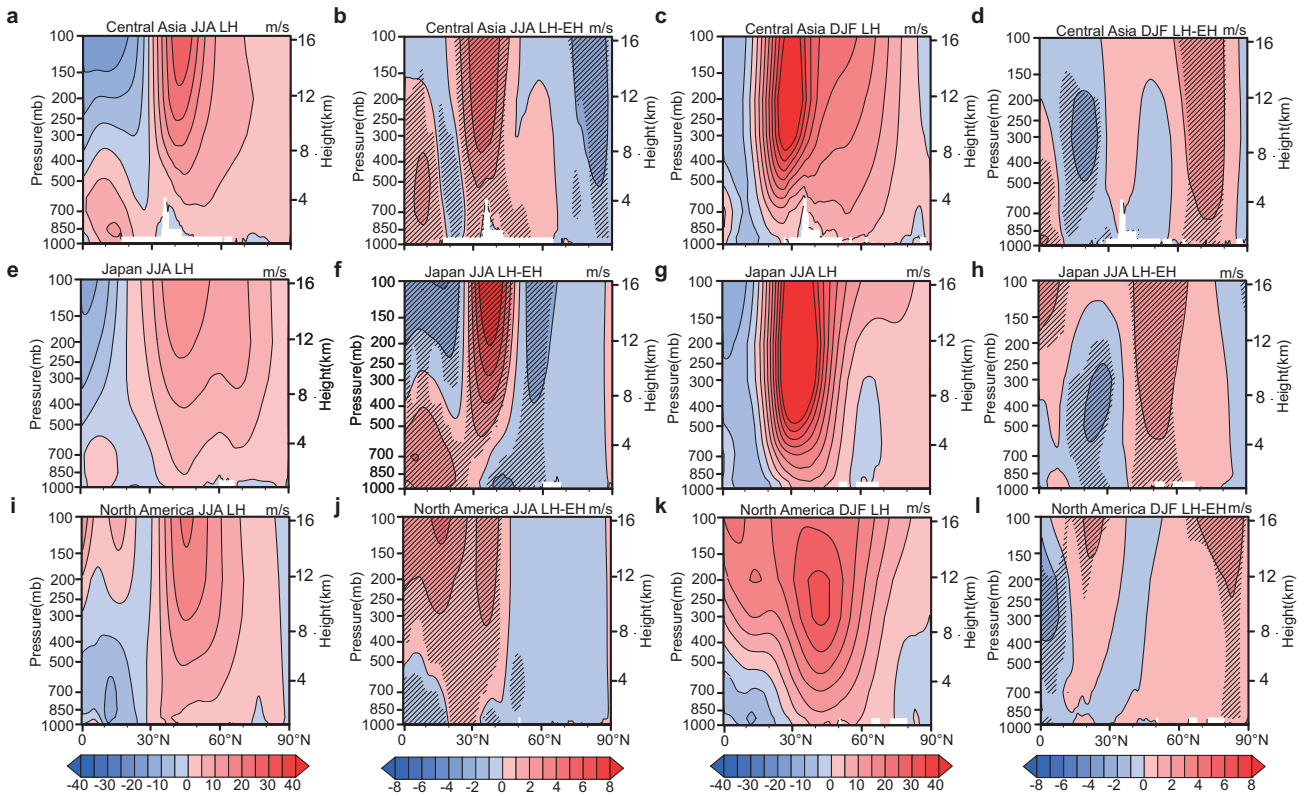

FIGURE 5 | Vertical profile of zonal mean westerly winds in boreal summer and winter averaged for Central Asia **(a–d)**, Japan **(e–h)**, and North America **(i–l)**. The values for LH and the differences between LH and EH are both shown. Black shades indicate the differences at the 95% significance level.

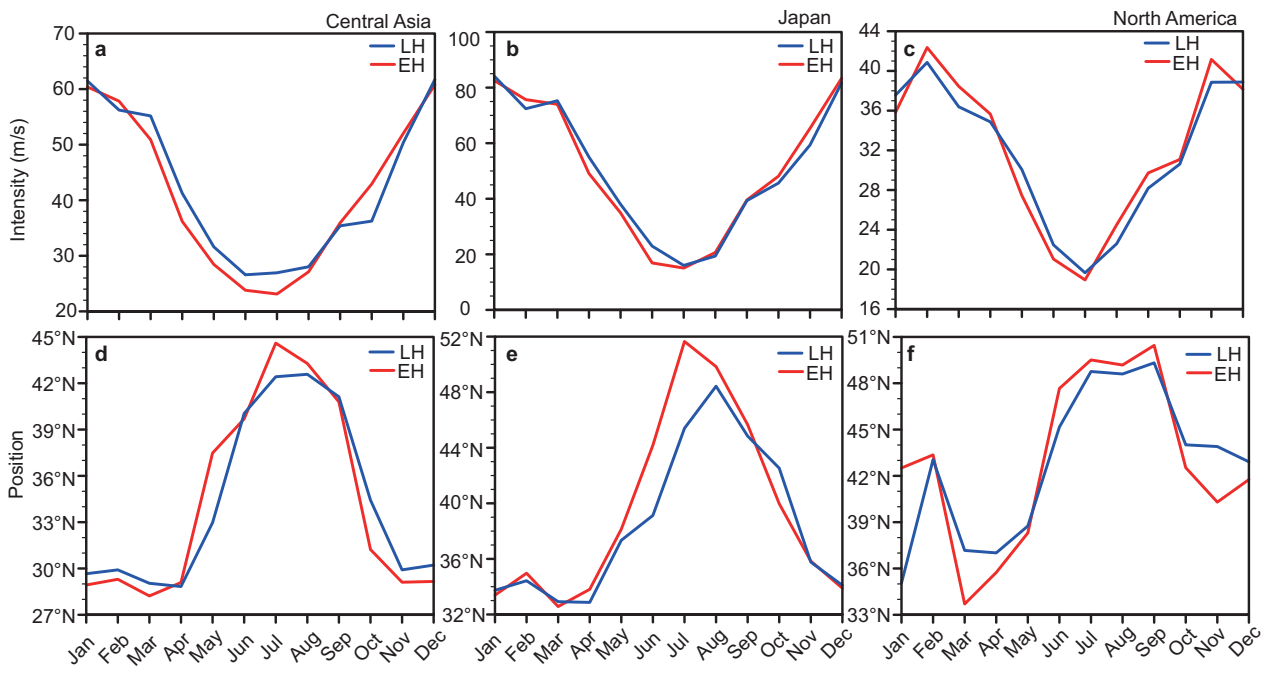

FIGURE 6 | Monthly variation of intensity and position of WJ over Central Asia **(a,d)**, Japan **(b,e)**, and North America **(c,f)**. The red and blue lines represent the EH and LH, respectively.

last 1 ka, the spatial distributions of the simulated summer and winter mean surface temperature are in good agreement with the ERA data.

The spatial distributions and values of simulated summer and winter WJ are broadly consistent with the general features of ERA data, especially over the Asia (**Figure 2**). In summer,

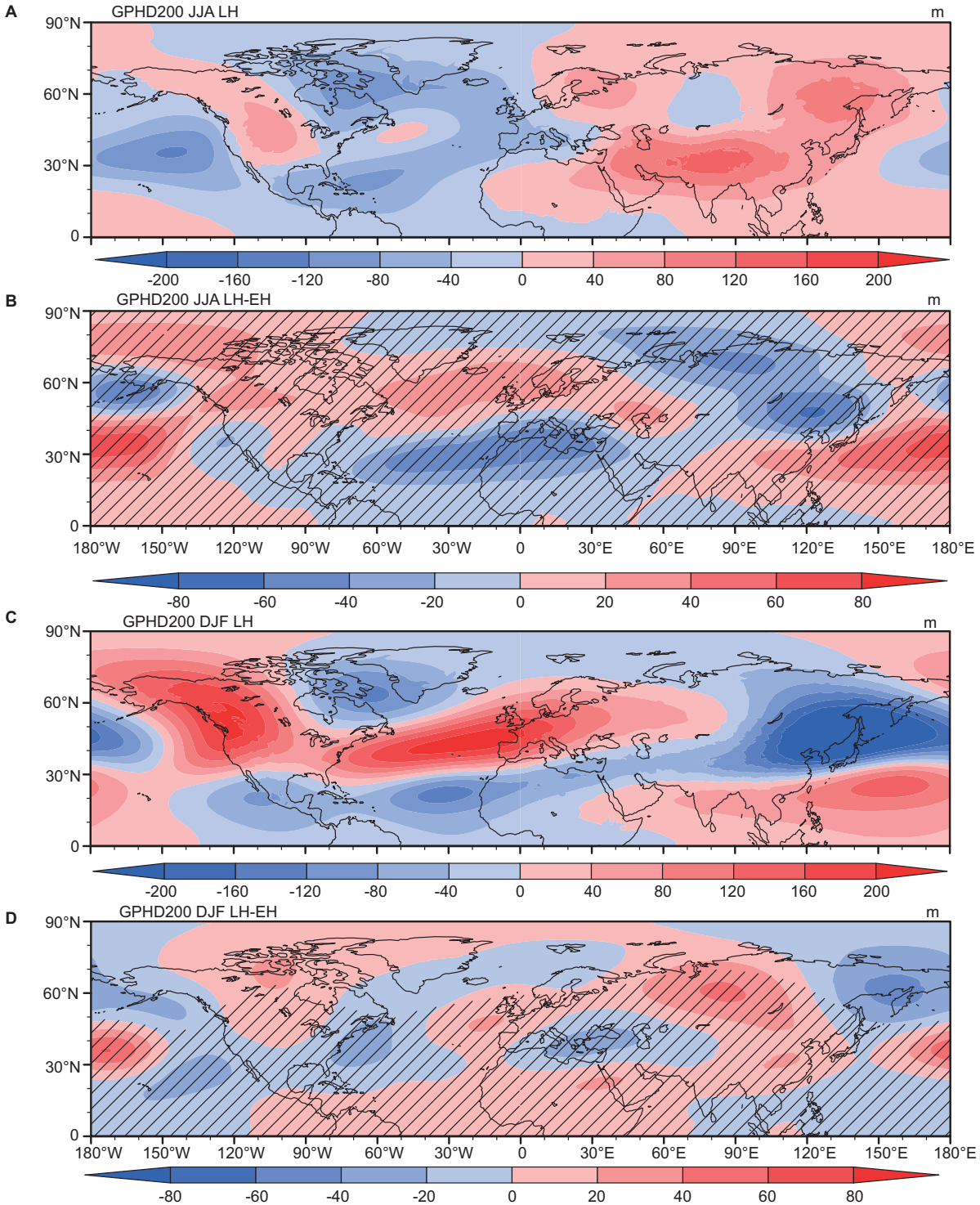

FIGURE 7 | The 200 hPa geopotential height disturbance over the Northern Hemisphere during the Holocene. Summer and winter 200 hPa geopotential height disturbance in LH **(A,C)** and the LH-minus-EH difference **(B,D)**. The line indicates the differences at the 95% significance level.

the WJ is located at 40°N with the center of the north of the Tibetan Plateau (**Figures 2a,b**). Our simulation underestimates the intensity of summer WJ, especially in the Japan and North America. In winter, the WJ generally shifts southward and the center over the North Pacific Ocean becomes stronger. Overall, both the intensity and position of WJ are well captured by our

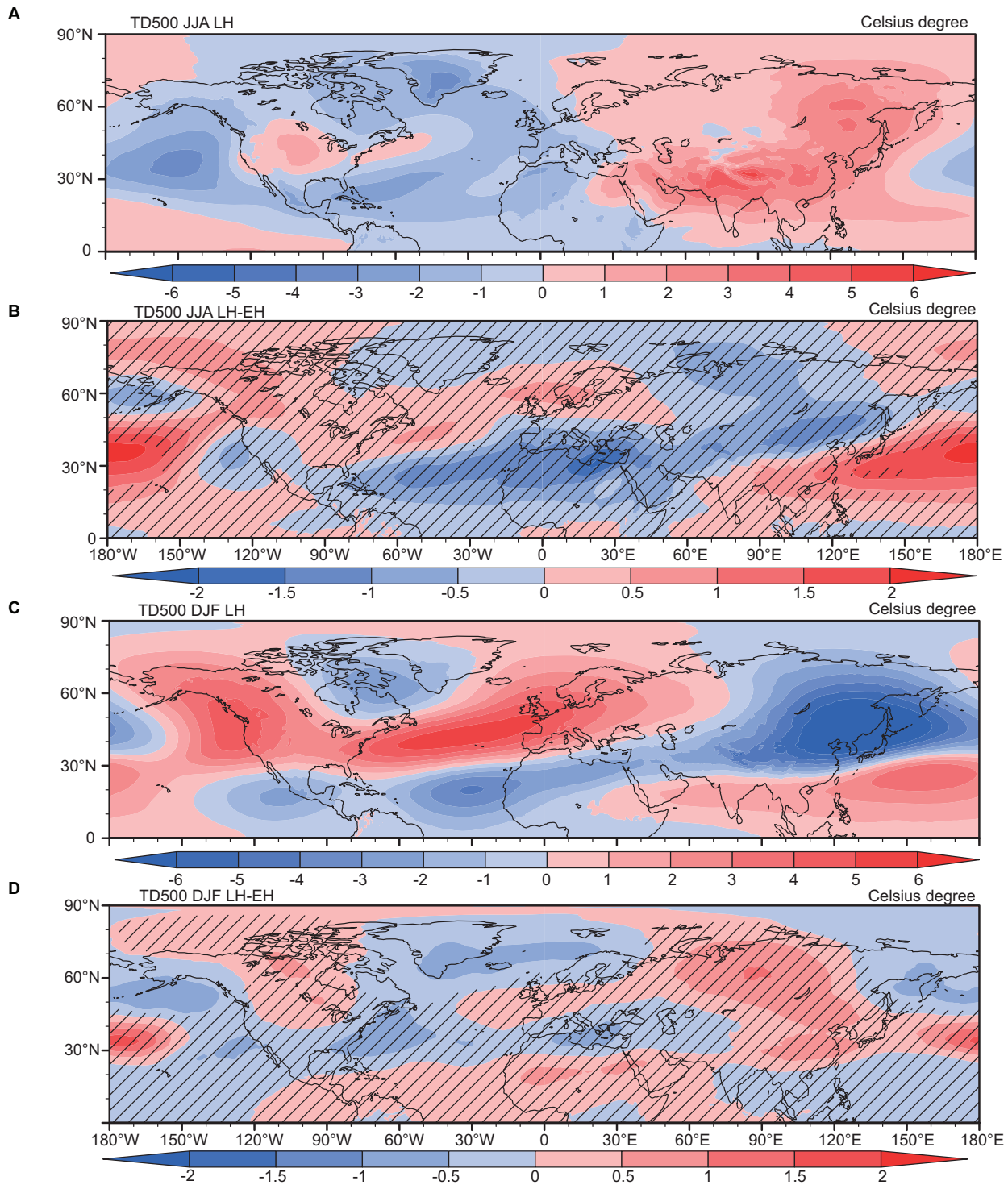

FIGURE 8 | The 500 hPa temperature disturbance over the Northern Hemisphere during the Holocene. Summer and winter 500 hPa temperature disturbance in LH **(A,C)** and the LH-minus-EH difference **(B,D)**. The line indicates the differences at the 95% significance level.

simulation, allowing us to further analyze the response of WJ to astronomical insolation during the Holocene.

The Spatiotemporal Variations of WJ

In order to evaluate the changes of WJ, we focus on three center areas including: the Central Asia (CA; 70–100°E, 15–55°N), the Japan (125–155°E, 15–55°N), and Northern America (NA; 60–100°W, 15–55°N). The intensity of WJ is defined as the mean 200 hPa wind speed in which the maximum westerly wind located on each longitude and its position is corresponding to the latitude of maximum wind speed at each region. **Figure 3** illustrates the changes in intensity and position of winter and summer WJ over the three regions during the Holocene. Over the CA, the intensity and position of summer WJ show a gradual increasing trend (**Figure 3a**) and southward migration (**Figure 3b**) during the Holocene, respectively. In contrast, the intensity and position of winter WJ demonstrate a weakening but not significant trend (**Figure 3c**) and northward migration, respectively (**Figure 3d**). The intensity and position of summer WJ over the Japan illustrate a similar pattern with highly sensitive of its position compared with that of the CA (**Figure 3f**). A weakened trend of winter WJ is noticeable over the Japan (**Figure 3g**). However, the changes in

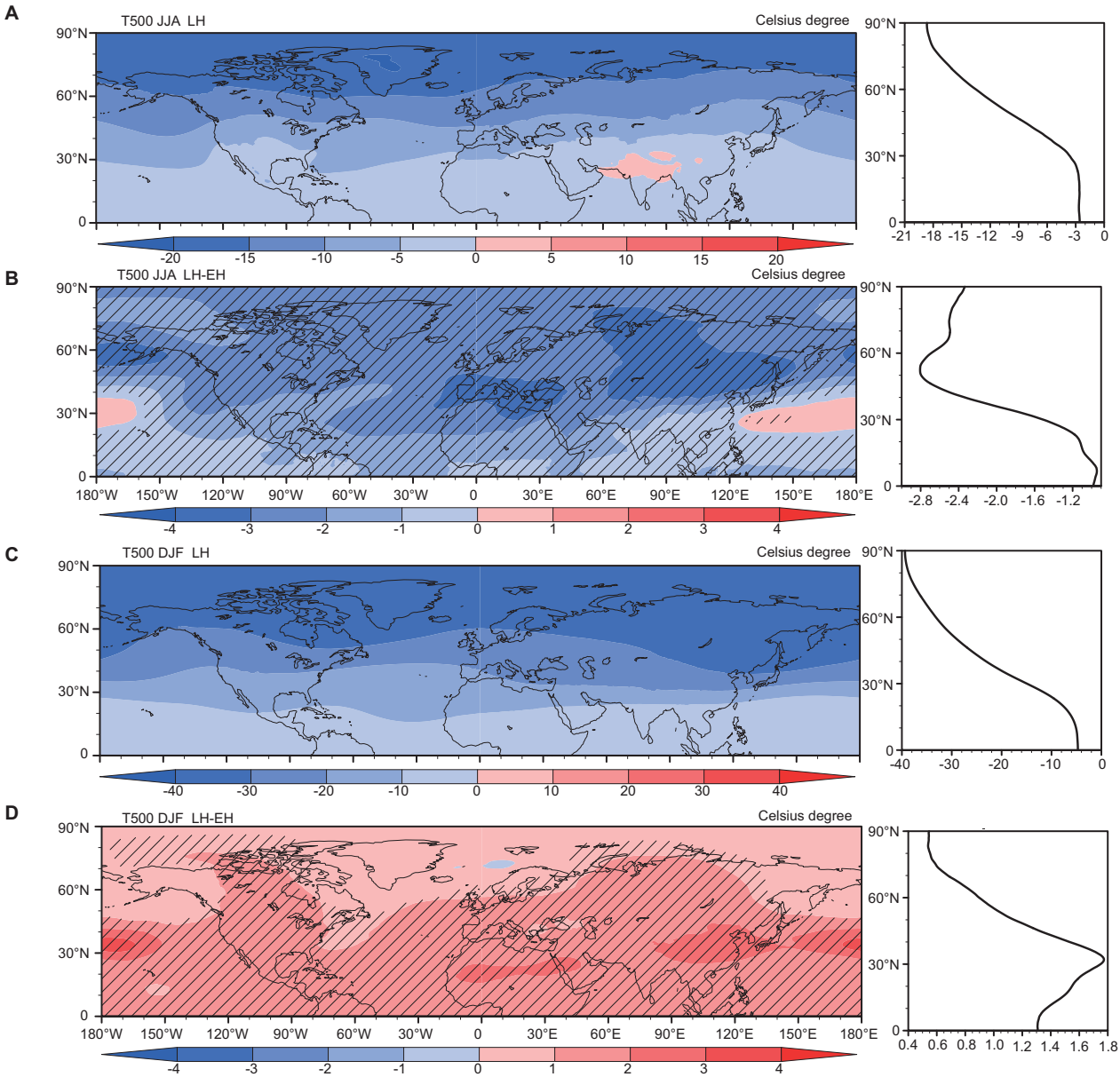

FIGURE 9 | The 500 hPa temperature distributions and the zonal mean temperature profiles. Summer and winter 500 hPa temperature distributions and zonal mean temperature profiles in LH **(A,C)** and the LH-minus-EH difference **(B,D)**. The line indicates the differences at the 95% significance level.

intensity and position over the NA during the Holocene are quite different with that of the CA and Japan. The position of WJ in NA shows a southward migration both in summer and winter (**Figures 3j,l**), with almost no significant change in intensity (**Figures 3i,k**).

To examine the spatial features of the WJ, we compared the 200 hPa wind vector difference between early Holocene (EH; 10–9 ka BP) and late Holocene (LH; 1-0 ka BP) in summer and winter. A long band-shaped region with positive values of westerly wind speed at 15–40°N in summer indicates obvious southward shift during the Holocene over the CA, Japan and NA (**Figure 4a**). However, the wind field in winter shows a quite different distribution (**Figure 4b**). There is showing a striking anticyclone-like pattern over the Northern Pacific, eastern North Atlantic Ocean, and Northwest Siberia and a cyclone-like pattern over the Eastern America and Mediterranean. As illustrated in vertical structure, the summer westerlies occupy the north of 30°N with the strongest centers at 40–50°N over CA, Japan, and NA (**Figures 5a,e,i**). The difference of LH-minus-EH shows significant maximal positive values at approximately 30–40°N,

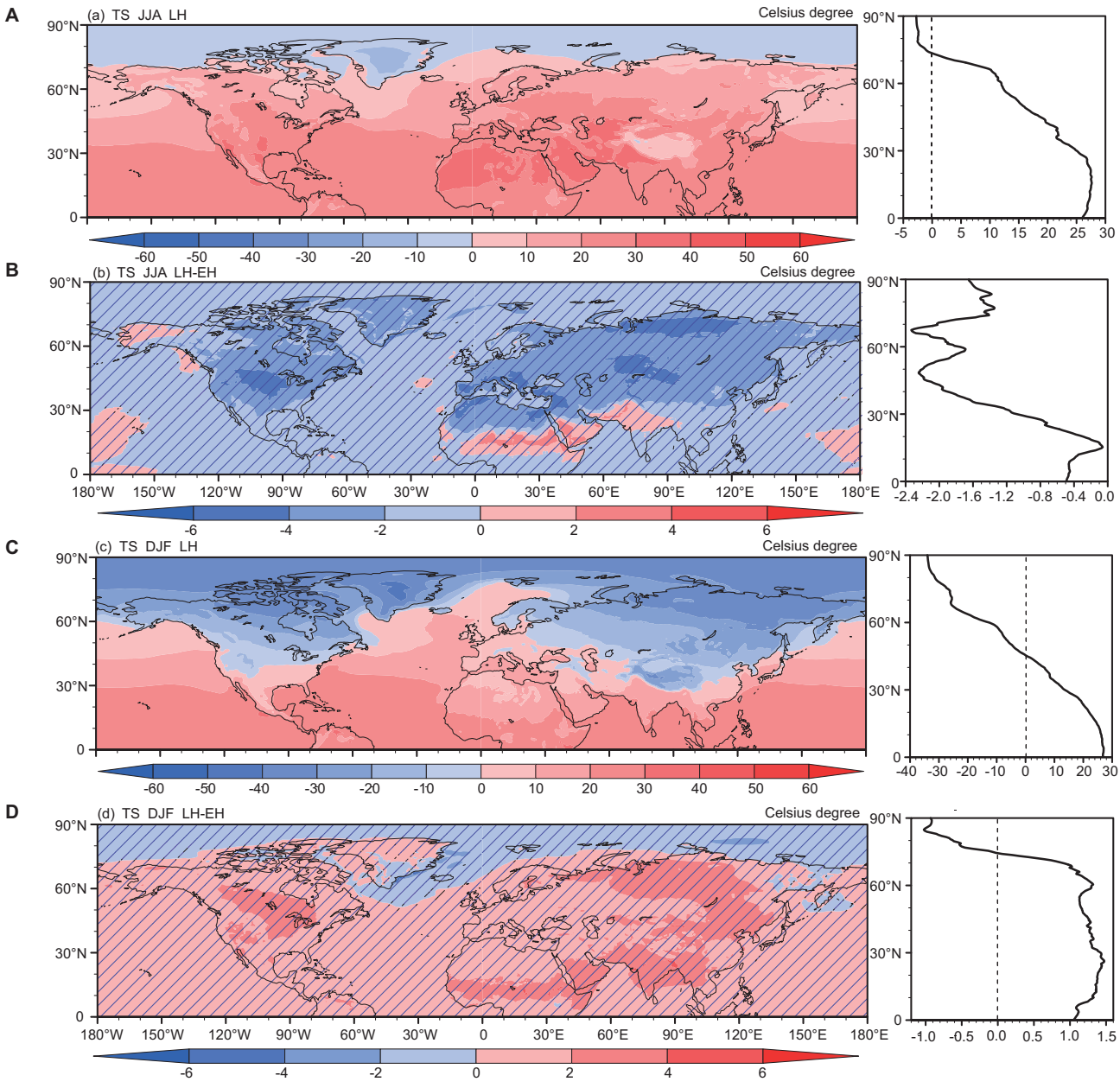

FIGURE 10 | Surface temperature distributions and the zonal mean temperature profiles. Summer and winter surface temperature distributions and zonal mean temperature profiles in LH **(A,C)** and the LH-minus-EH difference **(B,D)**. The line indicates the differences at the 95% significance level.

implying intensified and southward summer WJ during the LH (**Figures 5b,f,j**). The intensified WJ spreads from middle to high troposphere. The winter westerlies in CA are located at north of 15°N (**Figure 5c**) with a slightly northward migration and a decreasing trend during the LH. This result is evidently supported by the distribution of differences of LH-minus-EH, which show a slightly negative value at 15–55°N (**Figure 5d**). The changes of winter WJ in Japan are illustrated in **Figure 5g**, which shows a dramatic increasing trend in winter and locates at north of 15°N. Both of positive and negative values in difference of LH-minus-EH between 15 and 55°N in Japan are suggested, revealing a slightly decreasing trend of intensity in winter WJ (**Figure 5h**). In NA, the westerlies reach the maximum at 35°N (**Figure 5k**). The differences of LH-minus-EH show a slightly positive value, indicating strengthened westerlies during the Holocene (**Figure 5l**).

We calculate the monthly variations of the intensity and position of WJ during the Holocene to examine the seasonal characteristics (**Figure 6**). From the seasonal variation of the WJ wind speed, the intensity of the WJ is strongest in winter and weakest in summer (**Figures 6a–c**). The maximum intensity of difference between the LH and EH periods appears in summer, slightly changing in other seasons. Comparison with the intensity, the position of WJ also shows highly seasonal

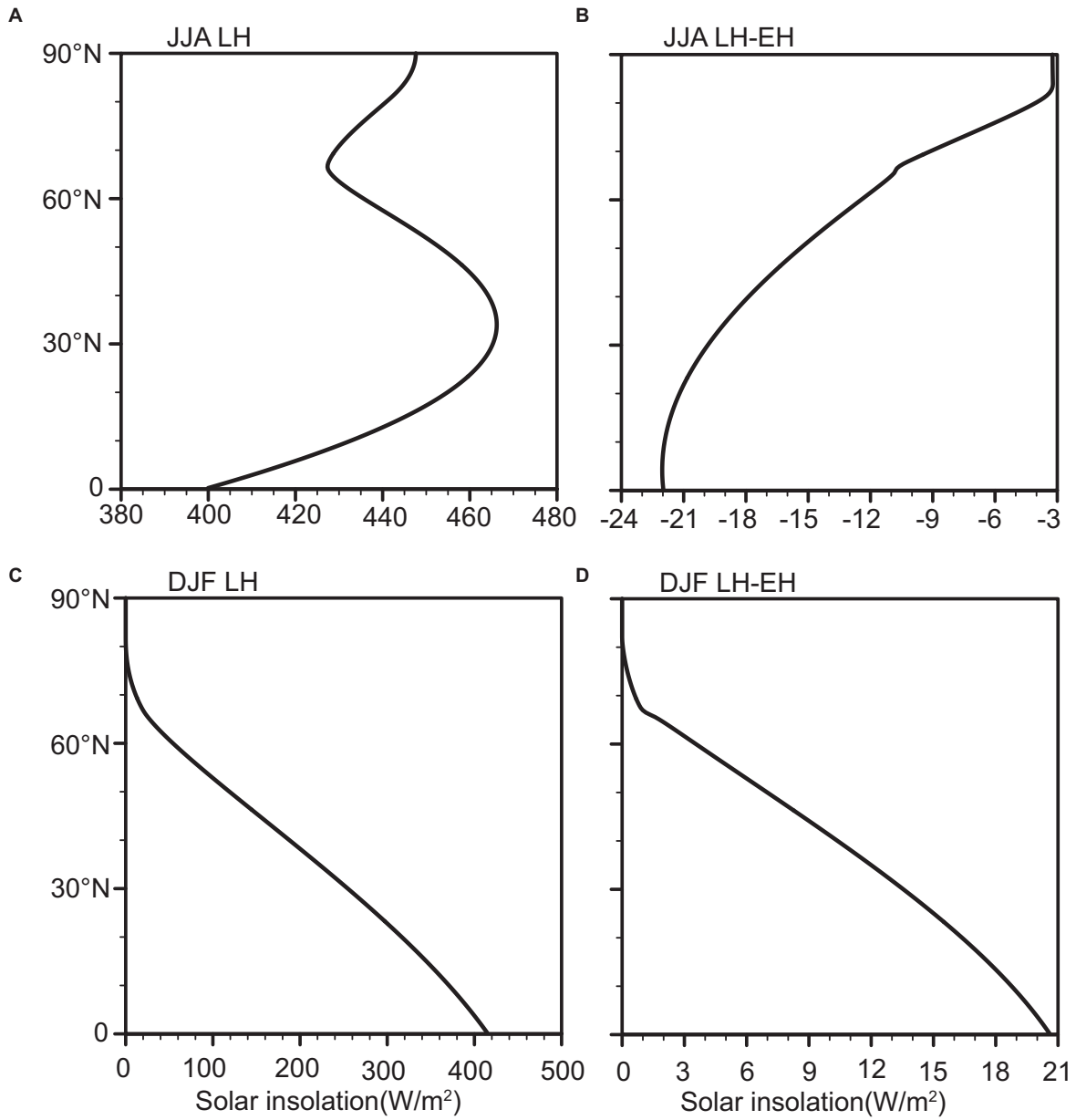

FIGURE 11 | Zonal mean profiles of solar insolation. Summer and winter solar insolation in LH **(A,C)** and the LH-minus-EH difference **(B,D)**.

variations. The WJ shifts to the northernmost position in summer, while it moves to the southernmost position in winter (**Figures 6b–d**). Over the CA and Japan, the WJ during the Holocene gradually and significantly shifted southward in spring and summer whereas it migrated northward in autumn and winter. Nevertheless, the shift of WJ over the NA is quite different with that of CA and Japan. It shifts southward in summer and winter whereas northward in spring and autumn. The maximum position of difference between the LH and EH appears in summer over the CA and Japan while in winter over the NA.

Physical Mechanisms for WJ Variations

As shown in **Figure 7**, the most significant response of the 200 hPa geopotential height disturbance occurs over the NH, which is consistent with the pattern of wind vector. The negative LH-minus-EH differences in geopotential height disturbances in summer lie over northern North Pacific, Mediterranean, and Southern Siberia (**Figure 7B**), corresponding with the cyclone-like pattern in the wind field (**Figure 4a**). However, the positive LH-minus-EH differences in geopotential height disturbances in winter occupy Northern Pacific, eastern North Atlantic Ocean, and Northwest Siberia (**Figure 7D**), which

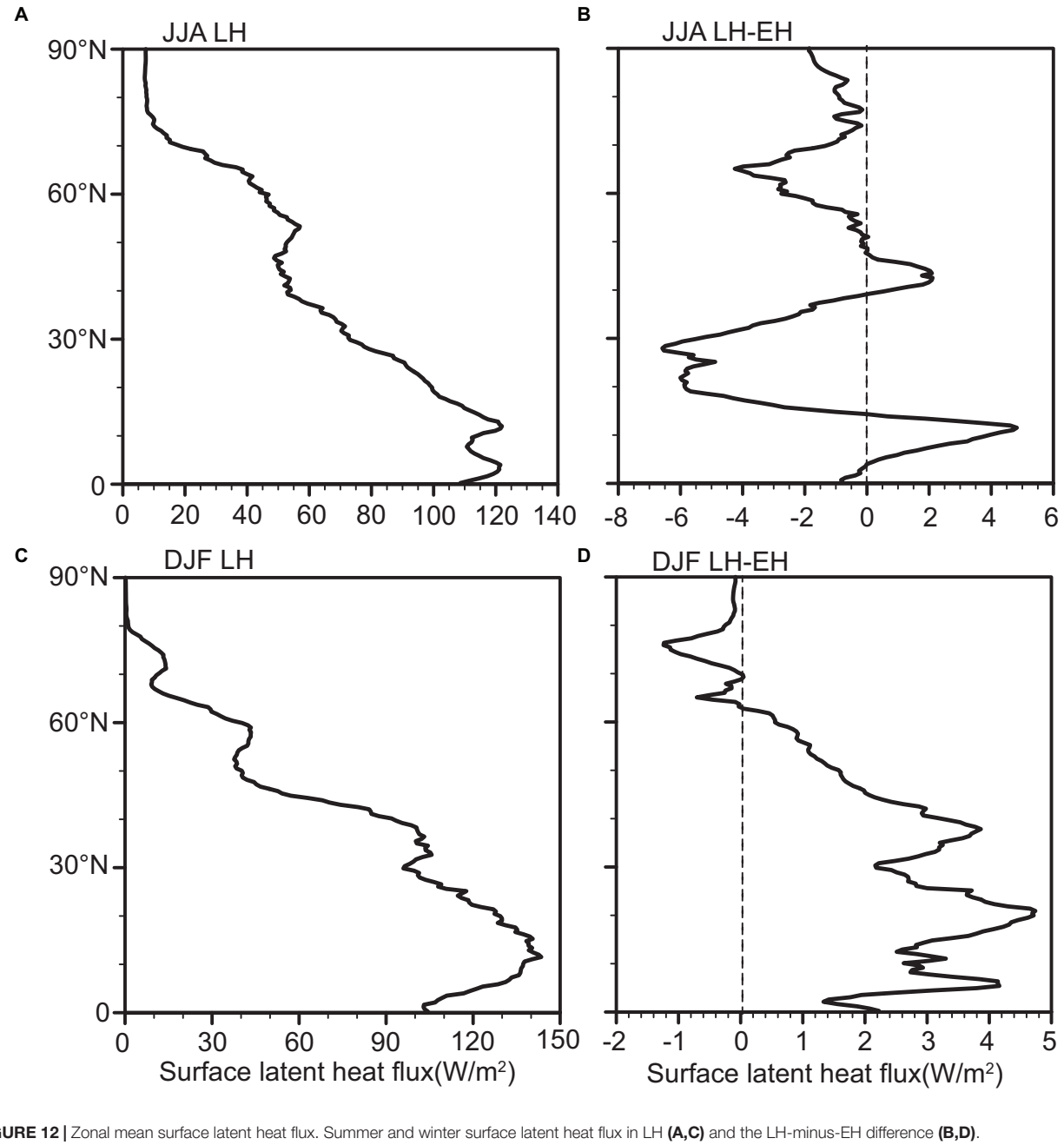

FIGURE 12 | Zonal mean surface latent heat flux. Summer and winter surface latent heat flux in LH **(A,C)** and the LH-minus-EH difference **(B,D)**.

are consistent with the anticyclone-like pattern in the wind field (**Figure 4b**). As illustrated in **Figures 7**, **8**, the upper tropospheric geopotential height disturbance and the mid-tropospheric temperature disturbance are highly synchronized in the spatial patterns. The results show that the anomaly areas of geopotential height disturbance are broadly synchronous with that of temperature disturbance (**Figure 8**). The geographic distribution of averaged 500 hPa temperature and the zonal mean for LH as well as its differences (LH-EH) over the North Hemisphere are shown (**Figure 9**). During the LH, the summer temperature at 500 hPa exhibits a decreasing trend from low to high latitudes (**Figure 9A**). While the difference of LH-minus-EH is generally showing negative values with the minimum at the mid-latitudes around 60°N, which clearly imply that the summer temperature at 500 hPa in EH is higher and its variation is stronger in mid and high latitudes (**Figure 9B**). The winter temperature at 500 hPa during the LH demonstrates a decreasing trend with increased latitudes (**Figure 9C**). The LH-minus-EH difference indicates that the winter warming reaches the maximum value at 30°N with declining for both polarward and equatorward (**Figure 9D**). In addition, the profile of zonal mean surface air temperature during the LH and the difference of LH-minus-EH (**Figure 10**) are generally coeval with the temperature pattern at 500 hPa (**Figure 9**), which supports that the 500 hPa temperature is largely controlled by the surface.

The surface temperature is presumably associated with the influence of solar insolation, surface latent and sensible heat flux during the Holocene (**Figures 11–13**). From the forcing of astronomical insolation, the absolute maximum solar insolation of the LH-minus-EH difference appears at the equator in summer and winter (**Figures 11B,D**). However, the surface air temperature difference reaches the negative maximum around 60°N in summer and positive maximum around 30°N in winter (**Figures 10B,D**). In summer, both the negative peaks of LH-minus-EH differences for the surface latent and the sensible heat

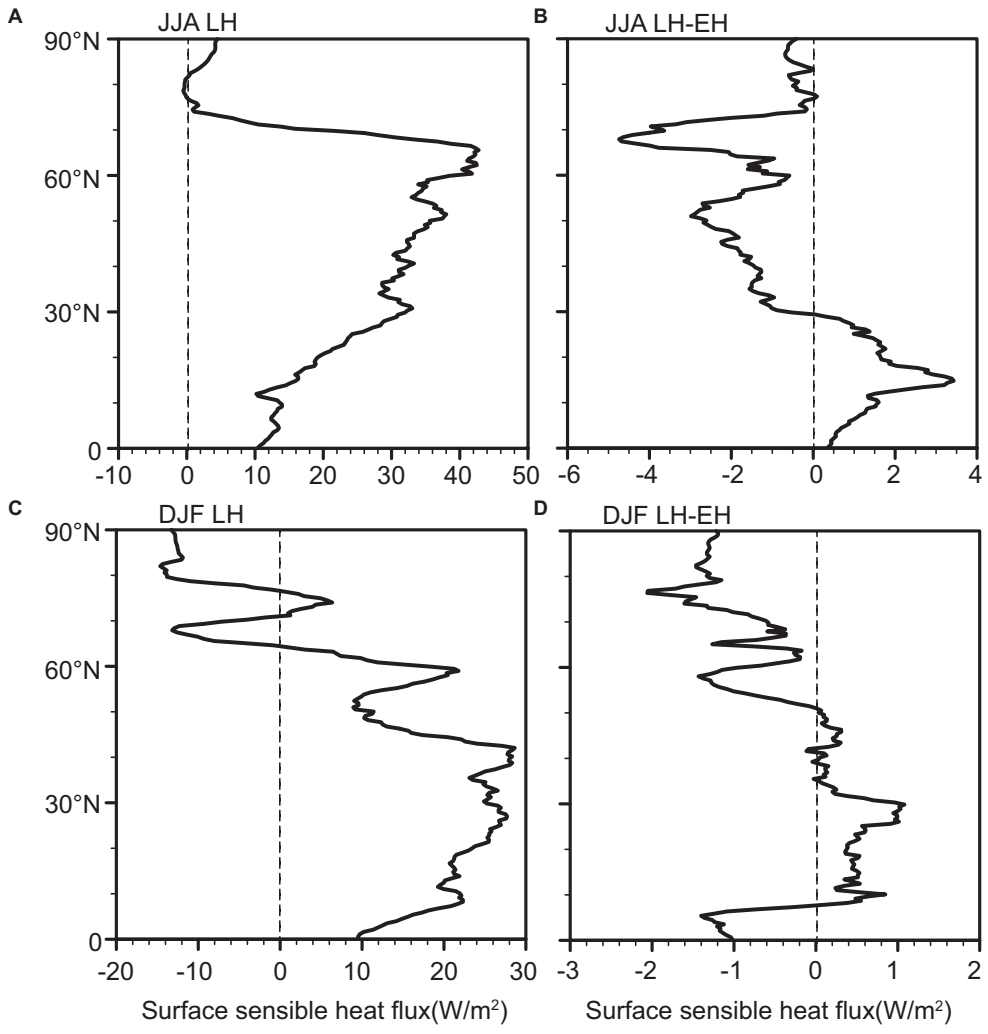

FIGURE 13 | Zonal mean surface sensible heat flux. Summer and winter surface sensible heat flux in LH **(A,C)** and the LH-minus-EH difference **(B,D)**.

flux at 60°N, probably modulated by the land-sea distribution, are roughly similar with that of the surface air temperature (**Figures 12B**, **13B**). The positive maximum of latent heat flux at 30°N is larger in winter which means more contributions on the surface air temperature (**Figures 12D**, **13D**). Therefore, we can conclude that the surface air temperature influenced by the latent and sensible heat flux has shown significant local characteristics with seasonal changes, which further result in seasonal changes in the intensity and position of the WJ.

DISCUSSION

By analysis of this study, the summer WJ has experienced a substantial change both in term of intensity and position in CA, Japan, and NA. The summer WJ migrated southward and showed a strengthening trend during the Holocene. The WJ carries out a large amount of heat and water vapor from the middle and low latitude oceans to Eurasian and Northern American continents and then has a profound impact on the climate and environmental changes in those regions. It has been widely recognized that change of precipitation in northwestern China and CA during the Holocene is also closely related to the change of WJ, transporting the water vapor from North Atlantic Ocean, Mediterranean Ocean, Black Sea, and Caspian Sea (Chen et al., 2008; Jin et al., 2012; Wang et al., 2013; Huang et al., 2015; Xu et al., 2019; Zhang et al., 2020). Furthermore, as a recent study, Cai et al. (2017) have illustrated precipitation seasonality in CA, in which implies that precipitation in most of CA occurs in summer half year. Therefore, the southward and strengthened summer WJ during the Holocene probably results in an increasing trend of precipitation in CA. Indeed, a growing body of evidence, including lake sediments, loess-paleosol sequences, and peats, has revealed a generally wetting trend in the ACA during the Holocene (Wang and Feng, 2013; Hong et al., 2014; Long et al., 2014, 2017; Chen et al., 2016), which might indicate an increasing trend of WJ as simulated by our experiments. In addition to the multi-proxy records, a long-term transient simulation by another climate model, forced by changes in orbital parameters, also demonstrated a strengthening trend of WJ during the Holocene (Zhang et al., 2016), which supports that this response of WJ during Holocene is not model dependent.

Beside the climate over CA, the change of WJ has also significantly influenced on the EASM by its north–south migration (Lin and Lu, 2008; Chiang et al., 2015; Lan et al., 2020). The sway of the WJ axis is closely associated to the intensity of EASM (Nagashima et al., 2011), and consequently influence on the latitudinal location of the summer monsoon precipitation through changes in its residence time on the north and south sides of the Tibetan Plateau (Sampe and Xie, 2010; Nagashima et al., 2011; Chiang et al., 2015; Herzschuh et al., 2019). When the NH summer solar insolation decreased, the southward migration of WJ accompanied by the intensified winter monsoon and southeastward migration of summer monsoon should decrease (increase) precipitation in northern (southern) EASM area (Chiang et al., 2015). For example, based on oppositional precipitation changes during the Heinrich event 1 (H1) and Younger Dryas (YD) indicated by the ratio of trace elements and oxygen isotope in stalagmite at Haozhu Cave in the middle Yangtze River, Zhang et al. (2018) have suggested that the westerly circulation regulates the changes in precipitation in central and eastern China by affecting the length of the Meiyu period in East Asia. Our results reveal that the summer WJ also shows a southward migration during the Holocene, which means longer time stay on the southern side of the Tibetan Plateau during the Holocene. It should block the northward movement of the EASM, causing more precipitation in southern part of EASM region. Recently, Herzschuh et al. (2019) also found that the southward migration of WJ-stream axis during the Holocene was tracked by the summer monsoon rain band, resulting in a gradual southward migration of the precipitation maximum.

CONCLUSION

In this study, we evaluated the response of position and intensity of WJ to the astronomical insolation during the Holocene based on a high-resolution transient simulation. Our results reveal that the changes in the position and intensity of WJ in CA, Japan, and NA are broadly consistent in summer, which have experienced southward migration and strengthening trend during the Holocene. However, the changes position and intensity of winter WJ over the three regions have shown regional features, with northward migration and weakening over the CA, slightly southward migration and weakening over the Japan, and southward migration and strengthening over the NA, respectively. We therefore suggest that the WJ is primarily controlled by the surface air temperature, ultimately triggered by the surface latent heat and sensible heat flux. Further researches are necessary to understand the influences and forcing mechanisms of WJ on regional precipitation/moisture variations, especially interplays between the WJ and EASM during the Holocene, which would provide helpful information for the human-induced global warming.

DATA AVAILABILITY STATEMENT

The raw data supporting the conclusions of this article will be made available by the authors, without undue reservation.

AUTHOR CONTRIBUTIONS

PZ performed the data analyses, drew the figures, and wrote the manuscript. ZS designed the research and also joined the analyses. XL conducted the climate model experiment. All authors contributed to the discussion and improvement of the manuscript.

FUNDING

This work was jointly supported by the Strategic Priority Research Program of Chinese Academy of Sciences (XDB40030000) and National Natural Science Foundation of China (41690115 and 41977382). ZS also acknowledges the support of Youth Innovation Promotion Association CAS.

REFERENCES

Cai, Y., Chiang, J. C. H., Breitenbach, S. F. M., Tan, L., Cheng, H., Edwards, R. L., et al. (2017). Holocene moisture changes in western China, Central Asia, inferred from stalagmites. *Quat. Sci. Rev.* 158, 15–28. doi: 10.1016/j.quascirev.2016.12.014

Chen, F., Jia, J., Chen, J., Li, G., Zhang, X., Xie, H., et al. (2016). A persistent Holocene wetting trend in arid central Asia, with wettest conditions in the late Holocene, revealed by multi-proxy analyses of loess-paleosol sequences in Xinjiang, China. *Quat. Sci. Rev.* 146, 134–146. doi: 10.1016/j.quascirev.2016.06.002

Chen, F., Yu, Z., Yang, M., Ito, E., Wang, S., Madsen, D. B., et al. (2008). Holocene moisture evolution in arid central Asia and its out-of-phase relationship with Asian monsoon history. *Quat. Sci. Rev.* 27, 351–364. doi: 10.1016/j.quascirev.2007.10.017

Chiang, J. C. H., Fischer, J., Kong, W., and Herman, M. J. (2019). Intensification of the pre-meiyu rainband in the Late 21st Century. *Geophys. Res. Lett.* 46, 7536–7545. doi: 10.1029/2019gl083383

Chiang, J. C. H., Fung, I. Y., Wu, C.-H., Cai, Y., Edman, J. P., Liu, Y., et al. (2015). Role of seasonal transitions and westerly jets in East Asian paleoclimate. *Quat. Sci. Rev.* 108, 111–129. doi: 10.1016/j.quascirev.2014.11.009

Herzschuh, U., Cao, X., Laepple, T., Dallmeyer, A., Telford, R. J., Ni, J., et al. (2019). Position and orientation of the westerly jet determined Holocene rainfall patterns in China. *Nat. Commun.* 10:2376. doi: 10.1038/s41467-019-09866-8

Hong, B., Gasse, F., Uchida, M., Hong, Y., Leng, X., Shibata, Y., et al. (2014). Increasing summer rainfall in arid eastern-Central Asia over the past 8500 years. *Sci. Rep.* 4:5279. doi: 10.1038/srep05279

Huang, W., Chen, F., Feng, S., Chen, J., and Zhang, X. (2013). Interannual precipitation variations in the mid-latitude Asia and their association with large-scale atmospheric circulation. *Chin. Sci. Bull.* 58, 3962–3968. doi: 10.1007/s11434-013-5970-4

Huang, W., Chen, J., Zhang, X., Feng, S., and Chen, F. (2015). Definition of the core zone of the "westerlies-dominated climatic regime", and its controlling factors during the instrumental period. *Sci. China Earth Sci.* 58, 676–684. doi: 10.1007/s11430-015-5057-y

Jiang, Q., Shen, J., Liu, X., Zhang, E., and Xiao, X. (2007). A high-resolution climatic change since Holocene inferred from multi-proxy of lake sediment in westerly area of China. *Chin. Sci. Bull.* 52, 1970–1979. doi: 10.1007/s11434-007-0245-6

Jin, L., Chen, F., Morrill, C., Otto-Bliesner, B. L., and Rosenbloom, N. (2012). Causes of early Holocene desertification in arid central Asia. *Clim. Dynam.* 38, 1577–1591. doi: 10.1007/s00382-011-1086-1

Kay, J. E., Deser, C., Phillips, A., Mai, A., Hannay, C., Strand, G., et al. (2015). The community Earth system model (CESM) large ensemble project: a community resource for studying climate change in the presence of internal climate variability. *B. Am. Meteorol. Soc.* 96, 1333–1349. doi: 10.1175/bams-d-13-00255.1

Kong, W., Swenson, L. M., and Chiang, J. C. H. (2017). Seasonal transitions and the westerly jet in the holocene East Asian summer monsoon. *J. Clim.* 30, 3343–3365. doi: 10.1175/jcli-d-16-0087.1

Kuang, X., and Zhang, Y. (2005). Seasonal variation of the East Asian Subtropical Westerly Jet and its association with the heating field over East Asia. *Adv. Atmos. Sci.* 22, 831–840. doi: 10.1007/BF02918683

Lan, J., Xu, H., Lang, Y., Yu, K., Zhou, P., Kang, S., et al. (2020). Dramatic weakening of the East Asian summer monsoon in northern China during the transition from the Medieval Warm Period to the Little Ice Age. *Geology* 48, 307–312. doi: 10.1130/g46811.1

Li, X., Liu, X., Qiu, L., An, Z., and Yin, Z.-Y. (2013). Transient simulation of orbital-scale precipitation variation in monsoonal East Asia and arid central Asia during the last 150 ka. *J. Geophy. Res* 118, 7481–7488. doi: 10.1002/jgrd.50611

Liang, X.-Z., and Wang, W.-C. (1998). Associations between China monsoon rainfall and tropospheric jets. *Q. J. Roy. Meteor. Soc.* 124, 2597–2623. doi: 10.1002/qj.49712455204

Lin, Z., and Lu, R. (2008). Abrupt northward jump of the East Asian upper-tropospheric jet stream in midsummer. *J. Meteorol. Soc. Jpn.* 86, 857–866. doi: 10.2151/jmsj.86.857

Long, H., Shen, J., Chen, J., Tsukamoto, S., Yang, L., Cheng, H., et al. (2017). Holocene moisture variations over the arid central Asia revealed by a comprehensive sand-dune record from the central Tian Shan, NW China. *Quat. Sci. Rev.* 174, 13–32. doi: 10.1016/j.quascirev.2017.08.024

Long, H., Shen, J., Tsukamoto, S., Chen, J., Yang, L., and Frechen, M. (2014). Dry early Holocene revealed by sand dune accumulation chronology in Bayanbulak Basin (Xinjiang, NW China). *Holocene* 24, 614–626. doi: 10.1177/0959683614523804

Nagashima, K., Tada, R., Matsui, H., Irino, T., Tani, A., and Toyoda, S. (2007). Orbital- and millennial-scale variations in Asian dust transport path to the Japan Sea. *Palaeogeogr. Palaeoclimatol. Palaeoecol.* 247, 144–161. doi: 10.1016/j.palaeo.2006.11.027

Nagashima, K., Tada, R., Tani, A., Sun, Y., Isozaki, Y., Toyoda, S., et al. (2011). Millennial-scale oscillations of the westerly jet path during the last glacial period. *J. Asian Earth. Sci.* 40, 1214–1220. doi: 10.1016/j.jseaes.2010.08.010

Nagashima, K., Tada, R., and Toyoda, S. (2013). Westerly jet-East Asian summer monsoon connection during the Holocene. *Geochem. Geophys. Geosyst.* 14, 5041–5053. doi: 10.1002/2013gc004931

Sampe, T., and Xie, S.-P. (2010). Large-scale dynamics of the meiyu-baiu rainband: environmental forcing by the westerly jet. *J. Clim.* 23, 113–134. doi: 10.1175/2009jcli3128.1

Schiemann, R., Lüthi, D., and Schär, C. (2009). Seasonality and interannual variability of the westerly jet in the tibetan plateau region. *J. Clim.* 22, 2940–2957. doi: 10.1175/2008jcli2625.1

Shi, Z. (2016). Response of Asian summer monsoon duration to orbital forcing under glacial and interglacial conditions: implication for precipitation variability in geological records. *Quat. Sci. Rev.* 139, 30–42. doi: 10.1016/j.quascirev.2016.03.008

Shi, Z., Liu, X., and Cheng, X. (2012). Anti-phased response of northern and southern East Asian summer precipitation to ENSO modulation of orbital forcing. *Quat. Sci. Rev.* 40, 30–38. doi: 10.1016/j.quascirev.2012.02.019

Shi, Z., Liu, X., Liu, Y., Sha, Y., and Xu, T. (2015). Impact of mongolian plateau versus tibetan plateau on the westerly jet over North Pacific Ocean. *Clim. Dyn.* 44, 3067–3076. doi: 10.1007/s00382-014-2217-2

Sung, M.-K., Kwon, W.-T., Baek, H.-J., Boo, K.-O., Lim, G.-H., and Kug, J.-S. (2006). A possible impact of the North Atlantic Oscillation on the east Asian summer monsoon precipitation. *Geophys. Res. Lett.* 33:L21713. doi: 10.1029/2006gl027253

Wang, W., and Feng, Z. (2013). Holocene moisture evolution across the Mongolian Plateau and its surrounding areas: a synthesis of climatic records. *Earth Sci. Rev.* 122, 38–57. doi: 10.1016/j.earscirev.2013.03.005

Wang, W., Feng, Z., Ran, M., and Zhang, C. (2013). Holocene climate and vegetation changes inferred from pollen records of Lake Aibi, northern Xinjiang, China: a potential contribution to understanding of Holocene climate pattern in East-central Asia. *Quat. Int.* 311, 54–62. doi: 10.1016/j.quaint.2013.07.034

Wei, W., Zhang, R., Wen, M., and Yang, S. (2017). Relationship between the Asian westerly jet stream and summer rainfall over Central Asia and North China: roles of the indian monsoon and the South Asian High. *J. Clim.* 30, 537–552. doi: 10.1175/jcli-d-15-0814.1

Xu, H., Zhou, K., Lan, J., Zhang, G., and Zhou, X. (2019). Arid Central Asia saw mid-Holocene drought. *Geology* 47, 255–258. doi: 10.1130/g45686.1

Yang, S., Lau, K.-M., and Kim, K.-M. (2002). Variations of the East Asian jet stream and Asian–Pacific–American winter climate anomalies. *J. Clim.* 15, 306–325.

Zhang, D., Chen, X., Li, Y., Wang, W., Sun, A., Yang, Y., et al. (2020). Response of vegetation to Holocene evolution of westerlies in the Asian Central Arid Zone. *Quat. Sci. Rev.* 229:106138. doi: 10.1016/j.quascirev.2019.106138

Zhang, H., Griffiths, M. L., Chiang, J. C. H., Kong, W., Wu, S., Atwood, A., et al. (2018). East Asian hydroclimate modulated by the position of the westerlies during Termination I. *Science* 362, 580–583. doi: 10.1126/science.aat9393

Zhang, X., Jin, L., Chen, J., Chen, F., Park, W., Schneider, B., et al. (2017). Detecting the relationship between moisture changes in arid central Asia and East Asia

during the Holocene by model-proxy comparison. *Quat. Sci. Rev.* 176, 36–50. doi: 10.1016/j.quascirev.2017.09.012

Zhang, X., Jin, L., Huang, W., and Chen, F. (2016). Forcing mechanisms of orbital-scale changes in winter rainfall over northwestern China during the Holocene. *Holocene* 26, 549–555. doi: 10.1177/0959683615612569

Zhao, Y., Wang, M., Huang, A., Li, H., Huo, W., and Yang, Q. (2014). Relationships between the West Asian subtropical westerly jet and summer precipitation in northern Xinjiang. *Theor. Appl. Climatol.* 116, 403–411. doi: 10.1007/s00704-013-0948-3

Conflict of Interest: The authors declare that the research was conducted in the absence of any commercial or financial relationships that could be construed as a potential conflict of interest.

Copyright © 2020 Zhou, Shi, Li and Zhou. This is an open-access article distributed under the terms of the Creative Commons Attribution License (CC BY). The use, distribution or reproduction in other forums is permitted, provided the original author(s) and the copyright owner(s) are credited and that the original publication in this journal is cited, in accordance with accepted academic practice. No use, distribution or reproduction is permitted which does not comply with these terms.

frontiers in Earth Science

ORIGINAL RESEARCH
published: 30 July 2020
doi: 10.3389/feart.2020.00234

Holocene East Asian Summer Monsoon Rainfall Variability in Taiwan

Xiaodong Ding[1], Liwei Zheng[2], Xufeng Zheng[3] and Shuh-Ji Kao[2]*

[1] College of Biological Science & Engineering, North Minzu University, Yinchuan, China, [2] State Key Laboratory of Marine Environmental Science, College of Ocean and Earth Sciences, Xiamen University, Xiamen, China, [3] Key Laboratory of Marginal Sea Geology, South China Sea Institute of Oceanology, Chinese Academy of Sciences, Guangzhou, China

Characterizing the spatiotemporal variability of the East Asian summer monsoon (EASM) advances our understanding of its rhythm, dynamics, and future impacts. East Asian summer monsoon variations during the Holocene have been reconstructed from a variety of geological archives and proxies. However, the spatiotemporal heterogeneity of EASM rainfall during the Holocene remains controversial. Taiwan is geographically suitable for studying the EASM history, through its geological archives. Herein, we synthesize the reported lake and peat sedimentary records of the entire Holocene, in addition to the records of mass-wasting and on-land deposition from cores collected from Taiwan to illustrate the EASM induced hydroclimate changes in Taiwan throughout the Holocene. Records from Taiwan indicate that the EASM rainfall maximum occurred during the early Holocene, concurring with other EASM records from monsoon regions in southern China. We suggest that the early Holocene EASM rainfall maximum in southern China was mainly forced by the higher Northern Hemisphere summer insolation and sea surface temperatures (SSTs) in the Western Pacific Warm Pool (WPWP). A synthesis of EASM rainfall records from across China shows that the timing of the Holocene EASM rainfall maximum occurred progressively later than that from southern to northern China. This time-transgressive EASM rainfall maximum may be due to the latitudinal shift of the westerlies and Western Pacific subtropical high (WPSH) that was induced by changes of interhemispheric temperature gradients (ΔT_{N-S}) and the northern high latitude ice volume. Moreover, records from Taiwan suggest a significant collapse of the EASM in Taiwan at ~4–2 ka BP. Based on the records from Taiwan, coastal East Asia, and the Tropical Pacific, we propose that the SSTs of the WPWP and/or El Niño-Southern Oscillation activity may have exerted a strong influence on the EASM rainfall changes during the late Holocene. Moreover, increased EASM rainfall in southern China during the last 2 ka was likely caused by a southward shift of WPSH, which is associated with gradual decreases in ΔT_{N-S} during the late Holocene.

Keywords: East Asian summer monsoon, Taiwan, Holocene, maximum rainfall, solar insolation, WPSH, ENSO

OPEN ACCESS

Edited by:
Hai Xu,
Tianjin University, China

Reviewed by:
Zhiping Tian,
Institute of Atmospheric Physics (CAS), China
Zhengguo Shi,
Institute of Earth Environment (CAS), China

****Correspondence:***
Xiaodong Ding
dingxd@nmu.edu.cn

Specialty section:
This article was submitted to Quaternary Science, Geomorphology and Paleoenvironment, a section of the journal Frontiers in Earth Science

Received: *10 March 2020*
Accepted: *02 June 2020*
Published: *30 July 2020*

Citation:
Ding X, Zheng L, Zheng X and Kao S-J (2020) Holocene East Asian Summer Monsoon Rainfall Variability in Taiwan. Front. Earth Sci. 8:234. doi: 10.3389/feart.2020.00234

INTRODUCTION

As an important component of the global atmospheric circulation system, the East Asian summer monsoon (EASM) plays a significant role in global hydrologic and energy cycles and is the primary driver of hydroclimatic changes in East Asia (Ding and Chan, 2005; An et al., 2015). Unlike the Indian summer monsoon, which consists of moisture sourced mainly from the Indian Ocean, the EASM is a combination of tropical and subtropical monsoon systems with complex moisture sources that include tropical sources in the Indian Ocean and the South China Sea, as well as subtropical sources in the western North Pacific (Ding and Chan, 2005; Wang et al., 2008). The EASM has a profound impact on the livelihood of people living in East Asia through the distribution of monsoon-related rainfall and any related disasters (e.g., floods, droughts, typhoons). It is vital to study the evolution of EASM variabilities on different timescales in order to understand their hemispheric and global teleconnections, possible forcing mechanisms, and future hydroclimatic changes.

The history of the EASM and its forcing mechanisms have been the subject of numerous paleoclimate studies. Various geological archives have been used to reconstruct the EASM history such as loess-paleosol sequences (An et al., 1990; Guo et al., 2000; Sun et al., 2006, 2015; Wang H. et al., 2014; Beck et al., 2018; Meng et al., 2018), lake and peat sediments (Zhou et al., 2004; Xiao et al., 2006; Selvaraj et al., 2007; Yancheva et al., 2007; Zhong et al., 2010; Chen F. et al., 2015; Park et al., 2016; Wang et al., 2016), marine sediments (Wang et al., 1999; Liu et al., 2003; Sun et al., 2003; Wan et al., 2010), and stalagmite records (Wang et al., 2001, 2005; Yuan et al., 2004; Dykoski et al., 2005; Cheng et al., 2009, 2016, 2019; Zhang et al., 2019). Among these, the stalagmite records have been widely used to reconstruct the variations in the EASM on different timescales due to their wide distribution, precise dating, and continuity over long timescales (Cheng et al., 2019). However, the paleoclimatic significance of the most important proxy obtained from stalagmites (stable oxygen isotopes; $\delta^{18}O$) remains debated because of the complex relationship between local rainfall and $\delta^{18}O$ in the EASM region (Maher, 2008; Pausata et al., 2011; Caley et al., 2014; Tan, 2014; Baker et al., 2015; Liu et al., 2015; Chen et al., 2016). It has been argued that the variabilities in the $\delta^{18}O$ of Chinese stalagmites are more likely controlled by changes in the moisture source (Maher, 2008; Maher and Thompson, 2012) or the atmospheric moisture pathway (Baker et al., 2015), rather than by local rainfall amounts. In addition, Pausata et al. (2011) concluded that changes in the stalagmite $\delta^{18}O$ records from China reflect changes in the intensity of the Indian rather than East Asian monsoon precipitation. However, by comparing simulations and observations from paleoclimatic records, Liu et al. (2014b) suggested that the stalagmite $\delta^{18}O$ records are a robust proxy for the EASM intensity in terms of the southerly monsoon winds and monsoon rainfall in northern China. Moreover, a synthesized stalagmite $\delta^{18}O$ record, which is based on 16 stalagmites from the EASM region of China, exhibits a Holocene EASM evolutionary pattern that is similar to other EASM records derived from the monsoonal region of China; this result confirms that the stalagmite $\delta^{18}O$ records are a valid indicator of EASM intensity, rather than the local rainfall amount (Yang et al., 2019).

The spatiotemporal heterogeneity of EASM rainfall during the Holocene is also a debated issue (Shi et al., 2012; Xie et al., 2013; Chen F. et al., 2015; Jia et al., 2015; Rao et al., 2016; Zhou et al., 2016; Goldsmith et al., 2017; Zhu et al., 2017; Huang X. et al., 2018; Ming et al., 2020; Xu et al., 2020). For example, stalagmite $\delta^{18}O$ records show an early Holocene EASM maximum (Dykoski et al., 2005; Wang et al., 2005; Cai et al., 2010; Dong et al., 2010; Zhang et al., 2019), which is also supported by lacustrine records from southern China (Zhou et al., 2004; Zhong et al., 2010; Wang et al., 2016; Sheng et al., 2017). However, numerous records from arid/semi-arid northern China show a middle Holocene EASM rainfall maximum (Lu et al., 2013; Wang and Feng, 2013; Li et al., 2014; Wang H. et al., 2014; Chen F. et al., 2015; Guo et al., 2018). By combining these records with the TraCE-21 ka transient simulation (Liu et al., 2009, 2014a). Lu et al. (2019) pointed out that the trend of the Holocene EASM rainfall in southern China (28°–38°N, 112°–124°E) matched with the decreasing trend in the Northern hemisphere solar insolation (NHSI), while the maximum rainfall in arid/semi-arid northern China (38°–53°N, 80°–105°E) lags behind the peak insolation by ∼4–5 ka. By comparing the full and single forcing transient simulations, Lu et al. (2019) also suggested that the northern high latitude ice volume suppressed the summer rainfall in northern China, but had little effect on southern China during the early Holocene, leading to the meridional asynchronous evolution of the EASM rainfall amounts. Note that "southern China" as defined by Lu et al. (2019) is not the traditional view of what is actually "southern China." It is a region located around the middle to lower reaches of the Yangtze River. Recently, Xu et al. (2020) noted a very different pattern of the EASM in southern China, based on lake level reconstructions. According to their reconstructions, the summer monsoon rainfall in southern China was high during the early and late Holocene, but low during the middle Holocene (Xu et al., 2020). Such a pattern is also evident in subtropical East Asia (20–27°N, 110–125°E) precipitation in the TraCE−21ka simulations (Xu et al., 2020). This pattern is also supported by several paleoclimate records from the middle Yangtze Valley which indicate wet conditions during the early and late Holocene, but dry conditions during the middle Holocene (Xie et al., 2013; Huang X. et al., 2018; Liu et al., 2019). However, these records are inconsistent with other proxy records from the same sites, including a pollen record from the Dajiuhu peatland (Zhu et al., 2010) and a stalagmite $\delta^{18}O$ record from Heshang Cave (Hu et al., 2008). This discrepancy may exist for a number of reasons, such as climatic sensitivity of the different proxy indicators (Li et al., 2018; Lu et al., 2019). However, pollen based quantitative rainfall reconstructions from the lower reaches of the Yangtze River show an early to middle Holocene (10–6 ka BP) EASM rainfall maximum (Li et al., 2018; Lu et al., 2019). These studies render the spatiotemporal evolution of the EASM rainfall elusive. Moreover, the early to middle Holocene has generally been characterized as a warm period (Renssen et al., 2012) and has thus been considered as a potential "analog" for modern climatic conditions. To better project any future changes

of the EASM-related hydroclimate under a background of global warming, it is essential to comprehend the spatiotemporal variations of EASM rainfall during the Holocene and its possible forcing mechanisms.

Located at the front edge of the East Asian continent (**Figure 1A**), Taiwan's climate is heavily influenced by the EASM; therefore, it is a suitable location for exploring past EASM variability by studying the geological archives in its lakes and swamps (Liew et al., 2006, 2014; Selvaraj et al., 2007, 2011, 2012; Lee and Liew, 2010; Lee et al., 2010; Yang et al., 2011; Wang L.-C. et al., 2014; Wang et al., 1999; Ding et al., 2016, 2017). However, due to the high relief, steep topography, extreme rainfall, and landslides induced by frequent typhoon activity that lead to high erosion and sedimentation rates, climate archives from Taiwan are rarely long enough to cover the entire Holocene. To date, only three lake and peat sediment cores have been retrieved that cover the entire Holocene. These sediment cores originate from the Retreat Lake (northern Taiwan, 24°29′N, 121°26′E; 2230 m above sea level; Selvaraj et al., 2007), the Toushe Basin (central Taiwan, 23°49′N; 120°53′E; 650 m above sea level; Liew et al., 2006), and the Dongyuan Lake (southern Taiwan, 22°10′N, 120°50′E, 360 m above sea level; Lee et al., 2010; **Figure 1B**). In addition, Taiwan is a mountainous island characterized by active rock uplift, rapid fluvial bedrock incision, frequent seismic activity, and episodic extreme rainfall events, rendering it exposed to frequent landslides and debris flows that are observed almost annually (Hsieh and Chyi, 2010). The deposited gravel from ancient landslide and debris flows, and their associated landforms (e.g., alluvial terraces) can be used to reconstruct paleo-mass-wasting events that are likely related to climatic changes (Hsieh et al., 2011, 2014). The mass-wasting events have been traced back to 14.8 ka using radiocarbon dating. Furthermore, Wu (2013) obtained a good record of the on-land depositional history during the Holocene by studying the 12 deep cores from the Lanyang Plain in northern Taiwan. In this study, we compiled data from all the three long sedimentary cores that covered the entire Holocene and combined them with the mass-wasting records and the depositional histories that were obtained from the on-land cores to illustrate the variability of EASM rainfall in Taiwan during the Holocene.

Study Area

The subtropical island of Taiwan is located off the southeastern coast of mainland China. Its climate is mainly influenced by the East Asian monsoon system, which has strong seasonal variabilities. Precipitation in Taiwan is influenced by the northeasterly monsoon during the cold season (September–April) and the southwesterly monsoon during the warm seasons (May–August) (Chen and Chen, 2003; Wang and Chen, 2008). The annual rainfall in Taiwan usually exceeds 2500 mm and can reach 3300 mm locally. More than 90% of the total rainfall occurs during the summer season. In addition to the EASM rainfall, Taiwan is often threatened by episodic typhoons that have caused enormous loss of life and property. On average, approximately four typhoons hit Taiwan every year (Chen and Chen, 2003). According to the Taiwan Central Weather Bureau,[1] the mean monthly temperature of Taiwan ranges from 14°C in January to 28°C in July.

[1]http://www.cwb.gov.tw

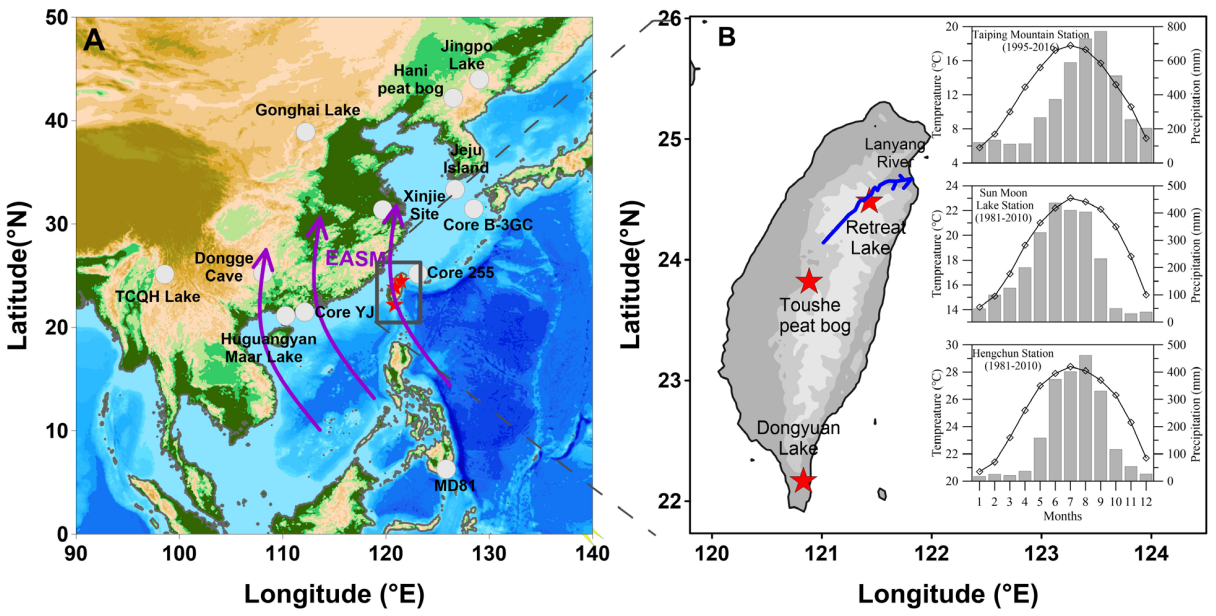

FIGURE 1 | (A) Locations of the climate records synthesized and discussed in this study. **(B)** Mean monthly temperature and precipitation in the meteorological stations near the three lakes and peat bog are provided (Taiping Mountain Station for Retreat Lake, Sun Moon Lake Station for Toushe peat bog and Hengchun Station for Dongyuan Lake).

Retreat Lake is a shallow (<1.5 m depth) sub-alpine lake with a small surface area (10^4 m^2) located in northern Taiwan (**Figure 1B**). Because its hydrological system is closed, the lake level is mainly controlled by precipitation and evaporation. The lake is filled by monsoon-related precipitation during the summer and is almost dried out during the winter. The sediment deposited in the lake is entirely derived from the surrounding mountains and consists of argillite, slate, and phyllite. The lake levels were likely higher during the early stages according to the basin shape. Retreat Lake lies on the route of the EASM and close to the main axis of the northward flowing Kuroshio Current. According to the nearest weather station in Taiping Mountain, the mean monthly temperature is 12°C and ranges from 6°C in January to 18°C in July. The mean annual precipitation is ∼4000 mm and has strong seasonal variations (ranges from 110 mm in winter to 770 mm in summer), suggesting influences dominated by the summer monsoon. Modern vegetation in the drainage basin of Retreat Lake is composed of subtropical species, dominated by *Cyclobalanopsis* and *Quercus* (Selvaraj et al., 2011).

Toushe Peat Bog is located in central Taiwan (**Figure 1B**). The mean annual rainfall in this area is 2400 mm, according to the nearest meteorological station, Sun Moon Lake. The mean monthly temperature is 19°C and ranges from 14 to 23°C. Subtropical evergreen *Lauro-Fagaceae* forests currently occupy the Toushe Basin (Liew et al., 2006). A 40 m long sediment core was previously collected from this site, covering the last glacial period (Liew et al., 2006). The bog was a lake prior to the last glacial period but became a peat bog by the early stage of the glacial period and desiccated at ∼1.7 ka BP (Liew et al., 2006).

Dongyuan Lake is located on the eastern coast of southern Taiwan (**Figure 1B**), has a surface area of 2 m × 10^4 m, and a catchment area of approximately 94 m × 10^4 m. According to the Hengchun meteorological station near Dongyuan Lake, the mean monthly rainfall ranges from 20 to 460 mm, with an annual rainfall of more than 2000 mm. More than 90% of the annual rainfall occurs during the summer season. The mean monthly air temperature ranges from 21 to 28°C, with a mean annual temperature of 25°C. The lake has been undisturbed for the last 21 ka and has become artificially managed in recent decades. The catchment of the lake is currently a swampy wetland dominated by species of *Poaceae* and *Cyperaceae*. The surrounding hills are covered by a subtropical evergreen forest (Lee and Liew, 2010).

The Lanyang River originates at Nan-Hu Mountain (3535 m above sea level) with a mean 5% gradient. The length of the Lanyang River is 73 km, with a drainage area of 980 km^2. The average annual precipitation in the Lanyang watershed is approximately 3250 mm, with rainfall being most abundant during the EASM season, particularly during typhoons. With a steep gradient and abundant rainfall, Lanyang River has one of highest sediment yields in the world, with a present-day annual sediment load of approximately 8–17 Mt/year (Jeng and Kao, 2002; Dadson et al., 2003; Milliman and Kao, 2005).

PROXY VARIATIONS AND DISCUSSION

EASM Rainfall Variation in Taiwan During the Holocene

In this synthesis, we compiled data from three individual lake and peat cores that span most of the Holocene period. The three cores were collected from the northern, central, and southern regions of Taiwan. We then compared these cores with the sedimentary history records derived from 12 on-land cores from northern Taiwan and landslide records based on accelerated mass spectrometer (AMS) ^{14}C from various locations in Taiwan (**Table 1**). For the sediment cores from the Toushe peat bog and Dongyuan Lake, we applied the interpretations presented in the original studies. The spore percentages (percentage of the sum of pollen and spores) in these two cores were used as an indicator of the moisture condition (Liew et al., 2006; Lee et al., 2010).

TABLE 1 | Paleoclimate records from Taiwan synthesized in this study.

Site name	Location	Lake areas	Core length	Time span	Dating method	Number of dates	Proxies used	References
Retreat Lake	Northern Taiwan, 24°29′N, 121°26′E	10^4 m^2	1.7 m	10.3 ka	^{14}C	10	TOC	Selvaraj et al., 2007, 2011
Toushe Basin	Central Taiwan, 23°49′N; 120°53′E	1.75 km^2	39.5 m	96 ka	^{14}C	13	Spores	Liew et al., 2006
Dongyuan Lake	Southern Taiwan, 23°49′N; 120°53′E	2 × 10^4 m^2	15 m	22 ka	^{14}C	18	Spores	Lee and Liew, 2010
Lanyang Plain	Northern Taiwan				^{14}C	116 for 12 cores	Sedimentation rate	Wu, 2013
Pa-chang River	Southwestern Taiwan				^{14}C	55	Number of ^{14}C dates	Hsieh et al., 2014
Hua-tung coast	Eastern Taiwan				^{14}C	34	Number of ^{14}C dates	Hsieh et al., 2011
Trunk Cho-shui River and Chen-yeo-lan River	Central-south Taiwan				^{14}C	25	Number of ^{14}C dates	Hsieh and Chyi, 2010
Lao-nung River	Central-south Taiwan				^{14}C	22	Number of ^{14}C dates	Hsieh and Chyi, 2010
Nan-tzu-hsien River	Southwestern Taiwan				^{14}C	7	Number of ^{14}C dates	Hsieh et al., 2012

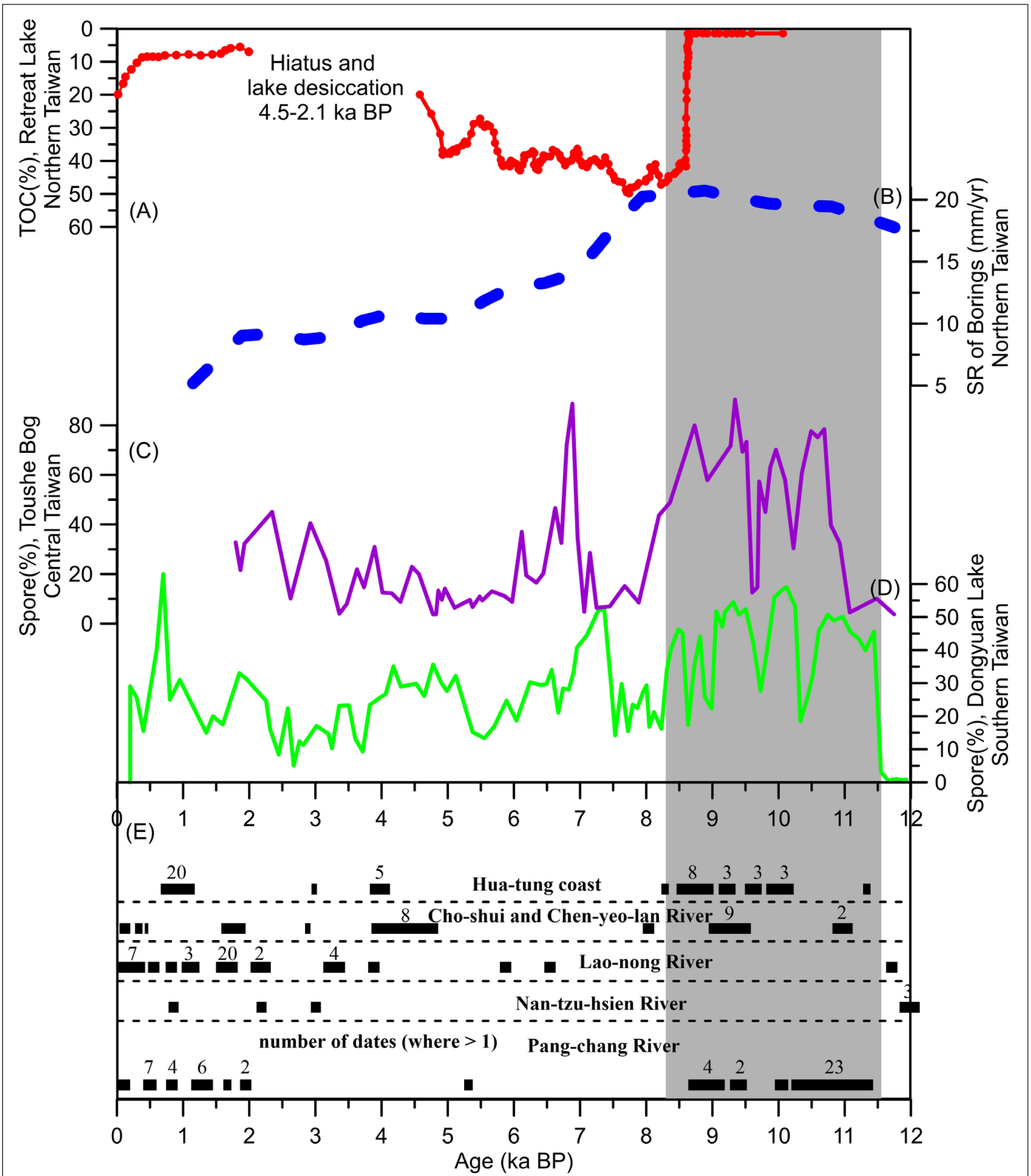

FIGURE 2 | Paleoclimate records from Taiwan. **(A)** TOC record from Retreat Lake (Selvaraj et al., 2011). **(B)** Variations in sedimentation rate from on-land cores in northern Taiwan (The blue dashed line, Wu, 2013). **(C)** Record of spore percentages from Toushe Basin (Liew et al., 2006). **(D)** Record of spore percentages from Dongyuan Lake (Lee and Liew, 2010). **(E)** Available radiocarbon dates derived from mass-wasting sequences compiled by Hsieh et al. (2014). Bars represent 1σ calibrated ranges or their combinations where more than one set of data are available. The numbers (>1) of dates are shown above the bars. The gray bar highlights the EASM rainfall maximum during the early Holocene.

However, the total organic carbon (TOC) content of the sediment core from Retreat Lake was used directly as an indicator of precipitation in the original studies (Selvaraj et al., 2007, 2011), which should be suspected. The extremely high TOC content during the middle Holocene was interpreted to represent a significantly increased summer monsoon rainfall (Selvaraj et al., 2007, 2011). However, the TOC proxy has been suggested to be sensitive to hydrological changes from peat conditions (high TOC) to a lacustrine status (low TOC) in southern China (Zhou et al., 2004). The much higher TOC content of the Retreat Lake during the middle Holocene might reflect a drier condition. This means that the water availability for Retreat Lake during the middle Holocene was low compared those during 10.3–8.6 ka BP and 2.1 ka BP to the present (**Figure 2A**). The C/N ratios in the same core (Selvaraj et al., 2011) also point to a lake status during the early Holocene and the last 2 ka but a mire status during the middle Holocene.

Records from Taiwan through the Holocene are compiled in **Figure 2**. As mentioned above, the TOC proxy in Retreat Lake might reflect the changes of relatively dry swampy peat and wet lacustrine mud sequences. The lower TOC content from 10.3–8.6 ka BP in Retreat Lake might suggest higher water availability due to wet conditions (**Figure 2A**). The percentages of Spores in the Toushe Basin and Dongyuan Lake exhibit sharp increases at around 11.5 ka BP, indicating an intensification of the EASM after the Younger Dryas event. The percentages of spores in both lakes remained high until ∼8.2 ka BP, indicating high summer monsoon rainfall amounts during the early Holocene. Several centennial-scale oscillations punctuated this period (at 10.5, 9.7, and 9.2 ka BP) (**Figures 2C,D**). Moreover, the mass-wasting records show that the largest mass-wasting activity in Taiwan occurred during the early Holocene (**Figure 2E**, 11.3–8.7 ka BP). These mass-wasting events collectively created extensive alluvial terraces (Hsieh et al., 2014). Although earthquakes can initiate mass-wasting, the synchronicity of the ages of the terraces constructed among different landforms prefer frequent heavy rain associated with the enhanced EASM rather than earthquakes for the genesis of these mass-wasting events (Hsieh et al., 2014). Moreover, the sediment record based on the 12 on-land cores from the Lanyang Plain in northern Taiwan suggests that particularly high accumulation rates occurred at 12–8 ka BP (**Figure 2B**), which were mainly induced by increased summer monsoon rainfall (Wu, 2013). According to these observations, the records from Taiwan collectively show an early Holocene EASM rainfall maximum (∼11.5–8 ka BP).

The transition from lacustrine sediments to peat deposits are abrupt at 8.6 ka BP (drastic increase in TOC content) for Retreat Lake might reflect a decreased water availability due to drier conditions (**Figure 2A**). The sedimentation rate of on land cores from Lanyang Plain exhibit a decreasing trend since 8 ka BP (**Figure 2B**), which might attribute to a decreasing precipitation. Both of the spore records from central and southern Taiwan suggest a decreased EASM rainfall since 8 ka BP, with a wet excursion at ∼7 ka BP (**Figures 2C,D**). Strikingly, the radiocarbon dates of the mass-wasting sequences also decreased since 8 ka BP. The driest interval occurred at ∼4–2 ka BP, which is most pronounced in the records from Retreat Lake and Dongyuan Lake. Retreat lake totally dried up during 4.5–2.1 ka BP as reflected by a hiatus during this interval, which is attributable to a collapse of the EASM at that time (Selvaraj et al., 2007, 2011). Although the spore record in the Toushe basin shows a slightly increasing trend since 3.3 ka BP, the dry interval during 4–2 ka BP has been widely reported in many other records from Taiwan (Liew and Huang, 1994; Chen and Wu, 1999; Wenske et al., 2011; Liew et al., 2014; Wang et al., 2015). Over the last two millennia, both the TOC record from Retreat Lake in northern Taiwan and the spore percentage record from Dongyuan Lake in southern Taiwan suggest an increased EASM rainfall (**Figures 2A,C**). Additionally, a significant increase in the number of radiocarbon dates of the mass-wasting sequences since 2 ka BP (**Figure 2E**) likely suggests that more landslide events occurred and were probably induced by frequent heavy rainfall. However, the sedimentation rate of on land cores from Lanyang Plain further decreased during last 2 ka (**Figure 2B**), which may be ascribed to the strong influences of human activity.

Large uncertainties in the reconstructions of Holocene EASM rainfall in Taiwan may exist due to the small number of records available. Moreover, uncertainties might also be raised from the different proxies used as EASM rainfall indicators for different sites (i.e., TOC for northern Taiwan and spore percentages for central and southern Taiwan). The different proxies used as precipitation indicators could be complicated by additional factors such as sampling resolution, local surface processes, and climatic sensitivity to the large-scale climatic forcing factors for each individual proxy. For example, the wet excursion at ∼7 ka BP registered in pollen records from central and southern Taiwan is not detected in TOC records from northern Taiwan. This discrepancy might be caused by the climatic sensitivity of different proxies. Despite the large uncertainties in their details, the general consistency in temporal patterns among different records indicate that these records can be used for regional comparisons.

Early Holocene EASM Rainfall Maximum in Taiwan and Spatiotemporal Pattern of the Holocene EASM Rainfall Maximum Across China

A detailed comparison of EASM proxies from Taiwan with other regional paleoclimate records is shown in **Figure 3**. The temporal pattern of the EASM rainfall during the Holocene, registered in archives from Taiwan, appears to vary in agreement with other monsoon rainfall records from southern China, collectively suggesting an early Holocene EASM rainfall maximum and a relatively drier middle to late Holocene (**Figure 3**). Well-dated high-resolution pollen records from Huguangyan Maar Lake clearly show an early Holocene EASM maximum (11.5–8 ka BP) and a relatively dry middle to late Holocene (**Figure 3E**; Wang et al., 2016; Sheng et al., 2017). Small grain-size fractions from Tengchongqinghai Lake in southwestern China, which have been interpreted as an indicator of monsoon precipitation (Zhang et al., 2017), also show similar trends than the records from Taiwan throughout the Holocene, with an early Holocene rainfall maximum (**Figure 3F**). It is worth noting that the general trend of

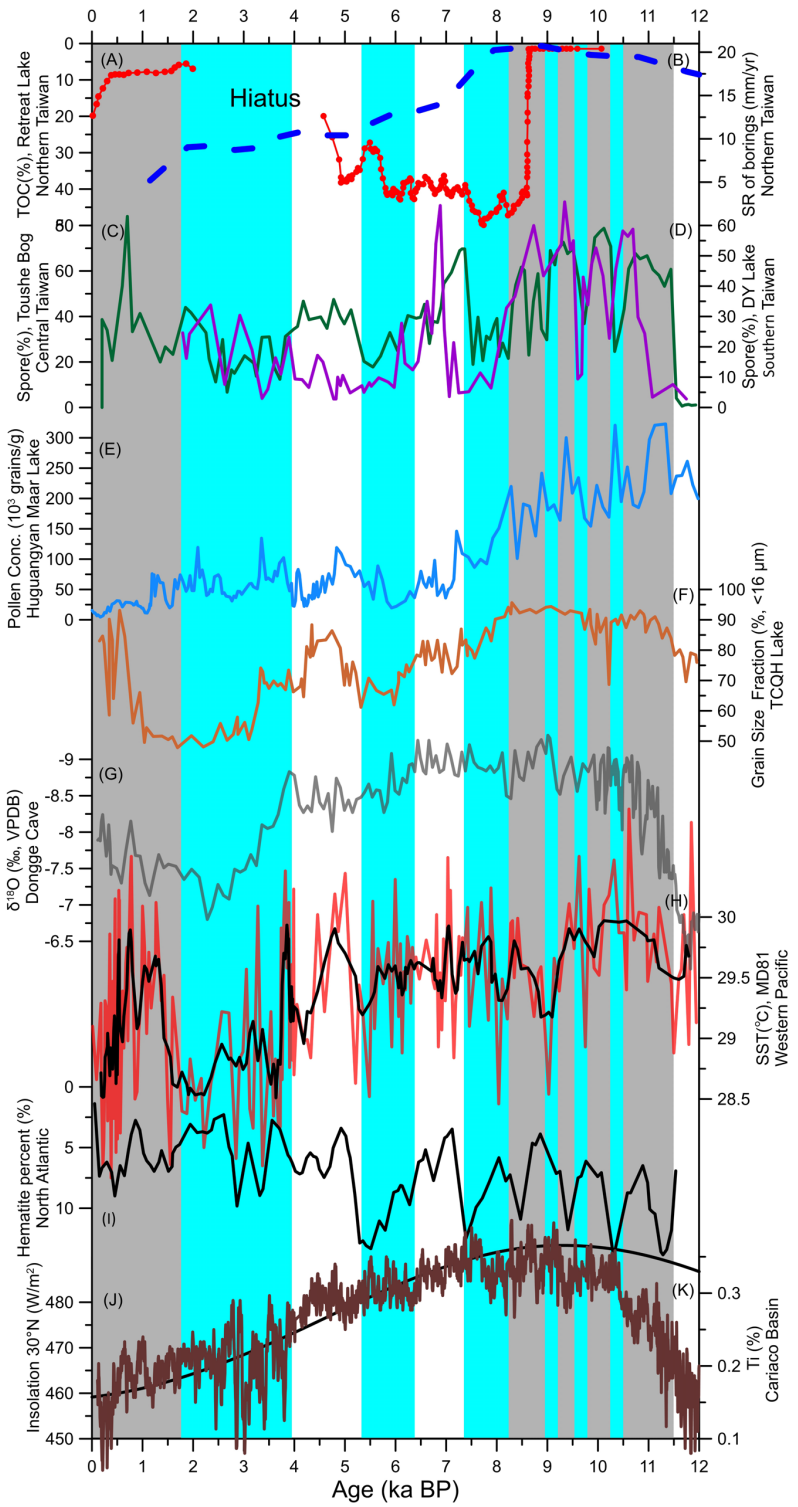

FIGURE 3 | Comparisons of paleoclimate records from Taiwan **(A–D)** with regional and global climatic records **(E–K)**. **(A)** TOC record from Retreat Lake (Selvaraj et al., 2011). **(B)** Variations in sedimentation rate from on-land cores in northern Taiwan (The blue dashed line, Wu, 2013). **(C)** Record of spore percentage from Toushe Basin (The purple line, Liew et al., 2006). **(D)** Record of spore percentage from Dongyuan Lake (The green line, Lee and Liew, 2010). **(E)** Variations in pollen concentrations from Huguangyan Maar Lake (Wang et al., 2016). **(F)** Small grain size contents from Tengchongqinghai Lake. **(G)** Speleothem $\delta^{18}O$ records from Dongge (Dykoski et al., 2005). **(H)** SST records from the MD81 site in the western tropical Pacific (Stott et al., 2004). **(I)** Hematite percentages in the North Atlantic (Bond et al., 2001). **(J)** Summer insolation at 30°N (The black line, Berger and Loutre, 1991). **(K)** Ti records from the Cariaco Basin, off the coast of Venezuela (The brown line, Haug et al., 2001). The gray bars highlight the early Holocene rainfall maximum and the "2-ka shift." The cyan bars indicate dry events.

EASM rainfall was punctuated by a series of centennial-timescale dry events (10.5, 9.7, and 9.2 ka BP) that have also been identified in various paleoclimatic records from southern China (Wang et al., 2016; Yang et al., 2019; Xu et al., 2020). These events coincide with low sea surface temperature (SST) events in the Western Pacific Warm Pool (WPWP; **Figure 3H**; Stott et al., 2004) and may correspond to North Atlantic ice-rafting events (**Figure 3I**; Bond, 1997; Bond et al., 2001). The in-phase pattern and consistencies in timing of these oscillations may suggest a strong teleconnection between the climate systems in low latitude and northern high latitude regions.

It has previously been assumed that precession-induced changes in the Northern Hemisphere summer insolation (NHSI) modulated EASM rainfall variations on an orbital timescale during the Holocene (Wang et al., 2001, 2017; Cheng et al., 2016; Lu et al., 2019; Yang et al., 2019; Zhang et al., 2019). The monsoon rainfall records from Taiwan and other records from southern China do track changes in the NHSI, showing an increased summer rainfall during the early Holocene and decreased summer rainfall during the middle to late Holocene (**Figure 3**). Asynchronous responses of surface temperatures over the land and ocean to insolation heating generate enhanced land–ocean thermal gradients and increased onshore moist air flow in the summer during precession maxima, resulting in increased EASM rainfall during the early Holocene. Furthermore, elevated NHSI during the early Holocene (**Figure 3J**) may have induced higher SSTs in the WPWP (**Figure 3F**; Stott et al., 2004), causing an elevated seawater evaporation rate and a northward migration of the mean annual location of the Intertropical Convergence Zone (ITCZ; **Figure 3K**). This would have enhanced monsoon circulation and brought a large amount of evaporated water vapor from tropical and subtropical oceanic regions to the East Asian continent, which in turn caused more summer rainfall in subtropical monsoonal East Asia (Stott et al., 2004; Sun and Feng, 2013; Li et al., 2018; Lu et al., 2019). However, the changes in the NHSI and SSTs of the WPWP cannot explain all of the observed EASM rainfall variability during the Holocene or the existence of the spatiotemporal heterogeneity of EASM rainfall in China (Chen F. et al., 2015; Lu et al., 2019; Xu et al., 2020).

As mentioned above, the monsoon rainfall records from southern China collectively show an early Holocene rainfall maximum at ∼11.5–8 ka BP. However, quantitative reconstructions of annual and summer rainfall amounts, based on high-resolution pollen records from the Xinjie site on the lower reaches of the Yangtze River, indicate that the maximum summer rainfall occurred between ∼10–6 ka BP (**Figure 4**; Lu et al., 2019), which is slightly later than records from southern China. Li et al. (2018) reported a similar pattern (EASM rainfall maximum at ∼10–7 ka BP) based on three high-resolution fossil pollen sequences from the lower Yangtze region ∼220 km west of the Xinjie site. Moreover, paleoclimate records from arid/semi-arid northern China exhibit a very different pattern, indicating a middle Holocene EASM rainfall maximum (Lu et al., 2013; Wang and Feng, 2013; Li et al., 2014; Wang H. et al., 2014; Chen F. et al., 2015; Guo et al., 2018). For example, a quantitative reconstruction of Holocene EASM rainfall, based on a well-dated high-resolution pollen record from

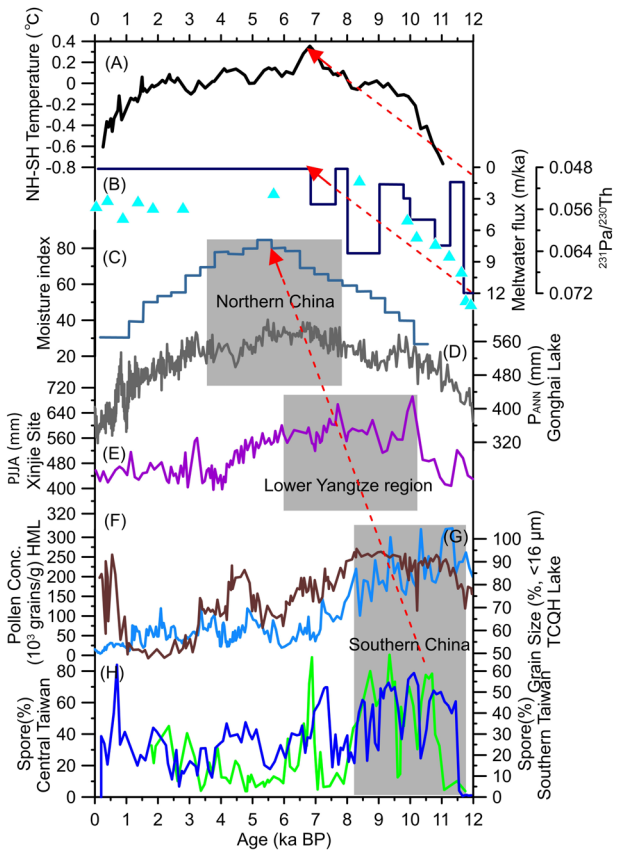

FIGURE 4 | Comparisons of the summer monsoon rainfall maximum across China. **(A)** North–South hemisphere temperature gradients (McGee et al., 2014). **(B)** Meltwater flux in the Northern Hemisphere in TRACE21 (dark blue line, Liu et al., 2014a) and ^{231}Pa/^{230}Th ratio in Western subtropical Atlantic (cyan triangles), a proxy for the AMOC (McManus et al., 2004). **(C)** Synthesized moisture index for arid/semiarid northern China (Li et al., 2014). **(D)** Annual rainfall from Gonghai Lake, northern China (Chen F. et al., 2015). **(E)** Summer rainfall reconstructions for the Xinjie site in the lower Yangtze region (Lu et al., 2019). **(F)** Variations in pollen concentrations from Huguangyan Maar Lake (The blue line, Wang et al., 2016). **(G)** Small grain size contents from Tengchongqinghai Lake (The brown line, Zhang et al., 2017). **(H)** Records of spore percentages from Toushe Basin (The green line, Liew et al., 2006) and from Dongyuan Lake (The dark blue line, Lee and Liew, 2010). The gray bars highlight the EASM rainfall maximum.

an alpine lake in northern China, indicates that the rainfall maximum occurred during the middle Holocene (**Figure 4**; Chen F. et al., 2015). A reconstruction of effective moisture levels, based on analyses of changes in sedimentary facies of aeolian deposits and vegetation types in the desert regions of northern China, indicates that the effective moisture reached a peak from 8–4 ka BP (**Figure 4**; Li et al., 2014). A pollen-based moisture index, synthesized from six Holocene sequences from the summer monsoon-influenced semi-arid belt, also indicates that a pronounced middle Holocene EASM rainfall maximum occurred at ∼8.5–4.5 ka BP (Wang and Feng, 2013).

To investigate the spatial patterns of the Holocene EASM rainfall maximum across China, we compared the rainfall records

from southern China with those from the lower Yangtze region and northern China (**Figure 4**). We found apparent time-transgressive onsets and terminations of the Holocene rainfall maximum between 11.5 and 8 ka BP in southern China, 10–6 ka BP for the lower reaches of the Yangtze region, and 8–4 ka BP for northern China. Increasing evidence and model results suggest that additional forcing mechanisms may also modulate the EASM rainfall patterns, such as westerlies and Western Pacific subtropical high (WPSH; Chiang et al., 2015; Kong et al., 2017; Zhang et al., 2018; Xu et al., 2020). Unlike the tropical Indian summer monsoon, the EASM has more complex moisture sources and rainfall structures and is closely associated with low-level southwesterly airflow and the migration of the rain belt—known as the mei-yu (in Korean: changma, and in Japanese: baiu) front in China (Ding and Chan, 2005; Wang et al., 2008). The summer rainfall varies significantly from southern to northern China because of the seasonal migration of the mei-yu front/WPSH. It should be noted that the mei-yu rain belt lies on the northwestern flank of the WPSH. Recently, Xu et al. (2020) argued that the intensity and location of the WPSH, which are induced by inter-hemispheric and/or zonal Pacific temperature gradients, modulated the summer monsoon rainfall in subtropical China during the Holocene. In addition, the north–south displacement of the westerlies has also been proposed to be responsible for the Holocene EASM rainfall variability (Chiang et al., 2015; Sun et al., 2015; Kong et al., 2017). Based on comparisons of model results with proxy data, Sun et al. (2015) note that insolation forcing has a greater impact on the precipitation change in southern than in northern China, whereas the glacial forcing has a weaker impact in southern China compared to northern China. They argued that the different summer precipitation responses to solar insolation and glacial forcing between northern China and southern China reflect the complex dynamics of the EASM, linked to high- and low-latitude climates through migrations of westerlies and WPSH (Sun et al., 2015). Here, we propose that the time-transgressive EASM rainfall maximum from southern to northern China might be induced by the migration of the meridional location of the westerlies and WPSH, which may have been modulated by inter-hemispheric temperature gradients.

Inter-hemispheric temperature gradients (ΔT_{N-S}) are important for modulating the meridional location of the planetary atmospheric circulation systems (Toggweiler, 2009; McGee et al., 2014; Xu et al., 2019). For example, increased ΔT_{N-S} can be expected to push the northern hemisphere westerlies and the ITCZ northward and *vice versa* (McGee et al., 2014; Putnam and Broecker, 2017). The NPSH is also expected to move synchronously. From modern observations, the WPSH shifts to its northernmost location at August, when the SSTs are highest in the northern Hemisphere and lowest in the southern Hemisphere. It is reasonable to expect a northward shift of the NPSH with an increasing ΔT_{N-S}. Thus, changes in ΔT_{N-S} could potentially change the meridional location of the westerlies and WPSH and consequently modulate the rain belt migration in China, especially on long timescales. As shown in **Figure 4A**, ΔT_{N-S} was relatively lower during the early Holocene compared to the middle Holocene. The location of the westerlies and WPSH might have been sustained at a more southern location, leading to increased monsoon precipitation in southern China and a short rainy season in northern China during the early Holocene (**Figure 4**). With gradual increases in ΔT_{N-S}, the westerlies and WPSH might have shifted further north, leading to the onset of the monsoon rainfall maximum in the lower Yangtze region at ∼10 ka BP (**Figure 4**). Eventually, the westerlies and WPSH reached its northernmost location at ∼7 ka BP when the Holocene monsoon rainfall peaked in northern China (**Figure 4**). Moreover, the ice volume in the northern high latitudes was still large during the early Holocene. The melting freshwater from the Laurentide ice sheet was continuously delivered to the North Atlantic until ∼7 ka (**Figure 4B**; Carlson et al., 2008; Liu et al., 2014a). The discharge of meltwater into the North Atlantic can slow down the Atlantic meridional overturning circulation (AMOC), which can change the inter-hemispheric thermal gradient (Toggweiler, 2009; McGee et al., 2014) and shift the mean position of the westerlies and perhaps the WPSH. The more southern position of the westerlies and WPSH during the early Holocene may be responsible for the drier climate in northern China. As shown in **Figure 4B**, with the gradually diminished meltwater flux and the recovered AMOC during the early Holocene, the westerlies and WPSH might also shift northward gradually. The northward shift of the WPSH is generally accompanied by a stronger southerly wind over eastern China, which increases the monsoon rainfall in northern China (Liu et al., 2014b). Paleoclimate Modeling Intercomparison Project (PMIP) models also simulated a stronger EASM than baseline EASM during the middle Holocene (Jiang et al., 2013).

Similar to our observations, a time-transgressive termination of the African Humid Period during the Holocene has been reported and was attributed to decreasing summer insolation and the gradual southward migration of the tropical rain belt (Shanahan et al., 2015). An et al. (2000) reported a time-transgressive EASM rainfall maximum from northwest to southeast China throughout the Holocene, which was attributed to the southeastward shift of the monsoon front and weakening summer insolation. However, due to the poor chronological controls and low sampling resolution, the timing of the EASM rainfall maximum is not well constrained. Subsequent evidence from the last 20 years also does not support a southward shift of the maximum precipitation belt. Recently, Zhou et al. (2016) suggested the opposite pattern, based on tree pollen records across China, with a marked northward migration of the onset of the "Holocene optimum" in East Asia, from ∼10 ka BP in southern China to ∼6 ka BP in northeastern China. However, the "Holocene Optimum" in their study depended on the thermal or moisture condition in different regions, which may not solely reflect the summer monsoon rainfall maximum (Zhou et al., 2016). In this study, we focused on the rainfall maximum without considering the temperature. As shown in **Figure 4**, well-dated and quantitative reconstructions of EASM rainfall records (from the Gonghai Lake and Xinjie site) were selected as the representative records for northern China and the lower reaches of the Yangtze region. Although palynological records from Taiwan are not quantitative reconstructions, like those from the Gonghai Lake and Xinjie site, similar temporal patterns

between spore percentages, sedimentary history records, and mass-wasting records across Taiwan (which are independent with temperature condition) suggest that the spore percentages can faithfully reflect the EASM rainfall variations in Taiwan. Moreover, pollen analyses of the same records based on a biomization technique (Liew et al., 2006; Lee et al., 2010) pointed out that the Holocene Thermal Optimum in Taiwan occurred at ∼8–4 BP which is different from the early Holocene rainfall maximum indicated by spore percentages. Additional quantitative reconstructions of summer precipitation, especially in southern China, are needed in the future to illustrate the spatial and temporal variabilities of EASM precipitation during the Holocene.

Drought in Taiwan During 4–2 ka BP and a Possible Link to El Niño-Southern Oscillation

During the late Holocene, the EASM rainfall exhibits a more complex pattern. A catastrophic drought occurred in Taiwan from 4 to 2 ka BP, followed by an increase in EASM rainfall during the last 2 ka. The dry interval at 4–2 ka BP has also been reported in other records from Taiwan (Liew and Huang, 1994; Chen and Wu, 1999; Wenske et al., 2011; Wang et al., 2015). In addition, this dry interval has been broadly reported in records from coastal East Asia and/or subtropical East Asia (**Figure 4**). Chen R. et al., 2015 reported a dry interval between ∼3.6 and 2.1 ka BP based on a sediment record retrieved from Jingpo Lake in northeastern China (**Figure 5A**). Similar results have also been obtained from a peat core from the Haini Peat in northeastern China (**Figure 5B**; Hong et al., 2005). Multi-proxy evidence obtained from a sediment core retrieved from the Mulyoungari crater swamp on Jeju Island, South Korea, also suggests a dry interval between 4.3 and 1.9 ka BP (**Figure 5C**; Park et al., 2016). Near cessation of peat deposition and negligible sedimentation between 4 and 2 ka BP in the Kimotsuki lowland delta plain of Southern Japan, suggests greatly reduced precipitation (Ishii, 2018). Multi-proxy evidence from a marine sediment core from the inner shelf of the northern South China Sea also suggests reduced summer rainfall at 3.5–2 ka BP (**Figure 5E**; Huang C. et al., 2018). The grain size fraction in Tengchongqinghai Lake (Zhang et al., 2017) and the redness values in Qinghai Lake (Ji et al., 2005) also suggest decreased summer monsoon rainfall. Moreover, the dry interval from 4 to 2 ka BP can also be identified in stalagmite $\delta^{18}O$ records, such as those from Dongge Cave (**Figure 3H**; Dykoski et al., 2005) in southern China, Jiuxian Cave in central China (Cai et al., 2010), Tianmen Cave on the southern Tibetan Plateau (Cai et al., 2012), and Qunf Cave in southern Oman (Fleitmann, 2003).

Since the water vapor supply for the EASM region is mainly derived from the WPWP (Ding and Chan, 2005; Liu et al., 2014b), variations in SST in the WPWP are likely to influence the water vapor availability and hence summer precipitation in East Asia. Furthermore, increased El Niño-Southern Oscillation (ENSO) activity since the late Holocene might also have a significant impact on the EASM rainfall (Conroy et al., 2008; Cai et al., 2010; Selvaraj et al., 2011; Park et al., 2016; Xu et al., 2016; Huang C. et al., 2018). The catastrophic droughts at 4–2 ka may have coincided with decreased SSTs in the WPWP and increased ENSO activity (**Figures 5H,I**). It has been reported that the frequency and intensity of ENSO significantly increased since ∼4 ka BP (**Figure 5I**; Rein, 2007; Conroy et al., 2008). Reconstructions suggest that El Niño events occurring at 4–2 ka BP were among the strongest in the Holocene (Rein, 2007). Cores from coral reef frameworks along an upwelling gradient in the tropical eastern Pacific show that reef ecosystems in the tropical eastern Pacific collapsed between 4 and 1.5 ka BP, which coincided with greatly increased El Niño events (Toth et al., 2012). It is likely that El Niño-like conditions persisted during 4–2 ka BP. During El Niño-like conditions, a decline in the SST of the WPWP due to the amount of warm water mass brought to the eastern tropical Pacific, may have induced less formation of water vapor over the WPWP and thus less moisture was available for the subtropical East Asian monsoon region (Chen R. et al., 2015; Park et al., 2016; Huang C. et al., 2018; Li et al., 2018). In addition, a significantly southward shift of the ITCZ with high variabilities at 4–2 ka BP (**Figure 3K**) might also have contributed to decreased EASM rainfall. Moreover, a corresponding attenuation of warm Kuroshio currents at 4–2 ka BP (as indicated by a decrease in the abundance of foraminifera *Pulleniatina obliquiloculata* in sediment cores from the Okinawa Trough, **Figure 5D**) might also have significantly decreased the summer monsoon rainfall in Taiwan and northeastern Asia (**Figure 5**; Selvaraj et al., 2007; Park et al., 2016).

The 2-ka Shift

For the past 2 ka, it seems the EASM rainfall has increased according to the records from Taiwan. Proxies from both northern and southern Taiwan suggest increased summer precipitation. Moreover, mass-wasting records also indicate that landslide events have increased significantly during last 2 ka. A strengthening of the Asian summer monsoon for the last 2 ka was identified in numerous paleoclimatic records from monsoonal regions in Asia and seems to be a robust feature (Zhao et al., 2013). Most of these monsoon rainfall records in their synthesis are from subtropical East Asia (see in Zhao et al., 2013). Recently, Cheng et al. (2016) noted that the Asian summer monsoon registered in stalagmite records deviated from the downward trend in NHSI through the Holocene over the last 2 ka. They termed this late Holocene anomaly as the "2-ka shift." They also suggested that this "shift" anti-correlated with monsoon records from South America and some temperature records from Antarctica, a scenario very similar to the millennial-scale events throughout the past glacial-interglacial cycles, which is mainly caused by changes in the intensity of the AMOC. Cheng et al. (2016) suggested that a possible increase in the intensity of the AMOC may explain the "2-ka shift." Moreover, progressive increases in the concentrations of greenhouse gases have been proposed as being responsible for the intensification of the Asian monsoon since 2 ka BP (Zhao et al., 2013; Lu et al., 2019). However, records from northern China show a persistently decreasing trend during the late Holocene (**Figure 4**; Li et al., 2014; Chen F. et al., 2015) which likely contradicts with the increased intensity of the AMOC and greenhouse gas

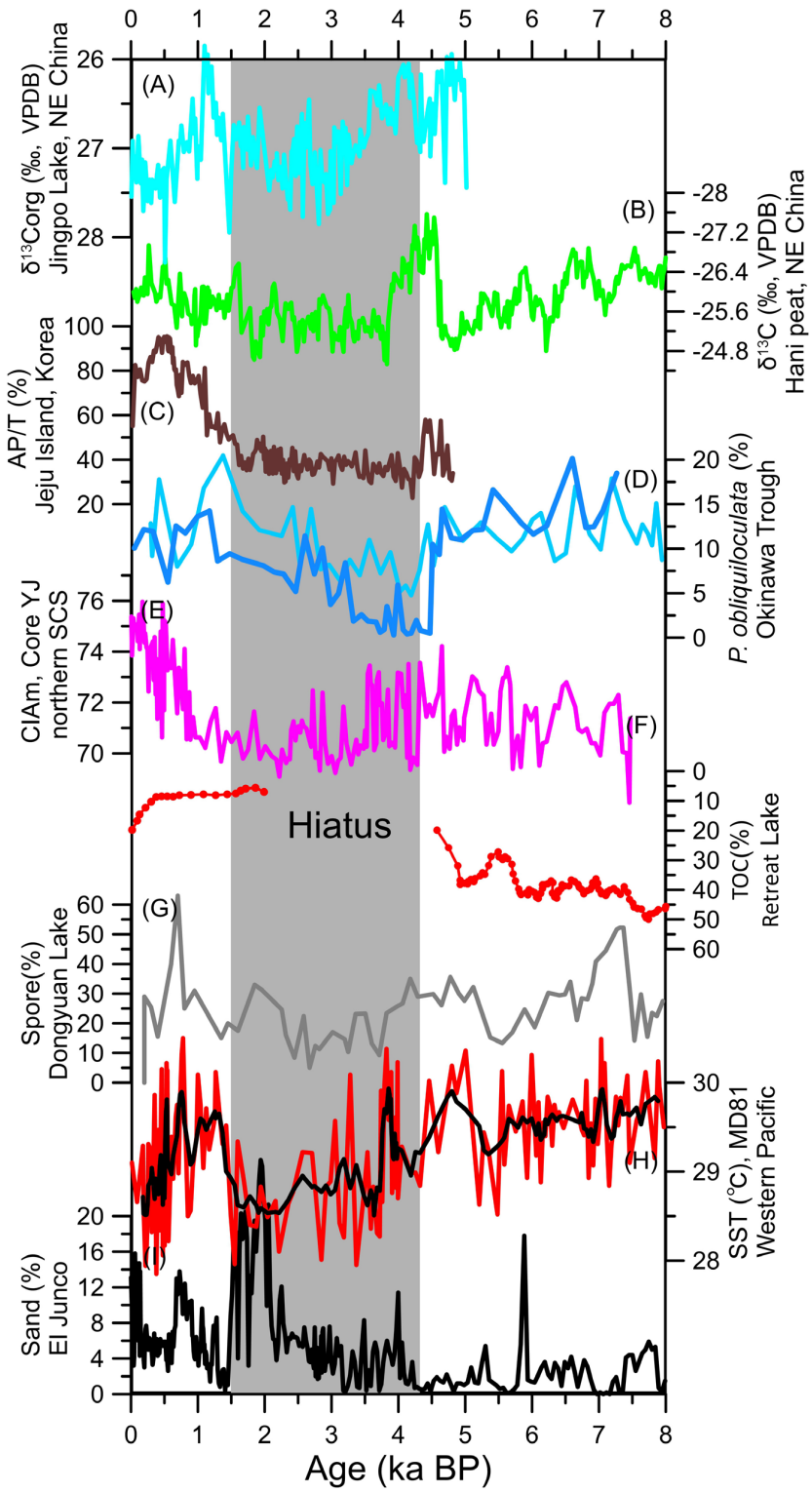

FIGURE 5 | Records showing the prolonged dry interval from 4 to 2 ka BP. **(A)** δ^{13}Corg values from Jingpo Lake, northeastern China (Chen R. et al., 2015). **(B)** Cellulose δ^{13}C record from Hani peat (Hong et al., 2005). **(C)** Arboreal pollen/total pollen (AP/T) ratios from Jeju Island, South Korea (Park et al., 2016). **(D)** Abundances of the foraminifera *Pulleniatina obliquiloculata* from the Okinawa Trough (Jian et al., 2000). **(E)** Records of chemical weathering proxies (CIAm) from the northern inner shelf of the South China Sea (Huang C. et al., 2018). **(F)** TOC record from Retreat Lake (Selvaraj et al., 2007). **(G)** Record of spore percentages from Dongyuan Lake (Lee and Liew, 2010). **(H)** SST records from the MD81 site in the western tropical Pacific (Stott et al., 2004). **(I)** Sand percentages from El Junco Lake, eastern tropical Pacific (Conroy et al., 2008).

forcing. We propose that the "2-ka shift" might also, or at least partly, be induced by a southward shift of the WPSH, associated with a gradual decrease in ΔT_{N-S} during the late Holocene (**Figure 4**). This proposal is supported by the opposing trends of EASM rainfall between northern and southern China during the last 2 ka.

CONCLUSION

In this study, we integrate the lake and peat records that cover the entire Holocene epoch with mass-wasting records and depositional history records from Taiwan, to illustrate the variations in EASM rainfall in Taiwan throughout the Holocene. Records from Taiwan indicate an early Holocene EASM rainfall maximum and agree with other EASM records from southern China. We suggest that the early Holocene EASM rainfall maximum in southern China was mainly forced by a higher NHSI and elevated SSTs in the WPWP. In addition, we observed the transgressive timing of the EASM rainfall maximum across China, which may be due to the latitudinal shift of the westerlies and WPSH that were induced by a gradually increasing ΔT_{N-S} and diminishing ice volume during the early to middle Holocene. Combined with other records from the East Asian monsoon region and the tropical Pacific, we found a pronounced dry interval at 4–2 ka BP, which probably resulted from prevailing El Nino-like conditions and drastically decreased SSTs in the WPWP during this interval. For the last 2 ka, the EASM has increased abnormally as compared to the downward trend of the NHSI. Besides the changes in the intensity of AMOC and/or increased concentrations of greenhouse gases during the last 2 ka, a southward shifting WPSH, associated with a gradual decrease ΔT_{N-S} during the late Holocene, might have contributed to the EASM rainfall anomaly in southern China. The meridional SST gradients are expected to increase as global warming continues (Rind, 1998), which might cause a northward shift of the WPSH (analogous to the conditions during the middle Holocene), leading to an increased EASM rainfall in northern China and a decreased EASM rainfall in southern China. Our discussions on the spatiotemporal variability of the Holocene EASM rainfall, which are helpful for understanding the potential forcing mechanisms for EASM variations and predicting future hydroclimate changes in East Asia under the scenario of global warming. However, well-dated high-resolution records of Holocene EASM rainfall in subtropical East Asia are still sparse. Additional high-resolution and quantitative reconstructions of EASM rainfall in low latitude regions are warranted to illustrate the detailed information of the spatiotemporal variabilities in the EASM precipitation during the Holocene. More simulation works with high resolution are also needed in the future to investigate the possible forcing mechanisms on the spatiotemporal heterogeneity of EASM rainfall during the Holocene.

DATA AVAILABILITY STATEMENT

The raw data supporting the conclusions of this article will be made available by the authors, without undue reservation, to any qualified researcher.

AUTHOR CONTRIBUTIONS

XD conceived the research idea and wrote the manuscript with contributions from all authors. LZ discussed and conducted the figure drafting for this manuscript. XZ and S-JK carried out a lot of the paleoenvironmental explanations and improved the manuscript. All authors contributed to the article and approved the submitted version.

FUNDING

This research was funded by the school-level general research project of North Minzu University (2020XYZSK03), the Doctoral Scientific Research Foundation of the North Minzu University, and the National Natural Science Foundation of China (NSFC 41806062).

ACKNOWLEDGMENTS

We acknowledge the editor HX and the reviewers for their insightful comments and constructive suggestions which significantly improved this manuscript.

REFERENCES

An, Z., Liu, T., Lu, Y., Porter, S. C., Kukla, G., Wu, X., et al. (1990). The long-term paleomonsoon variation recorded by the loess-paleosol sequence in Central China. *Quat. Int.* 7, 91–95. doi: 10.1016/1040-6182(9)90042-3

An, Z., Porter, S., Kutzbach, J., Wu, X., Wang, S., Liu, X., et al. (2000). Asynchronous Holocene optimum of the East Asian monsoon. *Quat. Sci. Rev.* 19, 743–762. doi: 10.1016/S0277-3791(99)00031-1

An, Z., Wu, G., Li, J., Sun, Y., Liu, Y., Zhou, W., et al. (2015). Global monsoon dynamics and climate change. *Annu. Rev. Earth Planet. Sci.* 43, 29–77. doi: 10.1146/annurev-earth-060313-054623

Baker, A. J., Sodemann, H., Baldini, J. U. L., Breitenbach, S. F. M., Johnson, K. R., van Hunen, J., et al. (2015). Seasonality of westerly moisture transport in the East Asian summer monsoon and its implications for interpreting precipitation δ18O. *J. Geophys. Res-Atmos.* 120, 5850–5862. doi: 10.1002/2014jd022919

Beck, J. W., Zhou, W., Li, C., Wu, Z., White, L., Xian, F., et al. (2018). A 550,000-year record of East Asian monsoon rainfall from 10Be in loess. *Science* 360, 877–881. doi: 10.1126/science.aam5825

Berger, A., and Loutre, M. F. (1991). Insolation values for the climate of the last 10 million years. *Quat. Sci. Rev.* 10, 297–317. doi: 10.1016/0277-3791(91)90033-q

Bond, G. (1997). A pervasive millennial-scale cycle in north atlantic holocene and glacial climates. *Science* 278, 1257–1266. doi: 10.1126/science.278.5341.1257

Bond, G., Kromer, B., Beer, J., Muscheler, R., Evans, M. N., Showers, W., et al. (2001). Persistent solar influence on North Atlantic climate during the Holocene. *Science* 294, 2130–2136. doi: 10.1126/science.1065680

Cai, Y., Tan, L., Cheng, H., An, Z., Edwards, R. L., Kelly, M. J., et al. (2010). The variation of summer monsoon precipitation in central China since the last deglaciation. *Earth Planet. Sci. Lett.* 291, 21–31. doi: 10.1016/j.epsl.2009.12.039

Cai, Y., Zhang, H., Cheng, H., An, Z., Edwards, R. L., Wang, X., et al. (2012). The Holocene Indian monsoon variability over the southern Tibetan Plateau and its teleconnections. *Earth Planet. Sci. Lett.* 335, 135–144. doi: 10.1016/j.epsl.2012.04.035

Caley, T., Roche, D. M., and Renssen, H. (2014). Orbital Asian summer monsoon dynamics revealed using an isotope-enabled global climate model. *Nat. Commun.* 5:5371. doi: 10.1038/ncomms6371

Carlson, A. E., LeGrande, A. N., Oppo, D. W., Came, R. E., Schmidt, G. A., Anslow, F. S., et al. (2008). Rapid early Holocene deglaciation of the Laurentide ice sheet. *Nat. Geosci.* 1, 620–624. doi: 10.1038/ngeo285

Chen, C.-S., and Chen, Y.-L. (2003). The rainfall characteristics of Taiwan. *Mon. Weather Rev.* 131, 1323–1341. doi: 10.1175/1520-04932003131(1323:TRCOT(2.0.CO;2

Chen, F., Xu, Q., Chen, J., Birks, H. J. B., Liu, J., Zhang, S., et al. (2015). East Asian summer monsoon precipitation variability since the last deglaciation. *Sci. Rep.* 5:11186. doi: 10.1038/srep11186

Chen, R., Shen, J., Li, C., Zhang, E., Sun, W., and Ji, M. (2015). Mid-to late-Holocene East Asian summer monsoon variability recorded in lacustrine sediments from Jingpo Lake, Northeastern China. *Holocene* 25, 454–468. doi: 10.1177/0959683614561888

Chen, J., Rao, Z., Liu, J., Huang, W., Feng, S., Dong, G., et al. (2016). On the timing of the East Asian summer monsoon maximum during the Holocene—Does the speleothem oxygen isotope record reflect monsoon rainfall variability? *Sci. China Earth Sci.* 59, 2328–2338. doi: 10.1007/s11430-015-5500-5

Chen, S.-H., and Wu, J.-T. (1999). Paleolimnological environment indicated by the diatom and pollen assemblages in an alpine lake in Taiwan. *J. Paleolimnol.* 22, 149–158. doi: 10.1023/A:1008067928365

Cheng, H., Edwards, R. L., Broecker, W. S., Denton, G. H., Kong, X., Wang, Y., et al. (2009). Ice age terminations. *Science* 326, 248–252. doi: 10.1126/science.1177840

Cheng, H., Edwards, R. L., Sinha, A., Spotl, C., Yi, L., Chen, S., et al. (2016). The Asian monsoon over the past 640,000 years and ice age terminations. *Nature* 534, 640–646. doi: 10.1038/nature18591

Cheng, H., Zhang, H., Zhao, J., Li, H., Ning, Y., and Kathayat, G. (2019). Chinese stalagmite paleoclimate researches: a review and perspective. *Sci. China Earth Sci.* 62, 1–25. doi: 10.1007/s11430-019-9478-3

Chiang, J. C. H., Fung, I. Y., Wu, C.-H., Cai, Y., Edman, J. P., Liu, Y., et al. (2015). Role of seasonal transitions and westerly jets in East Asian paleoclimate. *Quat. Sci. Rev.* 108, 111–129. doi: 10.1016/j.quascirev.2014.11.009

Conroy, J., Overpeck, J., Cole, J., Shanahan, T., and Steinitz-Kannan, M. (2008). Holocene changes in eastern tropical Pacific climate inferred from a Galápagos lake sediment record. *Quat. Sci. Rev.* 27, 1166–1180.

Dadson, S. J., Hovius, N., Chen, H., Dade, W. B., Hsieh, M.-L., Willett, S. D., et al. (2003). Links between erosion, runoff variability and seismicity in the Taiwan orogen. *Nature* 426, 648–651. doi: 10.1038/nature02150

Ding, X., Bao, H., Zheng, L., Li, D., and Kao, S. J. (2017). Lacustrine lignin biomarker record reveals a severe drought during the late Younger Dryas in southern Taiwan. *J. Asian Earth Sci.* 135, 281–290. doi: 10.1016/j.jseaes.2017.01.003

Ding, X., Zheng, L., Li, D., Yang, T.-N., Lee, T.-Q., and Kao, S.-J. (2016). Lacustrine record of centennial-and millennial-scale rainfall variability of the East Asian summer monsoon during the last deglaciation: multi-proxy evidence from Taiwan. *Palaeogeogr. Palaeoclimatol. Palaeoecol.* 450, 38–49. doi: 10.1016/j.palaeo.2016.02.048

Ding, Y., and Chan, J. (2005). The East Asian summer monsoon: an overview. *Meteorol. and Atmos. Phys.* 89, 117–142. doi: 10.1007/s00703-005-0125-z

Dong, J., Wang, Y., Cheng, H., Hardt, B., Edwards, R. L., Kong, X., et al. (2010). A high-resolution stalagmite record of the Holocene East Asian monsoon from Mt Shennongjia, central China. *Holocnene* 20, 257–264. doi: 10.1177/0959683609350393

Dykoski, C. A., Edwards, R. L., Cheng, H., Yuan, D., Cai, Y., Zhang, M., et al. (2005). A high-resolution, absolute-dated Holocene and deglacial Asian monsoon record from Dongge Cave. *China. Earth Planet. Sci. Lett.* 233, 71–86. doi: 10.1016/j.epsl.2005.01.036

Fleitmann, D. (2003). Holocene Forcing of the Indian Monsoon Recorded in a Stalagmite from Southern Oman. *Science* 300, 1737–1739. doi: 10.1126/science.1083130

Goldsmith, Y., Broecker, W. S., Xu, H., Polissar, P. J., Porat, N., Lan, J., et al. (2017). Northward extent of East Asian monsoon covaries with intensity on orbital and millennial timescales. *Proc. Natl. Acad. Sci. U.S.A.* 114, 1817–1821. doi: 10.1073/pnas.1616708114

Guo, L., Xiong, S., Ding, Z., Jin, G. Y., Wu, J., and Ye, W. (2018). Role of the mid-Holocene environmental transition in the decline of late Neolithic cultures in the deserts of NE China. *Quat. Sci. Rev.* 190, 98–113. doi: 10.1016/j.quascirev.2018.04.017

Guo, Z., Biscaye, P., Wei, L., Chen, X., Peng, S., and Liu, T. J. G. R. L. (2000). Summer monsoon variations over the last 1.2 Ma from the weathering of loess-soil sequences in China. *Geophys. Res. Lett.* 27, 1751–1754. doi: 10.1029/1999GL008419

Haug, G. H., Hughen, K. A., Sigman, D. M., Peterson, L. C., and Röhl, U. (2001). Southward migration of the intertropical convergence zone through the Holocene. *Science* 293, 1304–1308. doi: 10.1126/science.1059725

Hong, Y. T., Hong, B., Lin, Q. H., Shibata, Y., Hirota, M., Zhu, Y. X., et al. (2005). Inverse phase oscillations between the East Asian and Indian Ocean summer monsoons during the last 12000 years and paleo-El Niño. *Earth Planet. Sci. Lett.* 231, 337–346. doi: 10.1016/j.epsl.2004.12.025

Hsieh, M.-L., Ching, K.-E., Chyi, S.-J., Kang, S.-C., and Chou, C.-Y. (2014). Late Quaternary mass-wasting records in the actively uplifting Pa-chang catchment, southwestern Taiwan. *Geomorphology* 216, 125–140. doi: 10.1016/j.geomorph.2014.03.040

Hsieh, M.-L., and Chyi, S.-J. (2010). Late Quaternary mass-wasting records and formation of fan terraces in the Chen-yeo-lan and Lao-nung catchments, central-southern Taiwan. *Quat. Sci. Rev.* 29, 1399–1418. doi: 10.1016/j.quascirev.2009.10.002

Hsieh, M.-L., Lai, L. S.-H., Lin, C. D.-J., and Shyu, J. B. H. (2012). Late Quaternary landscape evolution and genesis of the 2009 catastrophic landslide in the Hsiao-lin area, southwestern Taiwan. *Geomorphology* 179, 225–239. doi: 10.1016/j.geomorph.2012.08.014

Hsieh, M.-L., Liew, P.-M., and Chen, H.-W. (2011). Early Holocene catastrophic mass-wasting event and fan-delta development on the Hua-tung coast, eastern Taiwan. *Geomorphology* 134, 378–393. doi: 10.1016/j.geomorph.2011.07.012

Hu, C., Henderson, G. M., Huang, J., Xie, S., Sun, Y., and Johnson, K. R. (2008). Quantification of Holocene Asian monsoon rainfall from spatially separated cave records. *Earth Planet. Sci. Lett.* 266, 221–232. doi: 10.1016/j.epsl.2007.10.015

Huang, C., Zeng, T., Ye, F., Xie, L., Wang, Z., Wei, G., et al. (2018). Natural and anthropogenic impacts on environmental changes over the past 7500 years based on the multi-proxy study of shelf sediments in the northern South China Sea. *Quat. Sci. Rev.* 197, 35–48. doi: 10.1016/j.quascirev.2018.08.005

Huang, X., Pancost, R. D., Xue, J., Gu, Y., Evershed, R. P., and Xie, S. (2018). Response of carbon cycle to drier conditions in the mid-Holocene in central China. *Nat. comm.* 9, 1–9. doi: 10.1038/s41467-018-03804-w

Ishii, Y. (2018). Middle to late Holocene delta plain evolution of the Kimotsuki lowland. Kyushu (southern Japan). *Palaeogeogr. Palaeoclimatol. Palaeoecol.* 502, 74–85. doi: 10.1016/j.palaeo.2018.04.025

Jeng, W. L., and Kao, S. J. (2002). Lipids in suspended matter from the human-disturbed Lanyang River, northeastern Taiwan. *Environ. Geol.* 43, 138–144. doi: 10.1007/s00254-002-0619-7

Ji, J., Shen, J., Balsam, W., Chen, J., Liu, L., and Liu, X. (2005). Asian monsoon oscillations in the northeastern Qinghai-Tibet Plateau since the late glacial as interpreted from visible reflectance of Qinghai Lake sediments. *Earth Planet. Sci. Lett.* 233, 61–70. doi: 10.1016/j.epsl.2005.02.025

Jia, G., Bai, Y., Yang, X., Xie, L., Wei, G., Ouyang, T., et al. (2015). Biogeochemical evidence of Holocene East Asian summer and winter monsoon variability from a tropical maar lake in southern China. *Quat. Sci. Rev.* 111, 51–61. doi: 10.1016/j.quascirev.2015.01.002

Jian, Z., Wang, P., Saito, Y., Wang, J., Pflaumann, U., Oba, T., et al. (2000). Holocene variability of the Kuroshio current in the Okinawa Trough, northwestern Pacific Ocean. *Earth Planet. Sci. Lett.* 184, 305–319. doi: 10.1016/S0012-821X(00)00321-6

Jiang, D., Lang, X., Tian, Z., and Ju, L. (2013). Mid-Holocene East Asian summer monsoon strengthening: insights from Paleoclimate Modeling Intercomparison

Project (PMIP) simulations. *Palaeogeogr. Palaeoclimatol. Palaeoecol.* 369, 422–429. doi: 10.1016/j.palaeo.2012.11.007

Kong, W., Swenson, L. M., and Chiang, J. C. H. (2017). Seasonal Transitions and the Westerly Jet in the Holocene East Asian Summer Monsoon. *J. Climate* 30, 3343–3365. doi: 10.1175/JCLI-D-16-0087.1

Lee, C.-Y., and Liew, P.-M. (2010). Late Quaternary vegetation and climate changes inferred from a pollen record of Dongyuan Lake in southern Taiwan. *Palaeogeogr. Palaeoclimatol. Palaeoecol.* 287, 58–66. doi: 10.1016/j.palaeo.2010.01.015

Lee, C. Y., Liew, P. M., and Lee, T. Q. (2010). Pollen records from southern Taiwan: implications for East Asian summer monsoon variation during the Holocene. *Holocene* 20, 81–89. doi: 10.1177/0959683609348859

Li, J., Dodson, J., Yan, H., Wang, W., Innes, J. B., Zong, Y., et al. (2018). Quantitative Holocene climatic reconstructions for the lower Yangtze region of China. *Clim. Dyn.* 50, 1101–1113. doi: 10.1007/s00382-017-3664-3

Li, Q., Wu, H., Yu, Y., Sun, A., Marković, S. B., Guo, Z. J. G., et al. (2014). Reconstructed moisture evolution of the deserts in northern China since the Last Glacial Maximum and its implications for the East Asian Summer Monsoon. *Glob. Planet. Change* 121, 101–112. doi: 10.1016/j.gloplacha.2014.07.009

Liew, P.-M., and Huang, S.-Y. (1994). A 5000-year pollen record from Chitsai Lake, central Taiwan. *Terr. Atmos. Oceanic Sci.* 5, 411–419. doi: 10.3319/TAO.1994.5.3.411(PAGES)

Liew, P. M., Lee, C. Y., and Kuo, C. M. (2006). Holocene thermal optimal and climate variability of East Asian monsoon inferred from forest reconstruction of a subalpine pollen sequence. Taiwan. *Earth Planet. Sci. Lett.* 250, 596–605. doi: 10.1016/j.epsl.2006.08.002

Liew, P.-M., Wu, M.-H., Lee, C.-Y., Chang, C.-L., and Lee, T.-Q. (2014). Recent 4000 years of climatic trends based on pollen records from lakes and a bog in Taiwan. *Quat. Int.* 349, 105–112. doi: 10.1016/j.quaint.2014.05.018

Liu, H., Gu, Y., Huang, X., Yu, Z., Xie, S., and Cheng, S. (2019). A 13,000-year peatland palaeohydrological response to the ENSO-related Asian monsoon precipitation changes in the middle Yangtze Valley. *Quat. Sci. Rev.* 212, 80–91. doi: 10.1016/j.quascirev.2019.03.034

Liu, J., Chen, J., Zhang, X., Li, Y., Rao, Z., and Chen, F. (2015). Holocene East Asian summer monsoon records in northern China and their inconsistency with Chinese stalagmite δ18O records. *Earth-Sci. Rev.* 148, 194–208. doi: 10.1016/j.earscirev.2015.06.004

Liu, Z., Lu, Z., Wen, X., Otto-Bliesner, B. L., Timmermann, A., and Cobb, K. M. (2014a). Evolution and forcing mechanisms of El Nino over the past 21,000 years. *Nature* 515, 550–553. doi: 10.1038/nature13963

Liu, Z., Wen, X., Brady, E. C., Otto-Bliesner, B., Yu, G., Lu, H., et al. (2014b). Chinese cave records and the East Asia Summer Monsoon. *Quat. Sci. Rev.* 83, 115–128. doi: 10.1016/j.quascirev.2013.10.021

Liu, Z., Otto-Bliesner, B. L., He, F., Brady, E. C., Tomas, R., Clark, P. U., et al. (2009). Transient simulation of last deglaciation with a new mechanism for Bølling-Allerød warming. *Science* 325, 310–314. doi: 10.1126/science.1171041

Liu, Z., Trentesaux, A., Clemens, S. C., Colin, C., Wang, P., Huang, B., et al. (2003). Clay mineral assemblages in the northern South China Sea: implications for East Asian monsoon evolution over the past 2 million years. *Mar. Geol.* 201, 133–146. doi: 10.1016/S0025-3227(03)00213-5

Lu, F., Ma, C., Zhu, C., Lu, H., Zhang, X., Huang, K., et al. (2019). Variability of East Asian summer monsoon precipitation during the Holocene and possible forcing mechanisms. *Clim. Dyn.* 52, 969–989. doi: 10.1007/s00382-018-4175-6

Lu, H., Yi, S., Liu, Z., Mason, J. A., Jiang, D., Cheng, J., et al. (2013). Variation of East Asian monsoon precipitation during the past 21 k.y. and potential CO2 forcing. *Geology* 41, 1023–1026. doi: 10.1130/g34488.1

Maher, B. A. (2008). Holocene variability of the East Asian summer monsoon from Chinese cave records: a re-assessment. *Holocene* 18, 861–866. doi: 10.1177/0959683608095569

Maher, B. A., and Thompson, R. (2012). Oxygen isotopes from Chinese caves: records not of monsoon rainfall but of circulation regime. *J. Quat. Sci.* 27, 615–624. doi: 10.1002/jqs.2553

McGee, D., Donohoe, A., Marshall, J., and Ferreira, D. (2014). Changes in ITCZ location and cross-equatorial heat transport at the Last Glacial Maximum, Heinrich Stadial 1, and the mid-Holocene. *Earth Planet. Sci. Lett.* 390, 69–79. doi: 10.1016/j.epsl.2013.12.043

McManus, J., Francois, R., Gherardi, J.-M., Keigwin, L., and Brown-Leger, S. (2004). Collapse and rapid resumption of Atlantic meridional circulation linked to deglacial climate changes. *Nature* 428, 834–837. doi: 10.1038/nature02494

Meng, X., Liu, L., Wang, X. T., Balsam, W., Chen, J., Ji, J. J. E., et al. (2018). Mineralogical evidence of reduced East Asian summer monsoon rainfall on the Chinese loess plateau during the early Pleistocene interglacials. *Earth Planet. Sci. Lett.* 486, 61–69. doi: 10.1016/j.epsl.2017.12.048

Milliman, J. D., and Kao, S.-J. (2005). Hyperpycnal discharge of fluvial sediment to the ocean: impact of super-typhoon Herb (1996) on Taiwanese rivers. *J. Geol.* 113, 503–516. doi: 10.1086/431906

Ming, G., Zhou, W., Wang, H., Cheng, P., Shu, P., Xian, F., et al. (2020). Moisture variations in Lacustrine-eolian sequence from the Hunshandake sandy land associated with the East Asian Summer Monsoon changes since the late Pleistocene. *Quat. Sci. Rev.* 233:106210. doi: 10.1016/j.quascirev.2020.106210

Park, J., Shin, Y. H., and Byrne, R. (2016). Late-Holocene vegetation and climate change in Jeju Island. Korea and its implications for ENSO influences. *Quat. Sci. Rev.* 153, 40–50. doi: 10.1016/j.quascirev.2016.10.011

Pausata, F. S. R., Battisti, D. S., Nisancioglu, K. H., and Bitz, C. M. (2011). Chinese stalagmite δ18O controlled by changes in the Indian monsoon during a simulated Heinrich event. *Nat. Geosci.* 4, 474–480. doi: 10.1038/ngeo1169

Putnam, A. E., and Broecker, W. S. (2017). Human-induced changes in the distribution of rainfall. *Sci. Adv.* 3:e1600871. doi: 10.1126/sciadv.1600871

Rao, Z., Li, Y., Zhang, J., Jia, G., and Chen, F. (2016). Investigating the long-term palaeoclimatic controls on the δD and δ18O of precipitation during the Holocene in the Indian and East Asian monsoonal regions. *Earth-Sci. Rev.* 159, 292–305. doi: 10.1016/j.earscirev.2016.06.007

Rein, B. (2007). How do the 1982/83 and 1997/98 El Niños rank in a geological record from peru? *Quat. Int.* 161, 56–66. doi: 10.1016/j.quaint.2006.10.023

Renssen, H., Seppä, H., Crosta, X., Goosse, H., and Roche, D. (2012). Global characterization of the Holocene Thermal Maximum. *Quat. Sci. Rev.* 48, 7–19. doi: 10.1016/j.quascirev.2012.05.022

Rind, D. (1998). Latitudinal temperature gradients and climate change. *J. Geophys. Res-Atmos.* 103, 5943–5971. doi: 10.1029/97JD03649

Selvaraj, K., Chen, C. T. A., and Lou, J. Y. (2007). Holocene East Asian monsoon variability: links to solar and tropical Pacific forcing. *Geophys. Res. Lett.* 34:L01703. doi: 10.1029/2006GL028155

Selvaraj, K., Chen, C. T. A., Lou, J.-Y., and Kotlia, B. S. (2011). Holocene weak summer East Asian monsoon intervals in Taiwan and plausible mechanisms. *Quat. Int.* 229, 57–66. doi: 10.1016/j.quaint.2010.01.015

Selvaraj, K., Wei, K.-Y., Liu, K.-K., and Kao, S.-J. (2012). Late Holocene monsoon climate of northeastern Taiwan inferred from elemental (C, N) and isotopic (δ13C, δ15N) data in lake sediments. *Quat. Sci. Rev.* 37, 48–60. doi: 10.1016/j.quascirev.2012.01.009

Shanahan, T., McKay, N., Hughen, K., Overpeck, J., Otto-Bliesner, B., Heil, C., et al. (2015). The time-transgressive termination of the African Humid Period. *Nat. Geo.* 8, 140–144. doi: 10.1038/ngeo2329

Sheng, M., Wang, X., Zhang, S., Chu, G., Su, Y., and Yang, Z. (2017). A 20,000-year high-resolution pollen record from Huguangyan Maar Lake in tropical-subtropical South China. *Palaeogeogr. Palaeoclimatol. Palaeoecol.* 472, 83–92. doi: 10.1016/j.palaeo.2017.01.038

Shi, Z., Liu, X., and Cheng, X. (2012). Anti-phased response of northern and southern East Asian summer precipitation to ENSO modulation of orbital forcing. *Quat. Sci. Rev.* 40, 30–38. doi: 10.1016/j.quascirev.2012.02.019

Stott, L., Cannariato, K., Thunell, R., Haug, G. H., Koutavas, A., and Lund, S. (2004). Decline of surface temperature and salinity in the western tropical Pacific Ocean in the Holocene epoch. *Nature* 431, 56–59. doi: 10.1038/nature02903

Sun, A., and Feng, Z. (2013). Holocene climatic reconstructions from the fossil pollen record at Qigai Nuur in the southern Mongolian Plateau. *Holocene* 23, 1391–1402. doi: 10.1177/0959683613489581

Sun, X., Luo, Y., Huang, F., Tian, J., and Wang, P. (2003). Deep-sea pollen from the South China Sea: pleistocene indicators of East Asian monsoon. *Mar. Geol.* 201, 97–118. doi: 10.1016/s0025-3227(03)00211-1

Sun, Y., Clemens, S. C., An, Z., and Yu, Z. (2006). Astronomical timescale and palaeoclimatic implication of stacked 3.6-Myr monsoon records from the Chinese Loess Plateau. *Quat. Sci. Rev.* 25, 33–48. doi: 10.1016/j.quascirev.2005.07.005

Sun, Y., Kutzbach, J., An, Z., Clemens, S., Liu, Z., Liu, W., et al. (2015). Astronomical and glacial forcing of East Asian summer monsoon variability. *Quat. Sci. Rev.* 115, 132–142. doi: 10.1016/j.quascirev.2015.03.009

Tan, M. (2014). Circulation effect: response of precipitation δ18O to the ENSO cycle in monsoon regions of China. *Clim. Dyn.* 42, 1067–1077. doi: 10.1007/s00382-013-1732-x

Toggweiler, J. R. (2009). Shifting Westerlies. *Science* 323, 1434–1435. doi: 10.1126/science.1169823

Toth, L. T., Aronson, R. B., Vollmer, S. V., Hobbs, J. W., Urrego, D. H., Cheng, H., et al. (2012). ENSO drove 2500-year collapse of eastern Pacific coral reefs. *Science* 337, 81–84. doi: 10.1126/science.1221168

Wan, S., Tian, J., Steinke, S., Li, A., and Li, T. (2010). Evolution and variability of the East Asian summer monsoon during the Pliocene: evidence from clay mineral records of the South China Sea. *Palaeogeogr. Palaeoclimatol. Palaeoecol.* 293, 237–247. doi: 10.1016/j.palaeo.2010.05.025

Wang, B., Wu, Z. W., Li, J., Liu, J., Chang, C., Ding, Y., et al. (2008). How to measure the strength of the East Asian summer monsoon? *J. Climate* 21, 4449–4463. doi: 10.1175/2008JCLI2183.1

Wang, H., Chen, J., Zhang, X., and Chen, F. (2014). Palaeosol development in the Chinese Loess Plateau as an indicator of the strength of the East Asian summer monsoon: evidence for a mid-Holocene maximum. *Quat. Int.* 33, 155–164. doi: 10.1016/j.quaint.2014.03.013

Wang, L.-C., Behling, H., Chen, Y.-M., Huang, M.-S., Arthur Chen, C.-T., Lou, J.-Y., et al. (2014). Holocene monsoonal climate changes tracked by multiproxy approach from a lacustrine sediment core of the subalpine Retreat Lake in Taiwan. *Quat. Int.* 333, 69–76. doi: 10.1016/j.quaint.2014.02.014

Wang, L., Sarnthein, M., Erlenkeuser, H., Grimalt, J., Grootes, P., Heilig, S., et al. (1999). East Asian monsoon climate during the Late Pleistocene: high-resolution sediment records from the South China Sea. *Mar. Geol.* 156, 245–284. doi: 10.1016/s0025-3227(98)00182-0

Wang, L.-C., Behling, H., Kao, S.-J., Li, H.-C., Selvaraj, K., Hsieh, M.-L., et al. (2015). Late Holocene environment of subalpine northeastern Taiwan from pollen and diatom analysis of lake sediments. *J. Asian Earth Sci.* 114, 447–456. doi: 10.1016/j.jseaes.2015.03.037

Wang, P. X., Wang, B., Cheng, H., Fasullo, J., Guo, Z., Kiefer, T., et al. (2017). The global monsoon across time scales: mechanisms and outstanding issues. *Earth-Sci. Rev.* 174, 84–121. doi: 10.1016/j.earscirev.2017.07.006

Wang, S.-Y., and Chen, T.-C. (2008). Measuring East Asian summer monsoon rainfall contributions by different weather systems over Taiwan. *J. Appl. Meteorol. Clim.* 47, 2068–2080. doi: 10.1175/2007jamc1821.1

Wang, W., and Feng, Z. D. (2013). Holocene moisture evolution across the Mongolian Plateau and its surrounding areas: a synthesis of climatic records. *Earth Sci. Rev.* 122, 38–57. doi: 10.1016/j.earscirev.2013.03.005

Wang, X., Chu, G., Sheng, M., Zhang, S., Li, J., Chen, Y., et al. (2016). Millennial-scale Asian summer monsoon variations in South China since the last deglaciation. *Earth Planet. Sci. Lett.* 451, 22–30. doi: 10.1016/j.epsl.2016.07.006

Wang, Y., Cheng, H., Edwards, R. L., An, Z., Wu, J., Shen, C.-C., et al. (2001). A high-resolution absolute-dated late Pleistocene monsoon record from Hulu Cave. China. *Science* 294, 2345–2348. doi: 10.1126/science.1064618

Wang, Y., Cheng, H., Edwards, R. L., He, Y., Kong, X., An, Z., et al. (2005). The Holocene Asian monsoon: links to solar changes and North Atlantic climate. *Science* 308, 854–857. doi: 10.1126/science.1106296

Wenske, D., Böse, M., Frechen, M., and Lüthgens, C. (2011). Late Holocene mobilisation of loess-like sediments in Hohuan Shan, high mountains of Taiwan. *Quat. Int.* 234, 174–181. doi: 10.1016/j.quaint.2009.10.034

Wu, C. (2013). *Holocene Sedimentation on the Lanyang Plain and Adjacent Continental Shelf, Northwestern Taiwan*. Dissertations/master's thesis, College of William & Mary, Virginia, doi: 10.25773/v5-v8ng-wk84

Xiao, J., Wu, J., Si, B., Liang, W., Nakamura, T., Liu, B., et al. (2006). Holocene climate changes in the monsoon/arid transition reflected by carbon concentration in Daihai Lake of Inner Mongolia. *Holocene* 16, 551–560. doi: 10.1191/0959683606hl950rp

Xie, S., Evershed, R. P., Huang, X., Zhu, Z., Pancost, R. D., Meyers, P. A., et al. (2013). Concordant monsoon-driven postglacial hydrological changes in peat and stalagmite records and their impacts on prehistoric cultures in central China. *Geology* 41, 827–830. doi: 10.1130/G34318.1

Xu, H., Goldsmith, Y., Lan, J., Tan, L., Wang, X., Zhou, X., et al. (2020). Juxtaposition of western Pacific subtropical high on Asian Summer Monsoon shapes subtropical East Asian precipitation. *Geophys. Res. Lett.* 47:e2019GL084705. doi: 10.1029/2019GL084705

Xu, H., Lan, J., Sheng, E., Liu, B., Yu, K., Ye, Y., et al. (2016). Hydroclimatic contrasts over Asian monsoon areas and linkages to tropical Pacific SSTs. *Sci. Rep.* 6:33177. doi: 10.1038/srep33177

Xu, H., Song, Y. P., Goldsmith, Y., and Lang, Y. C. (2019). Meridional ITCZ shifts modulate tropical/subtropical Asian monsoon rainfall. *Sci. Bull.* 64, 1737–1739. doi: 10.1016/j.scib.2019.09.025

Yancheva, G., Nowaczyk, N. R., Mingram, J., Dulski, P., Schettler, G., Negendank, J. F., et al. (2007). Influence of the intertropical convergence zone on the East Asian monsoon. *Nature* 445, 74–77. doi: 10.1038/nature05431

Yang, T.-N., Lee, T.-Q., Meyers, P. A., Song, S.-R., Kao, S.-J., Löwemark, L., et al. (2011). Variations in monsoonal rainfall over the last 21 kyr inferred from sedimentary organic matter in Tung-Yuan Pond, southern Taiwan. *Quat. Sci. Rev.* 30, 3413–3422. doi: 10.1016/j.quascirev.2011.08.017

Yang, X., Yang, H., Wang, B., Huang, L.-J., Shen, C.-C., Edwards, R. L., et al. (2019). Early-Holocene monsoon instability and climatic optimum recorded by Chinese stalagmites. *Holocene* 29, 1059–1067. doi: 10.1177/0959683619831433

Yuan, D., Cheng, H., Edwards, R. L., Dykoski, C. A., Kelly, M. J., Zhang, M., et al. (2004). Timing, duration, and transitions of the last interglacial Asian monsoon. *Science* 304, 575–578. doi: 10.1126/science.1091220

Zhang, E., Zhao, C., Xue, B., Liu, Z., Yu, Z., Chen, R., et al. (2017). Millennial-scale hydroclimate variations in southwest China linked to tropical Indian Ocean since the Last Glacial Maximum. *Geology* 45, 435–438. doi: 10.1130/G38309.1

Zhang, H., Ait Brahim, Y., Li, H., Zhao, J., Kathayat, G., Tian, Y., et al. (2019). The Asian summer monsoon: Teleconnections and forcing mechanisms—A review from Chinese speleothem δ18O records. *Quaternary* 2:26. doi: 10.3390/quat2030026

Zhang, H., Griffiths, M. L., Chiang, J. C., Kong, W., Wu, S., Atwood, A., et al. (2018). East Asian hydroclimate modulated by the position of the westerlies during Termination I. *Science* 362, 580–583. doi: 10.1126/science.aat9393

Zhao, C., Chang, Y. P., Chen, M. T., and Liu, Z. (2013). Possible reverse trend in Asian summer monsoon strength during the late Holocene. *J. Asian Earth Sci.* 69, 102–112. doi: 10.1016/j.jseaes.2012.09.028

Zhong, W., Xue, J., Zheng, Y., Ouyang, J., Ma, Q., Cai, Y., et al. (2010). Climatic changes since the last deglaciation inferred from a lacustrine sedimentary sequence in the eastern Nanling Mountains, south China. *J. Quat Sci.* 25, 975–984. doi: 10.1002/jqs.1384

Zhou, W., Yu, X., Jull, A. J. T., Burr, G., Xiao, J. Y., Lu, X., et al. (2004). High-resolution evidence from southern China of an early Holocene optimum and a mid-Holocene dry event during the past 18,000 years. *Quat. Res.* 62, 39–48. doi: 10.1016/j.yqres.2004.05.004

Zhou, X., Sun, L., Zhan, T., Huang, W., Zhou, X., Hao, Q., et al. (2016). Time-transgressive onset of the Holocene Optimum in the East Asian monsoon region. *Earth Planet. Sci. Lett.* 456, 39–46. doi: 10.1016/j.epsl.2016.09.052

Zhu, C., Ma, C., YU, S. Y., Tang, L., Zhang, W., and Lu, X. (2010). A detailed pollen record of vegetation and climate changes in Central China during the past 16 000 years. *Boreas* 39, 69–76. doi: 10.1111/j.1502-3885.2009.00098.x

Zhu, Z., Feinberg, J. M., Xie, S., Bourne, M. D., Huang, C., Hu, C., et al. (2017). Holocene ENSO-related cyclic storms recorded by magnetic minerals in speleothems of central China. *Proc. Natl. Acad. Sci. U.S.A.* 114, 852–857. doi: 10.1073/pnas.1610930114

Conflict of Interest: The authors declare that the research was conducted in the absence of any commercial or financial relationships that could be construed as a potential conflict of interest.

Copyright © 2020 Ding, Zheng, Zheng and Kao. This is an open-access article distributed under the terms of the Creative Commons Attribution License (CC BY). The use, distribution or reproduction in other forums is permitted, provided the original author(s) and the copyright owner(s) are credited and that the original publication in this journal is cited, in accordance with accepted academic practice. No use, distribution or reproduction is permitted which does not comply with these terms.

frontiers in Earth Science

ORIGINAL RESEARCH
published: 31 July 2020
doi: 10.3389/feart.2020.00317

Monsoon Precipitation, Economy and Wars in Ancient China

Jixiao Zhang[1], Xin Zhou[1,2], Shiwei Jiang[1], Luyao Tu[1] and Xiaoyan Liu[1]*

[1] School of Earth and Space Sciences, University of Science and Technology of China, Hefei, China, [2] Laboratory for Marine Geology, Pilot National Laboratory for Marine Science and Technology (Qingdao), Qingdao, China

Northern China, particularly the Yellow River Basin, which is the birth place of Chinese civilization and has been the political center throughout most of China's history, is an ideal region for studying the response of human activities to climate change. However, studies on links between climate change and variations in earlier civilization are limited due to the scarcity of macroscale monsoon precipitation records. In the present study, a ∼4,000-year record of monsoon precipitation, which represents average rainfall in large areas in northern China, was reconstructed from sediments in Northern Yellow Sea Mud (NYSM). The record shows high monsoon precipitation during ∼4,000–2,500 BP, ∼1,350–750 BP and the past ∼250 years. In general, our record of monsoon precipitation exhibits trends similar to the percentages of planted Poaceae pollen in lake sediments and the Chinese economic index, contrasting with the frequency of wars over the past 2,000 years. We postulated that, in the agricultural society of ancient China, low monsoon precipitation in northern China may be an important factor that cause reduced agricultural production, declined economy and even the occurrence of wars.

Keywords: monsoon precipitation, Yellow Sea muddy sediment, median grain size, cereal production, war frequency in ancient China

OPEN ACCESS

Edited by:
Liangcheng Tan, Chinese Academy of Sciences (CAS), China

Reviewed by:
Aifeng Zhou, Lanzhou University, China
Shangbin Xiao, China Three Gorges University, China

****Correspondence:***
Xin Zhou
xinzhou@ustc.edu.cn

Specialty section:
This article was submitted to Quaternary Science, Geomorphology and Paleoenvironment, a section of the journal Frontiers in Earth Science

Received: *11 March 2020*
Accepted: *03 July 2020*
Published: *31 July 2020*

Citation:
Zhang J, Zhou X, Jiang S, Tu L and Liu X (2020) Monsoon Precipitation, Economy and Wars in Ancient China. Front. Earth Sci. 8:317. doi: 10.3389/feart.2020.00317

INTRODUCTION

Billions of people currently live in monsoon regions, with monsoon precipitation bringing significant influences to bear on human lives and wealth through severe climate conditions. Research on the relationship between prehistoric human activities and monsoon climate change provides long-term evidence for studying the response of human activity to climate change (Wigley et al., 1985; Pandey, 2005; Potts, 2012). This topic has been extensively researched over the past 20 years, and much progress has been achieved (Gupta et al., 2006; Xie et al., 2013; Zhang et al., 2016). However, studies of detailed links between macroscale monsoon climate change and ancient human activities have rarely been undertaken (Hsiang et al., 2013; Li et al., 2015; Wei et al., 2015), due to the lack of adequate macroscale monsoon climate records in key regions.

Northern China is an ideal region for studying the above question, because (i) it is the region known to be the birthplace of Chinese civilization, and has been the political center during most of the Chinese history (Schirokauer and Brown, 2012; Eberhard, 2013); and (ii) large areas of northern China are in monsoon regions, environments of which, especially around the monsoon margin, are sensitive to monsoon precipitation changes (Wang et al., 2013). The interactions between human activities and monsoon precipitation in northern China during the past several thousand years have been extensively studied (Fan, 2010; Yin et al., 2016).

However, macroscale monsoon precipitation records from the past several millennia in northern China are sparse, and precipitation evidence has been reconstructed from terrestrial materials, including stalagmite, lake sediment, peat sediment, tree ring and historical literature, but large regional scale records in northern China remain limited (Hong et al., 2000; Peng et al., 2005; Ge et al., 2008; Tan et al., 2008, 2011; Yi et al., 2012). Although the synthesis of precipitation records over large areas has helped toward resolving this question (Li J. et al., 2017), time series could be influenced by the distribution, resolutions and dating uncertainties of the records used. Thus, monsoon precipitation records that show average rainfall changes over large areas are essential.

Chinese coastal muddy sediments, which are transported from the land by rivers, have been widely used for reconstructing paleoclimate changes (Wang, 2018). As shown in previous studies (Zhou et al., 2012), sediments in some coastal areas were influenced by nearby runoff, and thus could be used to reconstruct average precipitation changes across river basins. In this study, we extended the macroscale monsoon precipitation records by more than 4,000 years, using coastal sediments from the Northern Yellow Sea Mud (NYSM) region. We then compared our record with records of economic index and war frequency in China reconstructed from historical literatures, and with pollen percentages of planted Poaceae from lake sediments, to discuss the links between climate change and human activities throughout Chinese history.

MATERIALS AND METHODS

Site 38002 (122°30.21′ E, 37°59.92′ N; water depth: 49.2 m) is in the southwestern part of the NYSM (**Figure 1**) region. Two sediment cores, named as 38002-A and 38002, and consisting mainly of gray clay silt, were collected in 2009 by staff of the expedition ship "Kexue 1", Institute of Oceanology, CAS, using a gravity corer and a box corer, respectively. The 238 cm long sediment Core 38002-A was subsampled at 1 cm intervals; Core 38002, 34 cm long, was subsampled at 0.5 cm intervals.

Of the samples from Core 38002, 18 were selected for ^{210}Pb–^{137}Cs analysis (Miguel et al., 2003). Radioactivity was measured using a germanium detector (AMETEK, United States) at the Institute of Polar Environment, USTC, Hefei, China. The samples were dried at 50°C, homogenized using a mortar and pestle, and passed through a 2 mm sieve. Samples (∼5–10 g) were then packed into standard counting geometries for gamma analysis, sealed and stored for approximately 1 week to allow radioactive equilibration between ^{226}Ra and its daughter product ^{214}Pb. Spectra were continuously measured over 24 h to obtain sufficient counts. The resulting spectra showed ^{210}Pb activity with a peak at 46.5 keV.

Benthic foraminifera of various species from Core 38002-A were used for accelerator mass spectrometry (AMS) ^{14}C dating (Cearreta and Murray, 2000). The ^{14}C dates were calibrated to calendar ages using the Marine13 calibration dataset via the "R" code of Bacon (version 2.2). The foraminifera were placed under a stereomicroscope and the AMS ^{14}C measurements made at Beta Laboratory, Miami, United States.

Grain size distributions were analyzed in the 238 samples from 38002-A. The samples were added to a 10–20 mL H_2O_2 solution (30%), after which the mixture was heated to 100°C for 0.5 h to remove organic matter, and then treated with 10 mL of HCl (10%) for 48 h to remove calcareous cement and shell material. All the samples were then washed and dispersed by adding 10 mL of $(NaPO_3)_6$ (10%) followed by ultrasonic treatment for 10 min before measurement. The grain-size distributions were measured using an LS13 320 laser diffraction particle-size analyzer (Beckman Coulter, Inc.). Analysis range was 0.04–2000 μm, size resolution was 0.01 Φ and the relative error of repeat tests was less than 2%.

The concentrations of elements (SiO_2, Al_2O_3, Sr and Rb) were determined with an X-ray fluorescence (XRF) spectrometer (Axios^{mAX}-Minerals, PANalytical B.V.) using the fusion method (Fabb, 1976). Air-dried sediments were ground to a particle size equivalent to that of powder sieved by a No. 200 (75 μm) mesh. In total, 0.7000 ± 0.0003 g of sample and 7.0000 ± 0.0003 g of lithium borate were dried and stored in a glass desiccator, mixed uniformly and then fused into a glass disc. The samples were then analyzed using a spectrometer (Rh-anode X-ray tube) with a relative error of 0.1–1.0%. Element analysis was performed in the Institute of Geology and Geophysics, China Academy of Sciences.

RESULTS

Chronology

Core 38002 and Core 38002-A were dated using the ^{210}Pb–^{137}Cs method and ^{14}C, respectively, in our previous research (Zhang et al., 2019; **Figure 2**). The chronology of the upper part of the Core 38002-A was established by comparing the sea surface temperature (SST) between the two cores. Previous studies have shown that the trend of SSTs in the region was opposite that of the total solar irradiance (TSI) during the past 100 years (He et al., 2014). The trend of the long-term SST record was also consistent with that of the TSI record, indicating that the chronology of the Core 38002-A was reliable, though ^{14}C dating on carbonate foraminifer shells could result in some dating uncertainties.

Median Grain Size and Element Ratios

Our results show that the median grain size in the sediments of Core 38002-A varied from 22 to 60 μm, with an average of 38 μm (**Figure 3C**). The relatively high median grain size occurred during 3,870–2,500 BP, 1,350–750 BP and throughout the past 250 years, and relatively low values occurred from 2,500–1,350 BP and 750–250 BP.

The ratio of SiO_2/Al_2O_3 (**Figure 3B**) ranged between 5.3 and 6.3, while the ratio of Rb/Sr (**Figure 3A**) ranged between 0.50 and 0.63. The ratio of SiO_2/Al_2O_3 changed in accordance with the median grain size; i.e., during 3,870–2,500 BP, 1,350–750 BP and the past 250 years, the ratio was relatively high, and during 2,500–1,350 BP and 750–250 BP, the ratio was relatively low. In contrast, the ratio of Rb/Sr showed the opposite trend. The results of correlation analysis also support the inference that the ratio of

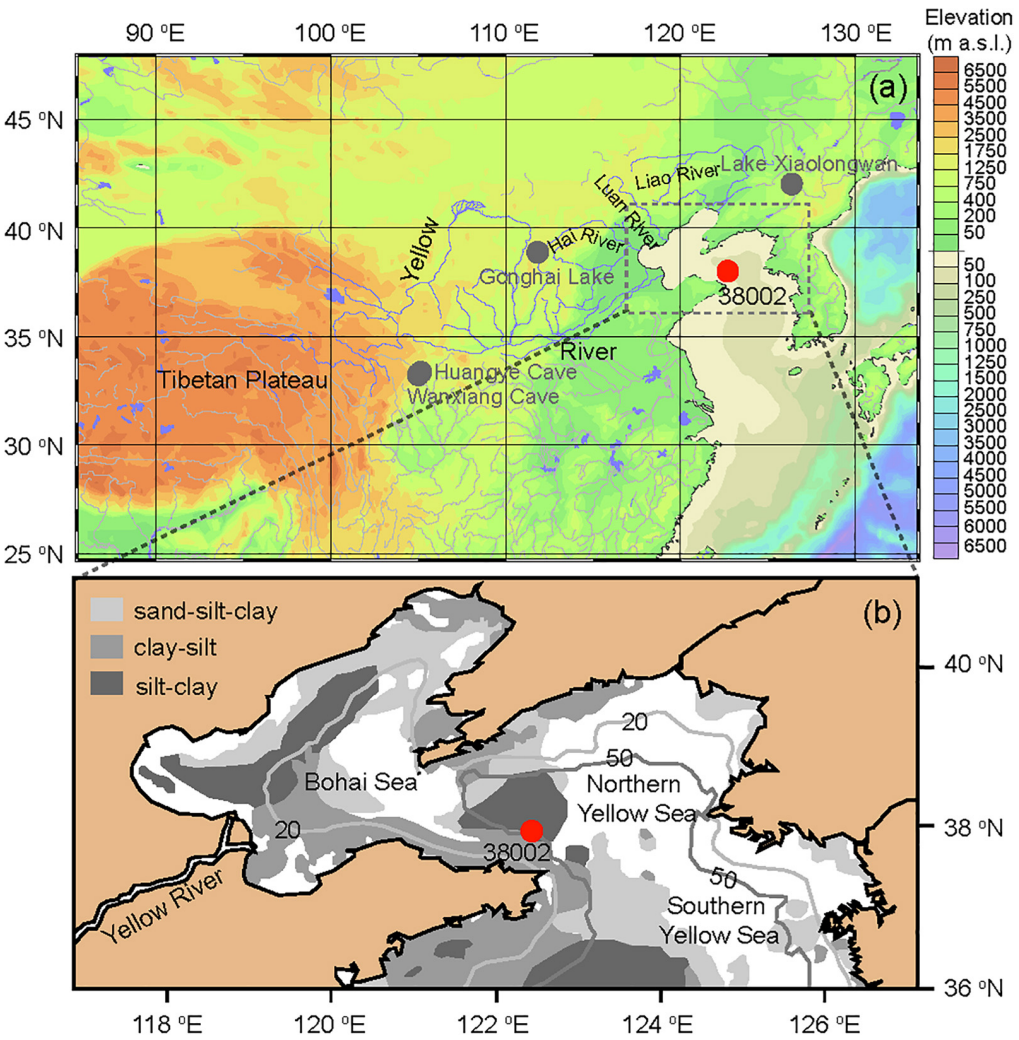

FIGURE 1 | Location of site 38002 and related sites. The base map was generated with Ocean Data View 4.0. **(a)** The main study sites involved in this article and **(b)** types of surface sediments in the Bohai Sea and the Yellow Sea.

SiO_2/Al_2O_3 exhibited strong positive linear correlation ($R = 0.76$) with the median grain size (**Figure 4A**), while the ratio of Rb/Sr exhibited negative linear correlation ($R = -0.52$) (**Figure 4B**).

DISCUSSION

Source and Climatic Significance of Median Grain Size in the NYSM Region

The sediments in Core 38002 originated mainly from the Loess Plateau and were transported by the discharge of the Yellow River and the current circulation of Bohai Sea; therefore, they reflect large regional climate especially summer monsoon precipitation in northern China (Li et al., 2016). However, the Yellow River has changed its course many times in history, during which the most significant diversion occurred between 1128–1855 AD, resulting in the instability of many indicators (Xue et al., 2011). Compared with other indicators, the median grain size was less affected by the diversion of Yellow River and had be used as an indicator of precipitation proxy in our previous study (Zhou et al., 2012, 2013).

Si and Al are relatively stable elements in the Loess Plateau; as such, the ratio of SiO_2/Al_2O_3 is not affected by pedogenic processes and can be used as an index that reflects the grain size of original eolian particles and to reconstruct the history of the East Asian monsoon (Peng and Guo, 2001). The strong positive linear correlation between the ratio of SiO_2/Al_2O_3 and median grain size in Core 38002 supports the reliability of the median grain size.

The ratio of Rb/Sr is related to regional weathering intensity and could indicate the intensity of East Asia Summer Monsoon (EASM) (Chen et al., 2003). During a strong EASM or high-precipitation period, Sr is transported more easily than Rb from inland to the coastal zone (Peng and Guo, 2001; Boulay et al., 2003; Sun et al., 2008, 2009; Zhao et al., 2008). Therefore, a low ratio of Rb/Sr in Core 38002-A indicates high precipitation,

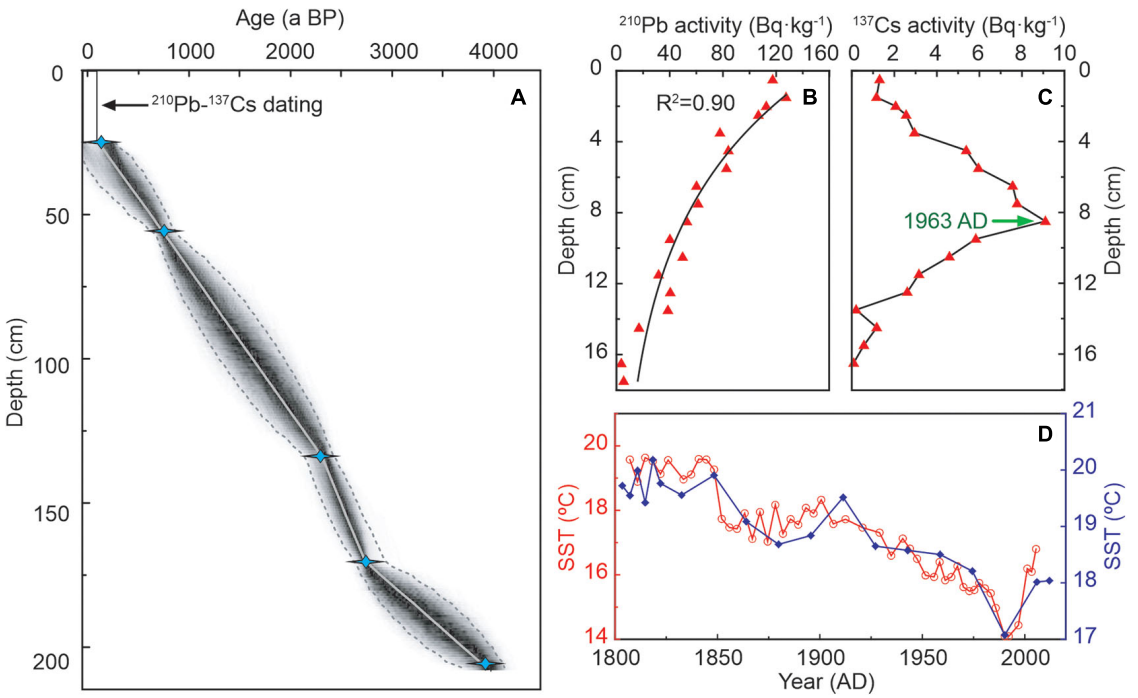

FIGURE 2 | Chronology of gravity Core 38002-A and box Core 38002. **(A)** ^{14}C age for Core 38002-A (Zhang et al., 2019), **(B,C)** ^{210}Pb and ^{137}Cs activities for Core 38002 (Zhou et al., 2012), **(D)** Comparison between SSTs from Cores 38002 (red) and 38002-A (blue) (Zhang et al., 2019).

and vice versa. When considering the linear correlation, the element ratios further support the reliability of median grain size in Core 38002-A as an indicator of historical precipitation in northern China.

In summary, the Rb/Sr and SiO_2/Al_2O_3 ratios of Core 38002, supported the reliability of median grain size as the indicator of monsoon precipitation changes in large areas of northern China. During 3,870–2,500 BP, 1,350–750 BP and the past 250 years, high median grain size, high ratio of SiO_2/Al_2O_3 and low ratio of Rb/Sr indicate there were high monsoon precipitation. In contrast, during 2,500–1,350 BP and 750–250 BP, there was low monsoon precipitation.

Monsoon Precipitation Changes and Civilization in Northern China During the Last 4,000 Years

Multiple studies have shown that temperature change plays important roles in the development and demise of human civilization (Haug et al., 2003; Issar and Zohar, 2004; Tsonis et al., 2010). Precipitation is closely related to the occurrence of floods and droughts, so it is as equally important as temperature in terms of climate change. In the past ~4,000 years, northern China has been ruled by many dynasties. Although some studies have discussed about regional precipitation changes and cultural development (Yin et al., 2005; Gu et al., 2007; Zhang et al., 2008; Tan et al., 2011), there are few research materials discussing the relationship between precipitation and cultural development in large areas.

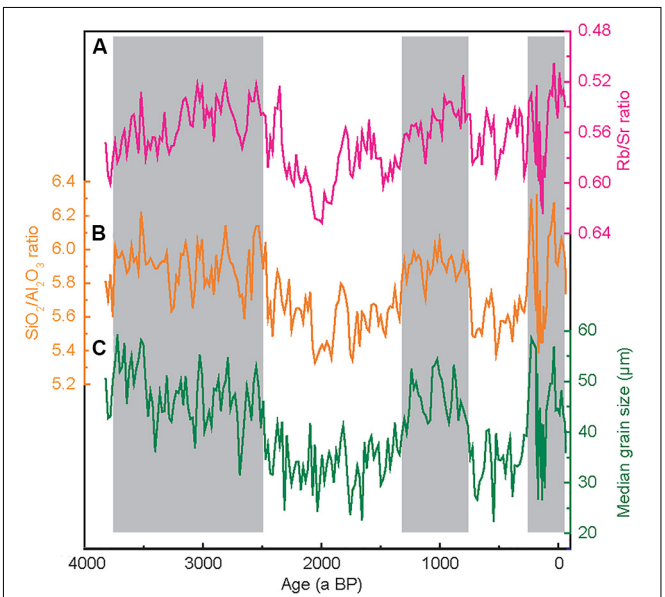

FIGURE 3 | Proxies from Core 38002-A. **(A)** Rb/Sr ratio, **(B)** SiO_2/Al_2O_3 ratio, **(C)** Median grain size.

The median grain size of NYSM region, as discussed above, is a good indicator of monsoon precipitation over a large area, which can compensate for the deficiency of previous research. To reconstruct past precipitation of the Yellow River Basin, we

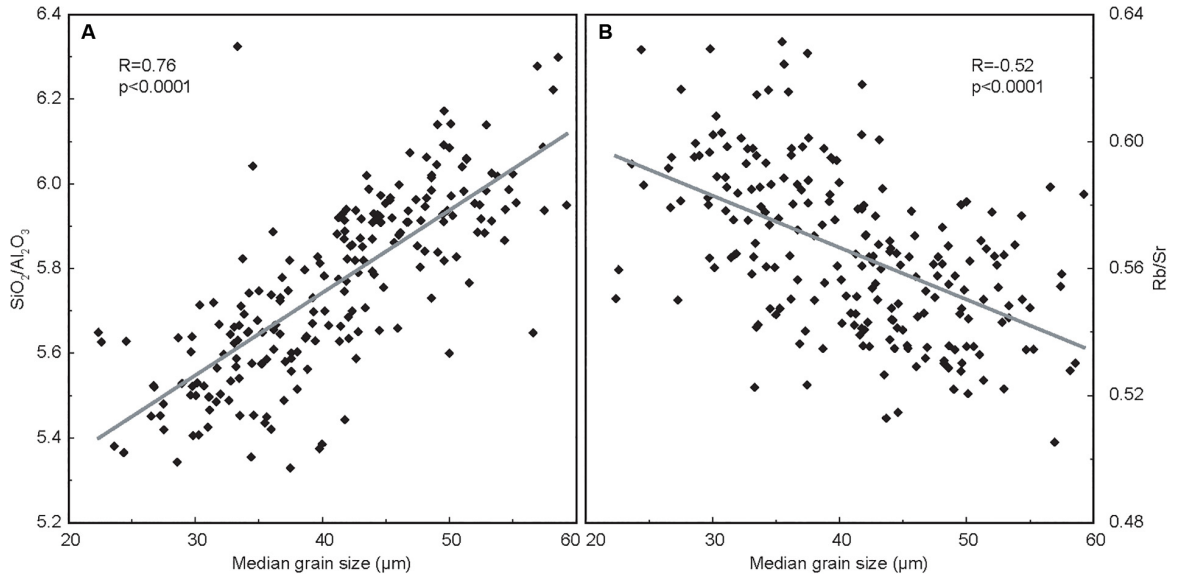

FIGURE 4 | Linear correlations between median grain size and element ratios in sediments from Core 38002-A. **(A)** Relationship between SiO_2/Al_2O_3 and median grain size, **(B)** Relationship between Rb/Sr and median grain size.

further compared these data with other indicators in northern China (**Figure 5**). Although the chronological results between them may have some errors that make it difficult to discuss specific climate events in detail, it is still possible to explore the precipitation and civilization history on centuries time scales.

In terms of the different physical–geographical settings, the Yellow River Basin has been divided into three water source areas: upper (above the Hekou station), middle (from the Hekou station to the Taohuayu station), and lower (below the Taohuayu station) reaches (He et al., 2013). Nearly 40% of runoff in Yellow River comes from the upstream basin. Therefore, changes in upstream precipitation and runoff have an important impact on the hydrodynamics of the entire Yellow River, and further affect the sediments exported to the Yellow Sea (Li X. et al., 2017; Wang et al., 2017). The area of the Qilian Mountains is located in the northwest of the Tibetan Plateau. Hence, the precipitation reconstructed by tree-ring of Qilian juniper (**Figure 5A**) can partially reflect the regional precipitation changes in the upper Yellow River Basin.

The wet-dry index data (**Figure 5B**) were extracted from ∼1,500-year flood and drought records from within the North China Plain region that mainly located in the middle and lower reaches of the Yellow River Basin (approximately 34–40°N) (Zheng et al., 2006); therefore, these data can indicate precipitation changes in large areas of the Yellow River Basin. In addition, the $\delta^{18}O$ values in stalagmites of Wanxiang cave (**Figure 5C**) and Huangye cave (**Figure 5D**), both located in the upper reaches of the Yellow River, were also considered as indicators of precipitation in the Yellow River Basin (Zhang et al., 2008; Tan et al., 2011).

Consistent changes among the above records show that the median grain size of the NYSM region can be used as a reliable indicator of monsoon precipitation changes in large areas of northern China, although there were slight variations between them due to regional differences or sensitivity of different indicators. The $\delta^{18}O$ values in stalagmites showed inconsistent trend changes with median grain size from ∼1,850 to 1,350 BP, as there factors other than monsoon precipitation may exist that can influence $\delta^{18}O$ values (Liu et al., 2015; Zhao et al., 2018).

Based on the median grain size and other indices, the precipitation history and civilization of northern China during the past ∼4,000 years can be broadly divided into the following intervals:

(i) ∼4,000 to ∼2,500 BP, roughly equivalent to the Xia Dynasty-Spring and Autumn Period during Chinese history (Li, 2002). Precipitation was generally high, but there was a slight downward trend, with short-term fluctuations. During this period, society was relatively stable and conflicts were infrequent.

(ii) ∼2,500 to 1,350 BP, roughly equivalent to the Warring States Period-Southern and Northern Dynasties during Chinese history. The precipitation during this period is comparably low, and shows a trend of descending first before rising again. During most of this period, the temperature was lower than that during modern times (Zheng, 2005).

(iii) ∼1,350 to ∼750 BP, roughly equivalent to the Sui Dynasty to the early Southern Song Dynasty during Chinese history. The precipitation during this period is relatively high, with some small fluctuations. During this period, China was in a state of unification for most of the time, with a developed economy, prosperous culture and fewer hostilities. Previous research shows that the temperature during this period was comparable to or slightly higher than in modern times (Ge et al., 2003; Liu et al., 2011).

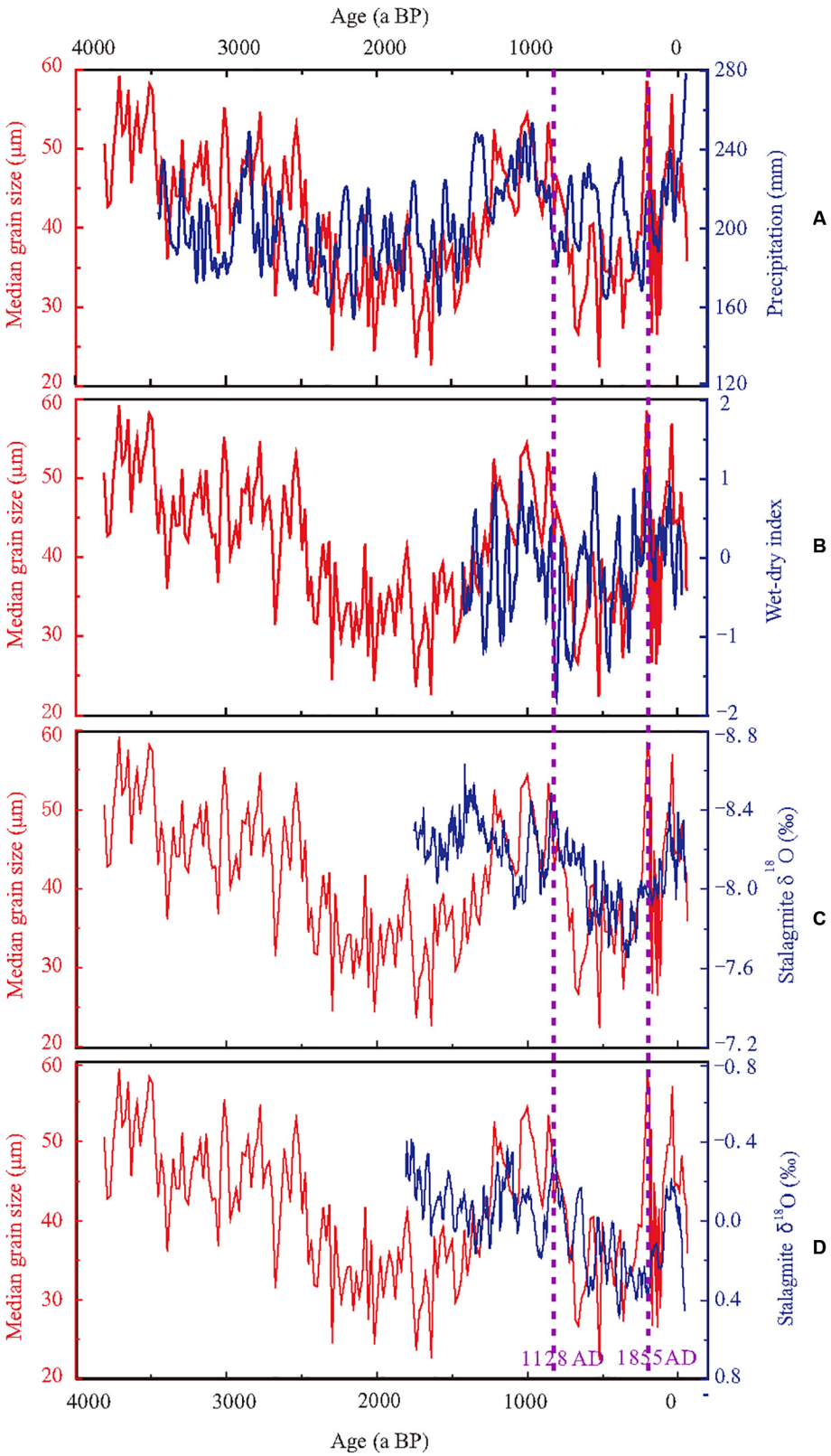

FIGURE 5 | Comparison of median grain size in sediments from Core 38002-A and other monsoon precipitation records. **(A)** Precipitation reconstructed by tree-ring analysis (Yang et al., 2014), **(B)** Wet-dry index of northern China (Zheng et al., 2006), **(C)** Stalagmites $\delta^{18}O$ from Wanxiang cave (Zhang et al., 2008), **(D)** Stalagmites $\delta^{18}O$ from Huangye cave (Tan et al., 2011).

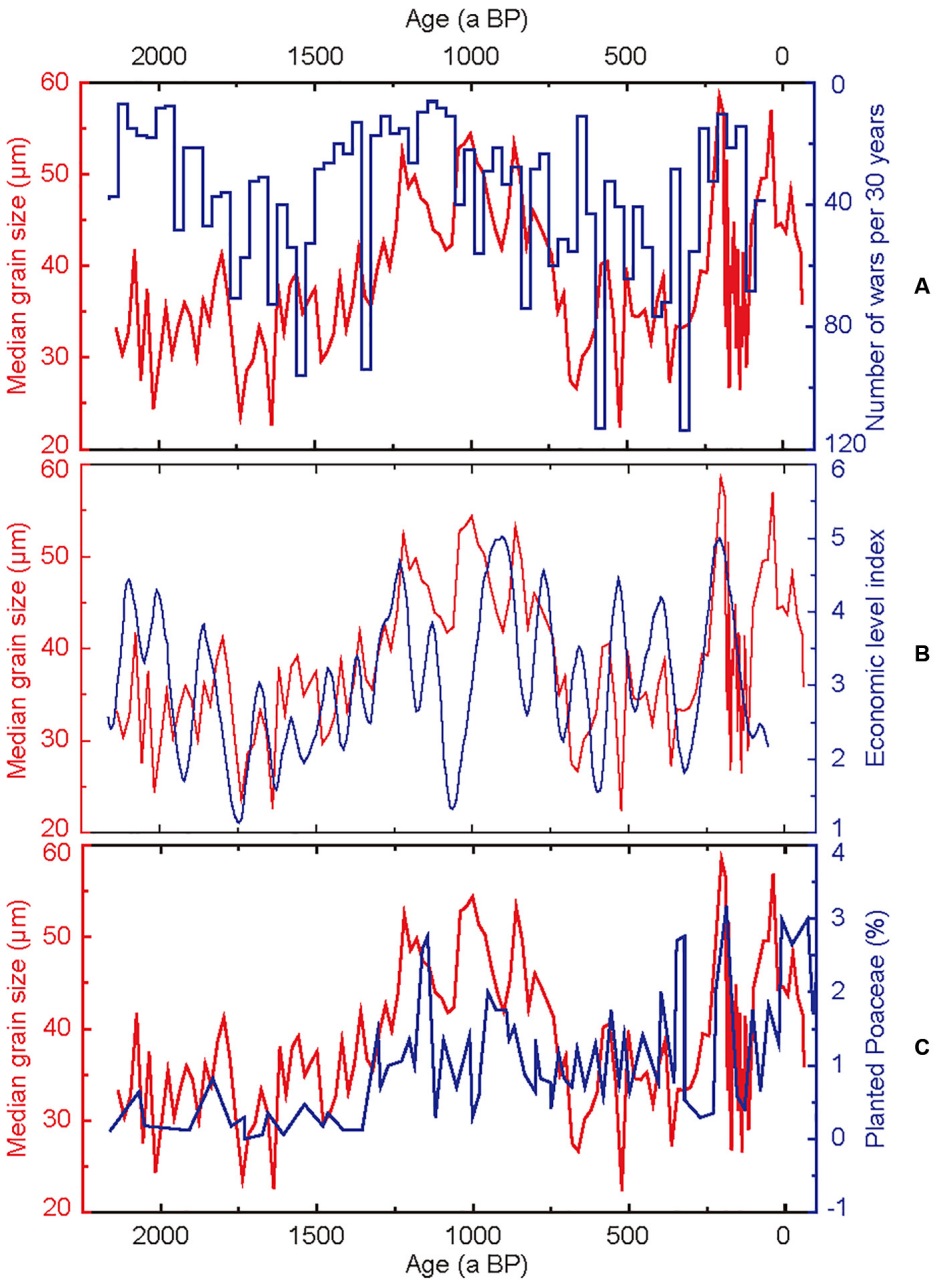

FIGURE 6 | Comparison of median grain size in sediments from Core 38002-A and records of **(A)** war frequency (Ge et al., 2014), **(B)** economic index (Wei et al., 2015), and **(C)** pollen percentages of planted Poaceae from Lake Gonghai (Xu et al., 2017).

It can be inferred that abundant precipitation and advantageous temperature may be the reasons for the prosperity and development of society during this period.

(iv) ∼750 to ∼250 BP, roughly equivalent to late Southern Song Dynasty to the early Qing Dynasty during Chinese history. Although the estuary of the Yellow River changed (1128 and 1855 AD, marked as purple dash lines in **Figure 5**) around this period' the median grain size still exhibited good consistency with other indices in the mass and thus can indicate precipitation. Precipitation during this period was relatively low, and showed a decreasing trend. This period was also approximately equivalent to the Little Ice Age, characterized by low temperatures (Wang et al., 2010).

(v) The past 250 years. Precipitation, as reconstructed by references to tree-ring and stalagmite $\delta^{18}O$ analysis is relatively high, but the median grain size of Core 38002-A does not correlate well with the perceived precipitation. The human activities during the past 200 years may well have interfered with the

change of the median grain size (Wang and Li, 2011; Yang et al., 2015).

In general, during most periods of the past ∼4,000 years, the median grain size of NYSM reflects a microscale precipitation change in the Yellow River Basin or northern China. The period of high precipitation usually corresponded to a warm phase and also a period of cultural prosperity, and a period of low precipitation usually corresponded to a cold phase and also a period of social unrest.

During 1128–1855 AD, although Yellow River changed its estuary, the median grain size still had a good correlation with other indicators. There are multiple reasons may cause the median grain size to be less affected by the diversion: (i) during 1128–1855 AD, the lower reaches of the Yellow River still flowed into the Bohai Sea, only the water from the middle and upper reaches was affected by the diversion; (ii) judging from the circulation of the Bohai Sea, the stronger circulation mainly passes through the Luanhe estuary, which is relatively far from the Yellow River estuary, may further weakened the impact of the Yellow River runoff during diversion (Ji et al., 2019); (iii) most time of 1128–1855 AD was in the Little Ice Age, which was a period of less monsoon precipitation, this may also weakened the impact of the Yellow River diversion.

Relationship Among Precipitation, Economy and War in Northern China During the Last 2,000 Years

By comparing the precipitation reconstructed by the median grain size in sediments from Core 38002-A with historical records, we made a preliminary assumption that precipitation is closely related to culture development. To further explore the underlying mechanism, we compared it with other indicators (**Figure 6**) during the last 2,000 years.

In ancient China, rice was the main crop in the southern region, while wheat and millet were the main crops in the northern region (Zeng, 2005; Betts et al., 2014). All these cereal crops belong to the Poaceae plant family. Therefore, the pollen percentage of planted Poaceae (>35 μm grain size) in Lake Gonghai sediments (**Figure 6C**) can be considered as a rough indicator of the cereal yield of nearby areas (Xu et al., 2017). Based on the planted Poaceae pollen in Gonghai, cereal production nearby can be divided into several phases. Before ∼1,300 BP, the planted Poaceae pollen percentage was relatively low, indicate that agricultural activities were limited. Throughout ∼1,300–750 BP, the planted Poaceae pollen percentage increased significantly, indicating increased agricultural activity and higher cereal yields in this region. From ∼750 to 250 BP, the decreased planted Poaceae pollen percentage indicated weakened agricultural activity and lower cereal yields in this region. Throughout the recent 250 years, the planted Poaceae pollen percentage increased again, indicating flourishing agricultural activities and higher cereal yields.

In northern China, cereal yields are closely related to precipitation, and low precipitation leads to a shortage of water resources, which in turn leads to a reduction in cereal yields. The Lake Gonghai is located in the Yellow River Basin, and its precipitation is related to the regional monsoon strength (Chen et al., 2013, 2015); thus, the median grain size in sediments from Core 38002-A and the Planted Poaceae pollen percentage in Lake Gonghai showed a similar trend although there were some differences in detail.

The cereal yields may further affected the economic level (Wei et al., 2015) and the number of wars (Ge et al., 2014). Looting for food may cause ancient conflicts: in the case of adequate food resources, society was relatively stable with increased economic level, there was no need to wage war for food; in the case of food shortage, humans needed to snatch limited food resources and thus may reduce economic level and cause war. As an example, there was a peak in number of wars between ∼600 and 300 BP, roughly equivalent to the Little Ice Age, which occurred during a period of drought and reduced cereal reduction (Wang et al., 2003).

However, the relationship among the economic level, the number of wars and the cereal yields was not always consistent. For instance, ∼1,100 to 900 BP corresponded to a period of humid climate and had relatively high cereal yields, but the economic index was extremely low. This shows that although precipitation could affect cereal production, it was not necessarily the only factor that determined economic level and wars in history, other factors such as technological development level and social structure may also play important roles.

CONCLUSION

In this study, we used sediments in the NYSM regions as the research material and reconstructed a ∼4,000-year record of monsoon precipitation via median grain size. The ratio of SiO_2/Al_2O_3 and the ratio of Rb/Sr showed close linear correlation with the median grain size, thus supporting the reliability of median grain size as an indicator of macroscale monsoon precipitation in northern China.

Based on the median grain size and indices including $\delta^{18}O$ values in stalagmites, wet-dry index from historical records and precipitation reconstructed by tree-ring data, the precipitation and civilization history of northern China during the past ∼4,000 years can be broadly divided into five intervals: throughout ∼4,000–2,500 BP, ∼1,350–750 BP and the past ∼250 years, the monsoon precipitation was relatively high, corresponding to the periods of cultural prosperity. During ∼2,500–1,350 BP and ∼750–250 BP, the monsoon precipitation was relatively low, corresponding to the periods of social unrest and change in dynasties.

Monsoon precipitation may play an important role on the economic index and frequency of wars in northern China during the last 2,000 years by affecting cereal yields. Relatively low precipitation could cause a decrease in cereal yields, and could lead to further instabilities in society, a downturn of the economy and even wars. Nevertheless, factors other than monsoon precipitation may also play roles in changing the economy and war frequencies.

DATA AVAILABILITY STATEMENT

The datasets generated for this study are available on request to the corresponding author.

AUTHOR CONTRIBUTIONS

XZ designed the research. SJ, LT, and XL performed the research. JZ analyzed the data and wrote the manuscript. All authors contributed to the article and approved the submitted version.

FUNDING

This study was jointly supported by the National Natural Science Foundation of China (grants 41822707, 41888101, and 41672159) and the Youth Innovation Promotion Association CAS (grant 2018498).

REFERENCES

Betts, A., Jia, P. W., and Dodson, J. (2014). The origins of wheat in China and potential pathways for its introduction: A review. *Quat. Int.* 348, 158–168. doi: 10.1016/j.quaint.2013.07.044

Boulay, S., Colin, C., Trentesaux, A., Pluquet, F., Bertaux, J., Blamart, D., et al. (2003). Mineralogy and sedimentology of Pleistocene sediment in the South China Sea (ODP Site 1144). *Proc. Ocean Drill. Prog. Sci. Results* 184, 1–21.

Cearreta, A., and Murray, J. W. (2000). AMS ^{14}C dating of Holocene estuarine deposits: consequences of high-energy and reworked foraminifera. *Holocene* 10, 155–159. doi: 10.1191/095968300669405262

Chen, F., Liu, J., Xu, Q., Li, Y., Chen, J., Wei, H., et al. (2013). Environmental magnetic studies of sediment cores from Gonghai Lake: implications for monsoon evolution in North China during the late glacial and Holocene. *J. Paleolimnol.* 49, 447–464. doi: 10.1007/s10933-012-9677-3

Chen, F., Xu, Q., Chen, J., Birks, H. J. B., Liu, J., Zhang, S., et al. (2015). East Asian summer monsoon precipitation variability since the last deglaciation. *Sci. Rep.* 5:11186. doi: 10.1038/srep11186

Chen, Y., Chen, J., Liu, L., Ji, J., and Zhang, J. (2003). Spatial and temporal changes of summer monsoon on the Loess Plateau of Central China during the last 130 ka inferred from Rb/Sr ratios. *Sci. China Ser. D Earth Sci.* 46:1022. doi: 10.1007/BF02959397

Eberhard, W. (2013). *A History of China*. Abingdon: Routledge.

Fabb, B. (1976). *X-Ray Fluorescence Analysis of 21 Selected Major, Minor.* US Geological Survey Professional Paper. Reston, VA: United States Geological Survey, 89.

Fan, K. (2010). Climatic change and dynastic cycles in Chinese history: a review essay. *Clim. Change* 101, 565–573. doi: 10.1007/s10584-009-9702-3

Ge, Q., Fang, X., and Zheng, J. (2014). Learning from the historical impacts of climatic change in China. *Adv. Earth Sci.* 29, 23–29. doi: 10.11867/j.issn.1001-8166.2014.01.0023

Ge, Q., Zheng, J., Fang, X., Man, Z., Zhang, X., Zhang, P., et al. (2003). Winter half-year temperature reconstruction for the middle and lower reaches of the Yellow River and Yangtze River, China, during the past 2000 years. *Holocene* 13, 933–940. doi: 10.1191/0959683603h1680rr

Ge, Q., Zheng, J., Tian, Y., Wu, W., Fang, X., and Wang, W. (2008). Coherence of climatic reconstruction from historical documents in China by different studies. *Int. J. Climatol.* 28, 1007–1024. doi: 10.1002/joc.1552

Gu, J., Zhao, J. B., and Zhou, J. (2007). Drought disaster and climate change in yuan dynasty in guanzhong area. *Mar. Geol. Quat. Geol.* 27:111. doi: 10.1016/S1872-5791(07)60044-X

Gupta, A. K., Anderson, D. M., Pandey, D. N., and Singhvi, A. K. (2006). Adaptation and human migration, and evidence of agriculture coincident with changes in the Indian summer monsoon during the Holocene. *Curr. Sci.* 90:1082. doi: 10.1029/2005JG000076

Haug, G. H., Günther, D., Peterson, L. C., Sigman, D. M., Hughen, K. A., and Aeschlimann, B. (2003). Climate and the collapse of Maya civilization. *Science* 299, 1731–1735. doi: 10.1126/science.1080444

He, B., Miao, C., and Shi, W. (2013). Trend, abrupt change, and periodicity of streamflow in the mainstream of Yellow River. *Environ. Monit. Assess.* 185, 6187–6199. doi: 10.1007/s10661-012-3016-z

He, Y., Zhou, X., Liu, Y., Yang, W., Kong, D., Sun, L., et al. (2014). Weakened Yellow Sea warm current over the last 2–3 centuries. *Quat. Int.* 349, 252–256. doi: 10.1016/j.quaint.2013.09.039

Hong, Y., Wang, Z., Jiang, H., Lin, Q., Hong, B., Zhu, Y., et al. (2000). A 6000-year record of changes in drought and precipitation in northeastern China based on a δ13C time series from peat cellulose. *Earth Planet. Sci. Lett.* 185, 111–119. doi: 10.1016/S0012-821X(00)00367-8

Hsiang, S. M., Burke, M., and Miguel, E. (2013). Quantifying the influence of climate on human conflict. *Science* 341:1235367. doi: 10.1126/science.1235367

Issar, A. S., and Zohar, M. (2004). *Climate Change-Environment and Civilization in the Middle East: Environment and Civilization in the Middle East.* Berlin: Springer Science & Business Media.

Ji, C., Li, K., Yu, B., Dong, L., and Liu, Q. (2019). The multi-time scale variations of water exchange across the Bohai Strait. *Oceanol. Limnol. Sin.* 50, 24–30.

Li, A., Qiao, L., Wan, X., and Ma, W. (2016). Distribution, flux and seasonal variation of suspended particulate matters in the Bohai Strait. *Oceanol. Limnol. Sin.* 47, 310–318. doi: 10.11693/hyhz20150700202

Li, H., An, C., Fan, W., Dong, W., Zhao, Y., and Wang, H. (2015). Population history and its relationship with climate change on the Chinese Loess Plateau during the past 10,000 years. *Holocene* 25, 1144–1152. doi: 10.1177/0959683615580200

Li, J., Dodson, J., Yan, H., Zhang, D., Zhang, X., Xu, Q., et al. (2017). Quantifying climatic variability in monsoonal northern China over the last 2200 years and its role in driving Chinese dynastic changes. *Quat. Sci. Rev.* 159, 35–46. doi: 10.1016/j.quascirev.2017.01.009

Li, X. (2002). The Xia-Shang-zhou chronology project: methodology and results. *J. East Asian Archaeol.* 4, 321–333. doi: 10.1163/15685230232245 4585

Li, X., Zhou, X., Liu, W., Fan, G., Cheng, P., and Xu, L. (2017). Oxygen isotopic composition of bulk carbonates in recent sediments from Lake Kuhai (NW China) and implications for hydroclimatic changes in headwater areas of the Yellow River on the northeastern Tibetan Plateau. *J. Asian Earth Sci.* 134, 150–159. doi: 10.1016/j.jseaes.2016.11.001

Liu, J., Chen, F., Chen, J., Xia, D., Xu, Q., Wang, Z., et al. (2011). Humid medieval warm period recorded by magnetic characteristics of sediments from Gonghai Lake, Shanxi, North China. *Sci. Bull.* 56, 2464–2474. doi: 10.1007/s11434-011-4592-y

Liu, J., Chen, J., Zhang, X., Yu, L., and Chen, F. (2015). Holocene East Asian summer monsoon records in northern China and their inconsistency with Chinese stalagmite δ18O records. *Earth Sci. Rev.* 148, 194–208. doi: 10.1016/j.earscirev.2015.06.004

Miguel, S., Bolivar, J. P., and García-Tenorio, R. (2003). Mixing, sediment accumulation and focusing using 210 Pb and 137 Cs. *J. Paleolimnol.* 29, 1–11. doi: 10.1023/a:1022864615111

Pandey, N. (2005). *Societal Adaptation to Abrupt Climate Change and Monsoon Variability: Implications for Sustainable Livelihoods of Rural Communities Report*. New Delhi: Winrock Int.

Peng, S., and Guo, Z. (2001). Geochemical indicator of original eolian grain size and implications on winter monsoon evolution. *Sci. China Ser. D Earth Sci.* 44, 261–266. doi: 10.1007/BF02911995

Peng, Y., Xiao, J., Nakamura, T., Liu, B., and Inouchi, Y. (2005). Holocene East Asian monsoonal precipitation pattern revealed by grain-size distribution of

core sediments of Daihai Lake in Inner Mongolia of north-central China. *Earth Planet. Sci. Lett.* 233, 467–479. doi: 10.1016/j.epsl.2005.02.022

Potts, R. (2012). Evolution and environmental change in early human prehistory. *Annu. Rev. Anthropol.* 41, 151–167. doi: 10.1146/annurev-anthro-092611-145754

Schirokauer, C., and Brown, M. (2012). *A Brief History of Chinese Civilization*. Boston, MA: Cengage Learning.

Sun, Q., Wang, Z., Chen, J., and Feng, W. (2009). Climate implications of major geochemical elements in the Holocene sediments of the North and East China monsoonal regions. *Front. Earth Sci. China* 3:291–296. doi: 10.1007/s11707-009-0035-3

Sun, Y., Wu, F., Clemens, S. C., and Oppo, D. W. (2008). Processes controlling the geochemical composition of the South China Sea sediments during the last climatic cycle. *Chem. Geol.* 257, 240–246. doi: 10.1016/j.chemgeo.2008.10.002

Tan, L., Cai, Y., An, Z., Edwards, R. L., Cheng, H., Shen, C., et al. (2011). Centennial-to decadal-scale monsoon precipitation variability in the semi-humid region, northern China during the last 1860 years: records from stalagmites in Huangye Cave. *Holocene* 21, 287–296. doi: 10.1177/0959683610378880

Tan, L., Cai, Y., Yi, L., An, Z., and Ai, L. (2008). Precipitation variations of Longxi, northeast margin of Tibetan Plateau since AD 960 and their relationship with solar activity. *Clim. Past* 4, 19–28. doi: 10.5194/cp-4-19-2008

Tsonis, A. A., Swanson, K. L., Sugihara, G., and Tsonis, P. A. (2010). Climate change and the demise of Minoan civilization. *Clim. Past* 6, 525–530. doi: 10.5194/cp-6-525-2010

Wang, G., Zhang, J., Jin, J., Weinberg, J., Bao, Z., Liu, C., et al. (2017). Impacts of climate change on water resources in the Yellow River basin and identification of global adaptation strategies. *Mitig. Adapt. Strateg. Glob. Chang.* 22, 67–83. doi: 10.1007/s11027-015-9664-x

Wang, H., Liu, H., Liu, Y., Cui, H., and Abrahamsen, N. (2010). Mineral magnetism and other characteristics of sediments from an alpine lake (3,410 m a.s.l.) in central China and implications for late Holocene climate and environment. *J. Paleolimnol.* 43, 345–367. doi: 10.1007/s10933-009-9335-6

Wang, N., Li, Z., Li, Y., and Cheng, H. (2013). Millennial-scale environmental changes in the Asian monsoon margin during the Holocene, implicated by the lake evolution of Huahai Lake in the Hexi Corridor of northwest China. *Quat. Int.* 313, 100–109. doi: 10.1016/j.quaint.2013.08.039

Wang, S., and Li, Y. (2011). Channel variations of the different channel pattern reaches in the lower Yellow River from 1950 to 1999. *Quat. Int.* 244, 238–247. doi: 10.1016/j.quaint.2010.09.002

Wang, S., Liu, J., and Zhou, J. (2003). The climate of little Ice Age maximum in China. *J. Lake Sci.* 15, 369–376. doi: 10.18307/2003.0412

Wang, X. (2018). *Sediment Dynamics of Chinese Muddy Coasts and Estuaries: Physics, Biology and Their Interactions*. Cambridge, MA: Academic Press.

Wei, Z., Rosen, A. M., Fang, X., Su, Y., and Zhang, X. (2015). Macro-economic cycles related to climate change in dynastic China. *Quat. Res.* 83, 13–23. doi: 10.1016/j.yqres.2014.11.001

Wigley, T. M. L., Ingram, M. J., and Farmer, G. (1985). Climate and history: studies in past climates and their impact on man. *CUP Arch.* 19, 305–367. doi: 10.1016/0012-8252(83)90002-8

Xie, S., Evershed, R. P., Huang, X., Zhu, Z., Pancost, R. D., Meyers, P. A., et al. (2013). Concordant monsoon-driven postglacial hydrological changes in peat and stalagmite records and their impacts on prehistoric cultures in central China. *Geology* 41, 827–830. doi: 10.1130/G34318.1

Xu, Q., Chen, F., Zhang, S., Cao, X., Li, J., Li, Y., et al. (2017). Vegetation succession and East Asian summer monsoon changes since fthe last deglaciation inferred from high-resolution pollen record in Gonghai Lake, Shanxi Province, China. *Holocene* 27, 835–846. doi: 10.1177/0959683616675941

Xue, C., Liu, J., and Kong, X. (2011). Channel shifting of lower Yellow River in 1128-1855 AD and its influence to the sedimentation in Bohai, Yellow and East China Seas. *Mar. Geol. Quat. Geol.* 31, 25–36. doi: 10.3724/SP.J.1140.2011.05025

Yang, B., Qin, C., Wang, J., He, M., Melvin, T. M., Osborn, T. J., et al. (2014). A 3,500-year tree-ring record of annual precipitation on the northeastern Tibetan Plateau. *Proc. Natl. Acad. Sci. U.S.A.* 111, 2903–2908. doi: 10.1073/pnas.1319238111

Yang, Z., Zhang, Y., Bi, N., Kanai, Y., and Saito, Y. (2015). Sedimentary records off the modern Huanghe (Yellow River) delta and their response to deltaic river channel shifts over the last 200 years. *J. Asian Earth Sci.* 108, 68–80. doi: 10.1016/j.jseaes.2015.04.028

Yi, L., Yu, H., Ge, J., Lai, Z., Xu, X., Qin, L., et al. (2012). Reconstructions of annual summer precipitation and temperature in north-central China since 1470 AD based on drought/flood index and tree-ring records. *Clim. Change* 110, 469–498. doi: 10.1007/s10584-011-0052-6

Yin, J., Su, Y., and Fang, X. (2016). Climate change and social vicissitudes in China over the past two millennia. *Quat. Res.* 86, 133–143. doi: 10.1016/j.yqres.2016.07.003

Yin, S., Huang, C., and Li, X. (2005). Historical drought and water disasters in the Weihe Plain. *J. Geogr. Sci.* 15, 97–105. doi: 10.1007/BF02873112

Zeng, X. (2005). Direct seeding rice in Chinese history. *Agric. Hist. China* 2, 3–16. doi: 10.3969/j.issn.1000-4459.2005.02.001

Zhang, D., Dong, G., Wang, H., Ren, X., Qiang, M., and Chen, F. (2016). History and possible mechanisms of prehistoric human migration to the Tibetan Plateau. *Sci. China Earth Sci.* 59, 1765–1778. doi: 10.1007/s11430-015-5482-x

Zhang, P., Cheng, H., Edwards, R. L., Chen, F., Wang, Y., Yang, X., et al. (2008). A test of climate, sun, and culture relationships from an 1810-year Chinese cave record. *Science* 322, 940–942. doi: 10.1126/science.1163965

Zhang, Y., Zhou, X., He, Y., Jiang, Y., Liu, Y., Xie, Z., et al. (2019). Persistent intensification of the Kuroshio current during late Holocene cool intervals. *Earth Planet. Sci. Lett.* 506, 15–22. doi: 10.1016/j.epsl.2018.10.018

Zhao, H., Han, X., Chen, R., Chu, F., and Gao, S. (2008). Characteristics of main elements and their palaeoenvironment significance of Core 191 in the northern South China *Sea. Acta Oceanol. Sin.* 30, 85–93. doi: 10.3321/j.issn:0253-4193.2008.06.010

Zhao, P., Tan, L., Zhang, P., Wang, S., Cui, B., Li, D., et al. (2018). Stable isotopic characteristics and influencing factors in precipitation in the monsoon marginal region of Northern China. *Atmosphere* 9:97. doi: 10.3390/atmos9030097

Zheng, J. (2005). Temperature variation in the Eastern China during Wei, Jin and South-North Dynasties(220 580 A.D.). *Quat. Sci.* 25, 129–140. doi: 10.3321/j.issn:1001-7410.2005.02.002

Zheng, J., Wang, W., Ge, Q., Man, Z., and Zhang, P. (2006). Precipitation variability and extreme events in eastern china during the past 1500 years. *Terr. Atmos. Ocean. Sci.* 17, 579–592. doi: 10.1111/j.1600-0889.2006.00188.x

Zhou, X., Jia, N., and Cheng, W. (2013). Relocation of the Yellow River estuary in 1855 AD recorded in the sediment core from the northern Yellow Sea. *J. Ocean Univ. China* 12, 624–628. doi: 10.1007/s11802-013-2199-4

Zhou, X., Sun, L., Huang, W., Cheng, W., and Jia, N. (2012). Precipitation in the Yellow River drainage basin and East Asian monsoon strength on a decadal time scale. *Quat. Res.* 78, 486–491. doi: 10.1016/j.yqres.2012.07.008

Conflict of Interest: The authors declare that the research was conducted in the absence of any commercial or financial relationships that could be construed as a potential conflict of interest.

Copyright © 2020 Zhang, Zhou, Jiang, Tu and Liu. This is an open-access article distributed under the terms of the Creative Commons Attribution License (CC BY). The use, distribution or reproduction in other forums is permitted, provided the original author(s) and the copyright owner(s) are credited and that the original publication in this journal is cited, in accordance with accepted academic practice. No use, distribution or reproduction is permitted which does not comply with these terms.

frontiers in Earth Science

REVIEW
published: 31 July 2020
doi: 10.3389/feart.2020.00316

Mercury Deposition, Climate Change and Anthropogenic Activities: A Review

Feng Li[1], Chunmei Ma[1] and Pingjiu Zhang[2]*

[1] School of Geography and Ocean Science, Nanjing University, Nanjing, China, [2] School of Geography and Tourism, Anhui Normal University, Wuhu, China

As a toxic and harmful global pollutant, mercury enters the environment through natural sources, and human activities. Based on large numbers of previous studies, this paper summarized the characteristics of mercury deposition and the impacts of climate change and human activities on mercury deposition from a global perspective. The results indicated that global mercury deposition changed synchronously, with more accumulation during the glacial period and less accumulation during the interglacial period. Mercury deposition fluctuated greatly during the Early Holocene but was stable and low during the Mid-Holocene. During the Late Holocene, mercury deposition reached the highest value. An increase in precipitation promotes a rise in forest litterfall Hg deposition. Nevertheless, there is a paucity of research on the mechanisms of mercury deposition affected by long-term humidity changes. Mercury accumulation was relatively low before the Industrial Revolution ca. 1840, while after industrialization, intensive industrial activities produced large amounts of anthropogenic mercury emissions and the accumulation increased rapidly. Since the 1970s, the center of global mercury production has gradually shifted from Europe and North America to Asia. On the scale of hundreds of thousands of years, mercury accumulation was greater in cold periods and less in warm periods, reflecting exogenous dust inputs. On millennial timescales, the correspondence between mercury deposition and temperature is less significant, as the former is more closely related to volcanic eruption and human activities. However, there remains significant uncertainties such as non-uniform distribution of research sites, lack of mercury deposition reconstruction with a long timescale and sub-century resolution, and the unclear relationship between precipitation change and mercury accumulation.

Keywords: mercury deposition, site distribution, climate change, anthropogenic activities, industrialization

OPEN ACCESS

Edited by:
Liangcheng Tan,
Chinese Academy of Sciences, China

Reviewed by:
Guanghui Dong,
Lanzhou University, China
Ruoyu Sun,
Tianjin University, China

****Correspondence:***
Chunmei Ma
chunmeima@nju.edu.cn

Specialty section:
This article was submitted to Quaternary Science, Geomorphology and Paleoenvironment, a section of the journal Frontiers in Earth Science

Received: *21 January 2020*
Accepted: *03 July 2020*
Published: *31 July 2020*

Citation:
Li F, Ma C and Zhang P (2020) Mercury Deposition, Climate Change and Anthropogenic Activities: A Review. Front. Earth Sci. 8:316. doi: 10.3389/feart.2020.00316

INTRODUCTION

As a toxic and harmful global pollutant, mercury enters the environment through natural sources (volcanic eruptions, oceans, soil, and forests, etc.), and human activities (fossil fuel combustion; gold, silver, and mercury mining; non-ferrous metal smelting; etc.; Tang et al., 2012; Guédron et al., 2018; Obrist et al., 2018; Pratte et al., 2018). Mercury in the atmosphere includes particulate mercury and gaseous mercury. Particulate mercury includes Hg(0) and $HgCl_2$, among others, which are adsorbed on the surface of particles or combined with particles; gaseous mercury mainly

exists in the form of Hg(O) (Wang, 2011). Due to its high volatility, low chemical activity, and low solubility, mercury is characterized by a long atmospheric life (0.5–2 years), and long-distance transport (Roos-Barraclough et al., 2002). Furthermore, there are a few other volatile mercury compounds, including $HgBr_2$, $HgCl_2$, and $Hg(OH)_2$, that are easily soluble in water and reduced to Hg(0), referred to as reactive gaseous mercury (RGM; Wang, 2011). Mercury under long-distance transportation can enter natural archives, including peatlands, lacustrine deposits, ice cores, coastal salt marsh sediments, and marginal pelagic sediments, through dry and wet deposition (Schuster et al., 2002; Tang et al., 2012; Donovan et al., 2013; Krabbenhoft and Sunderland, 2013; Guédron et al., 2018; Kim et al., 2019). These characteristics of mercury accumulation in natural archives can, to some extent, reflect the process of atmospheric mercury deposition during historical periods, and the deposition rate may be subject to factors such as climate change, geological conditions, volcanic eruptions, and human activities in the natural environment (Biester et al., 2007; Guédron et al., 2019).

In recent years, there have been many studies reconstructing atmospheric mercury deposition during historical periods using the natural archives. These studies focused mainly on the Northern Hemisphere, whereas studies in the Southern Hemisphere were limited to Chile (Biester et al., 2002, 2003; Hermanns and Biester, 2013a,b; Daga et al., 2016; Guédron et al., 2019), Brazil (Peìrez-Rodrìguez et al., 2015; De Lacerda et al., 2017), and Peru of South America (Cooke et al., 2009; Beal et al., 2014). In the Northern Hemisphere, European countries, represented by Switzerland (Roos-Barraclough et al., 2002; Roos-Barraclough and Shotyk, 2003; Zaccone et al., 2008; Thevenon et al., 2011), Spain (Martínez-Cortizas et al., 1999, 2012; Gallego et al., 2013; Serrano et al., 2013; Corella et al., 2017), Denmark (Shotyk et al., 2003), Greenland (Shotyk et al., 2003; Zheng, 2015; Pérez-Rodríguez et al., 2017), Scotland (Farmer et al., 2009; Küttner et al., 2014), Norway (Steinnes and Sjøbakk, 2005; Drevnick et al., 2012), and Sweden (Bindler et al., 2004), were studied mostly in terms of mercury deposition, followed by North America, represented by Canada (Givelet et al., 2004; Sunderland et al., 2008; Zdanowicz et al., 2015, 2016; Wiklund et al., 2017; Korosi et al., 2018; Štrok et al., 2019), and the United States (Benoit et al., 1998; Schuster et al., 2002; Arnason and Fletcher, 2003; Conaway et al., 2004; Gray et al., 2005; Roos-Barraclough et al., 2006; Donovan et al., 2013; Megaritis et al., 2014; Kurz et al., 2019). In contrast, there have been fewer studies on mercury deposition in China, with the research areas mainly distributed in the Shennongjia Dajiu Lake Basin (Li et al., 2016, 2017), the Greater Khingan Range (Bao et al., 2016), the Lesser Khingan Range (Xu et al., 2010; Tang et al., 2012), the Tibetan Plateau (Wang et al., 2010; Yang et al., 2010; Huang et al., 2013), and the South China Sea (Xu et al., 2010; Liu et al., 2012). In turn, there have numerous time series analyses that document changes in mercury deposition on 10^3 to 10^1 timescales that evaluate the impact of climate change and human activities on mercury deposition. However, these studies were almost always limited to a certain place or a certain area and explained only the mercury accumulation in a certain area. We are unaware of previous reviews of mercury deposition on a longer timescale from a global perspective. The authors hoped to find similarities and differences between different regions by analyzing and summarizing historical mercury deposition data at a global scale, and explored the relationship between mercury deposition and climate change and human activities.

This paper identified and analyzed relevant studies on atmospheric mercury deposition regarding climate change and human activities from a global perspective, discussing the prospects for future research. The global mercury deposition history reflected the global climate change and regional human activities during historical periods. Our work is conducive to the systematic understanding of mercury deposition and its influencing factors. On this basis, new methods and perspectives can be developed to conduct more in depth research.

DATA SOURCES

The data used in this study were mainly based on peer-reviewed papers and the data for Dajiu Lake Basin from our research group. The authors searched for documents in Elsevier SDOL, Nature, Science, Google Scholar, and the CNKI database, among others, using keywords such as "mercury deposition/mercury accumulation," "climate change," and "anthropogenic activities/human activities." Following the principles of a uniform spatial distribution and an extensive timescale, 36 sets of mercury deposition data from 60 papers were selected, covering the history of atmospheric mercury deposition on six continents (Asia, Europe, Africa, North America, South America, and Antarctica) recorded by natural archives (fen peat, lacustrine deposits, ice cores, and marine deposits, etc.) from 670 ka BP to now, as shown in **Table 1**.

According to the global studies on atmospheric mercury deposition, the authors found that the site distribution of global mercury deposition studies was characterized by an overall pattern of "more in the north and fewer in the south"; that is, the research areas were mostly distributed in the Northern Hemisphere, such as Europe (including Belgium, the Czech Republic, Denmark, Greenland, Ireland, Norway, Scotland, Spain, Sweden, and Switzerland), North America (including the United States and Canada), and China (including the Northeast Hani, Shennongjia Dajiu Lake Basin, Greater Khingan Range, Lesser Khingan Range, Sichuan Hongyuan, Huguangyan Maar Lake, Chao Lake, Tibetan Plateau, Xinjiang Mount Tianshan, East China Sea, Yellow Sea, and South China Sea), while in the Southern Hemisphere, the areas were distributed only in South America (including Chile, Peru, Brazil, and Bolivia), Africa (including the Berg River of South Africa and Lake Tanganyika in East Africa), and some parts of Antarctica, as shown in **Figure 1**.

RESULTS AND DISCUSSION

Regional Comparison of Global Mercury Deposition

At the global scale, atmospheric mercury deposition is closely related to climate variability (such as temperature and humidity changes) and human activities (such as mining, metal smelting,

TABLE 1 | Information of global mercury deposition research spots.

Number	Study site	Region	Location	Altitude/m	Materials dated	Depth/m	Dating methods	Age range	Selected references
a1	The Upper Fremont Glacier	Wyoming, United States	44°20′02″ N 111°36′49″ W	4100	Ice core	160	Isotope and chemical dating	1720–1993 AD	Schuster et al., 2002
a2	San Francisco Bay	United States	37°40′00″ N 122°25′00″ W	/	Coastal salt marsh	1.6	^{137}Cs, ^{210}Pb	1850–2000 AD	Donovan et al., 2013
a3	Southern Baffifin Island	Arctic Canada	63°57′53″ N 68°15′42″ W	1825	Firn	22.7	δ^{18}O	1970–2010 AD	Zdanowicz et al., 2015
a4	The Bay of Fundy	Canada	45°12′36″ N 66°54′12″ W	/	Peat bogs, Lake sediments, Coastal salt marsh	/	^{137}Cs, ^{210}Pb	1800–2000 AD	Sunderland et al., 2008
a5	Lake Ontario	Canada	49°48′00″ N 93°48′00″ W	/	Lake sediments	/	^{137}Cs, ^{210}Pb	1850–2000 AD	Wiklund et al., 2017
a6	Ellesmere Island	The Canadian High Arctic Archipelago	78°43′00″ N 74°27′00″ W	323	Lake sediments	12.1	^{137}Cs, ^{210}Pb	1850–2000AD	Korosi et al., 2018
a7	Caribou Bog	Central Maine, United States	44°58′97″ N 68°48′35″ W	80	Peat bogs	5	^{210}Pb, ^{14}C	8000 BC–2000 AD	Roos-Barraclough et al., 2006
a8	Lost Lake	Wyoming, United States	43°46′55″ N 110°06′00″ W	2889	Lake sediments	21	^{137}Cs, ^{210}Pb	1350–2000 AD	Kurz et al., 2019
a9	Oyster Point	California, United States	45°25′28″ N 111°20′28″ W	/	Coastal salt marsh	3	^{14}C	1700–2000 AD	Conaway et al., 2004
a10	Arlberg Bog	Minnesota, United States	46°56′00″ N 92°41′00″ W	/	Peat bogs	0.6	^{137}Cs, ^{210}Pb	1700–2000 AD	Benoit et al., 1998
a11	Narraguinnep Reservoir	Colorado, United States	40°31′26″ N 106°58′43″ W	2035	Lake sediments	10	^{137}Cs	1950–2000 AD	Gray et al., 2005
a12	Patroon Reservoir	New York, United States	42°41′05″ N 73°47′21″ W	/	Lake sediments	3	/	1955–2000 AD	Arnason and Fletcher, 2003
b1	Etang de la Gruère	Swiss Jura Mountains	47°15′34″ N 07°03′51″ E	1005	Peat bogs	6.5	^{210}Pb, ^{241}Am, ^{14}C	12500 BC–2000 AD	Roos-Barraclough et al., 2002
b2	Franches Montagnes	Swiss Jura Mountains	47°14′23″ N 07°02′57″ E	1020	Peat bogs	0.8	^{210}Pb, ^{14}C	1200 BC–2000 AD	Roos-Barraclough and Shotyk, 2003
b3	Lake Lucerne	Central Switzerland	46°13′25″ N 07°40′28″ E	2661	Lake sediments	1.2	^{14}C	14315 BC–2000 AD	Thevenon et al., 2011
b4	Roñanzas Bog	Asturias, Spain	43°20′13″ N 04°51′01″ W	/	Peat bogs	2	/	6000 BC–2000 AD	Gallego et al., 2013
b5	Galicia	Northwest Spain	43°32′00″ N 07°34′00″ W	/	Peat bogs	2.5	^{14}C	2635 BC–1995 AD	Martínez-Cortizas et al., 1999
b6	Lake Montcortès	Pyrenees, Spain	42°19′00″ N 00°19′00″ E	1031	Lake sediments	1.1	^{210}Pb, ^{14}C	1386–2010 AD	Corella et al., 2017
b7	Chao de Lamoso bog	Xistral Mountains, northwest Spian	43°14′35″ N 09°05′45″ W	1039	Peat bogs	1	^{210}Pb	1825–2000 AD	Martínez-Cortizas et al., 2012
b8	Portlligat Bay	Iberian Peninsula	42°17′32″ N 03°17′28″ E	/	Coastal salt marsh	5	^{14}C	2315 BC–2000 AD	Serrano et al., 2013
b9	Storelung Mose	Denmark	55°15′23″ N 10°15′22″ E	/	Peat bogs	1	^{14}C	2000 BC–2000 AD	Shotyk et al., 2003

(Continued)

TABLE 1 | Continued

Number	Study site	Region	Location	Altitude/m	Materials dated	Depth/m	Dating methods	Age range	Selected references
b10	Sandhavn	Southern Greenland	59°59′54″ N 44°46′36″ W	/	Peat bogs	0.4	^{210}Pb, ^{14}C	1270–2000 AD	Pérez-Rodríguez et al., 2017
b11	Raeburn Flow	Scotland, United Kingdom	55°02′04″ N 03°06′27″ W	/	Peat bogs	3.6	^{210}Pb, ^{14}C	1385 BC–2005 AD	Küttner et al., 2014
b12	Six ombrotrophic bogs	Norway	58°–69° N 04°–12° E	/	Peat bogs	1	^{210}Pb, ^{14}C	2000 BC–2000 AD	Steinnes and Sjøbakk, 2005
b13	Svalbard	Norwegian Arctic	80°03′05″ N 17°37′26″ E	/	Lake sediments	/	^{210}Pb	1800–1995 AD	Drevnick et al., 2012
b14	Store Mosse	South-central Sweden	57°15′00″ N 13°55′00″ E	/	Peat bogs	0.4	^{137}Cs, ^{210}Pb	1860–2000 AD	Bindler et al., 2004
b15	Marano and Grado Lagoon	Northern Adriatic Sea	40°12′–45°53′ N 12°13′–19°34′ E	/	Coastal salt marsh	1.1	^{137}Cs, ^{210}Pb	1650–2000 AD	Covelli et al., 2012
b16	Misten peat bog	Eastern Belgium	50°38′28″ N 03°11′17″ E	/	Peat bogs	1	^{210}Pb, ^{14}C	431–2011 AD	Allan et al., 2013
b17	Brdy Hills	The Czech Republic	49°42′42″ N 13°52′30″ E	/	Peat bogs	0.38	^{210}Pb	1807–2003 AD	Ettler et al., 2008
b18	Multiple lakes	Across England	50°–55° N 04° W–02° E	3–244	Lake sediments	1.5	^{137}Cs, ^{210}Pb, ^{241}Am	1850–2010 AD	Yang H. D. et al., 2016
c1	Tanghongling	Heilongjiang Province, northeast China	46°42′–48°40′ N 129°05′–129°55′ E	/	Peat bogs	1.05	^{210}Pb, ^{14}C	4480 BC–2000 AD	Tang et al., 2012
c2	Dajiu Lake Basin	Hubei Province, China	31°29′27″ N 109°59′45″ E	1760	Peat bogs	2.97	^{14}C	14141 BC–2004 AD	Li et al., 2017
c3	Motianling mountain	Western Great Hinggan Mountains, China	46°39′–47°39′ N 119°28′–121°23′ E	1200	Peat bogs	0.78	^{137}Cs, ^{210}Pb	1820–2005 AD	Bao et al., 2016
c4	Tibetan Plateau	Southwest China	28°41′–37°17′ N 85°23′–100°16′ E	2813–4652	Lake sediments	0.4	^{137}Cs, ^{210}Pb, ^{241}Am, ^{226}Ra	1830–2010 AD	Yang et al., 2010
c5	Qinghai Lake	Northeast Tibetan Plateau, China	36°24′00″ N 100°09′00″ E	/	Lake sediments	0.205	^{137}Cs, ^{210}Pb, ^{241}Am, ^{226}Ra	1860–2000 AD	Wang et al., 2010
c6	Guangjin Islan	South China Sea	16°27′07″ N 111°42′05″ E	/	Eggshells	1.05	^{210}Pb, ^{14}C	1280–2000 AD	Xu et al., 2010
c7	Xisha Islands	South China Sea	15°47′–17°08′ N 110°10′–112°55′ E	/	Coral sand	0.95	^{210}Pb, ^{14}C	1300–2000 AD	Liu et al., 2012
c8	Lake Sayram	Xinjiang Province, China	44°30′–44°42′ N 81°05′–81°15′ E	2072	Lake sediments	0.3	^{210}Pb	1810–2010 AD	Zeng et al., 2014
c9	Hani peat bog	Jilin Province, China	42°12′50″ N 126°31′05″ E	882–900	Peat bogs	9	^{14}C	11927 BC–2010 AD	Xiao, 2017
c10	Okinawa Trough	East China Sea	27°29′50″ N 126°41′16″ E	/	Marginal pelagic sediments	4.95	^{14}C	17990 BC–2010 AD	Lim et al., 2017

(Continued)

TABLE 1 | Continued

Number	Study site	Region	Location	Altitude/m	Materials dated	Depth/m	Dating methods	Age range	Selected references
c11	East China Sea	China	26°–32° N 120°–126° E	/	Marginal pelagic sediments	1.4	^{137}Cs, ^{210}Pb	1913–2015 AD	Zhang R. et al., 2018
c12	Shanghai	China	31°26′17″ N 121°23′02″ E	/	Lake sediments	0.35	^{137}Cs, ^{210}Pb	1750–2010 AD	Yang J. et al., 2016
c13	Chao Lake	Anhui Province, China	31°25′–31°43′ N 117°16′–117°51′ E	/	Lake sediments	0.3	^{210}Pb	1890–2009 AD	Zhang H. X. et al., 2018
c14	Hongyuan	Sichuan Province, China	32°46′46″ N 102°30′58″ E	3510	Peat bogs	0.25	^{210}Pb	1850–2006 AD	Shi et al., 2011
c15	Huguangyan Maar Lake	Guangdong Province, China	21°09′00″ N 110°17′00″ E	/	Lake sediments	0.94	^{137}Cs, ^{14}C	766–2005 AD	Han, 2018
c16	Huguangyan Maar Lake	Guangdong Province, China	21°09′00″ N 110°17′00″ E	/	Lake sediments	1.175	^{137}Cs, ^{210}Pb, ^{14}C	1350–2004 AD	Zeng et al., 2017
d1	Lake Titicaca region	Bolivia	15°50′–16°13′ S 68°03′–68°17′ W	3760–4040	Peat bogs	1.63	^{14}C	11430 BC–2014 AD	Guédron et al., 2018
d2	Lake Chungará	Chile	18°15′07″ S 69°09′47″ W	4520	Lake sediments	1.46	^{137}Cs, ^{210}Pb	686 BC–2014 AD	Guédron et al., 2019
d3	Lake Hambre	Patagonia, Chile	53°36′13″ S 70°57′08″ W	80	Lake sediments	13.94	^{14}C	14722 BC–2008 AD	Hermanns and Biester, 2013a
d4	The Gran Campo bog	Magellanic Moorlands, Chile	52°47′26″ S 72°56′37″ W	/	Peat bogs	1.5	^{210}Pb, ^{14}C	466 BC–1995 AD	Biester et al., 2002
d5	Lake Futalaufquen	Patagonia, Chile	42°49′00″ S 71°43′00″ W	518	Lake sediments	0.79	^{137}Cs	400–2000 AD	Daga et al., 2016
d6	Pinheiro Mire	Minas Gerais, Brazil	18°03′44″ S 43°39′42″ W	1230–1270	Peat bogs	2.2	^{14}C	54990 BC–2010 AD	Peìrez-Rodrìguez et al., 2015
d7	Yanacocha	Southeast Peru	13°56′42″ S 70°52′30″ W	4910	Lake sediments	3.33	^{210}Pb, ^{14}C	10290 BC–2010 AD	Beal et al., 2014
d8	Huancavelica	Central Peru	14°51′27″ S 75°24′38″ W	/	Lake sediments	/	^{210}Pb, ^{14}C	2800 BC–2000 AD	Cooke et al., 2009
e1	Berg River	South Africa	32°47′26″ S 18°12′05″ E	/	Coastal salt marsh	0.3	^{210}Pb	1900–2007 AD	Kading et al., 2009
e2	Lake Tanganyika	East Africa	04°40′–06°34′ S 29°37′–29°59′ W	/	Lake sediments	0.28	^{210}Pb, ^{14}C	1600–2000 AD	Conaway et al., 2012
f1	King George Island	Western Antarctica	62°11′57″ S 59°58′48″ W	/	Seal hairs	0.425	^{137}Cs, ^{14}C	18–2002 AD	Sun et al., 2006
f2	Adélie Basin	Southern Antarctica	66°12′53″ S 140°26′17″ E	/	Diatom ooze sediments	170	Diatom fossils	6600 BC–2000 AD	Zaferani et al., 2018
f3	Dome C	Antarctica	75°06′00″ S 123°21′00″ E	3233	Ice core	3062.4	δ^{18}O	652000 BC–2000 AD	Jitaru et al., 2009
f4	Dome C	Antarctica	77°39′00″ S 124°10′00″ E	3240	Ice core	905	δ^{18}O	31710 BC–1990 AD	Vandal et al., 1993

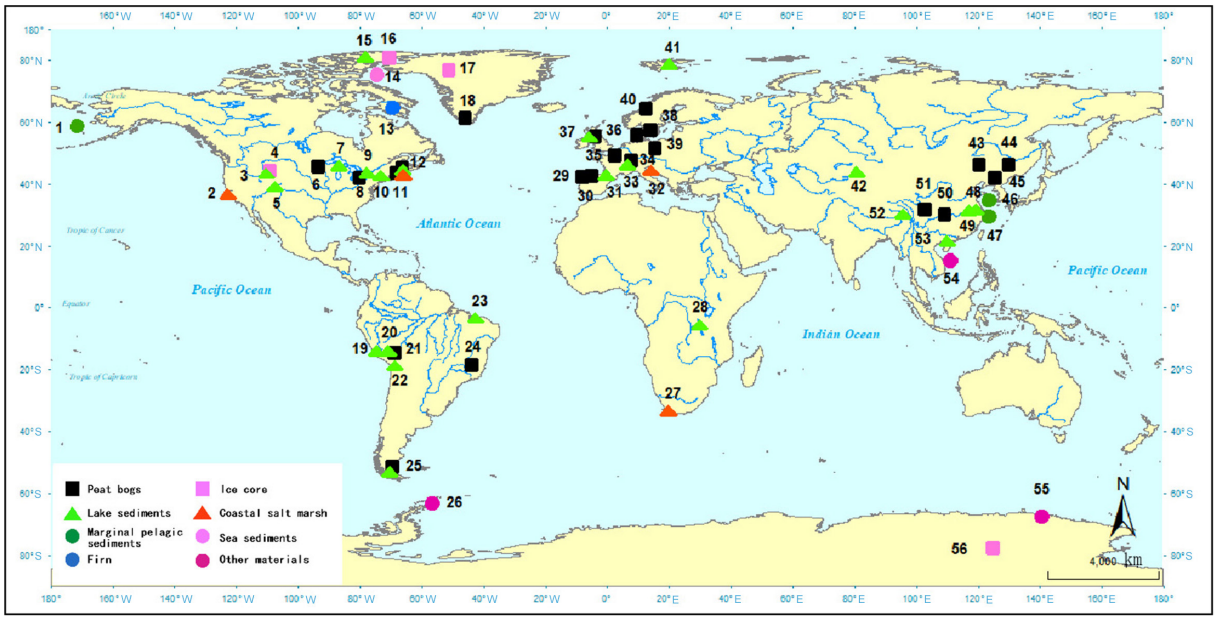

FIGURE 1 | Distribution of mercury deposition research spots. 1. Bering Sea (Kim et al., 2019); 2. San Francisco Bay (Donovan et al., 2013); 3. Wyoming (Kurz et al., 2019); 4. California (Conaway et al., 2004); 5. Colorado (Gray et al., 2005); 6. Minnesota (Benoit et al., 1998); 7. the Great Lakes (Grant et al., 2014); 8. Ontario (Givelet et al., 2004); 9. Lake Ontario (Wiklund et al., 2017); 10. New York (Arnason and Fletcher, 2003); 11. Maine (Roos-Barraclough et al., 2006); 12. the Bay of Fundy (Sunderland et al., 2008); 13. Baffifin Island (Zdanowicz et al., 2015); 14. the Arctic Archipelago (Štrok et al., 2019); 15. Ellesmere Island (Korosi et al., 2018); 16. Arctic Canada (Zdanowicz et al., 2016); 17. northwest Greenland (Zheng, 2015); 18. Narsaq Peninusla (Shotyk et al., 2003); 19. Huancavelica (Cooke et al., 2009); 20. Yanacocha (Beal et al., 2014); 21. Lake Titicaca region (Guédron et al., 2018); 22. Lake Chungará (Guédron et al., 2019); 23. Maranhão state (De Lacerda et al., 2017); 24. Minas Gerais (Peìrez-Rodrìguez et al., 2015); 25. Patagonia (Biester et al., 2002, 2003; Hermanns and Biester, 2013a; Daga et al., 2016); 26. King George Island (Sun et al., 2006); 27. Berg River (Kading et al., 2009); 28. Lake Tanganyika (Conaway et al., 2012); 29. Xistral Mountains (Martínez-Cortizas et al., 2012); 30. Asturias (Gallego et al., 2013); 31. Pyrenees (Corella et al., 2017); 32. Adriatic Sea (Covelli et al., 2012); 33. Lake Lucerne (Thevenon et al., 2011); 34. Swiss Jura Mountains (Roos-Barraclough and Shotyk, 2003); 35. Belgium (Allan et al., 2013); 36. Denmark (Shotyk et al., 2003); 37. Scotland (Farmer et al., 2009; Küttner et al., 2014); 38. Sweden (Bindler et al., 2004); 39. the Czech Republic (Ettler et al., 2008); 40. Norway (Steinnes and Sjøbakk, 2005); 41. Svalbard (Drevnick et al., 2012); 42. Mount Tianshan (Zeng et al., 2014); 43. Greater Khingan Range (Bao et al., 2016); 44. Lesser Khingan Range (Xu, 2010; Tang et al., 2012); 45. Hani peat bog (Xiao, 2017); 46. Yellow Sea (Kim et al., 2019); 47. East China Sea (Lim et al., 2017; Zhang H. X. et al., 2018; Zhang R. et al., 2018); 48. Shanghai (Yang H. D. et al., 2016); 49. Chao Lake (Zhang H. X. et al., 2018; Zhang R. et al., 2018); 50. Dajiu Lake Basin (Li et al., 2016, 2017); 51. Hongyuan (Shi et al., 2011); 52. Tibetan Plateau (Wang et al., 2010; Yang et al., 2010); 53. Huguangyan Maar Lake (Zeng et al., 2017; Han, 2018); 54. Xisha Islands (Xu et al., 2010; Liu et al., 2012); 55. Adélie Basin (Zaferani et al., 2018); and 56. Dome C (Vandal et al., 1993; Jitaru et al., 2009).

and other industrial activities). Due to the interaction between these factors and regional differences in human activities, the mercury deposition changes in different regions showed both certain commonalities and relatively large differences through time. Based on previous studies, the history of global mercury deposition was divided into the following four stages:

670 to 11.7 ka BP, Before the Holocene

The Dome C ice core in Antarctica provided a mercury deposition time series for past 670 ka (**Figure 2**). This record revealed mercury value peaks during glacial periods, while in the warm interglacial periods, the Hg concentration was relatively low (Jitaru et al., 2009). Similar trends occurred in the ice core records of Dome C for the past 34 ka, with greater temporal resolution (**Figure 3A**): The mercury concentration was relatively low 34 ka BP, and then it rose, maintaining a high value during 28 to 18 ka BP, corresponding to the Last Glacial Maximum (LGM, ∼26 to 16 ka BP); there was a reduction in 17 to 13 ka BP, representing the transition from the Last Glacial Period to the Holocene. According to peat records in southeastern Brazil (**Figure 3A**), the mercury concentration fluctuation 57 to 28 ka BP was relatively smooth, and the change in mercury concentration was mainly affected by atmospheric wet deposition related to precipitation and mineral input in the catchment area (Peìrez-Rodrìguez et al., 2015). The mercury concentration suddenly decreased to its lowest value 27 ka BP and then increased sharply and remained high from 26 to 17 ka BP, coinciding with the LGM (**Figure 3A**; Peìrez-Rodrìguez et al., 2015). Similar glacial to interstadial contrast in mercury levels was reported for lake sediment records in northeastern Brazil (De Lacerda et al., 2017). Records from this lake showed decreased Hg concentrations at ca. 17 to 13 ka BP, with subsequent recovery to the level prior to 17 ka BP, and until the sudden increase ca. 12 ka BP, corresponding to the Younger Dryas (YD) cooling event (De Lacerda et al., 2017). The mercury accumulations in the Dajiu Lake Basin, the Swiss Jura Mountains, and Peru also showed a significant increasing trend before and after the YD event (**Figure 3B**). Through the comparison of the above data, we concluded that glacial and interglacial timescales ca. the past 600 ka global mercury deposition appears to fluctuate in parallel

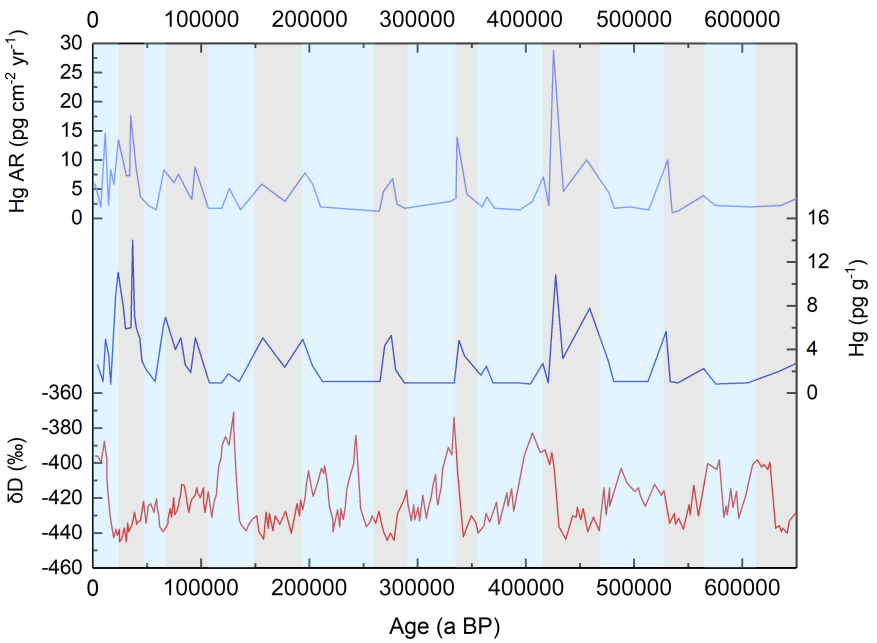

FIGURE 2 | Mercury deposition and temperature change in Antarctica since 670,000 a BP. The data were based on the research results of Petru Jitaru et al. in Dome C ice core of Antarctica, the red curve represents δD (‰), indicating the temperature change (Jitaru et al., 2009).

with broad climate variability with more Hg accumulation in the glacial periods and less accumulation in the interglacial periods.

11.7 to 8.2 ka BP, the Early Holocene

Post YD cooling, in general there was warming in to an interglacial climate. However, in the Early Holocene, the climate was still unstable and there were many climate oscillations sourced in the North Atlantic area, including the 11.1 ka BP event, 10.3 ka BP event, 9.4 ka BP event, 8.2 ka BP event, and possibly other climate variability (Bond et al., 1997). According to the mercury deposition records of the Dajiu Lake Basin, the Swiss Jura Mountains, Lake Titicaca, Yanacocha of Peru, and Maine United States (**Figure 3B**), both the mercury concentration and mercury accumulation rate for the Early Holocene were relatively low and Hg-depositional variability was linked to abrupt changes, especially during the 8.2 ka BP cooling event in the N. Atlantic. The mercury deposition in the Dajiu Lake Basin, the Swiss Jura Mountains, Lake Titicaca, Yanacocha in Peru, and Maine in the United States reached a peak. Through comparison of the regional data, it was discovered that in the Early Holocene, the mercury accumulation rate in the Dajiu Lake Basin of China was higher than that in the Swiss Jura Mountains and Maine in the United States, among other locations. Meanwhile, data from various regions showed that atmospheric mercury deposition was unstable during this period, with substantial fluctuations.

8.2 to 4.2 ka BP, the Mid-Holocene

Many studies showed that the climate in the Mid-Holocene was generally warm and humid (Dwyer et al., 1996; Haug et al., 2001; Kaufman et al., 2004). Global atmospheric mercury deposition was also characterized by relatively consistent values in the Mid-Holocene (**Figures 3B,C**). It is worth noting that the changes in mercury accumulation in some areas during this period were related to specific conditions. For example, the enrichment of mercury deposition from 8 to 6 ka BP in the Swiss Jura Mountains was related to volcanic eruptions (Roos-Barraclough et al., 2002); the mercury peaks of Lake Titicaca from 6 to 5 ka BP were caused by rich orographic precipitation in the eastern part of the Andes (Guédron et al., 2018). The comparison of the regional data showed that in the Mid-Holocene, the characteristics of atmospheric mercury deposition in the Dajiu Lake Basin and Lesser Khingan Range of China, the Swiss Jura Mountains, Spain, Norway, Maine, and Ontario, among other locations, were similar, and the atmospheric mercury accumulation rate and mercury concentrations were at a relatively low level, with the atmospheric mercury deposition being weaker and significantly lower than that during the Early Holocene.

4.2 to 0 ka BP, the Late Holocene

The Late Holocene is a stage when human civilization has developed rapidly and human activities have had a profound impact on natural systems. Since the Industrial Revolution, the population has increased dramatically and the impact of human activities on earth system reached an unprecedented magnitude. Under the multiple effects of natural systems and human activities, regional and global atmospheric mercury deposition changed significantly and the rate of atmospheric mercury accumulation increased to its highest value during historical periods. Atmospheric mercury deposition between 4.2 and 0 ka BP in all regions of the world continued to rise (**Figures 3C,D**), especially in the past hundreds of years. The atmospheric mercury accumulation rate and the mercury

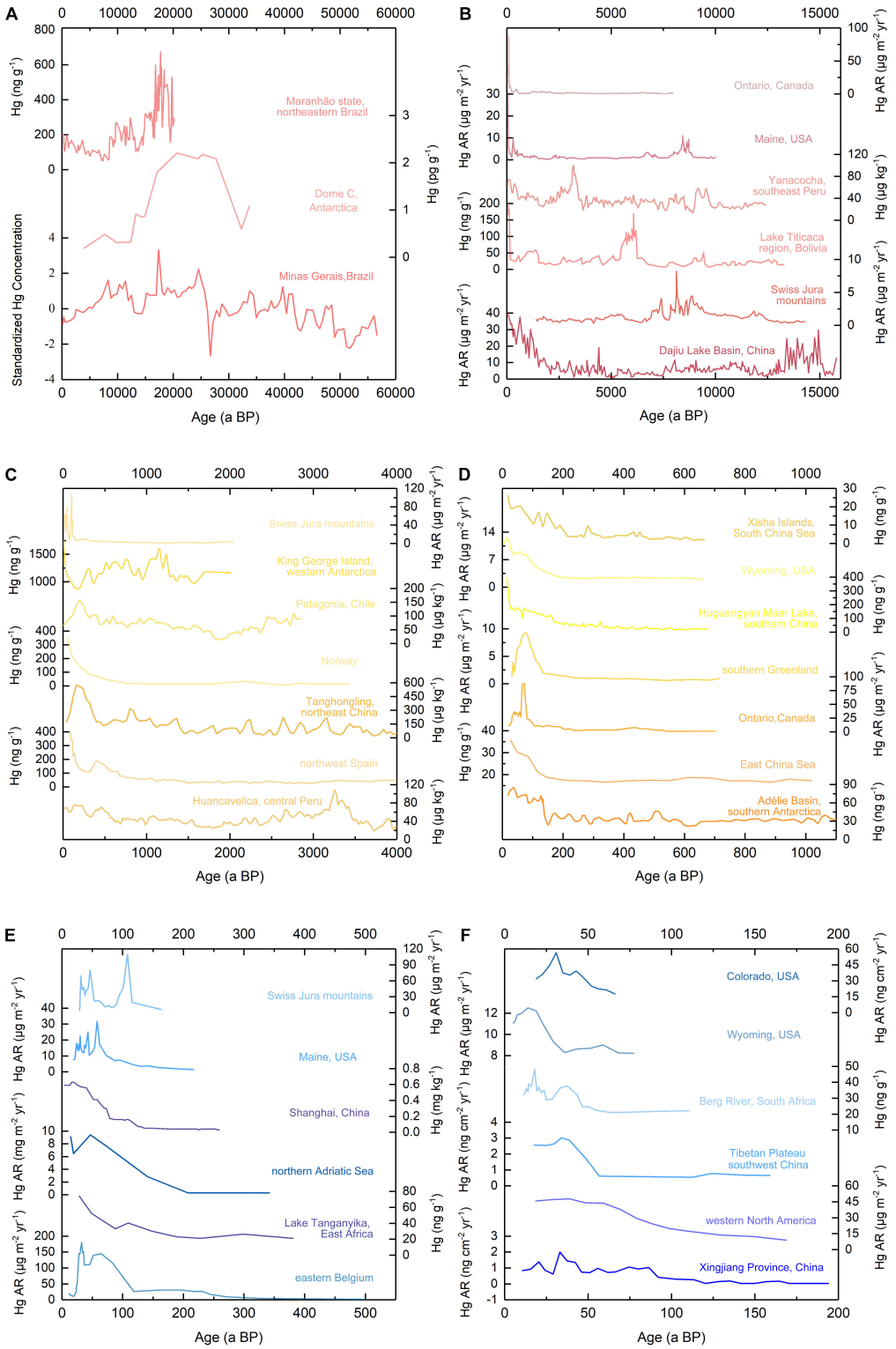

FIGURE 3 | Changes of mercury deposition in different time scales around the world. **(A)** From bottom to top: Standardized Hg concentrations in Minas Gerais, Brazil (Peirez-Rodrîguez et al., 2015); Hg concentrations in Dome C, Antarctica (Vandal et al., 1993); and Hg concentrations in Maranhão state, northeastern Brazil (De Lacerda et al., 2017). **(B)** From bottom to top: Hg Accumulation Rate (Hg AR) in Dajiu Lake Basin, China (Li et al., 2016); Hg AR in Swiss Jura Mountains (Roos-Barraclough et al., 2002); Hg concentrations in Lake Titicaca region, Bolivia (Guédron et al., 2018); Hg concentrations in Yanacocha, southeast Peru (Beal et al., 2014); Hg AR in Maine, United States (Roos-Barraclough et al., 2006); and Hg AR in Ontario, Canada (Givelet et al., 2004). **(C)** From bottom to top: Hg

(Continued)

FIGURE 3 | Continued
concentrations in Huancavelica, central Peru (Beal et al., 2014), northwest Spain (Martínez-Cortizas et al., 1999), Tanghongling, northeast China (Tang et al., 2012), Norway (Steinnes and Sjøbakk, 2005), Patagonia, Chile (Biester et al., 2003), King George Island, western Antarctica (Sun et al., 2006); and Hg AR in Swiss Jura Mountains (Roos-Barraclough et al., 2002). **(D)** From bottom to top: Hg concentrations in Adélie Basin, southern Antarctica (Zaferani et al., 2018), East China Sea (Kim et al., 2019); Hg AR in Ontario, Canada (Givelet et al., 2004), southern Greenland (Pérez-Rodríguez et al., 2017); Hg concentrations in Huguangyan Maar Lake, southern China (Zeng et al., 2017); Hg AR in Wyoming, United States (Kurz et al., 2019); and Hg concentrations in Xisha Islands, South China Sea (Huang et al., 2013). **(E)** From bottom to top: Hg AR in eastern Belgium (Allan et al., 2013); Hg concentrations in Lake Tanganyika, East Africa (Conaway et al., 2012); Hg AR in northern Adriatic Sea (Covelli et al., 2012); Hg concentrations in Shanghai, China (Yang H. D. et al., 2016); and Hg AR in Maine, United States (Roos-Barraclough et al., 2006), Swiss Jura Mountains (Roos-Barraclough et al., 2002). **(F)** From bottom to top: Hg AR in Xingjiang Province, China (Zeng et al., 2014), western North America (Drevnick et al., 2016), Tibetan Plateau, southwest China (Wang et al., 2010); Hg concentrations in Berg River, South Africa (Kading et al., 2009); and Hg AR in Wyoming, United States (Kurz et al., 2019), Colorado, United States (Gray et al., 2005).

concentration reached their highest values during the Mid- and Late Holocene (**Figures 3D,F**). This was mainly due to the significant increase in mercury emissions from human activities after the Industrial Revolution, which led to an increase in the rate of atmospheric mercury accumulation of several times or even tens of times.

Through the comparison of atmospheric mercury deposition data at a global scale, it could be inferred that the characteristics of mercury deposition in European countries represented by Switzerland, Greenland, Spain, and Belgium, among others, are similar to those of the North American countries represented by the United States and Canada. Specifically, beginning with the Industrial Revolution in the mid-19th century, the mercury deposition rate increased rapidly, and mercury accumulation reached a peak value in the mid- and late 20th century and then showed a downward trend. With the increasing emphasis on the environmental pollution caused by a large number of mercury emissions in European and North American countries, measures were taken in various regions to reduce mercury emissions (Roos-Barraclough and Shotyk, 2003; Bindler et al., 2004; Ettler et al., 2008; Sunderland et al., 2008; Farmer et al., 2009; Drevnick et al., 2012; Allan et al., 2013; Corella et al., 2017). The atmospheric mercury deposition rate in the Asian regions represented by Shanghai, the Xisha Islands, Huguangyan Maar Lake, and the East China Sea increased slowly after industrialization. The rate began to increase rapidly during the 1960s to 1970s, with mercury deposition continuing to rise. From the above comparison, it could be deduced that since the 1970s, the center of global mercury production has gradually shifted from Europe and North America to Asia (Xu et al., 2010; Zeng et al., 2017).

Mercury Deposition and Climate Change

In studies around the world, the impact of climate change on mercury deposition has been the focus of researchers with various outcomes. Most scholars believe that a cold and dry climate is conducive to mercury accumulation, while a warm and humid climate limits the accumulation of mercury (Roos-Barraclough et al., 2002, 2006; Jitaru et al., 2009; Gallego et al., 2013; Peìrez-Rodriìguez et al., 2015; Li et al., 2016; De Lacerda et al., 2017). Some scholars believe that there is more mercury accumulation during humid-climate periods and less accumulation of mercury during dry-climate periods (Guédron et al., 2018). Related to this issue, in the following section, two aspects of climate, namely, temperature change and humidity change, are analyzed and summarized.

Dry and Wet Deposition of Atmospheric Mercury

Mercury emitted from anthropogenic and natural sources to the atmosphere eventually falls back to the surface through dry and wet deposition. Dry deposition refers to the deposition of aerosol particles. An aerosol is a gas dispersion composed of solid or liquid particles suspended in a gas medium, which has a complex chemical composition (Wang, 2011). Wet deposition refers to the process of removing particles from the atmosphere through rainfall, snowfall, and other phenomena.

Atmospheric mercury deposition is a process through which various forms of mercury are removed from the atmosphere. The dry deposition of mercury mainly includes the direct deposition of Hg(0) and RGM, which occurs throughout the year as long as it does not rain heavily. The forms of mercury in wet deposition tend to be soluble and granular Hg(II). Due to the long-distance diffusion and water solubility of gaseous Hg(II), most of the mercury is deposited via Hg(II) dissolved in atmospheric water or adsorbed on the surface of raindrop particles (Fitzgerald et al., 1991). Mercury can react with O_3 in the atmosphere to form water-soluble Hg(II), which can be adsorbed on particles or dissolved in water and then deposited. Inorganic mercury compounds, such as methylmercury, deposit rapidly because of their solubility (Munthe et al., 1995). Although the wet deposition process of Hg(II) contributes greatly, it represents less than 5% of the total mercury in the atmosphere, and the continuous dry deposition of mercury almost all year is still dominant. Recent studies employing field monitoring and mercury isotopes showed that Hg(0) dry deposition far exceeds wet deposition by precipitation and the former can even be five times greater than the latter (Selin and Jacob, 2008; Enrico et al., 2016; Obrist et al., 2017; St. Louis et al., 2019).

At present, the deposition mechanism and long-term monitoring sites of mercury wet deposition flux in many countries are well established. As one of the countries emitting the most mercury in the world, China has yet to establish a relatively complete monitoring system for wet mercury deposition. Additionally, the measurement and evaluation of dry mercury deposition are mostly local or achieved by atmospheric models, and there are few published relevant records.

Impact of Temperature Change on Mercury Deposition

To evaluate the impact of temperature change on mercury deposition, the mercury deposition records of Maine of the United States, southeastern Peru, the Swiss Jura Mountains,

Patagonia of Chile, the Shennongjia Dajiu Lake Basin of China, Maranhão of Brazil, Dome C of Antarctica, and Minas Gerais of Brazil were selected for comparison, as shown in **Figure 4**. During the LGM (∼26–16 ka BP), the mercury concentration in Antarctica, as well as Minas Gerais and Maranhao, remained at a high level. From 17 to 13 ka BP, the mercury concentration showed a downward trend until it reached its peak again from 13 to11.5 ka BP, consistent with the YD event, and the mercury accumulation in the Dajiu Lake Basin and Patagonia also showed an obvious upward trend before and after the YD event. From 11.5 to 9 ka BP, the mercury concentration dropped gradually, but the decrease was small, and it increased significantly and reached its peak from 9 to 8 ka BP, corresponding to the 8.2 ka BP event, with the strongest cooling effect during the Holocene.

After 8.2 ka BP, the mercury accumulations generally showed a slow downward trend. The peak values of mercury accumulation in the Mid- and Late Holocene were mainly affected by volcanic eruptions and human activities (Vandal et al., 1993; De Lacerda et al., 2017). Volcanic emissions are thought to be an important natural source of atmospheric Hg. On millennial timescales, dust from volcanic eruptions might affect mercury deposition in paleoclimate records. Hg enrichment in Patagonia occurred during the periods of three volcanic eruptions two eruptions of Mt. Burney (8300 a BP and 4250 a BP) and one eruption of the Mt. Hudson volcano (7800 a BP; **Figure 4D**; Biester et al., 2003). Many volcanoes erupted between 8 and 6 ka BP in Europe, which explained the peaks of the Hg accumulation rate in the Swiss Jura Mountains (**Figure 4C**; Roos-Barraclough et al., 2002).

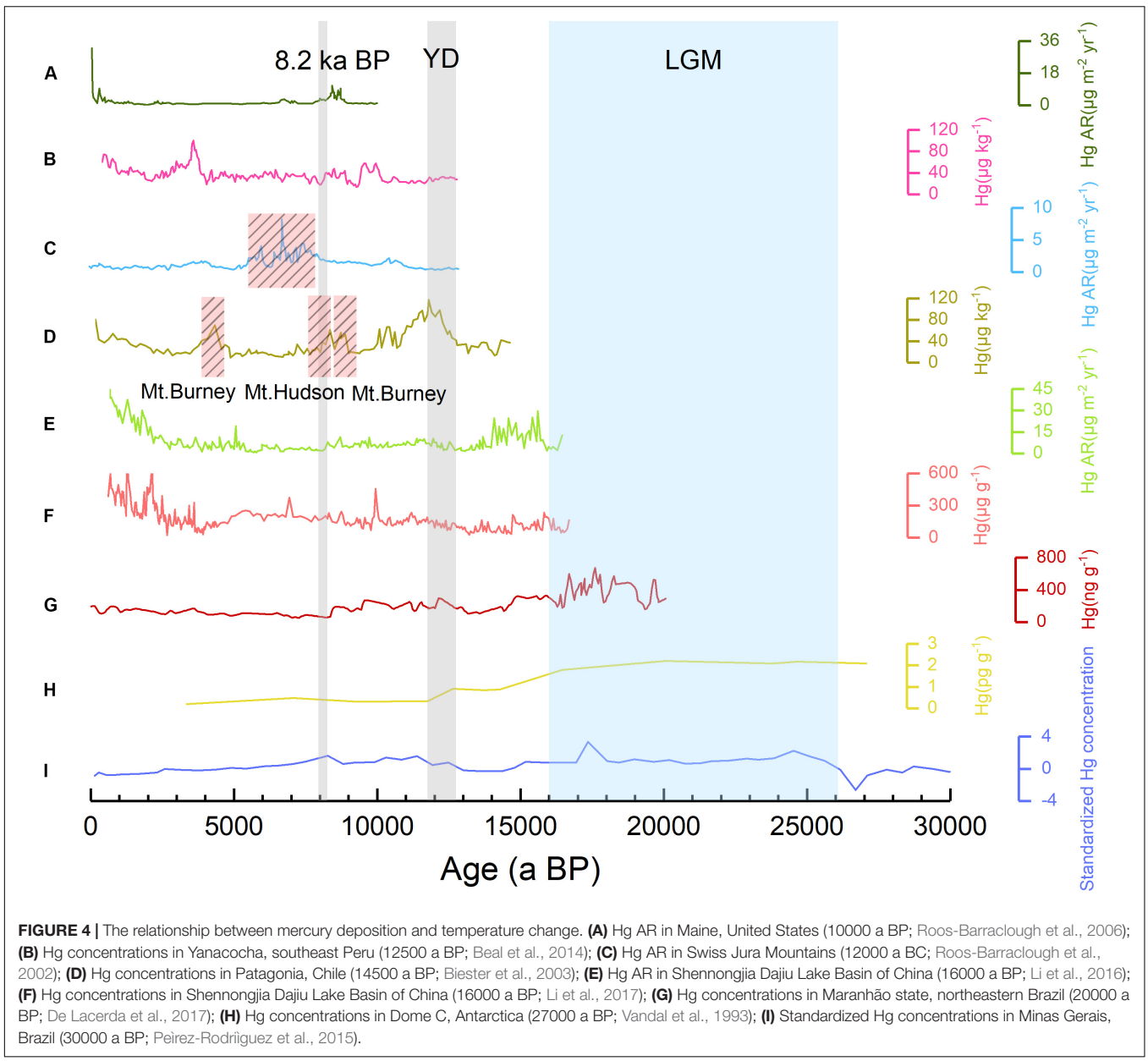

FIGURE 4 | The relationship between mercury deposition and temperature change. **(A)** Hg AR in Maine, United States (10000 a BP; Roos-Barraclough et al., 2006); **(B)** Hg concentrations in Yanacocha, southeast Peru (12500 a BP; Beal et al., 2014); **(C)** Hg AR in Swiss Jura Mountains (12000 a BC; Roos-Barraclough et al., 2002); **(D)** Hg concentrations in Patagonia, Chile (14500 a BP; Biester et al., 2003); **(E)** Hg AR in Shennongjia Dajiu Lake Basin of China (16000 a BP; Li et al., 2016); **(F)** Hg concentrations in Shennongjia Dajiu Lake Basin of China (16000 a BP; Li et al., 2017); **(G)** Hg concentrations in Maranhão state, northeastern Brazil (20000 a BP; De Lacerda et al., 2017); **(H)** Hg concentrations in Dome C, Antarctica (27000 a BP; Vandal et al., 1993); **(I)** Standardized Hg concentrations in Minas Gerais, Brazil (30000 a BP; Peìrez-Rodrìguez et al., 2015).

At longer timescales, it could be concluded that the temperature change from 30 to 8 ka BP was consistent with the fluctuation of atmospheric mercury deposition, especially during the LGM, YD event, and 8.2 ka BP event, and atmospheric mercury deposition showed a strong response. Petru Jitaru et al. reconstructed mercury deposition records and temperature changes since 670 ka BP at Dome C, Antarctica. As shown in **Figure 2**, there is a good correlation between peak mercury accumulation and cold periods. Based on these analyses, it could be concluded that a cold climate is conducive to mercury accumulation. According to the studies of different scholars, the following four reasons could be summarized regarding the specific mechanism: (1) Due to the high volatility of mercury, the mercury in the atmosphere is easily attached to objects such as particulate matter under cold conditions and then settles on the ground surface, known as the condensation effect (Roos-Barraclough et al., 2002; Gallego et al., 2013); (2) The atmospheric dust increases during cold periods, and this dust can carry the mercury in the atmosphere to the ground surface so that mercury accumulation is increased (Roos-Barraclough et al., 2002; Jitaru et al., 2009; Peìrez-Rodriìguez et al., 2015; De Lacerda et al., 2017; Li et al., 2017); (3) In colder environments, marine mercury emissions are higher (Vandal et al., 1993; Roos-Barraclough et al., 2002; Peìrez-Rodriìguez et al., 2015; De Lacerda et al., 2017) and the high-productivity marine emissions of gaseous mercury are important sources of atmospheric mercury (Vandal et al., 1993); and (4)The mercury released by soil degassing is lower during cold periods (Gallego et al., 2013). In conclusion, more exogenous dust inputs and an increase in mercury in the atmosphere during cold periods lead to mercury accumulation on the scale of tens of thousands of years, while on millennial timescales, mercury emitted from volcanic eruption to the atmosphere also has a certain impact on mercury deposition records.

Impact of Humidity Change on Mercury Deposition

The main effect of precipitation on mercury deposition is that an increase in precipitation promotes a rise in forest litterfall Hg deposition. Terrestrial vegetation often represents the first ecosystem compartment with which new atmospheric Hg interacts following deposition. It was recently demonstrated that a portion of newly wet-deposited Hg(II) may not initially pass directly through the forest canopy to the forest floor, but rather is retained over the growing season, only to be deposited later with litterfall (Graydon et al., 2006). Plant foliage provides an excellent surface for photochemical reduction of newly deposited Hg(II) remaining in the forest canopy following precipitation events (Lindberg et al., 1998). Litterfall Hg deposition is the major pathway for Hg loading into the forest (Zhou et al., 2013). Recent studies on the air-surface exchange of mercury and litterfall Hg deposition revealed that an increase in precipitation can elevate forest biomass, which in turn pumps more Hg(0) into litterfall and then soils (Lindberg et al., 1998; Graydon et al., 2006). It is generally believed that vegetation litter represents a net sink of atmospheric Hg (Lindberg et al., 1998; Demers et al., 2007; Pokharel and Obrist, 2011; Ma et al., 2017; Zhang et al., 2019). Therefore, an increase in precipitation may enhance absolute wet Hg deposition rather than wet deposition relative to dry deposition via vegetation. However, research on the mechanism of mercury deposition affected by long-term humidity change is lacking. The results of studies conducted in Brazil and Lake Titicaca showed that the atmospheric wet deposition of mercury during humid periods increased, so a humid climate is considered to be conducive to mercury accumulation (Peìrez-Rodriìguez et al., 2015; Guédron et al., 2018). However, most scholars found a significant relationship between a cold-dry climate and peak mercury deposition. Unfortunately, the influence of temperature could not be excluded to judge the relationships between humidity changes and mercury deposition. Furthermore, due to the small amount of data and conclusions available for reference, the relationship between humidity change and mercury deposition cannot be determined. The authors believe that studies of the relationship between precipitation changes and mercury deposition changes can be strengthened over long timescales and a more accurate conclusion can be drawn by comparing the two types of change.

Mercury Deposition and Anthropogenic Activities

According to a large number of previous studies, atmospheric mercury deposition caused by human activities began approximately 3,500 years ago. Before industrialization, gold, silver, and mercury mining and the widespread use of cinnabar were the main sources of anthropogenic mercury. After industrialization, coal combustion, mercury mining, non-ferrous metal smelting, liquid mercury production, steel manufacturing, cement manufacturing, gold mining, waste incineration, and the development of the chlor-alkali industry led to a sharp increase in anthropogenic emissions of mercury, which in turn caused a sharp increase in mercury deposition.

Preindustrial Era

With the development of human civilization, mercury is being increasingly used in all aspects of society. Cinnabar has a bright red color and never fades, so it has long been used as a pigment. According to the literature, the use of cinnabar can be traced back to the Shang Dynasty (∼1600–1046 BC) in China, and some characters engraved with cinnabar were found on unearthed animal bones or turtle shells (Li et al., 2016). Cinnabar was also used to color figurines and pottery; for example, the Terracotta Warriors were painted with cinnabar (Chen, 2017). In ancient times, mercury was considered an antiseptic, and mercury gas volatilized in underground palaces could prevent buried corpses and funerary objects from rotting for a long time. Since mercury is a highly toxic substance that can cause death in cases of inhalation at high volume, it was also used to poison tomb raiders (Liu and Wang, 2001; Duan, 2007). During the Qin and Han Dynasties of China (221 BC–220 AD), Chinese ancestors extracted elemental mercury from cinnabar, utilizing the easy solubility of gold and silver in mercury and the volatility of mercury to extract gold and silver from ores by using mercury, which was later called the "amalgamation process" (Li et al., 2016). For quite a long time in ancient times, the amalgamation process was the main method of gold smelting worldwide, until it was replaced by a more effective method with less mercury

pollution called the "cyanidation method" in the early 20th century (Sun et al., 2006). Mercury was also used in medicine. According to the manuscripts on silk named "Prescriptions for Fifty-two Diseases" in the Han Dynasty Changsha Mawangdui Tomb unearthed in 1973, transcription was performed during the Qin and Han Dynasties. It was the most ancient Chinese medicine prescription that has been discovered, in which mercury was used in four prescriptions. Moreover, mercury was once considered by Tibetans to be able to heal fractures, prolong life, and maintain good health (Wang et al., 2010; Yang et al., 2010).

At approximately 1400 BC, the Huancavelica cinnabar mine in Peru began to be mined. During the period of rapid development and expansion of mining and metallurgy in the Andes (∼500–1000 AD, ∼1000–1400 AD), mercury emissions increased continuously (Cooke et al., 2009). In Europe, the increase in anthropogenic mercury 2500 years ago was consistent with the high mercury mining activities and metallurgical history of Spain (Martínez-Cortizas et al., 1999). **Figure 5** shows that the mercury concentrations in various regions were higher in some stages between 2000 years ago and the beginning of industrialization, namely, the Roman Empire (27 BC–1453 AD), the Chinese Han Dynasty (202 BC–8 AD, 25–220 AD), the Mayan period (from approximately the 10th century BC to the 16th century AD), the Chinese Tang Dynasty (618–907 AD), and after the discovery of the New World (1650–1800 AD). The high mercury concentrations were closely related to the large-scale mining activities during these periods. However, between these periods, with the decrease in mining activities, the mercury concentrations showed a downward trend. Between 18 and 300 AD, both the Roman Empire and the Chinese Han Dynasty engaged in many mining activities when alchemy became popular at the time (Martínez-Cortizas et al., 1999; Sun et al., 2006). After 300 AD, the mercury concentrations declined. Between 300 and 750 AD, the mercury concentrations were relatively low, corresponding to the collapse of Rome and the decline in China's gold production (Brading and Cross, 1972; Sun et al., 2006). Between 1050 and 1250 AD, low mercury concentrations corresponded to the fall of Mayan civilization and the wars during the Southern Song Dynasty. In addition, the depletion of European silver mines and the suppression of gold mining also led to a decrease in mercury concentration (Sun et al., 2006). Since the beginning of 1250 AD, the mercury concentrations have increased, and during the period of Incan civilization in South America (from the 12th to 15th century), a large amount of gold was produced (Xiang and Huang, 2014). Meanwhile, new silver mines were discovered in Europe, and thousands of people joined the "Silver Tide" activities of the Christian Kingdom (Sun et al., 2006). After 1500 AD, the mercury concentrations fell to another low. Pizarro, a Spanish colonist, conquered the Inca in 1532 AD (Xiang and Huang, 2014), resulting in a reduction in mercury consumption. In the early 19th century, with the outbreak of the South American War of Independence, mercury consumption suddenly stopped and Spain, the main supplier of mercury in the world, also reduced mercury production (Martínez-Cortizas et al., 1999), leading to a decline in mercury concentration. With the rise of the Industrial Revolution in the mid-19th century, mercury concentrations began to rise sharply.

Industrial Age

Since the Industrial Revolution of 1840, coal combustion, non-ferrous metal smelting, and the chlor-alkali industry have become the main sources of anthropogenic mercury. Intensive industrial activities have caused unprecedented mercury pollution. According to previous studies, in Spain, the mercury accumulation after industrialization was 10 times as high as the level before industrialization (Serrano et al., 2013). In Norway, the figure was 15 (Steinnes and Sjøbakk, 2005); in Scotland, the figure was 20 (Farmer et al., 2009); and in Belgium, the figure was 63 (Allan et al., 2013). After the 1960s and 1970s, since European and North American countries began to pay attention to environmental issues and adopted a series of measures to reduce mercury emissions, such as closing the main mercury mines, reducing mercury emissions from flue gas emissions, reducing incinerator emissions, gradually phasing out mercury in waste streams, shutting down old facilities, and installing additional pollution control equipment (Benoit et al., 1998; Conaway et al., 2004; Sunderland et al., 2008; Yang H. D. et al., 2016; Yang J. et al., 2016; Corella et al., 2017; Obrist et al., 2018), mercury deposition was reduced to some extent. However, after the 1970s, with the rise of Asian countries, especially China and India, and the rapid development of industrialization and urbanization, Asia became the largest contributor to anthropogenic mercury, with its mercury emission accounting for more than half of the global emission in 2000 (Xu et al., 2010; Obrist et al., 2018). In recent decades, the massive production of mercury in Asia, coupled with the high mercury emissions from coal combustion, smelting, and waste incineration, has led to a significant increase in anthropogenic mercury emissions (Liu et al., 2012). This means that the mercury production center has gradually moved from Europe and North America to Asia.

Factors Influencing Mercury Deposition in Different Phases or at Different Timescales

Based on the previous analysis, it could be concluded that the main factors influencing mercury deposition include temperature change, human activities, and volcanic eruption, while the influencing factors vary among phases and timescales. According to **Figures 2**, **4**, before the Middle and Late Holocene, when human activities had limited environmental impact, mercury deposition was consistent with temperature changes. That is, on the scale of hundreds of thousands of years, mercury accumulated more in cold periods and less in warm periods, and mercury mainly came from exogenous dust inputs. On millennial timescales, the correspondence between mercury deposition and temperature change shows limited significance, while the former is more closely related to volcanic eruption and human activities (**Figures 4**, **5**; Vandal et al., 1993; De Lacerda et al., 2017). The frequent volcanic eruptions in the Middle Holocene led to the peak of mercury accumulation in this period (Roos-Barraclough et al., 2002). With the change in human activities in the past 3,500 years, mercury deposition has shown strong correspondence.

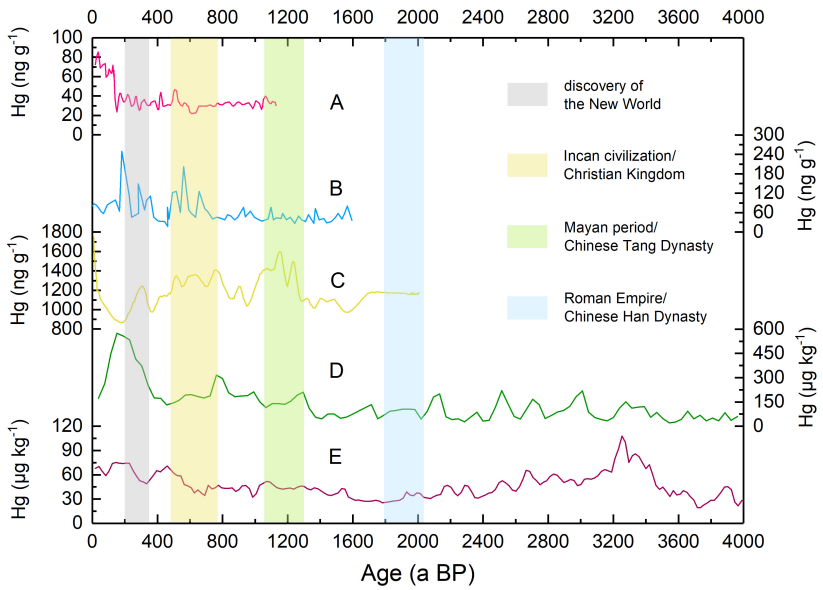

FIGURE 5 | Relationship between mercury deposition and human activities since 4000 a BP. **(A)** Hg concentrations in Adélie Basin, southern Antarctica (1100 a BP; Zaferani et al., 2018); **(B)** Hg concentrations in Patagonia, Chile (1600 a BP; Daga et al., 2016); **(C)** Hg concentrations in King George Island, western Antarctica (2000 a BP; Sun et al., 2006); **(D)** Hg concentrations in Lesser Khingan Range (4000 a BP; Tang et al., 2012); and **(E)** Hg concentrations in Huancavelica, central Peru (4000 a BP; Beal et al., 2014).

SUMMARY AND PROSPECTS

Summary

This study summarized the characteristics of mercury deposition from a global perspective by analyzing previous studies on mercury deposition on yearly to 100,000-year timescales. It was found that regarding the accumulation of mercury, there are certain commonalities within the regional range, while there are also differences among regions. In addition, both climate change and human activities have a significant impact on mercury deposition.

(1) The common feature of global mercury deposition in the Holocene is that the accumulation was generally lower before the start of the Industrial Revolution of 1840 and posthaste increased rapidly. Alternatively, due to regional volcanic activities or human activities, such as mining and metallurgy, there are differences in mercury accumulations among regions. It is worth noting that since the 1970s, emission reduction measures have been adopted in Europe and North America to reduce mercury accumulation, and Asia has gradually become the global center of anthropogenic mercury emissions.

(2) On the scale of hundreds of thousands of years, mercury accumulated more in cold periods and less in warm periods. On millennial timescales, the correspondence between mercury deposition and temperature change appears non-significant, and the former is more closely related to volcanic eruption and human activities. An increase in precipitation leads to a rise in forest litterfall Hg deposition. Little research has been performed on the effect of long-term humidity change on mercury deposition, with inconsistent conclusions, so the specific impact of humidity change on mercury deposition is unknown.

(3) The atmospheric mercury deposition caused by human activities can be traced back to 3500 years ago. Before industrialization, gold, silver, and mercury mining and the widespread use of cinnabar were the main anthropogenic mercury sources; after industrialization, coal combustion, non-ferrous metal smelting, waste incineration, and chlor-alkali industry development led to a significant increase in anthropogenic emissions of mercury, which in turn led to a sharp increase in mercury deposition.

Prospects

Although many studies have been conducted on the relationships of mercury deposition with climate change and human activities, with significant results, there remains some urgent challenges from a global perspective.

(1) The mercury deposition monitoring and research sites are unevenly distributed. The research sites are mostly distributed in the Northern Hemisphere, including Western Europe, North America, and China, while the number of research areas distributed in the Southern Hemisphere is relatively small, located in only a few regions of South America, Africa, and Antarctica. There are no research sites in Eastern Europe, Northern and Central Asia, Northern Africa, or Oceania. In future studies, mercury deposition research in these gap areas can be strengthened to provide data for the global reconstruction of the evolutionary history of mercury deposition.

(2) Most previous studies focused on the history of mercury deposition in the Holocene. There have been few studies on a longer timescale and even fewer studies on the relationship between precipitation change and mercury accumulation. As a result, the impact of climate change, especially humidity change, on the mercury accumulation mechanism has yet to be investigated. Therefore, it is suggested that studies of mercury deposition on a longer timescale and of the impact of precipitation on mercury accumulation be strengthened.
(3) There is a lack of high-resolution mercury deposition reconstruction. In previous studies, fen peat and lacustrine deposits were widely used as natural archives, with few ice core records with high resolution and almost no stalagmite records available. To accurately analyze the relationships of mercury deposition with climate change and human activities, mercury deposition reconstruction at a higher resolution should be performed.

AUTHOR CONTRIBUTIONS

FL and CM designed the research. FL presented a synthesis of the state of the art of mercury deposition worldwide. FL and PZ completed the data collection, analysis, and interpretation. All authors listed have made substantial, direct and intellectual contributions to the work, and approved it for publication. All authors contributed to the article and approved the submitted version.

FUNDING

This research was jointly funded by the National Natural Science Foundation of China (Nos. 41671196 and 41977389) and the National Key Research and Development Program of China (No. 2016YFA0600501).

ACKNOWLEDGMENTS

We are grateful to Renhui Huang and Chujun Yuan for their valuable suggestions about the final version of the manuscript. We also acknowledge Yunkai Deng and Haiyan Li for their assistance with the graphics. Our deepest gratitude goes to the two reviewers and the Associate Editor Liangcheng Tan as well as the Chief Editor Steven L. Forman for their careful work and thoughtful suggestions which have helped improve this manuscript substantially.

REFERENCES

Allan, M., Le Roux, G., Sonke, J. E., Piotrowska, N., Streel, M., and Fagel, N. (2013). Reconstructing historical atmospheric mercury deposition in Western Europe using: Misten peat bog cores, Belgium. *Sci. Total Environ.* 442, 290–301. doi: 10.1016/j.scitotenv.2012.10.044

Arnason, J. G., and Fletcher, B. A. (2003). A 40+ year record of Cd, Hg, Pb, and U deposition in sediments of Patroon Reservoir, Albany County, NY, USA. *Environ. Pollut.* 123, 383–391. doi: 10.1016/S0269-7491(03)00015-0

Bao, K., Shen, J., Wang, G., Sapkota, A., and McLaughlin, N. (2016). Estimates of recent Hg pollution in Northeast China using peat profiles from Great Hinggan Mountains. *Environ. Earth Sci.* 75:536. doi: 10.1007/s12665-015-5231-8

Beal, S. A., Kelly, M. A., Stroup, J. S., Jackson, B. P., Lowell, T. V., and Tapia, P. M. (2014). Natural and anthropogenic variations in atmospheric mercury deposition during the Holocene near Quelccaya Ice Cap, Peru. *Global Biogeochem. Cycles* 28, 437–450. doi: 10.1002/2013GB004780

Benoit, J. M., Fitzgerald, W. F., and Damman, A. W. H. (1998). The biogeochemistry of an ombrotrophic bog: evaluation of use as an archive of atmospheric mercury deposition. *Environ. Res.* 78, 118–133. doi: 10.1006/enrs.1998.3850

Biester, H., Bindler, R., Martinez-Cortizas, A., and Engstrom, D. R. (2007). Modeling the past atmospheric deposition of mercury using natural archives. *Environ. Sci. Technol.* 41, 4851–4860. doi: 10.1021/es0704232

Biester, H., Kilian, R., Franzen, C., Woda, C., Mangini, A., and SchÖler, H. F. (2002). Elevated mercury accumulation in a peat bog of the Magellanic Moorlands, Chile (53°S) – an anthropogenic signal from the Southern Hemisphere. *Earth Planet. Sci. Lett.* 201, 609–620. doi: 10.1016/S0012-821X(02)00734-3

Biester, H., Martinez-Cortizas, A., Birkenstock, S., and Kilian, R. (2003). Effect of peat decomposition and mass loss on historic mercury records in peat bogs from patagonia. *Environ. Sci. Technol.* 37, 32–39. doi: 10.1021/es025657u

Bindler, R., Klarqvist, M., Klaminder, J., and Förster, J. (2004). Does within-bog spatial variability of mercury and lead constrain reconstructions of absolute deposition rates from single peat records? The example of Store Mosse, Sweden. *Global Biogeochem. Cycles* 18:GB3020. doi: 10.1029/2004gb002270

Bond, G., Showers, W., Cheseby, M., Lotti, R., Almasi, P., De Menocal, P., et al. (1997). A pervasive millennial-scale cycle in North Atlantic Holocene and Glacial Climates. *Science* 278, 1257–1266. doi: 10.1126/science.278.5341.1257

Brading, D. A., and Cross, H. E. (1972). Colonial silver mining: Mexico and Peru. *Hisp. Am. Hist. Rev.* 52, 545–579. doi: 10.2307/2512781

Chen, G. Y. (2017). Cinnabar mercury industry in the Qin Empire. *J. Shaanxi Norm. Univ.* 46, 71–81.

Conaway, C. H., Swarzenski, P. W., and Cohen, A. S. (2012). Recent paleorecords document rising mercury contamination in Lake Tanganyika. *Appl. Geochem.* 27, 352–359. doi: 10.1016/j.apgeochem.2011.11.005

Conaway, C. H., Watson, E. B., Flanders, J. R., and Flegal, A. R. (2004). Mercury deposition in a tidal marsh of South San Francisco Bay downstream of the historic New Almaden mining district, California. *Mar. Chem.* 90, 175–184. doi: 10.1016/j.marchem.2004.02.023

Cooke, C. A., Balcom, P. H., Biester, H., and Wolfe, A. P. (2009). Over three millennia of mercury pollution in the Peruvian Andes. *Proc. Natl. Acad. Sci. U.S.A.* 106, 8830–8834. doi: 10.1073/pnas.0900517106

Corella, J. P., Valero-Garcés, B. L., Wang, F., Martínez-Cortizas, A., Cuevas, C. A., and Saiz-Lopez, A. (2017). 700 years reconstruction of mercury and lead atmospheric deposition in the Pyrenees (NE Spain). *Atmos. Environ.* 155, 97–107. doi: 10.1016/j.atmosenv.2017.02.018

Covelli, S., Langone, L., Acquavita, A., Piani, R., and Emili, A. (2012). Historical flux of mercury associated with mining and industrial sources in the Maranoand Grado Lagoon (Northern Adriatic Sea). *Estuar. Coast. Shelf Sci.* 113, 7–19. doi: 10.1016/j.ecss.2011.12.038

Daga, R., Ribeiro Guevara, S., Pavlin, M., Rizzo, A., Lojen, S., Vreèa, P., et al. (2016). Historical records of mercury in southern latitudes over 1600 years: lake Futalaufquen. Northern Patagonia. *Sci. Total Environ.* 553, 541–550. doi: 10.1016/j.scitotenv.2016.02.114

De Lacerda, L. D., Turcq, B., Sifeddine, A., and Cordeiro, R. C. (2017). Mercury accumulation rates in Caço Lake, NE Brazil during the past 20,000 years. *J. S. Am. Earth Sci.* 77, 42–50. doi: 10.1016/j.jsames.2017.04.008

Demers, J. D., Driscoll, C. T., Fahey, T. J., and Yavitt, J. B. (2007). Mercury cycling in litter and soil in different forest types in the Adirondack region, New York, USA. *Ecol. Appl.* 17, 1341–1351. doi: 10.1890/06-1697.1

Donovan, P. M., Blum, J. D., Yee, D., and Gehrke, G. E. (2013). An isotopic record of mercury in San Francisco Bay sediment. *Chem. Geol.* 349-350, 87–98. doi: 10.1016/j.chemgeo.2013.04.017

Drevnick, P. E., Cooke, C. A., Barraza, D., Blais, J. M., Coale, K. H., Cumming, B. F., et al. (2016). Spatiotemporal patterns of mercury accumulation in lake sediments of western North America. *Sci. Total Environ.* 568, 1157–1170. doi: 10.1016/j.scitotenv.2016.03.167

Drevnick, P. E., Yang, H., Lamborg, C. H., and Rose, N. L. (2012). Net atmospheric mercury deposition to Svalbard: estimates from lacustrine sediments. *Atmos. Environ.* 59, 509–513. doi: 10.1016/j.atmosenv.2012.05.048

Duan, Q. B. (2007). *Research on the Related Problems of the Mausoleum of the First Emperor of Qin Dynasty*. Kirkland, WA: Northwest University.

Dwyer, T. R., Mullins, H. T., and Good, S. C. (1996). Paleoclimatic implications of Holocene lake-level fluctuations, Owasco Lake, New York. *Geology* 24, 519–522.

Enrico, M., Roux, G. L., Marusczak, N., Heimbürger, L. E., Claustres, A., Fu, X. W., et al. (2016). Atmospheric mercury transfer to peat bogs dominated by gaseous elemental mercury dry deposition. *Environ. Sci. Technol.* 50, 2405–2412. doi: 10.1021/acs.est.5b06058

Ettler, V., Navrátil, T., Mihaljevič, M., Rohovec, J., Zuna, M., Šebek, O., et al. (2008). Mercury deposition/accumulation rates in the vicinity of a lead smelter as recorded by a peat deposit. *Atmos. Environ.* 42, 5968–5977. doi: 10.1016/j.atmosenv.2008.03.047

Farmer, J. G., Anderson, P., Cloy, J. M., Graham, M. C., Mackenzie, A. B., and Cook, G. T. (2009). Historical accumulation rates of mercury in four Scottish ombrotrophic peat bogs over the past 2000 years. *Sci. Total Environ.* 407, 5578–5588. doi: 10.1016/j.scitotenv.2009.06.014

Fitzgerald, W. F., Mason, R. P., and Vandal, G. M. (1991). Atmosphere cycling and air-water exchange of Hg over mid-continental Lacustrine regions. *Water Air Soil Pollut.* 56, 745–767. doi: 10.1007/bf00342314

Gallego, J. L. R., Ortiz, J. E., Sierra, C., Torres, T., and Llamas, J. F. (2013). Multivariate study of trace element distribution in the geological record of Roñanzas Peat Bog (Asturias, N. Spain). Paleoenvironmental evolution and human activities over the last 8000 cal yr BP. *Sci. Total Environ.* 454-455, 16–29. doi: 10.1016/j.scitotenv.2013.02.083

Givelet, N., Roos-Barraclough, F., and Shotyk, W. (2004). Predominant anthropogenic sources and rates of atmospheric mercury accumulation in southern Ontario recorded by peat cores from three bogs: comparison with natural "background" values past 8000 years. *J. Environ. Monit.* 5, 935–949. doi: 10.1039/B307140E

Grant, S. L., Kim, M., Lin, P., Crist, K. C., Ghosh, S., and Kotamarthi, V. R. (2014). A simulation study of atmospheric mercury and its deposition in the Great Lakes. *Atmos. Environ.* 94, 164–172. doi: 10.1039/B307140E

Gray, J. E., Fey, D. L., Holmes, C. W., and Lasorsa, B. K. (2005). Historical deposition and fluxes of mercury in Narraguinnep Reservoir, southwestern Colorado. USA. *Appl. Geochem.* 20, 207–220. doi: 10.1016/j.apgeochem.2004.05.011

Graydon, J. A., St. Louis, V. L., Lindberg, S. E., Hintelmann, H., and Krabbenhoft, D. P. (2006). Investigation of mercury exchange between forest canopy vegetation and the atmosphere using a new dynamic chamber. *Environ. Sci. Technol.* 40, 4680–4688. doi: 10.1021/es0604616

Guédron, S., Ledru, M. P., Escobar-Torrez, K., Develle, A. L., and Brisset, E. (2018). Enhanced mercury deposition by Amazonian orographic precipitation: evidence from high-elevation Holocene records of the Lake Titicaca region (Bolivia). *Palaeogeogr. Palaeoclimat. Palaeoecol.* 511, 577–587. doi: 10.1016/j.palaeo.2018.09.023

Guédron, S., Tolu, J., Brisset, E., Sabatier, P., Perrot, V., Bouchet, S., et al. (2019). Late Holocene volcanic and anthropogenic mercury deposition in the western Central Andes (Lake Chungará, Chile). *Sci. Total Environ.* 662, 903–914. doi: 10.1016/j.scitotenv.2019.01.294

Han, C. (2018). *The History of Atmospheric Mercury Deposition Since 1200 Years Recorded in the Sediments of Huguangyan Maar Lake, Zhanjiang*. Beijing: China University of Geosciences.

Haug, G. H., Hughen, K. A., Sigman, D. M., Peterson, L. C., and Röhl, U. (2001). Southward migration of the intertropical convergence zone through the Holocene. *Science* 293, 1304–1308. doi: 10.1126/science.1059725

Hermanns, Y. M., and Biester, H. (2013a). A 17,300-year record of mercury accumulation in a pristine lake in southern Chile. *J. Paleolimnol.* 49, 547–561. doi: 10.1007/s10933-012-9668-4

Hermanns, Y. M., and Biester, H. (2013b). Anthropogenic mercury signals in lake sediments from southernmost Patagonia, Chile. *Sci. Total Environ.* 445-446, 126–135. doi: 10.1016/j.scitotenv.2012.12.034

Huang, J., Kang, S. C., Zhang, Q. G., and Guo, J. M. (2013). "Study on atmospheric mercury wet deposition in the Tibet Plateau and its adjacent areas. Environmental Chemistry Committee of Chinese Chemical Society, Environmental Chemistry Branch of Chinese Society of Environmental Science," in *Summary of the 7th National Conference on Environmental Chemistry-S12 Heavy metal pollution and remediation. Environmental Chemistry Committee of Chinese Chemical Society, Environmental Chemistry Branch of Chinese Society of Environmental Science*.

Jitaru, P., Gabrielli, P., Marteel, A., Plane, J. M. C., Planchon, F. A. M., Gauchard, P. A., et al. (2009). Atmospheric depletion of mercury over Antarctica during glacial periods. *Nat. Geosci.* 2, 505–508. doi: 10.1038/ngeo549

Kading, T. J., Mason, R. P., and Leaner, J. J. (2009). Mercury contamination history of an estuarine floodplain reconstructed from a 210Pb-dated sediment core (Berg River, South Africa). *Mar. Pollut. Bull.* 59, 116–122. doi: 10.1016/j.marpolbul.2009.02.020

Kaufman, D. S., Ager, T. A., Anderson, N. J., Anderson, P. M., Andrews, J. T., Bartlein, P. T., et al. (2004). Erratum to: holocene thermal maximum in the western Arctic (0-180°W). *Quat. Sci. Rev.* 23, 529–560. doi: 10.1016/j.quascirev.2003.09.007

Kim, H., Lee, K., Lim, D., Nam, S., Han, S. H., Kim, J., et al. (2019). Increase in anthropogenic mercury in marginal sea sediments of the Northwest Pacific Ocean. *Sci. Total Environ.* 654, 801–810. doi: 10.1016/j.scitotenv.2018.11.076

Korosi, J. B., Griffiths, K., Smol, J. P., and Blais, J. M. (2018). Trends in historical mercury deposition inferred from lake sediment cores across a climate gradient in the Canadian High Arctic. *Environ. Pollut.* 241, 459–467. doi: 10.1016/j.envpol.2018.05.049

Krabbenhoft, D. P., and Sunderland, E. M. (2013). Global change and mercury. *Environ. Sci.* 341, 1457–1458. doi: 10.1126/science.1242838

Kurz, A. Y., Blum, J. D., Washburn, S. J., and Baskaran, M. (2019). Changes in the mercury isotopic composition of sediments from a remote alpine lake in Wyoming, USA. *Sci. Total Environ.* 669, 973–982. doi: 10.1016/j.scitotenv.2019.03.165

Küttner, A., Mighall, T. M., De Vleeschouwer, F., Maukuoy, D., Martínez-Cortizas, A., Foster, I. D. L., et al. (2014). A 3300-year atmospheric metal contamination record from Raeburn Flow raised bog, south west Scotland. *J. Archaeol. Sci.* 44, 1–11. doi: 10.1016/j.jas.2014.01.011

Li, Y. P., Ma, C. M., Zhu, C., Huang, R., and Zheng, C. G. (2016). Historical anthropogenic contributions to mercury accumulation recorded by a peat core from Dajiuhu montane mire, central China. *Environ. Pollut.* 216, 332–339. doi: 10.1016/j.envpol.2016.05.083

Li, Y. P., Ma, C. M., Zhu, C., Huang, R., and Zheng, C. G. (2017). Hg sedimentary records and influencing factors of Dajiuhu Lake Basin since 16,000 years ago. *China Environ. Sci.* 37, 1103–1110.

Lim, D., Kim, J., Xu, Z. K., Jeong, K., and Jung, H. (2017). New evidence for Kuroshio inflow and deepwater circulation in the Okinawa Trough, East China Sea: sedimentary mercury variations over the last 20 kyr. *Paleoceanography* 32, 571–579. doi: 10.1002/2017PA003116

Lindberg, S. E., Hanson, P. J., Meyers, T. P., and Kim, K. H. (1998). Air/surface exchange of mercury vapor over forests—the need for a reassessment of continental biogenic emissions. *Atmos. Environ.* 32, 895–908. doi: 10.1016/S1352-2310(97)00173-8

Liu, C. H., and Wang, Z. Y. (2001). From the view of "Taking mercury as rivers and seas", the antiseptic measures in the tombs of the Eastern Zhou, Qin and Han Dynasties in China. *Collect. Comment. Qin Cult.* 42, 1–439.

Liu, X. D., Xu, L. Q., Chen, Q. Q., Sun, L. G., Wang, Y. H., Yan, H., et al. (2012). Historical change of mercury pollution in remote Yongle archipelago, South China Sea. *Chemosphere* 87, 549–556. doi: 10.1016/j.chemosphere.2011.12.065

Ma, M., Du, H. X., Wang, D. Y., Sun, T., Sun, S. W., and Yang, G. (2017). The fate of mercury and its relationship with carbon, nitrogen and bacterial communities during litter decomposing in two subtropical forests. *Appl. Geochem.* 86, 26–35. doi: 10.1016/j.apgeochem.2017.09.008

Martínez-Cortizas, A., Peiteado Varela, E., Bindle, R., Biester, H., and Cheburkin, A. (2012). Reconstructing historical Pb and Hg pollution in NW Spain using multiple cores from the Chao de Lamoso bog (Xistral Mountains). *Geochim. Cosmochim. Acta* 82, 68–78. doi: 10.1016/j.gca.2010.12.025

Martínez-Cortizas, A., Pontevedra-Pombal, X., Garcı a-Rodeja, E., Nóvoa-Muñoz, C., and Shotyk, W. (1999). Mercury in a Spanish peat bog: archive of climate change and atmospheric metal deposition. *Science* 284, 939–942. doi: 10.1126/science.284.5416.939

Megaritis, A. G., Murphy, B. N., Racherla, P. N., Adams, P. J., and Pandis, S. N. (2014). Impact of climate change on mercury concentrations and deposition in the eastern United States. *Sci. Total Environ.* 487, 299–312. doi: 10.1016/j.scitotenv.2014.03.084

Munthe, J., Hultberg, H., Lee, Y. H., Parkman, H., Iverfeldt, A., and Renberg, I. (1995). Trends of mercury and methyl-mercury in deposition, run-off water sediments in relation to experimental manipulations and acidification. *Water Air Soil Pollut.* 85, 743–748. doi: 10.1007/BF00476918

Obrist, D., Agnan, Y., Jiskra, M., Olson, C. L., Colegrove, D. P., Hueber, J., et al. (2017). Tundra uptake of atmospheric elemental mercury drives Arctic mercury pollution. *Nature* 547, 201–204. doi: 10.1038/nature22997

Obrist, D., Kirk, J. L., Zhang, L., Sunderland, E. M., Jiskra, M., and Selin, N. E. (2018). A review of global environmental mercury processes in response to human and natural perturbations: changes of emissions, climate, and land use. *Ambio* 47, 116–140. doi: 10.1007/s13280-017-1004-9

Pérez-Rodríguez, M., Silva-Sánchez, N., Kylander, M. E., Bindler, R., Mighall, T. M., Edward Schofield, J., et al. (2017). Industrial-era lead and mercury contamination in southern Greenland implicates North American sources. *Sci. Total Environ.* 613–614, 919–930. doi: 10.1016/j.scitotenv.2017.09.041

Peirez-Rodriıguez, M., Horaik-Terra, I., Rodriıguez-Lado, L., Aboal, J. R., and Martínez-Cortizas, A. (2015). Long-term (˜57 ka) controls on mercury accumulation in the Southern Hemisphere reconstructed using a peat record from Pinheiro Mire (Minas Gerais, Brazil). *Environ. Sci. Technol.* 49, 1356–1364. doi: 10.1021/es504826d

Pokharel, A. K., and Obrist, D. (2011). Fate of mercury in tree litter during decomposition. *Biogeosciences* 8, 2507–2521. doi: 10.5194/bg-8-2507-2011

Pratte, S., Bao, K., Shen, J., Mackenzie, L., Klamt, A. M., Wang, G. P., et al. (2018). Recent atmospheric metal deposition in peatlands of northeast China: a review. *Sci. Total Environ.* 626, 1284–1294. doi: 10.1016/j.scitotenv.2018.01.183

Roos-Barraclough, F., Givelet, N., Cheburkin, A. K., Shotyk, W., and Norton, S. A. (2006). Use of Br and Se in peat to reconstruct the natural and anthropogenic fluxes of atmospheric Hg: a 10000-year record from Caribou Bog, Maine. *Environ. Sci. Technol.* 40, 3188–3194. doi: 10.1021/es051945p

Roos-Barraclough, F., Martínez-Cortizas, A., García-Rodeja, E., and Shotyk, W. (2002). A 14 500 year record of the accumulation of atmospheric mercury in peat: volcanic signals, anthropogenic influences and a correlation to bromine accumulation. *Earth Planet. Sci. Lett.* 202, 435–451. doi: 10.1016/S0012-821X(02)00805-1

Roos-Barraclough, F., and Shotyk, W. (2003). Millennial-scale records of atmospheric mercury deposition obtained from ombrotrophic and minerotrophic peatlands in the Swiss Jura Mountains. *Environ. Sci. Technol.* 37, 235–244. doi: 10.1021/es0201496

Schuster, P. F., Krabbenhoft, D. P., Naftz, D. L., Dewayne Cecil, L., Olson, M. L., Dewild, J. F., et al. (2002). Atmospheric mercury deposition during the last 270 years: a glacial ice core record of natural and anthropogenic sources. *Environ. Sci. Technol.* 36, 2303–2310. doi: 10.1021/es0157503

Selin, N. E., and Jacob, D. J. (2008). Seasonal and spatial patterns of mercury wet deposition in the United States: constraints on the contribution from North American anthropogenic sources. *Atmos. Environ.* 42, 5193–5204. doi: 10.1016/j.atmosenv.2008.02.069

Serrano, O., Martínez-Cortizas, A., Mateo, M. A., Biester, H., and Bindler, R. (2013). Millennial scale impact on the marine biogeochemical cycle of mercury from early mining on the Iberian Peninsula. *Global Biogeochem. Cycles* 27, 21–30. doi: 10.1029/2012GB004296

Shi, W. F., Feng, X. B., Zhang, G., Ming, L. L., Yin, R. S., Zhao, Z. Q., et al. (2011). High resolution mercury isotope records in rain fed peat of Hongyuan in the past 150 years. *Chin. Sci. Bull.* 56, 583–588.

Shotyk, W., Goodsite, M. E., Roos-barraclough, F., Frei, R., Heinemeier, J., Asmund, G., et al. (2003). Anthropogenic contributions to atmospheric Hg, Pb and As accumulation recorded by peat cores from southern Greenland and Denmark dated using the 14C "bomb pulse curve". *Geochim. Cosmochim. Acta* 67, 3991–4011. doi: 10.1016/S0016-7037(03)00409-5

St. Louis, V. L., Graydon, J. A., Lehnherr, I., Amos, H. M., Sunderland, E. M., St. Pierre, K. A., et al. (2019). Atmospheric concentrations and wet/dry loadings of mercury at the remote experimental lakes area, Northwestern Ontario, Canada. *Environ. Sci. Technol.* 53, 8017–8026. doi: 10.1021/acs.est.9b01338

Steinnes, E., and Sjøbakk, T. E. (2005). Order-of-magnitude increase of Hg in Norwegian peat profiles since the outset of industrial activity in Europe. *Environ. Pollut.* 137, 365–370. doi: 10.1016/j.envpol.2004.10.008

Štrok, M., Anabelle Baya, P., Dietrich, D., Dimock, B., and Hintelmann, H. (2019). Mercury speciation and mercury stable isotope composition in sediments from the Canadian Arctic Archipelago. *Sci. Total Environ.* 671, 655–665. doi: 10.1016/j.scitotenv.2019.03.424

Sun, L. G., Yin, X. B., Liu, X. D., Zhu, R. B., Xie, Z. Q., and Wang, Y. H. (2006). A 2000-year record of mercury and ancient civilizations in seal hairs from King George Island, West Antarctica. *Sci. Total Environ.* 368, 236–247. doi: 10.1016/j.scitotenv.2005.09.092

Sunderland, E. M., Cohen, M. D., Selin, N. E., and Chmura, G. L. (2008). Reconciling models and measurements to assess trends in atmospheric mercury deposition. *Environ. Pollut.* 156, 526–535. doi: 10.1016/j.envpol.2008.01.021

Tang, S. L., Huang, Z. W., Liu, J., Yang, Z. C., and Lin, Q. H. (2012). Atmospheric mercury deposition recorded in an ombrotrophic peat core from Xiaoxing'an Mountain, Northeast China. *Environ. Res.* 118, 145–148. doi: 10.1016/j.envres.2011.12.009

Thevenon, F., Guédron, S., Chiaradia, M., Loizeau, J. L., and Poté, J. (2011). (Pre-) historic changes in natural and anthropogenic heavy metals deposition inferred from two contrasting Swiss Alpine lakes. *Quat. Sci. Rev.* 30, 224–233. doi: 10.1016/j.quascirev.2010.10.013

Vandal, G. M., Fitzgerald, W. F., Boutron, C. F., and Candelone, J. P. (1993). Variations in mercury deposition to Antarctica over the past 34,000 years. *Nature* 362, 621–623. doi: 10.1038/362621a0

Wang, X. P., Yang, H. D., Gong, P., Zhao, X., Wu, G. J., Turner, S., et al. (2010). One century sedimentary records of polycyclic aromatic hydrocarbons, mercury and trace elements in the Qinghai Lake, Tibetan Plateau. *Environ. Pollut.* 158, 3065–3070. doi: 10.1016/j.envpol.2010.06.034

Wang, Y. M. (2011). *Study on Mercury and its Precipitation in the Main Urban Area of Chongqing*. Chongqing: Southwest University, doi: 10.7666/d.y1881755

Wiklund, J. A., Kirk, J. L., Muir, D. C. G., Evans, M., Yang, F., Keating, J., et al. (2017). Anthropogenic mercury deposition in Flin Flon Manitoba and the Experimental Lakes Area Ontario (Canada): a multi-lake sediment core reconstruction. *Sci. Total Environ.* 586, 685–695. doi: 10.1016/j.scitotenv.2017.02.046

Xiang, Y., and Huang, Z. F. (2014). The characteristics and influence of Spanish American colonial rule in the 15th-18th Century. *J. Qiongzhou Univ.* 21, 96–102. doi: 10.13307/j.issn.1008-6722.2014.06.16

Xiao, H. (2017). *Study of Holocene Climate Change and Atmospheric Mercury Deposition Recorded by Peat in Northeast China*. Wuhan: China University of Geosciences.

Xu, J. M. (2010). *Response Relationship between Atmospheric Mercury Deposition and Climate Change Recorded by Rain Fed Peat in Tanghongling, Xiaoxing'anling*. Jiaozuo: Henan Polytechnic University.

Xu, L. Q., Liu, X. D., Sun, L. G., Chen, Q. Q., Yan, H., Liu, Y., et al. (2010). A 700-year record of mercury in avian eggshells of Guangjin Island, South China Sea. *Environ. Pollut.* 159, 889–896. doi: 10.1016/j.envpol.2010.12.021

Yang, H. D., Battarbee, R. W., Turner, S., Rose, N. L., Derwent, R. G., Wu, G. J., et al. (2010). Historical reconstruction of mercury pollution across the Tibetan Plateau using lake sediments. *Environ. Sci. Technol.* 44, 2918–2924. doi: 10.1021/es9030408

Yang, H. D., Turner, S., and Rose, N. L. (2016). Mercury pollution in the lake sediments and catchment soils of anthropogenically-disturbed sites across England. *Environ. Pollut.* 219, 1092–1101. doi: 10.1016/j.envpol.2016.09.012

Yang, J., Chen, L., Steele, J. C., Chen, R. S., and Meng, X. Z. (2016). An extended study on historical mercury accumulation in lake sediment of Shanghai: the contribution of socioeconomic driver. *Environ. Pollut.* 219, 612–619. doi: 10.1016/j.envpol.2016.06.028

Zaccone, C., Santoro, A., Cocozza, C., Terzano, R., Shotyk, W., and Miano, T. M. (2008). Comparison of Hg concentrations in ombrotrophic peat and corresponding humic acids, and implications for the use of bogs as archives of atmospheric Hg deposition. *Geoderma* 148, 399–404. doi: 10.1016/j.geoderma.2008.11.017

Zaferani, S., Pérez-Rodríguez, M., and Biester, H. (2018). Diatom ooze-A large marine mercury sink. *Science* 361, 797–800. doi: 10.1126/science.aat2735

Zdanowicz, C. M., Kruemmel, E., Lean, D., Poulain, A., Kinnard, C., Yumvihoze, E., et al. (2015). Pre-industrial and recent (1970–2010) atmospheric deposition of sulfate and mercury in snow on southern Baffin Island, Arctic Canada. *Sci. Total Environ.* 509-510, 104–114. doi: 10.1016/j.scitotenv.2014.04.092

Zdanowicz, C. M., Krümmel, E. M., Poulain, A. J., Yumvihoze, E., Chen, J. B., Štrok, M., et al. (2016). Historical variations of mercury stable isotope ratios in Arctic glacier firn and ice cores. *Global Biogeochem. Cycles* 30, 1324–1347. doi: 10.1002/2016GB005411

Zeng, H. A., Wu, J. L., and Liu, W. (2014). Two-century sedimentary record of heavy metal pollution from Lake Sayram: a deep mountain lake in central Tianshan, China. *Quat. Int.* 321, 125–131. doi: 10.1016/j.quaint.2013.09.047

Zeng, Y., Chen, J. G., Yang, Y. Q., Wang, J. X., Zhu, Z. J., and Li, J. (2017). Huguangyan Maar Lake (SE China): a solid record of atmospheric mercury pollution history in a non-remote region. *J. Asian Earth Sci.* 147, 1–8. doi: 10.1016/j.jseaes.2017.07.009

Zhang, H., Nizzetto, L., Feng, X. B., Borgå, K., Sommar, J., Fu, X. W., et al. (2019). Assessing air-surface exchange and fate of mercury in a subtropical forest using a novel passive exchange-meter device. *Environ. Sci. Technol.* 53, 4869–4879. doi: 10.1021/acs.est.8b06343

Zhang, H. X., Huo, S. L., Yeager, K. M., Xi, B. D., Zhang, J. T., and Wu, F. C. (2018). A historical sedimentary record of mercury in a shallow Eutrophic Lake: impacts of human activities and climate change. *Engineering* 5, 296–304. doi: 10.1016/j.eng.2018.11.022

Zhang, R., Russell, J., Xiao, X., Zhang, F., Li, T. G., Liu, Z. Y., et al. (2018). Historical records, distributions and sources of mercury and zinc in sediments of East China Sea: implication from stable isotopic compositions. *Chemosphere* 205, 698–708. doi: 10.1016/j.chemosphere.2018.04.100

Zheng, J. C. (2015). Archives of total mercury reconstructed with ice and snow from Greenland and the Canadian High Arctic. *Sci. Total Environ.* 509-510, 133–144. doi: 10.1016/j.scitotenv.2014.05.078

Zhou, J., Feng, X. B., Liu, H. Y., Zhang, H., Fu, X. W., Bao, Z. D., et al. (2013). Examination of total mercury inputs by precipitation and litterfall in a remote upland forest of Southwestern China. *Atmos. Environ.* 81, 364–372. doi: 10.1016/j.atmosenv.2013.09.010

Conflict of Interest: The authors declare that the research was conducted in the absence of any commercial or financial relationships that could be construed as a potential conflict of interest.

Copyright © 2020 Li, Ma and Zhang. This is an open-access article distributed under the terms of the Creative Commons Attribution License (CC BY). The use, distribution or reproduction in other forums is permitted, provided the original author(s) and the copyright owner(s) are credited and that the original publication in this journal is cited, in accordance with accepted academic practice. No use, distribution or reproduction is permitted which does not comply with these terms.

frontiers in Earth Science

ORIGINAL RESEARCH
published: 07 August 2020
doi: 10.3389/feart.2020.00322

Migration of Afro-Asian Monsoon Fringe Since Last Glacial Maximum

Jun Cheng[1], Yiyi Ma[2], Haibin Wu[3,4], Hao Long[5] and Zhengyu Liu[6]*

[1] Laboratory of Meteorological Disaster, Ministry of Education (KLME)/Joint International Research Laboratory of Climate and Environment Change (ILCEC)/Collaborative Innovation Center on Forecast and Evaluation of Meteorological Disasters (CIC-FEMD), Nanjing University of Information Science and Technology, Nanjing, China, [2] Quzhou Meteorological Bureau, Zhejiang, China, [3] Key Laboratory of Cenozoic Geology and Environment, Institute of Geology and Geophysics, Chinese Academy of Sciences, Beijing, China, [4] CAS Center for Excellence in Life and Paleoenvironment, China University of Chinese Academy of Sciences, Beijing, China, [5] State Key Laboratory of Lake Science and Environment, Nanjing Institute of Geography and Limnology, Chinese Academy of Sciences, Nanjing, China, [6] Department of Geography, The Ohio State University, Columbus, OH, United States

OPEN ACCESS

Edited by:
Hai Xu,
Tianjin University, China

Reviewed by:
Zhongshi Zhang,
China University of Geosciences, China
Zhengguo Shi,
Institute of Earth Environment (CAS), China

***Correspondence:**
Jun Cheng
chengjun@nuist.edu.cn

Specialty section:
This article was submitted to Quaternary Science, Geomorphology and Paleoenvironment, a section of the journal Frontiers in Earth Science

Received: *01 June 2020*
Accepted: *10 July 2020*
Published: *07 August 2020*

Citation:
Cheng J, Ma Y, Wu H, Long H and Liu Z (2020) Migration of Afro-Asian Monsoon Fringe Since Last Glacial Maximum. Front. Earth Sci. 8:322. doi: 10.3389/feart.2020.00322

Geological records indicated the termination of the Holocene Thermal Maximum (dramatic drying) occurred progressively later at lower latitudes in both North Africa and East Asia, along with the coherent weakening of local summer monsoon. Here we show that this time-transgressive evolution was dominated by the southward migration of monsoon fringe (shrinking monsoon domain) under monsoon weakening, as illustrated in a transient climate-terrestrial ecosystem model simulation. The monsoon fringe retreating southward during the Holocene, as well as expanding northward during the last deglaciation, occurred synchronously in a belt extending from North Africa to East Asia, which induced a locally humid-arid transition and the subsequent dramatic environment impact. The migration of Afro-Asia monsoon fringe since the Last Glacial Maximum was modulated by the orbital forcing through its impact on land-ocean thermal contrast, aiding by the variation of CO_2 concentration.

Keywords: Afro-Asian monsoon, fringe, hydrological evolution, land-ocean thermal contrast, external forcing, vegetation

INTRODUCTION

Since the Last Glacial Maximum (LGM), the Afro-Asian monsoon system, including East Asian monsoon, South Asian monsoon and North African monsoon, has experienced a coherent strengthening during the last deglaciation and weakening during the Holocene (Fleitmann et al., 2003; Dykoski et al., 2005; Weldeab et al., 2007; Wang et al., 2008; Shi and Yan, 2019) with the maximum at the Holocene Thermal Maximum (HTM, around 8 ka, kilo years ago before 1950; Haug et al., 2001). Synthesis analysis of monsoon records in North Africa and East Asia illustrated a common asynchronous termination of the HTM, which occurred later in lower latitudes (An et al., 2000; Shanahan et al., 2015). The eco-environmental response to this time-transgressive termination of the HTM is much robust in the northern part of Afro-Asian monsoon domains,

as illustrated by the dramatic variation of paleo-lake and vegetation (Street and Grove, 1976; Yu and Harrison, 1996; Lézine et al., 1998; Enzel et al., 1999; Armitage et al., 2015; Goldsmith et al., 2017).

The time-transgressive evolution of paleo-hydrology during the period of the Holocene in North Africa and East Asia was previously attributed to the southward migration of monsoon rainbelt, which was forced by reduced summer insolation (Shanahan et al., 2015), or/and seasonality (An et al., 2000). The mechanism of rainbelt migration may work for East Asia, presented as the anti-phase changes of precipitation within large meridional range of the monsoon (Zhang et al., 2018), but it may not be so robust in North Africa (Doherty et al., 2000). For the uniform time-transgressive evolution of paleo-hydrology occurred in both North Africa and East Asia, is there a common mechanism? The southward shift of the Intertropical Convergence Zone (ITCZ) during this period (Haug et al., 2001) may have contributed to this time-transgressive evolution in the monsoon region, but its physical connection with the environment variation occurred at higher latitudes is not obvious. In addition, why is the environmental response in the northern part of the Afro-Asian monsoon domain so large? Meanwhile, is there any internal relationship between the time-transgressive evolutions of North Africa and East Asia?

To address these questions, the change of monsoon fringe, the limit of the monsoon domain, may be the critical factor. Besides the general monsoon precipitation which widely used to represent the intensity of monsoon (Shi and Yan, 2019), the fringe of Afro-Asian monsoon varied largely as documented in geological records (Winkler and Wang, 1993; Yan and Petit-Maire, 1994; Adams, 1997; Jiang and Liu, 2007; Schneider et al., 2014; Skonieczny et al., 2015; Yang et al., 2015; Goldsmith et al., 2017; Tierney et al., 2017; Sha et al., 2019), and simulated in climate models (Doherty et al., 2000; Jiang et al., 2015a,b). Reconstructions and simulations consistently indicated monsoon fringe swung northward during the last deglaciation, afterward swung southward during the Holocene. On the other hand, the Afro-Asian monsoon is accompanied by an abroad arid region on its northern side (**Figure 1A**), which is forced by atmospheric meridional circulation and favored by the Tibetan Plateau (Broccoli and Manabe, 1992). Therefore, the migration of northern Afro-Asian monsoon fringe, which corresponds to the expansion or shrink of the monsoon domain, may induce the time-transgressive evolution of local precipitation and the subsequent dramatic response of environment for reasons of possible humid-arid transition. Thus, we hypothesize the recorded time-transgressive evolution of paleo-hydrology in the Afro-Asian monsoon regions and the dramatic environment variation may be dominated by the migration of monsoon fringe.

To test this hypothesis, we investigate the fringe change of the Afro-Asian monsoon and the possible subsequent environment response in a transient climate-terrestrial ecosystem model simulation since the LGM, aided by some other snapshot simulations at the LGM and mid-Holocene. Furthermore, the potential contributions of external forcing to the possible change of monsoon fringe are investigated.

DATA AND METHOD

The transient climate-terrestrial ecosystem simulation starting from the LGM used here is TraCE21 (Liu et al., 2009). This simulation was performed using the fully coupled NCAR CCSM3 at a spatial resolution of T31 (3.75°× 3.75°; Collins et al., 2006), and forced by the realistic climatic forcing that consisted of orbital insolation (Orb; Berger, 1978), atmospheric CO_2 (Joos and Spahni, 2008), meltwater discharge (McManus et al., 2004), and continental ice sheets (ICE-5G; Peltier, 2004). TraCE21 involved the land processes with a dynamic vegetation component, whose outputs could be used to directly compare with the corresponding proxy records. Four sets of solo-forcing experiments are also performed to investigate their individual contributions to the total climate variation since the LGM (He et al., 2013). In this paper, we employ the full-forcing and two solo-forcing experiments (Orb and CO_2) of TraCE21 to study the variations of Afro-Asian monsoon fringe, the subsequent environmental impact and the underling mechanism. The monsoon fringe in model simulation is defined as the edge of monsoon domain, whose general migration represents the expansion or the shrink of monsoon domain. To focus on the long-term evolution of monsoon fringe and local environment, our analyses are all based on the centennial mean data. Aiding to this transient climate simulation, a series of Paleoclimate Modeling Intercomparison Project Phase 3 (PMIP3) simulations during the LGM and mid-Holocene (**Supplementary Table 1**) are also included to improve the reliability of the results derived from TraCE21.

Comparing to the paleoclimate records, the full-forcing simulation of TraCE21 reasonably reproduced the general evolution of the Afro-Asian monsoon (Otto-Bliesner et al., 2014; Liu et al., 2014; Shanahan et al., 2015; Wen et al., 2016; Cheng et al., 2019; Shi and Yan, 2019). The spatial distribution of the Afro-Asian monsoon and adjacent arid regions are all well simulated (**Figure 1A**), compared to those derived from observations (**Supplementary Figure 1**). The simulated variation of monsoon intensity (black curves in **Figures 1E–G**, averaged precipitation in the monsoon regions) is roughly consistent with the proxies (green dots in **Figures 1E–G**), strengthening during the last deglaciation and weakening during the Holocene. The migration of northern Afro-Asian monsoon fringe indicated by geological records (Winkler and Wang, 1993; Yan and Petit-Maire, 1994; Adams, 1997; Jiang and Liu, 2007; Yang et al., 2015; Goldsmith et al., 2017) is also qualitatively reproduced by TraCE21, even though the varying magnitude in the simulation is smaller than that of the reconstructions (**Figures 1B,C**). The reasonable reproduction of TraCE21 for the variation of the Afro-Asian monsoon since the LGM provides the basis to test our hypothesis.

The monsoon domain is the region where the annual precipitation range (local summer minus winter) exceeds 300 mm (2 mm/day) and where summer precipitation exceeds 50% of the annual precipitation. Here, local summer and winter are defined as May through September (MJJAS) and November through next March (NDJFM), respectively, following Wang and Ding (2008). Arid regions are where the local

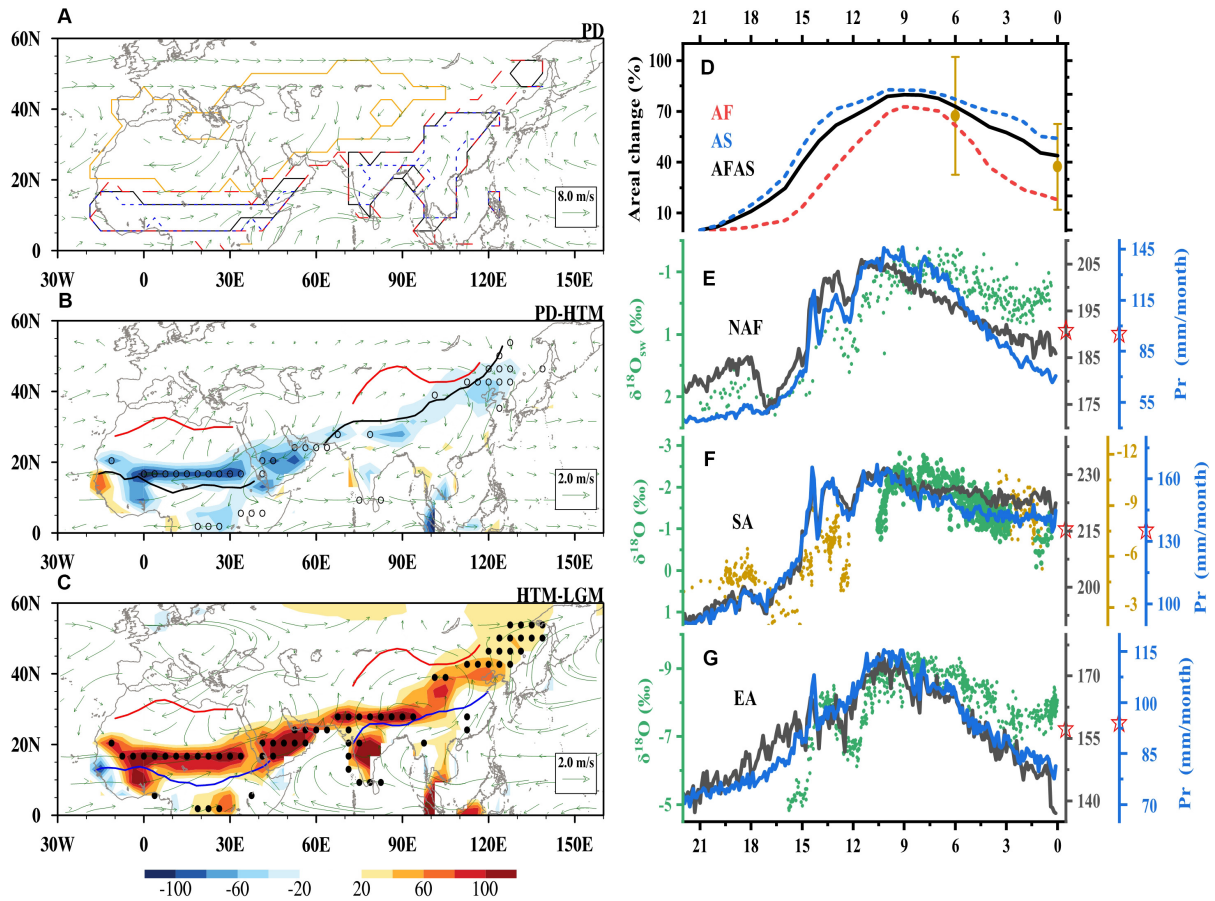

FIGURE 1 | (A) Simulated summer (JJA) 850-hPa wind (UV850; vector, units: m/s), Afro-Asian monsoon domain (black line) and arid domain (orange line) in present day (PD). Monsoon domains at Last Glacial Maximum (LGM) and Holocene Thermal Maximum (HTM) are also indicated by blue dotted and red dashed lines, respectively; **(B)** Changes of precipitation (Pr; shading, units: mm/month), UV850 (vector, units: m/s), and monsoon domain (black circles) between PD and HTM (PD – HTM); **(C)** Same as **(B)**, except for changes between HTM and LGM (HTM – LGM); **(D)** Areal changes (relative to LGM) of monsoon domain over Asia (blue dashed line), North Africa (red dashed line), and Afro-Asian (black solid line) with the unit of %. The multi-model ensemble results of PMIP3 and one intra-model standard deviation range of eight models are plotted in brown dots and bars; and **(E–G)** Simulated precipitation variation averaged over interior monsoon regions (gray curve; averaged over LGM domain illustrated in **(A)** and over fringe-migrationing regions (blue curve; averaged over monsoon domain difference between LGM and HTM). Their average values since LGM are labeled in the *y*-axis (units: mm/month). Records of oxygen isotope of MD03-2707 (Weldeab et al., 2007), Qunf cave (Fleitmann et al., 2003), Dongge cave (Dykoski et al., 2005) and Bittoo cave (Kathayat et al., 2016) are indicated by green/brown dots. The red curve in **(B,C)** depicts recorded monsoon fringe during HTM (Winkler and Wang, 1993; Adams, 1997; Jiang and Liu, 2007), black curve in **(B)** PD and blue curve in **(C)** LGM (Yan and Petit-Maire, 1994).

summer precipitation rate is below 1 mm/day (Liu et al., 2012). Here, we focus on the monsoon fringe (the limit of monsoon domain) close to the arid region, whose migration was robust and the subsequent environmental impact was dramatic as illustrated bellow.

RESULTS

Variation of Afro-Asian Monsoon Domain/Fringe

Since the LGM, Afro-Asian monsoon domains robustly co-varied in TraCE21. Along with the weakening of Afro-Asian monsoon during the Holocene (black curves in **Figures 1E–G**), the shrink of its domain (**Figure 1D**) was derived by the southward migration of northern monsoon fringe, with the amplitude of about 4 degrees in latitude (**Figure 1B**). Similar but reversed processes occurred during the last deglaciation (**Figure 1C**). Notably, referring to the state at the LGM, the varying magnitude of simulated Afro-Asian monsoon domain reached about 80% with the maximum at the HTM period (**Figure 1D**). In addition, the domain of Afro-Asian monsoon at present day (PD) is large by about 40% than that at the LGM (**Figure 1D**), expanded in the north, too (see **Supplementary Figure 2**). The multi-model mean results of PMIP3 indicated similar variation of the Afro-Asian monsoon domain (vertical bars in **Figure 1D**) and the migration of monsoon fringe (**Supplementary Figure 3**), with a slight difference in the varying magnitude. Therefore, the gradual variation of the monsoon domain, as indicated in the simulations, could induce the progressively meridional migration

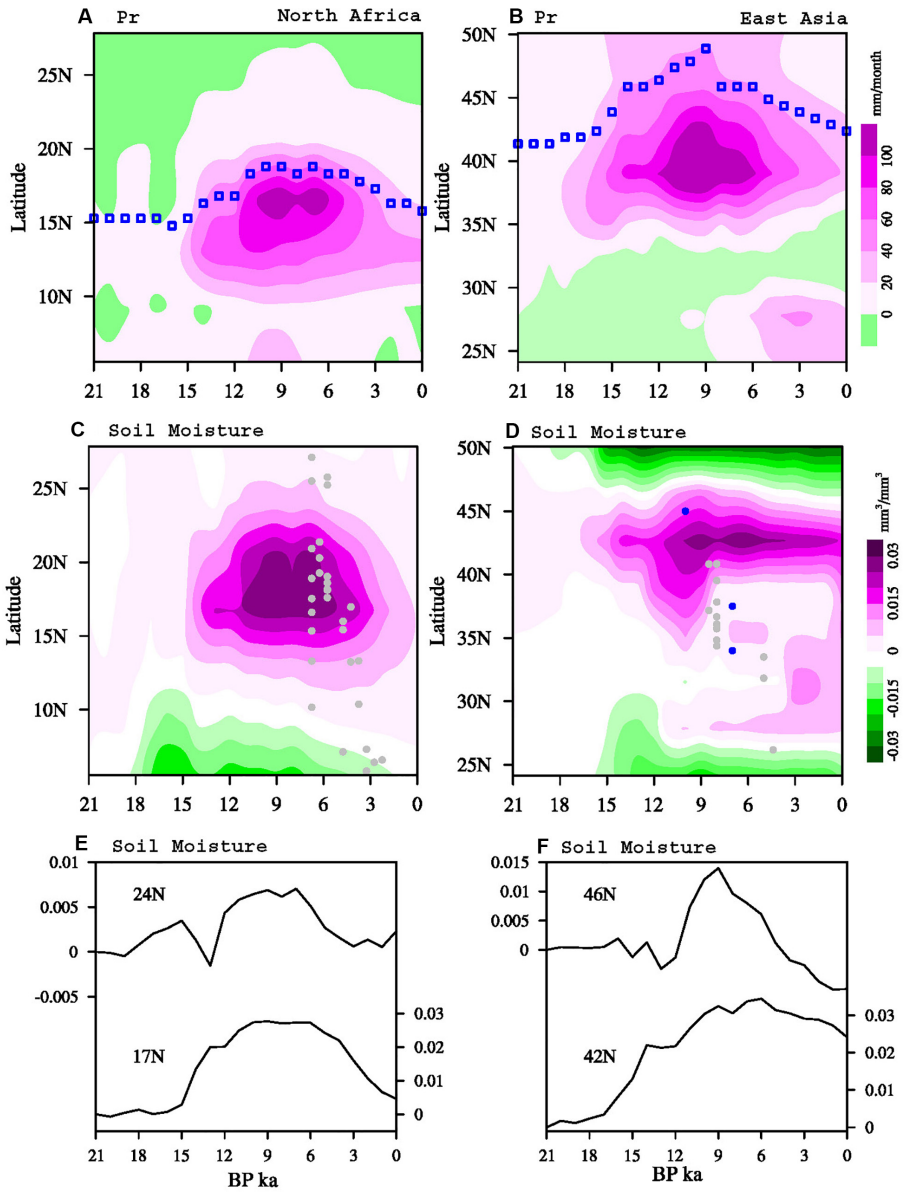

FIGURE 2 | (A) Hovmöller diagram of precipitation anomalies (relative to LGM, units: mm/month) over North Africa (0°–30°E); **(B)** Same as **(A)**, except for East Asia (110°–120°E). **(C,D)** Same as **(A,B)** except for soil moisture (units: mm^3/mm^3). **(E,F)** Typical soil moisture series in North Africa and East Asia. Northern monsoon fringe is shown using blue squares in **(A,B)**. Gray and blue dots show ending-time of HTM of individual paleo-hydrological record (An et al., 2000; Shanahan et al., 2015) in **(C,D)**.

of the northern monsoon fringe, and this simulated fluctuation of northern monsoon fringe is consistent with that reconstructed by geological records (**Figures 1B,C**).

According to the spatial configuration of Afro-Asian monsoon and arid regions (**Figure 1A**), the southward migration of northern monsoon fringe during the Holocene induced the transition from monsoonal humid climate to arid climate, which was accompanied by the dramatic decline of local precipitation (shading in **Figure 1B**). A reversed process occurred during the last deglaciation with a larger varying magnitude, which was due to mean state difference between LGM and PD (shading in **Figure 1C**). Whether the fringe migrated during the last deglaciation or Holocene, the associated precipitation changes all occurred in a belt crossing North Africa to East Asia. Further analysis indicated that the precipitation variation in the fringe-migrationing region (blue curves in **Figures 1E–G**) is synchronous with that of the interior monsoon (black curves in **Figures 1E–G**). Climatological precipitation in fringe-migrationing regions was just about half of that in the interior monsoon regions; however, their varying magnitude was nearly twice of that in the interior monsoon regions (**Figures 1E–G**).

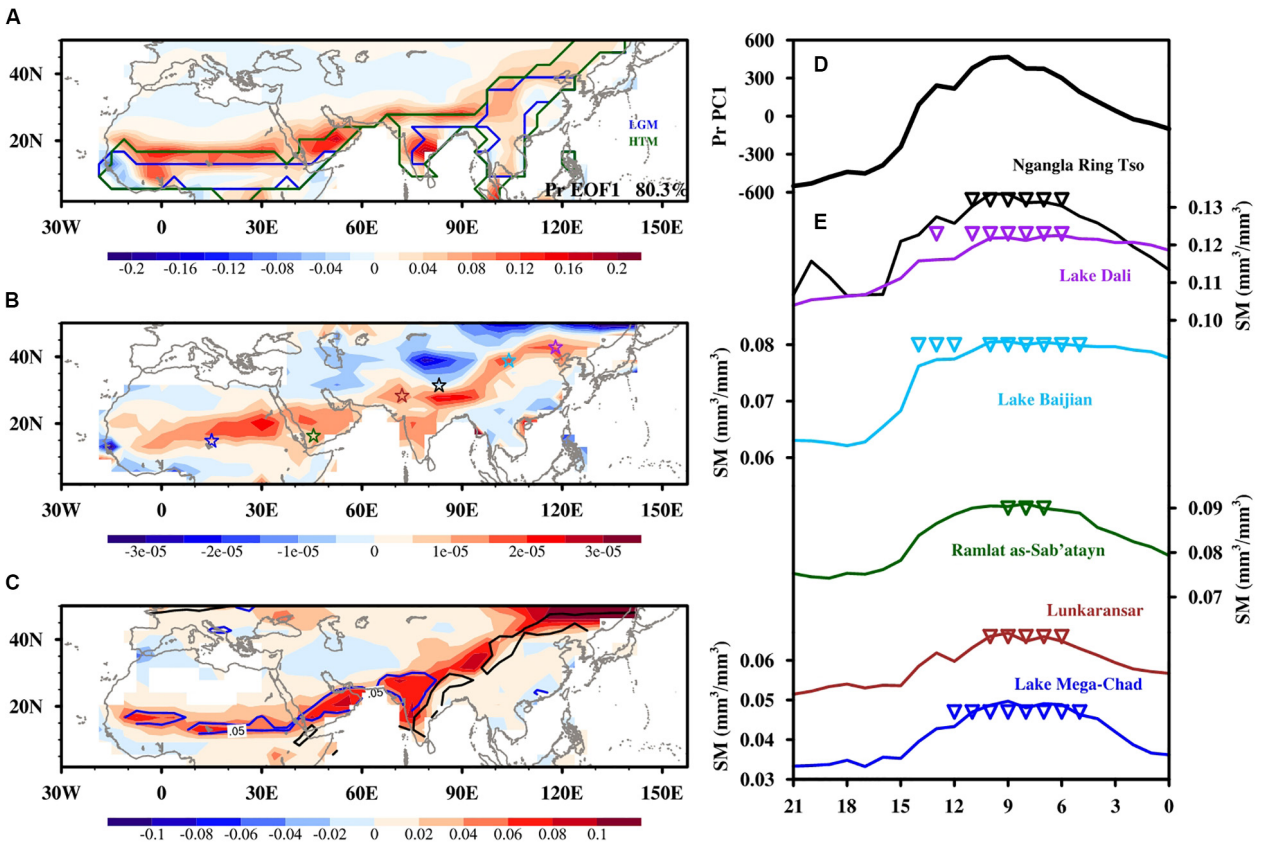

FIGURE 3 | (A) Spatial pattern and **(D)** corresponding principal component (PC1) of the first empirical orthogonal function (EOF) mode of Afro-Asian JJA precipitation in TraCE21; **(B)** Regression pattern of soil moisture on precipitation PC1 (units: $mm^3/mm^3/mm/month$). Stars indicate locations of Lake phase records (i.e., Ngangla Ring Tso, Hudson et al., 2015; Lake Dali, Goldsmith et al., 2017; Lake Baijian, Long et al., 2012; Ramlat as-Sab'atayn, Lézine et al., 1998; Lunkaransar, Enzel et al., 1999; and Lake Mega-Chad, Armitage et al., 2015); **(C)** Same as **(B)**, except for total vegetation percentage (units:%/mm/month). Blue curve shows the regression coefficients of C_3 grass; and black curve, total tree; **(E)** Recorded lake phase (triangles) and simulated soil moisture (curves) adjacent to these paleo-lakes. Curves in **(A)** show simulated Afro-Asian monsoon domains at LGM (blue) ad HTM (green).

Along with the progressively meridional migration of the northern fringe since the LGM, the associated dramatic precipitation changes are time-transgressive (**Figures 2A,B**). The southward migration of northern fringe during the Holocene, whether in North Africa or East Asia, induced the decline of precipitation occurred on the north side of the fringe first and then occurred on the interior side later with a larger amplitude. Similar to the precipitation changes, simulated soil moisture indicated a clearer time-transgressive feature (**Figures 2C–F**), which are roughly consistent to the recorded paleo-hydrological evolution (gray and blue dots in **Figure 2**; An et al., 2000; Shanahan et al., 2015). Similar but reversed processes occurred during the last deglaciation.

Different from the previous explanations which focusing on the migration of monsoon rainbelt (An et al., 2000; Shanahan et al., 2015), here we clearly show that in the model simulation, the Holocene time-transgressive evolution of hydrology in the Afro-Asian monsoon region was caused by the southward migration of the northern monsoon fringe because of shrinking monsoon domain. Along with the migration of the northern monsoon fringe, intensive precipitation changes occurred locally for the reason of humid-arid transition. Furthermore, the model simulation indicated there was a reversed process during the last deglaciation, which is consistent with the finding of previous studies in records and simulations (COHMAP Members, 1988).

The model simulation also clarified the high sensitivity region of climate change associated with the monsoon, which was located around its northern fringe. Our results highlight the integrated changes of the Afro-Asian monsoon, which involved not only monsoon intensity but also the monsoon fringe. Neglecting the changes of monsoon fringe and just focusing on monsoon intensity, the time-transgressive feature and unequal magnitude of climate variation in a broad Afro-Asian monsoon region cannot be well understood.

Eco-Environmental Impact of Monsoon Fringe Migration

As shown above, the intensive precipitation changes, associated with the migration of the northern monsoon fringe, occurred

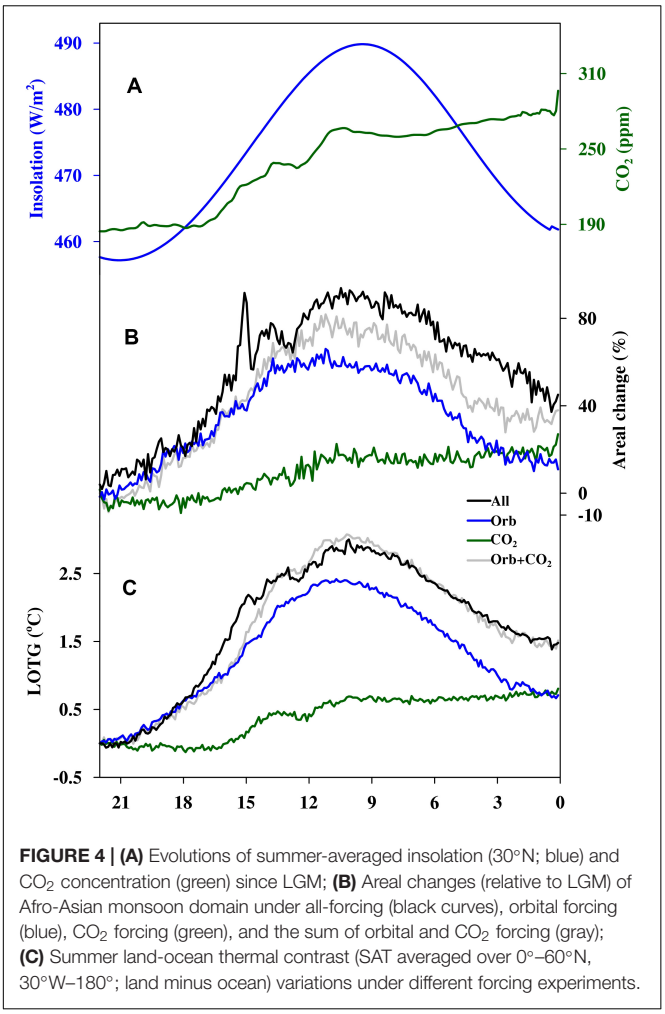

FIGURE 4 | (A) Evolutions of summer-averaged insolation (30°N; blue) and CO_2 concentration (green) since LGM; **(B)** Areal changes (relative to LGM) of Afro-Asian monsoon domain under all-forcing (black curves), orbital forcing (blue), CO_2 forcing (green), and the sum of orbital and CO_2 forcing (gray); **(C)** Summer land-ocean thermal contrast (SAT averaged over 0°–60°N, 30°W–180°; land minus ocean) variations under different forcing experiments.

over the humid-arid boundary region. However, in this semi-arid region, the spatial gradient of precipitation is usually large, which induces high sensitivity of local eco-environment to precipitation changes (Huang et al., 2017). Therefore, a dramatic eco-environmental response to the intensive precipitation change in this fringe-migrationing region is expected, and the simulation confirms it.

The intensive precipitation change along the northern fringe of the Afro-Asian monsoon, the dominant variation mode of precipitation over this area (**Figure 3A**), induced robust variations of local soil moisture (**Figure 3B**), and vegetation (**Figure 3C**). With the northward migration of northern monsoon fringe during the last deglaciation, the intensive increasing precipitation over the newly-formed monsoon region increased local soil moisture and then improved local vegetation. After that, a decreasing precipitation in the region monsoon retreated during the Holocene reduced the local moisture and destroyed the local vegetation intensively. The records of paleo-lakes along the northern fringe of Afro-Asian monsoon confirmed the robust change of local soil moisture simulated in TraCE21 (curves in **Figure 3E**). These lakes only existed during the period of the HTM (triangles in **Figure 3E**) and disappeared during the LGM and PD, indicating the dramatic variation of local hydrological condition and implying a reasonable simulation of local soil moisture variation in TraCE21. This dramatic hydrological variation around the northern fringe of Afro-Asian monsoon significantly controlled the abundance of local vegetation, grasses in low-latitude North Africa and trees in mid-latitude East Asia, as indicated by TraCE21 (**Figure 3C**).

Combined the geological records and model simulation, although the simulation is not validated for every process by limited records, we propose the recorded dramatic eco-environmental variation along northern fringe of Afro-Asian monsoon was caused by the migration of the northern monsoon fringe through the associated intensive variation of precipitation since the LGM. Owning to the intensive migration of monsoon fringe since the LGM, the sensitivities of both climate and eco-environment in the abroad region along northern fringe of Afro-Asian monsoon are all high, which provided the insight for the projection of future changes of climate and eco-environment under ongoing global warming.

Cause for Varying Monsoon Domain

The monsoon is a complex climate system. The monsoon circulation is an extension of the cross equatorial Hadley Cell (Bordoni and Schneider, 2008; Merlis et al., 2013; Schneider et al., 2014) in the monsoon season, it is shaped in further by the local large-scale land-ocean thermal contrast (Webster et al., 1998). The moisture transported by the monsoon circulation converges over the monsoon domain, which induces the formation of monsoon precipitation. Thus, the past recorded and the future projected changes of monsoon (Biasutti, 2013; Boos and Korty, 2016; Bischoff et al., 2017; Seth et al., 2019), involving that in the circulation, the precipitation and the domain, could be dominated by the land-ocean thermal contrast (Chou et al., 2001; Bordoni and Schneider, 2008), the meridional temperature gradient (Wang et al., 2001; D'Agostino et al., 2019; Seth et al., 2019), the large scale circulation (Bordoni and Schneider, 2008), the local moist static energy (Neelin and Held, 1987), and the net energy input (Texier et al., 2000; Schneider et al., 2014; Boos and Korty, 2016; D'Agostino et al., 2019). Among all these potential mechanisms, our transient simulations indicate that the changes of land-ocean thermal contrast coincided with the changes of the Afro-Asian monsoon under long-term climate changes since the LGM, which were mainly forced by orbital and CO_2 forcing (Cheng et al., 2019).

The solo-forcing experiments of TraCE21 of orbital and CO_2 clearly indicate the dominance of land-ocean thermal contrast on the Afro-Asian monsoon domain (**Figure 4**). Precession-dominated orbital forcing modulates the deglacial expansion and the Holocene shrink of the Afro-Asian monsoon domain through the in-phase change of land-ocean thermal contrast. The increasing CO_2 concentration, especially for the period of the last deglaciation, also could expand the domain of the Afro-Asian monsoon through enlarged land-ocean thermal contrast, which basically established the climatological difference between LGM and PD. Similar to the full-forcing experiment of TraCE21 (**Figures 1B,C**), the migration of the northern monsoon fringe is all dominant for the change of monsoon domain, and could

induce the intensive environment impact in the belt shown above (see **Supplementary Figure 4**). The sum of these two solo-forcing experiments (gray curve in **Figures 4B,C**) is roughly equal to the full-forcing experiment of TraCE21 (black curve in **Figures 4B,C**), which illustrates the dominance of these two external forcing during the long-term change of the Afro-Asian monsoon since the LGM. Comparing to the forcing of CO_2, orbital forcing is the dominated factor in the simulated migration of monsoon fringe.

CONCLUSION AND DISCUSSION

Combining model simulation with geological records, we proposed the recorded time-transgressive hydrological evolution around the northern fringe of the Afro-Asian monsoon and the recorded dramatic eco-environmental variation in the same region were caused by the gradual migration of the northern monsoon fringe since the LGM. The migration of the northern monsoon fringe could induce intensive variation of precipitation locally due to the humid-arid transition. Our results clarified the sensitive response of climate and eco-environment of monsoon located around its northern fringe, not the interior. We also propose the LGM-PD difference of climate and eco-environment was mainly attributed to the increasing CO_2 concentration, but their intensive long-term fluctuation was caused by orbital forcing through the impact on the land-ocean thermal contrast.

Our analyses clearly illustrated, besides monsoon intensity, we should pay more attention to the accompanying change of monsoon domain (migration of monsoon fringe) under long-term climate change. The clarification about the subsequence of monsoon fringe migration, as illustrated here, is important to understand the diverse evolution of individual geological record in the regions of the Afro-Asian monsoon, which was usually asynchronous in time and unequal in amplitude. The insight about the monsoon fringe, which was derived from its past changes, is important for the projection of future changes of monsoon-related climate and eco-environment under global warming.

Coherent long-term evolution of the Afro-Asian monsoon, as indicated by geological records and model simulation, illustrated the integrity of the Afro-Asian monsoon again, which is consistent with the analyses using the observations. For the long-term variation of the Afro-Asian monsoon, our analyses highlighted the importance of large-scale land-ocean thermal contrast (Webster et al., 1998). Comparing to the meridional scales of North Africa monsoon, it's large for the East Asia monsoon, which leads to an opposite rainfall changes over the East Asia during the Holocene era as indicated in geological records (An et al., 2000; Xu et al., 2020) and model simulation (Liu et al., 2014). This asynchronous rainfall changes over interior regions of East Asia monsoon was caused by the migration of monsoon rainbelt, which is clearly different to the asynchronous rainfall changes around norther monsoon fringe caused by the migration of monsoon fringe.

Another point should be noticed is that the amplitude of northward migration of the Afro-Asian monsoon fringe and associated environment impact may be small under future warming, even the warming amplitude may be larger than that in the past. As illustrated in Cheng et al. (2019), the varying amplitude of land-ocean thermal contrast relies on the external forcing of temperature change, high under the orbital forcing and small under CO_2 forcing. Comparing to the past changes of Afro-Asian monsoon fringe which dominated by orbital forcing, its future changes dominated by CO_2 will be relative small.

DATA AVAILABILITY STATEMENT

Publicly available datasets were analyzed in this study. This data can be found here: https://www.earthsystemgrid.org/dataset/ucar.cgd.ccsm3.trace.html.

AUTHOR CONTRIBUTIONS

JC: conceptualization and writing—original draft preparation. JC and YM: methodology and investigation. YM: formal analysis. HW, HL, and ZL: resources. HW and ZL: writing—review and editing. All authors have read and agreed to the published version of the manuscript.

FUNDING

This research was supported by the Program of Global Change and Mitigation, Ministry of Science and Technology of the People's Republic of China (2016YFA0600504), and by the National Natural Science Foundation of China (41776017, 41630527, and 41977381).

SUPPLEMENTARY MATERIAL

The Supplementary Material for this article can be found online at: https://www.frontiersin.org/articles/10.3389/feart.2020.00322/full#supplementary-material

REFERENCES

Adams, J. M. (1997). *Global Land Environments Since the Last Interglacial*. Oak Ridge, TN: Oak Ridge National Laboratory.

An, Z. S., Porter, S. C., Kutzbach, J. E., Xihao, W., Suming, W., and Xiaodong, L. (2000). Asynchronous Holocene optimum of the East Asian monsoon. *Quatern. Sci. Rev.* 19, 743–762. doi: 10.1016/s0277-3791(99)00031-1

Armitage, S. J., Bristow, C. S., and Drake, N. A. (2015). West African monsoon dynamics inferred from abrupt fluctuations of Lake Mega-Chad. *Proc. Natl. Acad. Sci. U.S.A.* 112, 8543–8548. doi: 10.1073/pnas.1417655112

Berger, A. (1978). Long-term variations of daily insolation and quaternary climatic changes. *J. Atmos. Sci.* 35, 2362–2367. doi: 10.1175/1520-0469(1978)035<2362:ltvodi>2.0.co;2

Biasutti, M. (2013). Forced Sahel rainfall trends in the CMIP5 archive. *J. Geophys. Res. Atmos.* 118, 1613–1623. doi: 10.1002/jgrd.50206

Bischoff, T., Schneider, T., and Meckler, A. N. (2017). A conceptual model for the response of tropical rainfall to orbital variations. *J. Clim.* 30, 8375–8391. doi: 10.1175/jcli-d-16-0691.1

Boos, W. R., and Korty, R. L. (2016). Regional energy budget control of the intertropical convergence zone and application to mid-Holocene rainfall. *Nat. Geosci.* 9, 892–897. doi: 10.1038/ngeo2833

Bordoni, S., and Schneider, T. (2008). Monsoons as eddy-mediated regime transitions of the tropical overturning circulation. *Nat. Geosci.* 1, 515–519. doi: 10.1038/ngeo248

Broccoli, A. J., and Manabe, S. (1992). The effects of orography on Midlatitude Northern Hemisphere dry climates. *J. Climate* 5, 1181–1201. doi: 10.1175/1520-0442(1992)005<1181:teooom>2.0.co;2

Cheng, J., Ma, W., Liu, Z., and Wu, H. (2019). Varying sensitivity of East Asia summer monsoon circulation to temperature change since Last Glacial Maximum. *Geophys. Res. Lett.* 46, 9103–9109. doi: 10.1029/2019GL083405

Chou, C., Neelin, J., and Su, H. (2001). Ocean-atmosphere-land feedbacks in an idealized monsoon. *Q. J. Roy. Meteor. Soc.* 127, 1869–1891. doi: 10.1002/qj.49712757602

Collins, W. D., Bitz, C. M., Blackmon, M. L., Bonan, G. B., Bretherton, C. S., Carton, J. A., et al. (2006). The community climate system model version 3 (CCSM3). *J. Clim.* 19, 2122–2143. doi: 10.1175/jcli3761.1

D'Agostino, R., Bader, J., Bordoni, S., Ferreira, D., and Jungclaus, J. (2019). Northern Hemisphere monsoon response to mid-holocene orbital forcing and greenhouse gas-induced global warming. *Geophys. Res. Lett.* 46, 1591–1601. doi: 10.1029/2018gl081589

Doherty, R., Kutzbach, J., Foley, J., and Pollard, D. (2000). Fully coupled climate/dynamical vegetation model simulations over North Africa during the mid-Holocene. *Clim. Dyn.* 16, 561–573. doi: 10.1007/s003820000065

Dykoski, C. A., Edwards, R. L., Cheng, H., Yuan, D., Cai, Y., Zhang, M., et al. (2005). A highresolution, absolute-dated Holocene and deglacial Asian monsoon record from Dongge Cave, China. *Earth Planet. Sci. Lett.* 233, 71–86. doi: 10.1016/j.epsl.2005.01.036

Enzel, Y., Ely, L. L., Mishra, S., Ramesh, R., Amit, R., Lazar, B., et al. (1999). High-resolution Holocene environmental changes in the Thar Desert, northwestern India. *Science* 284, 125–128. doi: 10.1126/science.284.5411.125

Fleitmann, D., Burns, S. J., Mudelsee, M., Neff, U., Kramers, J., Mangini, A., et al. (2003). Holocene forcing of the Indian monsoon recorded in a stalagmite from southern Oman. *Science* 300, 1737–1739. doi: 10.1126/science.1083130

Goldsmith, Y., Broeckera, W. S., Xu, H., Polissara, P. J., deMenocala, P. B., Poratc, N., et al. (2017). Northward extent of East Asian monsoon covaries with intensity on orbital and millennial timescales. *Proc. Natl. Acad. Sci. U.S.A.* 114, 1817–1821. doi: 10.1073/pnas.1616708114

Haug, G. H., Hughen, K. A., Sigman, D. M., Peterson, L. C., and Röhl, U. (2001). Southward migration of the intertropical convergence zone through the Holocene. *Science* 293, 1304–1308. doi: 10.1126/science.1059725

He, F., Shakun, J. D., Clark, P. U., Carlson, A. E., Liu, Z., Otto-Bliesner, B. L., et al. (2013). Northern hemisphere forcing of southern hemisphere climate during the last deglaciation. *Nature* 494, 81–85. doi: 10.1038/nature11822

Huang, J., Li, Y., Fu, C., Chen, F., Fu, Q., Dai, A., et al. (2017). Dryland climate change: recent progress and challenges. *Rev. Geophys.* 55, 719–778. doi: 10.1002/2016rg000550

Hudson, A. M., Quade, J., Huth, T. E., Lei, G. L., Cheng, H., Edwards, L. R., et al. (2015). Lake level reconstruction for 12.8–2.3ka of the Ngangla Ring Tso closed-basin lake system, southwest Tibetan Plateau. *Quatern. Res.* 83, 66–79. doi: 10.1016/j.yqres.2014.07.012

Jiang, D. B., Tian, Z. P., and Lang, X. M. (2015a). Mid-Holocene global monsoon area and precipitation from PMIP simulations. *Clim. Dyn.* 44, 2493–2512. doi: 10.1007/s00382-014-2175-8

Jiang, D. B., Tian, Z. P., Lang, X. M., Kageyama, M., and Ramstein, G. (2015b). The concept of global monsoon applied to the last glacial maximum: a multi-model analysis. *Quat. Sci. Rev.* 126, 126–139. doi: 10.1016/j.quascirev.2015.08.033

Jiang, W., and Liu, T. (2007). Timing and spatial distribution of mid-Holocene drying over northern China: response to a southeastward retreat of the East Asian Monsoon. *J. Geophys. Res. Atmos.* 112, 1984–2012.

Joos, F., and Spahni, R. (2008). Rates of change in natural and anthropogenic radiative forcing over the past 20,000 years. *Proc. Natl. Acad. Sci. U.S.A.* 105, 1425–1430. doi: 10.1073/pnas.0707386105

Kathayat, G., Cheng, H., Sinha, A., Spötl, C., Edwards, R. L., Zhang, H., et al. (2016). Indian monsoon variability on millennial-orbital timescales. *Sci. Rep.* 6:24374. doi: 10.1038/srep24374

Lézine, A. M., Saliege, J. F., Robert, C., Wertz, F., and Inizan, M. L. (1998). Holocene lakes from Ramlat as-Sab'atayn (Yemen) illustrate the impact of monsoon activity in Southern Arabia. *Quatern. Res.* 50, 290–299. doi: 10.1006/qres.1998.1996

Liu, J., Wang, B., Yim, S. Y., Lee, J., Jhun, J., and Ha, K. (2012). What drives the global summer monsoon over the past millennium? *Clim. Dyn.* 39, 1063–1072. doi: 10.1007/s00382-012-1360-x

Liu, Z., Otto-Bliesner, B. L., He, F., Brady, E. C., Tomas, R., Clark, P. U., et al. (2009). Transient simulation of Last Deglaciation with a new mechanism for Bolling-Allerod warming. *Science* 325, 310–314. doi: 10.1126/science.1171041

Liu, Z., Wen, X., Brady, E. C., Otto-Bliesner, B., Yu, G., Lu, H., et al. (2014). Chinese cave records and the East Asia Summer Monsoon. *Quat. Sci. Rev.* 83, 115–128. doi: 10.1016/j.quascirev.2013.10.021

Long, H., Lai, Z. P., Fuchs, M., Zhang, J. R., and Li, Y. (2012). Timing of Late Quaternary palaeolake evolution in Tengger Desert of northern China and its possible forcing mechanisms. *Glob. Planet. Change* 9, 119–129. doi: 10.1016/j.gloplacha.2012.05.014

McManus, J. F., Francois, R., Gherardi, J. M., Keigwin, L. D., and Brown-Leger, S. (2004). Collapse and rapid resumption of Atlantic meridional circulation linked to deglacial climate changes. *Nature* 428, 834–837. doi: 10.1038/nature02494

COHMAP Members (1988). Climatic changes of the last 18,000 years: observations and model simulations. *Science* 241, 1043–1052. doi: 10.1126/science.241.4869.1043

Merlis, T., Schneider, T., Bordoni, S., and Eisenman, I. (2013). Hadley circulation response to orbital precession. Part I: aquaplanets. *J. Clim.* 26, 754–771. doi: 10.1175/jcli-d-12-00149.1

Neelin, J., and Held, I. (1987). Modeling tropical convergence based on the moist static energy budget. *Mon. Weather Rev.* 115, 3–12. doi: 10.1175/1520-0493(1987)115<0003:mtcbot>2.0.co;2

Otto-Bliesner, B. L., Russell, J. M., Clark, P. U., Liu, Z., Overpeck, J. T., Konecky, B., et al. (2014). Coherent changes of southeastern equatorial and northern African precipitation during the last deglaciation. *Science* 346, 1223–1227. doi: 10.1126/science.1259531

Peltier, W. (2004). Global glacial isostasy and the surface of the ice-age earth: the ICE-5G (VM2) model and GRACE. *Annu. Rev. Earth Plant. Sci.* 20, 111–149. doi: 10.1146/annurev.earth.32.082503.144359

Schneider, T., Bischoff, T., and Haug, G. H. (2014). Migrations and dynamics of the inter-tropical convergence zone. *Nature* 513, 45–53. doi: 10.1038/nature13636

Seth, A., Giannini, A., Rojas, M., Rauscher, S. A., Bordoni, S., Singh, D., et al. (2019). Monsoon responses to climate changes—connecting past, present and future. *Curr. Clim. Change Rep.* 5, 63–79. doi: 10.1007/s40641-019-00125-y

Sha, L., Ait Brahim, Y., Wassenburg, J. A., Yin, J., Peros, M., Cruz, F. W., et al. (2019). How far north did the African Monsoon fringe expand during the African Humid Period? Insights from Southwest Moroccan speleothems. *Geophys. Res. Lett.* 46, 14093–14102. doi: 10.1029/2019GL084879

Shanahan, T., McKay, N., Hughen, K., Overpeck, J., Otto-Bliesner, B., Heil, C., et al. (2015). The time-transgressive termination of the African Humid Period. *Nat. Geosci.* 8, 140–144. doi: 10.1038/ngeo2329

Shi, J., and Yan, Q. (2019). Evolution of the Asian–African monsoonal precipitation over the last 21 kyr and the associated dynamic mechanisms. *J. Clim.* 32, 6551–6569. doi: 10.1175/jcli-d-19-0074.1

Skonieczny, C., Paillou, P., Bory, A., Bayon, G., Biscara, L., Crosta, X., et al. (2015). African humid periods triggered the reactivation of a large river system in Western Sahara. *Nat. Commun.* 6:8751. doi: 10.1038/ncomms9751

Street, F. A., and Grove, A. T. (1976). Environmental and climatic implications of late quaternary lake-level fluctuations in Africa. *Nature* 261, 385–390. doi: 10.1038/261385a0

Texier, D., de Noblet, N., and Braconnot, P. (2000). Sensitivity of the African and Asian monsoons to mid-holocene insolation and data-inferred surface changes. *J. Climate* 13, 164–181. doi: 10.1175/1520-0442(2000)013<0164:sotaaa>2.0.co;2

Tierney, J. E., Pausata, F. S. R., and deMenocal, P. B. (2017). Precipitation regimes of the green Sahara. *Sci. Adv.* 3:e1601503. doi: 10.1126/sciadv.1601503

Wang, B., and Ding, Q. (2008). Global monsoon: dominant mode of annual variation in the tropics. *Dyn. Atmos. Oceans* 44, 165–183. doi: 10.1016/j.dynatmoce.2007.05.002

Wang, B., Wu, R. G., and Lau, K. M. (2001). Interannual variability of the Asian summer monsoon: contrasts between the India and the western north pacific-east Asian monsoons. *J. Clim.* 14, 4073–4090. doi: 10.1175/1520-0442(2001)014<4073:ivotas>2.0.co;2

Wang, Y., Cheng, H., Edwards, R. L., Kong, X., Shao, X., Chen, S., et al. (2008). Millennial-and orbital scale changes in the East Asian monsoon over the past 224 000 years. *Nature* 7182, 1090–1093. doi: 10.1038/nature06692

Webster, P. J., Magana, V., Palmer, T., Shukla, J., Tomas, R., Yanai, M., et al. (1998). Monsoons: processes, predictability and the prospects for prediction. *J. Geophys. Res.* 1031, 14451–14510. doi: 10.1029/97jc02719

Weldeab, S., Lea, D. W., Schneider, R. R., and Andersen, N. (2007). 155000 years of West African monsoon and ocean thermal evolution. *Science* 316, 1303–1307. doi: 10.1126/science.1140461

Wen, X., Liu, Z., Wang, S., Cheng, J., and Zhu, J. (2016). Correlation and anti-correlation of the East Asian summer and winter monsoon during the last 21,000 years. *Nat. Commun.* 7:11999.

Winkler, M. G., and Wang, P. K. (1993). *The Late-Quaternary Vegetation and Climate of China, Global Climates Since the Last Glacial Maximum*. Minneapolis: University of Minnesota Press, 221–264

Xu, H., Goldsmith, Y., Lan, J., Tan, L., Wang, X., Zhou, X., et al. (2020). Juxtaposition of western Pacific subtropical high on Asian Summer Monsoon shapes subtropical East Asian precipitation. *Geophys. Res. Lett.* 47:e2019GL084705.

Yan, Z., and Petit-Maire, N. (1994). The last 140 ka in the Afro-Asian arid/semi-arid transitional zone. *Palaeogeogr. Palaeocl.* 110, 217–233. doi: 10.1016/0031-0182(94)90085-x

Yang, S., Ding, Z., Li, Y., Wang, X., Jiang, W., and Huang, X. (2015). Warming-induced northwestward migration of the East Asian monsoon rain belt from the Last Glacial Maximum to the mid-Holocene. *Proc. Natl. Acad. Sci. U.S.A.* 112, 13178–13183. doi: 10.1073/pnas.1504688112

Yu, G., and Harrison, S. P. (1996). An evaluation of the simulated water balance of Eurasia and northern Africa at 6000 yr BP using lake status data. *Clim. Dyn.* 12, 723–735. doi: 10.1007/s003820050139

Zhang, H., Griffiths, M. L., Chiang, J. C. H., Kong, W. W., Wu, S., Atwood, A., et al. (2018). East Asian hydroclimate modulated by the position of the westerlies during termination I. *Science* 362, 580–583. doi: 10.1126/science.aat9393

Conflict of Interest: The authors declare that the research was conducted in the absence of any commercial or financial relationships that could be construed as a potential conflict of interest.

Copyright © 2020 Cheng, Ma, Wu, Long and Liu. This is an open-access article distributed under the terms of the Creative Commons Attribution License (CC BY). The use, distribution or reproduction in other forums is permitted, provided the original author(s) and the copyright owner(s) are credited and that the original publication in this journal is cited, in accordance with accepted academic practice. No use, distribution or reproduction is permitted which does not comply with these terms.

frontiers in Earth Science

ORIGINAL RESEARCH
published: 07 August 2020
doi: 10.3389/feart.2020.00314

Lake-Level Oscillation Based on Sediment Strata and Geochemical Proxies Since 11,000 Year From Tengger Nuur, Inner Mongolia, China

Zhang Chengjun, Zhang Li, Zhang Wanyi, Tao Yunhan, Liu Yang, Wan Xiangling, Zhang Zhen and Safarov Khomid*

College of Earth Sciences & Key Laboratory of Mineral Resources in Western China (Gansu Province), Lanzhou University, Lanzhou, China

A 794-cm section was collected from Tengger Nuur in the Inner Mongolian Plateau. Accelerator mass spectrometry ^{14}C data were determined to set an age-depth model after removing about 1920 years of the carbon reservoir effect. Based on the multi-proxies grain size, carbonate-content, total organic carbon-content, ratio of C/N, ratios of Mg/Ca and Sr/Ca, and carbonate carbon and oxygen isotopes, paleoenvironmental changes since the last deglaciation were reconstructed. Tengger Nuur was very shallow during the last deglaciation under a cool and wet climate, especially during the interval of the cold Younger Dryas event. Although, temperature and humidity increased from the early Holocene (~10,450–8750 cal a BP), low lake levels indicated that the summer monsoon was not sufficiently strong to reach the modern monsoon boundary in Inner Mongolia. High monsoon precipitation caused lake expansion during 8750–5000 cal a BP, but the lake level oscillated in a shallow state under high evaporation. A low lake-level event occurred with the interval of a cold-wet climate during 5450–5100 cal a BP. The summer monsoon receded gradually to maintain a deep lake under high effective humidity during 5000–2000 cal a BP, punctuated by low lake-level events at intervals of 4300–3980 cal a BP and 3700–2750 cal a BP. With the arrival of the cold and dry westerly after 2000 cal a BP, lakes shrank gradually to become salinized or completely desiccated, but their levels oscillated at shallow depths during the four periods of 1900–1800 cal a BP, 1500–1050 cal a BP, 550–400 cal a BP (Little Ice Age), and 100 cal a BP–AD 1985. Therefore, the eastern summer monsoon was weak in the early Holocene, and lake-level oscillation was controlled by effective humidity in arid and semi-arid areas.

Keywords: Tengger Nuur, Holocene, stratigraphy, weak summer monsoon, effective humidity

OPEN ACCESS

Edited by:
Liangcheng Tan,
Institute of Earth Environment, Chinese Academy of Sciences, China

Reviewed by:
Hao Long,
Nanjing Institute of Geography and Limnology (CAS), China
Qianli Sun,
East China Normal University, China

****Correspondence:***
Zhang Chengjun
cjzhang@lzu.edu.cn

Specialty section:
This article was submitted to Quaternary Science, Geomorphology and Paleoenvironment, a section of the journal Frontiers in Earth Science

Received: *24 March 2020*
Accepted: *03 July 2020*
Published: *07 August 2020*

Citation:
Chengjun Z, Li Z, Wanyi Z, Yunhan T, Yang L, Xiangling W, Zhen Z and Khomid S (2020) Lake-Level Oscillation Based on Sediment Strata and Geochemical Proxies Since 11,000 Year From Tengger Nuur, Inner Mongolia, China. Front. Earth Sci. 8:314. doi: 10.3389/feart.2020.00314

INTRODUCTION

The region of mid and eastern Mongolia, which lies at the boundary of the modern summer monsoon, is controlled by the winter, summer monsoon, and westerlies. The interplay between the eastern monsoon and westerlies has been significantly affecting the ecological environment of this region since the last deglaciation. Therefore, reconstructions of the paleoenvironmental

change have high significance in understanding the evolution and mechanism of the eastern monsoon. The fragile ecological system at the monsoon boundary is sensitive to the monsoon, and thus a large number of lake-filling events triggered by the summer monsoon precipitation record the paleoenvironmental change. Such records based on lake and terrestrial sediments help in understanding the interplay between the climate and environment, and monsoon mechanisms since the last glaciation (Wang, 1992; Chen et al., 2003, 2010; Xiao et al., 2004), and the development of the ecological environment in arid and semi-arid regions in the future.

In the past several decades, several lakes at the modern eastern monsoon boundary of Inner Mongolia, i.e., Daihai Lake (Li et al., 1992; Xiao et al., 2004; Zheng et al., 2010; Zeng et al., 2013), Wulagai Lake (Yu et al., 2014), Baahar Nuur Lake (Guo et al., 2007), Dali Nor Lake (Wang et al., 2004), Haolaihure Paleolake (Liu et al., 2018), Diaojiao Lake (Song et al., 1996; Yang et al., 1997; Yang, 1998), Huangqihai (Li et al., 1992), Hulun Lake (Yang and Wang, 1996; Zhang and Wang, 2000; Wen et al., 2010), Dabusu Lake (Jie et al., 2001), and Angulinao (Zhai et al., 2000), had been used to reconstruct paleoenvironmental changes based on pollen and geochemical proxies. However, although the paleoenvironment records provided much information about environmental changes since last deglaciation, a few these studies did remove the carbon reservoir effect in the age-depth model established for lakes, for example, Xiao et al. (2004); Guo et al. (2007), Wen et al. (2010); Liu et al. (2018), and some of them did not calibrate the tree-ring calendar year. Nevertheless, they provided deep insight into the interplay eastern monsoon and westerlies in this region.

Tengger Nuur, which lies at the modern eastern Asian monsoon boundary in Inner Mongolia, is impacted both by the Asian summer and winter monsoons and westerlies (**Figure 1**). Studying lake-level fluctuations in Tengger Nuur would provide records of the Asian monsoon and its variability and linkage with the global climate change in the Holocene.

GEOLOGICAL SETTING, SAMPLING AND LITHOLOGICAL STRATIGRAPHY

Tengger Nuur, which means "sky lake" in Mongolian (Nuur means lake or swag) (110°38′–110°42′E, 42°24′–42°28′N, 1077.60 m asl), is located in northern Darhan Muminggan United Banner of Ulanqab League. Aeolian deposition is widely distributed around the lake shoreline. Tengger Nuur, a tectonic fault depression terminal lake, is 8.4 km long and 6.2 km wide, with a mean width of 3.4 km and an area of approximately 28.6 km^2. The maximum catchment area has been reported to be about 53 km^2 (Wang and Dou, 1998).

The lake area belongs to the middle temperate zone, which falls under a continental arid climate, and experiences a mean annual temperature of 3.4°C. The mean temperature in January is −15.9°C when the extreme minimum temperature can be as low as −41.0°C. In July, the mean temperature is 20.5°C, and the extreme maximum temperature could reach up to 36.6°C. The mean annual sunshine time reaches 2986 h, and the frost-free period is about 106 days. The annual precipitation ranges from 142.6 to 400.3 mm, which mean is about 236.6 mm, chiefly occurring between July and August. The evaporation is about 2360 mm. The lake depends on the supply of rainfall and surface runoff. Currently, seasonal Aibugai River is the only one flowing into the lake. The river is 154 km long, feeding the basin from Daqingshan in the south.

From 1979 onward, the water level of Tengger Nuur has been dropping gradually as the volume of runoff of Aibugai River decreased and wetlands shrunk to become almost completely desiccated in 1985, as historical records suggest. However, the lake began to rise again to reach the recorded highest level in 2018, and the water volume increased to 1×10^8 m^3.

A sediment stratum of 794 cm length (TGN-05, 42°27′7.7″N, 110°42′3.6″E, 1052 m asl), including 398 cm digging section and 396 cm core drilled with a UWITEC piston corer "Niederreiter 60", was obtained from Lake Tengger Nuur in 2005. The groundwater depth is about 398 cm. About 397 samples were collected at intervals of 2 cm. However, sediments in the interval of 346–374 cm were missed in the sampling.

The lithological strata of TGN-05 are as follows: a brown mud layer at 0–389 cm (in this paper, mud indicates sediment grain sizes less than 4 μm); a gray-black mud layer at 389–398 cm; a dark gray mud layer at 398–401 cm; a green-gray silt layer at 401–448 cm; a layer of well-sorted coarse sand with highly rounded fine gravel at 401–448 cm; a dark gray muddy silt layer at 469–521 cm; a blown gray coarse sandy mud layer at 521–540 cm; a layer of well-sorted and highly rounded bluish-gray coarse muddy sand at 540–602 cm; a bluish-gray mud layer 602–609 cm; a layer of highly rounded coarse sandy fine gravel at 609–620 cm; a muddy silt layer at 620–685 cm; a layer of alternating bluish-gray coarse sand and poorly sorted, highly rounded fine gravel at 685–757 cm; a brown silty mud layer at 757–794 cm.

AGE DATA AND AGE-DEPTH MODEL

A total of 11 samples of bulk organic matter were used for radiocarbon dating of TGN-05 in ^{14}C radioactivity isotope labs, BETA in United States and Beijing University in China. However, the total organic carbon (TOC) contents of the last three samples, TGN-05-828 (828–830 cm), TGN-05-704 (704–706 cm), and TGN-05-792 (792–794 cm), were too low for analysis (**Table 1**).

Recently, several studies found that the lake carbon reservoir effect (LCRE, also "dead carbon" or "old carbon" or "hard water" effect) can result in anomalously old ^{14}C ages of lacustrine sediments. Therefore, LCRE correction should be applied before the construction of an age-to-depth model. Lake carbon reservoir effect has a great spatial and temporal change. For example, that is very small in the Qingtu Lake (Long et al., 2011). Five hundred and seventy year of the age of Lake Bayanchagan in Inner Mongolia could be attributed to LCRE (Jiang et al., 2006), 685 year in Hulun Lake (Wen et al., 2010), 2570 year in Haolaihure Paleolake (Liu et al., 2018), that of Baahar Nuur has been reported to be around 1935 year (Guo et al., 2007), the ca. 360 year can be considered to result from the hard water effect on

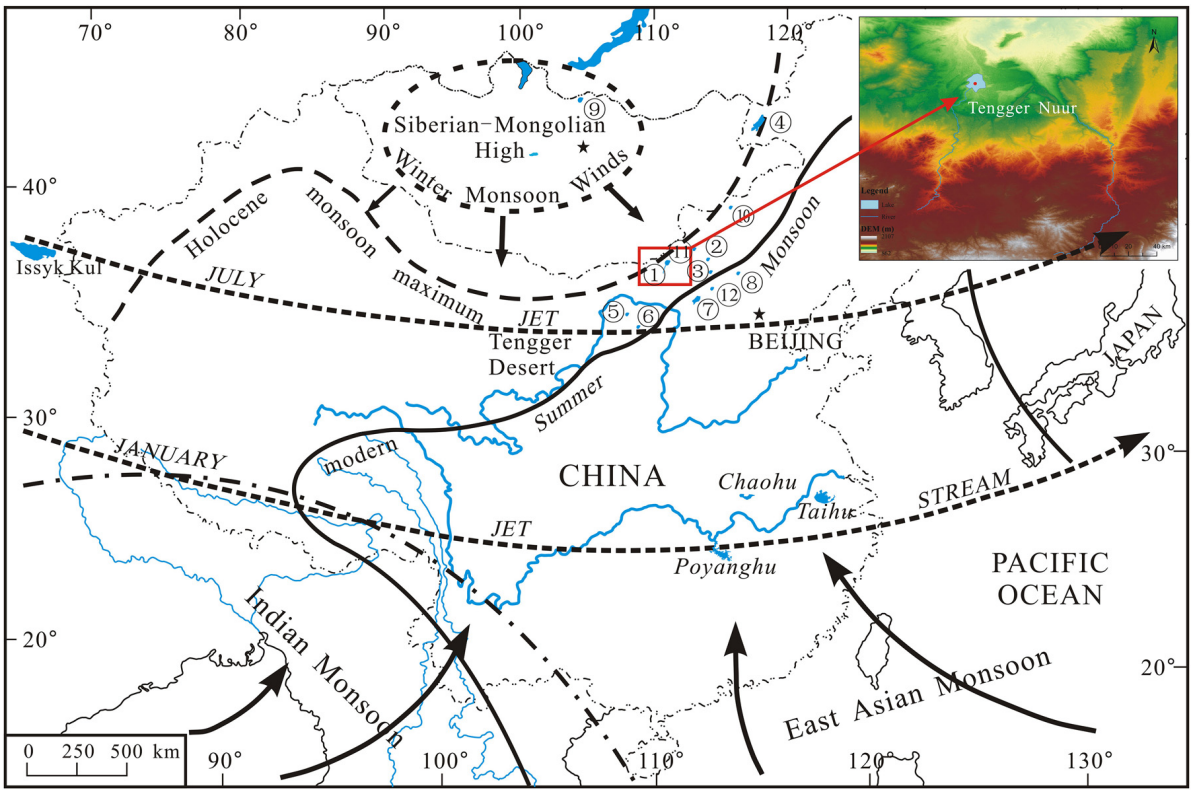

FIGURE 1 | Map of Asian monsoon region showing locations of paleoclimate records used in this study. ① Tengger Nuur, ② Daojiaohaizi, ③ Dali Lake, ④ Hulun Lake, ⑤ Yanhaizi, ⑥ Baahar Nuur, ⑦ Daihai Lake, ⑧ Bayanchagan Lake, ⑨ Gun Nuur, ⑩ Haolaihure, ⑪ Angulinao, ⑫ Huangqihai. Lines indicate modern extent of East Asian and Indian monsoons (dashed lines) and maximum area extent of monsoons during the Holocene (solid line), as mapped by Winkler and Wang (1993).

TABLE 1 | Radiocarbon dating results for section TGN-05 determined in the BETA ^{14}C Lab (BETA) and Beijing University ^{14}C Lab (BA).

Lab ID	Sample ID	Depth (cm)	Material	$\delta^{13}C_{org}$ (‰)	^{14}C a BP	cal a BP (1σ) eliminating LCRE
BETA408723	TGN-05-325	72–74	sediment	−23.2	3050 ± 30	980–1037
BETA408725	TGN-05-225	172–174	sediment	−23.2	4520 ± 30	2730–2754
BETA408726	TGN-05-205	192–194	sediment	−23.2	5210 ± 30	3517–3557
BETA408724	TGN-05-165	232–234	sediment	−23.2	6090 ± 30	4693–4761
BETA408727	TGN-05-85	312–314	sediment	−23.9	6420 ± 30	5101–5141
BETA408728	TGN-05-480	480–482	sediment	−25.1	8130 ± 30	7023–7118
BA120651	TGN-05-402	402–404	Sediment	–	7570 ± 40	6400–6484
BA120650	TGN-05-564	564–566	Sediment	–	10600 ± 35	9555–9633
BA120649	TGN-05-828	628–630	Sediment	–	No data	–
BA120648	TGN-05-704	704–708	Sediment	–	No data	–
BA120647	TGN-05-792	792–794	Sediment	–	No data	–

LCRE, lake carbon reservoir effect, 1920 years in Tengger Nuur sediment.

the radiocarbon dating of Daihai Lake sediments as extrapolated linearly to the core depth of 0 m (Xiao et al., 2004). Chen et al. (2003) regarded that LCRE of Lake Yanhaizi in the Mu Us Desert to be about 879 year according to comprehensively analyzed ^{14}C age of surface and lacustrine core sediments, and pollens. The hard water effect was estimated at 1000–2000 year for lakes in Inner Mongolia (Ren, 1998). Hou et al. (2012) discussed the spatial and temporal pattern of LCREs in Tibetan lakes, and found that they mostly range from 1000 to 3000 ^{14}C years.

Lake carbon reservoir effect is generally identified by the difference of macrophyte remains and TOC in bulk lake sediments. However, a large number of analysis results show that macrophyte remains in lacustrine sediments could also be affected by the hard water effect. For instance, Li et al. (2017) used surface macrophyte remains and determined the LCRE of Lake Koucha as 1812 ± 22 year. Therefore, the ^{14}C dating value of organic matter from lacustrine surface sediments could be roughly recognized as the value of LCRE (Chen et al., 2003;

Xiao et al., 2004; Jiang et al., 2006; Guo et al., 2007; Li et al., 2017). In addition, ^{210}Pb-^{137}Cs of lacustrine sediments could be occasionally used to calibrate the ^{14}C ages of surface sediments (Zhang et al., 2004). Otherwise, when ^{14}C ages of lacustrine horizons of sediments cannot be measured directly, LCRE data can be obtained through linear extrapolation to the top (Chen et al., 2003; Xiao et al., 2004).

According to the analysis values of the ^{14}C ages of Tengger Nuur (**Figure 2**), there are measurable differences between the ^{14}C ages of the upper stratum around 200 cm, which are 3050 ± 30 a BP (72–74 cm) and 4520 ± 30 a BP (172–174 cm), and the lower stratum. Meanwhile, the mean grain size of the upper deposits remains at around 6 μm, and the carbonate content is stable at approximately 10% (**Figure 2**), indicating that the sedimentary environment and the sedimentary rate are relatively consistent. Consequently, the linearly extrapolated ^{14}C age of surface sediments was 1920 a BP, which can also be considered as the LCRE of Tengger Nuur. The Daqingshan Mts, which serve as the water source to Tengger Nuur, also supply water to Diaojiao Lake as the main source. The ^{14}C ages of Diaojiao Lake were estimated at 2380 ± 90 a BP (Song et al., 1996) and 2170 ± 70 a BP (Yang et al., 1997) from shallow lacustrine sediments at 3–5 cm. That of Hulun Lake was 685 ± 21 a BP from sediment at 0–1 cm (Wen et al., 2010).

To produce an age-depth model for TGN-05, we first subtracted the reservoir age of 1920 year from all the original ^{14}C ages, assuming that it is constant throughout the stratum, and then performed calibrations on the reservoir-effect-free ^{14}C dates. The conventional ages were converted to calibrated ages using the OxCal 4.2 and IntCal13 calibration curves (Reimer et al., 2013). An age-depth model was then created with the linear relation and sedimentation rate. The sedimentation rate between 400 and 460 cm was about 0.14 cm/a. Because the sediments consist of coarse sand and fine gravel below 550 cm, which is the same as the 400–460 cm interval, we assumed the sedimentation rate of 0.14 cm/a and extrapolated the ^{14}C age-depth model below 550 cm (**Figure 2**). The sedimentation rate in the offshore lake of the Bojianghaizi Lake near the Tennger Nuur is about 1.62 and 0.92 mm/a to the center (Zhai et al., 2000).

MATERIALS AND METHODS

Paleoenvironmental proxies, TOC-content, C/N, carbonate-content, carbon and oxygen isotope, element, and grain size were analyzed for sediment samples from TGN-05.

Total organic carbon was determined using the anti-titration method, which uses concentrated sulfuric acid (H_2SO_4) and potassium dichromate ($K_2Cr_2O_7$), with an error of less than ±0.5%. Both carbonate and TOC content were determined in the environmental lab of the School of Resources and Environmental Sciences, Lanzhou University. The content of carbon (C), nitrogen (N) in the organic matter were determined by a Vario EL III Elemental Analyzer (at the Chemistry Department of Lanzhou University) after the samples were treated with 1 N HCl.

A common method to analyze carbonate content in soils is the so-called "Scheibler method," in which samples are treated with hydrochloric acid and the released CO_2 is volumetrically determined, and the volume of CO_2 is then converted into carbonate concentration (%) (Tatzber et al., 2007). Error is less than ±1%.

For carbonate stable isotopic analyses, all the organic matter were removed by roasting the finer portion (<200 μm) of the samples at about 300°C in a vacuum system before analysis. For carbon and oxygen isotopic composition analyses, 100% phosphoric acid at 90°C was added to the pre-treated samples, and then the acid-produced CO_2 gas was purified and transferred into a Finnigan 253 mass spectrometer. The analyses were conducted at the Lanzhou Institute of Geology (Chinese Academy of Sciences) and the isotopic values are reported as the standard δ-per mil notation in V-PDB standard calibrated with NBS-19 ($\delta^{18}O = -2.20‰$, $\delta^{13}C = +1.95‰$). The sample error is less than 0.3‰.

Metal elements of the bulk lake sediments were determined by the XRF method (PW2403 X, Netherlands) in the Key Laboratory of Western China's Environmental System (Ministry of Education), Lanzhou University. Then the paleoclimatic indicator Sr/Ca and Mg/Ca ratios (Chivas et al., 1985, 1986; Zhang et al., 2013), a widely used proxy for lake temperature and salinity, were calculated to infer relative environmental change.

The grain sizes of bulk samples were measured using a Malvern Mastersizer 2000 laser granulometer, which was fitted to the limit of grain sizes lower than 2000 μm, and the traditional manual sieve method to determine the weight percentages of three parts, <63–900 μm, and 900–20,000 μm as the fixed hole sizes of sieves 63, 900, and 20,000 μm. After sieving off particles larger than 900 μm, the samples were used for laser granulometer analysis using the following method: (1) adding H_2O_2 to remove organic matter and soluble salts, (2) using diluted 1N HCl to remove carbonate, and (3) using Na-hexametaphosphate as the dispersing agent to disperse the aggregates. The final results include three part percent concentration, that is <4 μm standing for mud, 4–63 μm for silt, and 63–900 μm for sand, and each part was calibrated with the total weight.

RESULTS AND DISCUSSION

Proxies

Grain Size

The grain size of Tengger Nuur sediments (TGN-05) showed obvious changes since the last deglaciation from sand and fine gravel layers in the low part (400–794) (**Figure 3**) to fine silty mud layer (0–400 cm) in the upper part, punctuated by several coarse particle layers (**Figure 4**). Gravels are based on quartz grains with high roundness and poor sorting, reflecting off-nearshore shoreline shallow lake deposition.

Generally, hydrodynamic force controls the distribution of the lake sediment particles. Under ideal condition, gravel and silt to clay size sediments deposit from the shoreline to the center of lake following hydrodynamic weakness. Xiao et al. (2013) and Fan et al. (2016) analyzed the grain size distribution of the modern sediments from Daihai Lake and Dali Lake, respectively, which site near the Tengger Nuur. The results showed that particles

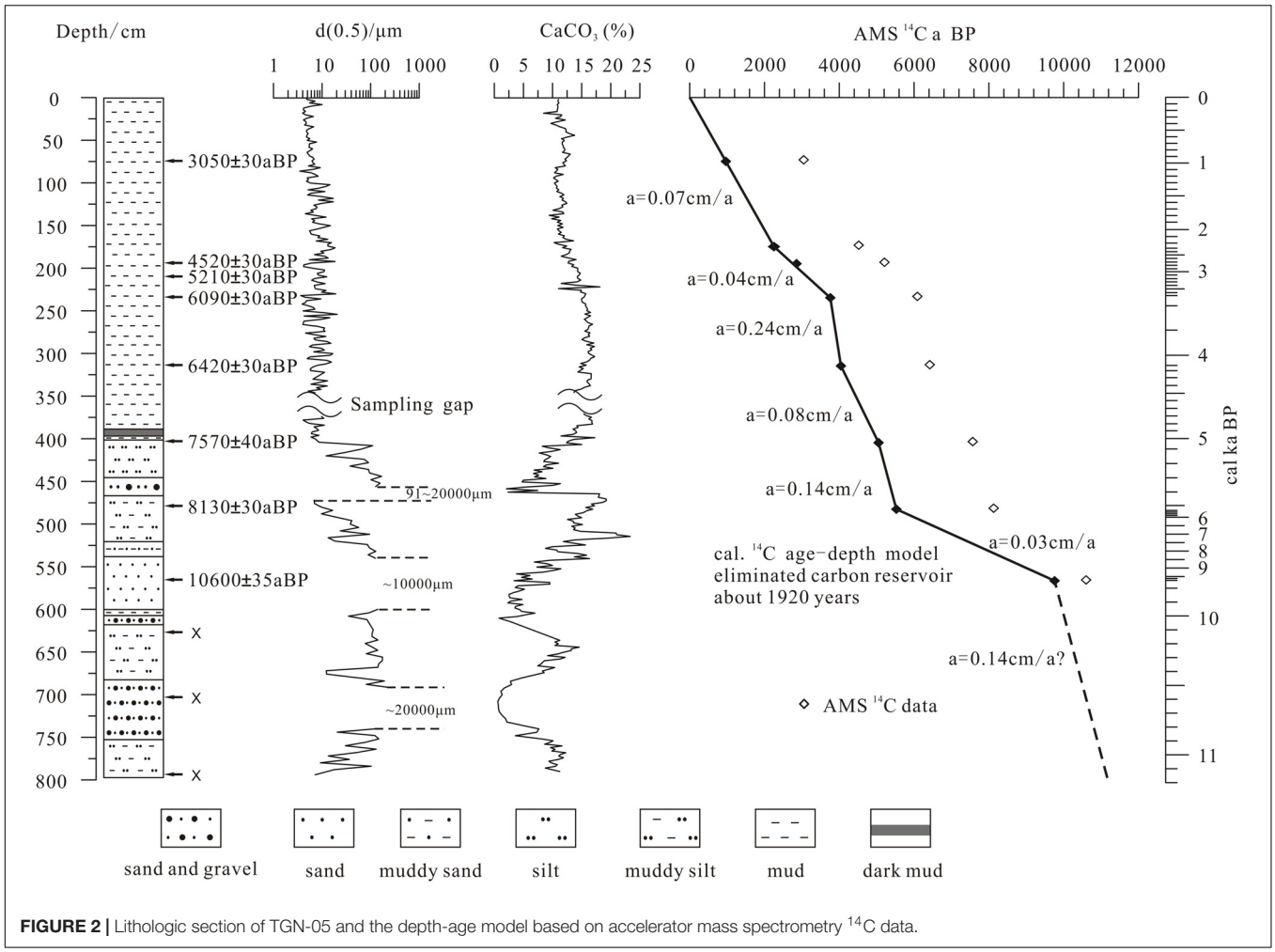

FIGURE 2 | Lithologic section of TGN-05 and the depth-age model based on accelerator mass spectrometry ^{14}C data.

of sediments declined gradually from shoreline to the center of lake, and five distinct belts are nearshore suspension fine sand, saltation medium sand, offshore suspension fine silt, medium to coarse silt, and long term suspension clay. The percentage of the nearshore components displays a negative correlation with water depth across the modern lakebed. And, that of the nearshore component increases in the annual precipitation decreasing based on the field observation. Guo et al. (2016) analyzed the modern surface sediments from 68 lakes and reservoirs in the Inner Mongolia Autonomous Region, Gansu Province and Ningxia Hui Autonomous Region, they found that the sediments near lake center mainly contain clay (0.4–1.9 μm), clay-to-fine silt (2.0–12.0 μm) and medium-to-coarse silt (17–58 μm). The sediments in the transitional area (shallow lake) mainly include medium-to-coarse silt (17–58 μm) and fine sand (70–150 μm). The sediments near the shoreline mainly contain medium-to-coarse sands (170–500 μm). The grain sizes of sediments near the regions of river filling are more than 600 μm.

Numerous modern process researches testify that the lake-level decreases with coarse grain sediments increasing, and that deposits under the dry and cold condition. Chen et al. (2003) regarded that coarse sediments were deposited during a shrinkage phase of Lake Yanhaizi in Mongolia under an arid environment, whereas fine sediments were deposited during a period of high lake-level in a humid environment. The lake-level of Qinghai Lake was low and particle was focused on coarse size, and the percents of medium and grain size more than 64 μm were high all during Younger Dryas (YD) event (Liu et al., 2003).

However, aeolian activity can impact the lake near the desert and grain size of sediment loads change with it. For example, a strong storm event can blow coarse particles near the shoreline of lakes into the center of lakes. Fan et al. (2016) analyzed the particles on the surface ice of Dali Lake in the winter, and found that mode grain size of particles is main 17.4 μm or so, and has a small coarse part of mode size 400 μm. Aeolian particles fixed in the sediments of shallow lakes under the cold and dry climate background, but it is difficult to distinct them from the lake sediments in the Tengger Nuur.

Organic Matter

Organic matter as an important fraction of lake sediments originates mainly from the complex mixture non-vascular plants that contain little or no carbon-rich cellulose and lignin, such as phytoplankton, and vascular plants that contain large

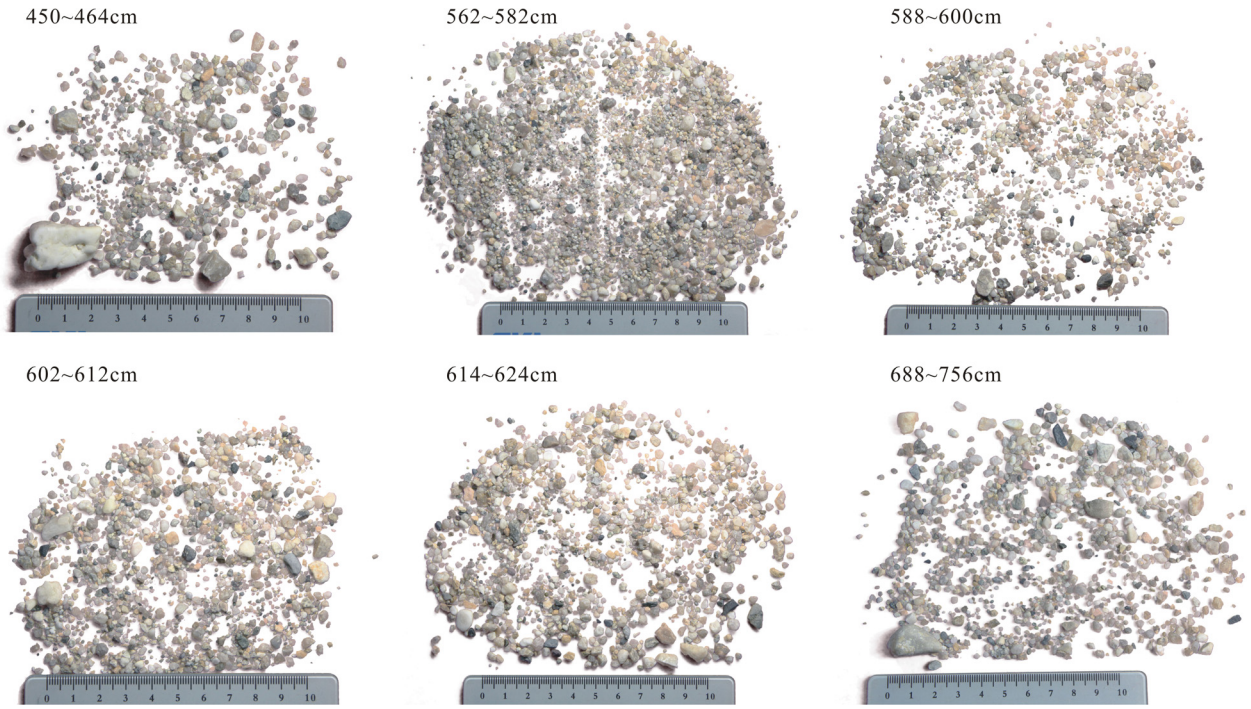

FIGURE 3 | Gravels in the Tengger Nuur lake sediments at depth of 450–756 cm, removed particle parts less than 63 μm size.

proportions of these fibrous tissues, such as grasses, shrubs, and trees. So, it can be an effective proxy to interpret the lacustrine paleoenvironments, histories of climate change, and the effects of humans on local and regional ecosystems around the catchments (Meyers and Vergés, 1999). Higher TOC indicates a warm and humid environment, whereas lower TOC indicates a cold and dry environment. The limiting factor of plant growth is effective humidity in semi- and arid areas. Changes in the lake water level have also impacted the organic matter content, and it is low in the shallow water, and the C/N ratios can indicate the type of organic matter delivered to the lake sediments (Meyers and Vergés, 1999; Müller and Ulrike, 1999). Normally, algae typically have atomic C/N ratios between 4 and 10, lacustrine sedimentary C/N ratios of between 10 and 20 represent a mixture of aquatic and higher plant material, whereas C/N ratios >20 indicate higher plant dominance (Meyers, 1994). Plankton has average C/N ratios of ∼6, withmost diatoms varying between 5 and 8 (Lerman, 1979).

As shown in **Figure 5**, TOC was relatively low (0.1–0.2%) in TGN-05 before 8750 cal a BP (794–540 cm); it was slightly higher at 0.3–0.8% during 8750–2750 cal a BP (540∼200 cm). Since 2750 cal a BP, TOC increased in the range of 0.8–2.2% and reached the maximum value of 2.5–5% under the influence of the marsh environment and human activity.

The C/N ratios of Tengger Nuur sediments are at 3–11 and the preponderant value is at 5–6 since the last deglaciation in **Figure 5**. The ratio is a little higher to 8–11 after about 2000 cal a BP. That inferred the organic matter came from the algae and aquatic plants, but some land higher plants maybe mixed since 2000 cal a BP.

Carbonate

Lacustrine carbonates form mainly in warm and alkaline water bodies. According to the study of lakes in western China, calcite forms in most shallow freshwater environments with low percentages in sediments, and low-Mg calcite and high-Mg calcite to aragonite form with increasing lake depth and salinity (Zhang et al., 2013).

The carbonate content can be divided into several stages, as shown in **Figure 5**. Carbonate contents were low (1–4%) in the 3 layers formed during 10,920–10,450 cal a BP, 10,050–8750 cal a BP, and 5450–5100 cal a BP with coarse sand to fine gravel. Most of the carbonate was authigenic, forming in western Chinese lakes with fine size, and coarse quartz and feldspar particles in the sediments can dilute the values of carbonate-content such that the determined values become lower than the true values (Zhang et al., 2013). The low content of carbonates during ∼10,920 cal a BP and 10,450–10,050 cal a BP suggests shallow freshwater lake and low-temperature conditions. The high carbonate content (13–8%) during 8750–2750 cal a BP indicates a relatively warm and saline water. Since 2750 cal a BP, carbonate content has been decreasing gradually from 14 to 10% or so, indicating decreases in temperature lowering and salinity.

$\delta^{13}C$ and $\delta^{18}O$ of Carbonate Bulk Sediments

$\delta^{13}C$ and $\delta^{18}O$ values are shown in the **Figure 5**. Lake water chemical conditions and sources can be well traced using carbon and oxygen isotopic signatures ($\delta^{13}C$ and $\delta^{18}O$) in lacustrine carbonates. They are controlled by many factors, among which the salinity and temperature of lake water are

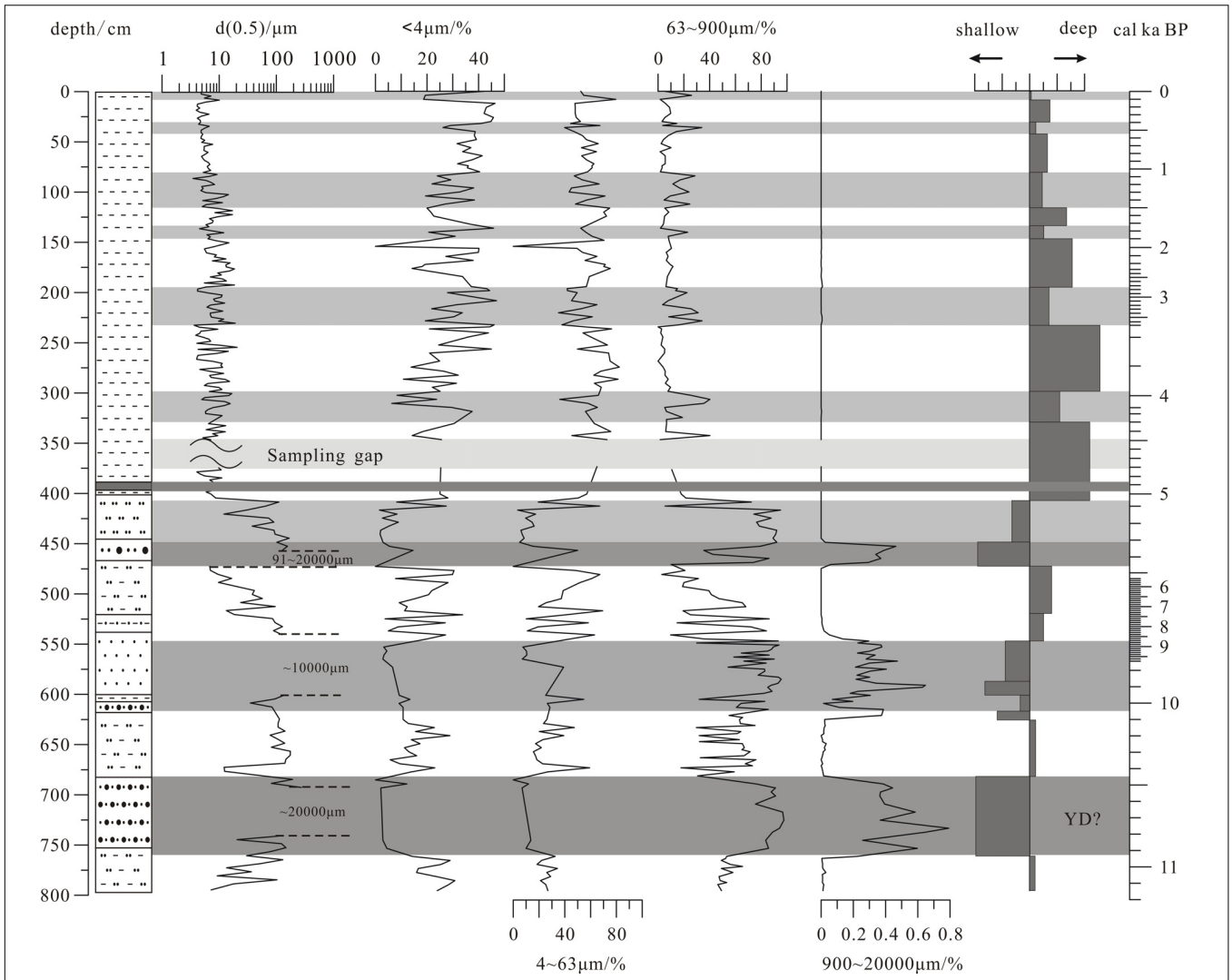

FIGURE 4 | Grain size changes in TGN-05 sediments since the last deglaciation.

the leading ones. The controlling factors on $\delta^{13}C$ variations in lake sediments are inflow $\delta^{13}C$ value, biological productivity, respiration within the lake, exchange of CO_2 between the lake and atmosphere, groundwater input, residence time, and changes in the vegetation cover of watersheds (Li and Ku, 1997). Among these, the residence time and biogeochemical features of the lake water are generally considered the most important factors affecting $\delta^{13}C$ (Leng and Marshall, 2004). The oxygen isotope compositions of water in lakes ($\delta^{18}O_{water}$) are dominantly controlled by the local evaporation/precipitation (both rain and snowfall), inflow water (both river and groundwater), and lake water temperature (Talbot, 1990; Menking et al., 1997). The oxygen isotopic composition of the water in a closed lake basin is largely dependent on the ratio of evaporation over precipitation in arid to semi-arid areas. The covariance between $\delta^{13}C$ and $\delta^{18}O$ can well describe the closed conditions of lakes (Talbot, 1990). Normally, $\delta^{13}C$ and $\delta^{18}O$ will be synchronously increase with water residence time in lakes (Leng and Marshall, 2004). However, it is also well documented that the two may change asynchronously when extreme temperature or evaporation/precipitation control the isotopic fractionation processes; that is, temperature and evaporation/precipitation have much stronger control over $\delta^{18}O$ fractionation than over $\delta^{13}C$ fractionation (Wu and Wang, 1997).

Ratio of Mg/Ca in Bulk Sediments

Ratio of the Mg/Ca in bulk sediments is shown in **Figure 5**. In closed and semi-closed lakes, authi-chemogenic carbonate minerals are formed widely. In general, biogenic and chemogenic carbonates from calcite to low-magnesium calcite, high-magnesium calcite, and aragonite form with increasing Mg/Ca ratio in water (Müller et al., 1972). Mg/Ca has a positive relationship with salinity and can indicate the characteristic of residence time due to the evaporation effect in the closed to semi-closed lakes in northwestern China (Zhang et al., 2013). However, the higher the lake waterbody temperature is, the higher the

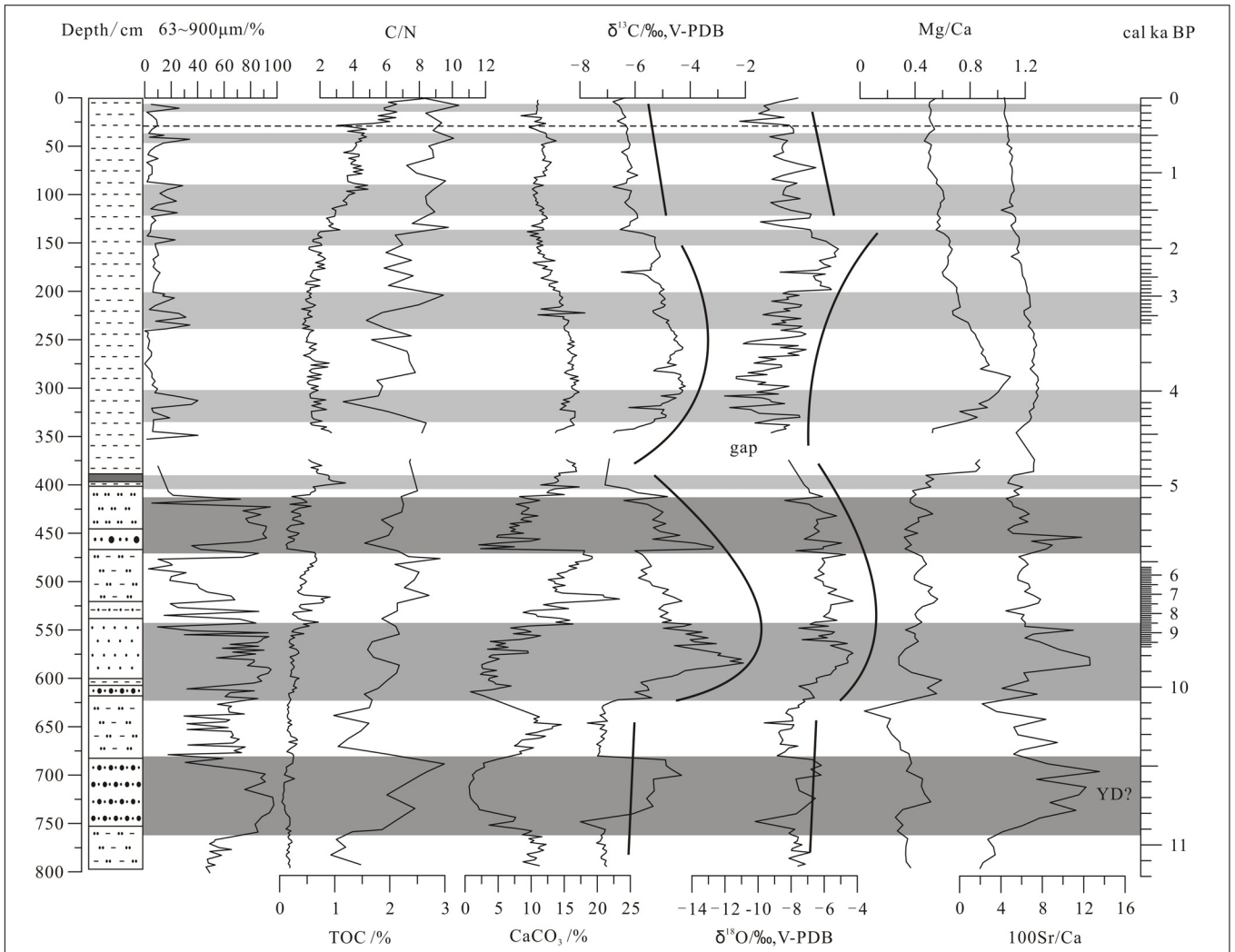

FIGURE 5 | Changes in geochemical proxies in TGN-05 since the last deglaciation. The ratio of Sr/Ca amplifies 100 times to fit for the figure show.

evaporation is, that leading to higher salinity in closed-lakes. The dominating carbonate mineral in Las Coladas Lake in the south of the San Francisco Basin, Argentina, is aragonite because of the high Mg/Ca ratio of the lake water (Valero-Garces et al., 1995). So, Mg/Ca and Sr/Ca ratio have a positive relationship in lake sediments, indicating residence time and evaporation effect.

Paleoenvironment

The characteristics of TGN-05 sediment particles can be inferred from the lake-level oscillation history of Tengger Nuur since the last deglaciation. Coarse sediments indicate a shallow lake, and fine sediments indicate a stable lake. The results of the grain size analysis of TGN-05 showed that the lake was shallow in the periods of 10,920–8750 cal a BP and 5450–5100 cal a BP, deep and relatively stable during 8750–5450 cal a BP and 5100 cal a BP to present. The chemical characteristics of water differed during different periods owing to the different climate setting (**Figure 5**).

About >757 cm (∼10,920 cal a BP), fine-grained sediment layer, low Mg/Ca and Sr/Ca ratios indicate a shallow lake with freshwater formed under a cool climate and much higher water supply than evaporation and rudimentary vegetation.

About 757–685 cm (10,920–10,450 cal a BP), coarse sand and fine gravel sediment layer, heavy $\delta^{13}C$ and $\delta^{18}O$, high Mg/Ca and higher Sr/Ca ratios represent a shoreline lake with very shallow shoreline brackish-water lake under cold climate and long residence time. This corresponds to the global cold YD event (Hughen et al., 1985; Mikolajewicz et al., 1997), which happened during the Last Glacial Termination recorded the onset of YD was dated to 10,800–10,600 ^{14}C years BP and that the end was dated to 10,000–10,050 ^{14}C years BP (Ammann and Lotter, 1989; Björck et al., 2003; Muscheler et al., 2008). It was at 11–10 ka BP cooling of Europe and eastern North America (Mathewes, 1993). After calibrating based on the tree-ring chronology, YD was a millennial-scale cold period between approximately 12,900 and 11,500 year BP (Muscheler et al., 2008). The beginning of the YD event recorded at stalagmite of Yamen Cave was nominally at 12,850 ± 50 a BP and the end of the YD dates to 11,500 ± 40 a BP (Yang et al., 2010). And YD event

recorded at Hulu Cave from 12,823 ± 60 a BP to 11,473 ± 100 a BP (Wang et al., 2001). However, the YD event recorded in Qinghai Lake was 11.3–10.8 cal ka BP calibrated by the tree-ring (Shen et al., 2005). The Younger Dryas cooling event recorded in the Tibet lakes occuring in 11,000-10,000 a BP, and coldest period was at 10.5–10.7 ka BP (Shen et al., 1996). Cooling wet-type YD event was at 10.80–10.50 ka BP recorded at Inner Mongolian salt lakes (Chen et al., 1996). The duration of the YD is 300 years as recorded at the salt lakes of Inner Mongolian (Chen et al., 1996) to 1350 years at the stalagmites from Hulu Cave and Yamen Cave (Wang et al., 2001; Yang et al., 2010). But till to now, the timing and length of the Younger Dryas remain controversial.

The cold and extremely low lake-level records in Tengger Nuur also had been found in the other lakes around this area. It was a cold desert during 10,950–10,300 a BP, as recorded in Daojiaohaizi sediments; the temperature was 5°C lower and precipitation was 100 mm lower than those today (Yang et al., 1997). The level of Daihai Lake ascended during 13–11 ka BP and declined sharply from 11 to 10 ka BP (Sun et al., 2009). The lake-level of Jalai Nur fell rapidly at the YD event during 10.9–10.6 ka BP, the flaser and lenticular bedding coarse sediment sets suggested the near shore environments (Wang et al., 1994). The aeolian sand layer correlated with the cold and dry YD event at 11.6-11.3 cal ka BP in the Haolaihure Paleolake (Liu et al., 2018). Grain size at 16-64μm in the Qinghai Lake sediments increased obviously during YD event at 11,000–10,400 a BP (Liu et al., 2003). Low lake-level and prevailing aeolian sediment deposition at Gun Nuur under dry conditions were recorded during the earliest Holocene (>10,800–10,300 cal a BP) (Zhang et al., 2012). The ^{14}C age was unequivocal and uncertainty, but we correlated this gravel layer (757–685 cm) to the YD event (10,920–10,450 cal a BP) in Tengger Nuur.

About 685–620 cm (10,450–10,050 cal a BP), sandy silt sediment, light $\delta^{13}C$ and $\delta^{18}O$, low Mg/Ca and Sr/Ca ratios indicate gradual increase in lake area to a shallow lake under a low-temperature freshwater environment with evaporation less than water supply.

About 620–540 cm (10,050–8750 cal a BP), silty sand and fine gravel sediment, heavy $\delta^{13}C$ and $\delta^{18}O$, and high Mg/Ca and Sr/Ca ratios reflect lake-levels dropped, fluctuating between a shoreline and shallow lake due to a high ratio of evaporation/filling water under increasing temperature. According to the paleoenvironment recorded from Tengger Nuur lake sediments, the Holocene started from 10,050 cal a BP and with the characteristics of temperature increase. However, Tengger Nuur was very shallow with slightly high salinity and high evaporation during 10,050–8750 cal a BP. Several paleoenvironmental records around Tengger Nuur suggest this phenomenon. Hulun Lake was shallow and sand blowing activity strengthened in the early Holocene (10,000–7200 a BP) under cold-dry to warm-dry climate conditions (Zhang and Wang, 2000). According to diatom data, Hulun Lake shrank gradually (Yang et al., 1995). Huangqihai experienced transgressions under a cold and wet climate in the early Holocene (11,000–8000 a BP), and Daihai also had a low level during 12,000–8000 a BP (Li et al., 1992). At the same time, Li et al. (1992) considered Daihai to be brackish water or have slightly high salinity based on ostracod components. They also considered lake level to have dropped to form a river environment under a cold and dry climate during 9000–8000 a BP, and lake level retreated again under a warm climate condition after 8000 a BP. In contrast, Sun et al. (2009) suggested that the lake level of Daihai expanded temporarily as effective precipitation increased under the summer monsoon-related humid climate during ca. 10–9 ka BP.

About 540–469 cm (8750–5450 cal a BP), sandy silt sediment, light $\delta^{13}C$ and $\delta^{18}O$, high Mg/Ca and Sr/Ca ratios indicate a gradually increase in lake area to a shallow lake under relatively warm water and evaporation slightly higher than water supply. The temperature increased and vegetable was abundant. However, a low lake-level event interrupted with a cold-wet climate during 5450–5100 cal a BP. Around this area, Lake Baahar Nuur was under a warm and humid climate between ∼7.65 and ∼5.40 ka BP (Guo et al., 2007). Temperature and humidity increased synchronously in the course of 8200–6350 a BP, and then, the climate oscillated from wet to dry from 6350 to 5100 a BP (Song et al., 1996).

The Holocene climatic optimum in the Huangqihai region can be placed between 8000 and 6000 a BP when the temperature was much more than 2–3°C, precipitation was high, and the lake level was also high (Li et al., 1992). Angulinao was deep during 8400–5500 a BP, warming during 8.4–7.3 ka BP, stable during 7.3–6.2 ka BP, and fluctuating during 5.5–5.0 ka BP (Zhai et al., 2000). Effective humidity in the Dali Nor region reached the maximum prior to ∼8000 years BP (Wang et al., 2004). Paleosol thickness reached the maximum in the Mu Us desert during 7000–5500 a BP; and it was in the extreme state in the Ordos Plateau during 6500–5500 a BP (Yang et al., 1997).

About 469–401 cm (5450–5100 cal a BP), coarse sediment layer, heavy $\delta^{13}C$ and light $\delta^{18}O$, and low Mg/Ca and Sr/Ca ratios indicate a rapid lake-level decline to form a shoreline lake, and interrupted by a shallow lake during 5300–5100 cal a BP under a low temperature and evaporation environment.

About 401–0 cm (5100 cal a BP ∼AD 1985), silty mud or muddy silt sediments, heavy $\delta^{13}C$ and $\delta^{18}O$, high Mg/Ca and Sr/Ca ratios indicate a relatively stable deep lake at the interval 5100–1800 cal a BP. After 1900 cal a BP, lighter $\delta^{13}C$ and $\delta^{18}O$, low Mg/Ca and Sr/Ca ratios indicate a freshwater environment under low evaporation with relatively higher effective humidity. Tengger Nuur was completely desiccated in 1985 as history recorded due to a gradual decrease in water supply. It was punctuated by several centennial- to millennial-scale shallow lake events, 330–300 cm (4300–3980 cal a BP), 240–200 cm (3700–2750 cal a BP), 150–140 cm (1900–1800 cal a BP), 120–85 cm (1500–1050 cal a BP), 40–30 cm (550–400 cal a BP), 10–0 cm (100 cal a BP ∼AD 1985). A layer of dark mud in the 389–398 cm interval (4960–4850 cal a BP) suggests a short–stage tidal flat environment as the lake-level started to increase.

Tengger Nuur expanded quickly to reach a high lake level during 5000–2000 cal a BP, under the condition of effective humidity increasing with decreasing temperature in oscillation. This implies that humidity and temperature fluctuated in the opposite directions. Gun Nuur was deep in the mid-Holocene (7000–2500 cal a BP), but three periods of low lake levels and

significantly drier conditions were recorded between 7000–5700, 4100–3600, and 3000–2500 cal a BP (Zhang et al., 2012).

Tengger Nuur shrank gradually and became completely desiccated under a cool climate from 2000 cal a BP to 1985 AD, and the period of 1050–550 cal a BP corresponds to the Medieval Warm Period (MWP). Four periods of low lake levels were recorded during 1900–1800 cal a BP, 1500–1050 cal a BP, 550–400 cal a BP (Little Ice Age), and 100 cal a BP–AD 1985. Owing to the retention of a very shallow lake level over a long time, a marsh environment formed around Lake Tengger Nuur and various aquatic plants such as reeds increased TOC of the sediments. The paleoenvironment of most regions in Inner Mongolia indicate a dry climate and gradual shrinking of lakes. For instance, Baahar Nuur Lake was under a dry climate characterized by complete desiccation of the lake after 3700 a BP (Guo et al., 2007). According to paleoenvironmental records of Haolaihure, the regional environment deteriorated after 2.2 cal ka BP as the climate shifted to generally cooler and drier conditions, with a brief return to a warm and wet climate during the MWP (AD 800–1100) (Liu et al., 2018). Daihai and Huangqihai shrank sharply and several periods of retreat have been oscillating since 3000 a BP (Li et al., 1992).

Paleoclimate

The northern region of the East-Asian monsoon transition zone, where Daqingshan is a boundary in the mid-eastern part of Inner Mongolia, is controlled by the westerly and Siberian-Mongolian high winter monsoon winds (WSMHM), and the southern region is controlled by the Eastern Asian Summer monsoon (EASM; **Figure 1**; Winkler and Wang, 1993). Paleoenvironmental records show that the climate was dry and cold and precipitation was less during the last deglaciation than that today in the WSMHM area of Gun Nuur (Zhang et al., 2012), Daojiaohaizi Lake (Yang et al., 1997), Haolaihure (Liu et al., 2018), feet of the Daqingshan (Cui and Song, 1992), and Baahar Nuur (Guo et al., 2007). The Qingtu paleolake westward of the Tengger Sandy Desert was an aeolian non-lake environment (Zhao et al., 2008). Influenced by EASM Daihai Lake had a low lake-level under the dry and cold climate (Sun et al., 2009). Kutzbach and Street-Perrott (1985) suggested that solar radiation culminated at 11–10 a BP since 18 ka BP in the Northern Hemisphere. Paleoenvironmental records of Tengger Nuur and other lakes testified that the summer monsoon did not strengthen to pass the modern monsoon boundary of Inner Mongolia. However, India's summer monsoon strengthened since 14–12 ka BP in the India monsoon dominated region of the Tibetan Plateau. Temperature and humidity increased greatly after interrupted by the short YD cold climate event. It became dry after 5 ka BP (He et al., 2004). Selin Co was a deep closed lake that formed stably for a long period with abundant vegetation under a warm and humid climate background from 15.5 to 10.4 cal ka BP (Zhang C. J. et al., 2018). The temperature and humidity increased quickly and lake-levels of Ximenco in eastern Tibetan Plateau (Zhang et al., 2009), Lake Naleng Co (Opitz et al., 2015), Koucha Lake (Mischke et al., 2008), and Luanhaizi in the Qilian Mountain (Mischke et al., 2005), etc., expanded since about 13,000 cal a BP in the interplay of EASM and the Indian monsoon.

Temperature and humidity increased and lakes expanded gradually with the strengthening of solar radiation since the early Holocene according to records, such as in Greenland Ice cores (Greenland Ice-core Project (GRIP) Members, 1993), stalagmites of Dongge cave in the EASM-dominated region (Dykoski et al., 2005), loess sequences (Zhou et al., 2014), and Qinghai Lake (Liu et al., 2007). However, the humidity (Chen et al., 2019) and lake-level oscillation (Guo et al., 2014) in the Arid Central Asia (ACA) the westerly dominated region, Indian Summer Monsoon (ISM)-dominated region, and Eastern Asian Summer Monsoon (EASM)-dominated region had different spatio-temporal characteristics (**Figure 6**). The lake surface area of Daihai Lake in the southern part of Daqingshan in the modern Eastern Asian monsoon boundary expanded temporarily according to the amelioration of monsoon-related effective precipitation and a relatively humid climate during 10–9.0 ka BP (Sun et al., 2009; Wen et al., 2010). The wettest climate occurred between 10,500 and 6500 cal a BP, during which annual precipitation was up to 30–60% higher than today recorded by Bayanchagan Lake sediments (Jiang et al., 2006). At the same time, in this study, Tengger Nuur in the northern part of Daqingshan was found to have a low lake level during 10,050–8750 cal a BP. Hulun Lake was also had a low lake level and strong aeolian activity under a warm-dry climate in the early Holocene during 10,000–7200 a BP (Yang et al., 1995; Zhang and Wang, 2000; Wen et al., 2010). Haolaihure was under a cool and dry period from 12.2 to 8.7 cal ka BP (Liu et al., 2018). Baahar Nuur Lake (Guo et al., 2007) and Qingtu Lake in the Tengger Sandy Desert (Zhao et al., 2008) had not formed in the early Holocene. Sediments at the feet of Daqingshan recorded a cold climate (Cui and Song, 1992). It was obvious that lake that did not form or low-lake-level sediments were derived from the northern part of the modern summer monsoon boundary and the climate was cold in the early Holocene. Nevertheless, lakes expanded and achieved high levels under a relatively warm-wet climate in the southern part of the modern summer monsoon boundary.

An atmospheric general-circulation model simulated a maximum summer solar radiation (7% more than the present value) at interval 11,000–10,000 cal a BP, during which precipitation increased in the Northern Hemisphere, such that lake-levels increased across parts of Africa, Arabia, and India between 10,000 and 5000 a BP (Kutzbach, 1981; Kutzbach and Street-Perrott, 1985). Summer monsoon strengthening was followed by high solar irradiation in the early Holocene, especially in correlation with the lake-level rise in China (Bond et al., 2001). Various paleoclimatic records show that a wetter condition prevailed during the early Holocene since ∼10,000 a BP in China (An, 2000; Chen et al., 2003). However, the low lake-level record in Tengger Nuur showed that the summer monsoon was not sufficiently strong to reach northward of the monsoon boundary, and thus, precipitation was low. A little warm paleoclimate based on pollen and diatom data indicates that solar radiation led to temperature increases in this area in the early Holocene (Chen et al., 2003; Liu et al., 2018).

According to our paleoenvironmental record of Gun Nuur in Mongolia, the lake expanded in the early Holocene (ca. 10.3 cal ka BP), but the significant moisture was probably not

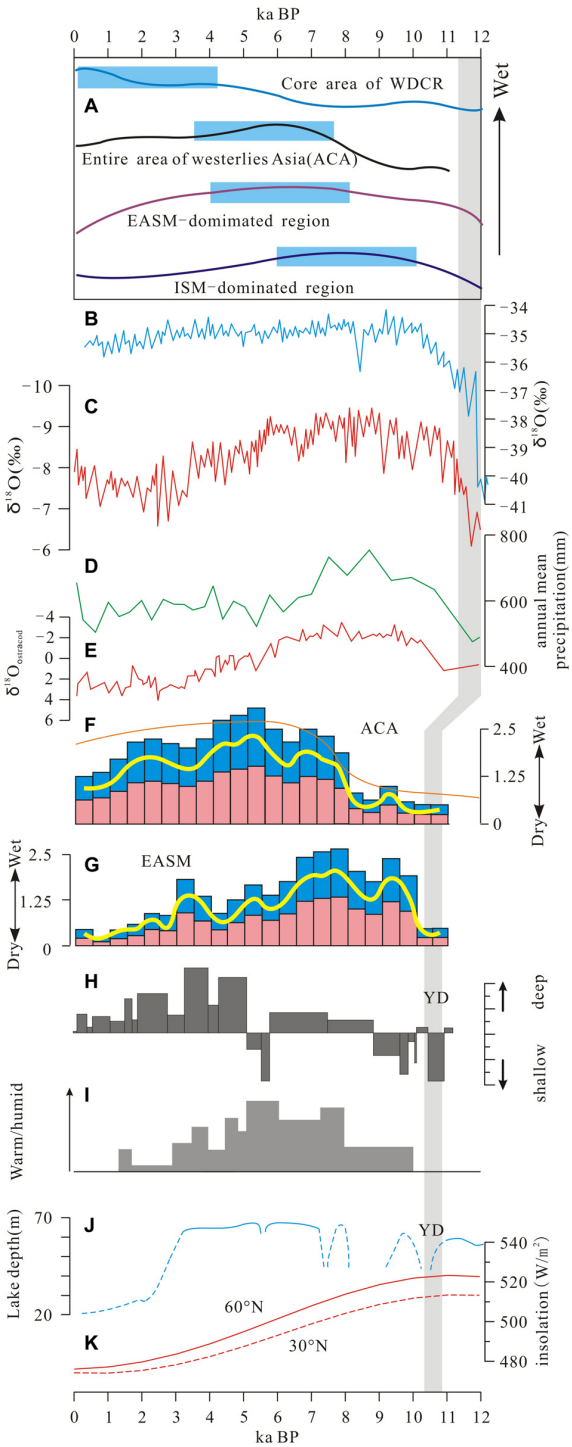

FIGURE 6 | Paleoenvironmental records in different climate regions. **(A)** westerlies-dominated climatic regime (WDCR), ACA, Eastern Asian Summer Monsoon (EASM), and Indian Summer Monsoon (ISM) (Chen et al., 2019), **(B)** GRIP (Greenland Ice-core Project (GRIP) Members, 1993), **(C)** Dongge Cave (Dykoski et al., 2005), **(D)** Luochuan Loess (Zhou et al., 2014), **(E)** Qinghai Lake (Liu et al., 2007), **(F)** Central Asia (ACA) westerly dominated region (Guo et al., 2014), **(G)** Eastern Asian Summer Monsoon (EASM)-dominated region (Guo et al., 2014), **(H)** Tengger Nur (this paper), **(I)** Daihai (Xiao et al., 2004), **(J)** Daihai (Sun et al., 2009), **(K)** solar irradiation in the Northern Hemisphere.

related to the northward shift of the present summer monsoon boundary or the moisture delivery from the northern Atlantic through the westerlies. The water source was melting snow, ice and frozen ground or the generation of precipitation from the local recycling of moisture (Zhang et al., 2012). Therefore, solar radiation strengthened in the early Holocene to drive summer monsoon to the modern monsoon boundary in Inner Mongolia, but monsoon precipitation did not influence the northern area of Daqingshan, where the summer monsoon should occur. It is inferred that the summer monsoon was not sufficiently strong to pass the boundary in the early Holocene. Furthermore, this can be deduced that the Daqingshan (height of 2338 m asl at the highest peak) was not covered by ice-snow during the last glacial maximum, and thus, the temperature increase in the early Holocene could not thaw enough ice and snow to fill Tengger Nuur.

Yang and Wang (1996) considered that the westerlies prevailed in the Hulun Lake area at intervals 10.0–7.0 ka BP and 5.0–3.0 ka BP, and eastern monsoon winds reached the northwest region of the summer monsoon boundary at about 7.0–5.0 ka BP. This also shows that the eastern summer monsoon was weak in the early Holocene.

Tengger Nuur started to expand during 8750–5000 cal a BP with high evaporation and a brackish water environment and entered a stable deep state during 5000–2000 cal a BP, punctuated by several millennial- and centennial-scale low lake levels. As researched in the past, the summer monsoon strengthened from the early Holocene to mid-Holocene, the most humid conditions occurred at approximately 5500–2700 cal a BP (Xiao et al., 2002), or 8200–5700 cal a BP in southern Inner Mongolia (Zhou et al., 2001). The summer monsoon exceeded the modern monsoon boundary to the northward region to Mongolia. Abundant precipitation led to the expansion of almost all lakes in the Mongolia Plateau. For example, the boundary of the eastern monsoon winds reached the Hulun Lake region during about 7.0–5.0 ka BP (Yang and Wang, 1996); Angulinao was deep during 8400–5500 a BP and cooled down from 3.0 ka BP to present (Zhai et al., 2000) and aeolian activity strengthened (Zhang and Wang, 2000); Daihai and Huangqihai had high lake levels during 8500–3500 a BP and shrank gradually since 5000 a BP (Li et al., 1992), and grasses and birch forests expanded during 8000–6400 cal year BP, implying a remarkable increase in the monsoon precipitation (Wen et al., 2010). However, the Yanhaizi region was dry between 8.0 and 4.3 ka BP. Chen et al. (2003) regarded that enhanced evaporation over higher monsoon precipitation reduced the effective humidity in the warm climate.

Cold events during 5450–5100 and 4300–3980 cal a BP recorded in Tengger Nuur significantly impacted human activities in northwestern China. Denton and Karlen (1973) defined 5800–4900 a BP as the second neoglaciation and 3300–2400 a BP as the third neoglaciation in the Holocene. Human activity had greatly been set back in the farming-animal husbandry zigzag zone of northern China at this stage of late Yangshao Culture (5500–5000 a BP) (Yang and Suo, 1996). The cold event in northwestern China during 4300–3500 a BP also contributed to the advancement of the Qijia Culture (Zhang H. R. et al., 2018).

After 2000 cal a BP, the Tengger Nuur region was controlled by the westerly current (Chen et al., 2019). The lake shrank gradually with decreasing water supply under the cold and dry climate, and it was completely desiccated in 1985. Moreover, several centennial-scale lake-level oscillations occurred during this stage.

CONCLUSION

Paleoenvironmental records from Tengger Nuur sediments (TGN-05) showed that solar radiation strengthened to stimulate the strengthening of the eastern monsoon in the Northern Hemisphere since the last deglaciation. However, the eastern summer monsoon in the early Holocene was not sufficiently strong to influence the northern region of the modern monsoon boundary in the Inner Mongolian Plateau. Water from the thawing of ice and snow covering the Daqingshan mountains was not sufficient to fill Tengger Nuur and other lakes in this region. The summer monsoon passed to the northward and northwestward regions of the monsoon boundary during 8750–5000 cal a BP. Lakes expanded rapidly under the associated high monsoon precipitation, but lake levels oscillated in a shallow state owing to high evaporation under high temperatures during this period. The summer monsoon receded gradually during 5000–2000 cal a BP. Nevertheless, lakes entered a stable deep state under high effective humidity with decreasing temperature, punctuated by several centennial-scale low lake-level events. The westerlies influenced this region and the climate was cold and dry after 2000 cal a BP. Lakes changed gradually to become salinized or completely desiccated. The lake state and vegetation cover have a close relationship with effective humidity in the arid Mongolian Plateau.

DATA AVAILABILITY STATEMENT

All datasets presented in this study are included in the article/supplementary material.

AUTHOR CONTRIBUTIONS

ZC and ZW contributed to fieldwork and manuscript perparation. ZL, TY, LY, WX, ZZ, and SK contributed to laboratory work and helped perparing the experiments. All authors contributed to the article and approved the submitted version.

FUNDING

We are thankful to the National Natural Science Foundation of China for providing the fund (grant NSFC 41571177) and the Fundamental Research Funds for the Central Universities (grant 2022019zr46).

ACKNOWLEDGMENTS

We wish to thank LT, HL, and QS for their thorough reviews and many helpful comments.

REFERENCES

Ammann, B., and Lotter, A. F. (1989). Late-glacial radiocarbon- and palynostratigraphy on the Swiss Plateau. *Boreas* 1989, 109–126. doi: 10.1111/j.1502-3885.1989.tb00381.x

An, Z. S. (2000). The history and variability of the East Asian paleomonsoon climate. *Quat. Sci.Rev.* 19, 171–187. doi: 10.1016/s0277-3791(99)00060-8

Björck, S., Koc, N., and Skog, G. (2003). Consistently large marine reservoir ages in the Norwegian Sea during the Last Deglaciation. *Quat. Sci. Rev.* 22, 429–435. doi: 10.1016/s0277-3791(03)00002-7

Bond, G., Kromer, B., Beer, J., Muscheler, R., Evans, M. N., Showers, W., et al. (2001). Persistent solar influence on North Atlantic climate during the Holocene. *Science* 294, 2130–2136. doi: 10.1126/science.1065680

Chen, C. T. A., Lan, H. C., Lou, J. Y., and Chen, Y. C. (2003). The Dry holocene megathermal in inner Mongolia. *Palaeogeogr. Palaeoclimatol. Palaeoecol.* 193, 181–200. doi: 10.1016/s0031-0182(03)00225-6

Chen, F. H., Chen, J. H., Huang, W., Chen, S. Q., Huang, X. Z., Jin, L. Y., et al. (2019). Westerlies Asia and monsoonal Asia: spatiotemporal differences in climate change and possible mechanisms on decadal to sub-orbital timescales. *Earth Sci. Rev.* 192, 337–354. doi: 10.1016/j.earscirev.2019.03.005

Chen, H. F., Song, S. R., Lee, T. Q., Löwemark, L., Chi, Z. Q., Wang, Y., et al. (2010). A multiproxy lake record from Inner Mongolia displays a late Holocene teleconnection between Central Asian and North Atlantic climates. *Quat. Int.* 227, 170–182. doi: 10.1016/j.quaint.2010.03.005

Chen, Y. C., Wei, D. Y., Wang, J. J., Guan, S. Z., Qian, Z. H., Yang, Q. T., et al. (1996). Determination and recognization of Younger Dryas and its important significance in the salt lakes sediments of Inner Mongolian. *Geol. Chem. Miner.* 18, 163–169. (in Chinese).

Chivas, A. R., De Deckker, P., and Shelley, J. M. C. (1985). Strontium content of ostracods indicates lacustrine palaeosalinity. *Nature* 316, 251–253. doi: 10.1038/316251a0

Chivas, A. R., De Deckker, P., and Shelley, J. M. G. (1986). Magnesium and strontium in non-marine ostracod shells as indicators of palaeosalinity and palaeotemperature. *Hydrobiologia* 143, 135–142. doi: 10.1007/bf00026656

Cui, Z. J., and Song, C. Q. (1992). Holocene periglacial process es and environmental changes in Daqingshan Mountains, Mongolia, China. *Permafr. Periglac. Process.* 3, 55–62. (in Chinese), doi: 10.1002/ppp.3430030108

Denton, G. H., and Karlen, W. (1973). Holocene climatic variations- their pattern and possible cause. *Quat. Res.* 3, 155–205. doi: 10.1016/0033-5894(73)90040-9

Dykoski, C. A., Edwards, R. L., Cheng, H., Yuan, D. X., Cai, Y. J., Zhang, M. L., et al. (2005). A high-resolution, absolute-dated Holocene and deglacial Asian monsoon record from Dongge Cave, China. *Earth Planet. Sci. Lett.* 233, 71–86. doi: 10.1016/j.epsl.2005.01.036

Fan, J. W., Xiao, J. L., Wen, R. L., Zhai, D. Y., Zhang, S. R., and Qin, X. G. (2016). A model for the linkage between grain size component in the Dali lake sediments and lake level status. *Quat. Sci.* 36, 612–622. (in Chinese), doi: 10.11928/j.issn.1001-7410.2016.03.11

Greenland Ice-core Project (GRIP) Members (1993). Climate instability during the last interglacial period recorded in the GRIP ice core. *Nature* 364, 203–207. doi: 10.1038/364203a0

Guo, C., Ma, Y. Z., Hu, C. L., Wu, Y. Q., and Lu, R. J. (2014). Holocene humidity changes in inland China inferred from lake sediments. *Prog. Geogr.* 33, 786–798. (in Chinese), doi: 10.11820/dlkxjz.2014.06.007

Guo, L. L., Feng, Z. D., Li, X. Q., Liu, L. Y., and Wang, L. X. (2007). Holocene climatic and environmental changes recorded in Baahar Nuur Lake core in

the Ordos Plateau, Inner Mongolia of China. *Chin. Sci. Bull.* 52, 959–966. doi: 10.1007/s11434-007-0132-1

Guo, X. G., Wang, W., Wang, G. L., Liu, L. N., Ma, Y. Z., and He, J. (2016). Within-lake distributions of grain-size components and environmental implications based on the survey of lake surface sediment of Chinese monsoon marginal area. *Geogr. Res.* 35, 677–691. (in Chinese), doi: 10.11821/dlyj201604007

He, Y., Theakstone, W. H., Zhang, Z. L., Zhang, D., Yao, T. D., Chen, T., et al. (2004). Asynchronous holocene climatic change across China. *Quat. Res.* 61, 52–63. doi: 10.1016/j.yqres.2003.08.004

Hou, J. Z., D'Andrea, W. J., and Liu, Z. H. (2012). The influence of ^{14}C reservoir age on interpretation of paleolimnological records from the Tibetan Plateau. *Quat. Sci. Rev.* 48, 67–79. doi: 10.1016/j.quascirev.2012.06.008

Hughen, K. A., Overpeck, J. T., Lehman, S. J., Kashgarian, M., Southon, J., Petersonk, L. C., et al. (1985). Deglacial changes in ocean circulation from an extended radiocarbon calibration. *Nature* 391, 65–68. doi: 10.1038/34150

Jiang, W. Y., Guo, Z. T., Sun, X. J., Wu, H. B., Chu, G. Q., Yuan, B. Y., et al. (2006). Reconstruction of climate and vegetation changes of Lake Bayanchagan (Inner Mongolia): holocene variability of the East Asian monsoon. *Quat. Res.* 65, 411–420. doi: 10.1016/j.yqres.2005.10.007

Jie, D. M., Liu, J. F., Li, Z. M., Leng, X. T., Wang, S. Z., and Zhang, G. R. (2001). Carbonate content of sedimentary core and Holocene lake-level fluctuation of Dabusu lake. *Mar. Geol. Quat. Geol.* 21, 77–82. (in Chinese), doi: 10.2307/2786328

Kutzbach, J. E. (1981). Monsoon climate of the Early Holocene: climate experiment with the Earth's orbital parameters for 9000 years age. *Science* 214, 59–61. doi: 10.1126/science.214.4516.59

Kutzbach, J. E., and Street-Perrott, F. A. (1985). Milankovitch forcing of fluctuations in the level of tropical lakes from 18 to 0 kyr BP. *Nature* 317, 130–134. doi: 10.1038/317130a0

Leng, M. J., and Marshall, J. D. (2004). Palaeoclimate interpretation of stable isotope data from lake sediment archives. *Quat. Sci. Rev.* 23, 811–831. doi: 10.1016/j.quascirev.2003.06.012

Lerman, A. (1979). *Geochemical Processes-Water and Sediment Environments*. New York, NY: John Wiley.

Li, H. C., and Ku, T. L. (1997). $\delta^{13}C$-$\delta^{18}O$ covariance as a paleohydrological indicator for closed-basin lakes. *Palaeogeogr. Palaeoclimatol. Palaeoecol.* 133, 69–80. doi: 10.1016/s0031-0182(96)00153-8

Li, H. Z., Liu, Q. S., and Wang, J. X. (1992). Study of evolution of Huangqihai and Daihai lakes in Holocene in Inner Mongolia Plateau. *J. Lake Sci.* 4, 31–39. (in Chinese), doi: 10.18307/1992.0104

Li, X. Z., Liu, W. G., Zhou, X., Xu, L. M., and Cheng, P. (2017). A 700-year macrophyte productivity record inferred from isotopes of macrophyte remains and bulk carbonates in Lake Koucha, northeast Qinghai-Tibetan Plateau. *Quat. Int.* 430, 32–40. doi: 10.1016/j.quaint.2015.11.053

Liu, J., Wang, Y., Wang, Y., Guan, Y. Y., Dong, J., and Li, T. D. (2018). A multi-proxy record of environmental changes during the Holocene from the Haolaihure Paleolake sediments, Inner Mongolia. *Quat. Int.* 479, 148–159. doi: 10.1016/j.quaint.2016.12.015

Liu, X. Q., Shen, J., Wang, S. M., Wang, Y. B., and Liu, W. G. (2007). Southwest monsoon changes indicated by oxygen isotope of ostracode shells from sediments in Qinghai Lake since the late glacial. *Chin. Sci. Bull.* 52, 539–544. doi: 10.1007/s11434-007-0086-3

Liu, X. Q., Wang, S. M., and Shen, J. (2003). The grainsize of the core QH-2000 in Qinghai Lake and its implication for paleoclimate and paleoenvironment. *J. Lake Sci.* 15, 112–117. (in Chinese), doi: 10.18307/2003.0203

Long, H., Lai, Z. P., Wang, N. A., and Zhang, J. R. (2011). A combined luminescence and radiocarbon dating study of Holocene lacustrine sediments from arid northern China. *Quat. Geochronol.* 6, 1–9. doi: 10.1016/j.quageo.2010.06.001

Mathewes, R. W. (1993). Evidence for younger Dryas-age cooling on the North Pacific coast of America. *Quat. Sci. Rev.* 12, 321–331. doi: 10.1016/0277-3791(93)90040-s

Menking, K. M., Bischoff, J. L., Fitzpatrick, J. A., Burdette, J. W., and Rye, R. O. (1997). Climate/hydrologic oscillation since ˜155000 yr B.P. at Owens lake, reflected in abundance and stable isotope composition of sediment carbonate. *Quat. Res.* 48, 58–68. doi: 10.1006/qres.1997.1898

Meyers, P. A. (1994). Preservation of elemental and isotopic source identification of sedimentary organic matter. *Chem. Geol.* 144, 289–302. doi: 10.1016/0009-2541(94)90059-0

Meyers, P. A., and Vergés, E. L. (1999). Lacustrine sedimentary organic matter records of Late Quaternary paleoclimates. *J. Paleolimnol.* 21, 345–372.

Mikolajewicz, U., Crowley, T. J., Schiller, A., and Voss, R. (1997). Modelling teleconnections between the North Atlantic and North Pacific during the Younger Dryas. *Nature* 387, 384–387. doi: 10.1038/387384a0

Mischke, S., Herzschuh, U., Zhang, C. J., Jan, B., and Riedel, F. (2005). A late Quaternary lake record from the Qilian Mountains (NW China): lake level and salinity changes inferred from sediment properties and ostracod assemblages. *Global Planet. Change* 46, 337–359. doi: 10.1016/j.gloplacha.2004.09.023

Mischke, S., Kramer, M., Zhang, C. J., Shang, H. M., Herzschuh, U., and Erzinger, J. (2008). Reduced early Holocene moisture availability in the Bayan Har Mountains, northeastern Tibetan Plateau, inferred from a multi-proxy lake record. *Palaeogeogr. Palaeoclimatol. Palaeoecol.* 267, 59–76. doi: 10.1016/j.palaeo.2008.06.002

Müller, A., and Ulrike, M. (1999). The palaeoenvironments of coastal lagoons in the southern Baltic sea: the application of sedimentary C/N ratios as source indications of organic matter. *Palaeogeogr. Palaeoclimatpl. Palaeoecol.* 145, 1–16. doi: 10.1016/s0031-0182(98)00094-7

Müller, G., Iron, G., and Forstner, U. (1972). Formation and diagenesis of inorganic Ca-Mg carbonates in the lacustrine environment. *Naturwissenschaften* 59, 158–164. doi: 10.1007/bf00637354

Muscheler, R., Kromer, B., Bjorck, S., Svensson, A., Friedrich, M., Kaiser, K. F., et al. (2008). Tree rings and ice cores reveal ^{14}C calibration uncertainties during the Younger Dryas. *Nat. Geosci.* 4, 263–276.

Opitz, S., Zhang, C. J., Herzschuh, U., and Mischke, S. (2015). Climate variability on the south-eastern Tibetan Plateau since the Lateglacial based on a multiproxy approach from Lake Naleng Co comparing pollen and non-pollen signals. *Quat. Sci. Rev.* 115, 112–122. doi: 10.1016/j.quascirev.2015.03.011

Reimer, P. J., Bard, E., Bayliss, A., Beck, J. W., Blackwell, P. G., Bronk Ramsey, C., et al. (2013). IntCal13 and Marine13 radiocarbon age calibration curves 0-50,000 years cal BP. *Radiocarbon* 55, 1869–1887. doi: 10.2458/azu_js_rc.55.16947

Ren, G. Y. (1998). A finding of the influence of hard water on radio carbon dating for lake sediments in inner Mongolia, China. *J. Lake Sci.* 10, 80–82. (in Chinese), doi: 10.18307/1998.0314

Shen, J., Liu, X. Q., Wang, S. M., and Ryo, M. (2005). Palaeoclimatic changes in the Qinghai Lake area during the last 18,000 years. *Quat. Int.* 136, 131–140. doi: 10.1016/j.quaint.2004.11.014

Shen, Y. P., Liu, G. X., Shi, Y. F., and Zhang, P. Z. (1996). Climate and environment in the Tibetan Plateau during the younger Dryas cooling event. *J. Glaciol. Geocryol.* 18, 219–226. (in Chinese).

Song, C. Q., Wang, B. Y., and Sun, X. J. (1996). Implication of paleovegetational changes in Diaojiao lake, Inner Mongolia. *Acta Bot. Sin.* 38, 568–575. (in Chinese).

Sun, Q. L., Wang, S. M., Zhou, J., Shen, J., Cheng, P., Xie, X. P., et al. (2009). Lake surface fluctuations since the late glaciationat Lake Daihai, North central China: a direct indicator of hydrological process response to East Asian monsoon climate. *Quat. Int.* 194, 45–54. doi: 10.1016/j.quaint.2008.01.006

Talbot, M. R. (1990). A review of the palaeohydrological interpretation of carbon and oxygen isotopic ratios in primary lacustrine carbonates. *Chem. Geol.* 80, 261–279. doi: 10.1016/0168-9622(90)90009-2

Tatzber, M., Stemmer, M., Spiegel, H., Katzlberger, C., Haberhauer, G., and Gerzabek, M. N. (2007). An alternative method to measure carbonate in soils by FI-IR spectroscopy. *Environ. Chem. Lett.* 5, 9–12. doi: 10.1007/s10311-006-0079-5

Valero-Garces, B., Kelts, K., and Ito, E. (1995). Oxygen and carbon isotope trends and sedimentological evolution of a meromictic and saline lacustrine system: the Holocene Medicine Lake Basin, North American Great Plains, USA. *Palaeogeogr. Palaeoclimatpl. Palaeoecol.* 17, 253–278. doi: 10.1016/0031-0182(94)00136-v

Wang, H. Y., Li, H. Y., Liu, Y. H., and Cui, H. T. (2004). Mineral magnetism of lacustrine sediments and Holocene palaeoenvironmental changes in Dali Nor area, southeast Inner Mongolia Plateau, China. *Palaeogeogr. Palaeoclimatol. Palaeoecol.* 208, 175–193. doi: 10.1016/j.palaeo.2004.02.026

Wang, P. F. (1992). Preliminry study on the environmental changes of Hulun Buir Sandy Land since the Holocene. *J. Desert Res.* 12, 13–19. (in Chinese).

Wang, S. M., and Dou, H. S. (1998). *Chinese Lakes*. Beijing: Science Press. (in Chinese).

Wang, S. M., Ji, L., Yang, X. D., Xue, B., Ma, Y., and Hu, S. Y. (1994). The record of younger Dryas event in lake sediments from Jalai Nur, Inner Mongolia, China. *Sci. Bull.* 39, 831–835.

Wang, Y. J., Cheng, H., Edwards, R. L., An, Z. S., Wu, J. Y., Shen, C. C., et al. (2001). A high-resolution absolute-dated Late Pleistocene monsoon record from Hulu Cave, China. *Science* 294, 2345–2348. doi: 10.1126/science.1064618

Wen, R. L., Xiao, J. L., Chan, Z. G., Zhai, D. Y., Xu, Q. H., Li, Y. C., et al. (2010). Holocene climate changes in the mid-high-latitude-monsoon margin reflected by the pollen record from Hulun Lake, northeastern Inner Mongolia. *Quat. Res.* 73, 293–303. doi: 10.1016/j.yqres.2009.10.006

Winkler, M. G., and Wang, P. K. (1993). "The late Quaternary vegetation and climate of China," in *Global Climates Since the Last Glacial Maximum*, ed. H. E. Wright (Minneapolis, MN: University of Minnesota Press), 221–261.

Wu, J. L., and Wang, S. M. (1997). Carbonate δ^{18}O- and δ^{13}C-recorded environmental changes in RM lake core in Zoige of the eastern Tibetan Plateau. *Mar. Geol. Quat. Geol.* 17, 63–71. (in Chinese).

Xiao, J. L., Fan, J. W., Zhou, L., Zhai, D. Y., Wen, R. L., and Qin, X. G. (2013). A model for linking grain-size component to lake level status of a modern clastic lake. *J. Asian Earth Sci.* 69, 149–158. doi: 10.1016/j.jseaes.2012.07.003

Xiao, J. L., Nakamura, T., Lu, H. Y., and Zhang, G. Y. (2002). Holocene climate changes over the desert/loess transition of north-central China. *Earth Planet. Sci. Lett.* 197, 11–18. doi: 10.1016/s0012-821x(02)00463-6

Xiao, J. L., Xu, Q. H., Nakamura, T., Yang, X. L., Liang, W. D., and Inouchi, Y. (2004). Holocene vegetation variation in the Daihai Lake region of north-central China: a direct indication of the Asian monsoon climatic history. *Quat. Sci. Rev.* 23, 1669–1679. doi: 10.1016/j.quascirev.2004.01.005

Yang, X. D., and Wang, S. M. (1996). The vegetation and climatic-environmental changes in Hulun Lake during Holocene. *Oceanol. Limnol. Sin.* 27, 67–72. (in Chinese).

Yang, X. D., Wang, S. M., and Xue, B. (1995). Vegetational development and environmental changes in Hulun Lake since Late Pleistocene. *Acta Palaeontol. Sin.* 34, 647–656. (in Chinese). doi: 10.19800/j.cnki.aps.1995.05.008

Yang, Y., Yuan, D. X., Cheng, H., Zhang, M. L., Qin, J. M., Lin, Y. S., et al. (2010). Precise dating of abrupt shifts in the Asian monsoon during the last deglaciation based on stalagmite data from Yamen Cave, Guizhou Province, China. *Sci. China Earth Sci.* 53, 633–641. doi: 10.1007/s11430-010-0025-z

Yang, Z. R. (1998). A study on the low temperature fluctuations since the Holocene in Diaojiaohaizi lake area, Daqingsha mountains, Inner Mongolia. *Geogr. Res.* 17, 138–144. (in Chinese). doi: 10.11821/yj1998020005

Yang, Z. R., Shi, P. J., and Fang, X. Q. (1997). Preliminary study on paleovegetation and environmental changes since 11ka B.P. in Diaojiaohaizi lake area, Daqingmountains, Inner Mongolia. *Acta Phytoecol. Sin.* 21, 551–563. (in Chinese).

Yang, Z. R., and Suo, X. F. (1996). Preliminary study on relations between human activities and environment in framing-animal husbandry zigzag zone of north China. *J. Beijing Norm. Univ. Nat. Sci.* 32, 415–420. (in Chinese).

Yu, Z. T., Liu, X. Q., Wang, Y., Chi, Z. Q., Wang, X. J., and Lan, H. Y. (2014). A 48.5-ka climate record from Wulagai Lake in Inner Mongolia, Northeast China. *Quat. Int.* 333, 13–19. doi: 10.1016/j.quaint.2014.04.006

Zeng, Y., Chen, J., Xiao, J., and Qi, L. (2013). Non-residual Sr of the sediments in Daihai Lake as a good indicator of chemical weathering. *Quat. Res.* 79, 284–291. doi: 10.1016/j.yqres.2012.11.010

Zhai, Q. M., Qiu, W. L., Li, R. Q., Zhao, Y., and Zheng, L. M. (2000). The middle and late Holocene lacustrine sediments and its climate significance of Angulinao -Bojianghaizi lakes, Inner Mongolia. *J. Palaeogeogr.* 2, 84–91. (in Chinese).

Zhang, C. J., Cao, J., Lei, Y. B., and Shang, H. M. (2004). The chronological characteristics of bosten lake Holocene sediment environment in Xinjiang, China. *Acta Sedimentol. Sin.* 22, 494–499. (in Chinese). doi: 10.1007/BF02873097

Zhang, C. J., Dembele, B., Zhang, W. Y., Zhang, J. Y., Wang, H. S., Gang, E., et al. (2018). The low lake-level record according to the Selin Co stratigraphical basis and multi-proxies during the last glacial maximum in the central Tibetan Plateau. *Acta Geol. Sin.* 92, 2058–2059. doi: 10.1111/1755-6724.13707

Zhang, C. J., Fan, R., Li, J., Mischke, S., Dembele, B., and Hu, X. L. (2013). Carbon and oxygen isotopic compositions: how lacustrine environmental factors respond in Northwestern and Northeastern China. *Acta Geol. Sin.* 87, 1344–1354. doi: 10.1111/1755-6724.12133

Zhang, C. J., Mischke, S., Zheng, M. P., Prokopenko, A., Guo, F. Q., and Feng, Z. D. (2009). The carbon and oxygen isotopic composition of surface-sediment carbonate in Bosten Lake (Xinjiang, China) and its controlling factors. *Acta Geol. Sin.* 2, 386–395. doi: 10.1111/j.1755-6724.2009.00029.x

Zhang, C. J., Zhang, W. Y., Feng, Z. D., Mischke, S., Gao, X., Gao, D., et al. (2012). Holocene hydrological and climatic change on the northern Mongolian Plateau based on multi-proxy records from Lake Gun Nuur. *Palaeogeogr. Palaeoclimatol. Palaeoecol.* 32, 75–86. doi: 10.1016/j.palaeo.2012.01.032

Zhang, H. R., Dembele, B., Zhang, W. Y., Zhang, J. Y., Ma, Y., and Zhang, C. J. (2018). The dry-cold climate of the Qijia archeological civilization in Chankou of the Loess Plateau along the silk road since the Neolithic Period. *Acta Geol. Sin. Res. Adv.* 92, 2466–2467.

Zhang, Z. K., and Wang, S. M. (2000). Paleoclimate significance of lake level fluctuation, peat development and Eolian Sand-paleosoil series in Hulun Lake Area during Past 13ka. *J. Arid Land Resour. Environ.* 14, 56–59. (in Chinese). doi: 10.3969/j.issn.1003-7578.2000.03.009

Zhao, Y., Yu, Z. C., Chen, F. H., and Li, J. (2008). Holocene vegetation and climate change from a lake sediment record in the Tengger Sandy Desert, northwest China. *J. Arid Environ.* 72, 2054–2064. doi: 10.1016/j.jaridenv.2008.06.016

Zheng, Y. E., Zhou, L. P., and Zhang, J. F. (2010). Optical dating of the upper 22m of cored sediments from Daihai Lake, northern China. *Quat. Geochronol.* 5, 228–232. doi: 10.1016/j.quageo.2009.05.010

Zhou, W. J., Head, M. J., and Deng, L. (2001). Climate changes in northern China since the late Pleistocene and its response to global change. *Quat. Int.* 83-85, 285–292. doi: 10.1016/s1040-6182(01)00046-5

Zhou, W. J., Xian, F., Du, Y. J., and Kong, X. H. (2014). The last 130 ka precipitation reconstruction from Chinese loess ^{10}Be. *J. Geophys. Res. Solid Earth* 119, 191–197. doi: 10.1002/2013jb010296

Conflict of Interest: The authors declare that the research was conducted in the absence of any commercial or financial relationships that could be construed as a potential conflict of interest.

Copyright © 2020 Chengjun, Li, Wanyi, Yunhan, Yang, Xiangling, Zhen and Khomid. This is an open-access article distributed under the terms of the Creative Commons Attribution License (CC BY). The use, distribution or reproduction in other forums is permitted, provided the original author(s) and the copyright owner(s) are credited and that the original publication in this journal is cited, in accordance with accepted academic practice. No use, distribution or reproduction is permitted which does not comply with these terms.

frontiers in Earth Science

ORIGINAL RESEARCH
published: 09 September 2020
doi: 10.3389/feart.2020.562426

Pollen Record of Humidity Changes in the Arid Western Qilian Mountains Over the Past 300 Years and Comparison With Tree-Ring Reconstructions

Jiale Wang[1], *Xiaozhong Huang*[1]*, *Jun Zhang*[1], *Lixiong Xiang*[1], *Yulin Xiao*[1], *Luciane Fontana*[2], *Xiuxiu Ren*[1] *and Zongli Wang*[1]*

[1] Key Laboratory of Western China's Environmental System, Ministry of Education, College of Earth and Environmental Sciences, Lanzhou University, Lanzhou, China, [2] Department of Engineering, Modeling and Applied Social Sciences, University Federal of ABC, São Paulo, Brazil

OPEN ACCESS

Edited by:
Davide Tiranti,
Agenzia Regionale per la Protezione Ambientale (ARPA), Italy

Reviewed by:
Santosh Kumar Shah,
Birbal Sahni Institute of Palaeobotany, India
Olga Nikolaevna Solomina,
Institute of Geography (RAS), Russia

***Correspondence:**
Xiaozhong Huang
xzhuang@lzu.edu.cn
Zongli Wang
zlwang@lzu.edu.cn

Specialty section:
This article was submitted to Quaternary Science, Geomorphology and Paleoenvironment, a section of the journal Frontiers in Earth Science

Received: 18 May 2020
Accepted: 17 August 2020
Published: 09 September 2020

Citation:
Wang J, Huang X, Zhang J, Xiang L, Xiao Y, Fontana L, Ren X and Wang Z (2020) Pollen Record of Humidity Changes in the Arid Western Qilian Mountains Over the Past 300 Years and Comparison With Tree-Ring Reconstructions. Front. Earth Sci. 8:562426. doi: 10.3389/feart.2020.562426

In arid central Asia, the geo-ecological environment of the well-vegetated high mountains differs from that of the extensive arid Gobi desert areas, with the forested areas having experienced a different pattern of humidity variations compared to the dryland regions. Therefore, the moisture history of the forest areas reconstructed by tree rings may differ from that of the dryland areas. In the extremely arid area of the western Qilian Mountains and the surrounding dryland areas, where forest is absent, it is unclear how humidity conditions have changed over the past several centuries. Here, we use a pollen record from Tian'E Lake, with a chronology based on ^{210}Pb and ^{137}Cs, and with an average temporal resolution of ~2 years, to reconstruct the humidity changes over the past 300 years. The results show that the pollen assemblage is dominated by *Artemisia* and Amaranthaceae (=Chenopodiaceae), and therefore, the A/C (*Artemisia*/Chenopodiaceae) ratio can be used to reconstruct changes in humidity conditions. Based on the pollen A/C ratio, two relatively wet periods are identified: ~1740–1750 and 1840–1980, and two dry intervals: ~1750–1840 and 1980–2018. This pattern of variation is similar to that reconstructed from nearby humidity records based on tree-ring width adjacent to the Tian'E Lake area and with instrumental records from meteorological stations over the past several decades. However, there are significantly different records between pollen-based and tree-ring based humidity during ~1760–1830, 1880–1910, and 1920–2018 in the Qilian Mountains on long timescales. We conclude that pollen-based humidity records from dryland areas may differ from those reconstructed from tree-ring widths in forested mountain areas, especially when the temperature was increasing. It was further suggested that there was an antiphased relationship in humidity conditions between westerlies-dominated central Asia and monsoon areas over the past century.

Keywords: western Qilian Mountains, A/C ratio, tree rings, global warming, humidity changes

INTRODUCTION

Although instrumental climate records show a clear record of increasing temperature in the Northern Hemisphere during the 20th century, humidity variations exhibit complex spatial patterns at the regional scale (IPCC, 2007). Increased global warming could lead to more frequent and sustained droughts (Cook et al., 2004; Dai et al., 2004), with consequently increased aridity in arid and semiarid areas (Feng and Zhang, 2015; Huang et al., 2016). It has been shown that on the global scale, drylands have experienced a significant intensification of warming in the past 100 years, together with inter-decadal fluctuations in drier/wetter conditions (Li et al., 2007; Guan et al., 2019). The Qilian Mountains, in the northern part of the Qinghai–Tibetan Plateau, is located in the marginal area of the arid region in central Asia and the semiarid or semi-humid region in the east. The Qilian Mountains is climatically influenced by the westerlies in the west and the summer monsoon in the east (Chen et al., 2008). The high mountains of the region have diverse geo-ecological environments along vertical and longitudinal gradients, including forest, shrubland, grassland, tundra, and sparse desert-like vegetation. The precipitation in the Qilian Mountains decreases from east to west. In recent decades, the climate of the region has warmed, and there is an increasing frequency and intensity of severe drought events (Zou et al., 2005).

In the Qilian Mountains, numerous dendrochronological studies have been conducted, including reconstructions of moisture conditions at the lower tree line (Kang et al., 2003; Yang et al., 2011; Zhang et al., 2011; Deng et al., 2013; Sun and Liu, 2013; Yang et al., 2019) and temperature at the upper tree line (Wang et al., 2001; Gou et al., 2012). However, it can be concluded that the pattern of climate change in the Qilian Mountains reconstructed by tree-ring records is complex on both the spatial and temporal scales. Moreover, because of the absence of forest in the arid area of the western Qilian Mountains and the surrounding arid areas, it is unclear how humidity conditions have evolved over the past three centuries, in the context of the significant temperature variations.

Pollen records from closed alpine lakes are reliable indicators of regional changes in moisture conditions. Moisture reconstructions from such lakes can potentially fill the gaps in the spatial distribution of paleoclimate records from dryland areas in central Asia, which may have experienced a different pattern of moisture changes from those of forested areas. Tian'E Lake is an alpine lake located in the western Qilian Mountains. Zhang et al. (2018) used the A/C ratio from this lake to reconstruct the history of regional humidity, and it had a relatively wetting trend after AD 1600 with some fluctuations (all subsequent dates are AD). A geotropism index suggests that the region was relatively warm and dry during the Medieval Warm Period and relatively cold and wet during the Little Ice Age (LIA) (Yan et al., 2018; Zhang et al., 2018). The past 300 years is a critical interval bridging the gap between meteorological records and geological records, and it also corresponds to the transition period from the LIA to the Current Warming Period. The high sediment accumulation rate of the alpine Tian'E lake enables high-resolution paleoenvironmental records to be obtained. Based on pollen analysis of 128 samples from the sediments of the lake, we reconstructed the pattern of humidity changes in the surrounding dryland area over the past ~300 years, and attempt to address whether the tree-ring records from the semiarid area have the representation of humidity over the large arid region in central Asia or not.

STUDY AREA

Tian'E Lake (39°14′20″N, 97°55′26″E, 3,012 m.a.s.l.) is an alpine lake located in the arid western part of the Qilian Mountains (**Figure 1**), ~35 km from the nearest forested area. The lake is ~0.12 km^2 in area and has a water depth of ~14.5 m. The lake basin is closed and is mainly fed by groundwater from glaciers, and its sediments can potentially provide a record of regional climate change (Zhang et al., 2018). As recorded at the nearby Sunan Meteorological Station (150 km from the lake, at 2,330 m.a.s.l.), from 1981 to 2010, the regional average annual precipitation was ~267 mm and the evaporation was ~2,200 mm. At the same time, the mean January temperature was −9.4°C and the mean July temperature was 16.8°C (**Figure 1B**).

The vegetation coverage of the Tian'E Lake region is sparse, and forest is absent (**Figure 1A**). The region is characterized by a desert-steppe landscape, with the natural vegetation consisting of desert and dry grassland plants, very similar to the vegetation of the Hexi Corridor. The vegetation consists mainly of *Artemisia* and Amaranthaceae, together with Asteraceae, Poaceae, Ranunculaceae, Rosaceae, Fabaceae, Labiatae, Caryophyllaceae, and Brassicaceae (Yi and Wang, 2013).

MATERIALS AND METHODS

Sediment Sampling and Chronology

A 66-cm-long sediment core (core TE18A) was collected from Tian'E Lake in October 2018 using a gravity corer (**Figure 1A**). The core was mainly subsampled at a 0.5-cm interval, with some samples (TE18A-81, 82, 83, and 84) at a 1-cm interval. The samples were transported to the laboratory and then freeze-dried.

Eighteen samples were analyzed for ^{210}Pb and ^{137}Cs at the Key Laboratory of Western China's Environmental System, Ministry of Education, Lanzhou University. For ^{210}Pb analysis, subsamples were freeze-dried and homogenized before being stored for three weeks to reach radioactive equilibrium. The samples were then analyzed for ^{210}Pb using gamma spectrometry with a low background intrinsic germanium detector. Gamma emissions at 46.5 keV were used to determine the radioactivity level of ^{210}Pb downcore. Unsupported ^{210}Pb activity ($^{210}Pb_{ex}$) was calculated by subtracting the activity of supported ^{210}Pb (as ^{226}Ra) from the total ^{210}Pb activity. The final chronology was established using the constant rate of supply model (Appleby and Oldfield, 1978).

$^{210}Pb_{ex}$ decreases irregularly with increasing depth (**Figure 2B**). Equilibrium between the total ^{210}Pb and supported ^{210}Pb activity is reached at the depth of 18.5–19 cm. ^{137}Cs first appears in the core sample at the depth of 12.0–12.5 cm and reaches a maximum value of 33.3 Bq kg^{-1} at the depth of 10.0–10.5 cm. Hence, these

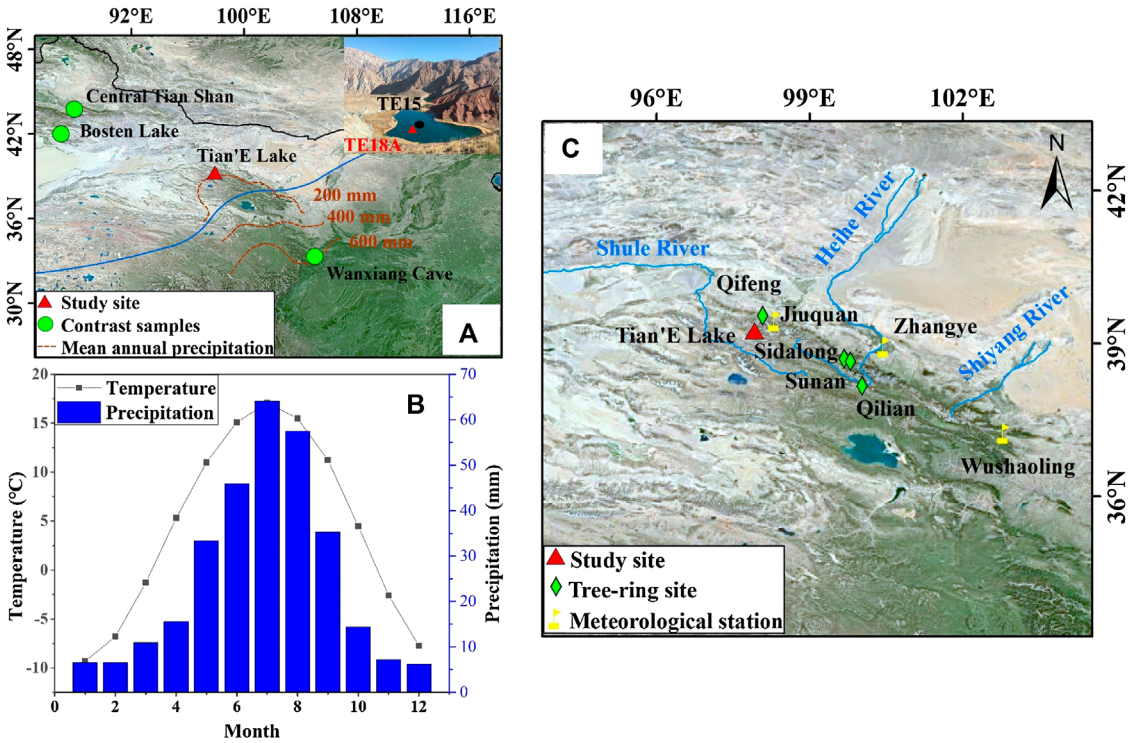

FIGURE 1 | Location and environmental setting of the Tian'E Lake area. **(A)** Location of Tian'E Lake in northwestern China and locations of other sites mentioned in the text. Inset image is a photo of Tian'E Lake showing the location of cores TE18A and TE15. The blue line is the modern limit of the summer monsoon (Chen et al., 2008), and the red dashed lines denote the mean annual precipitation. **(B)** Monthly temperature and precipitation at the Sunan Meteorological Station during 1981–2010. **(C)** Location of Tian'E Lake and tree-ring records from the Qilian Mountains referenced in the text.

levels were dated to 1952 and 1963, respectively, which is in good agreement with the ^{210}Pb chronology.

Below 19 cm of TE18A, there are no direct AMS ^{14}C dates based on plant material. Considering the lake has a stable sedimentation environment and the two sediment cores of TE15 and TE18A (**Figure 1A**) have close coring locations and a relatively small grain-size (**Figure 2**), we assume that the sedimentation rate was consistent and extrapolate the chronology of TE18A based on that of core TE15. The TE15 core has three radiocarbon dates of terrestrial plants in the upper 56 cm and four dates in the upper 166 cm (Zhang et al., 2018), so we use the average sedimentation rate of the top 100 cm of TE15 (0.29 cm/a) to calculate the age model of TE18A considering the errors of ^{14}C dates and variable sedimentation rates based on ^{14}C dates (**Figure 2B**). Based on this age model, the median grain-size data of TE18A have good consistency with TE15 (**Figure 2C**), which increased the confidence of this age model additionally.

Pollen Analysis

Pollen grains were extracted from 1 to 3 g of dried sediment using sequential treatments with 10% HCl, 40% HF, and 10% HCl. Before chemical pretreatment, tablets containing a known number of *Lycopodium* spores were added to estimate pollen concentrations. The samples were mounted in glycerin and counted using a light microscope at ×400–600 magnification. At least 300 terrestrial pollen grains were counted per sample, and pollen percentages were calculated based on the sum of total terrestrial pollen. Pollen identifications were based on photographs in Tang et al. (2016). A pollen diagram was produced using Tilia software (Grimm, 2011), and pollen assemblage zones were defined using stratigraphically constrained cluster analysis implemented with CONISS, using all pollen types (Grimm, 1987).

RESULTS

A total of 128 samples from core TE18A were used for pollen analysis, and 27 pollen types were identified. The average temporal resolution of the pollen data is ~2 years. The tree pollen percentages are relatively low, including some types of *Pinus*, *Picea*, *Betula*, and *Salix*; the main shrub pollen types are *Ephedra*, *Nitraria*, Rosaceae, and Zygophyllaceae; and the main herb pollen types are *Artemisia*, Amaranthaceae, Poaceae, Cyperaceae, *Thalictrum*, Polygonaceae, Asteraceae, Brassicaceae, Labiatae, and Ranunculaceae. The main aquatic pollen type is *Typha*. The pollen assemblages are divided into four main zones based on CONISS (**Figure 3**), and they are described below.

Zone I (66–61 cm, ~1740–1750)

Amaranthaceae (31.7–44.8%, average of 38.1%) and *Artemisia* (37.5–52.3%, average of 44.1%) are the main pollen types.

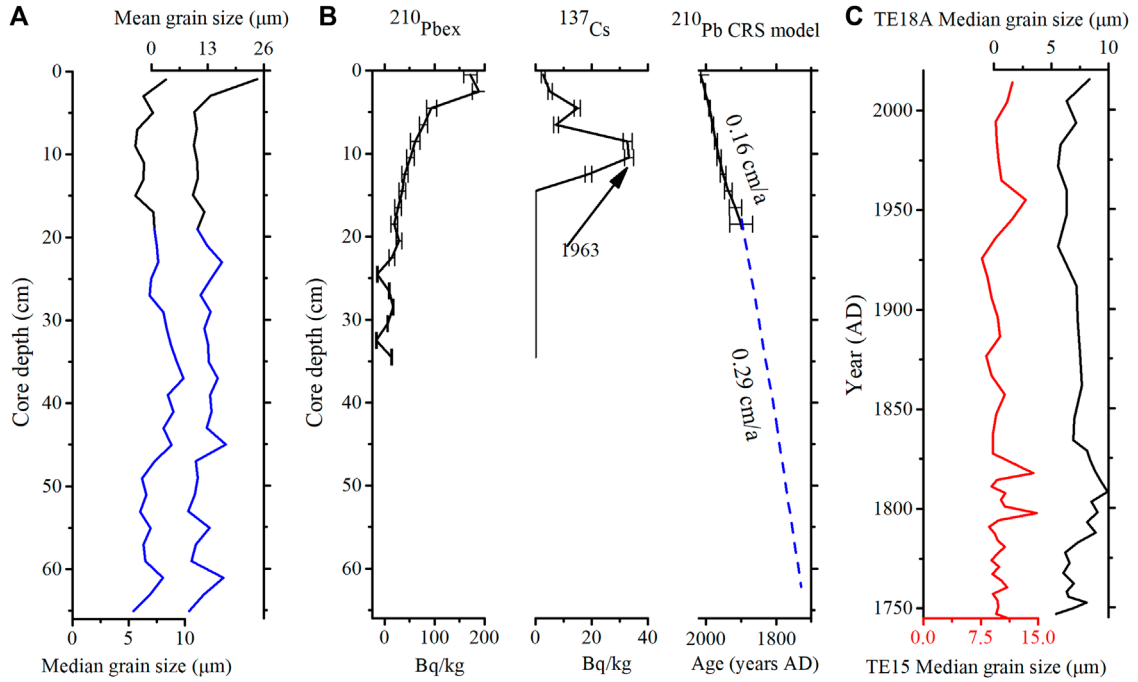

FIGURE 2 | Age model for core TE18A from Tian'E Lake. **(A)** Depth profiles of median grain size and mean grain size of TE18A. Parts below 19 cm are shown in blue. **(B)** ^{210}Pb and ^{137}Cs activity and the constant rate of supply age-depth model. **(C)** Comparison of the median grain sizes of TE15 and TE18A.

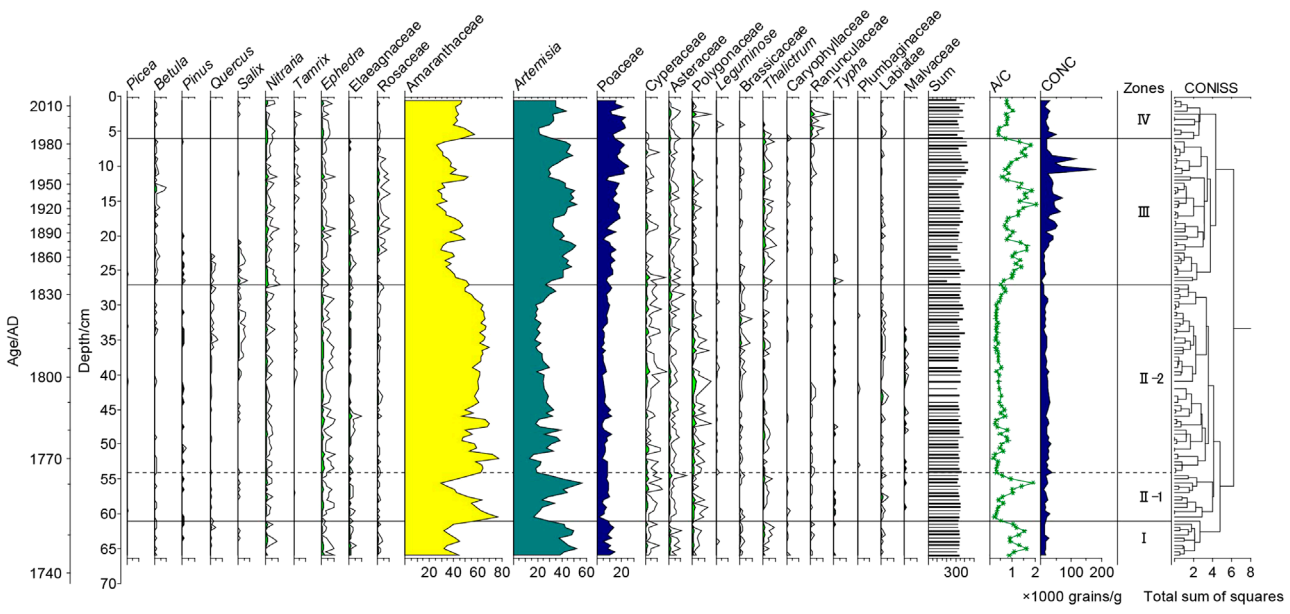

FIGURE 3 | Pollen percentage diagram (%) for core TE18A spanning the last 300 years (open curves are a 5× exaggeration of scale).

Asteraceae (average of 1%), Cyperaceae (average of 1%), and *Ephedra* (average of 1%) are also represented. The A/C ratio is variable (0.87–1.65, average of 1.18). The pollen concentration ranges from 11,381 to 26,886 grains/g (average of 15,492 grains/g).

Zone II (61–27 cm, ~1750–1840)

Amaranthaceae (29.4–76.9%, average of 58.9%) has a substantially increased representation, while *Artemisia* (16.9–56.9%) decreases to its lowest values. Other taxa with an average representation above 1% are Cyperaceae (1.2%), *Ephedra*

(1.1%), and Polygonaceae (1%). Compared to Zone I, the representation of *Artemisia* is substantially decreased and that of Amaranthaceae is significantly increased. This zone has the lowest A/C ratio, with an average of 0.49. The pollen concentration decreases markedly, fluctuating within the range of 9,049–38,022 grains/g (average of 19,479 grains/g). Based on the percentages of contents of *Artemisia* and Amaranthaceae, the zone can be divided into two subzones, II-1 and II-2. The average representation of Amaranthaceae increases from 53.5% in subzone II-1 to 60.2% in subzone II-2 and that of *Artemisia* decreases from 32.1% in subzone II-1 to 24.9% in subzone II-2.

Zone III (27–6 cm, ~1840–1980)

This zone is dominated by Amaranthaceae (25.8–53.2%, average of 37.3%) and *Artemisia* (26.6–52.9%, average of 41.3%). Compared to Zone II, the representation of *Betula* (average of 0.4%), *Artemisia*, and Rosaceae substantially increases, while that of Amaranthaceae and *Typha* decreases. The A/C ratio has the range of 0.5–2.05 and shows an increasing trend. The pollen concentration increases substantially compared with the previous zone, to 36,288 grains/g.

Zone IV (6–0 cm, ~1980–2018)

Amaranthaceae (41.8–57.7%, average of 46.1%) and *Artemisia* (21.1–43.5%, average of 31.2%) are still the dominant pollen types throughout the zone. Compared to Zone III, *Artemisia* decreases slightly and Amaranthaceae increases. The A/C ratio averages 0.69, and there is a slight decrease throughout the zone. The pollen concentration has the range of 11,968–51,779 grains/g (average of 24,908 grains/g), and there is a decreasing trend compared with Zone III.

DISCUSSION

Changes in Humidity Conditions in Western Qilian Mountains Over the Past 300 Years

Artemisia and Amaranthaceae are the main pollen types in the arid and semiarid areas, and both are overrepresented in pollen assemblages because of their high dispersal ability. Amaranthaceae percentages in areas with desert vegetation are generally higher than those of *Artemisia* (Xu et al., 2007), and the sum of the two pollen types typically exceeds 40%, indicating the occurrence of desert-steppe vegetation (Li et al., 2005; Xu et al., 2007). In core TE18A from Tian'E Lake, the average percentages of Amaranthaceae and *Artemisia* are 48.9 and 33.2%, respectively, and therefore, the vegetation is desert steppe at Tian'E Lake and the surrounding area. The A/C ratio is widely used as a proxy for reconstructing changes in humidity conditions in arid and semiarid areas (Tarasov et al., 1997; Huang et al., 2009; Zhao et al., 2009; Zhang et al., 2018). A paleoenvironmental study of a 50-year pollen record with a near-annual resolution from Gahai Lake in the Qaidam basin showed that the A/C ratio was well correlated with moisture data from the Delingha Meteorological Station (Zhao et al., 2008). A study of modern surface pollen in northwestern China demonstrated a statistically significant relationship between the A/C ratio and humidity when the sum percentage of the two pollen types exceeded 50%, with a higher A/C ratio indicating more humid conditions in a semiarid environment (Zhao et al., 2012).

To assess the reliability of humidity reconstruction, we compared it to the records from meteorological stations and historical documents. It was demonstrated that the A/C ratio fluctuations of TE18A were related to both the temperature and precipitation records from the Jiuquan station (**Figure 4**). The higher A/C ratio was related to lower temperature and higher precipitation during 1970–1980s, and the fast increases in temperature in the 1990s and 2010s led to lower humidity even with some higher precipitation (**Figure 4**). In addition, the moisture history revealed by the A/C ratio from Tian'E Lake was generally consistent with documentary records from the Hexi Corridor. For ~1876–1878, the low A/C ratio indicates a dry interval, which corresponds to the drought event of "Ding-Wu Disaster"; this was a major drought in northern China in the early Guangxu reign period, which resulted in millions of deaths with extremely adverse social impacts (Li et al., 2018). According to the Jiuquan city annals (Jiuquan City Annals Compilation Committee, 2008), after 1953, there was a prolonged drought and insect disaster in Jinta County of Jiuquan city. As documented in the Dunhuang city annals (Dunhuang City Annals Compilation Committee, 1994), floods occurred in 1939, 1946, 1971, and 1979. The timing of the drought and flood years documented in historical Chinese texts was generally in accord with the pollen record from Tian'E Lake. Therefore, the A/C ratio was a tested reliable indicator of humidity in this region.

In the small lake basin, Poaceae plants mainly include aquatic plants of *Phragmites australis* and terrestrial plants of *Stipa* and *Achnatherum splendens*, and therefore, it is difficult to use Poaceae pollen to reconstruct climatic signals. *Ephedra* and *Nitraria* are typical desert plants, and their increase in pollen assemblage indicates climatic drought. For example, *Ephedra* had a high content during ~1750–1840 (**Figure 3**) and this period has the lowest A/C ratio, and both of them indicate drier climate.

The reconstructed humidity record for the western Qilian Mountains, based on the A/C ratio from Tian'E Lake, is presented in **Figure 5H**, together with other climate records for the region. For the interval of ~1740–1750, the high A/C ratio indicates the occurrence of relatively high humidity at this time (**Figure 5H**). From ~1750 to 1840, the A/C ratio decreased markedly and reached its lowest values, indicating that this interval was the driest within the entire sequence (**Figure 5H**), which is also reflected by an increase in the representation of Amaranthaceae, *Ephedra*, and *Nitraria* and a gradual decrease in the pollen concentration (**Figure 3**). Some of the tree-ring records from the Qilian Mountains also revealed a drought condition during ~1760–1820s (Wang et al., 2001; Zhang et al., 2011; Kang et al., 2013). As indicated by the A/C ratio, this dry interval was interrupted by a notable wet period in ~1760 (**Figure 5H**). The subsequent rapid increase in the A/C ratio indicates that the interval of ~1840–1980 was the wettest in the western Qilian Mountains during the past 300 years (**Figure 5H**). During this period, the desert pollen types of *Ephedra* and Amaranthaceae decreased, while *Artemisia* and the total pollen concentration increased (**Figure 3**). During ~1980–2018, the lower A/C ratio

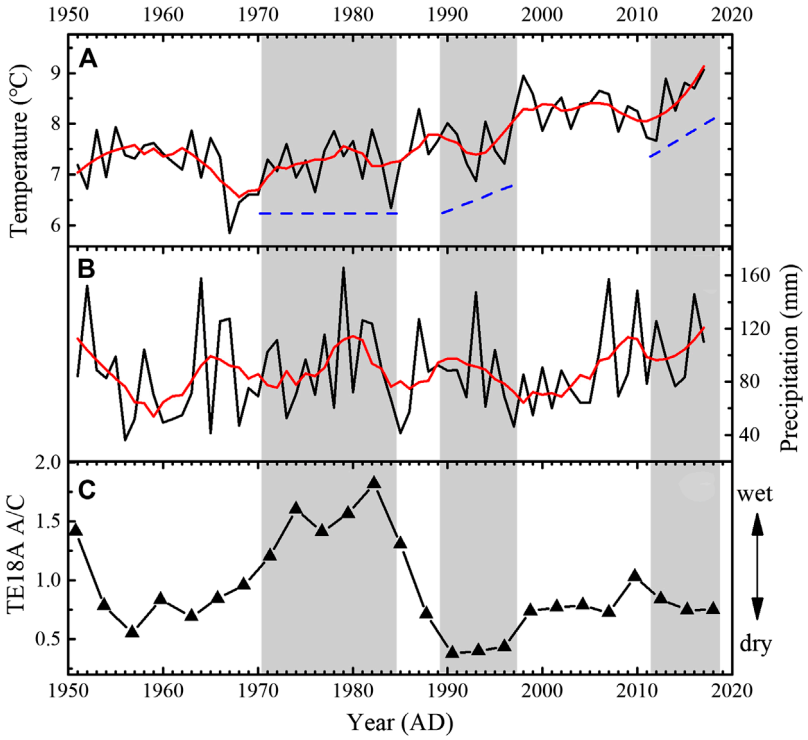

FIGURE 4 | Comparison of the A/C ratio with the meteorological information from the Jiuquan station during 1951–2017. **(A)** Mean annual temperature (°C). **(B)** Mean annual precipitation (mm). **(C)** Pollen A/C ratio from Tian'E Lake. The red curve is the result of 10-point smoothing. The blue dashed line indicates the trend of temperature. Some high precipitation periods are indicated by gray shading.

suggests that the climate became drier than the previous stage (**Figure 5**). The tree-ring record from Qifeng, in the western Qilian Mountains and close to our study area, indicates a drying trend during the recent decades (Gou et al., 2015; Yang et al., 2019).

Overall, the most obvious pattern of climatic changes in the western part of the Qilian Mountains during the last ~300 years is alternation of warm-dry and cold-wet conditions; however, the changes in humidity conditions may have been affected by temperature fluctuations on the inter-decadal scale as that in the recent decades we discussed in **Figure 4**.

Differences Between the Pollen-Based Regional Humidity Record Evolution and Tree-Ring Records on Decadal to Centennial Timescales

Several moisture-sensitive tree-ring width series for the central and western Qilian Mountains (with gradients of humidity and precipitation) have been produced, and their reconstructed humidity/precipitation have consistencies and differences (**Figures 1C,5**) (**Supplementary Table S1**). Differences in reconstructed moisture conditions between the pollen and tree-ring records are evident during ~1760–1830, 1890–1910, and 1920–2018 (**Figure 5**).

During ~1760–1830, the low pollen A/C ratio indicates the occurrence of the most intense and extended dry interval within the last 300 years, whereas the intensity and timing of drought indicated by the tree-ring records differ from the pollen record. On the central Qilian Mountains, the lower Palmer Drought Severity Index (PDSI) indicates that it experienced severe drought conditions at this time (Sun and Liu, 2013) (**Figure 5B**), which is consistent with low precipitation records from tree rings, Sunan County (Zhang et al., 2011) (**Figure 5D**). And a low precipitation period also occurred in the 1800s (Wang et al., 2001) (**Figure 5C**). However, the duration of the drought is not so long as that indicated by the pollen record (**Figure 5H**). At the western Qilian Mountain area, tree-ring records indicate that the Hexi Corridor had a humid climate during this period of 1760–1830 (Yang et al., 2019) (**Figure 5E**). A 2,700-year high-resolution (ca. 10-year) pollen record from the annually varved Sugan Lake in the Qaidam basin was presented, and the pollen A/C ratio suggests a relatively moister climate during ~1700–1800 and a drying trend from ~1790 (Zhang et al., 2010) (**Figure 5F**). During ~1890–1910, there was a slight increase in temperature in the Northern Hemisphere (Mann et al., 1998) (**Figure 5A**), and the pollen record from Tian'E Lake indicates a relatively dry climate (**Figure 5H**), whereas tree-ring records from the Qilian Mountains display high precipitation or wetter conditions (Wang et al., 2001; Hou et al., 2011; Zhang et al., 2011; Sun and Liu, 2013; Yang et al., 2019). Although the tree-ring record was obtained from a site closer to Tian'E Lake (Yang et al., 2019), the pattern of moisture changes differs substantially from that of Tian'E Lake. Furthermore, the moisture/precipitation conditions recorded by tree-ring records from the central Qilian Mountains spanning the

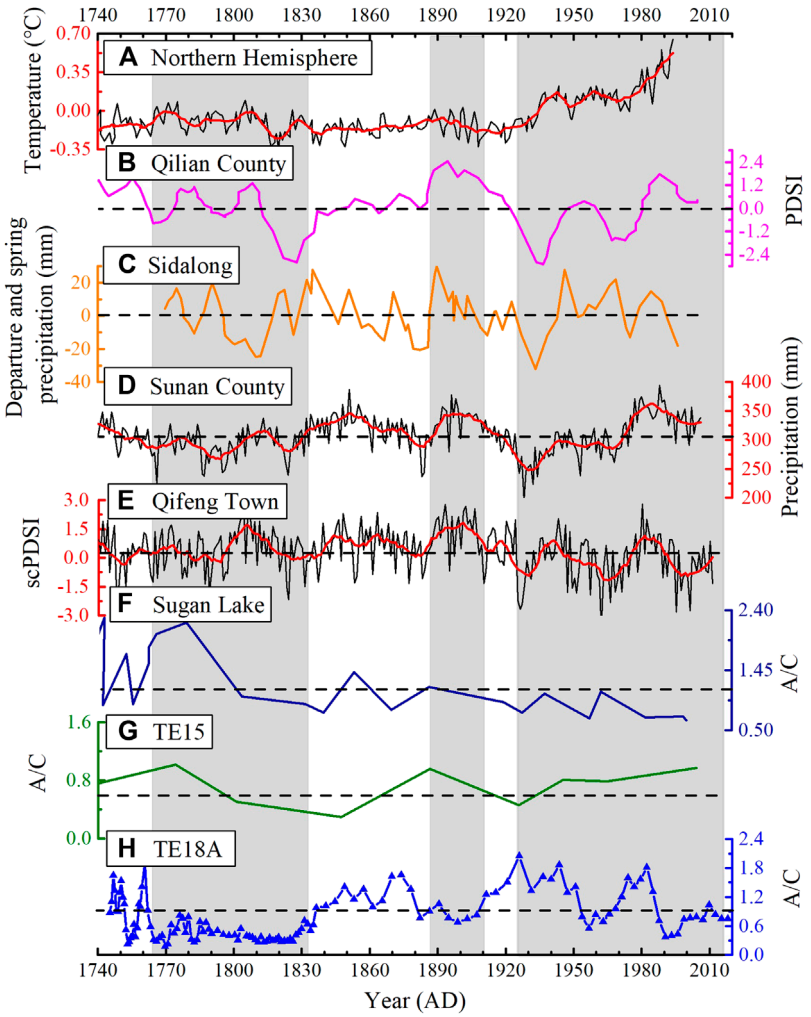

FIGURE 5 | Comparison of the humidity reconstruction for Tian'E Lake based on the A/C ratio with tree-ring and pollen records from Qilian Mountains and other temperature signals. **(A)** Northern Hemisphere temperature (Mann et al., 1998). **(B)** Palmer Drought Severity Index (PDSI) from May to July, a tree-ring record from central Qilian Mountains (Sun and Liu, 2013). **(C)** Tree-ring-based precipitation anomaly from Sidalong, in the central Qilian Mountains (Wang et al., 2001). **(D)** Annual precipitation reconstruction since 775 based on tree-ring records from the Qilian Mountains (Zhang et al., 2011). **(E)** scPDSI-based tree-ring records from Qifeng in the western Qilian Mountains (Yang et al., 2019). **(F)** Pollen A/C ratio from Sugan Lake (Zhang et al., 2010). **(G)** Pollen A/C ratio from core TE15 of Tian'E Lake in the western Qilian Mountains (Zhang et al., 2018). **(H)** Pollen A/C ratio from core TE18A of Tian'E Lake in the western Qilian Mountains (this study). Horizontal dashed lines represent the average value. Significant differences between the pollen and tree-ring-based humidity reconstructions are indicated by gray shaded areas. The red curves are the result of 20-point smoothing.

intervals of ~1920–2018 suggest a trend of wetting conditions with the temperature increasing rapidly (Wang et al., 2001; Zhang et al., 2011; Sun and Liu, 2013) (**Figures 5B–D**), while it shows a phase of drying recorded by pollen from Tian'E Lake and Sugan Lake (Zhang et al., 2010; Zhang et al., 2018) (**Figures 5F–H**) and tree-ring records from the western Qilian Mountain areas (Yang et al., 2019) (**Figure 5E**). Notably, three significant differences in the pollen records from Tian'E Lake compared with tree-ring records occurred during ~1760–1830, 1890–1910, and 1920–2018 (**Figure 5**), and these three intervals broadly correspond to the warm periods in the Northern Hemisphere (Mann et al., 1998) (**Figure 5A**). The good correspondence suggests that the pollen-indicated desert-steppe vegetation in the arid region is more temperature sensitive than tree-ring-indicated forest.

In addition, the humidity reconstruction based on pollen records is similar to the nearest tree-ring records of the Qifeng site from the western Qilian Mountains in the last few decades, but substantially different for previous periods (Yang et al., 2019) (**Figures 5E,H**). Therefore, there are differences between tree-ring and pollen-inferred humidity on a longer timescale. Although an offset between the two types of records could be caused by dating uncertainties at Tian'E Lake, there are also different types of response modes of tree rings and pollen spectra to long-term climate change.

Tree rings have the advantages of covering wide areas, a high temporal resolution (seasonal to annual), precise dating, and overall high reliability (Esper et al., 2002). However, at the centennial scale, studies of tree-ring widths have revealed

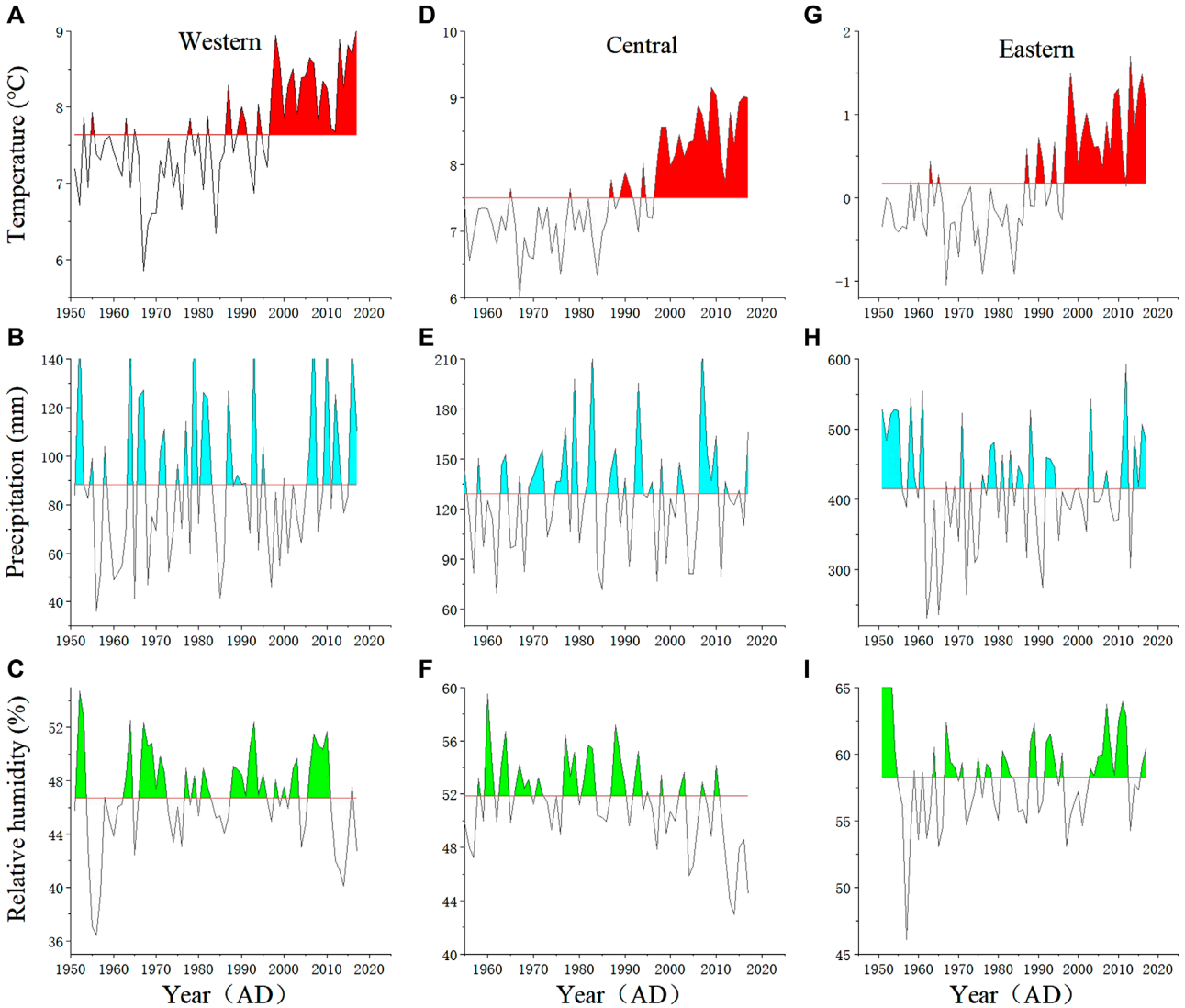

FIGURE 6 | Annual precipitation (mm), annual average temperature (°C), and relative humidity (%) in the eastern, central, and western parts of the northern slopes of the Qilian Mountains (data from China Meteorological Data Network http://data.cma.cn/). **(A)** Annual temperature at the Jiuquan Meteorological Station during 1951–2017. **(B)** Annual precipitation at Jiuquan. **(C)** Relative humidity at Jiuquan. **(D)** Annual temperature at the Zhangye Meteorological Station during 1951–2017. **(E)** Annual precipitation at Zhangye. **(F)** Relative humidity at Zhangye. **(G)** Annual temperature at the Wushaoling Meteorological Station during 1951–2017. **(H)** Annual precipitation at Wushaoling. **(I)** Relative humidity at Wushaoling. Black horizontal lines represent the mean value.

several influences which may introduce uncertainties into climate reconstructions, for example, the complex interactions between environmental factors such as soil water, temperature, soil, CO_2 concentration, and changes in groundwater status caused by the thawing of frozen soil and glacier meltwater supply (Liu et al., 2011; Zhang et al., 2011; Gou et al., 2012). In addition, the response of woody and herbaceous plants to climatic seasonality is different. Tree-ring growth is more sensitive to winter precipitation, while desert grassland vegetation may be sensitive to spring or summer precipitation. For example, it was suggested that high temperatures favor tree growth and that the warming trend after the LIA resulted in an increase in tree density and an advance of the tree line in the eastern Qilian Mountains (Gou et al., 2012). The results of the correlation analysis showed that tree-ring growth in the central Qilian Mountains was most strongly related to total water-year precipitation from the prior August to the current July (Zhang et al., 2011). Liu et al. (2011) suggested that there was a significant increase in the water-use efficiency of *Picea crassifolia* with increasing atmospheric CO_2 concentration at all sampling locations from east to west in the Qilian Mountains. Based on the above discussion, humidity conditions in dryland areas may be more sensitive to climatic warming than forested mountain areas which have a more variable environment. We infer that forested mountain areas reflect local climate and may experience a different pattern of humidity variations than extensive dryland areas on a longer timescale.

With regard to differences in humidity conditions indicated by the pollen and tree-ring records during ~1920–2018 (**Figure 5**),

in relation to increasing temperature, it is important to determine whether pollen records from desert-steppe environments reflect moisture changes and whether they differ from tree-ring records. The three meteorological stations of Wushaoling, Zhangye, and Jiuquan (from 1951 to 2017) provide climate records from east to west across the study area, and they indicate spatial differences in climate between the eastern, central, and western parts of the Qilian Mountains (**Figure 6**). The results from Wushaoling, Zhangye, and Jiuquan show that from 1951 to 2017, the average precipitation in the eastern, central, and western parts of the study area was 414.9, 129.1, and 88.4 mm, respectively (**Figures 6B,E,H**). It is clear that with rising temperature, there has been a fluctuating but overall increasing trend of precipitation in the Qilian Mountains (**Figures 6B,E,H**). Relative humidity in central and western Qilian Mountains shows a decreasing trend (**Figures 6C,F**), while there is an increasing trend in the eastern part (**Figure 6I**). It is obvious that there is a similar pattern of variation between PDSI and precipitation reconstruction based on different tree-ring records from the central Qilian Mountains (**Figures 5B–D**).

The humidity of dryland areas is mainly controlled by a combination of temperature and precipitation, which is likely to be a dominant factor affecting vegetation growth in the dryland areas. And temperature plays a more important role in dryland areas than in forested areas, which are a more complex environment with more precipitation for tree growth. According to the records from meteorological stations, we further suggest that pollen from desert-steppe areas can reflect the humidity conditions of a broad area of dryland in the northwestern China.

Comparison of Various Moisture Reconstructions From Different Climate Regions

There were substantial differences in moisture conditions between westerlies-influenced Asia and mid-latitude monsoonal Asia during the Holocene, on suborbital, centennial, and decadal timescales (Chen et al., 2019). In addition, it has been suggested that the climate of the western Qilian Mountain region was alternately affected by the westerlies and Asian monsoon, and by both circulation systems together through time (Zhang et al., 2009).

In the westerlies-dominated region of the Tian Shan, records of tree-ring width indicate a trend of increasing moisture in the 20th century (**Figure 7B**), along with increasing temperature (Mann et al., 1998) (**Figure 7A**). In the lower Yanqi basin, adjacent to the Tian Shan Mountains, records of sedimentary carbonate content and pollen A/C ratio from Bosten Lake (**Figure 7C**) indicate a dry climate from the end of the 19th century onward (Chen et al., 2006, with new data of this study; Fontana et al., 2019), which was contrary to tree-ring records from the Tian Shan Mountains. Huang

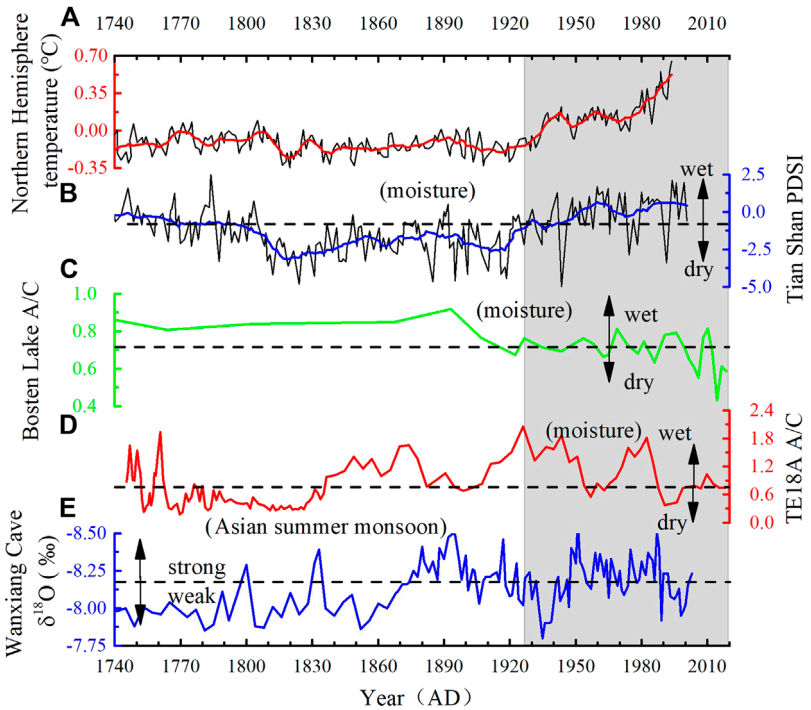

FIGURE 7 | Comparison of various climate reconstructions from different climatic regions in northwestern China with Northern Hemisphere temperature. **(A)** Northern Hemisphere temperature (Mann et al., 1998); the red line represents 20-point smoothing. **(B)** April–June Palmer Drought Severity Index derived from tree rings from the Tian Shan area in northwestern China (Li et al., 2006); the blue line represents 20-point smoothing. **(C)** Pollen A/C ratio from Bosten Lake (Chen et al., 2006), which is extended to 2018 using new data from the new core BST19C-1 (this study). **(D)** Pollen A/C ratio from Tian'E Lake (this study). **(E)** Stalagmite $\delta^{18}O$ record from Wanxiang Cave in northwestern China, reflecting variations in the intensity of the Asian summer monsoon circulation (Zhang et al., 2008). Horizontal dashed lines represent average values. Periods of rapid temperature increase are shown by gray shading.

et al. (2018) studied the Holocene vegetation and climate dynamics in the Altai Mountains and surrounding areas and suggested that, compared with the lower basins/plains, the vegetation of mountain environments responded differently to temperature forcing.

In the Qaidam basin, the pollen A/C ratio at Hurleg and Toson lakes decreased substantially since 1700 (Zhao et al., 2010), and a tree-ring-based precipitation record from Delingha (~30 km from Lake Kruk; 3,700–4,000 m.a.s.l.) shows the opposite trend (Shao et al., 2005). In the Qilian Mountains, tree-ring records of hydroclimatic variations also show substantial regional differences (Yang et al., 2019). The climate of the Hexi Corridor was generally dry during the Medieval Climate Anomaly, with a subsequent drying trend during the 20th century, whereas the Qaidam basin experienced high precipitation during the Medieval Climate Anomaly and the 20th century (Yang et al., 2019). Moreover, Yang et al. (2019) suggested that the Qaidam basin will receive more precipitation with ongoing global warming, whereas the Hexi Corridor will become drier in the future. Tree-ring records from the Helan Mountains, to the northeast of the Qilian Mountains, show a clear drying trend since the 1930s (Li et al., 2007), which is the opposite of the wetting trend in northwestern China (Li et al., 2006; Chen et al., 2014).

The pollen A/C ratio from Tian'E Lake indicates a trend of decreasing moisture conditions in the western Qilian Mountains from the 1920s onward (this study, **Figure 7D**), which is consistent with humidity records from Bosten Lake and Sugan Lake in the dryland areas (**Figures 5F,7C**). However, in the monsoon region, the oxygen isotope record from Wanxiang Cave indicates an interval of strong monsoon during the same interval (Zhang et al., 2008) (**Figure 7E**). Notably, the stalagmite $\delta^{18}O$ record from Wanxiang Cave is out of phase with the climate reconstruction from Tian'E Lake. The pollen record from Tian'E Lake indicates that the humidity record of the vast dryland area of central Asia was different from that suggested by tree-ring and stalagmite records from the monsoon region (**Figure 7E**), especially during the period of rapid temperature rise (**Figure 7A**). These spatiotemporal discrepancies among different records may also reflect the interaction of the monsoon and the westerlies.

CONCLUSION

We have obtained a high-resolution pollen record spanning the last 300 years from the sediments of Tian'E Lake in the western Qilian Mountains which is used to reconstruct humidity changes in the extensive dryland area of central Asia. The record helps fill the spatial gap in recent climate records from the region. The A/C ratio indicates the occurrence of high humidity during ~1740–1750 and dry conditions during ~1750–1840, with a notable wet interval around 1760. The interval of 1840–1980 was the most extended and pronounced wet period in the western Qilian Mountains during the past 300 years. During 1980–2018, the lower A/C ratio suggests that the climate became drier than previously.

Over the past few decades, the humidity of dryland areas is mainly controlled by a combination of temperature and precipitation. And pollen-indicated desert-steppe vegetation in the arid region is more temperature sensitive than tree-ring-indicated forest. There are significantly different records between pollen-based and tree-ring-based humidity during ~1760–1830, ~1880–1910, and ~1920–2018 in the Qilian Mountains. It was inferred that forested mountain areas may experience a different pattern of humidity variations than vast dryland areas at the background of substantial temperature changes on long timescales. We further suggest that pollen from desert-steppe areas can reflect the humidity conditions of a broad area of dryland in the northwestern China on the basis of evidences from meteorological stations.

A comparison of various climate records from westerlies-dominated central Asia and monsoon areas suggests that there was an antiphased relationship in humidity conditions between these two climatic domains over the past 100 years.

DATA AVAILABILITY STATEMENT

The raw data supporting the conclusions of this article will be made available by the authors, without undue reservation.

AUTHOR CONTRIBUTIONS

XH conceived this study. JW undertook the identification of pollen. JW and XH wrote the manuscript. JZ, LX, YX, LF, XR, and ZW discussed the data. LF improved the language.

FUNDING

The study was funded by the Second Tibetan Plateau Scientific Expedition and Research (STEP) program (Grant No. 2019QZKK0601) and the NSFC key project (Grant No. 41790422).

ACKNOWLEDGMENTS

We thank Davide Tiranti for his valuable comments on the manuscript. We gratefully acknowledge the friendly and constructive comments of the two reviewers.

REFERENCES

Appleby, P. G., and Oldfield, F. (1978). The calculation of lead-210 dates assuming a constant rate of supply of unsupported ^{210}Pb to the sediment. *Catena* 5, 1–8. doi:10.1016/S0341-8162(78)80002-2

Chen, F., Chen, J., Huang, W., Chen, S., Huang, X., Jin, L., et al. (2019). Westerlies Asia and monsoonal Asia: spatiotemporal differences in climate change and possible mechanisms on decadal to sub-orbital timescales. *Earth Sci. Rev.* 192, 337–354. doi:10.1016/j.earscirev.2019.03.005

Chen, F., Huang, X., Zhang, J., Holmes, J. A., and Chen, J. (2006). Humid Little Ice age in arid central Asia documented by Bosten Lake, Xinjiang, China. *Sci. China Ser. D* 49, 1280–1290. doi:10.1007/s11430-006-2027-4

Chen, F., Yu, Z., Yang, M., Ito, E., Wang, S., Madsen, D. B., et al. (2008). Holocene moisture evolution in arid central Asia and its out-of-phase relationship with

Asian monsoon history. *Quat. Sci. Rev.* 27, 351–364. doi:10.1016/j.quascirev.2007.10.017

Chen, F., Yuan, Y.-J., Wei, W.-S., Zhang, T.-W., Shang, H.-M., and Zhang, R. (2014). Precipitation reconstruction for the southern Altay Mountains (China) from tree rings of Siberian spruce, reveals recent wetting trend. *Dendrochronologia* 32, 266–272. doi:10.1016/j.dendro.2014.06.003

Cook, E. R., Woodhouse, C. A., Eakin, C. M., Meko, D. M., and Stahle, D. W. (2004). Long-term aridity changes in the western United States. *Science* 306, 1015–1018. doi:10.1126/science.1102586

Dai, A., Trenberth, K. E., and Qian, T. (2004). A global dataset of Palmer Drought Severity Index for 1870–2002: relationship with soil moisture and effects of surface warming. *J. Hydrometeorol.* 5, 1117–1130. doi:10.1175/JHM-386.1

Deng, Y., Gou, X., Gao, L., Zhao, Z., Cao, Z., and Yang, M. (2013). Aridity changes in the eastern Qilian Mountains since AD 1856 reconstructed from tree-rings. *Quat. Int.* 283, 78–84. doi:10.1016/j.quaint.2012.04.039

Dunhuang City Annals Compilation Committee (1994). *Dunhuang city annals*. Beijing, China: Xinhua Publishing House [in Chinese].

Esper, J., Cook, E. R., and Schweingruber1, F. H. (2002). Low-frequency signals in long tree-ring chronologies for reconstructing past temperature variability. *Science* 295, 2250–2253. doi:10.1126/science.1066208

Feng, H., and Zhang, M. (2015). Global land moisture trends: drier in dry and wetter in wet over land. *Sci. Rep.* 5, 18018. doi:10.1038/srep18018

Fontana, L., Sun, M., Huang, X., and Xiang, L. (2019). The impact of climate change and human activity on the ecological status of Bosten Lake, NW China, revealed by a diatom record for the last 2,000 years. *Holocene* 29, 1871–1884. doi:10.1177/0959683619865586

Gou, X., Gao, L., Deng, Y., Chen, F., Yang, M., and Still, C. (2015). An 850-year tree-ring-based reconstruction of drought history in the western Qilian Mountains of northwestern China. *Int. J. Climatol.* 35, 3308–3319. doi:10.1002/joc.4208

Gou, X., Zhang, F., Deng, Y., Ettl, G. J., Yang, M., Gao, L., et al. (2012). Patterns and dynamics of tree-line response to climate change in the eastern Qilian Mountains, northwestern China. *Dendrochronologia* 30, 121–126. doi:10.1016/j.dendro.2011.05.002

Grimm, E. C. (1987). CONISS: a FORTRAN 77 program for stratigraphically constrained cluster analysis by the method of incremental sum of squares. *Comput. Geosci.* 13, 13–35. doi:10.1016/0098-3004(87)90022-7

Grimm, E. C. (2011). *Tilia 1.7.16 software*. Springfield, IL: Illinois State Museum, Research and Collection Center.

Guan, X., Ma, J., Huang, J., Huang, R., Zhang, L., and Ma, Z. (2019). Impact of oceans on climate change in drylands. *Sci. China Earth Sci.* 62, 891–908. doi:10.1007/s11430-018-9317-8

Hou, Y., Wang, N. A., Zhang, X. M., Cheng, H. Y., and Lu, J. W. (2011). Precipitation reconstruction from tree ring width over the eastern part of the Qilian Mountains, northwestern China. *J. Mt. Sci.* 29, 12–18 [in Chinese]. doi:10.16089/j.cnki.1008-2786.2011.01.006

Huang, J., Yu, H., Guan, X., Wang, G., and Guo, R. (2016). Accelerated dryland expansion under climate change. *Nat. Clim. Change* 6, 166–171. doi:10.1038/nclimate2837

Huang, X., Peng, W., Rudaya, N., Grimm, E. C., Chen, X., Cao, X., et al. (2018). Holocene vegetation and climate dynamics in the Altai Mountains and surrounding areas. *Geophys. Res. Lett.* 45, 6628–6636. doi:10.1029/2018GL078028

Huang, X. Z., Chen, F. H., Fan, Y. X., and Yang, M. L. (2009). Dry late-glacial and early Holocene climate in arid central Asia indicated by lithological and palynological evidence from Bosten Lake, China. *Quat. Int.* 194, 19–27. doi:10.1016/j.quaint.2007.10.002

IPCC (2007). "WGI fourth assessment report, summary for policymakers," in The 10th session of working group I of the IPCC, February 2, Paris, France.

Jiuquan City Annals Compilation Committee (2008). *Jiuquan city annals*. Beijing, China: Fangzhi Publishing House [in Chinese].

Kang, S., Yang, B., Qin, C., Wang, J., Shi, F., and Liu, J. (2013). Extreme drought events in the years 1877-1878, and 1928, in the southeast Qilian Mountains and the air-sea coupling system. *Quat. Int.* 283, 85–92. doi:10.1016/j.quaint.2012.03.011

Kang, X. C., Cheng, G. D., Chen, F. H., and Gou, X. H. (2003). A record of rought and flood series by tree-ring data in the middle section of Qilian Mountain since 904 A.D. *J. Glaciol. Geocryol.* 25, 518–525 [in Chinese]. doi:10.3969/j.issn.1000-0240.2003.05.007

Li, J., Chen, F., Cook, E. R., Gou, X., and Zhang, Y. (2007). Drought reconstruction for North Central China from tree rings: the value of the Palmer drought severity index. *Int. J. Climatol.* 27, 903–909. doi:10.1002/joc.1450

Li, J., Gou, X., Cook, E. R., and Chen, F. (2006). Tree-ring based drought reconstruction for the central Tien Shan area in northwest China. *Geophys. Res. Lett.* 33, L07715. doi:10.1029/2006gl025803

Li, Y. C., Xu, Q. H., Yang, X. L., and Zheng, Z. H. (2005). Pollen assemblages of major steppe communities in China. *Acta Ecol. Sin.* 25, 169–178 [in Chinese]. doi:10.3321/j.issn:1000-0933.2005.03.024

Li, Y. K., Zhang, L., Ye, Y., and Lu, Y. J. (2018). Drought event in the midwest region of northwest China in 1876–1878. *Sci. Geogr. Sin.* 38, 780–789 [in Chinese]. doi:10.13249/j.cnki.sgs.2018.05.016

Liu, X. H., An, W. L., Liang, E. Y., Wang, W. Z., Shao, X. M., Huang, L., et al. (2011). Spatiotemporal variability in tree ring's $\delta^{13}C$ of *Picea crassifolia* in the Qilian Mountains: climatic significance and responses to rising CO_2. *Sci. Cold Arid Reg.* 3, 93–102 doi:10.3724/SP.J.1226.2011.00093

Mann, M. E., Bradley, R. S., and Hughes, M. K. (1998). Global-scale temperature patterns and climate forcing over the past six centuries. *Nature* 392, 779–787. doi:10.1038/33859

Shao, X., Huang, L., Liu, H. B., Liang, E. Y., Fang, X. Q., and Wang, L. L. (2005). Reconstruction of precipitation variation from tree rings in recent 1,000 years in Delingha, Qinghai. *Sci. China Ser. D* 48, 939–949. doi:10.1360/03yd0146

Sun, J., and Liu, Y. (2013). Drought variations in the middle Qilian Mountains, northeast Tibetan Plateau, over the last 450 years as reconstructed from tree rings. *Dendrochronologia* 31, 279–285. doi:10.1016/j.dendro.2012.07.004

Tang, L. Y., Mao, L. M., Shu, J. W., Li, C. H., Shen, C. M., and Zhou, Z. Z. (2016). *An illustrated handbook of quaternary pollen and spores in China*. Beijing, China: Science Press [in Chinese]. ISBN 978-7-03-050568-2.

Tarasov, P. E., Jolly, D., and Kaplan, J. O. (1997). A continuous late glacial and Holocene record of vegetation changes in Kazakhstan. *Palaeogeogr. Palaeoclimatol. Palaeoecol.* 136, 281–292. doi:10.1016/S0031-0182(97)00072-2

Wang, Y. J., Chen, F. H., Gou, X. H., and Du, S. Y. (2001). Study on response relationship between tree ring width and climate factors and climate reconstruction in middle region of Qilian Mountains. *J. Desert Res.* 21, 135–140 [in Chinese].doi:10.3321/j.issn:1000-694X.2001.02.006

Xu, Q. H., Li, Y. C., Yang, X. L., and Zheng, Z. H. (2007). Quantitative relationships between modern pollen rain and vegetation in Northern China. *Sci. China Earth Sci.* 37, 192–205 [in Chinese]. doi:10.3969/j.issn.1674-7240.2007.02.007

Yan, T. L., Wang, Z. T., He, J. Q., Huang, X. Z., Xia, D. S., and Wang, Z. L. (2018). A 3500 Year environmental changes recorded by sediment of Tian'E Lake, central part of the Qilian Mountains, China. *Acta Sedimentol. Sin.* 36, 521–530 [in Chinese]. doi:10.14027/j.issn.1000-0550.2018.041

Yang, B., Qin, C., Bräuning, A., Burchardt, I., and Liu, J. (2011). Rainfall history for the Hexi Corridor in the arid northwest China during the past 620 years derived from tree rings. *Int. J. Climatol.* 31, 1166–1176. doi:10.1002/joc.2143

Yang, B., Wang, J., and Liu, J. (2019). A 1556 year-long early summer moisture reconstruction for the Hexi Corridor, Northwestern China. *Sci. China Earth Sci.* 62, 953–963. doi:10.1007/s11430-018-9327-1

Yi, Y. Y. and Wang, H. Y. (2013). Characteristics of vertical distribution of vegetation community in the north slope of Qilian Mountains. *Protect. For. Sci. Technol.* 10, 6–9 [in Chinese]. doi:10.3969/j.issn.1005-5215.2013.10.003

Zhang, J., Huang, X., Wang, Z., Yan, T., and Zhang, E. Y. (2018). A late-Holocene pollen record from the western Qilian Mountains and its implications for climate change and human activity along the Silk Road, Northwestern China. *Holocene* 28, 1141–1150. doi:10.1177/0959683618761548

Zhang, K., Zhao, Y., Yu, Z., and Zhou, A. (2010). A 2700-year high resolution pollen record of climate change from varved Sugan Lake in the Qaidam Basin, northeastern Tibetan Plateau. *Palaeogeogr. Palaeoclimatol. Palaeoecol.* 297, 290–298. doi:10.1016/j.palaeo.2010.08.008

Zhang, P., Cheng, H., Edwards, R. L., Chen, F., Wang, Y., Yang, X., et al. (2008). A test of climate, sun, and culture relationships from an 1810-year Chinese cave record. *Science* 322, 940–942. doi:10.1126/science.1163965

Zhang, Y., Gou, X., Chen, F., Tian, Q., Yang, M., Peng, J., et al. (2009). A 1232-year tree-ring record of climate variability in the Qilian Mountains, Northwestern China. *IAWA J.* 30, 407–420. doi:10.1163/22941932-90000228

Zhang, Y., Tian, Q., Gou, X., Chen, F., Leavitt, S. W., and Wang, Y. (2011). Annual precipitation reconstruction since AD 775 based on tree rings from the Qilian

Mountains, northwestern China. *Int. J. Climatol.* 31, 371–381. doi:10.1002/joc.2085

Zhao, Y., Liu, H., Li, F., Huang, X., Sun, J., Zhao, W., et al. (2012). Application and limitations of the Artemisia/Chenopodiaceae pollen ratio in arid and semi-arid China. *Holocene* 22, 1385–1392. doi:10.1177/0959683612449762

Zhao, Y., Xu, Q., Huang, X., Guo, X., and Tao, S. (2009). Differences of modern pollen assemblages from lake sediments and surface soils in arid and semi-arid China and their significance for pollen-based quantitative climate reconstruction. *Rev. Palaeobot. Palynol.* 156, 519–524. doi:10.1016/j.revpalbo.2009.05.001

Zhao, Y., Yu, Z., Chen, F., Liu, X., and Ito, E. (2008). Sensitive response of desert vegetation to moisture change based on a near-annual resolution pollen record from Gahai Lake in the Qaidam Basin, northwest China. *Global Planet. Change* 62, 107–114. doi:10.1016/j.gloplacha.2007.12.003

Zhao, Y., Yu, Z., Liu, X., Zhao, C., Chen, F., and Zhang, K. (2010). Late Holocene vegetation and climate oscillations in the Qaidam Basin of the northeastern Tibetan plateau. *Quat. Res.* 73, 59–69 [in Chinese]. doi:10.1016/j.yqres.2008.11.007

Zou, X., Zhai, P., and Zhang, Q. (2005). Variations in droughts over China: 1951–2003. *Geophys. Res. Lett.* 32, 353–368. doi:10.1029/2004GL021853

Conflict of Interest: The authors declare that the research was conducted in the absence of any commercial or financial relationships that could be construed as a potential conflict of interest.

Copyright © 2020 Wang, Huang, Zhang, Xiang, Xiao, Fontana, Ren and Wang. This is an open-access article distributed under the terms of the Creative Commons Attribution License (CC BY). The use, distribution or reproduction in other forums is permitted, provided the original author(s) and the copyright owner(s) are credited and that the original publication in this journal is cited, in accordance with accepted academic practice. No use, distribution or reproduction is permitted which does not comply with these terms.

Advantages of publishing in Frontiers

OPEN ACCESS
Articles are free to read for greatest visibility and readership

FAST PUBLICATION
Around 90 days from submission to decision

HIGH QUALITY PEER-REVIEW
Rigorous, collaborative, and constructive peer-review

TRANSPARENT PEER-REVIEW
Editors and reviewers acknowledged by name on published articles

Frontiers
Avenue du Tribunal-Fédéral 34
1005 Lausanne | Switzerland

Visit us: www.frontiersin.org
Contact us: frontiersin.org/about/contact

REPRODUCIBILITY OF RESEARCH
Support open data and methods to enhance research reproducibility

DIGITAL PUBLISHING
Articles designed for optimal readership across devices

FOLLOW US
@frontiersin

IMPACT METRICS
Advanced article metrics track visibility across digital media

EXTENSIVE PROMOTION
Marketing and promotion of impactful research

LOOP RESEARCH NETWORK
Our network increases your article's readership